Design, validation and application of wave-to-wire models for heaving point absorber wave energy converters

Markel Penalba

A thesis submitted for the degree of
Doctor of Philosophy

Faculty of Science and Engineering
Electronic Engineering Department
Maynooth University

Supervisor: **Prof. John V. Ringwood**
Head of the Department: Dr. Ronan Farrell

July 2018

Table of Contents

Abstract

Ocean waves represent an untapped source of renewable energy which can significantly contribute to the energy transition towards a sustainable energy mix. Despite the significant potential of this energy source and the multiple solutions suggested for the extraction of energy from ocean waves, some of which have demonstrated to be technically viable, no commercial wave energy farm has yet been connected to the electricity grid. This means that none of the technologies suggested in the literature has achieved economic viability.

In order to make wave energy converters economically viable, it is essential to accurately understand and evaluate the holistic behaviour and performance of wave energy converters, including all the different conversion stages from ocean waves to the electricity grid. This can be achieved through wave tank or open ocean testing campaigns, which are extremely expensive and, thus, can critically determine the financial sustainability of the developing organisation, due to the risk of such large investments. Therefore, precise mathematical models that consider all the important dynamics, losses and constraints of the different conversion stages (including wave-structure hydrodynamic interaction and power take-off system), known as wave-to-wire models, are crucial in the development of successful wave energy converters. Hence, a comprehensive literature review of the different mathematical approaches suggested for modelling the different conversion stages and existing wave-to-wire models is presented, defining the foundations of parsimonious wave-to-wire models and their potential applications.

As opposed to other offshore applications, wave energy converters need to exaggerate their motion to maximise energy absorption from ocean waves, which breaks the assumption of small body motion upon which linear models are based. An extensive investigation on the suitability of linear models and the relevance of different nonlinear effects is carried out, where control conditions are shown to play an important role. Hence, a computationally efficient mathematical model that incorporates nonlinear Froude-Krylov forces and viscous effects is presented. In the case of the power take-off system, mathematical models for different hydraulic transmission system configurations and electric generator topologies are presented, where the main losses are included using specific loss models with parameters identified via manufacturers' data. In order to gain confidence in the mathematical models, the models corresponding to the different conversion stages are validated separately against either high-fidelity well-established software or experimental results, showing very good agreement.

The main objective of this thesis is the development of a comprehensive wave-to-wire model. This comprehensive wave-to-wire model is created by adequately combining the subsystems corresponding to the different components or conversion stages. However, time-step requirements vary significantly depending on the dynamics included in each subsystem. Hence, if the time-step required for capturing the fastest dynamics is used in all the subsystems, unnecessary computation is performed in the subsystems with slower dynamics. Therefore, a multi-rate time-integration scheme is implemented, meaning that each subsystem uses the sample period required to adequately capture the dynamics of the components included in that conversion stage, which significantly reduces the overall computational requirements. In addition, the relevance of using a high-fidelity

comprehensive wave-to-wire model in accurately designing wave energy converters and assessing their capabilities is demonstrated. For example, energy maximising controllers based on excessively simplified mathematical models result in dramatic consequences, such as negative average generated power or situations where the device remains stuck at one of the end-stops of the power take-off system.

Despite the reasonably high-fidelity of the results provided by this comprehensive wave-to-wire model, some applications require the highest possible fidelity level and have no limitation with respect to computational cost. Hence, the simulation platform HiFiWEC, which couples a numerical wave tank based on computational fluid dynamics to the high-fidelity power take-off model, is created. In contrast, low computational cost is the main requirement for other applications and, thus, a systematic complexity reduction approach is suggested in this thesis, significantly reducing the computational cost of the HiFiWEC platform, while retaining the adequate fidelity level for each application. Due to the relevance of the nonlinearity degree when evaluating the complexity of a mathematical model, two nonlinearity measures to quantify this nonlinearity degree are defined. Hence, wave-to-wire models specifically created for each application are generated via the systematic complexity reduction approach, which provide the adequate trade-off between computational cost and fidelity level required for each application.

Declaration of authorship

I, Markel Penalba, declare that this thesis titled 'Design, validation and application of wave-to-wire models for wave energy converters' and the work presented in it are my own. I confirm that:

- This work was done wholly or mainly while in candidature for a research degree at this University.
- Where any part of this thesis has previously been submitted for a degree or any other qualification at this University or any other institution, this has been clearly stated.
- Where I have consulted the published work of others, this is always clearly attributed.
- Where I have quoted from the work of others, the source is always given. With the exception of such quotations, this thesis is entirely my own work.
- I have acknowledged all main sources of help.
- Where the thesis is based on work done by myself jointly with others, I have made clear exactly what was done by others and what I have contributed myself.

Date: _____

Signature: _____

Acknowledgement

My most sincere gratitude to my supervisor John Ringwood, for giving me the opportunity to join the COER lab, his invaluable guidance and support, and the inspiring discussions that stimulated my reflections. I would also like to thank all the staff from the Electronic Engineering Department, with a special mention to Ann Dempsey and Joanne Bredin for their constant availability and efficacy in solving any administrative problem, and to Denis Buckley and John Maloco for their support with any technical issue.

A very special thank goes to the former and present members of the COER lab, who made the countless hours in the lab amusing and pleasant: Andrej Rössling, Paula Garcia-Rosa, Victor Ramos, Romain Genest, Francesco Paparella, Simone Giorgi, Thomas Kelly, Josh Davidson, Alexis Mérigaud, Giuseppe Giorgi, Yerai Peña, Christian Windt, Nicolás Ezequiel Faedo, LiGuo Wang and Demián García-Violini. I very much enjoyed the interesting discussions on and off our research topics and I am very grateful for their willingness to lend a hand.

I would also like to thank all the external researchers who collaborated with me either providing experimental data or widening my scope to analyse different aspects of wave energy: Nathan P. Sell and Andy J. Hillis from University of Bath and José-Antonio Cortajarena, Alain Ulazia, Gabriel Ibarra-Berastegui and Jon Saénz from University of the Basque Country.

I must also specially thank my parents for supporting me before, during and after my PhD and especially for constantly encouraging and inspiring me to find my way. Finally, my deepest gratitude goes to my partner Jone, for her understanding, patience and support, but specially for her ability to make me smile. *Loak hartu arte amets egin dezagun*.

Acronyms

2BPA	A two-body point absorber.
AC	Alternating-current.
AMETS	Atlantic Marine Energy Test Site.
AMPP	Annual mean power production.
AMR	Adaptive mesh refinement.
ANN	Artificial neural network.
ARX	Autoregressive with exogenous input.
AWS	Archimedes wave swing.
B2B	Back-to-back.
BBDB	Backward Bent Duct Buoy.
BEM	Boundary element method.
BVP	Boundary value problem.
CAPEX	Capital expenditure.
CFD	Computational fluid dynamics.
cHyPTO	Complete hydraulic PTO.
cHyW2W	Comprehensive HyW2W.
CNWT	CFD-based numerical wave tank.
CPTMC	Centre for Power Transmission and Motion Control.
CR	Complexity reduction.
CSA	Cross-sectional area.
DAQ	Data acquisition.
DAS	Randomly chosen phases and deterministic amplitudes.
DC	Direct-current.
DDC	Discrete displacement cylinder.
DDM	Discrete displacement motors.
DFIG	Doubly-fed induction generator.
DNS	Direct numerical simulation.
DoF	Degree of freedom.
ElecM	Electric sub-model.
EMEC	European Marine Energy Centre.
EWEA	European Wind Energy Association.
FC	Full cylinder.
FD	Frequency-domain.
FEA	Finite element analysis.
FK	Froude-Krylov.
fNLPF	Fully-nonlinear potential flow.
GenSC	Generator-side PEC.
GHE	Greenhouse emissions.

GR	Grading ratio.
GridSC	Grid-side PEC.
HdM	Hydrodynamic sub-model.
HE	High-energetic.
HIL	Hardware-in-the-loop.
HOS	High order spectral.
HP	High-pressure.
HPA	Heaving point absorber.
HyM	Hydraulic transmission system sub-model.
HyPTO	Hydraulic power take-off system.
HyW2W	Wave-to-wire model with a hydraulic power take-off system.
IG	Induction generator.
IPCC	International Panel on Climate Change.
ISPH	Incompressible SPH.
KC	Keulegan-Carpenter.
KGP	Kolmogorov-Gabor Polynomial.
LE	Low-energetic.
LES	Large eddy simulation.
LFK	Linear Froude-Krylov force.
LP	Low-pressure.
LPF	Linear potential flow.
LPMG	Linear permanent magnet generator.
MANRMSE	Moving average normalised root mean square error.
MAPE	Mean average percentage error.
maxXC	Maximum cross-correlation.
ME	Medium-energetic.
mLPF	Multi-linear models based on potential flow theory.
MLS	Magnetic lead screw.
MOR	Model order reduction.
MR	Multi-rate.
M-D	Mass-damper.
NARX	Nonlinear autoregressive with exogenous input.
NLFK	Nonlinear Froude-Krylov force.
NRMSE	Normalised root mean square error.
NWT	Numerical wave tank.
OPC	Oscillating pitching converter.
OPEX	Operation expenditure.
OWC	Oscillating water column.
OWSC	Oscillating wave surge converter.
parW2W	Parsimonious wave-to-wire.
PEC	Power electronic converter.
PF-CFD	Combined CFD and potential flow methods.
PLL	Phase locked loop.
PMSG	Permanent magnet synchronous generator.
PMSM	Permanent magnet synchronous motor.
pNLPF	Partially-nonlinear potential flow.
POD	Proper orthogonal decomposition.
PTO	Power take-off.
PWM	Pulse width modulation.
RANS	Reynolds-Average Navier-Stokes.
RAO	Response amplitude operator.
RAS	Randomly chosen amplitudes.

RARP	Random-amplitude random-phase.
RES	Renewable energy system.
rHyPTO	Reduced hydraulic power take-off system.
RK	Runge-Kutta.
RMS	Root mean square.
RMSr	Root mean square ration.
rWSHI	Reduced wave-structure hydrodynamic interaction.
SCIG	Squirrel-cage induction generator.
SAPA	Submerged axisymmetric point absorber.
SPH	Smoothed-particle hydrodynamics.
SR	Single-rate.
SST	Shear stress transport.
SWL	Still water level.
TPL	Technology performance level.
TRL	Technology readiness level.
viscLPF	LPF with viscous effects included externally.
VOF	Volume of fluid.
W2W	Wave-to-wire.
WCSPH	Weekly compressible SPH.
WEC	Wave energy converter.
wNLPF	Weakly-nonlinear potential flow.
WSHI	Wave-structure hydrodynamic interaction.
XC	Cross-correlation.
ZIC	Zero initial conditions.

List of symbols

This section only lists the symbols used "globally" throughout this thesis.

α_M	Fractional displacement of the hydraulic motor.
A_{cs}	Cross-sectional area.
A_p	Hydraulic piston area.
A_{rad}	Radiation added-mass.
A_v	Valve opening area.
A_w	Amplitude function of the wave spectrum.
β_{eff}	Effective bulk modulus of the hydraulic fluid.
B_{PTO}	Linear PTO damping.
B_{rad}	Radiation damping.
C_{drag}	Viscous drag coefficient.
D_ω	Displacement of the hydraulic motor.
δt	Time-step.
Δ	Deviation between two models.
Δp_{cyl}	Pressure difference between two chambers in the hydraulic cylinder.
Δp_M	Pressure difference between the inlet and outlet ports of the hydraulic motor.
η_w	Free-surface elevation time-series.
η_{PTO}	Efficiency of the hydraulic power take-off system as a whole.
η_{W2W}	Wave-to-wire efficiency.
F_{diff}	Diffraction force.
F_{ex}	Excitation force.
F_{FK}	Froude-Krylov force.
F_{fric}	Friction force in the hydraulic cylinder.
F_g	Gravity force.
F_{in}	Inertia force in the hydraulic cylinder.
F_{PTO}	PTO force.
F^*_{PTO}	Reference PTO force.
F_{pis}	Hydraulic piston force applied on the absorber.
F_{rad}	Radiation force.
F_{vis}	Viscosity force.
g	Acceleration due to gravity.
H_s	Significant wave height.
H_w	Wave height.
i_{sd}	Stator current in the *d-axis*.
i_{sq}	Stator current in the *q-axis*.
i_{rd}	Rotor current in the *d-axis*.
i_{rq}	Rotor current in the *q-axis*.
J	Power flow per meter of wavefront.
J_{shaft}	Moment of inertia of the rotor in the electric generator.

K_{diff}	Diffraction impulse response function.
K_{FK}	Froude-Krylov impulse response function.
K_{rad}	Radiation impulse-response function.
K_{PTO}	Linear PTO stiffness.
λ_w	Wavelength.
λ_{PM}	Permanent magnet flux.
λ_{sd}	Stator flux linkage in the *d-axis*.
λ_{sq}	Stator flux linkage in the *q-axis*.
λ_{rd}	Rotor flux linkage in the *d-axis*.
λ_{rq}	Rotor flux linkage in the *q-axis*.
L_r	Rotor inductance of an electric generator.
L_s	Stator inductance of an electric generator.
M	Mass of the absorber.
μ_∞	Added mass coefficient at infinite frequency.
ω_M	Rotational velocity of the hydraulic motor shaft.
ω_r	Angular velocity of the rotor.
p_{cyl}	Pressure in the hydraulic cylinder chamber.
p_{WSHI}	Pressure of the total incident flow acting on the body.
P_e	Active power generated in the electric generator.
P_{loss}	Power losses in the electrical system.
Q_{cyl}	Fluid flow exiting or entering the hydraulic cylinder.
Q_e	Reactive power generated in the electric generator.
Q_{loss}	Volumetric losses in the hydraulic motor.
Q_M	Flow through the hydraulic motor.
R_r	Rotor resistance of an electric generator.
R_s	Stator resistance of an electric generator.
ρ_w	Sea water density.
S	Instantaneous wetted surface of the absorber.
$\overline{S}$	Mean wetted surface of the absorber.
S_w	The spectral density function.
T_e	Electromagnetic torque.
T_{loss}	Mechanical losses in the hydraulic motor.
T_M	Torque generated in the hydraulic motor.
T_p	Peak period.
T_w	Wave period.
V_{acc}	Hydraulic accumulator volume.
V_{cyl}	Minimum oil volume in the hydraulic cylinder.
V_{DC}	Voltage in the CD-bus of the B2B power converter.
V_{sd}	Stator voltage in the *d-axis*.
V_{sq}	Stator voltage in the *q-axis*.
V_{rd}	Rotor voltage in the *d-axis*.
V_{rq}	Rotor voltage in the *q-axis*.
x_{abs}, $\dot{x}_{abs}$, $\ddot{x}_{abs}$	Position, velocity and acceleration of the absorber, respectively.
z_{abs}, $\dot{z}_{abs}$, $\ddot{z}_{abs}$	Position, velocity and acceleration of the absorber in heave, respectively.

Chapter 1

Introduction

"The struggle for existence is the struggle for available energy"
Ludwig Boltzmann

The social and economical development of human society since the industrial revolution is strongly correlated with a continuous increase in energy demand. The availability of easily accessible and cheap energy resources, i.e. fossil fuels such as oil, coal and gas, made that development possible, which brought prosperity and stability to modern society.

Nevertheless, easily accessible and cheap fossil fuels are rapidly depleting, which seriously questions the foundations of the current energy supply system and, consequently, the development of modern society. Therefore, different studies have tried to forecast the point where the extraction of oil will reach the maximum rate, referred to as the *oil peak* by Marion King Hubbert in 1956, after which the oil extraction will steadily decline. Different predictions place the *oil peak* at different points in time: some studies suggest the *oil peak* has already happened [1], while others conclude it will happen before 2030 [2]. However, the relevant point regarding the *oil peak* is that, while energy demand continues to increase, as illustrated in Figure 1.1, fossil fuel resources are depleting.

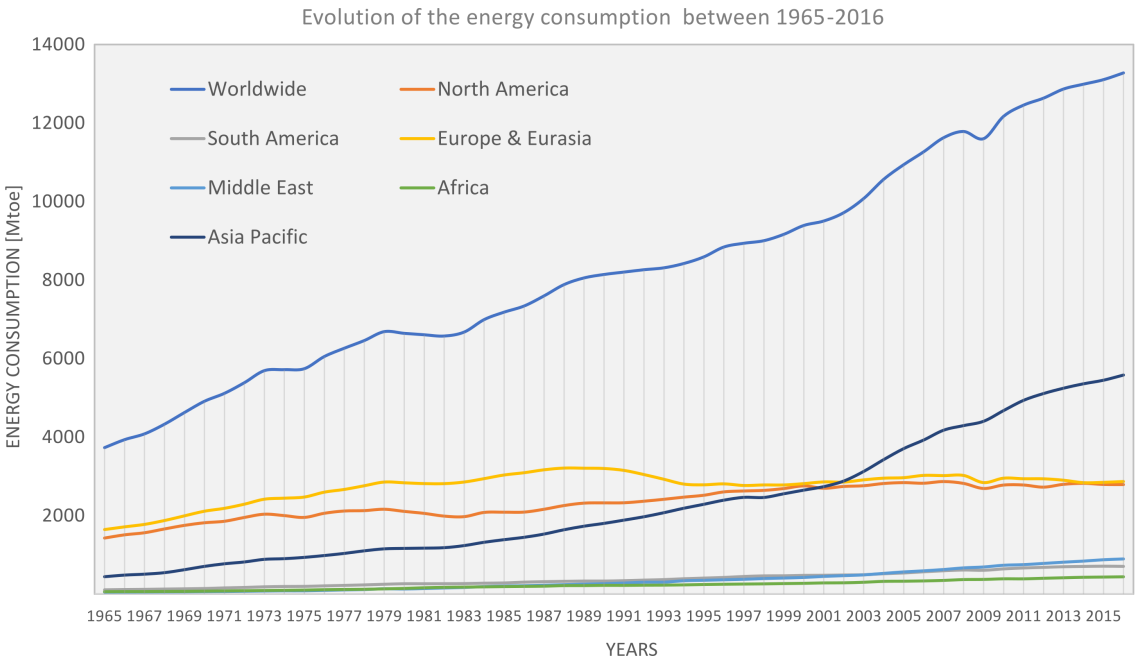

Figure 1.1: Evolution of the energy consumption worldwide in the last decades, based on the data from [3].

Moreover, comparisons between climatic models and observations suggest that human activities, particularly greenhouse emissions (GHE) from the combustion of fossil fuels, are responsible for the increase in global temperature during the second half of the 20th century [4]. The first 17 years of the 21st century only confirmed the trend: 17 of the 18 warmest years occurred within this period and the global average temperature rose by almost 1°C compared to the mean temperature of the 20th century [5].

Finally, the worldwide population is constantly and continuously increasing over recent decades and the probabilistic predictions by the United Nations estimate that the population will increase to over 11 billion by the end of the century [6]. Hence, the combination of the ever increasing worldwide population and energy demand, the fast depletion of traditional fossil fuels, and the unequivocal impact of the combustion of these traditional fossil fuels on climate change, make energy supply one of the most important challenges of the 21st century [7]. In addition, other aspects, such as the dependency of the energy supply system on external resources, *e.g.* Europe imports over 53% of the energy it consumes [8], or the potential to create a new and powerful economic sector [9], also suggest that a shift from fossil fuels to renewable energy systems (RESs) is necessary.

In this sense, the first legally binding global climate deal, known as the Paris Agreement, was signed by 195 countries in 2015 at the Paris climate conference COP21. All the signatories agreed to reduce GHE so that global average temperature remains 'well below 2°C above pre-industrial levels' [10]. More recently, the European Parliament has approved the proposal to increase the 2030 renewable energy target from 27% to 35% of the energy consumption in the EU.

The contribution of RESs to the final energy consumption worldwide has significantly increased in the 21st century in absolute values, more than doubling the installed power capacity of RESs from 800 GW to 2017 GW between 2004 and 2016 [11]. However, because the energy demand increased by over 20% within the same period [3], the share of RESs on the final energy demand only increased 2.3%, from 17% to 19.3% [11]. Figure 1.2 illustrates the share of RESs and the contribution of each renewable energy technology.

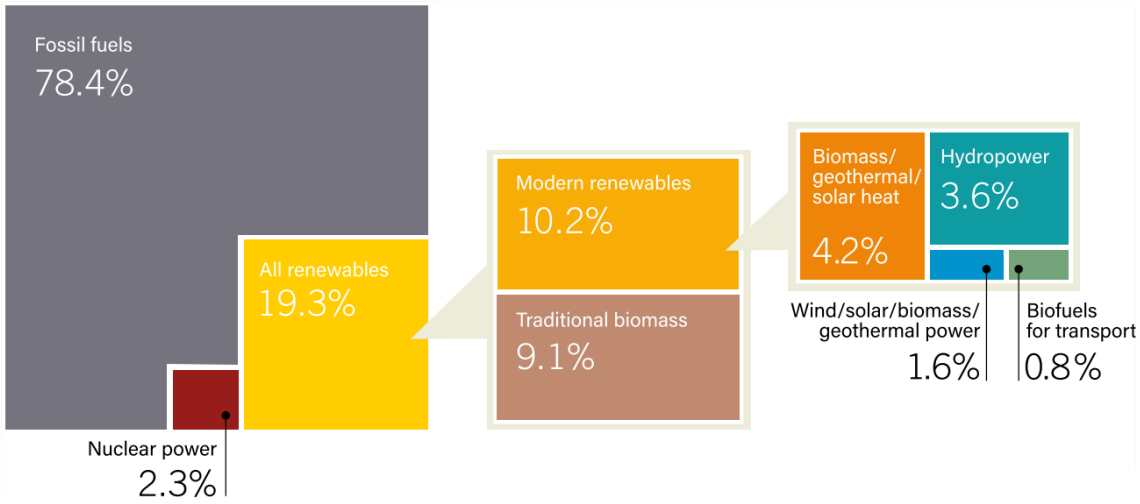

Figure 1.2: Worldwide contribution of RESs in the final energy consumption, based on the consumption data from 2015 [11].

Traditional biomass, which is the main contributor among the different RESs, makes up almost one half of the total renewable energy generation (9.1% out of the 19.3% share of all RESs). Nevertheless, traditional biomass has only grown at a 1.2% average yearly rate over the last decade, which is considerably lower than the average growth rate of modern RESs (4.7%) [11]. Modern RESs include hydropower, modern biomass, geothermal, solar (PV and thermal), wind and biofuels.

When only electricity production is considered, the figures of RESs are even more encouraging: 30% of worldwide power generation capacity and an estimated 24.5% of the total electricity demand was supplied from RESs in 2016 [11]. In addition, the non-hydro RESs achieved significant penetration levels throughout 2016 in different countries, such as the 37.6%, 27% and 24% of the electricity demand covered by wind energy in Denmark, Ireland and Portugal, respectively, or the 7.3%, 7.2% and 6.4% covered by PV solar in Italy, Greece and Germany, respectively [11].

These trends in the global energy market show the increasing role of modern RESs, which account for 10.2% of the total energy consumption. However, apart from a higher participation of the established RES technologies, i.e. hydropower, wind and solar, the contribution of new renewable sources into the national electricity networks will be crucial to fulfil the objective of significant GHE reduction.

Offshore renewable energy technologies, such as offshore wind (fixed and floating), tidal or ocean current energy, ocean energy thermal conversion and wave energy, have the potential to significantly support traditional RESs in the short- medium-term future. The European Wind Energy Association (EWEA) suggests that offshore wind installed power capacity could be of up to 460 GW and could produce about 1800 TWh annually by 2050 [12]. Similarly, the European Commission estimated the contribution of offshore renewable energy systems (excluding offshore wind) could meet 10% of the total power demand in the European Union by 2050, with about 100GW installed power capacity and an annual production of about 350 TWh [13].

1.1 Wave Energy

1.1.1 Wave energy resource

Ocean waves represent an untapped source of energy. The worldwide wave energy resource has been estimated to be around 3.7 TW and about 32000 TWh/yr in [14] and [15], while around 2.1 TW and 18500/yr TWh in [16]. Comparing these resource estimates to global energy consumption, 152411 TWh [3] in 2015, from which only 22386 TWh [17] corresponded to electric energy, one can note that wave energy could only cover a small fraction of the global energy demand, even when the wave energy resource is fully extracted.

Figure 1.3 illustrates the power flow per meter of wavefront (J) in different locations worldwide, given in kW/m, which corresponds to the average power per metre of wavefront, where the wavefront refers to the crest line of waves. The average power is obtained by evaluating the wave energy potential over different sea-states, defined using significant wave height (H_s) and peak period (T_p). Assuming deep water conditions, the power flow per meter of wavefront of a specific sea-state can be expressed as follows,

$$J_{ss} = \frac{\rho_w g^2}{64\pi} H_s^2 T_p \approx 0.5 H_s^2 T_p, \tag{1.1}$$

where ρ_w is the sea water density and g the acceleration due to gravity. It is important to note that resource potential increases with the square of the wave height, while increasing linearly with wave period.

However, a large part of that energy resource is located in remote areas, as illustrated in Figure 1.3, where deployment of real wave energy converter (WEC) farms may not be technically feasible due to the large transmission distance to consumption centres. In addition, WECs are designed to produce power within a pre-defined operational space limited by wave periods and wave heights, beyond which the focus is on protecting the device from critical damage. In this respect, recent studies have demonstrated that part of the estimated resource may correspond to storms [19, 20], which are not exploitable. In addition, the analysis of wave trends over the 20th century in different points of the European coast, suggests that the wave energy resource is becoming more energetic, especially in recent decades, which entails more frequent non-exploitable extreme events [21, 22].

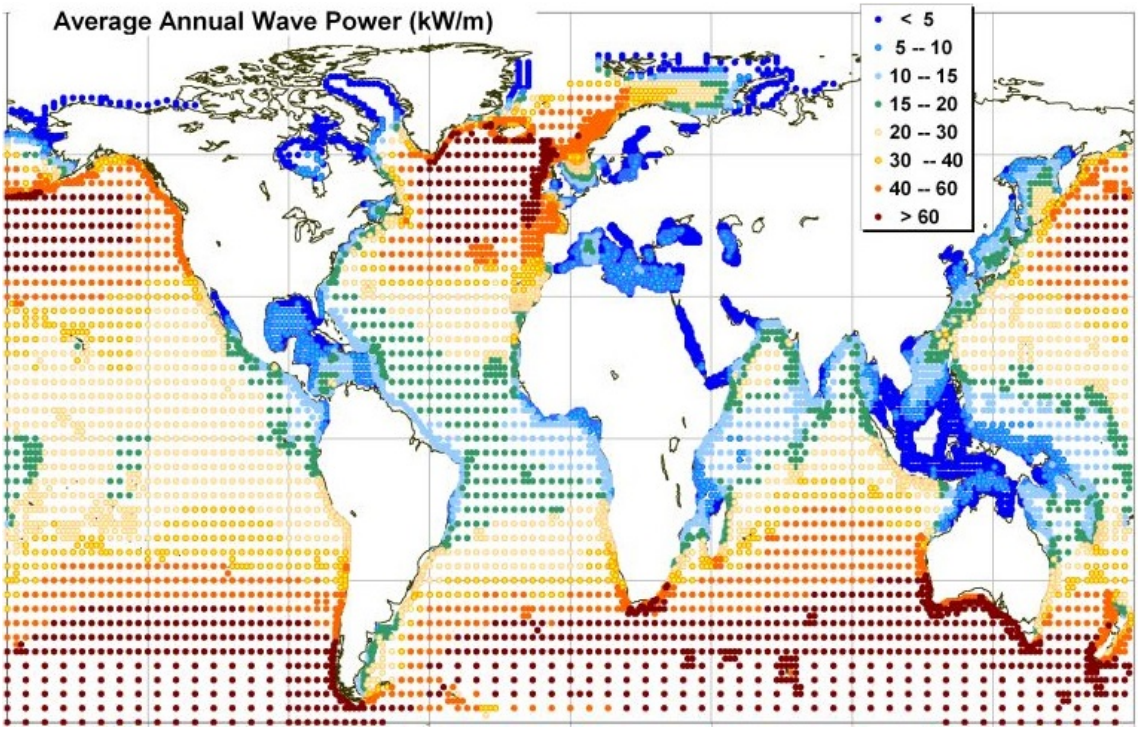

Figure 1.3: Global annual mean wave energy resource estimation in kW/m, retrieved from [18].

Therefore, the International Panel on Climate Change (IPCC) defined, in 2007, the *"technical potential"* of wave energy, which assumes that the deployment of WECs will only be possible along 2% of the total length of coastline worldwide, estimating a more realistic resource of about 500 GW based on a WEC conversion efficiency of about 40% [23]. Other similar studies place the *"technical potential"* of wave energy between 2000-4000 TWh/yr [24]. In fact, due to the early stage of development of the wave energy industry, and the uncertainties of its evolution in the medium- and long-term future, the *"technical potential"* of wave energy becomes quite unpredictable.

Technological developments of the wave energy industry in the next years/decades will define the role of wave energy in the future energy-mix. In any case, it seems reasonable to anticipate that this *"technical potential"* of wave energy will be significantly below the theoretical resource estimates and, thus, cannot be the only solution for the decarbonisation of the energy sector, but a complementary source.

1.1.2 WEC classification

Due to the large number of devices suggested by inventors, researchers and developers, different classifications have been proposed to organise WECs into groups. When considering the orientation and the size of the WEC [31], three type of devices can be distinguished: *point absorbers*, *attenuators* and *terminators*. *Point absorbers* are small devices with respect to the wavelength and are, in general, multi-directional devices. In contrast, *attenuators* and *terminators* are large devices (similar to, or greater than, a wavelength) whose main dimensions are aligned with, and facing the waves, respectively.

A second classification is based on the working principle [32], using three main groups to classify all the different WECs: oscillating water column (OWC), wave-activated oscillating bodies, and overtopping devices. In OWC devices, the action of the wave makes the water-column in the lower part of the chamber oscillate, which, in turn, drives the oscillating air-flow trapped in the upper part of the chamber through an air-turbine located at the top-end of the chamber. Wave-

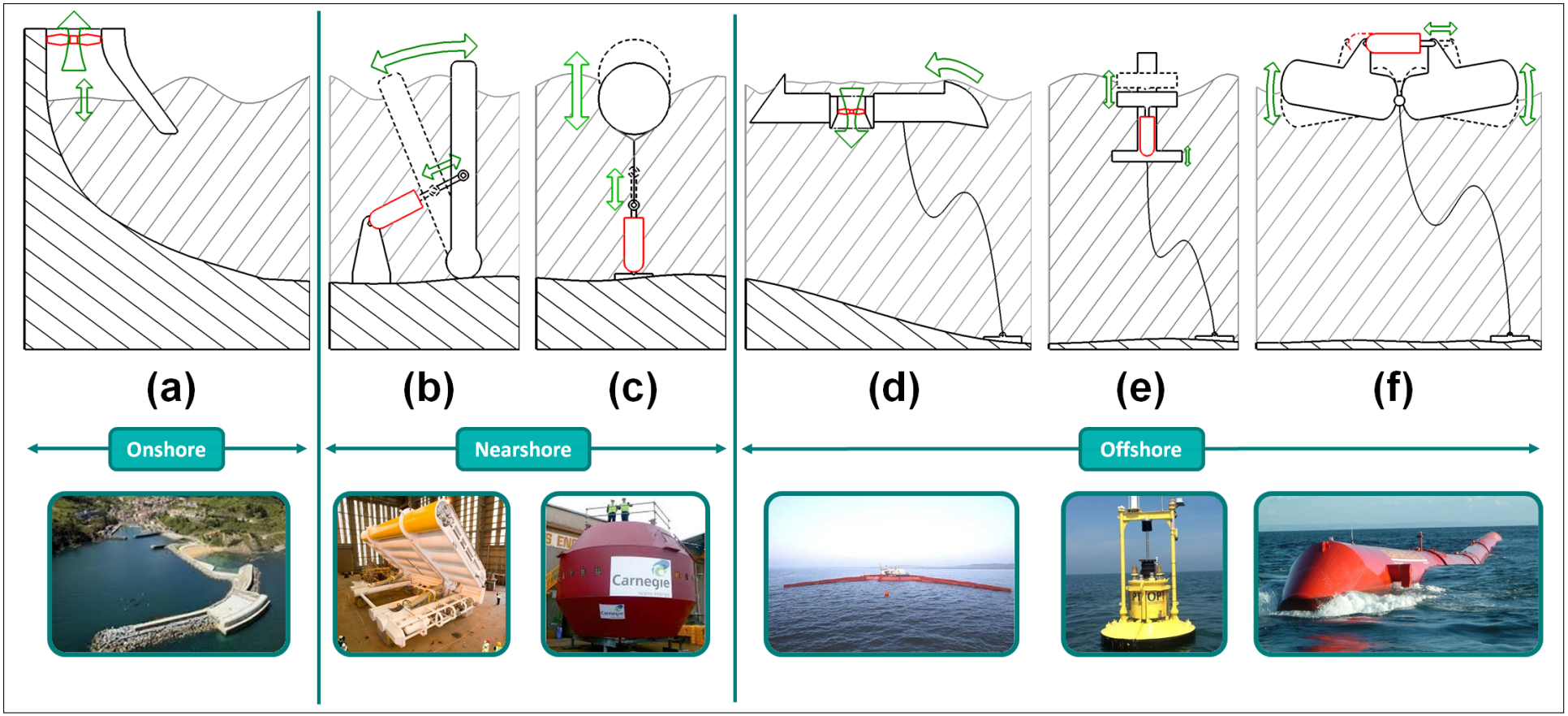

Figure 1.4: Different types of wave energy converters: (a) is an onshore OWC like the Mutriku OWC plant [25], (b) a nearshore OWSC as the Oyster device by Aquamarie Power Ltd. [26], (c) a nearshore point absorber like the CETO device by Carnegie [27], (d) an offshore overtopping device like WaveDragon [28], (e) an offshore self-reacting point absorber as PowerBuoy by OPT [29], and (f) an offshore attenuator like Pelamis [30].

activated oscillating bodies react to ocean waves with oscillatory motion of the body. Depending on the principal motion of the device, two categories can be distinguished within wave-activated oscillating bodies: heaving point absorbers (HPAs), when the device mainly reacts with vertical oscillations, and oscillating wave surge converters (OWSCs), when the device mainly uses the horizontal components of the wave motion.

Finally, a third classification is possible based on the location of devices [33]. WECs located on the coastline are known as onshore devices, while WECs installed in the ocean are referred to as near-shore devices when located close to shore and use the seabed as the reference point for the motion, and offshore devices when deployed far from the coastline (water depths of about 100m) using loose mooring lines.

Figure 1.4 illustrates different WECs, showing the working principle, and an example of a real device, for each case. Figure 1.4 (a) shows an onshore OWC device, for which a real example includes the Mutriku power plant, where 16 OWC cavities are built into a breakwater [25]. Oscillating water column devices can also be floating and be deployed offshore, such as the case of the Sparbuoy [34]. Figure 1.4 (b) illustrates an OWSC located near-shore, where the device is shown to rotate around a reference point on the seabed, and the Oyster device [26] is one of the physical examples. Also, OWSC devices can be floating and be deployed offshore, such as the Langlee concept [35]. Figures 1.4 (c) and (e) show two HPAs located near-shore, *e.g.* the CETO device [27], and offshore, *e.g.* the OPT Powerbuoy [29], respectively. The near-shore HPA uses the seabed as its reference point, while the offshore HPA reacts against itself. Figure 1.4 (d) illustrates a floating overtopping device, such as the Wavedragon [28], where waves break on a ramp, capturing the water of the waves in the reservoir to use the potential energy of the water in the reservoir by means of a turbine located at the bottom of the floating structure. Overtopping devices can also be located onshore, as the TAPCHAN device [36]. Finally, Figure 1.4 (f) shows an attenuator located offshore, such as the Pelamis device [30], which extracts energy from the relative motion of the different bodies.

1.1.3 Brief historical perspective

Despite the general belief that wave energy is a new technological solution for energy production, [37] shows that the first idea to harvest power from ocean waves goes back to 1799, when the first patent on wave energy was presented in Paris. The WEC suggested in this first patent is a pontoon connected to an onshore power station by means of a lever. Other pioneering ideas to use wave energy were suggested in the following decades: an OWC was built in 1910, using natural cavities in cliffs, to light a house [38], and another OWC, also built in natural cavities, was used to pump sea-water from 1898 to 1910 [39]. Dhaille [40] states that more than 600 patents related to wave energy conversion were already presented by 1956.

However, the wave energy industry, as we know it nowadays, defined as the ”modern age” in [41], started to develop with the energy crisis originated after the oil crisis in 1973. The key inventions and advancements suggested in the years after the energy crisis provided a breakthrough in the development of the wave energy industry. Stephen Salter published two articles in 1974 and 1975 in the influential scientific journal *Nature*, where he presents the WEC known as *Salter's duck* [42, 43]. Also in 1975, and also in *Nature*, Budal and Falnes introduced the point-absorber concept and the theoretical foundation for optimal control of WECs [44], and extended their work on the control of point absorbers in 1980 [45]. Another important theoretical contribution of the 1970's is the paper by David Evans [46], where the maximum theoretical wave energy absorption by an oscillating device is presented.

One of the first WECs to be tested in real conditions was the KAIMEI, which basically consisted of a large ship with several OWCs. Although Yoshio Masuda invented the OWC device in the early 1940's, it was in 1978 when the prototype suggested by Masuda was tested in Japan [37]. The KAIMEI evolved in time into the well known OWC Backward Bent Duct Buoy (BBDB). A significant contribution for OWC devices also happened in the 1970's, when Alan Arthur Wells

invented the first air turbine, known as the Wells turbine, specifically designed for wave energy conversion. The Wells turbine was the first self-rectifying air turbine and provided such a significant improvement to absorb energy from ocean waves, using the OWC concept, that most OWC prototypes at that time utilised a Wells turbine.

Also in 1978, Sir Christopher Cockerell invented the Cockerell raft [37], which is considered to be the first attenuator. The Cockerell raft consisted of three hinged pontoons and energy was extracted by means of hydraulic components installed in the hinges. A 1/10 scale prototype of the Cockerell raft was tested in the Solent, south of England, and was considered to be the first WEC to produce electricity in the UK. Later in 1985, an onshore overtopping device called TAPCHAN was installed in Norway. This concept was invented by a research group at the Centre for Industrial Research and the installed power of the first prototype was 350kW. The TAPCHAN stopped working after three years of operation due to the damage inflicted by storms and was never repaired.

The significant contributions, both theoretical and experimental, of the 1970's and 1980's were crucial for an accurate understanding of wave-body interactions and significantly aided the development of future WEC concepts. However, after the high activity of the 1970's and early 1980's, the subsequent significant drop in oil prices, making oil affordable again, dramatically cut the financial support for ocean energy research [47]. As a consequence, the ocean energy research and industry fell into a crisis. Figure 1.5 clearly illustrates this crisis, which is expressed by the dramatic reduction of ocean energy patents highlighted in blue.

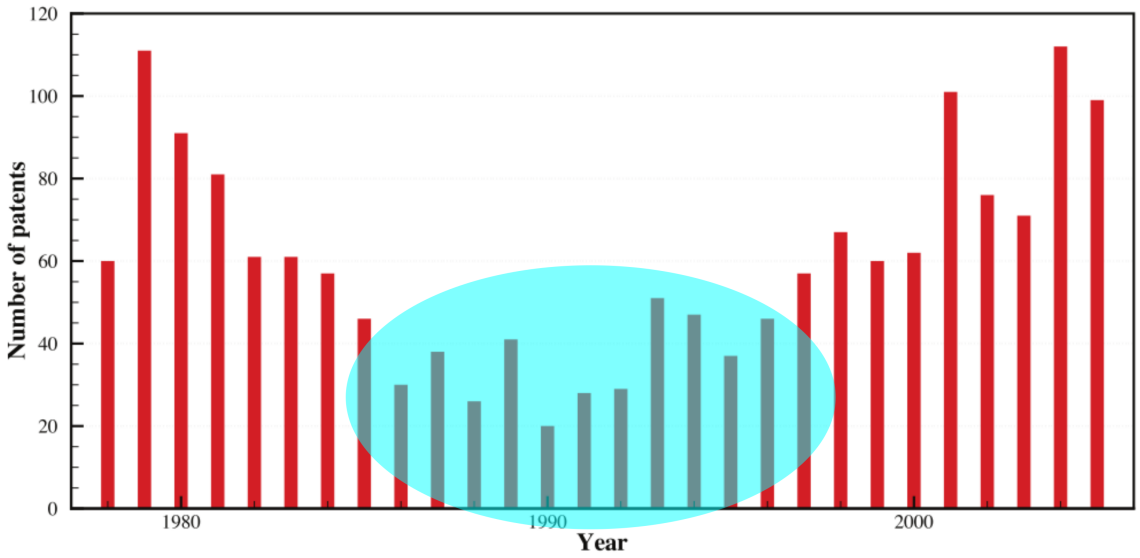

Figure 1.5: Number of patents for wave and tidal/stream energy technologies between 1978 and 2005, where the blue circle highlights a strong trough. Figure adapted from [41].

However, the interest of researchers focused again on ocean energy just before the end of the millennium, when a second generation of wave energy converters started to emerge. The interest of different funding agencies and private companies increased, and ocean energies re-emerged in the spotlight. As a consequence, different WEC concepts were invented and tested all over the world, and the number of patent publications recovered the levels of the 1970's and early 1980's by 2005, as shown in Figure 1.5.

For further details about the historical perspective, the readers are referred to [41], where Babarit thoroughly reviews the historical development of WECs from the first patent in 1799 to the present.

1.1.4 Current status and future challenges

Despite better understanding of WEC behaviour, and the significant development of different technologies achieved during recent decades, none of the prototypes suggested so far has yet shown true commercial viability. The resounding bankruptcy of important wave energy companies, such as Pelamis, Wavestar or Aquamarine, and the lack of successful prototypes showing economical viability of wave energy made the involved companies and funding agencies become somewhat sceptical.

Several WEC prototypes have been demonstrated to be technically successful while only a few have suffered tragic failure, where [41] states that only 5% of the prototypes have failed. Unfortunately, the impact of failure is strong in an industry where good news is scarce and, thus, the wave energy industry and research seems to be falling into a second crisis.

However, the reason why important wave energy companies went into bankruptcy may not be their specific technology, but the development methodology of such technologies. Investors want to see their prototypes at full-scale (or close to full-scale) installed in the ocean to demonstrate the technical maturity as soon as possible, which requires colossal investment. The idea was that once the prototype demonstrated its capacity to harvest energy and survive extreme events, the economical viability would be further developed over time.

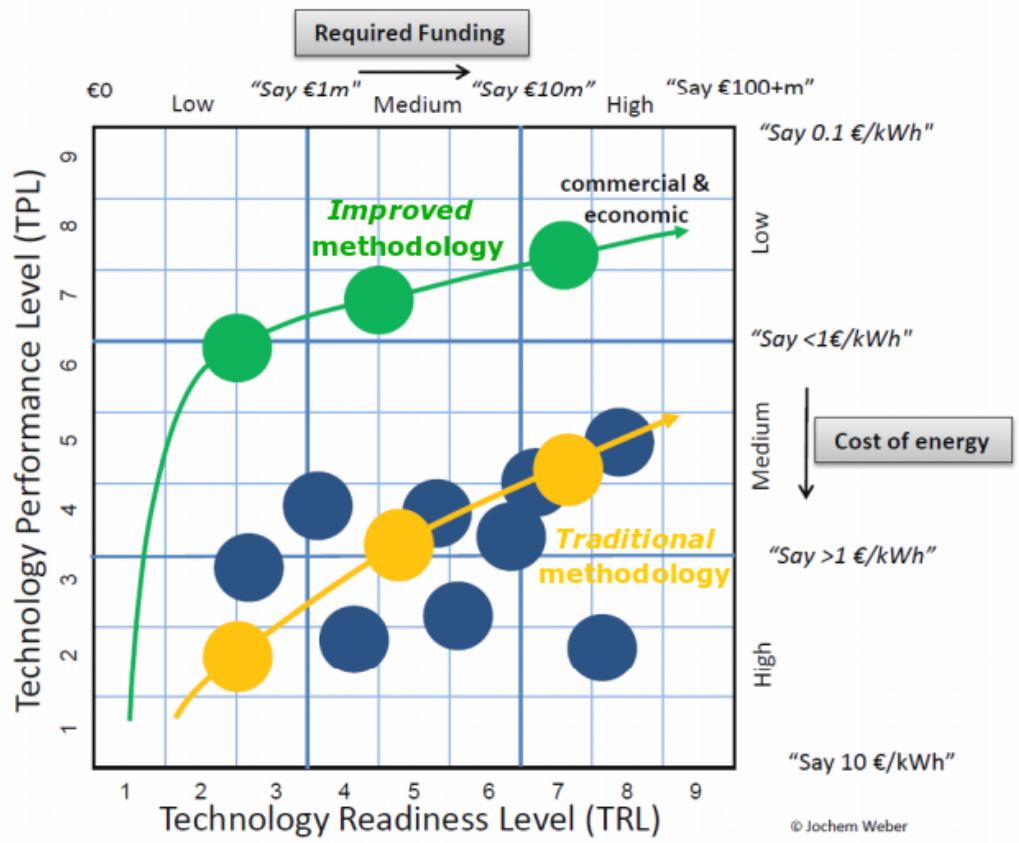

Figure 1.6: Two technology development methodologies: yellow line shows the *traditional* methodology where the technology maturity is the main objective, green line shows the *improved* methodology where energy cost is included in the development from the beginning, and blue dots correspond to the development status of real WEC technologies. Figure adapted from [48].

Hence, the performance of a WEC concept was only measured by its technical maturity. To that end, the metric known as technology readiness level (TRL) was used, originally designed for defence and aerospace industries, for which the cost of the technology is secondary. However, cost is crucial for the wave energy industry. Therefore, Weber [48] suggests a new metric to com-

plement the TRL, which includes the economical performance of the technology: the technology performance level (TPL). The combination of the TRL and TPL metrics allows for the design of an 'improved' technology development methodology that assesses the overall performance of a WEC, including economic aspects, and minimises the investment risk, as suggested in [49]. Figure 1.6 shows the *traditional* (in yellow) and the *improved* (in green) development methodologies, with respect to TRL and TPL values. In addition, blue dots in Figure 1.6 correspond to the development status of real WEC technologies.

Therefore, the wave energy industry now has the chance to shift the development methodology to assess technology and economic performance from the early stages of development. Indeed, economic viability, that is, making wave energy generation cost-effective, is the main challenge of the wave energy industry today. Babarit [41] presents an interesting analysis regarding the marketability of wave energy, comparing the price of electric energy in different regions around the world and the current estimation of the cost of energy generated from ocean waves (estimated to be about 0.5€/kWh today). The remarkable conclusion of this analysis is that pre-commercial wave energy projects require a cost reduction by a factor of 2 in order to be attractive for public and/or private investors.

Significant improvements are thus required in different aspects related to wave energy to reduce the cost of energy by a factor of 2, meaning that the cost reduction challenge further implies other more specific challenges:

- **Power take-off design**: The design of the power take-off (PTO) system must allow for efficient conversion from mechanical energy absorbed from ocean waves into electric energy, suitable for integration into national grids. The PTO configuration and efficiency strongly affect the final cost of energy.

- **Energy extraction performance**: The configuration of the WEC, *i.e.* the geometry and the specific degree(s) of freedom (DoF) in which energy is absorbed, strongly affects energy extraction. In addition, the device can be controlled to maximise energy extraction performance. Optimally selecting the working principle of the device, and accurately maximising energy absorption by means of control, is vital in making a WEC economically viable.

- **Survivability**: Apart from extracting energy from ocean waves, WECs have to survive in extreme conditions, such as storms. Within its lifetime, typically considered between 20-30 years, a WEC can encounter extremely harsh conditions, which suggests that a survivability strategy to minimise structural damage is essential. An efficient survivability strategy should not greatly affect energy extraction, but directly affects the sizing of different components and, as a consequence, the cost of energy.

- **Construction, deployment and maintenance**: Due to the harsh environment where WECs operate, construction, deployment and maintenance activities are difficult and expensive. Reducing the capital expenditure (CAPEX), and especially the operation expenditure (OPEX), is essential to make a WEC commercially viable.

These specific challenges individually affect the cost of energy produced from ocean waves, but analysing them independently may not reflect their real implication on the cost of energy, since the different specific challenges are strongly interconnected, as illustrated in Figure 1.7. For example, the design of the PTO system not only facilitates an efficient energy conversion, but also restricts the energy extraction performance, affects the survivability, and influences maintenance requirements. This thesis focuses on aspects related to the PTO system and the energy extraction performance, as highlighted in Figure 1.7, so survivability and construction/maintenance analysis is beyond the scope of this thesis.

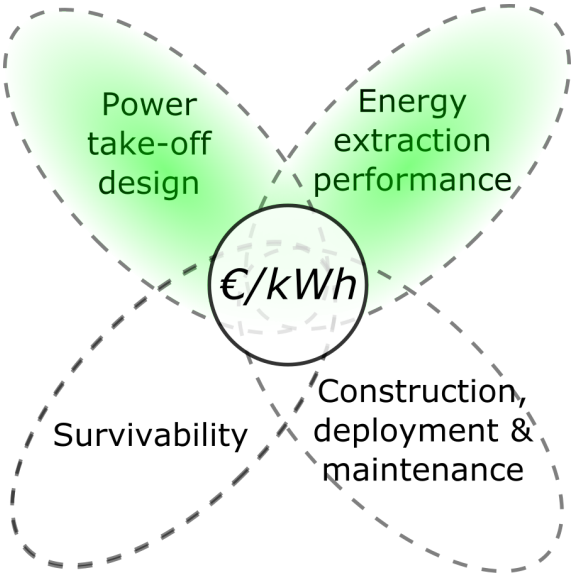

Figure 1.7: Main challenges for the development of successful WECs and the illustration of the relation between the specific challenges and the final cost of energy.

1.2 Motivation

Mathematical models are crucial tools in designing a successful WEC that can achieve economic viability, which can be used for simulation of WEC behaviour, power production assessment, or as a basis for the design of model-based control strategies. The accuracy of mathematical models is essential, so that WEC developers can rely on the results provided by these mathematical models, and minimise expensive wave tank experiments or open ocean tests. Most commonly, WECs are tested by combining mathematical models with wave tank and/or test rig experiments, so that mathematical models can be validated and, in some cases, tuned to improve the accuracy of the results.

In general, WECs are developed through independent stages, where different subsystems of the WEC are analysed independently, in the following order:

A. The concept of the absorber[1] is established based on significantly simplified and computationally fast hydrodynamic models, which determines the working principle of the absorber;

B. The suitability of the concept is verified in wave tank experiments with a small scale prototype, ensuring that the prototype responds as expected to the action of the waves and that the motion of the device can actually be used to extract energy from ocean waves;

C. The geometry of the absorber is optimised via simplified hydrodynamic models tuned based on the wave tank experiments with small scale prototypes;

D. A PTO system is designed for the WEC, based on mathematical models and test rigs that often ignore the performance of the absorber in extracting energy from ocean waves; and

E. An energy maximising control strategy is designed for the WEC, based on simplified hydrodynamic models and neglecting or excessively simplifying the effect of the PTO system.

The result is a WEC with individually optimised subsystems, where the effect of the energy maximising control is not included in the geometry or PTO optimisation, and/or the PTO system

[1]Note that the absorber and the WEC are intentionally distinguished in the following, where absorber(s) is referred to the part of the WEC that absorbs energy from ocean waves and the WEC corresponds to the whole energy conversion system, including the absorber(s) and the PTO system.

is designed to ensure the highest possible efficiency of the individual components. However, similarly to the specific challenges presented in Figure 1.7, the different subsystems, from ocean waves to the electricity grid, are interconnected. Thus, following the traditional development strategy described in stages A-E, the final WEC may be composed of optimised subsystems, but be suboptimal as a whole [50].

To design a successful WEC, the holistic performance of the WEC should be evaluated, so that the different subsystems are designed and optimised according to their impact on the overall WEC economic performance. To that end, mathematical models that adequately incorporate all these subsystems, known as wave-to-wire (W2W) models, must be developed.

1.3 Objectives and Contributions

The main objective of the present thesis is to design a comprehensive W2W model that includes all the required dynamics (including nonlinearities if necessary), constraints and losses of the different subsystems from ocean waves to the electricity grid. A further objective of this thesis is to demonstrate the need for accurate W2W models in different potential applications, such as identification of model parameters, power production assessment or simulation of the WEC behaviour, and constructing application-specific W2W models that fulfil the specific requirements of these applications.

Wave-to-wire models created in this thesis are W2W models based on hydraulic PTO (HyPTO) systems (HyW2W). The main contributions of this thesis are summarised as follows:

1. The primary contribution of this thesis is the construction of a comprehensive parsimonious W2W (parW2W) model that includes accurate mathematical models for the different subsystems from ocean waves to the electricity grid. This unique parW2W model is referred to as the *comprehensive HyW2W* (*cHyW2W*) model, and includes the following aspects:

    - A computationally efficient partially-nonlinear model to solve wave-structure hydrodynamic interactions (WSHIs), where nonlinear Froude-Krylov (FK) forces and viscous effects are considered, showing significantly more accurate results than the commonly employed linear models. The influence of the partially-nonlinear model is demonstrated to be particularly relevant when the device is actively controlled to maximise the energy extracted from ocean waves.
    - Mathematical models for two different hydraulic transmission system configurations, i.e. constant- and variable-pressure configurations, where all the important dynamics, losses, and constraints are included. In addition, mathematical models for three different electric generators and back-to-back (B2B) power converters are incorporated, which also include the main dynamics and losses. The mathematical models for the hydraulic transmission systems, electric generators and B2B power converters are validated against experimental results obtained using different test rigs.
    - The HyW2W model is efficiently implemented by utilising a multi-rate time-integration scheme, so that each subsystem uses the time-step required to adequately capture the dynamics of the components included in that subsystem and avoids unnecessary computation in the subsystems where components with slower dynamics are included.

2. In addition, the relevance of the *cHyW2W* model in accurately designing a WEC and assessing its capabilities is demonstrated in this thesis. Hence, the *cHyW2W* model is shown to be vital in demonstrating the benefits of active control strategies, evaluating the performance of different PTO configurations, accurately maximising energy generation of a WEC, and assessing power generation capabilities of a WEC.

3. A further novel contribution presented in this thesis is the design of a high-fidelity HyW2W simulation platform, referred to as the *HiFiWEC*, where a numerical wave tank (NWT)

based on computational fluid dynamics (CFD) is coupled to a high-fidelity PTO model. The *HiFiWEC* provides an unprecedented numerical platform to evaluate the performance of the WEC at medium-high TPLs and low-medium TRLs, which can be crucial in the development of the successful WEC.

4. Finally, a *systematic* complexity reduction (CR) approach is presented in this thesis to design application-specific W2W models that fulfil the specific requirements of different applications, which have particular fidelity and/or complexity requirements. In addition, two nonlinearity measures, to quantify the nonlinearity degree of the behaviour of a WEC, are presented in this thesis as part of the *systematic* CR approach.

1.3.1 List of publications

1.3.1.1 Conference publications

[A] Penalba, M., Giorgi, G., & Ringwood, J. V. A Review of non-linear approaches for wave energy converter modelling. In Proceedings of the 11th European Wave and Tidal Energy Conference, Nantes, France, no. 08C1-3, 2015.

[B] Penalba, M., Mérigaud, A., Gilloteaux, J., & Ringwood, J. V. Nonlinear Froude-Krylov force modelling for two heaving wave energy point absorbers. In Proceedings of the 11th European Wave and Tidal Energy Conference, Nantes, France, no. 08C1-4, 2015.

[C] Giorgi, G., Penalba, M., & Ringwood, J. V. Nonlinear Hydrodynamic Models for Heaving Buoy Wave Energy Converters. In Proceedings of the 3rd Asian Wave and Tidal Energy Conference, Singapore, pp. 144-153, 2016.

[D] Giorgi, G., Penalba, M., & Ringwood, J. V. Nonlinear Hydrodynamic Force Relevance for Heaving Point Absorber and Oscillating Surge Converters. In Proceedings of the Asian Wave and Tidal Energy Conference, Singapore, pp. 154-162, 2016.

[E] Penalba, M., Kelly, T., & Ringwood, J. V. Using NEMOH for Modelling Wave Energy Converters: A Comparative Study with WAMIT. In Proceedings of the 12th European Wave and Tidal Energy Conference, Cork, Ireland, no. 631, 2017.

[F] Penalba, M., & Ringwood J. V. The Impact of a Wave-to-Wire Model in Control Parameter Optimisation and Power Assessment. In Proceedings of the ASME 37th International Conference on Ocean, Offshore and Arctic Engineering, Madrid, Spain, OMAE2018-77501, 2018.

[G] Penalba, M., & Ringwood J. V. Reduced wave -to-wire model for Control Parameter Optimisation and Power Assessment. Proceedings of the 3rd International Conference on Renewable Energies Offshore, Lisbon, Portugal, 2018.

1.3.1.2 Journal publications

[H] Penalba, M., & Ringwood, J. V. A review of wave-to-wire models for wave energy converters. Energies, 9(7), 506, 2016.

[I] Penalba, M., Mérigaud, A., Gilloteaux, J.-C., & Ringwood, J. V. Influence of nonlinear Froude-Krylov forces on the performance of two wave energy point absorbers. Journal of Ocean Engineering and Marine Energy, 3(3), 209-220, 2017.

[J] Penalba, M., Giorgi, G., & Ringwood, J. V. Mathematical modelling of wave energy converters: A review of nonlinear approaches. Renewable and Sustainable Energy Reviews, 78, 1188-1207, 2017.

[K] Penalba, M., Sell, N., Hillis, A., & Ringwood, J. Validating a Wave-to-Wire Model for a Wave Energy Converter - Part I: The Hydraulic Transmission System. Energies, 10(7), 977, 2017.

[L] Penalba, M., Cortajarena, J.-A., & Ringwood, J. V. Validating a Wave-to-Wire Model for a Wave Energy Converter - Part II: The Electrical System. Energies, 10(7), 1002, 2017.

[M] Ulazia, A., Penalba, M., Ibarra-Berastegui, G., Ringwood, J.V., & Sanz, J. Wave energy trends over the Bay of Biscay and the consequences for wave energy converters. Energy 141, 624-634, 2017.

[N] Penalba, M., Ulazia, A., Ibarra-Berastegui, G., Ringwood, J.V., & Saenz, J. Wave Energy Resource Variation off the West Coast of Ireland and its Impact on Realistic Wave Energy Converters' Power Absorption. Applied Energy, 224, 205-219, 2018.

[O] Penalba, M., Davidson, J., Windt, C., & Ringwood, J. V. A high-fidelity wave-to-wire simulation platform for wave energy converters: Coupled numerical wave tank and power take-off models. Applied Energy, vol. 226 C, pp. 655-669, 2018.

[P] Ulazia, A., Penalba, M., Ibarra-Berastegui, G., Ringwood, J.V., & Sanz, J. Historical Evolution of the Wave Resource and Energy Production off the Chilean Coast over the 20th Century. *Energies*, 11(9), 2289, 2018.

1.3.1.3 Submitted publications

[Q] Penalba, M., & Ringwood, J. V. A High-Fidelity Wave-to-Wire Model for Wave Energy Converters. Submitted to Renewable Energy.

[R] Penalba, M., & Ringwood, J. V. Linearisation-based nonlinearity measures for wave-to-wire models in wave energy. Submitted to Ocean Engineering.

[S] Penalba, M., & Ringwood J. V. Systematic Complexity Reduction of Wave-to-Wire models for Wave Energy System Design. Submitted to Ocean Engineering.

[T] Ulazia, A., Penalba, M., Ibarra-Berastegui, G., Ringwood, J.V., & Sanz, J. Reduction of the capture width of wave energy converters due to long-term seasonal wave energy trends. Submitted to Renewable and Sustainable Energy Reviews.

[U] Windt, C., Faedo, N., Penalba, M., & Ringwood, J.V. Evaluation of Energy Maximising Control Systems for the Wavestar Wave Energy Converter. In preparation for the American Control Conference, Philadelphia, USA, 2019.

1.4 Thesis outline

The thesis consists of nine additional chapters, the subjects of which are outlined in the following part of this section:

- Chapter 2 introduces W2W models and defines different potential applications for W2W models. The chapter divides the path from ocean waves to the electricity grid into different subsystems and conversion stages, and provides a comprehensive literature review of the approaches used to model each of the subsystems. The last part of the chapter analyses existing HyW2W models, evaluating their advantages and limitations based on the applications they were designed for. In addition, the foundations of parsimonious HyW2W modelling are defined in this last part.

- In Chapter 3, the fundamental aspects of potential flow theory which describe WSHIs are described in detail. The chapter first describes the linear potential flow (LPF) theory, including linear wave theory and the identification of frequency-domain (FD) hydrodynamic coefficients using boundary element method (BEM) solvers. Then, the influence of nonlinear effects in WSHIs is evaluated, including nonlinear FK and viscous forces, and nonlinear waves. The last part of the chapter briefly presents the computationally-efficient partially-nonlinear hydrodynamic model implemented in the *cHyW2W* model.

- Chapter 4 presents the different mathematical models for the HyPTO systems implemented in the *cHyW2W* model and is divided into two main parts: the hydraulic transmission system, including constant- and variable-pressure configurations, and the electrical system, including models for three different generators and the B2B power converter.

- Chapter 5, is divided into three main parts. On the first part, the different mathematical models presented in Chapter 3 are compared, demonstrating the relevance of considering nonlinear effects in the WSHI. In the second and third parts, the mathematical models for the hydraulic and electrical systems presented in Chapter 4 are validated against high-fidelity numerical models or experimental results obtained from different test rigs.

- Chapter 6 describes the efficient implementation of the *cHyW2W* model, comparing the single-rate and multi-rate time-integration schemes, and various different numerical methods. In addition, results of the *cHyW2W* model are shown for different HyPTO configurations, and the relevance of using the *cHyW2W* model to accurately design a WEC and assess its capabilities is demonstrated.

- In Chapter 7 the *HiFiWEC* simulation platform is presented, a high-fidelity HyW2W simulation platform composed of a CFD-based NWT (CNWT) and the HyPTO model described in Chapter 4. The coupling between the CNWT and the HyPTO is verified in the first part of the chapter and the value of using such a high-fidelity platform is shown in the last part of the chapter.

- In Chapter 8, a *systematic* CR approach is presented. The specific requirements of each application described in Chapter 2 and the complexity of a mathematical model are defined in the introduction to Chapter 8, where the nonlinearity degree is shown to be an important factor. Therefore, the first part of the chapter presents two nonlinearity measures to quantify the nonlinearity degree of mathematical models. Then, the *systematic* CR that considers the application requirements is presented in the second part of the chapter. Finally, the last section of the chapter evaluates the reduced models, selecting specifically designed HyW2W models for each application (*specific HyW2W*) and testing the *specific HyW2W* models for power assessment and controller design applications.

- Conclusions of the thesis are drawn in Chapter 9, where a summary and a discussion on the contributions and results of the thesis is presented along with a short discussion on potential future work.

Chapter 2

Wave-to-wire modelling: A literature survey

The different subsystems involved in energy generation from ocean waves and the interconnections between these subsystems are illustrated in Figure 2.1. The initial and final subsystems refer to the ocean waves and the electricity grid, respectively, mooring lines employed to keep the WEC on station only interact with the absorber, and the WEC comprises all the subsystems required for energy generation, including the absorber and the PTO system. Hence, the path from ocean waves to the electricity grid is divided into five main subsystems: ocean waves, absorber, moorings, PTO and electricity grid.

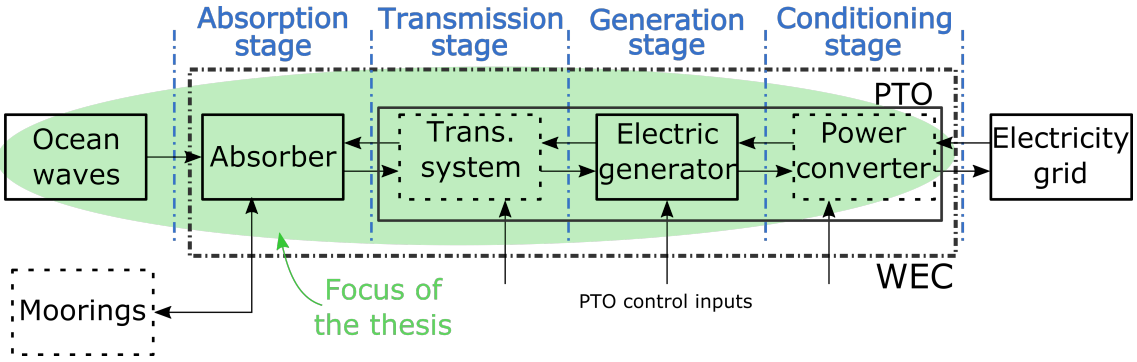

Figure 2.1: Schematic representation of the different subsystems involved in wave energy generation and the interconnection between these subsystems. Dashed rectangles represent the subsystems that are included only in certain WECs.

Wave energy converters deployed in the ocean interact with ocean waves to absorb energy in the form of kinetic and/or potential energy, depending on the type of WEC. That mechanical energy needs to be converted into electrical energy, which often requires conditioning so that the requirements imposed by the electricity grid are adequately fulfilled. Thus, the energy from ocean waves passes through between two and four different conversion stages, depending on the PTO system integrated into the WEC, before it is delivered to the electricity grid. Figure 2.1 illustrates the different subsystems and conversion stages, where the dashed rectangles represent the subsystems that are included only in certain WECs.

For instance, in the case of a wave-activated WEC with a HyPTO system [27, 30, 51], the *absorption* stage comprises the conversion of wave motion into oscillating motion of the absorber. This absorbed mechanical energy is then transmitted into hydraulic energy in the *transmission* stage and converted into electricity in the *generation* stage. Finally, the power signal from the electric generator is adapted for delivery into the electricity grid in the *conditioning* stage. As shown in

Section 2.3, the hydraulic PTO system can be replaced by a mechanical or magnetic transmission system, in the case of a wave-activated body, or by a pneumatic transmission system, in the case of an OWC, preserving, in both cases, the four-conversion-stage chain (*absorption-transmission-generation-conditioning*). In some particular cases, known as direct conversion, wave-activated WECs are directly connected to the electric generator using a linear electric generator, in which case the *transmission* stage is eliminated, resulting in a three-conversion-stage chain (*absorption-generation-conditioning*).[1]

Wave-to-wire models should include all the subsystems shown in Figure 2.1, for a holistic study of a WEC. However, the focus of this thesis is on PTO systems and the energy extraction performance, as illustrated in Figure 1.7. Thus, moorings and electricity grid are beyond the scope of this thesis, as illustrated in Figure 2.1.

The *improved* technology development trajectory presented in Figure 1.6 illustrates the need for accurate mathematical models to improve the TPL of a WEC, while preserving a relatively low TRL. These mathematical models are particularly crucial at the initial steep portion of the *improved* trajectory, where the WEC concept, including the absorber and the PTO system, is being established and optimised.

More specifically, some of the most relevant decisions to be made, at this initial stage, are the design of the absorber, and the type and configuration of the PTO system. Though these decisions may seem to be independent of each other, they are actually tightly connected. The design of the absorber can significantly influence the optimum design of the PTO system and, in turn, the configuration of the PTO system can considerably influence the performance of the absorber. In addition, optimally controlling the WEC to maximise energy generation, can significantly influence the design of the absorber and PTO system [52, 53], and vice versa. As a consequence, the correct decisions concerning the design of a WEC can only be made if the overall performance of the WEC system is evaluated, for which a W2W model, where control inputs are accommodated, is vital. Hence, in the initial stages of the design process, W2W models are essential for the assessment of WECs' power production capabilities (*PowAss*), the optimisation of the PTO system configuration and sizing of PTO system components (*PTOopt*), and the design of upper-level model-based control strategies to maximise energy generation (*MBC*).

Once the concept and size of the absorber, and the PTO system configuration, are established, W2W models are also necessary to accurately simulate the behaviour of WECs and evaluate their performance (*SimWEC*). Excessive simplification of mathematical models can lead to significant overestimation of the device motion and, as a consequence, power generation, which can lead to unrealistic optimism of the real behaviour and performance of a WEC. Another potential application of W2W models is the modelling of electrical power systems and power quality analysis (*PowSyst*). Unless the mathematical models for *PowSyst* accurately incorporate all the different conversion stages presented in Figure 2.1, the power flows estimated from these mathematical models are likely to be inaccurate. This may result in an inappropriate design of energy storage systems and/or electric interconnection between the WEC, or WEC array, and the electricity grid. Another consequence of inaccurate power flow estimates is the potential violation of the restrictions stipulated in the grid code, with the consequence that energy generated by the WEC will not be delivered/sold into the electricity grid.

Also, high-fidelity W2W models can be utilised as validation tools for simpler mathematical models or as verification platforms to test the effectiveness of different control strategies (*ValVer*). Similarly, mathematical models used for the identification of model parameters (*Ident*) need to accurately represent the holistic performance of WECs, so that the identified models capture the behaviour of the device precisely.

Each of these potential applications of W2W models has very specific requirements and, as a consequence, require specific W2W models, as discussed in Chapter 8.

[1] Note that the distinction between energy absorption and generation is made intentionally, where absorption refers to the mechanical energy absorbed from ocean waves and generation to the electric energy generated through the power take-off system.

Including nonlinearities in mathematical models can be crucial for an accurate representation of WECs' behaviour. Any WEC deployed in the ocean deals with a wide range of sea states. Therefore, the operation of WECs is divided into two operational modes, as illustrated in Figure 2.2. The *power production mode* refers to the operational mode when the device produces energy from ocean waves without compromising its integrity, while the *survival mode* is activated during extreme conditions to avoid structural damage in the WEC. Similar operational modes are also utilised in other offshore engineering applications, where nonlinear behaviour is assumed to be particularly relevant during extreme conditions, but relatively negligible in *power production mode*.

In fact, WECs are commonly designed and studied by utilising numerical models previously employed in other offshore engineering applications. However, in contrast to other offshore engineering applications, WECs are designed to maximise power by encouraging exaggerated motion of the absorber via a control strategy. Therefore, large motion, which lead to nonlinear behaviour, should also appear within the power production mode. Accordingly, linear approaches, originally created for the traditional offshore engineering applications (where small deviations from equilibrium are both present and desired), may not be adequate to accurately reproduce the behaviour of WECs. Some evidence on the nonlinear behaviour of different WECs, within the power production mode, can be found in [54–56] for HPAs, oscillating pitching converters [57] or oscillating surge converters [58–60]. The impact of different nonlinear effects is further discussed in Section 2.2.

This evidence challenges typical WEC modelling approaches and suggests a scenario divided into three different regions: a *linear region*, a *nonlinear region* and a *highly nonlinear region*, as shown in Figure 2.2. In such a scenario, nonlinear models would also be important within the *power production mode*.

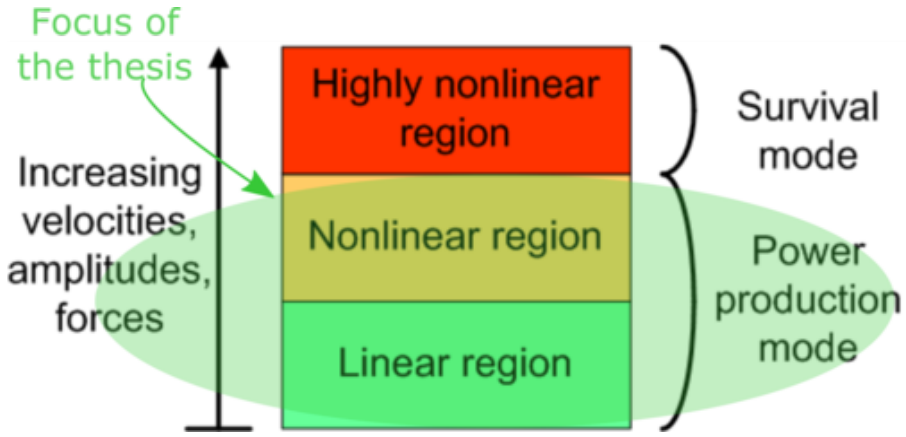

Figure 2.2: Different operating regions for wave energy devices

This thesis focuses on the design of W2W models for the *power production mode*, as highlighted in Figure 2.2, while the behaviour of WECs during the *survival mode* is beyond the scope of this thesis. Sources of nonlinear effects within the *power production mode* have been identified in all the different subsystems involved in wave energy generation: ocean waves [61], WSHIs [56–58] and PTO systems [62–64]. Therefore, the relevance of nonlinear effects and the mathematical approaches to articulate these nonlinear effects, are evaluated for each subsystem in this section.

Although not all WECs are designed for electricity production, *i.e.* some produce potable water, this thesis only studies the WECs that generate electricity from ocean waves. The W2W models developed in this thesis consist of three main subsystems, *i.e.* ocean waves, absorber and the PTO system, and four different conversion stages, as illustrated in Figure 2.1. This chapter is divided into six different sections, based on the separation of the path from ocean waves to the electricity grid presented in Figure 2.1: Ocean waves in Section 2.1, *Absorption* stage in Section

2.2, *Transmission* stage in Section 2.3, *Generation* stage in Section 2.4, *Conditioning* stage in Section 2.5 and an application-based *HyW2W* survey in Section 2.6.

2.1 Ocean waves

Incoming waves, originally produced by consistent wind activity, can be represented in many different ways, from linear monochromatic waves, where waves are basically adjustable (in amplitude and frequency) sinusoidal signals, to irregular and fully nonlinear (including viscous effects) waves in three dimensions. Figure 2.3 illustrates the appropriate wave theory to be used as a function of wave height, wave period and water depth. These three terms should be considered when analysing nonlinear waves, with special emphasis on the wave height and period. Wave steepness, defined as the ratio between the wave height and the wavelength ($\frac{H_w}{\lambda_w}$) is commonly used as the indicator of nonlinearity of ocean waves, where nonlinearity increases with steepness. Hence, short and high waves result in steep nonlinear waves.

Since the thesis focuses on devices operating in *power production mode*, only waves that are suitable for power production are considered, avoiding extreme, highly nonlinear, waves. Indeed, it is believed that a large percentage of the wave resource in operational conditions (some researchers suggest over 90%) can be covered by linear wave theory. Unfortunately, no reference has been found that addresses the importance of modelling nonlinear waves for wave power production purposes.

Therefore, defining a region of the wave theory diagram where *power production mode* is activated, is useful for identifying the relevance of nonlinear effects and finding an appropriate wave modelling approach. However, operational conditions of WECs are highly device-dependent. For each device, data from open ocean tests can be used to determine the upper boundary of the power production region in relation to the location characteristics (water depth). Figure 2.3 shows the upper boundary of three different devices, the *Oyster* (near-shore) [65] and the *Pelamis* (off-shore) WECs [66], deployed at the European Marine Energy Centre (EMEC), and the *Sea Power* device (off-shore) [67], deployed at the Atlantic Marine Energy Test Site (AMETS). The boundaries of these three devices provide a reasonable spread of different WEC types and location characteristics. Hence, an approximate *power production mode operation area*, the blue area in Figure 2.3, is defined.

This *power production mode operation area* suggests that Stokes water waves [69] up to third order should be considered in intermediate and deep water waves. Stokes' theory, nevertheless, breaks down in shallow water [70], where a possible alternative is Cnoidal theory [71], providing waves with sharper crests and flatter troughs. However, it should be noted that the data from open ocean tests is provided for different sea-states, that is, polychromatic waves, while the wave theory diagram represents the different wave theories required for monochromatic waves. The difference between the energy contained in a monochromatic (E_m) and a polychromatic wave (E_p), with the same wave height and period characteristics, is significant ($E_m \approx 2E_p$). Therefore, the *power production mode operational area* delimited in Figure 2.3 may be too conservative, meaning that second-order Stokes theory may be sufficient in the power production region.

Fenton [70] shows that fifth-order expansions of Stokes' and Cnoidal theories are of acceptable accuracy almost everywhere within the range of validity of each theory, but very high-order expansions are required to get really accurate results. However, expansions of up to fifth order largely cover the *power production mode operation area*. Rienecker and Fenton presented an efficient method [72], where the equations are solved via the Newton's method and coefficients are calculated numerically by solving fully nonlinear equations. Further details on different numerical modelling techniques for the propagation of nonlinear waves can be found in [73].

In any case, regular (monochromatic) wave theory cannot represent real waves, since two consecutive waves are never identical in real seas. Therefore, irregular wave models are used to reproduce real sea-states. The most established way of describing real sea-states is via the Fourier

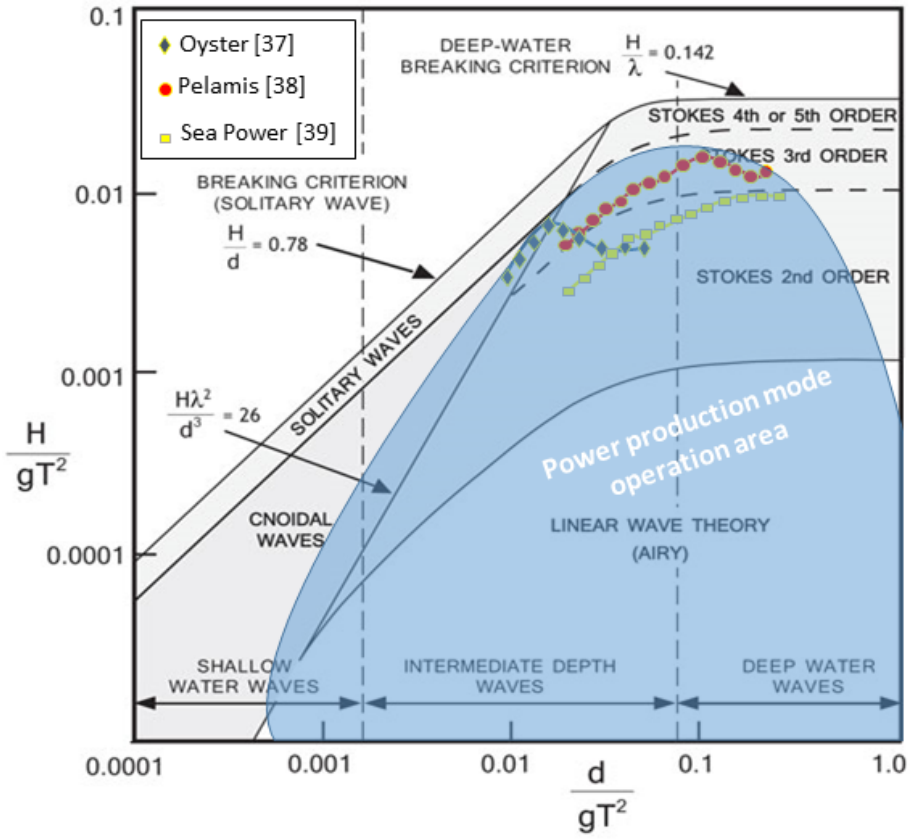

Figure 2.3: Wave theory diagram with the application area for power production in wave energy. Figure modified from [68], based on data published in [65] for the Oyster prototype, in [66] for the Pelamis WEC and in [67] for the Seapower platform.

analysis of records taken in different sites. These records are used to create a wave spectrum for each sea-state in a given location, giving the distribution of wave energy among different wave frequencies or wave-lengths on the sea surface. Various idealized spectra are used in ocean engineering and oceanography, such as Pierson-Moskowitz [74], JONSWAP spectra [75], Bretschneider [76] (all representing single-peaked spectra) or Ochi-Hubble [77], which is able to describe a multi-peak spectrum. A recent study describes two different methods to generate free-surface elevation time-series ($\eta_w(t)$) for wave energy applications, using harmonic sinusoidal components either with randomly chosen phases and deterministic amplitudes (DAS), or randomly chosen amplitudes (RAS) [78]. More realistic irregular waves can also be modelled using nonlinear wave theories. In fact, the same Rienecker and Fenton method suggested in [72] is also used for irregular waves in [79], where the impact of the nonlinear wave theory on the pressure field is shown to be always lower than 5% within the operational space.

Other alternatives include the high order spectral (HOS) methods, developed independently in [80] and [81], created to simulate nonlinear free-surface waves [82]. These HOS methods use a spectral expansion and the Fourier transforms, together with a modified Taylor series expansion, and are also used for the representation of nonlinear irregular waves, in [83] or [84], for example.

2.2 Absorption stage

This section focuses on WSHIs, with the section divided into three main parts: the different effects involved in WSHIs are first identified and described in Section 2.2.1, the relevance of the nonlinear representation of these effects is studied for different WECs in Section 2.2.2, and the different nonlinear modelling approaches are analysed in Section 2.2.3.

2.2.1 WSHI effects

The response of the absorber is represented as a function of different effects that participate in the WSHI,

$$(x_{abs}, \dot{x}_{abs}, \ddot{x}_{abs}) \leftarrow f(F_g, F_{FK}, F_{diff}, F_{rad}, F_{vis}, F_{other}), \tag{2.1}$$

where diverse effects acting on the absorber are shown, without specifying the mathematical description of these effects, nor the way the different effects interact with each other, that is, without assuming superposition of these effects.

The WSHI, which only considers the interaction between waves and the absorber, can be represented by the effects of the gravity (F_g) and the four main hydrodynamic effects: Froude-Krylov (FK) effect (F_{FK}), diffraction effect (F_{diff}), radiation effect (F_{rad}) and viscous effects (F_{visc}). In addition, other external effects, for example, the effect of the wind, tides or the coriolis effect, can also affect the behaviour of the absorber, for which F_{other} is included in Equation (2.1). The following subsections analyse the different effects involved in the WSHI.

2.2.1.1 Froude-Krylov effect

The FK effect is the load introduced by the unsteady pressure field generated by undisturbed waves. It is generally divided into static ($F_{FK_{stat}}$) and dynamic ($F_{FK_{dyn}}$) effects. The static part, also known as the buoyancy effect, represents the hydrostatic effect in a static situation with a still ocean ($F_{FK_{stat}}$, combined with F_g, results in hydrostatic force), while the dynamic part represents the effect of the incident wave.

Linear codes compute the FK force over the *mean* surface of the body, while nonlinear computation requires the integration of the incident wave pressure and the hydrostatic force over the *instantaneous* wetted surface, at each time step.

2.2.1.2 Diffraction effect

The diffraction effect is the effect associated with the action of the diffracted wave. Diffracted waves are introduced into the wave system by the presence of the floating structure. Froude-Krylov forces, together with the diffraction force, make up the total non-viscous hydrodynamic forces acting on a floating body in LPF theory. In fact, the commonly used excitation force (F_{ex}) is formed by the sum of the diffraction and dynamic FK forces. With respect to the diffraction due to a floating structure, [85] mentions that neglecting the diffraction term in F_{ex} is a reasonable approximation if the body is very small in comparison to the wavelength.

2.2.1.3 Radiation effect

The radiation effect, on the other hand, is the hydrodynamic force associated with the motion of a floating body. In the LPF theory, the radiation force is expressed by a convolution product, following the Cummins' equation [86], where the convolution term describes the water memory effects. In general, a linear approach for the radiation force is reasonably good for devices which are much smaller than the wavelength [87, 88].

2.2.1.4 Viscous effects

In the traditional offshore industry, in which hydrodynamic models have been mainly based on LPF theory, viscous losses are considered relevant for structures that are small compared to the wavelength (high λ_w/L_{charac} ratios, where λ_w and L_{charac} are the wavelength and characteristic length of the structure, respectively) [89]. This ratio is known as the KeuleganCarpenter (KC) number, which shows the importance of viscous effects over inertia effects [90]. The smaller the KC number, the more dominant inertia effects are. However, offshore structures (offshore oil and

gas platforms or ships) are, in general, large, with relatively low λ_w/L_{charac} ratios, meaning that diffraction forces are dominant and viscous losses are minor losses, except for localized effects, such as vortex shedding generation around sharp edges. However, WECs are generally small structures with high λ_w/L_{charac} ratios, especially point-absorbers, and so viscous effects, at least in theory, can be relevant.

In addition, viscous effects depend on the relative structure/fluid velocity. Offshore platforms are generally designed to remain still, so the relative structure/fluid velocity is low, while WECs are designed to maximise energy absorption by exaggerating their motion, which significantly increases the relative structure/fluid velocity. Therefore, viscous effects in WECs should not be neglected without a thorough study.

2.2.1.5 Device specific effects

Some WECs, due to their particular working principles, may experience particular hydrodynamic effects that can significantly affect the behaviour of the WEC. Three effects that can be relevant for specific WECs include parametrically excited motion, sloshing phenomena and slamming events.

Parametrically excited motion is caused by the nonlinear coupling of at least two DoFs, and mainly appear in pitch and/or roll. This coupling appears when the incident wave has a frequency of approximately twice the resonance roll/pitch frequency. This nonlinear effect is also known in the literature as a Mathieu-type instability [91], and has been investigated since the 60s in the offshore and shipping industries [92]. When a floating body is angularly displaced, its buoyancy centre moves and the body starts oscillating about a new reference point. This new point is known as the metacentre, and the distance between the metacentre and the centre of gravity is known as the metacentric height. The instability due to parametric motion is caused by the dynamic variation of the metacentre position, as a consequence of heave motion. Basically, the metacentric height becomes negative at some points during the simulation/experiment, which makes the object unstable, causing large roll/pitch motion amplitudes.

The sloshing phenomenon has been studied in ships and trucks transporting liquids, and is highly nonlinear. When a liquid is enclosed in a container and the liquid has a free-surface within that container, slosh dynamics refer to the movement of the liquid in the container, which can severely affect the overall system dynamics [93]. Hence, the sloshing effect is effectively restricted to OWC devices [94], where the sea water enclosed in the OWC can be considered as a slosh tank, or specific concepts with an internal fluid tank [95, 96].

Finally, slamming is the impact of a structure onto the free surface, which is very common in some WECs when the device rises from the free surface and subsequently impacts it. Impact events are typical under extreme conditions, which are beyond the scope of this thesis, but may also appear when operating within the *power production mode*, especially in devices where energy is extracted by means of a rotating motion. Slamming is a highly nonlinear phenomenon, for which key variables are the pressure magnitude, duration of the event and the spatial distribution of the impact [97].

2.2.2 Relevance of nonlinear effects

The relevance of nonlinear effects for WECs is discussed in this section. However, due to the wide variety of different WECs, based on diverse working principles, it is extremely difficult to analyse the relevance of nonlinear effects in general. Therefore, WECs are classified into four groups, based on the classifications presented in Section 1.1.2, with special attention paid to the relevance of different nonlinear effects:

- OWC,
- HPA,
- oscillating pitching converter (OPC), and

- OWSC.

Examples of each WEC group are given in Table 2.2. Overtopping devices, which form a group in all the aforementioned classifications and are shown in Figure 1.4, are omitted in this literature review due to their very particular working principle, described in Section 1.1.2. In fact, the overtopping phenomenon itself is extremely nonlinear, which can only be analysed by using fully nonlinear mathematical models. However, an empirical approach to estimate the time-varying overtopping discharge-rate [98]. The relevance of nonlinear effects for each WEC group is analysed in the following subsections.

2.2.2.1 Oscillating water columns

Oscillating water columns extract energy from the motion of the water column inside the device chamber. The behaviour of the free-surface inside this chamber is irregular and nonlinear [99]. Hence, the free-surface elevation modelled by linear approaches, such as the piston model used in commercial codes such as WAMIT [100], AQWA [101] or Aquaplus [102], may under- or over-estimate the free-surface elevation, and, as a consequence, pressure differential in the chamber [103, 104].

Apart from the water column, nonlinear effects are also relevant to WSHIs of OWC devices. Nonlinear FK forces are, for example, an important factor for floating OWC devices, as the variation of the entrained water mass in the chamber depends on the relative motion between the OWC device and the free-surface. Therefore, the pressure of the water mass inside the chamber and, as a consequence, the absorbed power can be more accurately computed when nonlinear FK forces are considered [105]. In addition, and related to nonlinear FK forces, parametrically excited motion can appear in floating OWCs, as shown in [106, 107].

Viscous effects are also important in OWCs. In onshore located fixed OWCs, waves arrive at the chamber with high components of turbulence and generate shedding vortices around the outer wall of the chamber. A similar phenomenon also appears in the case of floating devices. Zhang [94] demonstrates this phenomenon by simulating the fluid around and inside a fixed OWC converter, covering the whole cycle of vortex generation and free surface elevation, as illustrated in 2.4. These viscous effects can be analysed by using models that incorporate viscous effects automatically, as in [108], or by including them externally via a calibration process, where results from experiments or fully viscous simulations are utilised [109].

Finally, especially in the case of a floating oscillating water column, where a partially empty chamber is moving, a sloshing effect may appear [89]. Seakeeping software (*e.g.* WAMIT or AQWA), fail to accurately capture sloshing effects and, therefore, fully nonlinear modelling approaches become necessary [110]. Sloshing phenomena in floating structures create a non-uniform force field in the chamber, with direct consequences on the whole body dynamics and stability, as seen in [111].

2.2.2.2 Heaving point absorbers

Linear computation of FK forces can be accurate for small motion, or even in situations where the device behaves as a wave follower, but lose accuracy when the relative motion between the device and the free-surface increases. Therefore, considering only the nonlinear restoring force, that is, the static FK force, appears acceptable in some cases [112]. However, when the relative motion between the device and the free-surface is large enough, for example, when the device resonates due to a control strategy, the influence of nonlinear FK forces on the dynamics of the system becomes relevant [56], as shown in Figure 2.5.

Motion and absorbed power overestimation from linear models when the device is actively controlled to maximise energy absorption, illustrated in Figure 2.5, is further investigated in Chapter 3, where this overestimation of device motion is clearly demonstrated. In addition, Chapter 3

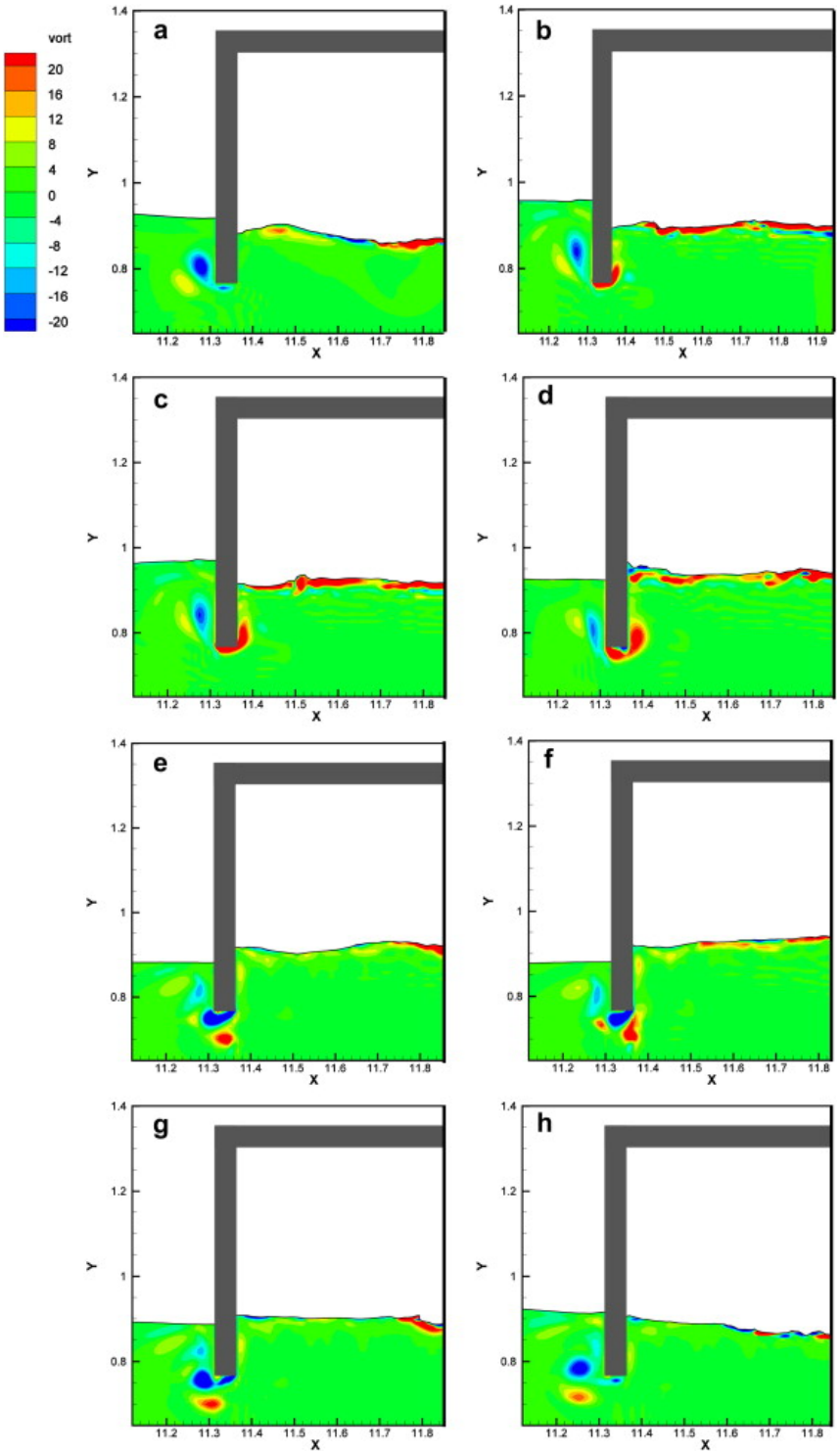

Figure 2.4: The cycle of the water-column behaviour within one wave period, [94]

demonstrates that the implementation of nonlinear restoring force alone, as in [112], can lead to unbalanced mathematical models that provide even lower accuracy than linear models. Finally, a geometric factor in the relevance of nonlinear FK forces is shown in Chapter 3, highlighting that nonlinear FK effects can be important, even for small and flat waves, in the case where the cross-sectional area is non-uniform, such as a sphere, while the linear model representation appears to be reasonable for the case where the cross-section is uniform.

In contrast, viscous effects appear to have a low influence in small HPAs [112–114]. Vortex shedding is generated by the motion of the body relative to the surrounding fluid, but this shedding

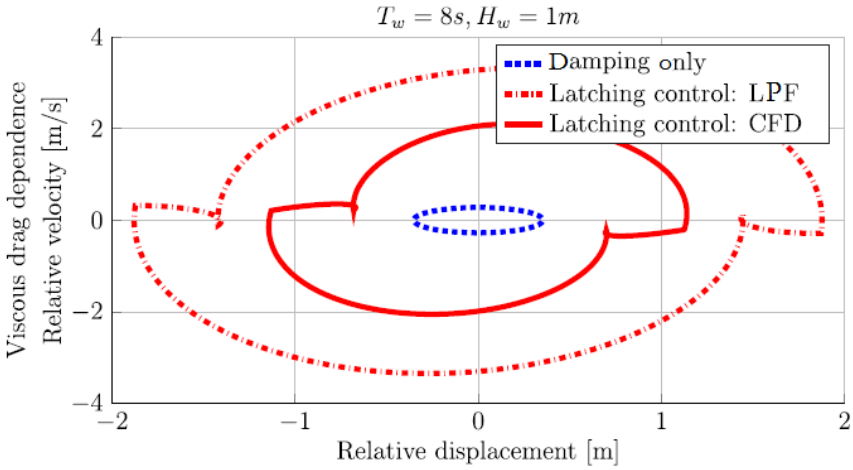

Figure 2.5: Operational space as a function of relative displacement and velocity for a spherical HPA for uncontrolled and controlled (via latching control) case evaluated with LPF and CFD [56]. The uncontrolled case is identical in both numerical models, for which only one curve (the dashed blue curve) is shown.

is not powerful enough, in general, to produce significant changes in the behaviour of the body and its power production capacity, as shown in Table 2.1. However, when the HPA is controlled via an relatively aggressive control strategy, such as reactive or latching control, viscous effects appear to gain relevance [56]. In addition, some two-body HPAs use a damping plate attached to the bottom of the central floater, which changes the hydrodynamic properties of the device by introducing extra damping (viscous damping) and increasing the added-mass [115]. As a consequence, the vortex shedding process is significantly enhanced in HPAs with damping plates. Hence, if a damping plate is included, the extra viscous damping should not be neglected [116]. In any case, Chapter 3 demonstrates that the FK force is the most relevant force for HPAs, meaning that nonlinear FK forces should be considered for an accurate representation of HPAs.

Due to the relevance of nonlinear FK forces in HPAs, parametrically excited motion can also be significant for HPAs that use more than one degree of freedom. For instance, self-reacting devices, are highly sensitive to the nonlinear coupling between heave, roll or pitch [117, 118].

2.2.2.3 Oscillating pitching converters

The nonlinear hydrodynamic behaviour of OPCs has been demonstrated in [57], where wave tank experiments show parametrically excited motion, as illustrated in Figure 2.6 for roll motion. Similarly to HPAs, the computation of nonlinear FK forces is crucial for OPCs, in order to predict these parametrically excited modes [57]. In addition, fast and large motion, typical in OPCs, encourage the formation of vortex shedding and other viscous effects. Therefore, viscous effects become important and lead to highly nonlinear effects, such as slamming events, which dissipate energy and limit the amplitude of the motion.

Such nonlinear behaviour can only be predicted by fully nonlinear models which include viscosity effects. Indeed, [57] shows that even fully-nonlinear models may not be able to accurately represent the behaviour of OPCs, including the nonlinear behaviour, unless the turbulence model is adequately tuned.

2.2.2.4 Oscillating wave surge converters

In the case of OWSCs, radiation and diffraction effects prevail over other forces [60], which suggests that the impact of nonlinear radiation and diffraction may not be negligible, as in OWCs,

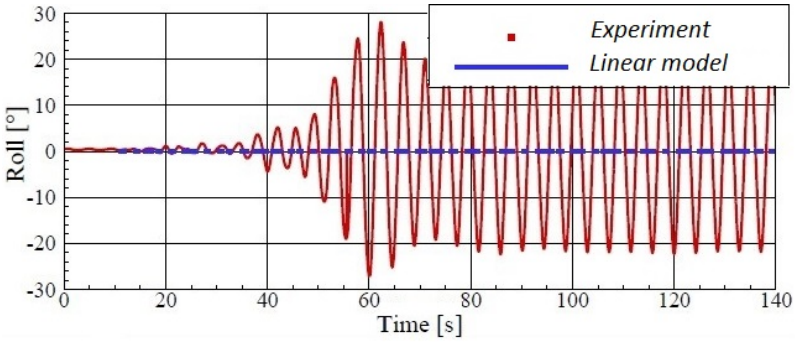

Figure 2.6: Nonlinear behaviour of the SEAREV device for large motion, where parametric roll is not captured by the linear model, modified from [57]

HPAs or OPCs. Although the number of studies in the literature that deal with nonlinear radiation/diffraction effects in OWSCs is rather scarce, a recent publication [119], using a nonlinear representation of radiation and diffraction effects, concludes that nonlinear radiation and diffraction effects could be more significant than viscosity effects in OWSCs.

In addition to radiation and diffraction effects, viscous effects also appear to be important for OWSCs. Different studies have analysed viscous effects in OWSCs, where strong turbulent vortices around the devices have been found, which have a significant impact on the motion of OWSCs [58]. Table 2.1 presents the impact of viscous effects on power production for OWSCs, where overestimation of the absorbed power by mathematical models that neglect viscous effects is demonstrated.

Table 2.1: Viscous effects and their impact on the power production, in terms of annual mean power production (AMPP) of HPAs and OWSCs. Table created with the data from [113] and [58].

WEC type	**Without viscous term**	**With viscous term**
HPAs	58 kW	56 kW
OWSCs	114 kW	74.4 kW

Slamming events in OWSCs are studied in [97, 120], demonstrating the need to satisfactorily capture the slamming phenomenon to accurately predict the behaviour of the device. Unfortunately, very little research has been carried out about slamming events in WECs, meaning that further investigation in required to fully understand, for example, the cause of the sudden plunge of the water level, in front of the device prior to the impact. In addition, due to the slamming phenomenon, a water jet is created as the device re-enters the water [121]. This water jet travels up the face of the flap and is finally ejected when the flap enters the water.

Table 2.2 summarises the relevance of the different nonlinear effects for each WEC group, providing literature references for each case. In addition, particular nonlinear effects that are important to consider in each WEC group are given.

2.2.3 Nonlinear modelling approaches

A critical classification of the existing modelling approaches to solve WSHIs is presented in this section. This classification is organised following, first of all, the physical theory the models are based on and, secondly, the way in which nonlinear effects are treated. Hence, the main existing models are divided into three groups: *Navier-Stokes and smoothed-particle hydrodynamics*, *potential flow models* and *parametric models*, in Sections 2.2.3.1, 2.2.3.2 and 2.2.3.3, respectively.

Table 2.2: A comparison of the impact of different nonlinear effects on different WECs.

WEC-type	Reference WEC	Particular effects	Relevance of nonlinear effects		
			Froude-Krylov	**Radiation/Diffraction**	**Viscosity**
OWC	Mutriku [25] SparBuoy [34]	Breaking waves Sloshing Parametric excitation	*High*: essential to account for the time-variant entrained water mass in the chamber [105] and predict parametrically excited motion [106, 107].	*Negligible*: nonlinear radiation and diffraction effects are negligible for devices much smaller than the wavelength [87, 88].	*High*: crucial to predict the vortex shedding at chamber walls [94], behaviour of the free-surface in the chamber [94] (sloshing phenomena [89, 110, 111]) and highly turbulent broken waves.
HPA	Wavestar [64] CETO [27] PowerBuoy [29]	Parametric excitation	*High*: crucial under large relative motion (*i.e.* under control), for reproducing devices' behaviour [56], including parametrically excited motion [117, 118].		*Low*: viscous effects are low in general [112, 113], but may become important for HPAs under aggressive control [56] or with damping plates [115, 116].
OPC	SEAREV [122]	Parametric excitation Slamming	*High*: essential to predict parametrically excited motion [57].		*High*: crucial to predict the vortex shedding on the edges and slamming events [57].
OWSC	Waveroller [123]	Slamming	*Low*: the contribution of FK forces is low in OWSCs [60, 114].	*N/A*: although dominated by radiation and diffraction forces [60, 114], the relevance of nonlinear effects is not proven.	*High*: crucial to predict the vortex shedding on the sides of the flaps [58] and slamming events [97, 121].

2.2.3.1 Navier-Stokes and smoothed-particle hydrodynamics

Navier-Stokes and smoothed-particle hydrodynamics (SPH) are both fully nonlinear mathematical modelling approaches. The main difference between the two options is the domain discretisation method: mesh-based in CFD and mesh-free in SPH. In addition, another important difference between CFD and SPH models is the way they deal with viscous effects. CFD uses turbulent models, described in Section 2.2.3.1.1, while viscous effects in SPH cannot be accurately considered.

The behaviour of a fluid is analysed by solving a set of differential equations known as the Navier-Stokes equations. The fundamental basis of almost all problems are governed by the transfer of mass and momentum (Navier-Stokes equations), described by the following equations: the continuity equation (2.2) and the equation of motion (2.3):

$$\frac{\partial \rho_w}{\partial t} + \bigtriangledown(\rho_w v) = 0, \tag{2.2}$$

$$\frac{\partial v}{\partial t} + (v\bigtriangledown)v = -\frac{1}{\rho_w} \bigtriangledown p_f + F + \frac{\mu}{\rho_w} \bigtriangledown^2 v, \tag{2.3}$$

where $v(x,y,z)$ is the fluid flow velocity vector, p_f the pressure field, F the external force per unit mass and μ the fluid viscosity.

However, Equations (2.2) and (2.3) cannot be solved analytically, and so numerical discretisation is necessary to obtain a solution. It is at this point that computational codes must be employed to implement the complete Navier-Stokes equations. The phenomenon to be simulated, the computation capacity of our machine and/or the fidelity requirement drive the decision between the different approaches.

In the case of wave energy, wave tank experiments or open water tests can be implemented in NWTs [124]. These simulations have been used for decades in offshore and ocean engineering for fluid-body interaction analysis.

2.2.3.1.1 Computational fluid dynamics

Computational fluid dynamics software solves the Navier-Stokes equation by numerically discretising space and time. The main issue when modelling WECs, using CFD, is the presence of a free-surface, dividing the domain into two phases: air and water. Specific free-surface modelling techniques have been developed, which can be classified into two main categories [125]: fitting methods (also known as tracking methods) [126] and capturing methods [127]. Tracking methods model the free surface as a sharp boundary [128], while interface-capturing methods include water and air in the mesh, adopting either the volume of fluid (VOF) method [129] or the level-set formulation [130]. Free surface capturing methods are more common in hydrodynamic applications [131], mainly because they are more robust, since remeshing is not required. Further details on numerical CFD discretization methods are given in [132].

In wave energy, especially in real devices, the flow is considered turbulent, which suggests the use of the Reynolds decomposition of the fluid velocity. The Reynolds decomposition consists of decomposing instantaneous quantities into time-averaged and fluctuating quantities. Therefore, Navier-Stokes equations become Reynolds-Average Navier-Stokes (RANS) equations, giving approximate time-averaged solutions to the Navier-Stokes equations. Reynolds-Average Navier-Stokes is the most widely used method, due to the high computational requirements of other methods like large eddy simulation (LES) or direct numerical simulation (DNS).

In order to produce a closed system of solvable equations, RANS equations require a turbulence model. The two most common turbulence models are the two-equation $k-\varepsilon$ [133, 134] and the $k-\omega$ models [134], where k refers to the turbulent kinetic energy, ε represents the dissipation of the turbulence kinetic energy and ω is the turbulence frequency. The $k-\varepsilon$ model is more robust and computationally cheaper, but performs poorly under severe pressure gradients, while the $k-\omega$ model shows superior performance under adverse pressure gradients and separation,

although separation is typically exaggerated and predicted too early. Shear stress transport (SST) turbulence models have also been suggested, using $k-\varepsilon$ away from walls and the $k-\omega$ near walls [55, 135]. Although the SST model is stated to be more appropriate for separated flows, giving highly accurate predictions of the onset and the amount of flow separation under adverse pressure gradients [136], [135] concludes there is a week dependency on changes in the turbulence model. A complete comparative study of the different turbulence models can be found in [137].

In addition, [138] presents the main advantages and drawbacks of using CFD methods in the design process of a WEC, with the main weakness being the high computational requirements. In addition, wave energy specific literature survey on CFD modelling approaches can be found in [139].

2.2.3.1.2 Smooth-particles hydrodynamics

Smooth-particles hydrodynamics is a purely Lagrangian meshless interpolation method that can approximate continuous field quantities and their derivatives by using discrete sample points, known as smoothed particles [140]. These discrete elements, or particles, are transported with the local velocity and they carry the information of the field, such as mass, pressure and density.

Thus, the fields are only defined at these discrete points. In order to define continuous fields, smoothing kernel functions (or weighting functions) are used, which specify the contribution of a typical field variable at any position. This means for example, that pressure at any position (r) depends on the pressure of all the particles within a radial distance h, also known as smoothing length.

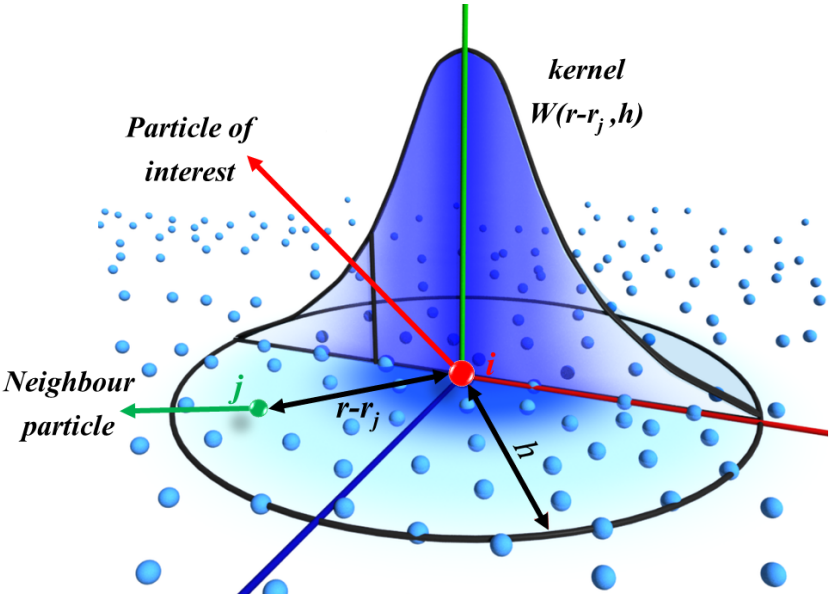

Figure 2.7: The principle of the SPH kernel function, modified from [141].

The contribution of all the particles within this radial distance to a property of the particle being analysed is not equal. This contribution is weighted relative to the distance between the analysed particle and the contributor particle ($r-r_j$) and their density. This is mathematically governed by the kernel function, illustrated in Figure 2.7. As a consequence, the field variable is known at a discrete set of points (N_{SPH}) within this radial distance and can be defined as follows:

$$A(r) = \sum_{j=1}^{N_{SPH}} \frac{m_{p,j}}{\rho_{p,j}} A(r_j) W(r-r_j,h), \tag{2.4}$$

where $A(r)$ could be any field variable at any position r, m_p the mass and ρ_p the density associated with the particle, and W is the kernel function.

Two main variables need to be selected for each specific problem: the smoothing kernel and the smoothing length. Several smoothing kernels have been used in the literature, such as the Gaussian kernel [142], the q-spline kernel [143], the 6th order polynomial kernel [144] or the quintic Wendland kernel [145]. The quintic Wendland kernel is the most commonly implemented kernel for wave energy applications [97, 146–148], probably because it was found to give the best compromise between accuracy and computation [149]. On the other hand, the smoothing length can be fixed in space and time or can be assigned to each particle and make it vary in time, adapting the resolution of the simulation depending on the local conditions of the area where that particle is located. This adaptability is comparable to the adaptive mesh refinement (AMR) codes in grid-based methods and can be introduced via two different methods: changing a particle's smoothing length or dividing the particle into 'daughter' particles, with smaller smoothing lengths.

Different SPH techniques may be implemented, as shown in [150], depending on the characteristics of the flow and the problem to be studied. SPH was originally developed for astrophysics [151], but has been applied to diverse applications [140, 152], including marine environment hydrodynamic problems [143] and, more specifically, hydrodynamic interactions in the presence of a free-surface [153]. The interpolation of the smoothing kernel outside the boundary may lead to inconsistent behaviour of the system [154], and so may require special treatment. Other alternative particle methods, such as the moving-particle semi-implicit method [155] or the consistent particle method [156], have also been suggested in the literature, but have never been implemented in a wave energy problem, to the best knowledge of the author.

In SPH, two main approaches are available to calculate the pressure: the weekly compressible SPH (WCSPH) and the incompressible SPH (ISPH). In wave energy applications, the WCSPH method has been typically used [97, 146, 157–159], although the ISPH method has also been implemented [147, 148] in order to reduce the pressure oscillations (pressure noise) typical of WCSPH.

Most of the studies using SPH in wave energy applications are focused on extreme events [97, 147, 148, 159], where the SPH can have significantly greater fidelity than CFD. However, such extreme events are beyond the scope of this thesis. When SPH has been implemented to study WECs' behaviour under operational conditions, results showed good agreement with experimental results.

2.2.3.2 Potential flow models

Potential flow theory describes the velocity flow as the gradient of the velocity potential ($\Phi(x,y,z)$). Thus, the pressure of the total incident flow acting on the body (p_{WSHI}) can be obtained by deriving Φ in Bernoulli's equation as follows,

$$p_{WSHI} = -\rho_w g x_{abs} - \rho_w \frac{\partial \Phi}{\partial t} - \rho_w \frac{|\nabla \Phi|^2}{2}, \tag{2.5}$$

where $\rho_w g x_{abs}$ is the hydrostatic pressure applied on the body. Further details concerning the assumptions considered in the LPF theory and the derivation of the equations of motion that describe the behaviour of a floating body are provided in Chapter 3.

2.2.3.2.1 Linear potential flow model

Analysing the linear approximation of the WSHI, the governing equation based on Newton's second law, previously presented in Equation (2.1) for the general case, can be described as:

$$M\ddot{x}_{abs} = F_g - \int_{S(t)} p_{WSHI} n \, dS, \tag{2.6}$$

where $S(t)$ is the instantaneous wetted surface and n the unit vector normal to the absorber's surface. However, $S(t)$ is approximated using the mean wetted surface ($\overline{S}$) in the LPF model,

where the quadratic term shown in Equation (2.5) is neglected. Therefore, the governing equation presented in Equation (2.6) is developed as follows:

$$M\ddot{x}_{abs} = -K_H x_{abs} + \int_{-\infty}^{\infty} K_{ex}(t-\tau)\eta_w(0,0,\tau)d\tau - \mu_\infty \ddot{x}_{abs} - \int_{-\infty}^{t} K_{rad}(t-\tau)\dot{x}_{abs}(\tau)d\tau, \qquad (2.7)$$

where K_{ex} is the excitation force kernel and K_H the hydrostatic stiffness, which represents the relationship between F_g and the buoyancy force. The radiation force is expressed as a convolution product based on the Cummins' equation [86], where μ_∞ is the added mass coefficient at infinite frequency and K_{rad} the radiation impulse-response function.

2.2.3.2.2 Multi-linear potential flow model

Multi-linear models based on LPF theory (mLPF) provide an alternative to LPF models. These mLPF models consist of multiple linear models, where each of these linear models is designed to represent the behaviour of the absorber at a different operational point. That way, the whole operational space can be covered by adequately combining different LPF models. For the specific case of wave energy applications, a pioneering work is presented in [160] for OWSCs. In this case, the model structure is the same as in Equation (2.7) and remains the same over the whole operational space. Only the parameters of the model vary with the position of the device. In [160], the only parameter that varies, depending on the position of the OWCS, is the K_{ex}, but an extension of this work could be carried out varying the parameters corresponding to the radiation force, *i.e.* μ_∞ and K_{rad}. The same approach is applicable to any type of WEC.

2.2.3.2.3 Partially-nonlinear potential flow model

The partially-nonlinear potential flow (pNLPF) model is essentially an extension of the LPF model. The pNLPF maintains the same structure as the LPF, but modifies the linear description of specific forces to include nonlinear effects. Two main extensions are found in the literature, where the first extension considers nonlinear FK forces and the second one allows a more precise computation of radiation-diffraction forces. One of the first contributions to pNLPF models is presented in [161], where the two extensions are analysed for the SEAREV device. The same approach is then adapted to a two-body HPA [87] and a single-body heaving sphere [88].

The extension to include nonlinear FK forces is implemented by integrating p_{WSHI} over the *instantaneous* wetted surface of the absorber, as in Equation (2.6). However, quadratic terms of p_{WSHI} are neglected in this case, meaning that all the forces except the FK force remain linear. The efficacy of this partially-nonlinear extension is extremely sensitive to inaccuracies in the instantaneous wetted surface. With a fixed mesh for the absorber, the panels on the boundary of the free-surface can be partly submerged and partly out of the water, leading to a misestimation of the instantaneous wetted surface and, as a consequence, the FK force. Therefore, different strategies to accurately estimate the wetted surface at each time-step are presented in the literature. A fixed but fairly fine mesh is utilised in [57], considering only those cells below the instantaneous free-surface at each time-step. On the other hand, [57, 87, 88] use a remeshing routine, modifying those cells of the mesh which are partly submerged and partly out of the water. Both strategies are compared for the same device and the same simulation conditions in [57], where both strategies show an accurate estimation of the wetted surface at each time-step. However, the technique using a fixed, but fine, mesh seems to be computationally more efficient.

An alternative method to compute FK forces over the instantaneous wetted surface is suggested in [162], based on an algebraic solution, which substantially reduces computational requirements. The pNLFK model is thoroughly evaluated in Chapter 3 for a HPA, using both the remeshing routine and the algebraic solution, highlighting the advantages and disadvantages of both methods.

A second extension of the LPF model, considering a more accurate computation of radiation and diffraction forces, is also included in this literature review. There exist two different

approaches: expanding the forcing terms around the mean wetted surface or directly expanding the equation for hydrodynamic force. The expansion to second order is carried out in two steps, where the linear hydrodynamic force is developed to second order in the first step and the quadratic terms in Bernoulli's equation are added in the second. This nonlinear extension requires a recalculation of the hydrodynamic parameters at each sampling instant, resulting in a high computational overhead.

However, it should be considered that the pNLFK approach in theoretically inconsistent and, thus, requires a comprehensive validation in order to gain confidence on the approach.

2.2.3.2.4 Weakly-nonlinear potential flow model

While the pNLPF method aims to extend the LPF method maintaining the same structure as the LPF method, the approach pursued by the so-called weakly-nonlinear potential flow (*wNLPF*) method is to simplify the fully-nonlinear potential flow (*fNLPF*) formulation.

An option for wNLPF models is to perform a perturbation expansion of the equations describing the interactions between waves and structure with respect to the wave steepness (kA), where the boundary conditions are approximated by their Taylor expansion. The perturbation method solves the WSHI for the lowest degree of steepness and uses the results as an input for the higher terms. Typically, a second order approximation is used, where the (linear) solution in kA is used to solve for $(kA)^2$. Different codes which use a second order approximation, are able to more effectively describe the diffraction and the excitation problem [163, 164].

An alternative approach to simplify the fully-nonlinear problem is the weak-scatter approximation [165], which assumes the perturbation potential (composed by radiation and diffraction potential) small, compared to the incident potential. Such an approximation is valid for bodies whose characteristic dimension is much smaller than the wave length. The boundary value problem (BVP) is then solved iteratively on the exact free surface elevation and the instantaneous wetted surface. This weak-scatter approach is applied in [166] to a submerged body constrained to move only in heave, where different schemes are integrated to capture the motion of the submerged body by adapting the mesh. More recently, [119] presents a new flow solver based on the weak-scatter approach, which is compared to the LPF method, providing identical results under linear conditions (differences between the wNLPF and LPF methods being lower than 1%), but large differences under nonlinear conditions with large body motion and wave steepness.

2.2.3.2.5 Fully-nonlinear potential flow model

When sea conditions exceed the operational limits of power production mode, any simplification of the complete model becomes unacceptable, and the only way to describe the response of the device in extreme conditions is to consider all the nonlinearities. In spite of the neglected viscous, green water, slamming or sloshing effects, *fNLPF* models seem to provide accurate results even in extreme conditions thanks to the calculation of the exact instantaneous boundary conditions. Therefore, *fNLPF* models have been used effectively to simulate NWTs in 2D by Guerberg [167, 168] and, in 3D, by Grilli [169].

Weakly- and fully-nonlinear potential flow models are both in an early stage of development, so further research is necessary to extract more definitive conclusions, particularly for wave energy applications. However, [170] presents a comparison of *wNLPF* and *fNLPF* by analysing a fully submerged cylinder, and concludes that both methods give good agreement on hydrodynamic coefficient values. Although the low complexity of the analysis is recognised, *i.e.* a fully submerged cylinder, [170] remarks that expectations have been met with both methods. A final table summarising the main characteristics of each method in [170] highlights the much higher computational requirements of the fully nonlinear method.

Other approaches which consider nonlinear effects have combined CFD and potential flow methods (PF-CFD). The SWENSE method presented in [171] is one of the existing codes in this sense, used in [172] to simulate the CALM buoy and in [57] to study the behaviour of the SEAREV

device. Two main challenges, *i.e.* the development of numerically stable two-phase equations and the mapping of the potential flow solver to the CFD grid, are recently identified for the development of the SEWENSE method [173]. However, [174] demonstrates the capabilities of the SWENSE method, where a novel formulation is presented to solve two-phase problems, showing significant improvement in accuracy and stability compared to conventional two-phase VOF solvers. In [175], a fully nonlinear potential flow solver was combined with a fully nonlinear Navier-Stokes VOF solver by an efficient and geometrically flexible one-way coupling method. Different tests for surface piercing circular cylinders were simulated, showing good agreement between the code and experimental results. Another alternative was presented in [176], coupling a linear BEM code, NEMOH [177], with a finite element analysis (FEA) tool, CodeAster, to analyse numerical vibration of an oscillating surge converter. Hydrodynamic coefficients, with a special focus on the added mass, are first computed by a linear BEM method for different rates of immersion and then used in numerical vibrational analysis, considerably reducing the required computational effort. Results obtained from the coupled methodology are compared to experimental results, returning good results and proving its functionality.

2.2.3.2.6 Viscous effects in potential flow model

Viscous effects are neglected by all potential flow models, as the fluid is considered inviscid. However, their relevance has been demonstrated in Table 2.2 for different WECs, which suggests that viscous effects should be externally included. There exist two main methods to externally include viscous losses into potential flow models: using an additional linear damping term or through the Morison equation [178], using a quadratic viscous term. The most widely used method in wave energy, and other offshore applications, is the Morison form expressed as follows:

$$F_{vis} = -\frac{1}{2}\rho A_{cs} C_{drag}(\dot{x}_{abs} - \dot{\eta}_w) \mid \dot{x}_{abs} - \dot{\eta}_w \mid, \tag{2.8}$$

where A_{cs} is the cross-sectional area and C_{drag} the viscous drag coefficient. Thus, the LPF model with viscous effects included, following Equation (2.8), is referred to as *viscLPF*.

The true nature of viscous drag is nonlinear, and can only be identified when using wave tank experiments [57, 106, 121, 179] or fully viscous modelling methods that are generally based on Navier-Stokes equations: NWT simulations implemented in CFD codes [58, 113] or some other specific hydrodynamic codes [57, 108].

Drag coefficient values used in different studies come from offshore industry publications [180], identification procedures utilising fully nonlinear methods [58, 113] or experimental tests [181, 182]. However, discrepancies between different studies lead to uncertainty in the correct drag coefficient. As an example of the uncertainty, drag coefficients for OWSCs found in the literature can vary from 1.9 [58] to 8 [183]. The uncertainty and inconsistency of C_{drag} is confirmed in [184], highlighting the infeasibility of a single representative C_{drag} for all the different operational conditions. In addition, [184] concludes that the viscous model is usually used to cover other modelling errors, apart from viscous effects. Finally, [184] suggests that "it is preferable to choose a larger rather than smaller" C_{drag} in the case of uncertainty, since the inaccuracies derived from overestimated C_{drag} coefficients are lower than the inaccuracies which arise from underestimated C_{drag} coefficients. The inconsistency of the Morison equation and the C_{drag} coefficient, and their impact on the performance of WECs estimated via BEM-based hydrodynamic models, are also demonstrated in Chapter 7.

2.2.3.3 Parametric models identified from data

Sometimes, the physical system being analysed is so complex that it can be practically impossible to create a model which includes all the components that comprise the 'system', or needs a mathematical model with excessive computational requirements.

In such cases, alternative modelling approaches, successfully tested in other fields, can be used. Parametric models identified from data (*ParaM*) are well established, for example, in the control systems community, where complex models are determined from input/output (u/y) data. Hence, the model is based on the data, rather than the physical process, as in the case of conventional models. System identification models use statistical methods to build mathematical models of dynamic systems from measured data, which is particularly interesting for very complex systems, where the physical principles are too complicated to formulate.

The identification procedure comprises:

- conducting a series of representative tests on the 'system',
- selecting a series of representative data of the 'system' to be reproduced,
- determining the structure of the model (model type and order, nonlinear terms, etc.),
- defining the fitting criteria, and
- using numerical optimisation to identify the system parameters.

Thus, there are three key elements in system identification: the representative data, the model structure and the identification algorithm.

Using representative data of the system dynamics, that entirely covers the whole range of frequencies/amplitudes the system is likely to deal with, is crucial. In the particular case of hydrodynamic applications, such data can be obtained from wave tank experiments [185, 186], or from NWT simulations implemented in BEM or CFD codes [187–189]. Numerical wave tank simulations have certain advantages compared to experimental tests, since intermediate variables, such as fluid force, can be measured. In addition to access, measurements are accurate in NWT simulations (within the numerical precision of the computing hardware and the numerical model), since there is no reflection effect or measurement noise, as in experimental tests. The main disadvantages of NWT simulations are the heavy computational requirement and the uncertainty of the results' accuracy, for which previous model validation is recommendable.

In order to generate adequate data for the identification of model parameters, various experiments can be carried out to provide data related to different characteristics: free decay tests (no external input) [188], tests with input waves (free surface elevation as input) [190], tests using external forces (*e.g.* PTO force) as inputs [189] or prescribed motion tests [187].

Once the data is generated, the structure of the model must be determined, which is probably the key point in order to create a representative model. The majority of system identification techniques are based on discrete-time models [191], which can be of very diverse form. The choice of the model structure essentially depends on the features of the system.

If the system to be modelled is considered linear, an autoregressive with exogenous input (ARX) model can be suitable [188]. In order to capture nonlinear effects, nonlinear autoregressive with exogenous input (NARX) models are suggested [192]. Figure 2.8 illustrates a general block diagram for NARX models, where n_a and n_b represent the order of the model, and n_d the input delay.

There are several candidate model structures, g[ ] in Figure 2.8, from a structure based on the knowledge of the physical principals of the system (grey-box) to a structure completely ignorant of these principals (black-box) [191]. Apart from the model structure, the way to analyse nonlinearities (the form), and its complexity, need to be selected. ARX, Hammerstein/Wiener and Feedback block-oriented models have already been analysed for wave energy applications [187, 188]. The Hammerstein and feedback block-oriented models are nonlinear in u/y relationship, but linear in the parameters. While the ARX model is unable to capture nonlinear behaviour, both Hammerstein and Feedback block-oriented models show good agreement in reproducing the response of the data containing significant nonlinear behaviour.

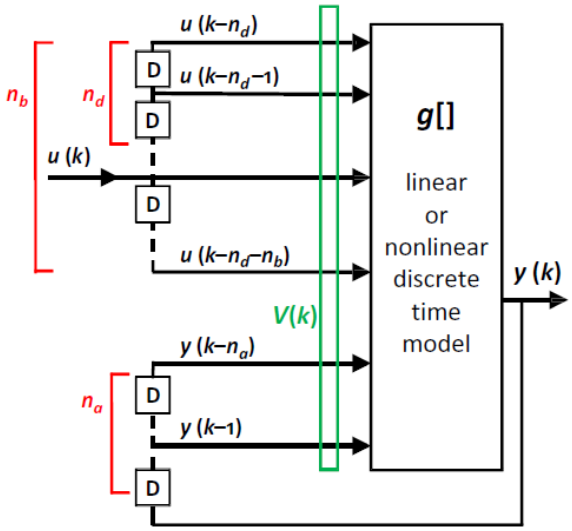

Figure 2.8: Block diagram of a general NARX discrete-time model.

Other alternatives tested for wave energy applications include the Kolmogorov-Gabor Polynomial (KGP) model in [193], which is a black-box model that uses polynomial nonlinearities to describe the u/y relationship of the data [192]. KGP structures with a low polynomial order (order 2) show good agreement with the data generated in a NWT, while higher-order polynomials are shown to perform better in training than in validation, which suggests overfitting. Overfitting is a common problem in system identification and shows the importance of parsimoniously selecting the structure of the models.

Finally, artificial neural networks (ANNs) have also been suggested in the literature for wave energy applications [189, 194]. There exist a variety of ANN structures. However, the complexity of these structures, which are nonlinear in u/y relationship and in the parameters, may lead to complex identification processes, since local minima can be found in the parameter optimisation problem, which can strongly affect the performance of ANNs [189].

Similarly to Table 2.2, a summary of the different modelling approaches reviewed in Section 2.2.3 is shown in Table 2.3, where the fluid and hydrodynamic models, the expected accuracy and computational cost, and the main advantages and drawbacks of each method are evaluated. The ratings included in Table 2.3 are relative ratings, where $+++++$ is the best rating and $-----$ the poorest. It should be noted that all the characteristics are not applicable to all the methods, *e.g.* the ANN model does not use any fluid or hydrodynamic model, which is denoted by using the N/A abbreviation that means 'not applicable'. In addition, the capabilities of *ParaM* models are still untapped due to the lack of comprehensive validation. Therefore, the **Accuracy** column in Table 2.3 reads N/I for *ParaM* models, which means 'not enough information'.

2.3 *Transmission* stage

The conversion from wave-induced mechanical motion into useful mechanical energy can be carried out by means of different technologies. The main challenge for the technologies to be implemented in the transmission stage, is to reliably and efficiently convert the power absorbed by the absorber, dealing with extreme variations between maximum power peaks and average power flow (which can be higher than a factor of 10).

Table 2.3: A comparative study of the different numerical modelling approaches for wave energy converters evaluated in Section 2.2.3.

	Modelling Approach	Fluid model	Hydrodynamic model	Accuracy	Computation	Main Advantages	Main Drawbacks
Navier-Stokes SPH	CFD	Viscous fluid	RANS	++++	− − − −	Flow field considered entirely	Computationally expensive Dynamic mesh complexity
	SWENSE IHVOF		RANS	+++++	− − −	Lower computation for CFD-similar fidelity	
	SPH	N/A*	SPH	++++	− − − − −	Meshless approach	Computationally prohibitive
Potential flow	Partially nonlinear	Perfect fluid	Linear BEM Instantaneous FK	++/+++	−−	Computationally beneficial	Viscous effects neglected
	Weakly nonlinear		Nonlinear BEM	+++	− − −	Nonlinear boundary conditions	Computationally expensive Viscous effects neglected
	Fully nonlinear		Nonlinear BEM	+++	− − −	All potential-flow nonlinearities included	
	Viscous drag	Empirical viscosity	Linear/Nonlinear BEM	Improves inviscid BEMs	Same as BEM	Computationally convenient	Drag coefficient uncertainty
Models from data	Hammerstein	N/A*	N/A*	N/I** (data dependent)	−	Linear in parameters Physical meaning available (Grey-box)	Model rigidity
	Feedback block-oriented				−		
	KGP				−	Linear in parameters	No physical meaning (Black-box)
	ANN				−	Model flexibility	Nonlinear in parameters No physical meaning (Black-box)

*N/A means not applicable.
**N/I means not enough information for evaluation.

2.3.1 Pneumatic transmission system

Pneumatic transmission systems are implemented in OWCs, either fixed (*e.g.*, the LIMPET shoreline plant [195], the PICO power plant [196], the Mutriku wave power plant [25] or the recently built Yongsoo plant [62]), or floating converters (*e.g.*, the BBDB converter [197, 198], the Mighty Whale concept [199] or the Oceanlinx converter [62]). The interaction between ocean waves and the air trapped in the OWC chamber, illustrated in Figure 2.9, is studied using thermodynamic relations, to determine the evolution of the air mass in the chamber and the air flow through the turbine.

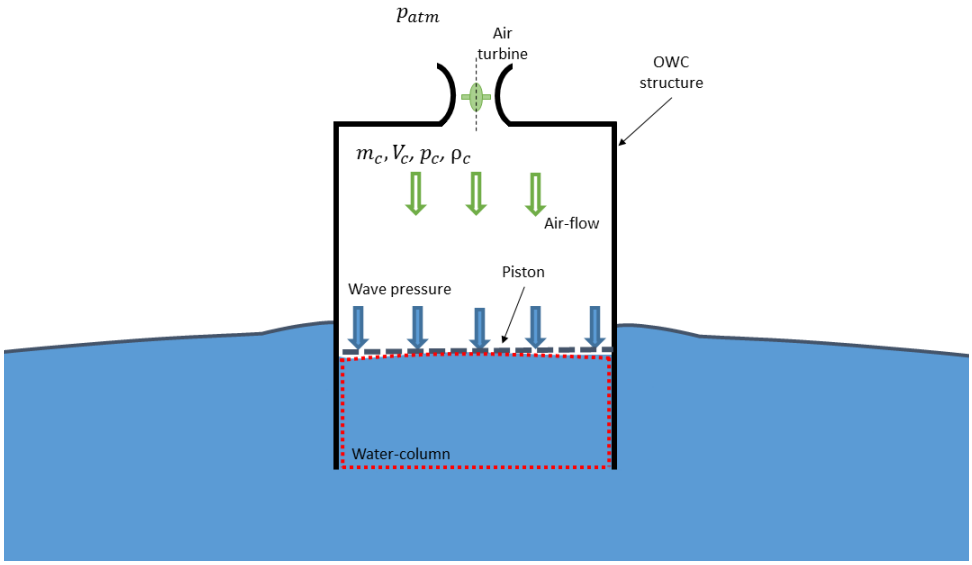

Figure 2.9: Schematic representation of OWC devices, including the water column, turbine and the horizontal piston that represents the air-water interface in the piston-model approach.

The compressibility effect in the chamber is important in OWC devices, especially in full-size OWC converters [62], which is very often modelled utilising a simple isentropic relationship between the pressure (p_c) and density (ρ_c) of air in the OWC chamber [200–202], as

$$\frac{p_c}{\rho_c^{\gamma_a}} = \frac{p_{atm}}{\rho_{atm}^{\gamma_a}}, \tag{2.9}$$

where γ_a is the specific heat ratio of the air ($\gamma_a = 1.4$), and p_{atm} and ρ_{atm} the pressure and density of atmospheric air. The assumption of an isentropic process in the chamber is reasonable, since the heat exchange in the chamber during a wave cycle is considered to be small [203].

Therefore, the pressure in the chamber can be given [204], as follows:

$$\Delta\dot{p}_c = -\gamma_a p_c \frac{\dot{V}_c}{V_c} - \gamma_a p_c^{\kappa} \frac{(p_{atm})^{\frac{1}{\gamma_a}}}{\rho_{atm}} \frac{\dot{m}_t}{V_c}, \tag{2.10}$$

where V_c is the air volume in the OWC chamber, m_t the air mass flow through the turbine and $\kappa = \frac{\gamma_a - 1}{\gamma_a}$. Hence, V_c is proportional to the displacement of the water column, and $\dot{V}_c$ is proportional to the velocity of the water column.

Air mass flows in (inhalation) and out (exhalation) of the chamber through the air turbine. When $p_c > p_{atm}$, air in the chamber is pressurised and is exhaled from the chamber. In contrast, when $p_c < p_{atm}$, air is depressurised in the chamber and is inhaled into the chamber.

The density of air can change during inhalation and exhalation phases, due to compressibility. Therefore, the air mass flow rate should be considered differently for inhalation and exhalation, using ρ_{atm} for inhalation and ρ_c for exhalation [203, 205].

The pressure difference, created in the chamber by ocean waves, drives the air turbine located at the top of the OWC structure. The most widely used method for modelling air turbines is based on dimensional analysis [203, 206–208], where the dimensionless flow and power are given as a function of the dimensionless pressure head [209],

$$\Phi = f_{\Phi}(\Psi), \qquad \Pi = f_{\Pi}(\Psi), \tag{2.11}$$

where

$$\Psi = \frac{\Delta p_t}{\rho_{ref} \omega_t{}^2 D_t{}^2}, \tag{2.12}$$

$$\Phi = \frac{\dot{m}_t}{\rho_{ref} \omega_t D_t{}^3}, \tag{2.13}$$

$$\Pi = \frac{P_t}{\rho_{ref} \omega_t{}^3 D_t{}^5}, \tag{2.14}$$

and Δp_t, ω_t and D_t are the pressure drop across the turbine, the rotational speed and diameter of the turbine, respectively, ρ_{ref} is the reference density, measured at stagnation inlet conditions (when velocity of the fluid is zero and static pressure is at its maximum value), P_t the turbine power output and Φ, Ψ and Π are the dimensionless flow rate, pressure head and the aerodynamic torque or turbine power output, respectively. However, it should be noted that, under normal operating conditions, Reynolds and Mach number effects can be ignored, and the air flow through the turbine is considered to be incompressible [203].

Different options to model the air turbine have been presented in the literature [62, 210], such as turbine induced damping. In general, a linear relationship between chamber pressure and air mass flow is used for Wells turbines, via Equation (2.15), and a nonlinear relation for self-rectifying impulse turbines, via Equation (2.16),

$$\Psi = K_1 \Phi, \tag{2.15}$$

$$\Psi = K_2 \Phi^l, \tag{2.16}$$

where the constants K_1 and K_2 depend only on the turbine geometry, if Reynolds and Mach number effects are neglected, and typically $1.5 \leq l \leq 2$.

Although conventional turbines can be used in OWC devices, the reciprocating motion of ocean waves requires a rectifying system, since reciprocating unidirectional turbines have been proven to be impractical in large OWC plants [62, 210]. Therefore, different self-rectifying air turbines were developed for OWC devices, which can be divided into two main turbine categories: Wells turbines [211] and impulse turbines [212], shown in Figures 2.10 (a) and (b), respectively. Other turbine configurations have also been suggested, such as the modified Wells turbines [18], the Dennis-Auld turbine [213, 214] or the recently developed bi-radial turbine [215]. Falcão [210] presents a good overview of the different air turbine configurations for OWC converters and their main characteristics.

A comparison between Wells, axial-impulse and bi-radial turbines is shown in Figure 2.10 (c), where the efficiency of the different turbines (η_t) is shown against flow rate. The operational flow range of axial-flow impulse turbines is wider compared to the range of Wells turbines, since the efficiency of Wells turbines drops sharply when stalling occurs at rotor blades [216].

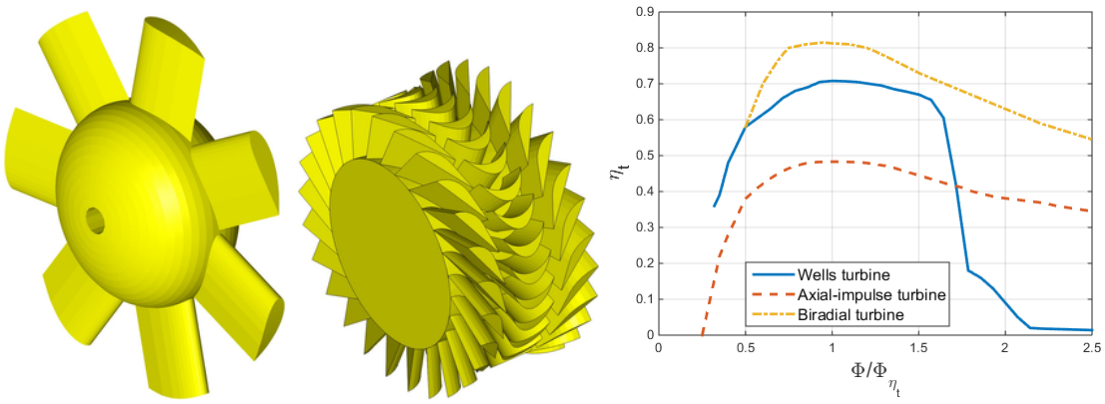

(a) (b) (c)

Figure 2.10: Two self-rectifying axial turbines, Wells turbine without guide vanes (a) and impulse turbine (b), and the efficiency of Wells turbines, axial-impulse turbines and bi-radial turbines plotted against the flow coefficient ratio Φ/Φ_{η_t} (c), where Φ_{η_t} expresses peak efficiency conditions, adapted from [210] and [62].

2.3.2 Mechanical transmission system

Mechanical transmission systems may be one of the best known transmission technologies due to their application in several different but acknowledged industrial sectors, such as the automotive industry. Nevertheless, due to the reciprocating motion of WECs, traditional mechanical transmission systems may not be adequate. Different conventional mechanical transmission mechanisms, such as rack and pinion, ratchet wheel or screw mechanisms, have already been suggested for use in WECs.

2.3.2.1 Rack and Pinion Mechanism

The well-known rack and pinion mechanism has inspired many different patents for wave energy conversion, where the difference between the patents is basically the rectification system facilitating unidirectional rotation of the generator, irrespective of the direction of motion of the absorber. Figure 2.11 illustrates two different mechanisms based on a rack/pinion assembly.

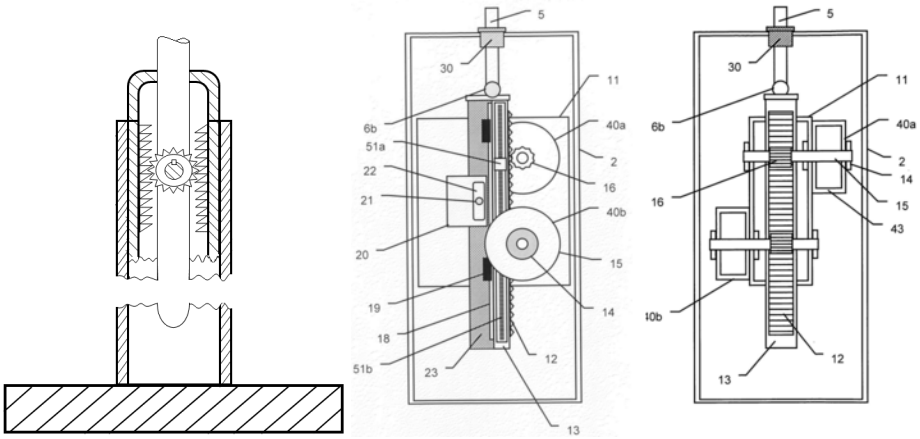

(a) (b)

Figure 2.11: Rack and pinion mechanisms: (a) double rack system adapted from [217] and (b) double pinion system, reproduced with kind permission from Ocean Power Technologies as published in their US Patent US 8487459 B2, 14 April 2011 [218].

The CorPower point absorber [219] converts the linear motion into rotation by using a cascade gear box, based on a rack and pinion system, as presented in [220]. The efficiency of rack and pinion mechanisms is one of the main advantages of this technology, up to 97% [221], while the biggest challenge is the relatively short lifetime.

2.3.2.2 Winch-based system

A winch-based system is a mechanical transmission mechanism which can convert linear motion into rotation. This rotation is bi-directional, but can be rectified with a rectification system. Some systems consist of a rope connected to the absorber on one end, and wound on a winch on the other. That way, the linear motion of the buoy is converted into the rotation of the winch that drives the gearbox, realised as a winch-based system, which in turn drives the electric generator.

Such a winch-based system has been suggested, for example, for the Lifesaver WEC [222]. In this case, the rectification is realised by means of a gearbox, based on a belt drive system, which only produces energy during the upwards motion of the absorber, while operates in motor mode during the downwards motion of the absorber, to wind the rope on the winch. The design of the mechanical PTO is shown in Figure 2.12 (a). This innovative system splits the gearbox into two small pulleys, which create a torque on both sides of the large pulley, balancing the force. That way, bearing loads are minimised and the generator can be mounted with the pulley directly on the shaft, avoiding complex coupling solutions [223].

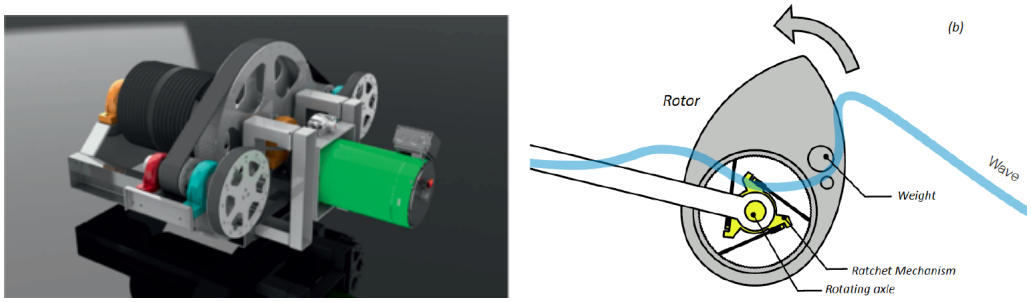

(a) (b)

Figure 2.12: The PTO design based on a belt-drive system for the Lifesaver converter [223] (a) and the ratchet mechanism in the WEPTOS converter [224] (b).

2.3.2.3 Ratchet-wheel mechanism

Another alternative for mechanical transmissions is the ratchet-wheel mechanism. The ratchet is implemented in the absorber, while the toothed wheel, is attached to the main shaft. This main shaft can only rotate in one direction and, as it drives the generator, the rotation speed is constant. Therefore, when a wave hits the absorber, this moves freely until the speed of the absorber reaches the shaft speed. At that moment, the ratchet mounted on the absorber clutches the main shaft, and locks the absorber and shaft motion together. Once the wave has passed, the absorber swings back towards the starting point due to the effect of the gravity force.

Single or double ratchet mechanism have been suggested in the literature. Using a single ratchet, only one direction of the absorber motion can be harnessed, while the double ratchet system allows wave energy to be harnessed in both directions. In spite of the advantage of the double ratchet mechanism, only the single ratchet version has been adopted by WEC developers: an early version of the Wavestar converter [225] and the Weptos WEC [224]. In the latter case, absorbers (rotors in Figure 2.12 (b)) are all located on a common axle, and the ratchet mechanism is included inside the absorber, as shown in Figure 2.12 (b). The pivoting motion of the absorber is only transferred to the common axle on the upstroke motion of the absorber, through the ratchet

mechanism. At the end of the axle, a generator is attached to produce electricity, where the axle is connected to the generator through a 1:3 gear.

2.3.2.4 Screw mechanisms

Different screw mechanisms have been suggested for the transmission of the energy absorbed from ocean waves. A lead screw is suggested to transform linear motion into rotational motion in [226]. However, lead screws present high friction on the thread, low gearing ratios and low efficiencies (about 25%). Alternatives to lead screws include roller screws or ball screws. A variety of screw mechanisms are illustrated in Figure 2.13.

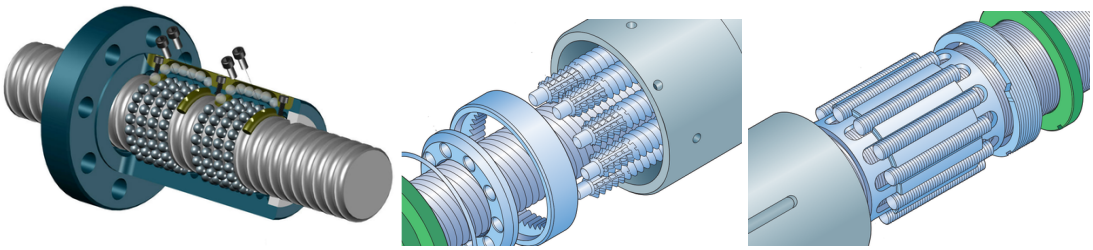

(a) (b) (c)

Figure 2.13: Screw mechanisms: (a) ball screws, reproduced with kind permission from Barness Industries Ltd. [227], (b) planetary roller screws, and (c) recirculating roller screws, reprinted with kind permission from SKF Group [228].

Ball screws allow for the application of high thrust loads with minimum friction, but a mechanism to return balls is necessary even for bi-directional motion. The use of a ball screw for wave energy conversion is suggested in [229, 230]. Providing more bearing points than ball screws within a given volume, roller screws can be more compact for a given load capacity, while providing similar efficiency. Roller screws can surpass ball screws in positioning precision, load rating, rigidity, speed, acceleration, and lifetime. In addition, roller screws require lower maintenance and have a longer lifetime. Efficiencies of up to 90% can be achieved with ball/roller screws [221].

An innovative alternative is the permanent-magnet piston/ball-screw/generator system presented in [231], referred to as a contact-less force transmission system. The ball screw mechanism is coupled to the generator using a one way clutch, which enhances the uni-directional rotation of the generator, and acts as a mechanical gear system for a direct drive permanent magnet linear generator.

2.3.3 Magnetic transmission system

Magnetic gears and couplings have been investigated to improve the relatively low force densities of permanent magnet generators. Studies carried out for rotary generators have shown considerably higher power densities for magnetic coupling compared to linear electric generators, which encouraged a study of magnetic coupling systems with regard to wave energy conversion.

A magnetic lead screw (MLS) was suggested for the Wavestar WEC [232], based on the same idea as mechanical screws. The advantage of the MLS is the lack of contact between the parts transferring the force, reducing the friction, and, consequently, losses and wear. An efficiency of about 95% is assessed for the MLS, from the mechanical input to the shaft output. Considering the MLS and the electric generator as a whole, the efficiency drops to 80%. However, the efficiency of the inverter, and other losses, such as idle losses of the generator or Coulomb-like losses in the MLS, must be considered as well, which may further diminish the final efficiency [233]. In addition, an important drawback of the MLS is the lack of power smoothing.

2.3.4 Hydraulic transmission system

Hydraulic transmission systems are the choice of the vast majority of developers working with a wave-activated WEC, since they offer unmatched force density at low velocities, high controllability, and relatively easy rectification (valves) and smoothing (accumulators) solutions. In addition, hydraulic transmission systems provide high flexibility in the required hydraulic transmission system topologies by combining different components. All the topologies include a hydraulic cylinder and a hydraulic motor, and the distinguishing factor is the way to connect both. Depending on the connection, different components may be necessary, and different types of hydraulic cylinders and motors can be used.

Several hydraulic transmission system topologies have been suggested for wave energy converters in the literature. The simplest topology includes a hydraulic cylinder, high- and low-pressure accumulators, a rectification bridge, and a fixed-displacement hydraulic motor, as suggested in several studies [234–238].

In order to improve the performance of such a 'standard' system, alternative hydraulic transmission system configurations have been suggested in the literature. Four configurations with higher flexibility are presented in [239], where the main difference among the four configurations is the arrangement of the accumulators. Another topology with direct connection between the hydraulic cylinder and a variable-displacement motor is suggested in [64]. Finally, an innovative configuration using a multi-chamber hydraulic cylinder connected to multiple accumulators with different pressure levels, which, in turn, are connected to a fixed-displacement motor, is presented in [240]. All these topologies can be organised into two main categories [241]: constant- and variable-pressure configurations.

The hydraulic cylinder, or hydraulic ram, is the mechanism for connecting the moving absorber to the hydraulic circuit, converting the mechanical energy absorbed from ocean waves into hydraulic energy. Conventional cylinders, single- or double-acting, and symmetric or asymmetric, have a single piston which divides the cylinder into two chambers. Thus, the pressure difference between these two chambers (Δp) determines the reaction force applied on the absorber (F_{pis}), and the torque induced in the hydraulic motor.

Pressure dynamics in hydraulic cylinder chambers are described by the flow continuity equation [242], as follows:

$$\dot{p}_{cyl} = \frac{\beta_{eff}(p_{cyl})}{V_{cyl} + A_p x_p}(Q_{cyl} - \dot{x}_p A_p), \tag{2.17}$$

$$F_{pis} = A_p \Delta p_{cyl} - F_{fric} - F_{in}, \tag{2.18}$$

where p_{cyl}, Q_{cyl}, $\beta_{eff}(p_{cyl})$ and V_{cyl} are the pressure, the flow entering or exiting the cylinder chamber, the effective bulk modulus and the minimum volume (calculated when the piston reaches its minimum or maximum position) in the cylinder chamber, respectively. In addition, A_p is the piston area, x_p and $\dot{x}_p$ the piston position and velocity, F_{fric} the friction force, and F_{in} the inertia force.

Friction losses in hydraulic cylinders arise from leakage/friction in piston and rod seals, which are estimated to represent an energy loss of about 5%, following a rule of thumb in [243].

In conventional hydraulic systems, the cylinder operates as a passive pump, where the pressure difference is manipulated via the control input of the hydraulic motor. An innovative system, consisting of multiple differently-sized cylinders mounted in parallel, is suggested in [244] for the Wavebob converter, where each cylinder has different damping characteristics, and a controller operates to select the desired PTO damping. The case presented in [244] is comprised of three cylinders, connected to a set of check valves to rectify the flow, and a high pressure accumulator for energy smoothing. Cylinders can be activated or de-activated by closing or opening a set of active valves, which results in 15 different PTO force settings, with 7 identical, but opposite, positive and negative force levels. Other WEC developers, for instance Pelamis, also analysed similar PTO systems [245].

The idea of a force-control strategy implemented via a hydraulic cylinder, *i.e.* by connecting or disconnecting cylinders from the hydraulic circuit, is a very appealing strategy, although the implementation of multiple cylinders may be problematic for some WECs. Therefore, [240] presents a discrete displacement cylinder (DDC), a cylinder with multiple chambers, as shown in Figure 2.14. These chambers are connected to a manifold with several electronic on/off valves, which present a combination of pressure and piston areas of the different chambers.

Hansen [240] presents two different configurations: One with four chambers and two pressure lines, high- and low-pressure, which results in 2^4=16 different PTO forces, and a second configuration with three chambers and three pressure lines, incorporating a medium-pressure line that enables 3^3=27 PTO-force possibilities, as shown in Figure 2.14. The controllability of the latter configuration is analysed in [246], where the role of active valves is found to be important.

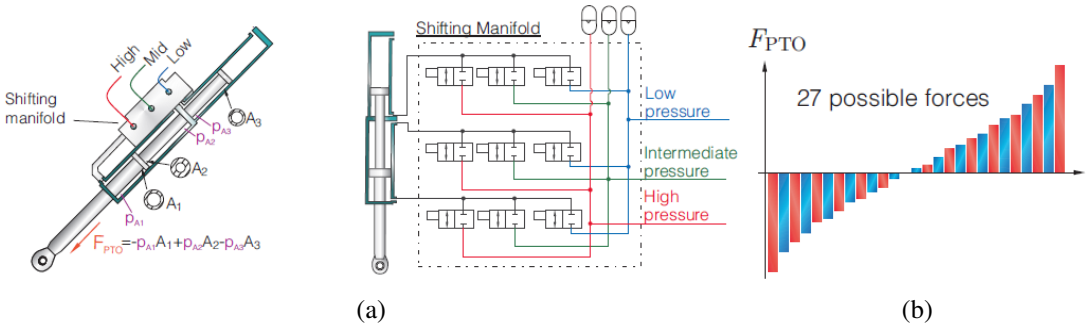

Figure 2.14: Discrete displacement cylinder: (a) configuration of the cylinder and the different pressure lines and (b) PTO force possibilities [240]. Reproduced with kind permission of Rico H. Hansen.

On the other hand, hydraulic motors convert the hydraulic pressure, and flow discharged from the cylinder, into torque (T_M) and angular displacement (ω_M) of the shaft. The flow through the motor (Q_M), and the torque produced by the motor, are calculated as in Equations (2.19) and (2.20), respectively, including volumetric (Q_{losses}) and mechanical (T_{losses}) losses,

$$Q_M = \alpha_M D_\omega \omega_M - Q_{losses}, \tag{2.19}$$

$$T_M = \alpha_M D_\omega \Delta p_M + T_{losses}, \tag{2.20}$$

where α_M is the fractional displacement of the hydraulic motor, D_M the displacement of the hydraulic motor and Δp_M the pressure difference between the inlet and outlet ports of the hydraulic motor.

Several types of hydraulic motors are currently available for diverse applications. Wave energy converters require fast hydraulic motors and, due to the variability of the resource, high efficiency is required not only at full-load, but also at part-load operating conditions. It is precisely this variability which suggests the use of variable-displacement motors, unless another component in the hydraulic circuit facilitates the adaptation of the system to ocean waves. Diverse hydraulic motor topologies with different characteristics are available to meet the requirements of each hydraulic transmission system topology: bent-axis, swash-plate, and digital displacement^{TM}, or discrete displacement, motors (DDMs).

The bent-axis motor, illustrated in Figure 2.15 (a), is a good option for a constant-pressure hydraulic transmission system, and offers either fixed- or variable-displacement versions. However, the bent-axis topology appears to be inappropriate for pressure control, due to their slow response, which requires more than 1 s to change from null to full displacement. Therefore, another alternative is needed to implement fast force control. In [240], for example, a fixed-displacement bent-axis motor is implemented, and force control is achieved via the DDC.

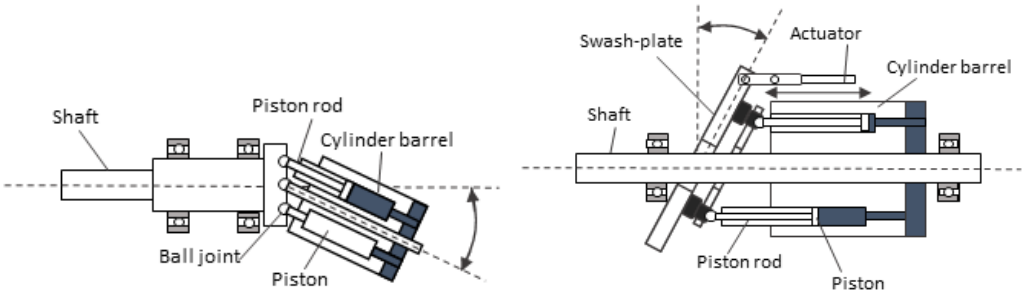

(a) (b)

Figure 2.15: The bent-axis (a) and swash-plate (b) hydraulic motors.

When force control is achieved, by adjusting the pressure through the hydraulic motor, swash-plate and DDMs provide the best alternatives. The response time of swash-plate machines from null to full displacement is usually below 50 ms.

The mechanism to modify the displacement in swash-plate motors is to mechanically vary the stroke of an actuator, which, in turn, modifies the angle of the swash-plate. Figure 2.15 (b) shows a generic illustration of a swash-plate motor. At full displacement, the efficiency of swash-plate machines can be over 80%, but dramatically drops as the displacement is reduced.

A new generation of hydraulic motors has been developed to overcome the poor performance of conventional machines at part-load conditions, which is one of the main challenges in wave energy applications. Instead of mechanically varying the stroke of an actuator, the output of a DDM is controlled by individually activating or de-activating the pistons of the DDM. Figure 2.16 (a) illustrates the structure of the E-dyn 96 digital displacement hydraulic pump.

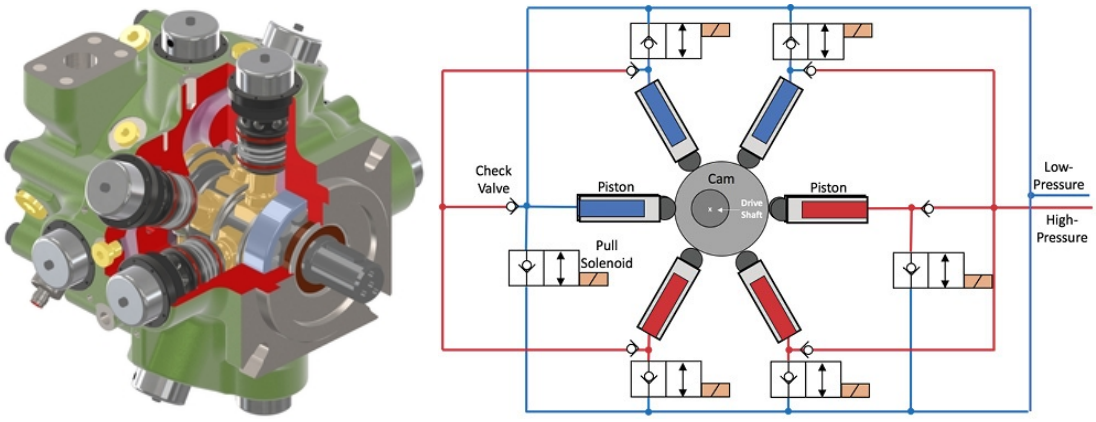

(a) (b)

Figure 2.16: (a) E-dyn 96 digital displacement hydraulic pump, reprinted with kind permission from Artemis Intelligent Power Ltd., Loanhead, Scotland (UK). (b) Simplified circuit diagram of a DDM with check valves and solenoid operated poppet valves [247].

Such control is achieved by electronically-controlled digital on/off valves, which switch the pistons from idling, motoring or pumping cycles, every shaft revolution. Figure 2.16 (b) shows a simplified circuit diagram of a DDM, illustrating the operation of different valves. The response time of these valves needs to be of the order of a few milliseconds. Digital displacement motors provide a much faster and more accurate control response, and superior efficiency, compared to the more common swash-plate motors.

Figure 2.17 illustrates efficiency curves for the bent-axis, swash-plate and DDM machines at different operating conditions: (a) at full displacement and constant pressure; (b) at 20% displa-

cement and constant pressure; and (c) at constant pressure and speed. The DDM appears to be superior to the swash-plate machine at all operating conditions, but the difference is especially significant at part-load conditions.

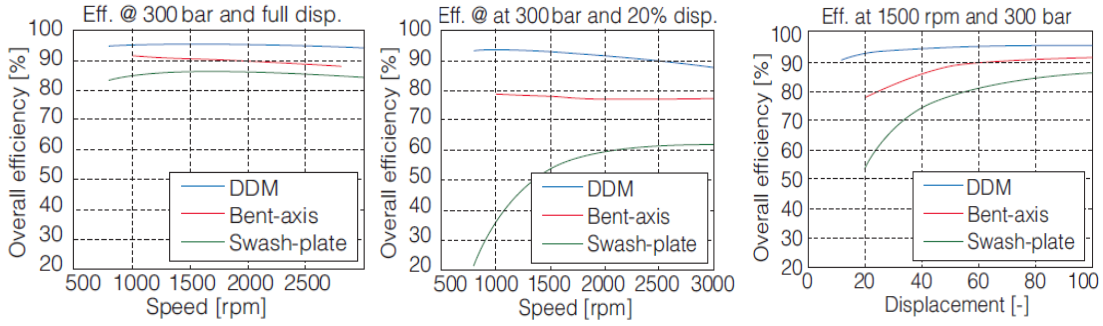

(a) (b) (c)

Figure 2.17: Efficiency comparison between bent-axis, swash-plate and Digital Displacement hydraulic motors [233]. (a) shows the efficiency at constant pressure (300 bar) and full displacement, (b) at constant pressure (300 bar) and 20% displacement and (c) at constant rotational speed (1500 rpm) and pressure (300 bar). Reproduced with the kind permission of Rico H. Hansen.

Chapter 4 provides further information about mathematical modelling of HyPTO systems, including different types of HyPTO system configurations, and the most relevant dynamics and losses of different components. In addition, Chapter 5 presents the validation of these mathematical models against results obtained from different test rigs and high-fidelity software.

2.4 *Generation* stage

The generation stage involves the conversion of absorbed energy into electricity, either directly or through a transmission stage. Hence, such a conversion can be carried out by means of two types of electric generators: rotary- and linear-generators. Rotary generators require, in general, a transmission mechanism (either pneumatic, mechanical, magnetic or hydraulic, as shown in Section 2.3) between the absorber and the generator, while linear generators are directly connected to the absorber. Since no intermediate conversion stage is used with linear-generators, this generation arrangement is also referred to as direct-conversion.

2.4.1 Rotary generator

Rotary electric power generation machines are basically divided into two different categories: fixed- and variable-speed generators. Fixed-speed generators are widely used in different conventional power plants. However, the high variability of renewable energy sources suggests that variable-speed generators are more appropriate. The superiority of variable-speed generators has been demonstrated in wind energy [248], but the same conclusion is not as clear in wave energy, which strongly depends on the type of PTO system and its configuration.

The most commonly used fixed-speed configuration in the *generation* stage is a squirrel-cage induction generator (SCIG) directly connected to the grid. The main advantage of fixed-speed configurations is that the generator is directly connected to the grid, which avoids expensive power converters and does not add any harmonics into the network. In contrast, the generator loses flexibility due to the fixed-speed restriction. Hence, the PTO system can provide controllability only through the equipment of the transmission stage.

The dynamics of an electric generator are represented in the rotor reference frame, also known as the *dq* frame, in most studies. The main advantage of *dq* models is that all the sinusoidal variables appear as direct-current quantities, referred to the synchronous rotating frame [249].

A configuration with a fixed-speed SCIG is implemented in the Pelamis WEC, driven by a variable displacement hydraulic motor [250]. SCIGs are also implemented, coupled to hydraulic transmission systems, in [238] and [251].

In the case of variable-speed generation, different configurations have been proposed by different WEC developers: a doubly-fed induction generator (DFIG) for an OWC converter [252], a permanent magnet synchronous generator (PMSG) for the *Lifesaver* [253] and the Wavedragon converters [254], and a variable-speed induction generator for the *Oceanlinx* [250] and the *Wavestar* [240] WECs.

Due to the frequency requirements of the grid, variable-speed generators cannot be directly connected to the grid. Therefore, power converters are required to decouple the generator from the grid. The dynamics of variable-speed rotary electric generators are also represented via the *dq* frame.

Chapter 4 includes mathematical models for fixed- and variable-speed electric generators, which are validated against experimental results in Chapter 5.

2.4.2 Linear generators

Several linear generator topologies currently exist, but only a few are suitable for wave energy conversion. Baker [255] examines various linear generator topologies, providing a discussion about the suitability of such machines for WECs. The study concludes that, among the conventional generator types, only linear permanent magnet generators (LPMG) may be suitable for wave energy conversion purposes.

The main drawback of linear generators is that the linear velocity of the translator, determined by the velocity of the absorber, is much lower than the equivalent rotational velocity of conventional rotary generators. Accordingly, the reaction force needs to be much greater (in the same proportion of the velocity, defined as between 15 and 50 times in [18]), in order to generate the same power. These large forces result in very large machines that involve large structures and several bearing points, to maintain the air gap between the stator and the translator, as illustrated in Figure 2.18.

The main advantages of LPMGs are a relatively high efficiency (over 86% [256]) and continuous force control possibility. In contrast, the main disadvantages are the low power to weight ratio (very large machines are required), and the necessity of a heavy structure (which implies high cost) due to the attractive forces between the stator and the translator. In order to avoid such large and heavy structures, air-cored/iron-less configurations [257, 258] have been suggested, which result in significant structural savings and magnetic force reductions.

The dynamics of linear electric generators are expressed similarly to rotary electric generators [249],

$$V_{sd} = R_s i_{sd} + L_s \frac{d}{dt} i_{sd} + \frac{\pi}{\tau} \dot{x}_t L_s i_{sq}, \tag{2.21}$$

$$V_{sq} = R_s i_{sq} + L_s \frac{d}{dt} i_{sq} + \frac{\pi}{\tau} \dot{x}_t (\lambda_{PM} - L_s i_{sd}), \tag{2.22}$$

where $\dot{x}_t$ represents the linear velocity of the translator, which is consistent with the motion of the absorber, τ is the pole pitch or pole width, R the resistance, L the inductance, λ_{PM} the permanent magnet flux, and V and i the voltage and current, respectively. In addition, the subscripts s, d and q refer to the stator, and direct and quadrature axes, respectively.

The original Archimedes wave swing (AWS) used direct conversion via a LPMG [259], and a LPMG is also suggested in [260] and [63] as the solution to generate electricity from ocean waves.

Alternatives to large and heavy LPMGs are magnetic coupling machines. These alternative generators use magnets mounted in the armature and the translator, generating a magnetic coupling, and are able to generate shear stresses of up to 10 times those generated in conventional electrical generators, with zero loss [261]. These magnetic couplings are able to achieve very high

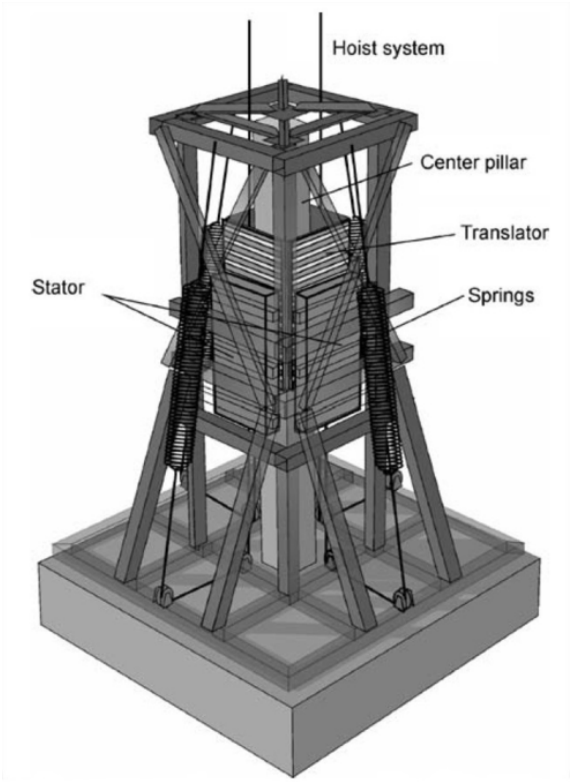

Figure 2.18: Illustration of a linear generator [18]. Photography supplied courtesy of João Cruz.

torque per volume densities, up to 400 $\mathrm{kNm/m^3}$, while, in the case of standard linear generators, this torque per volume density is about 10 $\mathrm{kNm/m^3}$, as reported in [262].

An example of such magnetic coupling machines is the Snapper concept. The Snapper is an electrical generator specifically created for wave energy conversion, that combines the magnetic gearing concept with a linear electric generator [261, 263].

Losses in electric generators, either rotary or linear, appear mainly due to large current requirements, especially in linear generators, manifested as large copper losses. Nevertheless, copper losses are not the only losses that affect the performance of a generator. The efficiency of electric generators is generally high at full-load operation, regardless of the topology of the generator. However, as in the case of hydraulic motors, the efficiency drops at part-load conditions.

The impact of each of these losses is described in [264] for an induction generator (IG) and a PMSG. Figure 2.19 illustrates power losses for an IG, where copper losses appear to be the most significant losses, and a PMSG, where iron losses appear to be the most important losses. Tamura [264] also considers losses of power converters in the PMSG, which are studied separately in this thesis. All the generators appear to perform similarly at nominal power rates, whereas the PMSG appears to be superior at part-load conditions.

The mathematical models for electric generators described in Chapter 4 also include the main losses of electric generators. The efficiency values obtained from these mathematical models are compared in Chapter 5 to those obtained from experimental results, showing very good agreement.

2.5 *Conditioning* stage

The conditioning stage is imperative for variable-speed electrical generators to adapt the frequency of the generated electric power to the frequency of the grid. Power electronic converters (PECs) have an AC-DC-AC configuration, which decouples the electric machine from the electric net-

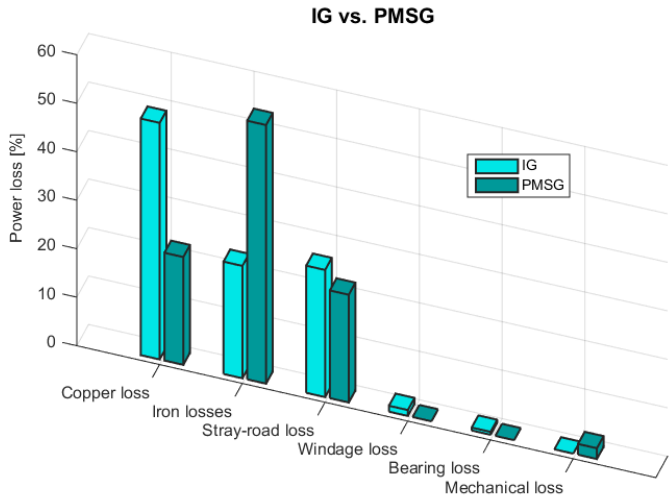

Figure 2.19: Relative power loss estimation for an induction generator and a permanent magnet generator, based on the information published in [264].

work, with an intermediate DC stage. Therefore, the speed of the generator can be modified, via the generator-side converter (GenSC), in order to absorb and generate power more efficiently, while the grid-side converter (GridSC) adapts the output power signal to meet the grid requirements. However, PECs incur extra losses and inject harmonics into the grid, which also need to be considered.

The AC-DC-AC conversion is achieved via a B2B converter, which consists of a rectifier and an inverter connected via a common DC-link. Many different B2B converter configurations, based on combinations of diodes and thyristors, are possible and used across a variety of different applications [265].

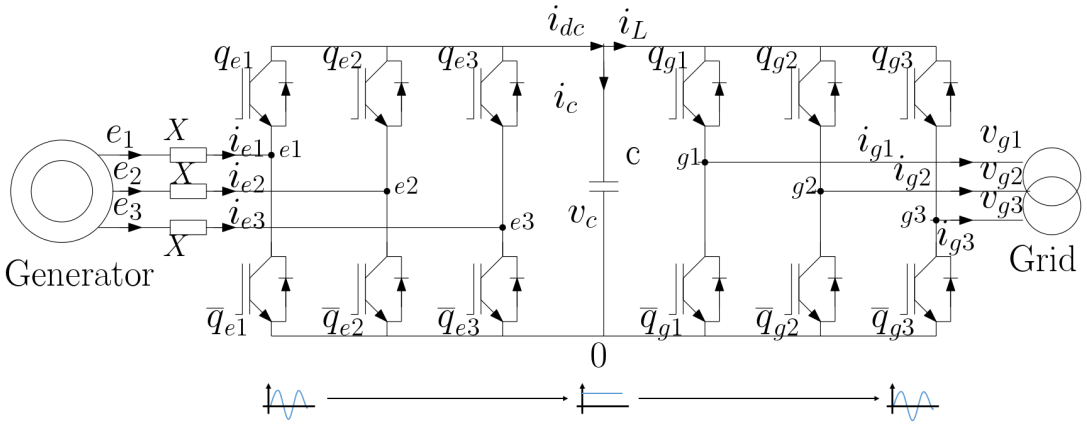

Figure 2.20: Schematic representation of the three-phase to three-phase B2B converter, adapted from [266].

However, since the control of power converters is crucial for wave energy applications, only fully-controlled PECs are studied here, where both the rectifier (GenSC stage) and the inverter (GridSC stage) use thyristors, rather than diodes. In general, a three-phase converter bridge is chosen over a single-phase bridge, due to the significant improvement in the output voltage waveform shape [267]. A three-phase to three-phase B2B converter, also known as the full-bridge converter, is shown in Figure 2.20.

Rectifier and inverter thyristors are controlled by regulating the switching periods, varying the on/off ratio time, where the control input is the firing angle or conduction angle. The different

objectives of the GenSC and GridSC demand specific controllers for each converter stage. In some cases, depending on the control strategy, the output signal from these controllers is converted by means of a pulse width modulation (PWM) approach, as shown in Chapter 4.

Power losses in the converters also need to be considered. Some studies include a constant efficiency, or an efficiency map [233], while others suggest a combined generator and converter loss model [222]. However, a more realistic consideration of power losses may be required. These losses in converters are divided into two different groups: conduction losses and switching losses [264]. Figure 2.21 illustrates the distribution of conduction and switching losses for an AC motor drive system with two type of connections. Switching losses are shown to be considerably higher in both cases.

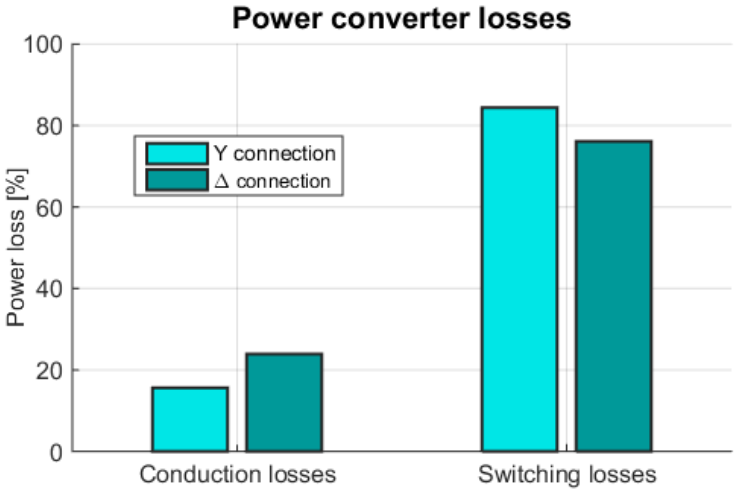

Figure 2.21: Power converter losses distribution, adapted from [266].

Chapter 4 analyses losses in PECs, and modelling approaches to include them into the mathematical model. These approaches include switching operations of PECs, prohibitively increasing computational requirements. Therefore, an alternative approach neglecting these switching operations, but retaining power losses, is suggested and validated in Chapter 5.

2.6 Wave-to-wire models with hydraulic transmission system: An application based survey

Accurate W2W models should include all the important dynamics, losses and constraints of the different conversion stages from waves to the electricity grid. However, the level of detail included in each sub-system varies significantly among the different W2W models in the literature.

Wave-to-wire models, for different WECs and type of PTO systems, have been suggested in the literature: an overtopping converter, including the hydraulic motor and the generator, is presented in [268], OWC devices with air-turbines coupled to electric generators are modelled in [208, 252, 269–271], wave-activated converters coupled to PTO mechanisms with mechanical and magnetic transmission systems are described in [222, 272] and [233], respectively, while examples of HPAs connected to linear generators are presented in [63, 259, 260].

However, HyPTO systems appear to be the choice of the vast majority of WEC developers, including Pelamis [30], Searev [234], Wavestar [246], Oyster [26], CETO [27], Waveroller [123] and Langlee [35]. Therefore, this thesis focuses on HyW2W models, as shown in Figure 2.22, where the different conversion stages of a HyW2W model are illustrated as a particular case of Figure 2.1.

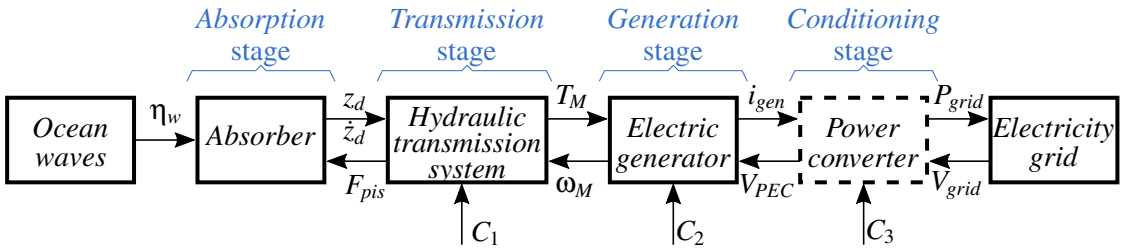

Figure 2.22: Diagram of a HyW2W including the interconnection between the different subsystems and the potential control inputs for the HyPTO components.

The vast majority of the HyW2W models suggested in the literature often incorporate high-fidelity into a specific component or stage, but fail to design a balanced (fidelity) parsimonious model. The main weakness of the HyW2W models suggested in the literature is, in general, the WSHI model. In the simplest version, the WSHI is represented as a mass-damper (*M-D*) system [273, 274], but the most widely used approach is the LPF model based on Cummins' equation [275], which in some cases includes viscous effects via the *viscLPF* [183]. However, the LPF and *viscLPF* models are demonstrated to overestimate the motion of WECs and, as a consequence, the absorbed energy. A number of modelling approaches, presented in Section 2.2, are suggested to improve the results of the LPF and *viscLPF* models.

Hydraulic PTO models have also been represented in many different ways in the literature, from an ideal HyPTO that completely neglects all the dynamics and losses [183], to a thoroughly modelled hydraulic transmission system, coupled to an excessively simplified electric generator [276], to a simplified hydraulic transmission system coupled to a detailed electric generator [238]. In order to critically evaluate the suitability of the different HyW2W models presented in the literature, it is essential to consider the application for which the HyW2W models in the literature were originally developed. Table 2.4 presents a summary of this critical evaluation.

Table 2.4: Critical evaluation of the different HyW2W models suggested in the literature. The following abbreviations are used in the table below: *Ref* for reference, *NL* for nonlinear, *App* for application, *Compr* for compressibility, *N/A* for not applicable, *const.* for constant, and η for efficiency.

Ref	Absorber		Hydraulic transmission system				Electric generator			Power converter		*App*
			Cylinder		Accumulators	Motor losses						
	LPF	*NL* effects	Internal dynamics	Losses			Shaft inertia	Electrical dynamics	Losses	Internal dynamics	Losses	
[235]	✓	✗	✗	✗	adiabatic	*const.* η	✓	✗	✗	✗	✗	*PowAss MBC*
[234]	✓	✗	*Compr*	✓	adiabatic	*const.* η	✗	✗	✗	✗	✗	*PowAss*
[277]		*viscLPF*	✗	✗	adiabatic	✓	✓	✗	*const.* η	✗	✗	*PowAss*
[237] [276]	*M-D*	✗	✗	✓	adiabatic	✓	✓	✗	✗	✗	✗	*PTOopt MBC*
[64] [240]	✓	✗	*Compr*	✓	Dynamic & compresible	✓	✓	✗	✓	✗	$\eta(\omega_M, P_{grid})$	*PTOopt MBC*
[278]	✓	✗	✗	✓ (ANFIS)	Dynamic & compresible	✓ (ANFIS)	✗	✗	$\eta(P_{grid})$	✗	✗	*MBC*
[279]	✓	✗	✗	✗	isothermal	*const.* P_{loss}	✓	✓	✓	*N/A*	*N/A*	*PowSyst*
[238]	✓	NL restoring	✗	✗	adiabatic	✓	✓	✓	✓	*N/A*	*N/A*	*PowSyst*

Ricci [235] suggests a HyW2W model for *MBC* and *PowAss*, where the compressibility of the hydraulic fluid and losses in hydraulic components are excessively simplified or neglected, and the electric generator is represented by an ideal constant load. Similar models for *PowAss* are presented in [234] and [277], where [234] also includes compressibility effects of the hydraulic system and [277] includes losses for the hydraulic motor. However, [234, 235, 277] miss, or excessively simplify, important losses and constraints in the HyPTO model. Chapter 7 demonstrates that such

simplifications result in generated power overestimation.

A HyW2W model is employed in [237, 276] for *PTOopt* and *MBC*. This HyW2W model includes losses in the hydraulic cylinder and motor, but neglects the electrical dynamics and losses. Therefore, the HyPTO model and the active PTO tuning strategy suggested in [276] may not be adequate, since *PTOopt* and *MBC* require the incorporation of losses of the electric generator to be articulated. The HyW2W model suggested in [64, 240] is also used for *PTOopt* and *MBC*, but includes losses in the electric generator and power converter, providing more reliable results. The only missing aspects in [64, 240] are the electrical dynamics, which are neglected, via a steady-state representation of the electric generator.

Due to the computationally fast models required for *MBC*, [278] suggests an adaptive neuro fuzzy inference system (ANFIS) to represent the losses in the hydraulic cylinder and motor. The HyW2W model suggested in [278] also neglects electrical dynamics in the electric generator and the efficiency is calculated with a polynomial approximation, using efficiency constants that represent part- (25% and 50% of the full load) and full-load operations of the electric generator. The HyPTO model presented in [278] for *MBC* seems to be appropriate from a complexity perspective, but the suitability of the HyPTO model strongly depends on the fidelity of the (black-box) ANFIS model, which is not clear from [278].

HyW2W models for *PowSyst* are suggested in [279] and [238], where electrical dynamics and losses are included in both models. However, losses in the hydraulic system are either excessively simplified, represented with a constant power loss value [279], or neglected [238], which results in overestimated power generation estimates. This generated power overestimation can have a relevant impact on the design of storage systems, incorporated to improve the smoothness of the power delivered to the electricity grid [279], or the design of the interconnection between a WEC array and the electricity grid.

Therefore, to date, and to the best of author's knowledge, no published HyW2W model captures all the main characteristics of the different sub-systems from wave to the electricity grid. In general, a parW2W model should include:

(c.1) Balanced parsimonious models for each conversion stage of the drive train (including non-linearities where required);

(c.2) Consideration of all possible control inputs at the various stages in the drive train;

(c.3) Articulation of constraints, energy losses and efficiency curves for each component;

(c.4) Specification of physical constraints for each component, e.g., displacement, velocity and force (for mechanical components), pressure (for hydraulic components), current, voltage (for electrical components) and power specification (at all levels).

In the case of WSHIs, the parsimonious model that accurately represents the hydrodynamic behaviour of WECs depends on the type of WEC and the application of the model, as demonstrated in Section 2.2. All the applications presented in the introduction can be divided into two groups, with a distinguishing dominant requirement: a balance of complexity vs. fidelity (accuracy). The complexity of a mathematical model includes aspects like computational requirements, nonlinearity degree and model order, and is also very application specific. Figure 2.23 (a) illustrates the compromise between complexity and fidelity of the modelling approaches described in Section 2.2.3.

Specific requirements of each application are described in Chatper 8, but, in general, *PowAss*, *PTOopt* and *MBC* require reasonably fast mathematical models, since a large number of cases need to be studied. In contrast, *VerVal* and *Ident* do not have restrictive computational requirements, while high-fidelity is crucial.

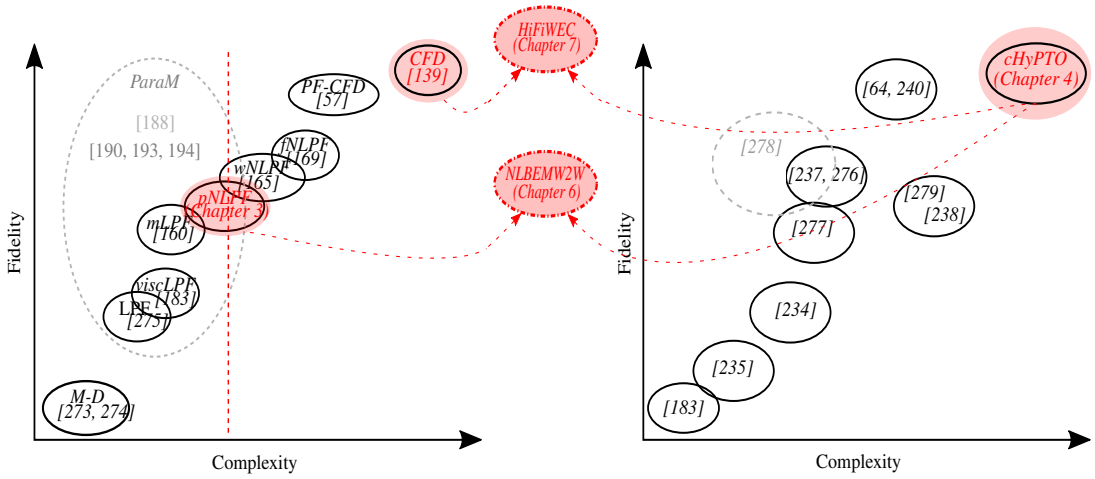

(a) WSHI modelling approaches.

(b) HyPTO modelling approaches.

Figure 2.23: Fidelity/complexity trade-off of different modelling approaches for WSHIs (a) and the HyPTOs (b), where the grey dashed ovals denote a lack of physical meaning of the modelling approach.

For applications that require fast mathematical models, the only approaches within the affordable computation region, delimited by the red dashed line in Figure 2.23 (a), are the *M-D*, LPF, *viscLPF*, *mLPF*, *pNPFL* and the parametric models. Due to the lack of validation of *ParaM*s for wave energy applications, it is hard to determine the real capabilities of these approaches. In addition, the *M-D*, LPF and *viscLPF* models seem to overestimate the motion and power absorption of WECs. The only exception to this might be the case of *viscLPF* models when applied to OWSCs. Therefore, the *pNLPF* model, with an externally added viscous force, is suggested for all the WEC groups, except for the OWSC, for which *viscLPF* seems accurate enough. Table 2.5 presents the modelling approaches suggested for each WEC group, where examples showing the performance of these modelling approaches are included.

In the case of *SimWEC* and *PowSyst*, high-fidelity is important, but computational requirements are more restrictive than in the case of *VerVal* and *Ident*. Therefore, *SimWEC* and *PowSyst* are also included in Table 2.5.

Table 2.5: Suggested WSHI modelling approaches for applications with low computational requirements.

	Low complexity (***PowAss, PTOopt, MBC, SimWEC*** **and** ***PowSyst***)
OWC	Partially nonlinear potential theory with viscous drag [107]
HPA	Partially nonlinear potential theory with viscous drag [117, 280, 281]
OPC*	Partially nonlinear potential theory with viscous drag [57]
OWSC	Linear potential theory with viscous drag [282]

*OPCs in this table include self-reacting HPAs with damping plates.

Where high-fidelity is the main requirement of the application, regardless of the complexity of the model, the suggested approaches vary significantly, compared to the applications that need fast mathematical models, as shown in Table 2.6.

Fully nonlinear approaches, such as CFD or *fNLPF*, seem to be necessary to accurately reproduce the WSHI behaviour of WECs. In the case of OWCs, viscosity effects seem predominant,

Table 2.6: Suggested WSHI modelling approaches for models with high fidelity requirements.

	High fidelity (*VerVal* and *Ident*)
OWC	CFD** [94, 133, 283, 284]
HPA	CFD*[285, 286]
OPC	Partially nonlinear potential theory combined with CFD [57]
OWSC	CFD** [58, 120, 134, 135]

*While *pNLPF* models with an external viscous model can provide relatively high-fidelity results [280], CFD is necessary in applications where the highest possible fidelity is required, due to the inconsistency of the viscous model.
**The additional computation of SPH models can be justified under specific (extreme) conditions in OWCs [158] or OWSCs [97, 148], but not in models for WECs operating within the *power production mode*.

which restricts the set of possibilities to CFD. Similarly, viscous effects appear to dominate the dynamics of OWSCs, along with radiation and diffraction forces, for which CFD seems again to be the only viable solution. For HPAs, the relevance of viscous effects is demonstrated to be significantly lower than potential flow nonlinearities. Therefore, a *pNLPF* model, with an externally added viscous force, seems to be accurate enough. However, due to the uncertainty and inconsistency of the external viscous model described in Section 2.2.3.2, high-fidelity WSHI results can only be obtained via CFD models. Finally, OPCs are in between OWCs and HPAs, where both potential flow nonlinearities and viscous effects are equally important. Therefore, mathematical models that combine a nonlinear potential flow method to account for the incident wave, and a CFD (RANS) model for the scattering and viscous effects, seem to be the best solution. Note that HPAs with damping plates may be considered as OPCs, due to the higher relevance of viscous effects compared to HPAs without damping plates.

With respect to the HyPTO, Figure 2.23 (b) illustrates the different modelling options suggested in the literature and presented in Section 2.6. None of the HyPTO models suggested in the literature includes all the relevant dynamics, losses and constraints of all the different components. Therefore, a complete HyPTO model (*cHyPTO*) that includes all the relevant dynamics and losses of the different components is presented in Chapter 4, which is validated against experimental results and high-fidelity established software in Chapter 5.

This *cHyPTO* can be coupled to the appropriate WSHI model, to design comprehensive parsimonious HyW2W models that fulfil the required characteristics (c.1)-(c.4). All HyW2W models presented in the following chapters involve a HPA. Hence, the HyW2W models *NLBEMW2W* and *HiFiWEC* are presented in Chapters 6 and 7, respectively, as illustrated in Figure 2.23. The *NLBEMW2W* model is initially designed for applications with low complexity requirements, and couples the *pNLPF* and the *cHyPTO* models. Alternatively, the *HiFiWEC* is designed for high-fidelity applications, and comprises a CNWT and the *cHyPTO* model. Finally, the *HiFiWEC* is also used in Chapter 8, as the basis for the *systematic* CR, to specifically design efficient comprehensive HyW2W models for each application described in the introduction of this chapter.

2.7 Summary

This chapter presents a comprehensive introduction to W2W models, including the different subsystems and conversion stages: *absorption*, *transmission*, *generation* and *conditioning* stages. In addition, the introduction of the chapter is dedicated to the potential applications of W2W models, where seven different applications have been identified and described briefly.

The chapter is divided into six different parts, where a comprehensive review of the diverse mathematical models to represent the different parts involved in W2W models is presented, inclu-

ding the relevance of different nonlinear effects within the *power production mode*. The first part of the chapter (Section 2.1) describes the different modelling approaches for ocean waves, where a *power production mode* operation area has been delimited in the wave theory diagram, which provides a preliminary idea about the need for nonlinear wave theories. In addition, Section 2.2 indicates the relevance of different nonlinear effects for diverse types of WECs, and different modelling approaches to consider these nonlinear effects. The different conversion stages included in the power take-off systems, *e.g. transmission*, *generation* and *conditioning* stages, are reviewed in Sections 2.3, 2.4 and 2.5, respectively, including the different technologies suggested by developers and researchers for each stage.

Finally, a survey of existing HyW2W models is presented in Section 2.6, based on the application for which each HyW2W model was designed. These HyW2W models are critically evaluated, summarised in Table 2.4, identifying the weak points of each HyW2W model, based on the requirements of the different applications. Furthermore, the requirements to create parsimonious HyW2W models are defined in Section 2.6, which are used as the basis to design the *cHyW2W* model in this thesis. In addition, WSHI modelling approaches suitable for low-complexity and high-fidelity applications are suggested in Tables 2.5 and 2.6, respectively, which are used in the following chapters to design different HyW2W models.

Chapter 3

Modelling the *cHyW2W* model: Ocean waves and wave-structure hydrodynamic interactions

Ocean waves and *Absorber*, which represents WSHIs, are the first two subsystems of any W2W model, as illustrated in Figure 2.1, and accurate mathematical models to represent both subsystems are essential. Ocean waves and WSHIs can be represented using several different approaches, as described in Sections 2.1 and 2.2, respectively, and the most suitable approach depends on the type of WEC, the operational conditions and the application the mathematical model is designed for.

This thesis focuses on the analysis of WECs in *power production mode*, excluding extreme events. In this context, potential flow theory is the most commonly used approach for modelling ocean waves and WSHIs, regardless of the type of WEC, due to its appealing computational requirements. In fact, LPF models are used in the vast majority of studies when modelling ocean waves and WSHIs, neglecting nonlinear effects. However, nonlinearities in ocean wave representation and WSHIs may be relevant even within the *power production mode*, and, as a consequence, linear models may be inaccurate. The objective of this chapter is suggesting the best mathematical models to be implemented in the *Ocean waves* and *Absorber* subsystems of the *cHyW2W* model presented in this thesis.

Section 2.6 suggests the optimum WSHI mathematical models, including nonlinear effects, for different WEC types and applications. Although the computationally demanding CFD approach may be required for some specific applications, where high-fidelity is essential, WSHIs can, in many cases, also be represented via the potential flow theory, with satisfactory fidelity and significantly lower computational effort. However, LPF models need to be extended to include the most relevant nonlinear effects to provide the required fidelity levels.

This chapter presents a brief introduction to potential flow theory, starting from the LPF model to represent ocean waves and WSHIs, described in Section 3.1. Hence, the assumptions considered in the LPF model are presented and the equations of motion that describe the behaviour of the absorber, using a linear approximation, are derived. Section 3.1.3 describes the method to obtain the hydrodynamic coefficients required in any mathematical model based on LPF theory and discusses the capabilities of the open-source BEM solver NEMOH [177], using the well-known commercial BEM solver WAMIT [100] as a benchmark. The extension of the linear model is presented in Section 3.2, where the *pNLPF* model is defined. This *pNLPF* model is evaluated for a HPA, analysing the impact of including different nonlinear effects: nonlinear FK forces, nonlinear viscous effects, and nonlinear waves. Finally, a computationally efficient version of the *pNLPF* model is presented in Section 3.3, which uses the analytical solution to solve nonlinear FK forces and is implemented in the *cHyW2W* model presented in Chapter 6.

3.1 Linear potential flow model

The system of nonlinear equations, composed of the continuity and motion equations defined in Equations (2.2) and (2.3), respectively, results in a complicated and computationally expensive problem to solve numerically. Therefore, a computationally more appealing technique can be used to solve WSHIs, considering a number of simplifying assumptions that lead to the formulation of the LPF model.

Figure 3.1 illustrates the BVP for a floating body, where S corresponds to the submerged part of the body in still water. Hence, the three-dimensional coordinate system is defined so that the z-axis represents the vertical axis perpendicular to the free-surface, with its origin on the undisturbed free-surface and positive values above the free-surface. In this coordinate system, ocean waves propagate in the positive sense of the x-axis. Hence, η_w is positive when the free-surface is above the x-y plane illustrated in Figure 3.1.

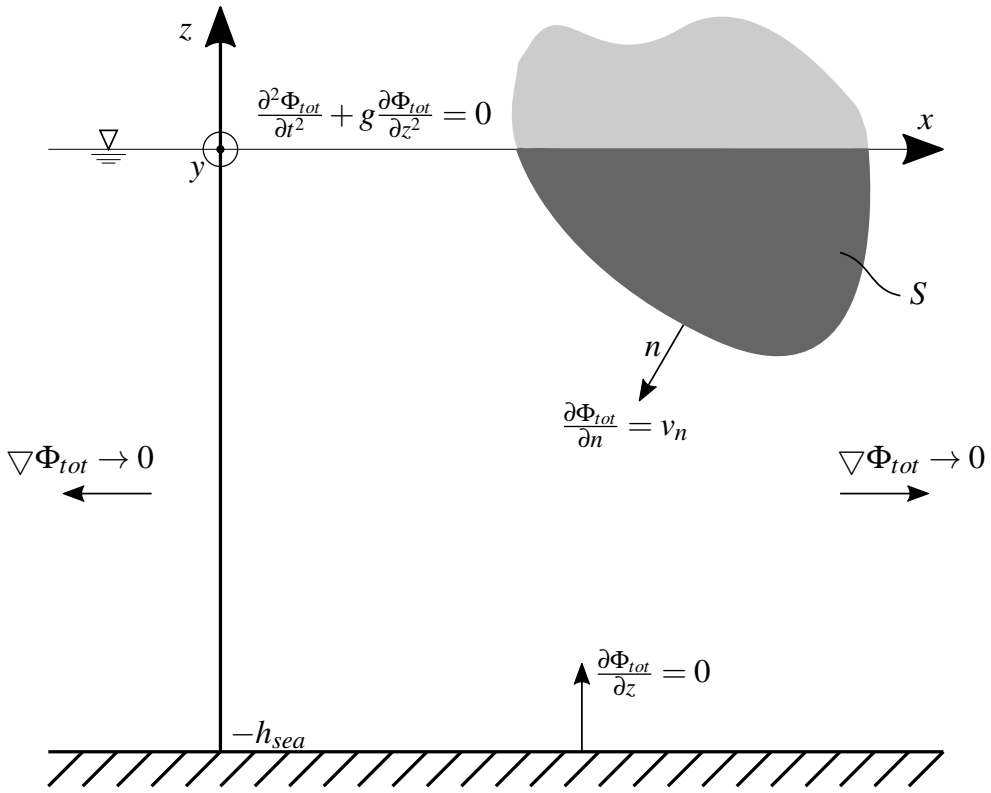

Figure 3.1: The BVP for a floating body assuming the hypothesis of the LPF theory, where the positive sense of the y-axis is out of the page.

The simplifying assumptions considered in the LPF model are the following:

(A.i) The fluid is incompressible ($\frac{\partial\rho_w}{\partial t} = 0$),

(A.ii) The fluid is inviscid ($\mu = 0$),

(A.iii) The flow is considered irrotational ($\nabla \times v = 0$),

(A.iv) Wave amplitude is small with respect to the wavelength, and

(A.v) The amplitude of the body motion is small compared to its dimensions.

Based upon assumption (A.i), the continuity equation presented in Equation (2.2) can be expressed [85] as follows,

$$\bigtriangledown \cdot v = 0, \tag{3.1}$$

stating the conservation of mass in the control volume defined in Figure 3.1. Similarly, using assumptions (A.ii) and (A.iii), the fluid flow velocity vector v can be defined as,

$$v = \bigtriangledown \Phi. \tag{3.2}$$

Thus, by substituting Equation (3.2) into Equation (3.1), the velocity potential can be solved using the Laplace equation [85] as follows,

$$\bigtriangledown^2 \Phi = 0. \tag{3.3}$$

In addition to the Laplace equation, the flow must satisfy the boundary conditions of the BVP at the free-surface, on the seabed and the floating body, and far from the floating body [287], as illustrated in Figure 3.1:

(BC.i) Two different conditions must be fulfilled at the free surface. Firstly, the pressure at the free-surface must be equal to the atmospheric pressure (dynamic boundary condition) and, secondly, the component of the fluid velocity normal to the free-surface must equal the free-surface velocity (kinematic boundary condition). Respectively, the dynamic and kinematic boundary conditions at the instantaneous free-surface, $z = \eta_w$, can be expressed as,

$$\frac{\partial \Phi}{\partial t} + \frac{1}{2}(\bigtriangledown \Phi)^2 + g\eta_w = 0 \qquad at \;\; z = \eta_w(x,y), \tag{3.4}$$

and

$$\frac{\partial \eta_w}{\partial t} + \frac{\partial \Phi}{\partial x}\frac{\partial \eta_w}{\partial x} + \frac{\partial \Phi}{\partial y}\frac{\partial \eta_w}{\partial y} - \frac{\partial \Phi}{\partial z} = 0 \qquad at \;\; z = \eta_w(x,y), \tag{3.5}$$

(BC.ii) The boundary condition on the seabed assumes its impermeability, which imposes a null vertical component of the fluid velocity,

$$\frac{\partial \Phi}{\partial z} = 0 \qquad at \;\; z = -h_{sea}, \tag{3.6}$$

where h_{sea} is the water depth.

(BC.iii) The boundary condition on the floating body also involves impermeability of the submerged body surface, which implies that the component of the fluid velocity vector normal to the body surface (v_n) must equal the body velocity in the direction normal to the body surface

$$\frac{\partial \Phi}{\partial n} = v_n. \tag{3.7}$$

(BC.iv) Finally, far from the oscillatory body, the wave field should appear undisturbed or identical to the incoming wave field (radiation condition). Therefore, the perturbation potential, which includes radiation and diffraction effects, must decay as the distance from the oscillatory body increases, resulting in

$$\Phi \propto (k_w d_{rad})^{-1/2} e^{-ik_w d_{rad}} \qquad as \;\; d_{rad} \to \infty, \tag{3.8}$$

where d_{rad} is the radial distance from the oscillatory body and k_w the wavenumber.

3.1.1 Linear wave theory

The Laplace equation defined in Equation (3.3) is linear, but boundary conditions at the free-surface (BC.i), expressed in Equations (3.4) and (3.5), are nonlinear. Thus, further simplifications are required to define the LPF model. Linearised boundary conditions at the free-surface, under assumptions (A.iv) and (A.v), can be obtained by neglecting the higher-order terms in Equations (3.4) and (3.5), and by considering free-surface boundary conditions at the undisturbed free-surface $z = 0$, instead of at the instantaneous free-surface $z = \eta_w$. Consequently, the linearised version of Equations (3.4) and (3.5) yields [287], respectively,

$$\frac{\partial \Phi}{\partial t} + g\eta_w = 0 \qquad at \;\; z = 0, \tag{3.9}$$

and

$$\frac{\partial \eta_w}{\partial t} - \frac{\partial \Phi}{\partial z} = 0 \qquad at \;\; z = 0. \tag{3.10}$$

Introducing Equation (3.10) into the time derivative of Equation (3.10), the linearised boundary condition at the free-surface can be given as,

$$\frac{\partial^2 \Phi}{\partial t^2} + g\frac{\partial \Phi}{\partial z} = 0 \qquad at \;\; z = 0. \tag{3.11}$$

Assuming a uniform water depth, the solution of the BVP takes a sinusoidal form, which allows for the spatial and temporal decomposition of the problem [287]. This decomposition allows each quantity to be represented as a frequency-dependent function. If the velocity potential oscillates harmonically in time, with an angular frequency ω_w, then

$$\Phi(x,y,z,t) = Re\{\hat{\Phi}(x,y,z)e^{i\omega_w t}\}, \tag{3.12}$$

where the $\hat{}$ sign represents complex amplitude and t is the time vector. Note that the harmonic content in Equation (3.12) is represented as $e^{-i\omega_w t}$ in NEMOH [177].

Initially, monochromatic waves are convenient, since they represent the basic problem, even if real waves are never monochromatic. In any case, the extension to polychromatic waves, which better represent real waves, is straightforward using the superposition of sinusoidal waves of different frequency and amplitude.

Based on Equation (3.12), the Laplace equation is represented as

$$\bigtriangledown^2 \hat{\Phi} = 0, \tag{3.13}$$

and the boundary conditions become,

$$-\omega_w^2 \hat{\Phi} + g\frac{\partial \hat{\Phi}}{\partial z} = 0 \qquad at \;\; z = 0, \tag{3.14}$$

$$\frac{\partial \hat{\Phi}}{\partial z} = 0 \qquad at \;\; z = -h_{sea}, \;\; \text{and} \tag{3.15}$$

$$\frac{\partial \hat{\Phi}}{\partial n} = \hat{v}_n. \tag{3.16}$$

The wave frequency ω_w is related to the wavenumber via the dispersion relation,

$$\frac{\omega_w^2}{g} = k_w \tanh(k_w h_{sea}), \tag{3.17}$$

and the wave elevation η_w for monochromatic waves can be given as follows,

$$\eta_w = Re\{A_w e^{(\omega_w t - ik_w(x\cos\beta_w + y\sin\beta_w) + \phi_w)}\} = A_w \cos(\omega_w t - k_w(x\cos\beta_w + y\sin\beta_w) + \phi_w), \tag{3.18}$$

where A_w is the wave amplitude, β_w the direction of propagation of the incident wave and ϕ_w the phase of the wave. In the case of more realistic polychromatic waves, assuming unidirectional waves and η_w measurements at the centre of the absorber, the most established way to generate η_w is by adding a finite number of sinusoidal Fourier components [78] as follows,

$$\eta_w(k) = \sum_{k=1}^{N_w} A_{w,k}\, cos(2\pi\, f_{w,k} t(k) + \phi_{w,k}), \tag{3.19}$$

where N_w is the number of frequency components, $f_{w,k}$ the frequency in Hz, $\phi_w \in [0, 2\pi]$ the vector of randomly chosen phases, $A_w = \sqrt{2S_w(f_{w,k})\Delta f_w}$ the amplitude function, $S_w(f_{w,k})$ the spectral density function that represents wave characteristics of a given location, and Δf_w the frequency step. The spectral density function S_w can be generated following different theoretical spectra, as described in Section 2.1.

3.1.2 Linear WSHI forces

The governing equation of the absorber is represented by Newton's second law, as shown in Equation (2.6), where the total fluid force acting on the absorber is calculated by integrating the pressure of the fluid over the wetted surface, and the pressure is calculated via Bernoulli's equation. In the linear case, based on the superposition principle, Φ can be represented as the superposition of the incident (Φ_I), diffracted (Φ_{diff}) and radiated (Φ_{rad}) potentials as follows,

$$\Phi = \Phi_I + \Phi_{diff} + \Phi_{rad}, \tag{3.20}$$

where the velocity potential of a propagating incident wave, based on Airy's theory and using the boundary conditions described in Equations (3.14) and (3.15), can be obtained [287] as,

$$\Phi_I = \frac{g}{\omega_w} A_w \frac{\cosh[k_w(z+h_{sea})]}{\cosh(k_w h_{sea})} e^{ik_w(x\cos\beta_w + y\sin\beta_w)}. \tag{3.21}$$

In addition, pressure is integrated over $\overline{S}$ and the nonlinear terms in Equation (2.5) are neglected. Hence, the pressure of the incident wave field acting on the body in the linear case, including hydrostatic and hydrodynamic pressure, can be given as,

$$p_I = -\rho_w g x_{abs} - \rho_w \frac{\partial \Phi_I}{\partial t} = - \underbrace{\rho_w g x_{abs}}_{\substack{\text{hydrostatic} \\ \text{pressure } (p_{I_{stat}})}} \underbrace{- \rho_w g A_w \frac{\cosh[k_w(z+h_{sea})]}{\cosh(k_w h_{sea})} e^{-ik_w(x\cos\beta_w + y\sin\beta_w)}}_{\text{hydrodynamic pressure } (p_{I_{dyn}})}. \tag{3.22}$$

Therefore, assuming the superposition principle of the different effects acting on the WSHI, Equation (2.6) can be replaced using Newton's second law,

$$M\ddot{x}_{abs} = F_g + F_{FK_{st}} + F_{FK_{dyn}} + F_{diff} + F_{rad} + F_{ext}, \tag{3.23}$$

where F_{ext} represents any external force, such as F_{visc}, F_{PTO} or F_{moo}. Apart from F_{ext}, the rest of the forces are calculated by computing the corresponding part of the pressure p_{WSHI} described in Equation (2.5) over $\overline{S}$:

- $F_{FK_{stat}}$ is the static FK force, also known as buoyancy force, formed by integrating $p_{I_{stat}}$ over $\overline{S}$,

$$F_{FK_{stat}} = -\iint_{\overline{S}} p_{I_{stat}} n\, dS, \tag{3.24}$$

- $F_{FK_{dyn}}$ is the dynamic FK force, obtained by integrating $p_{I_{dyn}}$ over $\overline{S}$,

$$F_{FK_{dyn}} = -\iint_{\overline{S}} p_{I_{dyn}} n\, dS, \tag{3.25}$$

- F_{diff}, given by integrating the pressure of the diffracted wave ($p_{diff} = -\rho\frac{\partial\Phi_{diff}}{\partial t}$) over $\overline{S}$,

$$F_{diff} = -\iint_{\overline{S}} p_{diff} n \, dS, \tag{3.26}$$

- F_{rad}, obtained by integrating the pressure of the radiated wave($p_{rad} = -\rho\frac{\partial\Phi_{rad}}{\partial t}$) over $\overline{S}$,

$$F_{rad} = -\iint_{\overline{S}} p_{rad} n \, dS. \tag{3.27}$$

Hence, as shown in Equation (2.7), the governing equation (3.23) can be represented following Cummins' equation, as follows,

$$M\ddot{x}_{abs} = -\underbrace{K_H x_{abs}}_{F_g+F_{FK_{stat}}} + \underbrace{\int_{-\infty}^{\infty} K_{ex}(t-\tau)\eta_w d\tau}_{F_{ex}=F_{FK_{dyn}}+F_{diff}} - \underbrace{\mu_\infty \ddot{x}_{abs} - \int_{-\infty}^{t} K_{rad}(t-\tau)\dot{x}_{abs}(\tau)d\tau}_{F_{rad}}, \tag{3.28}$$

where K_H is the hydrostatic stiffness and any F_{ext} is neglected. Hence, the mathematical model based on Equation (3.28) corresponds to the LPF model presented in Figure 2.23 (a).

3.1.3 Hydrodynamic coefficients

The solution of the LPF model, using Equation (3.28), requires the identification of hydrodynamic coefficients K_H, K_{ex}, μ_∞ and K_{rad}. To that end, BEM solvers are commonly used. These BEM solvers, also known as panel methods solvers, are numerical techniques which use systems of partial differential equations formulated into a boundary integral form. Boundary element method solvers attempt to fit boundary values into the integral equation and employ Green's functions to transform a flow problem into a problem of source distribution on the body surface [177]. In the hydrodynamic context, BEM solvers are used to solve the scattered and radiated velocity potentials, which are solved separately, and which arise from the interaction of a harmonic linear wave field with a body located within that field. The scattering potential is solved for the submerged part of the body when the body is held fixed and is used to determine the excitation force acting on the body due to the action of the waves ($\hat{F}_{ex}$). The radiation potential, where the potential is found for a moving body in the absence of incident waves, is commonly resolved into components in phase with the body acceleration and the body velocity, and gives rise to the added-mass (A_{rad}) and radiation damping (B_{rad}) terms.

A number of commercial software codes have been developed to implement the BEM and determine the hydrodynamic parameters of user-generated geometries. Such codes include FD (*e.g.* WAMIT [100], Aquaplus [102], Aqwa [101] or WADAM [288]) and time-domain (TD) solvers (*e.g.* ACHIL3D [289]). In 2014, the École Centrale de Nantes released NEMOH [177], an open-source FD BEM solver.

Capabilities of the open-source code NEMOH [177] for different types of WECs are verified in Appendix A, using the well-established commercial BEM solver WAMIT [100] as the benchmark. The results in Appendix A are only evaluated as relative agreement between NEMOH and WAMIT, showing the good performance of the NEMOH solver, meaning that it is able to produce results similar to WAMIT.

The suitability of the NEMOH solver is particularly good for wave-activated WECs, unless the wave-activated WECs include a damping plate that requires the use of thin elements, as demonstrated in Appendix A. The absorber utilised in this thesis is a spherical HPA of 5m diameter, restricted to heave motion for the sake of simplicity, as illustrated in Figure 3.2 (a). Therefore, hydrodynamic coefficients obtained with NEMOH can be considered reliable. In addition, the

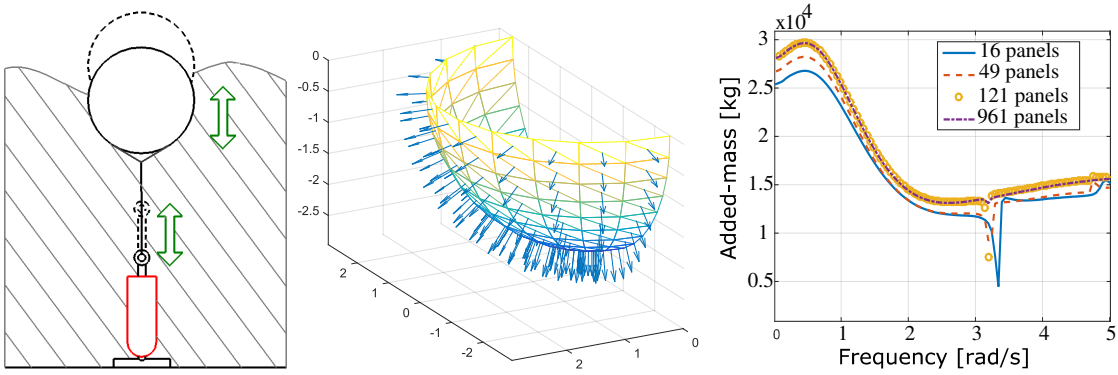

(a) Spherical HPA sketch. (b) Mesh of the spherical HPA. (c) Mesh convergence study.

Figure 3.2: Spherical HPA schematic representation (a), converged mesh (b) and results of the mesh convergence study (c).

device is assumed to operate in deep-water conditions. The device is modelled in NEMOH using 121 panels, following a mesh convergence study. Figure 3.2 (b) and (c) illustrate, respectively, the mesh of the spherical HPA and results of the convergence study.

Using the mesh shown in Figure 3.2 (b), FD hydrodynamic coefficients A_{rad}, B_{rad}, and $\hat{F}_{ex}$, illustrated in Figure 3.3, can be obtained. One can notice that the FD coefficients obtained from NEMOH include some undesirable spikes, which correspond to aforementioned irregular frequencies. These spikes should be removed, since they are numerical errors. In this thesis, the data corresponding to the irregular frequencies are manually removed and the curves are interpolated, using a spline interpolation function [290], to fit the gaps of the irregular frequencies. Results are shown in Figure 3.3, where the final FD coefficients without irregular frequencies ($\text{NEMOH}_{\text{adjusted}}$ in Figure 3.3) are compared with the coefficients obtained directly from NEMOH ($\text{NEMOH}_{\text{original}}$ in Figure 3.3) and from WAMIT.

In addition, FD coefficients need to be converted into TD coefficients to be used in Equation (3.28). The excitation IRF can be obtained as follows,

$$K_{ex}(t) = \frac{1}{\pi}\int_0^\infty \Re(\hat{F}_{ex}(\omega_w)e^{i\omega_w t})\, d\omega_w, \tag{3.29}$$

while Ogilvie's equations [291, 292] can be used to calculate TD radiation coefficients,

$$K_{rad}(t) = \frac{2}{\pi}\int_0^\infty B_{rad}\cos(\omega_w\tau)\, d\omega_w, \tag{3.30}$$

$$\mu_\infty = A(\omega_w) + \frac{1}{\omega_w}\int_0^\infty K_{rad}(\tau)\sin(\omega_w\tau)\, d\omega_w. \tag{3.31}$$

3.2 Partially-nonlinear extension of the linear model

The linear model presented in Equation (3.28) can be extended to include nonlinear effects. The relevance of different nonlinear effects is studied in Chapter 2, where the need for nonlinear waves is examined and the relevance of nonlinear effects for WSHIs are analysed separately for each WEC type. In the case of HPAs, Section 2.2.2.2 suggests that nonlinear FK forces are the most important nonlinear effects. However, since the characteristic length of the spherical HPA is considerably smaller than the wavelength, the linear representation for radiation and diffraction forces is considered to be accurate. Finally, viscous effects also seem to be important under control conditions.

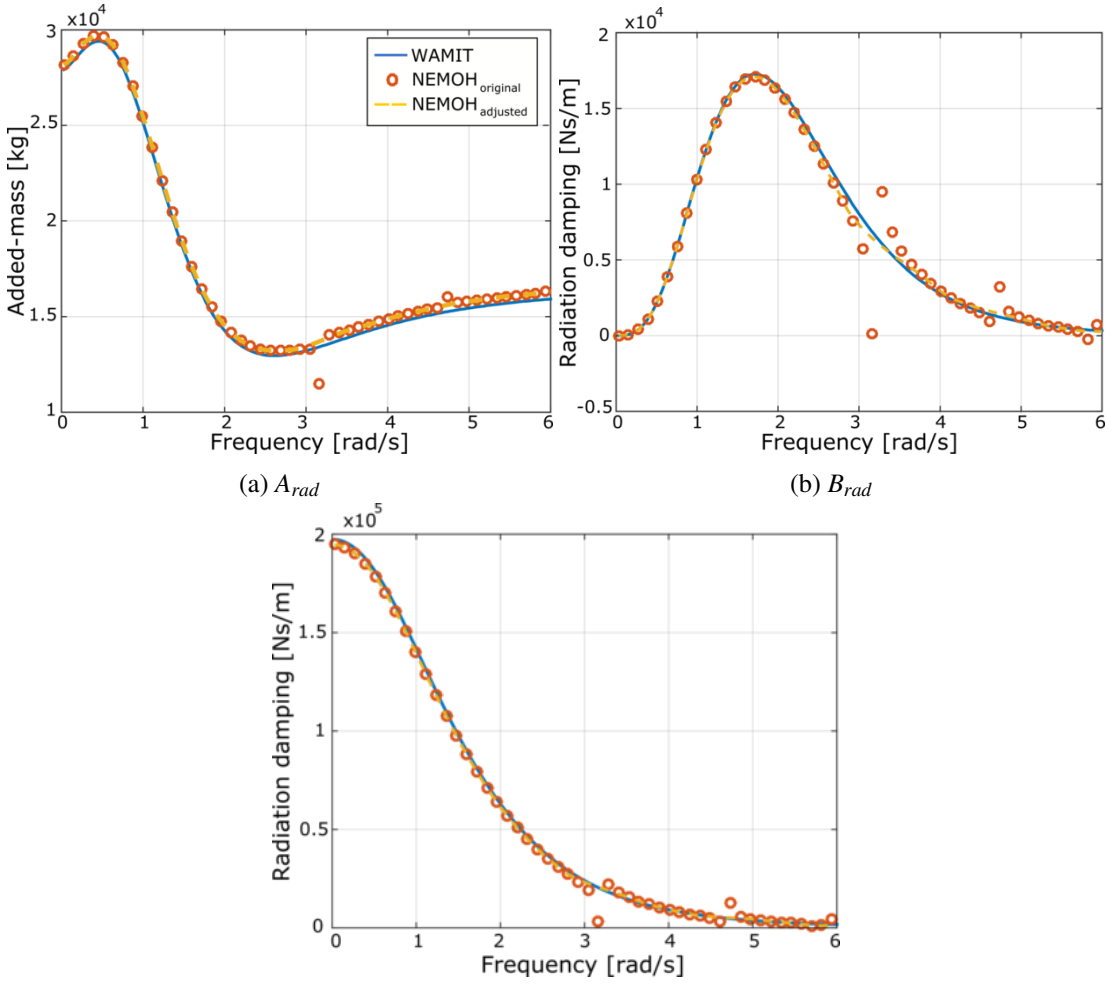

(a) A_{rad} (b) B_{rad}

(c) $\hat{F}_{ex}$

Figure 3.3: FD hydrodynamic coefficients for the spherical HPA.

Hence, approaches to include nonlinear waves (Section 3.2.1), nonlinear FK forces (Section 3.2.2) and viscous effects (Section 3.2.3) in the mathematical model are analysed in the following subsections.

3.2.1 Nonlinear waves

Two main approaches for nonlinear waves have traditionally been used: Stokes' and Cnoidal theory. Stokes' theory is suitable for deep water waves, while the Cnoidal theory is suitable for shallow water waves [293]. Due to the lack of universal applicability of Stokes' and Cnoidal theories, a numerical method based on the Fourier approximation technique was created: Rienecker-Fenton theory [72]. This mathematical formulation is based on potential flow theory and gives the numerical solution of a regular progressive wave.

Rienecker and Fenton presented a mathematical formulation using Airy's theory as the first approximation. The Rienecker-Fenton algorithm generates wave-trains for different ocean depths, wave amplitudes and wavelengths, respecting nonlinear limit conditions on the free-surface.

$$\Phi_I = \sum_{i=0}^{n} \Phi_i, \tag{3.32}$$

$$\Phi_i = B^i_{RF} \frac{\sinh(ik_w(z+h_{sea}))}{\cosh(ik_w h_{sea})} \cos(ik_w(x-c_w t)), \tag{3.33}$$

where B^i_{RF} is a coefficient defined in the algorithm presented in [72] and c_w the phase velocity. Figure 3.4 illustrates the free-surface elevation for Airy's theory (L_w) and Rienecker-Fenton' algorithm (NL_w) for an 8s monochromatic wave, where the free-surface elevation of the linear and nonlinear wave theories appear to be identical. However, the nonlinear wave has a slightly sharper crest and flatter trough, as expected.

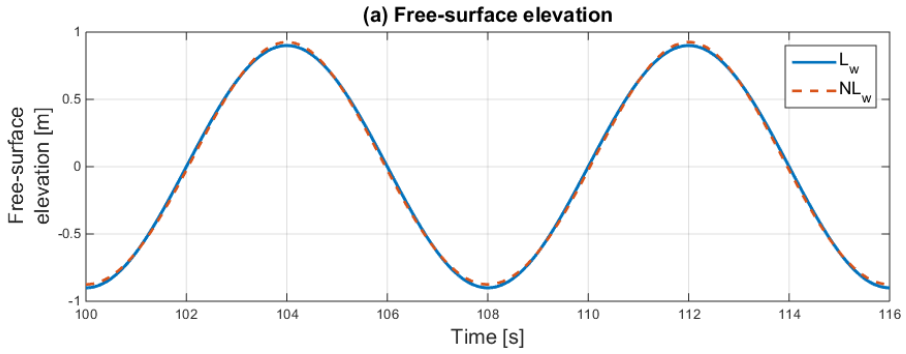

Figure 3.4: Free-surface elevation for a wave of 8s period based on linear and nonlinear wave theories.

3.2.2 Nonlinear Froude-Krylov forces

Nonlinear FK forces can be considered by computing the pressure of the potential flow acting on the body over the precise instantaneous wetted surface at each time-step.

3.2.2.1 Nonlinear restoring force

The simplest possibility to partially consider nonlinear FK forces is to include a nonlinear restoring force by integrating Equation (3.24) over S, instead of $\overline{S}$. The mean $\overline{S}$ and instantaneous wetted surface S are respectively depicted in Figures 3.5 (a) and (b) for a generic heaving body. The instantaneous wetted surface S can be described by subtracting the horizontal surface that defines the intersection between the floating body and the water plane S_{WP} to the closed surface S_c ($S = S_c - S_{WP}$), as shown in [238]. This S_{WP} is defined in Figure 3.5 (b) as the intersection between the body and the horizontal plane at the free surface elevation η_w. Consequently, $F_{FK_{stat}}$ can be computed as follows:

$$F_{FK_{stat}} = -\left(\iint_{S_c} p_{I_{stat}} n \, dS - \iint_{S_{WP}} p_{I_{stat}} n \, dS \right). \tag{3.34}$$

Applying Gauss's divergence theorem to the integral over the closed surface S_c, Equation (3.34) becomes:

$$F_{FK_{stat}} = (\rho_w g V_{sub} - \rho_w g \eta_w A_{cs}), \tag{3.35}$$

where V_{sub} is the submerged volume enclosed by S_c.

Since the instantaneous wetted surface is taken into account, it is possible to evaluate when the relative displacement between the vertical motion of the floater and the free surface elevation exceeds the vertical dimensions of the floater itself, i.e. when the floater is completely out of the water. In such an unrealistic situation, the fluid force is absent; therefore, the excitation force is set to zero.

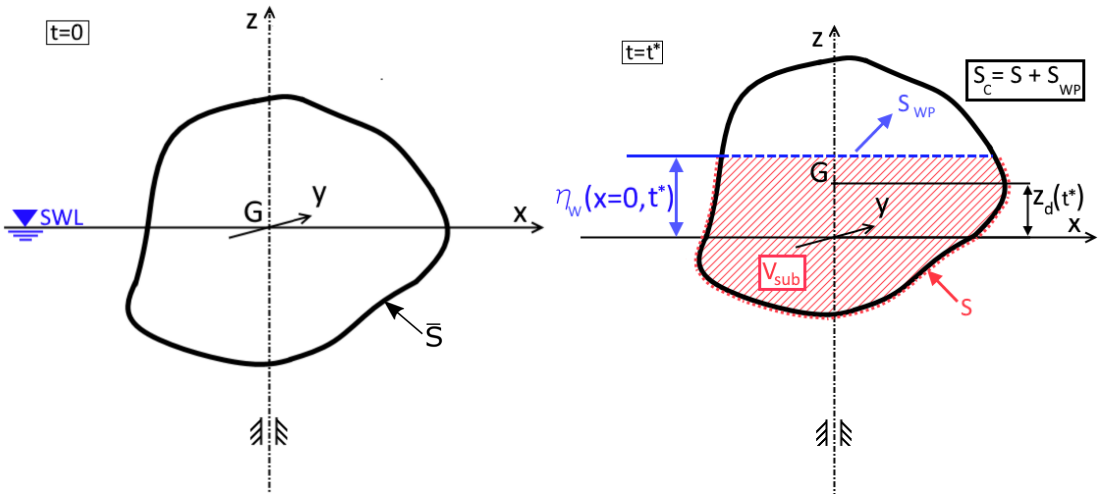

(a) A generic device floating in still water. (b) A generic device moving with waves.

Figure 3.5: A generic heaving device, with the centre of gravity G at the still water level (SWL) (a), and the free surface elevation η_w and the device's heave displacement z_d after a time t^* (b). The closed surface S_c surrounds the submerged volume V_{sub}, which is bounded from above by the water plane surface S_{WP}.

3.2.2.2 Nonlinear static and dynamic Froude-Krylov forces

A more consistent method to consider nonlinear FK forces is to include, both static and dynamic FK forces. In that case, Equation (3.28) is replaced as follows,

$$M\ddot{z}_d = F_g - \underbrace{\iint_S (p_{I_{stat}} + p_{I_{dyn}}) n \, dS}_{F_{FK}} - \underbrace{\int_{-\infty}^{\infty} K_{diff}(t-\tau)\eta_w d\tau}_{F_{diff}} - \underbrace{\mu_\infty \ddot{z}_d - \int_{-\infty}^{t} K_{rad}(t-\tau)\dot{x}_{abs}(\tau)d\tau}_{F_{rad}}, \tag{3.36}$$

where K_{diff} is the diffraction IRF. Since the spherical HPA is restricted to move only in heave, the generic displacement, velocity and acceleration terms x_{abs}, $\dot{x}_{abs}$ and $\ddot{x}_{abs}$ in Equation (3.28) are replaced by the more specific z_d, $\dot{z}_d$ and $\ddot{z}_d$, respectively, which only represent the heaving motion of the spherical HPA.

In order to integrate the Froude-Krylov forces over S, different methods are described in Section 2.2.3.2, which all provide identical results. The approach with the remeshing routine suggested in [161] is used in Section 3.2.4 to evaluate the impact of nonlinear static and dynamic FK forces.

3.2.3 Viscous effects

Finally, viscous effects, in potential flow theory, must be added as external forces, as described in Section 2.2.3.2. To that end, a Morison-like equation is commonly used [178], as shown in Equation (2.8), where viscous effects are captured by a quadratic drag term,

$$F_{vis} = -\frac{1}{2}\rho A_{cs} C_{drag}(\dot{x}_{abs} - V_{w0}) \mid \dot{x}_{abs} - V_{w0} \mid, \tag{3.37}$$

where V_{w0} represents the undisturbed flow velocity. Notwithstanding the simplicity of the viscous model in Equation (3.37), the identification of C_{drag} is not straightforward. Ideally, experimental tests can be used to identify C_{drag}, as in [182]. Nevertheless, in most cases, access to wave tank facilities is costly and time consuming, and the construction of a scaled prototype is not always possible. Such problems may be overcome by performing the identification of C_{drag} in a CNWT, as in [184, 294].

Alternatively, when the absorber's geometry under analysis is simple, it is possible to define an *a priori* C_{drag} based on established theoretical or tabulated knowledge. In the case of HPAs, the KC number, introduced in Section 2.2.1.4, can be used. In the case of sinusoidal motion, the KC number can be computed as:

$$KC = 2\pi \frac{A_{abs}}{L_c}, \tag{3.38}$$

where A_{abs} is absorber's amplitude of motion and L_c the characteristic length (spheres diameter in this case). For the spherical HPA studied in this thesis, A_{abs} is likely to be of the same order of magnitude as L_c, resulting in a Keulegan-Carpenter number KC of about 2π, for which a $C_{drag} = 1$ is a reasonable option, according to [180]. Hence, the *viscLPF* model presented in Figure 2.23 (a), where viscous effects are the only nonlinear effects, is given by extending Equation (3.28) to include F_{visc} as follows,

$$M\ddot{z}_d = -K_H z_d + \int_{-\infty}^{\infty} K_{ex}(t-\tau)\eta_w d\tau - \mu_\infty \ddot{x}_{abs} - \int_{-\infty}^{t} K_{rad}(t-\tau)\dot{z}_d(\tau)d\tau + F_{visc}. \tag{3.39}$$

3.2.4 Evaluation of the different nonlinearities

Once the mathematical models to represent the different relevant nonlinearities are described, the impact of each nonlinear effect can be evaluated. Equation (3.28) can be extended to include nonlinear FK forces and externally added viscous effects as follows

$$M\ddot{z}_d = F_g - \iint_S (p_{I_{stat}} + p_{I_{dyn}}) n \, dS + \int_{-\infty}^{\infty} K_{diff}(t-\tau)\eta_w d\tau - \mu_\infty \ddot{z}_d - \int_{-\infty}^{t} K_{rad}(t-\tau)\dot{x}_{abs}(\tau)d\tau + F_{visc} + F_{PTO} + F_{EndStop}. \tag{3.40}$$

To quantify the impact of each nonlinear effect, the simulation conditions, including the range of incoming waves and control strategies employed, need to be first defined.

3.2.4.1 Simulation conditions

A range of monochromatic waves is defined with waves of periods (T_w) between 3 and 8s, for which the wave steepness, the relationship between the wave height (H_w) and the wavelength (λ_w), remains constant over the complete range ($\frac{H_w}{\lambda_w} \approx 0.018$). Table 3.1 defines the main characteristics of the incoming waves analysed in this section.

Table 3.1: Range of monochromatic waves analysed, with a constant steepness of approximately 0.018.

T_w [s]	3	4	5	5.5	6	6.5	7	7.5	8
H_w [m]	0.25	0.45	0.7	0.85	1	1.19	1.38	1.58	1.8
λ_w [m]	14	25	39	47	56	66	77	88	100

In addition, in order to demonstrate the impact of the absorber's geometry on the relevance of nonlinear FK forces, a cylindrical HPA with a uniform CSA is included in the analysis. Table 3.2 provides the necessary information about the spheric and cylindrical HPA.

Finally, the control strategy used to maximise power absorption from ocean waves has an influence on the relevance of nonlinear effects. Therefore, the relevance of nonlinear effects is analysed under docile and aggressive control strategies. For the present study, resistive control,

Table 3.2: Geometrical and PTO characteristics of the bodies

Characteristics [unit]	Spherical HPA	Cylindrical HPA
Radius [m]	2.5	2.5
Draft [m]	-	2.5
Displacement [m^3]	32.72	49.1
Natural period [s]	3.2	4.1
$B_{PTO,1}$ [Ns/m]	25000	26000
$B_{PTO,2}$ [Ns/m]	42000	52000

described in Equation (3.41), is implemented as the docile control example, while the aggressive control strategy is represented by latching control. Resistive control is defined by

$$F_{PTO} = -B_{PTO}\,\dot{z}_d, \tag{3.41}$$

where B_{PTO} is the PTO damping coefficient. Table 3.2 includes the values of the B_{PTO} parameters implemented in the analysis. Two B_{PTO} parameters are provided for each absorber. The first set of B_{PTO} parameters ($B_{PTO,1}$) is optimised with the linear representation of FK forces to maximise power absorption. The second set ($B_{PTO,2}$) is also optimised with the linear representation of the FK forces, but the motion of the HPAs is constrained, so that they never get fully submerged nor fully out of the water. Thus, the set of $B_{PTO,2}$ parameters allows for a fair comparison of the effects of nonlinear FK forces for the two HPAs.

The latching strategy consists of locking (latching) the device when its velocity goes to zero and keeping the device latched until the wave force reaches the most advantageous phase, as shown in Figure 3.6, where θ_F is the phase offset between the force and the displacement. Latching control has proven to increase power absorption by a factor of 2 in polychromatic waves and a factor of 4 in monochromatic waves [295].

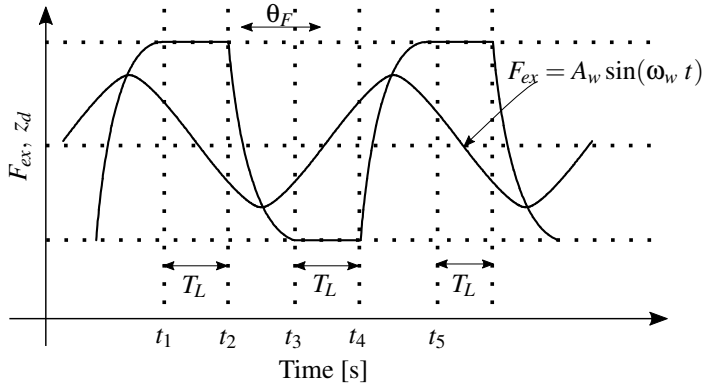

Figure 3.6: Latching calculations, [296]

The control variable is the duration of the latching period (T_L), calculated using the natural period of the device ($T_{\omega_0} = 2\pi/\sqrt{\frac{K_H}{(M+A_{rad}(\omega_w))}}$) and T_w. Equation ((3.42)) shows, to a first approximation, the calculation of the latching period as a function of the timings defined in Figure 3.6,

$$T_L = \frac{t_5 - t_1}{2} - (t_5 - t_4) = \frac{T_w}{2} - \frac{T_{\omega_0}}{2}. \tag{3.42}$$

The PTO system in the case under latching control is also modelled as in the case of the resistive control, following Equation (3.41). Equation (3.42) is designed for an optimal performance with linear WEC models, for which T_{ω_0} is constant. In the following, the latching strategy designed using a constant T_{ω_0} is referred to as the *fixed-time* latching strategy.

However, T_{ω_0} is not as clearly defined for a model containing a nonlinear computation of FK forces, since the hydrostatic stiffness varies significantly for the case where the cross-sectional area

(CSA) of the device is not constant. Therefore, the optimal latching period needs to be adaptively calculated to achieve the greatest motion and power absorption. A basic algorithm, referred to as the *adaptive* latching strategy and illustrated in Figure 3.7, is used here to determine the optimal latching period. This *adaptive* latching algorithm consists of modifying the latching period step-by-step in a direction that increases the motion amplitude. Between two consecutive updates, the algorithm waits for the motion to reach a steady state in order to get a reliable evaluation of the behaviour of the device. The criterion to confirm that steady state has been reached is to check whether the measured period of the device motion (T_m) is similar to the wave period (T_w). It should be noted that the *adaptive* strategy presented in Figure 3.7 can only be used with monochromatic waves.

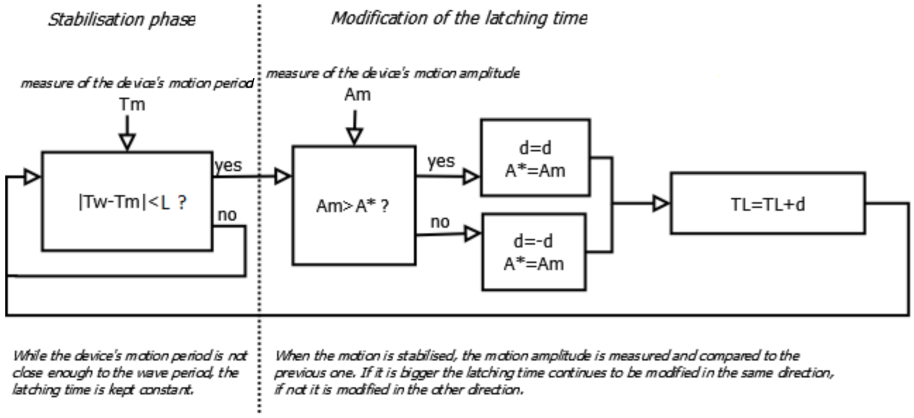

Figure 3.7: Diagram of the *adaptive* latching strategy algorithm.

In Figure 3.7, L is the threshold which determines whether the motion has reached steady state, A^* the memorised motion amplitude obtained with the previous latching time and d the variation in latching time. It is important to note that, when applied to the linear hydrodynamic modelling case, the *adaptive* latching strategy converges to the *fixed-time* latching strategy.

3.2.4.2 Results

Firstly, the impact of the absorber's geometry on the relevance of nonlinear FK forces is analysed comparing the response of the cylindrical and spherical HPA under latching control. For this case, the set of $B_{PTO,2}$ is used, so that the HPAs never clear the water or get fully submerged. Hence, discrepancies between the cylindrical and spherical HPA arise from their geometric differences, that is, the different CSA profiles. To that end, two representations of the FK forces are used: linear (*LFK*) and nonlinear FK forces (*NLFK*), where the latter includes nonlinear static and dynamic FK forces using a mesh-based approach [161], for which mesh conversion has been checked.

Figure 3.8 (a) illustrates the response of the cylindrical HPA, over the complete range of incoming waves described in Table 3.1, via the response amplitude operator (RAO), which illustrates the absorber's motion with respect to the free-surface elevation. Hence, RAO values for the *LFK* and *NLFK* simulation models show identical results, showing, as expected, that nonlinear FK effects are negligible for HPAs with a uniform CSA. Figure 3.8 (b) illustrates the velocity of the cylindrical HPA for the 8s monochromatic wave under *fixed-time* latching control, where the responses of the *LFK* and *NLFK* models are shown to be identical. In addition, Figure 3.8 (b) illustrates the device velocity to be perfectly in phase with the excitation force for the linear and partially-nonlinear models, which demonstrates the efficacy of the *fixed-time* latching strategy for both simulation models.

In contrast to the cylinder case, nonlinearities have a significant impact on the behaviour of the sphere, due to its non-uniform CSA. The solid and dashed curves in Figure 3.9 illustrate RAO

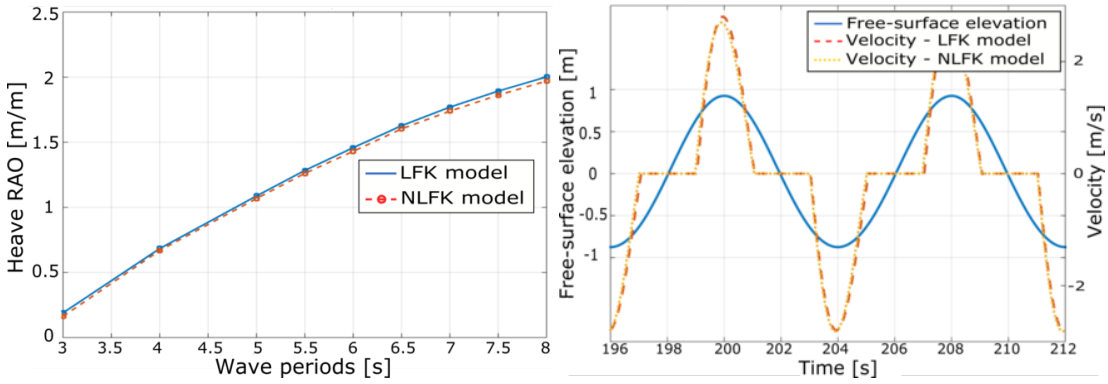

(a) (b)

Figure 3.8: Response of the cylindrical HPA represented via the *LFK* and *NLFK* models: RAOs over the complete range of input waves (a) and the velocity (b) for the 8s wave.

values for simulation under *fixed-time* latching control, using the *LFK* and *NLFK* representations, respectively. The difference between the *LFK* and *NLFK* models under the *fixed-time* latching strategy increases substantially as waves and, as a consequence, device motion become larger. Figure 3.10 (a) also illustrates the significant reduction of the oscillation amplitude for the *NLFK* representation, compared to the *LFK* representation, for the 8s wave.

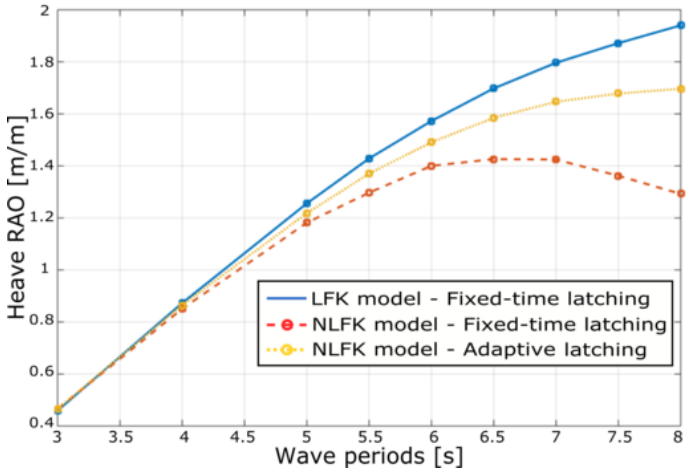

Figure 3.9: RAOs for the spherical HPA via the *LFK* and *NLFK* representations over the complete wave range and under *fixed-time* and *adaptive* latching strategies.

However, the difference between the *LFK* and *NLFK* simulation models is mostly due to the inability of the *fixed-time* latching strategy to align the peaks of the device velocity and the excitation force for the *NLFK* model, as shown in Figure 3.10 (c). Therefore, it is demonstrated that the accurate representation of FK forces is crucial to accurately design energy maximising control strategies, unless robust control strategies that are relatively insensitive to modelling errors are used. In the presence of significant nonlinearities, the control strategy that considers the effect of nonlinear FK forces (*adaptive* latching) shows the ability to maximise the motion of the device and, as a consequence, absorbed power. Figures 3.10 (a) and (b) illustrate the difference in performance of the *fixed-time* and the *adaptive* latching strategies. When applied to the *LFK* model, the *adaptive* latching strategy provides identical results to the *fixed-time* latching strategy. In contrast, when applied to the *NLFK* model, the *adaptive* latching strategy substantially enlarges the amplitude of device motion, compared to the case where the *fixed-time* strategy is applied.

Such improvement in the controller performance, arises from the adjustment of the latching

time to the slower nonlinear dynamics of the spherical HPA. The *adaptive* algorithm calculates the optimal latching time for the *NLFK* model ($T_L^{'}$), which is shorter than the optimal latching time for the linear case T_L, as shown in Figure 3.10 (b).

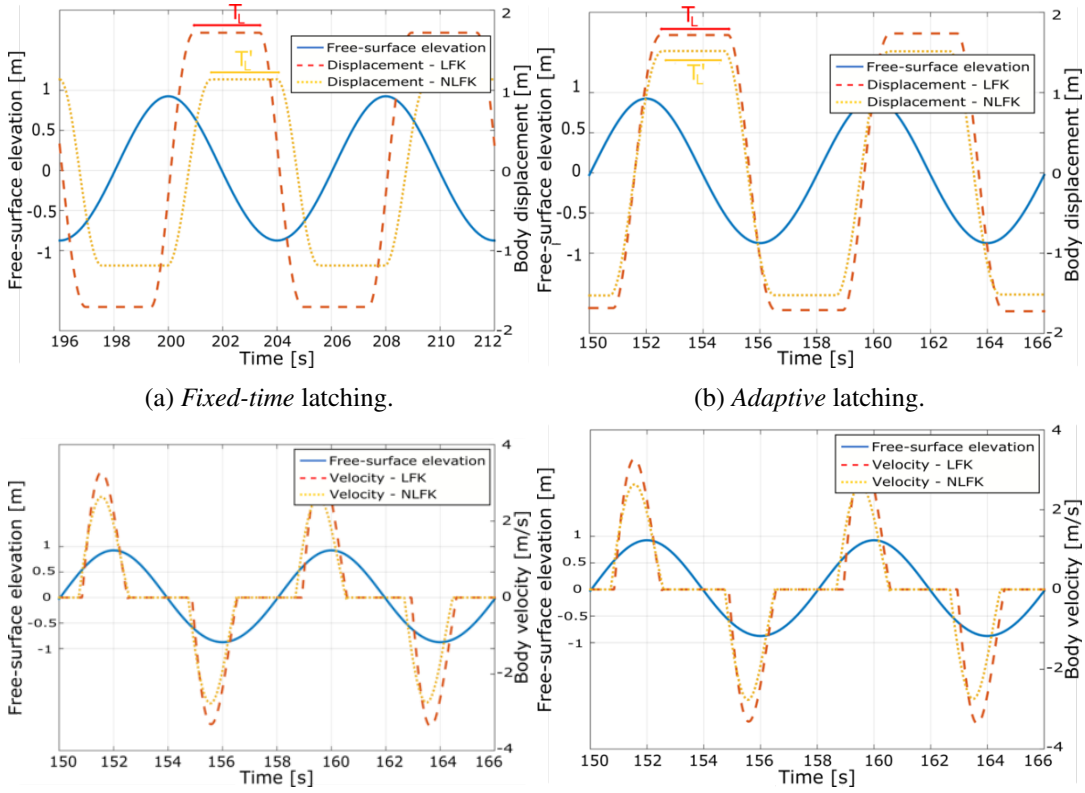

(a) *Fixed-time* latching.

(b) *Adaptive* latching.

(c) *Fixed-time* latching.

(d) *Adaptive* latching.

Figure 3.10: Free-surface elevation, and body displacement and velocity for the 8s wave via the *LFK* and *NLFK* simulation models under *fixed-time* latching (a) and (c), and *adaptive* latching control (b) and (d).

In fact, Figure 3.9 also illustrates RAO values for the *NLFK* representation using *adaptive* latching control, where the improvement of the *adaptive* strategy compared to the *fixed-time* latching strategy is shown to be significant.

The comparison between the *LFK* and *NLFK* representations can be extended to the analysis of the static and dynamic components of the FK forces. Due to the differences between Equations (3.28) and (3.36), static and dynamic FK forces from the *LFK* and *NLFK* models cannot be compared directly. The restoring force in the *LFK* model is given by means of the K_H, while in the *NLFK* model it is the sum of F_g and $F_{FK_{stat}}$. Similarly, excitation force in the *LFK* model is equivalent to the sum of F_{diff} and $F_{FK_{dyn}}$ in the *NLFK* model. Therefore, displacement, and restoring and excitation forces are compared in Figure 3.11, where differences are normalised against the results obtained in the *LFK* model.

Displacement, and restoring and excitation force amplitudes from the *NLFK* model, compared to the *LFK* model, are shown to be always lower in Figure 3.11, which means that the *LFK* representation overestimates the forces acting on the spherical HPA and, as a consequence, the response of the spherical HPA. In addition, this difference between the *LFK* and *NLFK* models increases for all the three variables as waves become longer and higher. However, while the excitation force for the *NLFK* representation is always close to the *LFK* representation, the difference between the linear and nonlinear restoring forces is significant. Furthermore, one can observe, in Figure 3.11, that differences between the *LFK* and *NLFK* representations for the displacement and the restoring

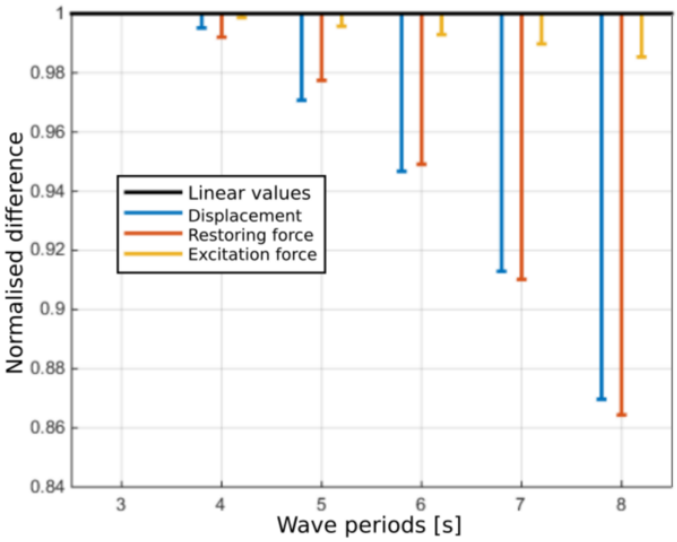

Figure 3.11: Normalised differences between the *LFK* and *NLFK* models for the displacement, restoring force and excitation force amplitudes over all the analysed wave periods. The amplitudes are normalised against the *LFK* model, 1 meaning results are identical to the *LFK* model.

force are very similar, which demonstrates the higher relevance of the static part. Thus, one may think that a mathematical model that only considers the nonlinear restoring force (*NLrest*) can be sufficient to accurately represent the behaviour of the spherical HPA.

To study the suitability of the *NLrest* model, the response of the spherical HPA is evaluated under the aggressive control strategy, *i.e adaptive* latching, over the complete wave range. In this case, the PTO damping optimised to maximise energy absorption without constraints ($B_{PTO,1}$) is used, to cover all the possible situations of a WEC, including the device getting fully submerged or fully out of the water. Hence, device motion increases considerably, compared to simulations where the PTO damping is optimised subject to constraints ($B_{PTO,2}$), as one can notice comparing Figures 3.9 and 3.12 (a).

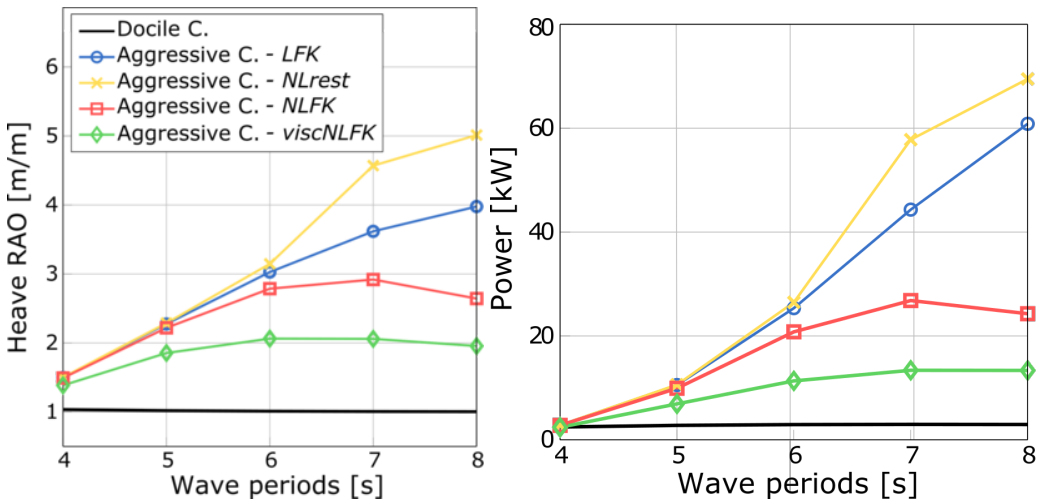

(a) (b)

Figure 3.12: Response of the spherical HPA estimated via different modelling approaches under docile and aggressive (*adaptive* latching strategy) control and using the $B_{PTO,1}$ parameter: displacement RAOs (a) and absorbed power (b) over the global wave range.

Under docile control, also using $B_{PTO,1}$, the spherical HPA behaves as a wave follower, since

the RAO is effectively 1 over the complete range of incoming waves, as illustrated in Figure 3.12 (a). Conversely, the aggressive control enhances the motion of the spherical HPA, specially for waves with periods greater than 6s, and, consequently, the nonlinear representation of FK forces becomes relevant. However, Figure 3.12 (a) illustrates that the *NLrest* model cannot accurately capture the behaviour of the spherical HPA. In fact, the *NLrest* model overestimates the motion of the spherical HPA even more than the *LFK* model. This happens because, in the *LFK* representation, the restoring force is computed as if the CSA were constant, so the restoring force increases as the absorber moves away from the equilibrium position. Hence, the restoring and the excitation forces are balanced in the *LFK* representation, meaning that the inaccuracies of the restoring force somewhat counterbalance the inaccuracies of the excitation force, and vice versa.

In contrast, the CSA decreases in the *NLrest* model as the body moves away from the equilibrium position and, thus, the restoring force decreases and a larger amplitude of motion ensues. Moreover, the magnitude of the nonlinear restoring force has an upper limit equal to the gravity force (when the body is completely out of the water or completely submerged) while, in the linear case, the restoring force is unbounded and directly proportional to the absorber's displacement. Therefore, the balance between the restoring force and the excitation force is broken in the *NLrest* model, resulting in greater overestimation of the displacement and absorbed power.

In addition to the *NLrest* model, an additional mathematical model that includes the nonlinear representation of the static and dynamic FK forces and viscous effects (*viscNLFK*) is also analysed in Figure 3.12. The *viscNLFK* model highlights the impact of viscous effects, which reduce the motion of the spherical HPA. Even though these viscous effects seem important, FK nonlinearities are the most relevant nonlinear effects in the case of the spherical HPA [114]. Similar trends can be observed in Figure 3.12 (b), where power estimates for the four different mathematical models analysed in this section are shown. The *LFK* and *NLrest* models significantly overestimate the power absorption of the spherical HPA, while the *viscNLFK* is the most conservative model.

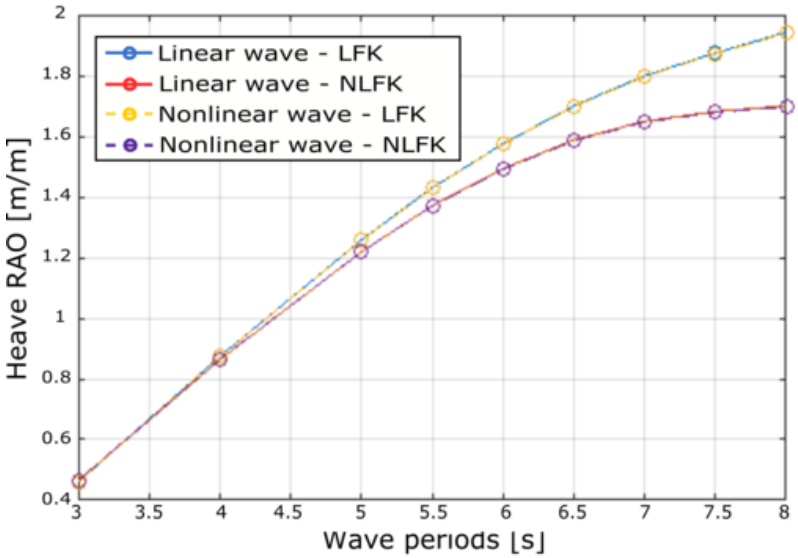

Figure 3.13: Comparison of the RAOs for the sphere, using linear and nonlinear waves and linear and nonlinear FK forces.

The implementation of the nonlinear FK forces is theoretically more consistent when nonlinear waves are considered, due to the nonlinear boundary condition on the free-surface ($p_{WSHI}(z = \eta_w) = 0$). However, comparing the RAOs obtained with the linear and nonlinear wave models, one can note that the difference is imperceptible, as illustrated in Figure 3.13. Therefore, for low-order nonlinear waves, the approximation using linear wave theory seems to be adequate even with nonlinear FK forces. In fact, waves within the power production region tend to be linear or

low-order nonlinear, as shown in Section 2.1, based on the power production data of different real devices during open-ocean tests. Therefore, higher order nonlinear waves may not be necessary within the power production region.

3.3 Computationally efficient partially-nonlinear extension

Despite the need for considering nonlinear FK forces to accurately predict the behaviour of the spherical HPA, the approach employed to compute the nonlinear FK forces in Section 3.2.4, via a remeshing routine to identify the submerged part of the absorber at each time-step, is computationally expensive: over 500% slower than the *LFK* approach. These computational time requirements may preclude the *NLFK* model for certain applications with low computational requirements presented in Table 2.5. Therefore, an approach that can compute nonlinear FK forces in, or close to, real-time is necessary.

A computationally efficient algebraic solution that considers nonlinear FK forces (*NLFKa*) of axisymmetric absorbers is presented in [162], which is briefly described in this section. This computationally efficient model is implemented in the *cHyW2W* model presented in this thesis.

In the *NLFKa* model, the integrals in Equations (3.24) and (3.25) are solved algebraically over the instantaneous wetted surface. Hence, the pressure applied on the surface of the absorber, shown in Equation (3.22), can be replaced by its deep-water ($h_{sea} \to \infty$) definition as follows,

$$p_{I_{dw}}(x,z,t) = -\rho_w g z_d + \rho_w g A_w e^{k_w z} \cos(\omega_w t - k_w x). \tag{3.43}$$

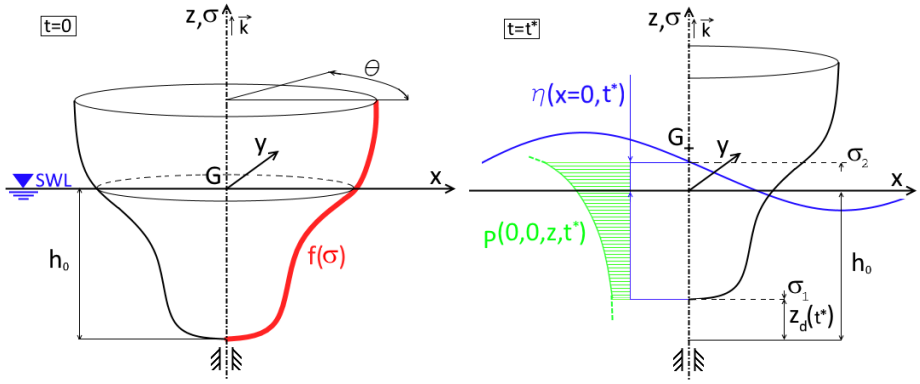

(a) (b)

Figure 3.14: Axisymmetric heaving device with generic profile $f(\sigma)$: (a) the absorber at rest, with the centre of gravity G at the SWL and draft h_0, and (b) the free surface elevation η_w and the device displacement z_d after a time t^*. The pressure is integrated over the surface between σ_1 and σ_2.

Figure 3.14 illustrates an axisymmetric absorber with a fixed vertical axis, which allows for a description of its surface in parametric cylindrical coordinates as follows,

$$\begin{cases} x(\sigma,\theta) = f(\sigma)\cos\theta \\ y(\sigma,\theta) = f(\sigma)\sin\theta \\ z(\sigma,\theta) = \sigma \end{cases}, \quad \sigma \in [\sigma_1,\sigma_2] \wedge \theta \in [0,2\pi). \tag{3.44}$$

Different $f(\sigma)$ corresponding to different revolution bodies are described in [162]. In the case of the spherical HPA, the resulting FK force is computed [162] as follows,

$$F_{FK} = \iint_S (p_{I_{stat}} + p_{I_{dyn}}) n \, dS = \int_0^{2\pi} \int_{\sigma_1}^{\sigma_2} p_I(x(\sigma,\theta), z(\sigma,\theta), t) f'(\sigma) f(\sigma) k d\sigma d\theta$$
$$= \int_0^{2\pi} \int_{\sigma_1}^{\sigma_2} (\rho_w g A_w e^{k_w \sigma} \cos(\omega_w t - k_w f(\sigma) \cos\theta) - \rho_w g z_d) \times f'(\sigma) f(\sigma) d\sigma d\theta, \quad (3.45)$$

where the algebraic solution of the static and dynamic pressure under the long wave approximation (wavelength considerably longer than the characteristic length of the device) for the spherical HPA are, respectively,

$$f(\sigma)_{stat} = -2\pi\rho_w g \Big[\frac{\sigma^3}{3} + z_d \frac{\sigma^2}{2}\Big], \quad (3.46)$$

$$f(\sigma)_{dyn} = -\frac{2\pi}{k_w} \rho_w g A_w \cos(\omega_w t) \Big[(z_d + \frac{1}{k_w} - \sigma) e^{k_w \sigma}\Big], \quad (3.47)$$

and the limits of integration defining the instantaneous wetted surface,

$$\begin{cases} \sigma_1 = z_d - h_0, \\ \sigma_2 = \eta_w, \end{cases} \quad (3.48)$$

where h_0 is the draft of the device at equilibrium, as shown in Figure 3.14 (a). In case the long wave approximation is not applicable, the FK force can also be solved using the McLaurin expansion of the cosine term in Equation (3.45) [162].

Hence, the algebraic solution provides identical results as the *NLFK* model via the remeshing routine, but only requires an overburden of about 50% with respect to the *LFK* model, significantly reducing the computational time of the *NLFK* model. Although not studied in this thesis, it is important to note that a similar approach can also be applied to WECs with several DoFs by numerically solving the FK force integrals in Equations (3.24) and (3.25), as demonstrated in [107, 118].

3.4 Summary

This chapter introduces the potential flow theory that underpins the most commonly used mathematical models in wave energy applications and presents the different possible mathematical models to consider the most relevant nonlinear effects for a spherical HPA.

Section 3.1 describes the foundations of potential flow theory, including the simplifying assumptions, and develops the governing equation to predict the behaviour of WECs. The identification of the required hydrodynamic coefficients of this governing equation is described in Section 3.1.3. The capabilities of the open-source BEM solver NEMOH are compared to the well-established commercial code WAMIT in Appendix A. In addition, the details of the spherical HPA used in this thesis are presented in Section 3.1.3, including its FD hydrodynamic coefficients.

The impact of different nonlinearities (nonlinear waves, nonlinear FK forces and viscous effects) and different modelling approaches to consider these nonlinearities, are analysed in Section 3.2, where results show that nonlinear FK forces and viscous effects are crucial to accurately reproduce the behaviour of spherical HPA, especially when the absorber is actively controlled to maximise energy generation. However, the use of nonlinear wave theory is demonstrated to have very little influence on the behaviour of the spherical HPA in *power production mode*. Finally, an efficient approach to consider nonlinear FK forces, based on an algebraic solution, is briefly presented in Section 3.3, which significantly reduces the computational overhead of the more conventional approach with the remeshing routine.

Chapter 4

Modelling the *cHyW2W* model: Hydraulic power take-off systems

The mechanical energy absorbed from ocean waves needs to be converted into electricity in an efficient way, either directly converting the mechanical energy into electricity or via an intermediate transmission system. In the *cHyW2W* model presented in this thesis, the energy absorbed from ocean waves is converted first into hydraulic energy and then into electricity, as illustrated in Figure 2.22. However, there exist a wide variety of possibilities to generate electricity via a hydraulic transmission system coupled to an electric generator, as reviewed in Section 2.3.4.

The main objective of this chapter is to present the mathematical models for the different components usually incorporated in hydraulic transmission systems and electrical systems (including the rotational electric generator and PECs) installed in real WECs. Mathematical models that provide high-fidelity results are crucial for an accurate evaluation of the performance of different PTO systems and, thus, all the relevant dynamics, losses and constraints are included in the mathematical models presented in this chapter, as suggested in Section 2.6. In addition, the mathematical models presented in this chapter incorporate the potential control-inputs of different components from ocean waves to the electricity grid (C_1, C_2 and C_3 in Figure 2.22), which is crucial in evaluating the practical implication and limitations of different control strategies.

Section 4.1 describes a mathematical model for hydraulic transmission systems, where the different hydraulic PTO configurations or topologies are first described, and the mathematical models to represent the different components included in the different configurations are then presented. The second part of the chapter, Section 4.2, describes the various possibilities for conversion of the hydraulic energy into electricity using rotational generators, including three electric generator topologies and power converter units. However, the solutions suggested in Section 4.2 are not only applicable to PTO topologies with hydraulic transmission systems, but for any transmission mechanism that converts the energy absorbed from ocean waves into rotational motion, for example, pneumatic or mechanic transmission systems, as described in Sections 2.3.1 and 2.3.2, respectively.

4.1 Hydraulic Transmission system

Hydraulic transmission systems have been and are used for a wide variety of applications in various engineering sectors, meaning that many companies and research groups have accumulated wide experience and knowledge about hydraulic systems. Hence, the solutions initially suggested for, and implemented in, real WECs (the Oyster OWSC by Aquamarine Power Ltd. [51], the Searev OPC [297] or the CETO HPA by Carnegie [285]) were rather conventional topologies, previously used in other applications, that consisted of well-known off-the-shelf components. However, wave energy is rather different to any other application for which hydraulic systems have been

suggested so far. Any PTO system implemented in a WEC needs to provide high force/torques under relatively low velocities, for which hydraulic systems are a good solution. However, the main challenge for PTO systems implemented in WECs is dealing with large peaks/average power values, derived from the variability of the wave resource. As a consequence, PTO components end up operating at part-load operational conditions most of the time, which results in significant losses.

4.1.1 Hydraulic transmission system configurations for wave energy

The simplest hydraulic transmission systems suggested for WECs use off-the-shelf components, where a hydraulic cylinder is connected to a hydraulic motor through low- (LP) and high-pressure (HP) hydrualic accumulators, as suggested in several studies [234–238]. This 'standard' configuration somewhat solves the problem of having hydraulic components operating at part-load operating conditions, but significantly reduces the possibility of maximising power absorption via an energy maximising control strategy.

In order to improve the performance of that 'standard' system, alternative configurations have been suggested in the literature. Four configurations with higher flexibility are presented in [239], where the main difference among the four configurations is the arrangement of the accumulators. Another topology with a direct connection between the hydraulic cylinder and a variable-displacement motor is suggested in [64], while a configuration using a multi-chamber hydraulic cylinder connected to multiple accumulators, with different pressure settings (which, in turn, are connected to a fixed-displacement motor), is presented in [240].

All these topologies can be organised in two main groups [241]: constant- and variable-pressure configurations. These two configurations are described in the following subsections.

4.1.1.1 Constant-pressure configuration

The typical constant-pressure configuration is described in [298]; and generally includes a hydraulic cylinder, a set of check-valves for the rectification of the flow, LP and HP accumulators, a hydraulic motor, a relief valve, and a boost pump powered by an electric motor, as illustrated in Figure 4.1. The reciprocating motion of the WEC and, as a consequence, of the cylinder piston, is rectified by means of the rectification valves. The HP and LP accumulators dictate the pressure difference in the cylinder and help to provide a smooth and slowly varying torque in the hydraulic motor. Relief valves only open when the pressure in the system exceeds the maximum pressure allowed by the different components of the system and the boost pump ensures that the pressure in the system never falls below a pre-defined minimum pressure level, avoiding undesirable effects such as cavitation.

An important advantage of the constant-pressure configuration is that the absorption and transmission stages can be completely separated, which allows the hydraulic motor to perform close to the optimal operating point most of the time. This enables a reasonably high HyPTO efficiency.

However, the control of the absorption stage to maximise the energy absorbed from ocean waves is, in general, quite limited in hydraulic transmission systems based on the constant-pressure configuration. The only control-input of the constant-pressure HyPTO configuration is accommodated in the hydraulic motor (C_1 in Figure 2.22), and, since large HP accumulators are installed between the hydraulic cylinder and motor, variations in the motor displacement take a long time to affect the pressure in the hydraulic cylinder and, eventually, the behaviour of the WEC. As a consequence, the power absorption of the wave energy converter is rather poor, with very limited possibilities for improvement, which may result in poor power generation. Only the use of extra (smaller) accumulators beside the hydraulic cylinder, as described in [235], can improve power absorption, by implementing control strategies such as latching or declutching, as shown in [233].

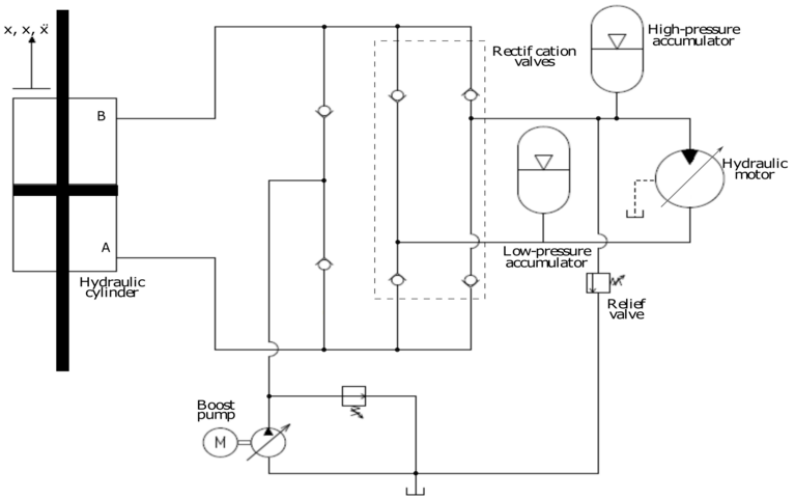

Figure 4.1: The scheme of a typical constant-pressure hydraulic transmission system.

4.1.1.2 Variable-pressure configuration

The typical alternative to the constant-pressure HyPTO configuration is shown in Figure 4.2, where the hydraulic cylinder is directly connected to the hydraulic motor. Only the LP accumulator is included in this configuration, which, along with the boost pump, avoids pressure drops in the low-pressure line. A boost pump is also necessary to replenish the fluid leaks in the motor. Similarly to the constant-pressure configuration, relief valves in the variable-pressure HyPTO configuration protect the system from overpressure. In contrast, the reciprocating motion of the WEC and the cylinder piston is rectified in the hydraulic motor.

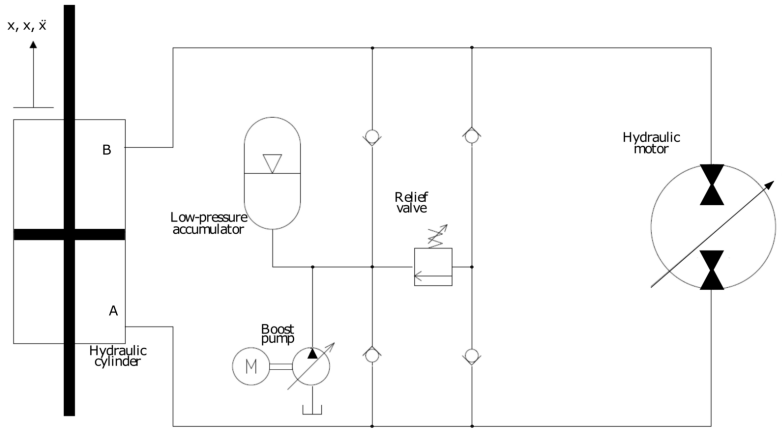

Figure 4.2: The scheme of a typical variable-pressure hydraulic transmission system.

The absence of a HP accumulator provides a more flexible hydraulic system, where variations in the hydraulic motor displacement rapidly affect the behaviour of the absorber, which facilitates effective control of the PTO force applied on the absorber, to maximise power absorption from ocean waves. However, the hydraulic motor may be required to provide four-quadrant operation, only if reactive power is required, *i.e.* capability to deliver and receive fluid power from either direction, to compensate for bi-directional flow. The four-quadrant operation is further described in Section 4.1.2.4.

The system shown in Figure 4.2 is the simplest version of a variable-pressure HyPTO configuration. Similar configurations have been suggested in [64, 239], including an energy overflow system connected to the relief valves, so that the extra flow, that the hydraulic motor cannot handle, is used to generate electricity, instead of leaking it into the LP accumulator, wasting the energy

contained in the HP fluid.

4.1.2 Mathematical modelling of hydraulic system components

Mathematical equations to model the different components included in hydraulic transmission systems, *i.e.* hydraulic cylinders, valves, accumulators and hydraulic motors, are common to any hydraulic system configuration or topology. Therefore, the equations for the different components are given in the following subsections, regardless of whether such components are used in the constant- or variable-pressure HyPTO configuration. The model structures used for each component are generic, in the sense that components of different characteristics, *e.g.* a hydraulic gear motor or a hydraulic radial piston motor, can be modelled using the same model structure. However, due to the very specific characteristics of each component, the parameters of the models may need to be adjusted for each specific component.

4.1.2.1 Hydraulic cylinder

Hydraulic cylinders consist of a piston that divides the cylinder into two chambers and can be symmetric or asymmetric. These two chambers are identical in symmetric cylinders, as illustrated in Figure 4.3 (a), meaning that the same piston area is used for pushing and retracting. In contrast, the two chambers of a hydraulic cylinder are significantly different in asymmetric cylinders, as shown in Figure 4.3 (b). Therefore, the active piston areas used in the pushing and retracting operations are also different. The active area used during the pushing or extension is the full piston area, while the active piston area used during the retraction is known as the annular area, as illustrated in Figure 4.3.

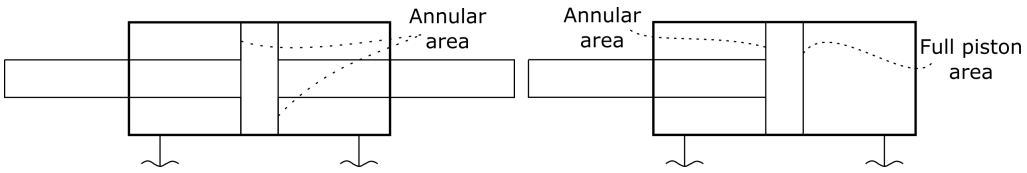

(a) Symmetric cylinder. (b) Asymmetric cylinder.

Figure 4.3: Schematic diagram of a symmetric and an asymmetric hydraulic cylinder.

Hence, the pressure difference between the two chambers determines the cylinder force(load) applied to the WEC. This pressure difference Δp_{cyl} is imposed by the pressure levels in the HP and LP accumulators in constant-pressure HyPTO configurations and the torque-control implemented in the hydraulic motor in variable-pressure HyPTO configurations. Following Equation (2.17), pressure dynamics in the different chambers of the cylinder can be given as:

$$\dot{p}^A_{cyl} = \frac{\beta_{eff}(p^A_{cyl})}{V_A + A_p x_p}(Q^A_{cyl} - \dot{x}_p A_p), \tag{4.1}$$

$$\dot{p}^B_{cyl} = \frac{\beta_{eff}(p^B_{cyl})}{V_B - A_p x_p}(\dot{x}_p A_p - Q^B_{cyl}), \tag{4.2}$$

where superscripts A and B refer to chambers *A* and *B* in Figures 4.1 and 4.2. The other parameters used in Equations (4.1) and (4.2) are defined after Equation (2.17), where they are used for the first time.

4.1.2.1.1 Fluid compressibility

Fluid compressibility is typically represented via the effective bulk modulus β_{eff}, which shows the relation between pressure and volume variations at a constant temperature. Hence β_{eff} varies

significantly with fluid pressure, as shown in Equations (2.17), (4.1) and (4.2), while the influence of temperature is negligible [242]. This bulk modulus varies due to the air entrained in the hydraulic fluid, which can reach up to 20% when the fluid is at atmospheric pressure [242], but dissolves into liquid as the pressure increases.

Therefore, different mathematical models have been suggested in the literature to represent variations in the bulk modulus, such as the isentropic model, and empirical models following Lee's and Hoffmann's formulae [242] illustrated in Equations (4.3), (4.4) and (4.5), respectively.

$$\beta_{eff}^{isen}(p) = \beta_{eff}^{isen,0} \frac{1 + r_v}{1 + (\frac{1}{p_{cyl}})^{1/\gamma_{oil}} r_v \frac{\beta_{eff}^0}{\gamma_{oil} p_{cyl}}}, \tag{4.3}$$

$$\beta_{eff}^{Lee} = a_1 \beta^{max} \log(a_2 \frac{p_{cyl}}{p_{cyl}^{max}} + a_3), \tag{4.4}$$

$$\beta_{eff}^{Hoffmann} = \beta^{max} \log(1 - e^{-0.4 - 2\times10^{-7} p_{cyl}}), \tag{4.5}$$

where $\beta_{eff}^{isen,0}$ is the isentropic bulk modulus of the liquid without entrained air, $r_v = \frac{V_{G0}}{V_{L0}}$ the relation between the volume of gas entrained in the liquid at atmospheric pressure (V_{G0}) and the volume of liquid at atmospheric pressure (V_{L0}), and $\gamma_{oil} = 1.4$ the adiabatic index. The isentropic bulk modulus is given as $\beta_{eff}^{isen,0} = \beta_{eff}^0 + K_p p_{cyl}$, where typical values are $\beta_{eff}^0 = 16500$bar and $K_p = 9.558$m [242].

As an alternative to Equations (4.3), (4.4) and (4.5), constant β_{eff} values are often used in the mathematical models that represent hydraulic transmission systems, based on a β_{eff} value provided by the manufacturer. Some studies directly use the air-free value provided by manufacturers (typically $\beta_{eff}^{air-free}$=17MPa [299]), while others recommend using a reduced value, with a reduction of between 25% [300] and 50% [301]. The reason why reduced values are recommended is because air-free values are, in general, determined via laboratory tests where the hydraulic fluid is carefully degassed. However, hydraulic fluids tend to aerate in use, making the air-free value inaccurate.

Thus, five different approaches are compared in this subsection: β_{eff}^{isen}, β_{eff}^{Lee}, $\beta_{eff}^{Hoffmann}$, $\beta_{eff}^{air-free}$ and a 40% reduced value ($\beta_{eff}^{60\%air-free}$), following the recommendation provided in [299]. Figure 4.4 illustrates effective bulk modulus variations as a function of pressure for the five different approaches compared in this subsection, where a pressure range between 1 bar (equivalent to atmospheric pressure) and 50 bar is analysed.

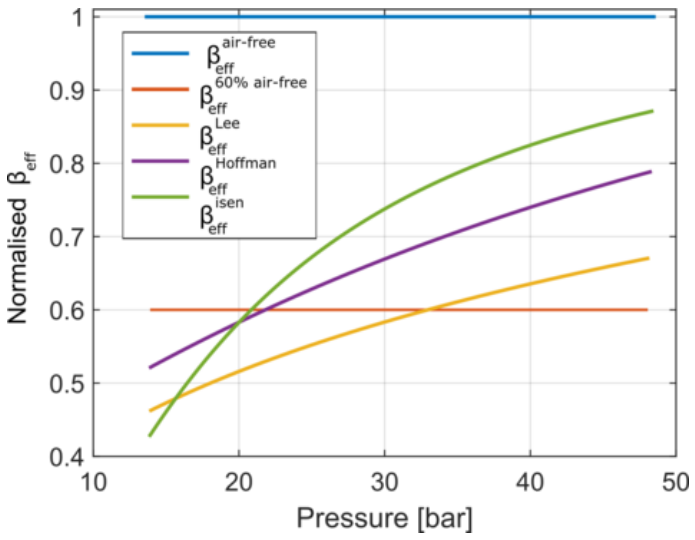

Figure 4.4: Effective bulk modulus as a function of pressure for different bulk modulus representations.

Significant differences can be observed in Figure 4.4 among the different approaches, which suggests that the impact of the different approaches on the pressure dynamics may be relevant. Therefore, the different approaches are compared under realistic operational conditions, using a mathematical model for the constant-pressure HyPTO configuration. The constant-pressure HyPTO configuration is selected since β_{eff} variations are expected to be more relevant than in variable-pressure configurations, due to the more severe compression-expansions cycles. Figure 4.5 (a) illustrates the normalised β_{eff} for the different approaches under these realistic operational conditions, where differences between the alternative approaches are significant. However, pressure values in the cylinder chamber, calculated using Equation (4.1), are almost identical for all the approaches, as shown in Figure 4.5 (b). Deviations among the different approaches can only be observed when the check valves of the constant-pressure HyPTO configuration open and close, resulting in very fast dynamics, as illustrated in the zoomed snapshot in Figure 4.5 (b).

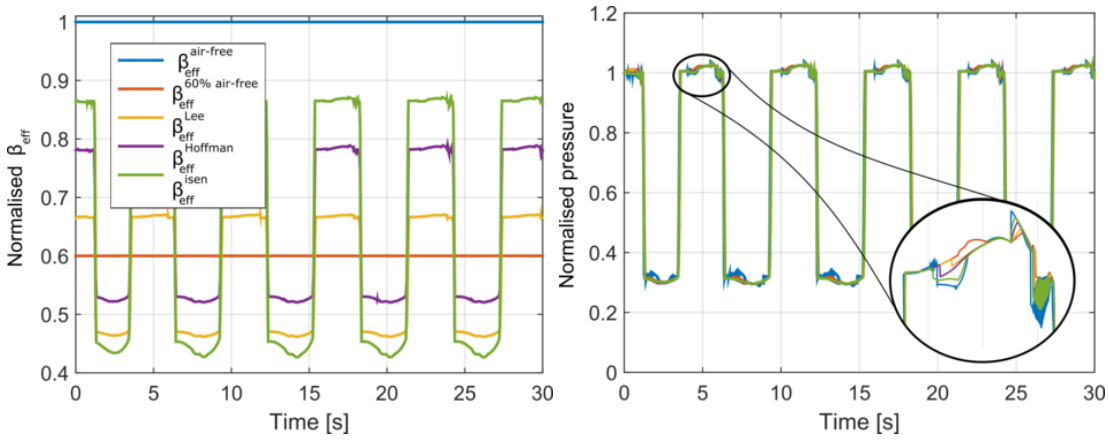

(a) (b)

Figure 4.5: Effective bulk modulus variations in time (a) and the impact of the different bulk modulus on the pressure variations (b).

Since almost identical results can be obtained with all the different approaches, a constant effective bulk modulus, the $\beta_{eff}^{60\%air-free}$, is implemented in the mathematical models presented in this thesis due to its simplicity.

Once the β_{eff} value is selected, the force(load) applied by the hydraulic cylinder to the absorber can be determined. The pressure difference between the different chambers in the hydraulic cylinder can be calculated via Equations (4.1) and (4.2), but, in that case, friction and inertia effects would be neglected, which can represent between 5% and 10% of energy losses in the cylinder [242]. A more accurate representation of the force applied on the absorber can be obtained as follows,

$$F_{pis} = A_p \Delta p_{cyl} + F_{fric} + F_{in}, \tag{4.6}$$

where $\Delta p_{cyl} = (p_{cyl}^A - p_{cyl}^B)$ and F_{in} includes the inertial force of the piston, the rod and the oil, which can be given as,

$$F_{in} = \ddot{x}_p (M_p + M_r + M_{oil}), \tag{4.7}$$

and M_p, M_r and M_{oil} are the mass of the piston, the rod and the oil stored in the cylinder chambers, respectively.

4.1.2.1.2 Friction model

The friction force F_{fric} is considered to be one of the main nonlinearities in hydraulic cylinders. Similarly to β_{eff}, several different approaches have been suggested in the literature to describe friction losses in hydraulic cylinders, including static and dynamic models [302].

The vast majority of these models divide the friction model into different effects: viscous friction, Coulomb friction and static friction. A well-known mathematical model, referred to as the *Stribeck* model, combines these three effects [242] as follows,

$$F_{fric} = \sigma_{st}\dot{x}_p + \text{sign}(\dot{x}_p)\left[F_c + F_{st}\exp\left(-\frac{|\dot{x}_p|}{c_{st}}\right)\right], \tag{4.8}$$

where σ_{st} is the linear viscous coefficient, F_c the Coulomb friction force, F_{st} the static friction force and c_{st} the characteristic velocity of the Stribeck curve. Figure 4.6 (a) illustrates the contribution of each friction effect, normalised against the maximum friction force.

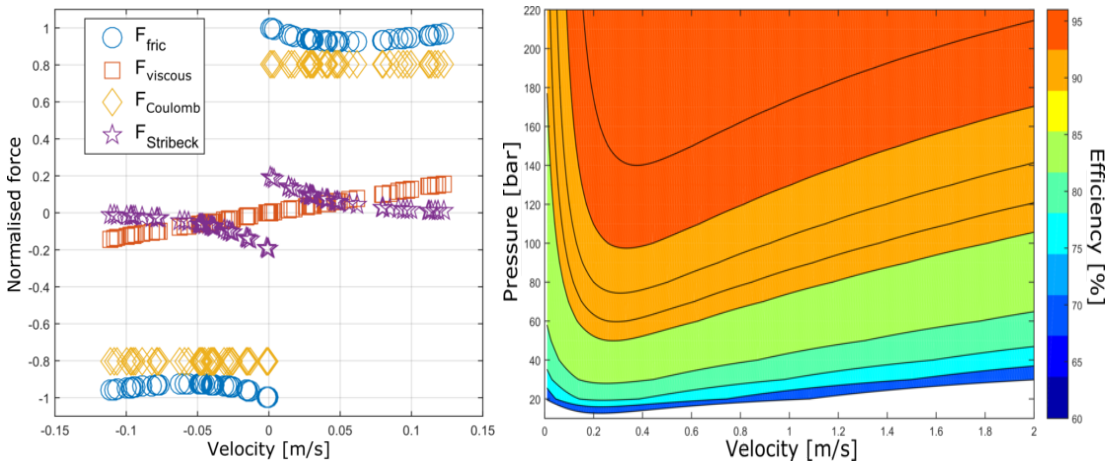

(a) (b)

Figure 4.6: Friction losses in the hydraulic cylinder: (a) the impact of different friction effects normalised against the maximum friction force; and (b) the approximated efficiency map of a cylinder, reproduced from [239].

Once the model structure is selected, the parameters (σ_{st}, F_c, F_{st} and c_{st}) of the model need to be defined. The most appropriate way to proceed would be to fit such parameters using experimental data from the hydraulic cylinder to be implemented in real life. However, experimental results are not always available, so parameters need to be identified using other relevant information, such as manufacturers' data. Therefore, the parameters for the present model are identified using an efficiency map, as a function of velocity and pressure difference presented in [239]. Figure 4.6 (b) shows the efficiency map of the hydraulic cylinder, reproduced with the model parameters fitted from [239].

The friction model presented in this section assumes friction losses are symmetric, as shown in Figure 4.6 (a). However, this is not always true, especially in asymmetric cylinders. In some cases, a lag exists between the pushing (positive velocity) and retracting (negative velocity) forces. To include such asymmetry, the model structure presented in Equation (4.8) is still useful, but needs to be duplicated to distinguish the performance during the pushing and retracting operations, separately identifying the parameters for each operation [242].

4.1.2.2 Valves

Valves are essential components for the successful performance of HyPTO systems, required to rectify or control the flow at different points in the circuit. Active and passive valves can be

included in the hydraulic system, depending on the purpose of the valve, and both can be described using the orifice equation [242] as follows,

$$Q_v = C_d A_v(\Delta p_v)\text{sign}(\Delta p_v)\sqrt{\frac{2}{\rho_{oil}}|\Delta p_v|}, \tag{4.9}$$

where Q_v is the flow through the valve, C_d the discharge coefficient, Δp_v the pressure difference between the inlet and the outlet of the valve, $A_v(\Delta p_v)$ the valve opening area as a function of Δp_v, and ρ_{oil} the density of the hydraulic oil.

Only passive valves, check valves in the rectification bridge and relief valves, are used in this thesis, which open and close as a function of the pressure difference across the valve, as expressed in Equation (4.9). The valve remains closed while the pressure difference across the valve is lower than the cracking pressure (Δp_{crack}). Once the cracking pressure is reached, the valve starts to open and continues to open until the valve is fully open. The pressure at which the valve is fully open is known as the maximum pressure (Δp_{max}). The maximum area of the valve (A_v^{max}), Δp_{crack} and Δp_{max} are, in general, provided in manufacturers' catalogues. However, the valve opening, from fully closed to fully open, can follow different profiles. Some of the most commonly used profiles [303] are illustrated in Figure 4.7.

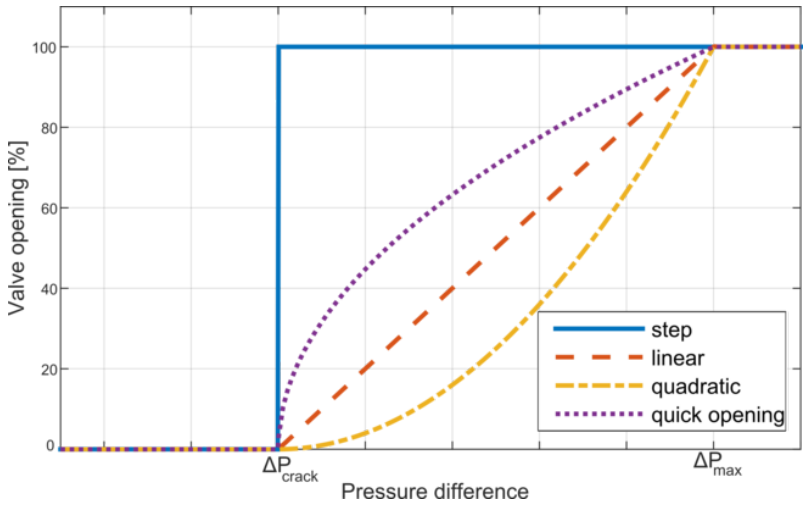

Figure 4.7: Valve opening functions.

4.1.2.3 Accumulators

The performance of hydraulic accumulators, typically compressed gas accumulators, can be described by means of an isentropic process, where the volume of hydraulic oil contained in the accumulator changes in time as follows,

$$V_{acc}(t) = \int_0^t Q_{acc}^{in}(t)dt, \tag{4.10}$$

where $Q_{acc}^{in}(t)$ is the input flow into the accumulator, which is positive if hydraulic oil flows in and negative if oil flows out. Hence, following isentropic compression, the pressure in the accumulator is given by

$$p_{acc} = p_{acc}^{pre}\left(\frac{V_{acc}^{tot}}{V_{acc}^{gas}}\right)^{\gamma_{oil}}, \tag{4.11}$$

where p_{acc}^{pre}, V_{acc}^{tot} and V_{acc}^{gas} are the pre-charge pressure, and the total volume and volume of compressed gas in the accumulator, respectively. However, accumulators are designed to store fluid up

to a pre-defined pressure level (p_{acc}^{max}). This maximum pressure level is normally defined as twice the pre-charge pressure, as illustrated in Figure 4.8.

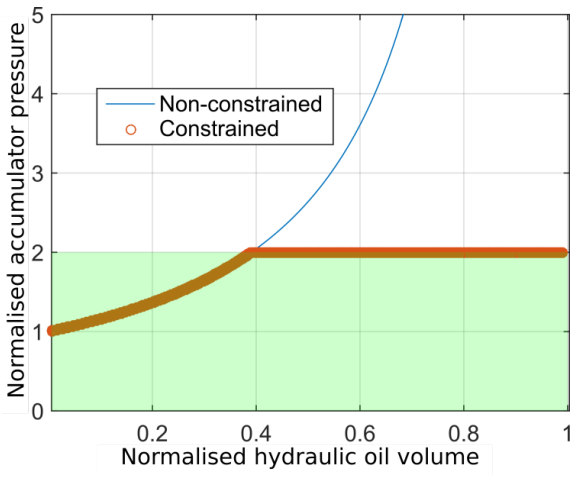

Figure 4.8: Non-constrained and constrained evolution of the pressure in the hydraulic accumulator as a function of the oil volume.

4.1.2.4 Hydraulic motor

As pressure increases in the cylinder chamber, oil flows from the hydraulic cylinder to the motor (through the check-valves and the HP accumulator, in the case of the constant-pressure HyPTO configuration), where pressure and flow discharged from the cylinder are converted into mechanical torque and rotation of the shaft. Once the motor extracts the energy from the high-pressure fluid, low-pressure oil flows back to the cylinder. As presented in Equations (2.19) and (2.20), the output flow, and the torque generated in the hydraulic motor, can be expressed, respectively, as,

$$Q_M = \alpha_M D_\omega \omega_M - Q_{losses}, \tag{4.12}$$

$$T_M = \alpha_M D_\omega \Delta p_M + T_{losses}. \tag{4.13}$$

With respect to the four quadrant operation capabilities, the diagram presented in Figure 4.9 illustrates the four different operation required in a hydraulic motor implemented in a variable-pressure HyPTO configuration. Hence, the piston can rise because the absorbers pulls, as in the qII case in Figure 4.9, or because the hydraulic motor sends high pressure fluid into the lower chamber of the hydraulic cylinder, as in the qI case in Figure 4.9. Same can be applied for the downwards motion of the piston, with the qIII and qIV cases in Figure 4.9. As a consequence, first and third quadrants (qI and qIII, respectively, in Figure 4.9) are only required when reactive power is used to enhance energy generation.

4.1.2.4.1 Loss model

Losses in hydraulic motors appear mainly due to friction and leakages, and can be significant, especially in part-load operations. Hydraulic motors in wave energy applications frequently operate at part-load operating conditions, due to the high variability of the wave resource and, thus, accurate estimation of the losses in hydraulic motors is essential. Different loss models have been suggested to approximate such losses, as described in [299]. The first loss model is suggested by Wilson [304], based on fixed-displacement gear pumps and motors, where the most widely used model structure, separating torque and volumetric efficiencies, is introduced. Wilson's model [304] uses constant loss coefficients, and is implemented in a wave energy context in [237].

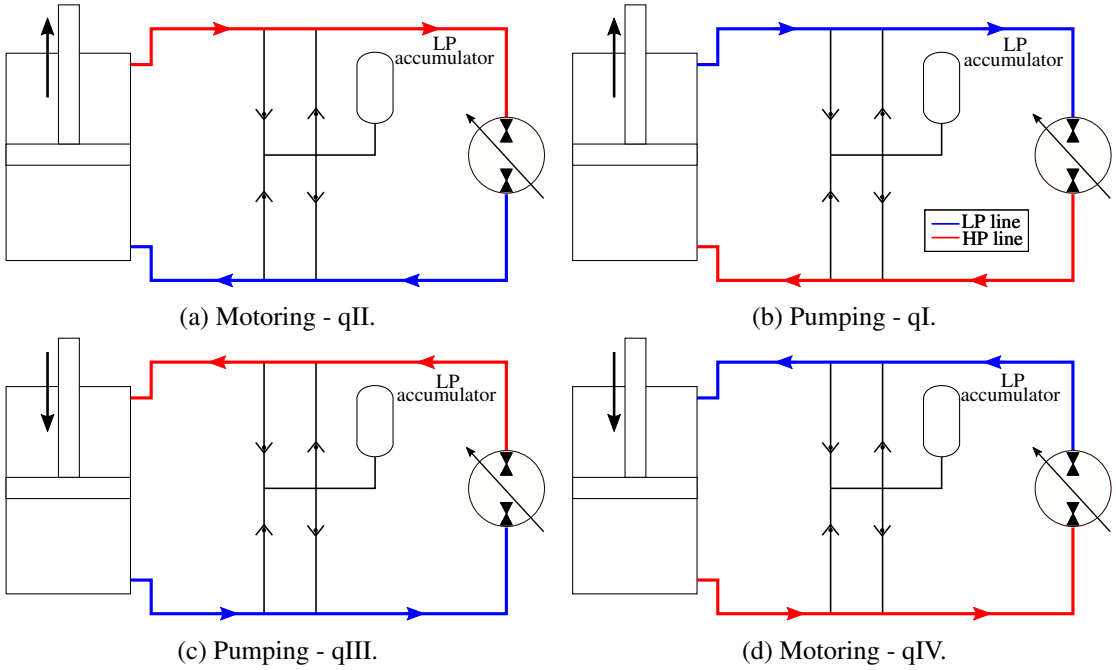

(a) Motoring - qII. (b) Pumping - qI.

(c) Pumping - qIII. (d) Motoring - qIV.

Figure 4.9: Four-quadrant operation hydraulic motor.

McCandish and Dorey [305] present an analytical model, described in detail in [306], to compute losses using variable loss coefficients for fixed- and variable-displacement motors. A polynomial based approach is suggested in [307], where the coefficients of the polynomial are identified using flow and torque data from experimental data.

The *cHyW2W* model presented in this thesis include the Schlösser model [308, 309], which includes losses due to friction and leakages in the motor. The beauty of the Schlösser model is that it can be fitted using data from manufacturers, so experimental data is not necessarily required:

$$Q_{losses} = \Delta p_M C_{Q1}, \tag{4.14}$$

$$T_{losses} = C_{T1} + C_{T2}\Delta p_M + C_{T3}\omega_M + C_{T4}\omega_M^2, \tag{4.15}$$

where C_{Q1}, C_{T1}, C_{T2}, C_{T3} and C_{T4} are model parameters of the Schlösser loss model.

Several types of hydraulic motors are currently available for diverse applications, which can also be suitable for wave energy, depending on the hydraulic transmission system implemented in the HyPTO system. In general, due to the variability of the resource, hydraulic motors that can rapidly vary the displacement are required. These hydraulic motors should ideally have high efficiency capabilities not only at the optimum, but also at part-load operating conditions. As described in Section 2.3.4, different hydraulic motor topologies with different performance characteristics have been suggested for inclusion in the HyPTO systems of diverse WECs: bent-axis, swash-plate or DDM. The model structure presented in Equations (4.12)–(4.15) is suitable for all the different hydraulic motor topologies. However, similarly to the case of the hydraulic cylinder, it is necessary to adapt the model parameters for each specific case, as shown in the following subsections. Due to the lack of available manufactures' data for the DDM, only the bent-axis and swash-plate topologies are analysed in this thesis.

Bent-axis motor

In the case of bent-axis hydraulic motors, the parameters of the loss model, presented in Equations (4.14) and (4.15), are identified using the data from manufacturers for the *Sauer-Danfoss* 51-1 Series bent-axis motor [310], which includes efficiency data for two specific cases, i.e., full-displacement ($\alpha_M = 1$) and partial-displacement ($\alpha_M = 0.3$). Figures 4.10 (a) and (c) illustrate

the efficiency map reconstructed from manufacturers' data for the full- and partial-displacement, respectively. The loss model presented in Equations (4.14) and (4.15) needs to be fitted using these sets of manufacturers' data.

The parameters of the loss model are identified for each operating case, *i.e.* the full- and partial-displacement operating conditions, using the linear least square fitting approach. Using the fitted parameters, efficiency maps for each operating condition can be reconstructed, as shown in Figures 4.10 (b) and (d) for the full- and partial-displacement operating conditions, respectively.

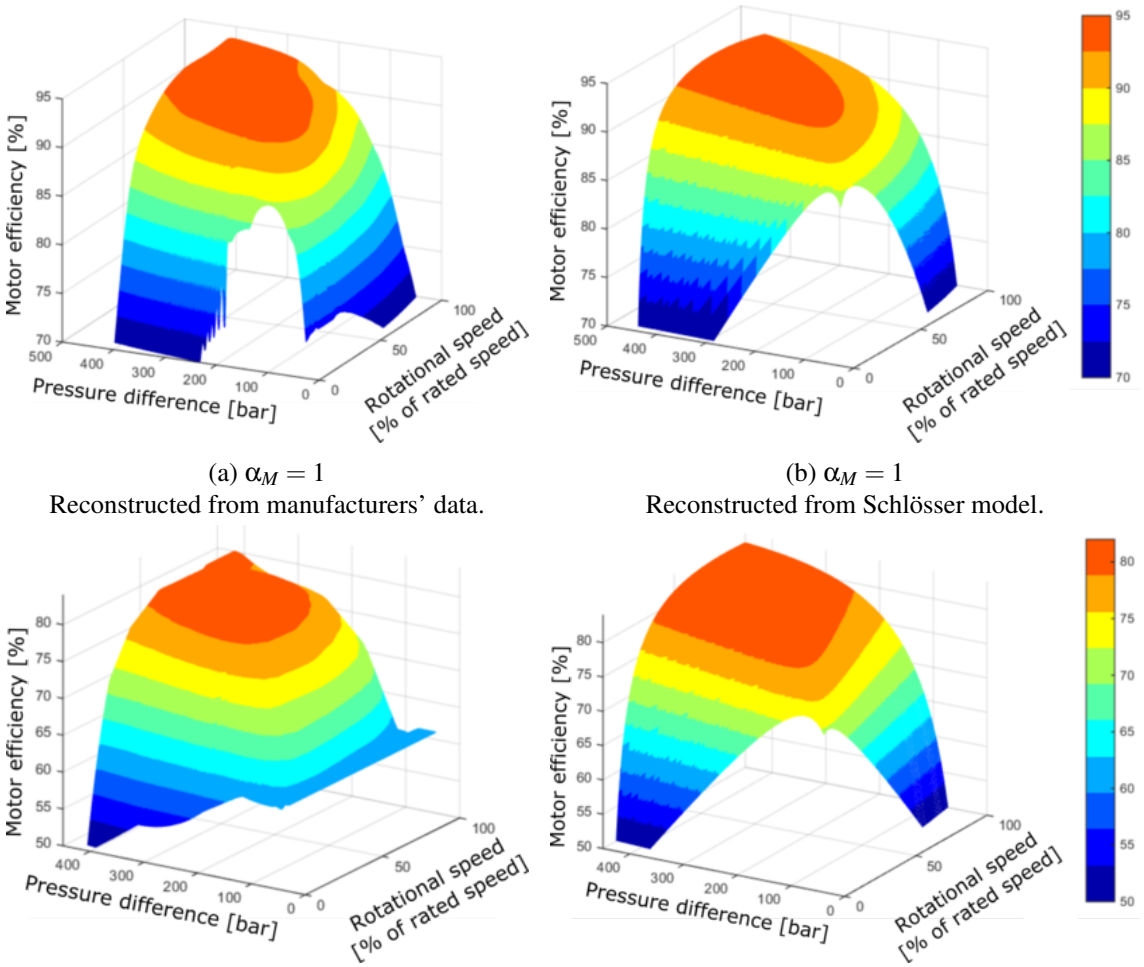

(a) $\alpha_M = 1$
Reconstructed from manufacturers' data.

(b) $\alpha_M = 1$
Reconstructed from Schlösser model.

(c) $\alpha_M = 0.3$
Reconstructed from manufacturers' data.

(d) $\alpha_M = 0.3$
Reconstructed from Schlösser model.

Figure 4.10: Efficiency maps of the Sauer-Danfoss 250 cc Series 51-1 bent-axis motor: top and bottom rows correspond to full- and partial-displacement operating conditions, respectively, while left and right columns correspond to reconstructions from manufacturers' data and the Schlösser loss model, respectively.

The agreement between the efficiency maps reconstructed from the manufacturers' data and the Schlösser model is reasonably good for both operating conditions, as illustrated in Figure 4.10. However, in variable-pressure HyPTO configurations, α_M varies rapidly, and can take any value between -1 and 1. Losses in the hydraulic motor can vary considerably for different operating conditions, as illustrated in Figure 4.10, and, thus, model parameters for all the different operating conditions need to be identified. Since manufacturers' data only covers two specific operating conditions, the model parameters for the rest of the cases can only be obtained by means of extrapolation. Hence, parameters can be expressed as a function of α_M using linear extrapolation between the two operating conditions, as shown in Figure 4.11 for the parameter C_{Q1}. Linear ex-

trapolation is convenient to obtain the parameters of the loss model at different operating points, since manufacturers only provide the data for two operating points, but it should be noted that the real behaviour of the motor is not expected to be linear.

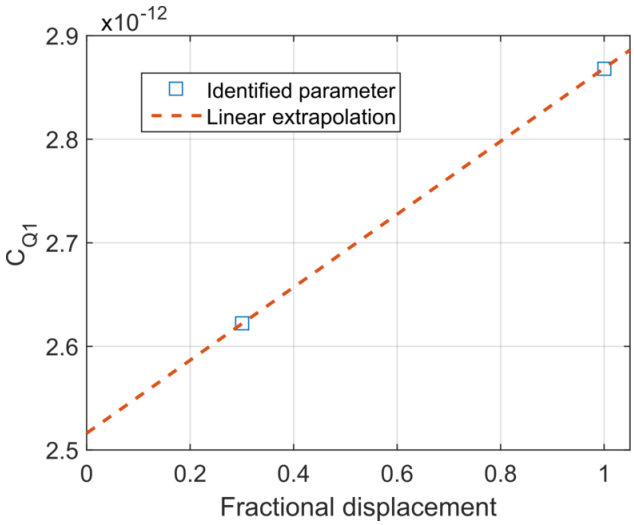

Figure 4.11: Identified parameter (C_{Q1}) for the two operating conditions available in [310] and the linear extrapolation function that fits the two parameters.

Swash-plate motor

Similarly to the bent-axis hydraulic motor, manufacturers' data for a swash-plate motor can be used to identify the parameters of the loss model presented in Equations (4.14) and (4.15). In the case of the swash-plate motor, the manufacturers' data corresponds to the *Kawasaki* K3VL Series [311], which provides the data for only one rotation speed: 1500rpm. However, the data covers different fractional displacement options. Figures 4.12 (a) and (b) illustrate the efficiency maps reconstructed from the manufacturers' data and the Schlösser model, respectively, where the agreement is again shown to be good.

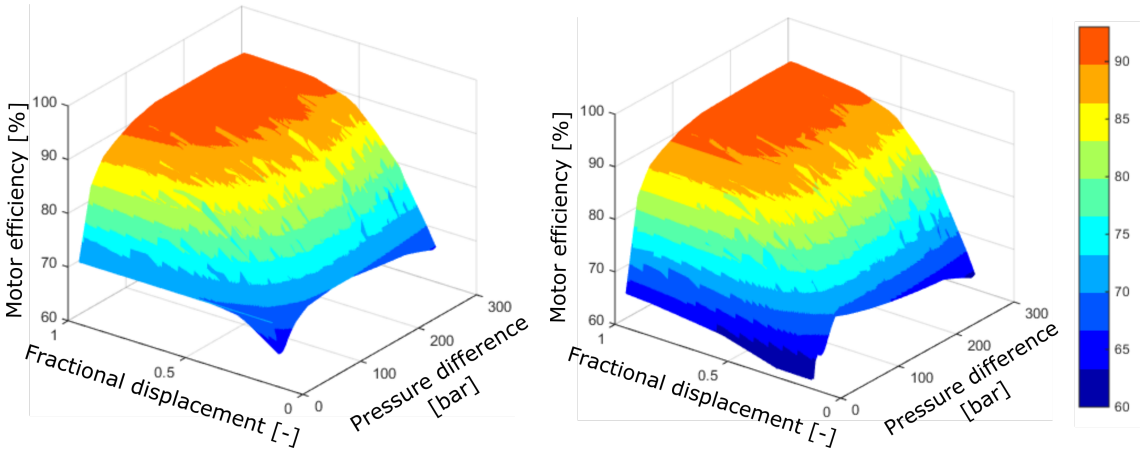

(a) Reconstructed from manufacturers' data.

(b) Reconstructed from Schlösser model.

Figure 4.12: Swash-plate motor efficiency maps reconstructed from (a) manufacturers' data [311] and from (b) the Schlösser model.

Similarly to the identification carried out for the bent axis motor, the parameters of the Schlösser model are identified for different values of α_M: 0.25, 0.5, 0.75 and 1. Thus, the behaviour of the

hydraulic motor can be approximated more accurately by using higher-order extrapolation. Figures 4.13 (a) and (b) illustrate the values for the C_{Q1} and C_{T2} parameters, respectively, including different α_M values. A quadratic extrapolation function is compared to the linear extrapolation in Figure 4.13, where the relative inaccuracy of the linear function is demonstrated.

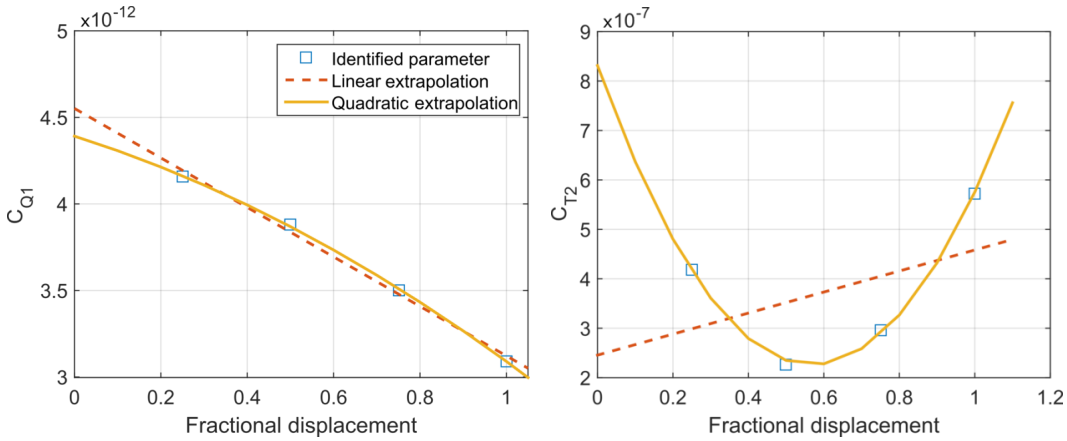

(a) (b)

Figure 4.13: Schlösser model parameters C_{Q1} (a) and C_{T2} (b) identified from manufacturers' data [311], and the linear and quadratic extrapolation functions to fit the identified parameters across different operating points.

Manufacturers' data is available for a specific hydraulic motor size (250cc/rev and 200cc/rev for the bent-axis and swash-plate, respectively). However, the mathematical model suggested in Equations (4.12)-(4.15) should ideally be applicable to different hydraulic motors, regardless of the dimension of the motor. To that end, the mathematical model for the hydraulic motor can be scaled, using the baseline motor characteristics, to be implemented in larger or smaller hydraulic motors [64] as follows:

$$Q_M^{RS} = \frac{D_\omega^{RS}}{D_\omega} \frac{\omega_M^{rated,RS}}{\omega_M^{rated}} Q_M\left(\frac{\omega_M^{rated}}{\omega_M^{rated,RS}}\omega_M, \Delta p_M\right), \tag{4.16}$$

$$T_M^{RS} = \frac{D_\omega^{RS}}{D_\omega} T_M\left(\frac{\omega_{rated}}{\omega_{rated}^{RS}}\omega_M, \Delta p_M\right), \tag{4.17}$$

where D_ω^{RS} is the displacement of the re-sized motor, and ω_M^{rated} and $\omega_M^{rated,RS}$ are the rated rotational speed of the baseline and re-sized motors, respectively.

Finally, it should be noted that, in the mathematical model of the hydraulic transmission system presented in this thesis, pressure losses in transmission lines are neglected, which is reasonable if short transmission lines are assumed.

4.2 Electrical systems

The mathematical model for the electrical system, which includes an electric generator occasionally complemented with PECs, is an essential part of any W2W model, regardless of the PTO mechanism incorporated in the WEC. Electrical systems implemented in WECs can include either a linear or rotational generator, as described in Section 2.4.2. However, rotational electric generators are (currently) most widely used in WECs, mainly because of their popularity in other renewable energy applications, such as wind turbines. In contrast, linear generators, despite their

potential for high efficiency performance [256], have been shown to be highly challenging in keeping the required air gap without using robust supporting structures, which considerably reduces the power-weight ratio [18].

The hydraulic transmission systems described in Section 4.1 require rotational generators and, thus, the following subsections analyse different rotational generators that can potentially be coupled to these hydraulic transmission systems. The most widely used rotational electric generators in wave energy applications, and also in other renewable energy applications, such as wind energy [264], can be reduced to three electric generator topologies: the SCIG [240], the PMSG [253] and the DFIG [252].

4.2.1 Electric generators

The dynamics of three-phase electrical machines are typically represented using the two-phase orthogonal rotating *dq* reference frame, regardless of the machine topology, as mentioned in Section 2.4. Thus, the original alternating-current (AC) signals become direct-current (DC) signals, as shown in Figure 4.14, which simplifies the analysis of the three-phase machines. In addition, this two-phase reference frame is also convenient for control calculations.

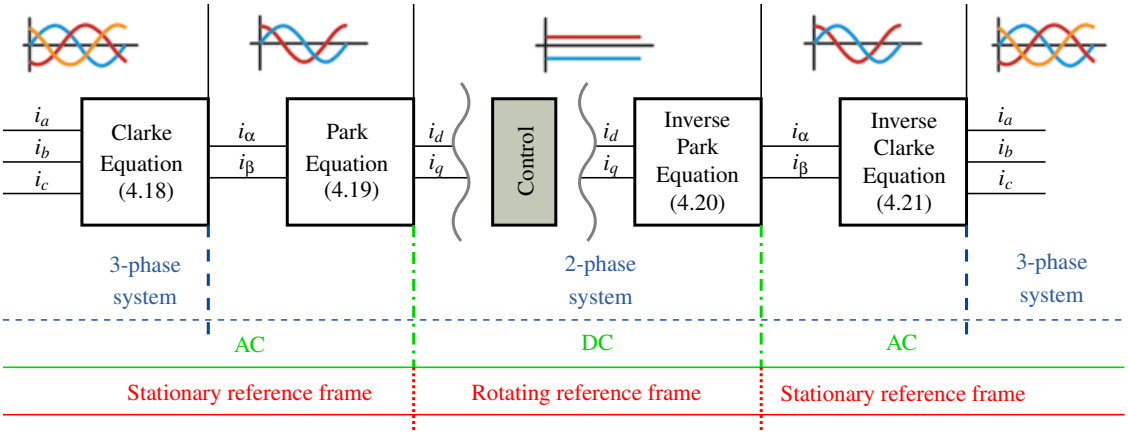

Figure 4.14: The reference frame transformation process from a three-phase stationary to a two-phase rotational reference frame, and vice versa, using the Park and Clarke transformations.

The transformation from a three-phase reference frame into the *dq* reference frame is carried out in two steps following the well-known Clarke and Park transformations [312], as illustrated in Figure 4.14. Hence, the three-phase reference is first transformed into an orthogonal stationary reference frame ($\alpha\beta$) using the transformation described in Equation (4.18). This two-phase $\alpha\beta$ representation is then converted into the *dq* reference frame via the vector rotation block described in Equation (4.19), where the $\alpha\beta$ reference frame is rotated over an angle θ_{dq} to follow the *dq* reference frame attached to the rotor flux.

$$\begin{bmatrix} i_\alpha \\ i_\beta \end{bmatrix} = \begin{bmatrix} 1 & -\frac{1}{2} & -\frac{1}{2} \\ 0 & -\frac{\sqrt{3}}{2} & -\frac{\sqrt{3}}{2} \end{bmatrix} \begin{bmatrix} i_a \\ i_b \\ i_c \end{bmatrix} \tag{4.18}$$

$$\begin{bmatrix} i_d \\ i_q \end{bmatrix} = \begin{bmatrix} \cos\theta_{dq} & \sin\theta_{dq} \\ \sin\theta_{dq} & \cos\theta_{dq} \end{bmatrix} \begin{bmatrix} i_\alpha \\ i_\beta \end{bmatrix} \tag{4.19}$$

Once the analysis has been carried out and all the necessary variables have been calculated in the *dq* reference frame, results can be converted back to three-phase quantities, as shown in Figure 4.14, by performing the inverse Park and Clarke transformations [267] as follows,

$$\begin{bmatrix} i_\alpha \\ i_\beta \end{bmatrix} = \begin{bmatrix} \cos\theta_{dq} & -\sin\theta_{dq} \\ \sin\theta_{dq} & \cos\theta_{dq} \end{bmatrix} \begin{bmatrix} i_d \\ i_q \end{bmatrix}, \tag{4.20}$$

$$\begin{bmatrix} i_a \\ i_b \\ i_c \end{bmatrix} = \begin{bmatrix} \frac{2}{3} & 0 \\ -\frac{1}{3} & \frac{1}{\sqrt{3}} \\ -\frac{1}{3} & -\frac{1}{\sqrt{3}} \end{bmatrix} \begin{bmatrix} i_\alpha \\ i_\beta \end{bmatrix}. \tag{4.21}$$

The mathematical models for the two induction machines, *i.e.* SCIG and DFIG, are identical except for the rotor voltages V_{rd} and V_{rq}, which are zero for the SCIG and non-zero for the DFIG. Thus, the model for the DFIG is presented in Section 4.2.1.1, which can also be used for the SCIG, setting the rotor voltages V_{rd} and V_{rq} to zero in Equations (4.24) and (4.25), respectively. The model for the PMSG is presented in Section 4.2.1.2.

4.2.1.1 Induction generators

The model for an induction machine is based on the equivalent two-phase circuit illustrated in Figure 4.15, where the circuits for the direct (d) and quadrature (q) axes are shown in Figures 4.15 (a) and (b), respectively.

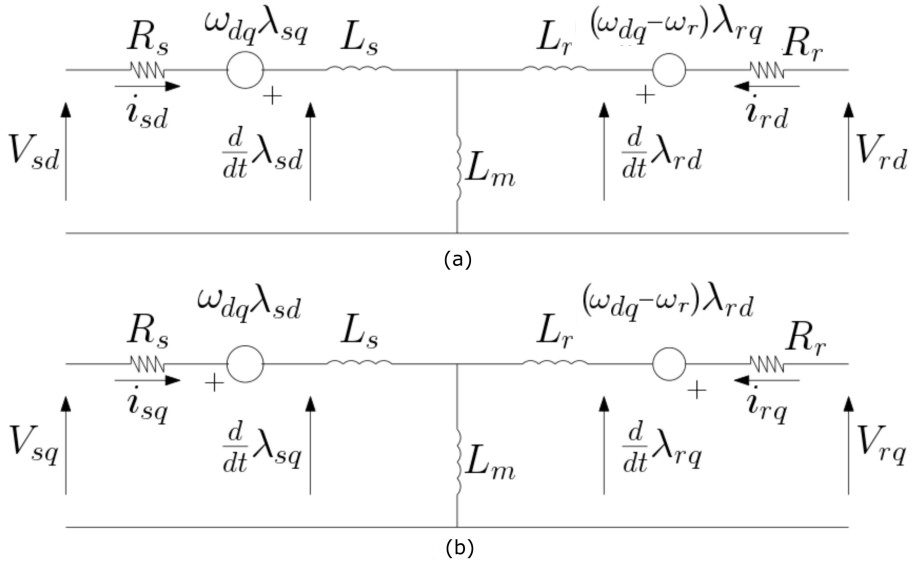

Figure 4.15: Induction generator dq equivalent circuit, based on [249], where (a) represents the *d-axis* and (b) represents the *q-axis*.

Equations for the induction machine model are given [313] as follows:

$$V_{sd} = R_s i_{sd} - \omega_{dq}\lambda_{sq} + L_s \frac{d}{dt} i_{sd} + L_m \frac{d}{dt}(i_{sd} + i_{rd}), \tag{4.22}$$

$$V_{sq} = R_s i_{sq} + \omega_{dq}\lambda_{sd} + L_s \frac{d}{dt} i_{sq} + L_m \frac{d}{dt}(i_{sq} + i_{rq}), \tag{4.23}$$

$$V_{rd} = R_r i_{rd} - (\omega_{dq} - \omega_r)\lambda_{rq} + L_r \frac{d}{dt} i_{rd} + L_m \frac{d}{dt}(i_{sd} + i_{rd}), \tag{4.24}$$

$$V_{rq} = R_r i_{rq} + (\omega_{dq} - \omega_r)\lambda_{rd} + L_r \frac{d}{dt} i_{rq} + L_m \frac{d}{dt}(i_{sq} + i_{rq}), \tag{4.25}$$

where ω_{dq} and ω_r are the angular velocities of the dq reference frame and the rotor, respectively, with the subscript r denoting the rotor of the electric generator, R_s and R_r the stator and rotor resistances, and L_s and L_r the stator and rotor inductances. In addition, i_{sd}, i_{rd}, i_{sq} and i_{rq} are the stator and rotor currents in the *d-* and *q-axis*, respectively. Note that, since the electric generator is coupled to the hydraulic motor, and assuming infinite rigidity of the shaft, ω_r is identical to ω_M. Finally, the flux linkages, λ_{ij} are represented as,

$$\lambda_{sd} = (L_s + L_m)i_{sd} + L_m i_{rd}, \tag{4.26}$$

$$\lambda_{sq} = (L_s + L_m)i_{sq} + L_m i_{rq}, \tag{4.27}$$

$$\lambda_{rd} = (L_r + L_m)i_{rd} + L_m i_{sd}, \tag{4.28}$$

$$\lambda_{rq} = (L_r + L_m)i_{rq} + L_m i_{sq}, \tag{4.29}$$

where L_m is the mutual inductance. Equations (4.22)-(4.25) include eight unknowns (dq voltages and currents in the stator and the rotor) for only four equations. Therefore, Equations (4.22)-(4.25) can only be solved by imposing the voltage in the stator (V_{sd} and V_{sq}) and the rotor (V_{rd} and V_{rq}) from the grid or the GenSC, depending on the grid-connection configuration of the electric generator. Finally, the electromagnetic torque developed in an induction machine is given by:

$$T_e = \frac{3N_p}{4}(\lambda_{sd} i_{sq} - \lambda_{sq} i_{sd}), \tag{4.30}$$

where N_p is the number of poles in the generator.

4.2.1.2 Permanent magnet generator

The mathematical model for the permanent magnet machine is different from the model for induction machines shown in Section 4.2.1.1, due to the major differences in the electrical machine topologies. Figure 4.16 illustrates the equivalent circuit for a PMSG, where one can note substantial differences compared to the equivalent circuit of induction machines, shown in Figure 4.15.

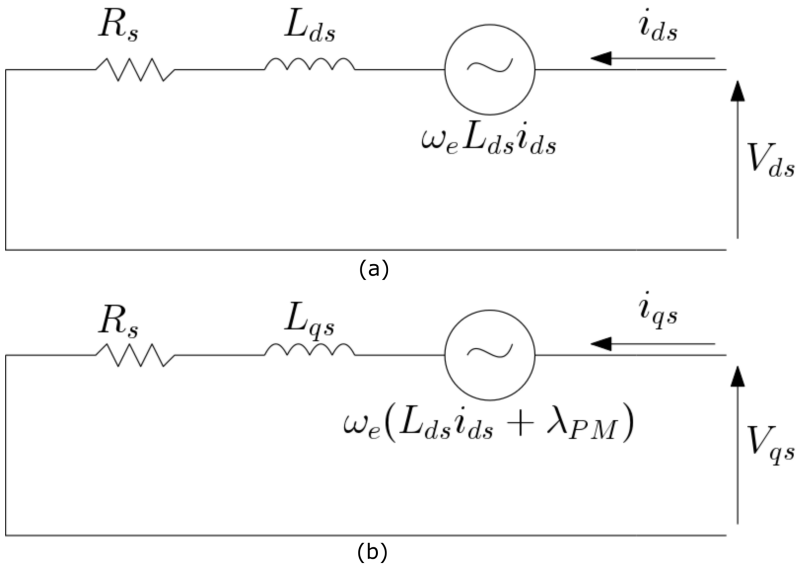

Figure 4.16: The dq equivalent circuit of the PMSG, based on [249], where (a) represents the *d-axis* and (b) represents the *q-axis*.

The voltage equations for the stator are given [249] as follows,

$$V_{sd} = R_s i_{sd} + L_{sd} \frac{d}{dt} i_{sd} - \omega_e L_{sd} i_{sd}, \tag{4.31}$$

$$V_{sq} = R_s i_{sq} + L_{sq} \frac{d}{dt} i_{sq} + \omega_e (L_{sq} i_{sq} + \lambda_{PM}), \tag{4.32}$$

where ω_e is the electric angular frequency of the generator. The electromagnetic torque, using the permanent magnet flux λ_{PM} of a PMSG, is given [249] by:

$$T_e = \frac{3N_p}{4} (i_{sq} \lambda_{PM} - i_{sd} i_{sq} (L_{sd} - L_{sq})). \tag{4.33}$$

Apart from voltage and electromagnetic torque equations, a mechanical equation for the acceleration of the rotor is required, which is identical for both induction and permanent magnet machines. The electromagnetic torque produced in the generator equals the driving torque (including mechanical losses due to friction and windage). Hence, the acceleration of the rotor can be expressed as:

$$\dot{\omega}_r = \frac{N_p}{2J_{shaft}} (T_e - T_M - B_{wind} \omega_r), \tag{4.34}$$

where J_{shaft} is the rotor's mechanical moment of inertia and B_{wind} the friction/windage linear damping.

Finally, voltages and currents from the stator of the generator are converted into active (P_e) and reactive power (Q_e) by means of Equations (4.35) and (4.36), respectively. Equations (4.35) and (4.36) are also identical for both induction machines and permanent magnet machines.

$$P_e = \frac{3}{2} (V_{sd} i_{sd} + V_{sq} i_{sq}), \tag{4.35}$$

$$Q_e = \frac{3}{2} (V_{sq} i_{sd} - V_{sd} i_{sq}). \tag{4.36}$$

4.2.2 Back-to-back power converter

Electric generators can be connected to the electricity grid directly (operating at fixed speed) or using a B2B power converter (operating at variable speed). In the latter case, the B2B power converter includes two inverters, a GenSC and a GridSC, linked through a smoothing DC line with a capacitor, as illustrated in Figure 4.17.

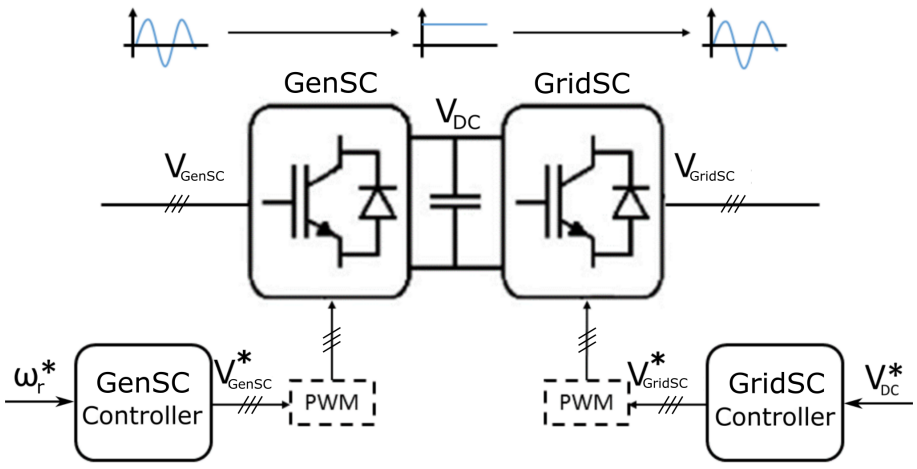

Figure 4.17: Diagram of a B2B power converter with controllers and pulse width modulators.

The inverters of the B2B power converter allow the rotational speed and air-gap flux in the electric generator to be controlled, and the output power to be suitably conditioned, for delivery into the grid. The air-gap flux is assumed to be constant, and the GenSC controller only controls the speed of the generator. Hence, reference signals for each inverter, reference rotor speed (ω_r^*) and DC voltage (V_{DC}^*), are delivered to the corresponding controllers, which are converted into voltage pulses for the inverters by means of a PWM unit, as shown in Figure 4.17.

Ideally, the mathematical model of an inverter, either GenSC or GridSC, includes the operation of the power switches, reproducing the pulses generated in PWM units. Despite the accuracy used to define and generate the switching instants in the PWM, it is well known that an inherent waveform distortion occurs in PWM units (due to switching operations), generating an output voltage signal that necessarily contains harmonics, unless some technique is used to eliminate such harmonics [314]. To examine the bulk performance of the electric generators, however, such harmonics can be neglected [315].

In addition, due to the high switching frequencies of PWM units (typically between 1–20 kHz in applications related to the control of AC motors), simulations require a very refined time step (1–10μs), which increases computational requirements to prohibitive levels. Therefore, the mathematical model of the B2B power converter presented in this chapter neglects the switching action (and consequent harmonics) of the PWM unit, and considers only the fundamental frequency of the voltage signals delivered into the electric generator and the electricity grid, referred to as V_{GenSC} and V_{GridSC} in Figure 4.17, respectively. Therefore, the PWM block in Figure 4.17 is represented by a simple unit gain, similarly to [223], meaning that reference voltage signals obtained in the controllers and the actual voltage signals are identical ($V_{GenSC}^* = V_{GenSC}$ and $V_{GridSC}^* = V_{GridSC}$, in Figure 4.17).

The DC-link between the GenSC and the GridSC can include a single capacitor or a bank of capacitors. These capacitors can absorb instantaneous active power fluctuation, smoothing the output power flow, and work as a voltage source for the converters. Variations of the DC voltage on the capacitor(s) can be calculated [316] as follows,

$$C\frac{d}{dt}V_{DC} = i_{DC_{GridSC}} - i_{DC_{GenSC}}, \tag{4.37}$$

where $i_{DC_{GridSC}}$ and $i_{DC_{GenSC}}$ are the current at the grid and generator side of the capacitor, in the DC link, respectively, C is the capacitance of the capacitor at the DC-link, and V_{DC} is the voltage on the capacitor.

4.2.3 Power losses in the electrical system

Modelling power losses in electric generators and power converters is vital to accurately evaluate final power generation. Electric generators are generally designed to minimise losses at full-load operational conditions, but losses increase substantially at part-load conditions, as shown later in Section 5.3.3.1 for the three different electric generator configurations studied in this thesis. Power losses may arise from different sources, and it is not always straightforward to include them in the mathematical model.

More insight into the efficiency characteristics of electrical machines is provided in [264], where losses in the SCIG, PMSG and DFIG, including the associated power converters, are studied.

4.2.3.1 Electric generators

Power losses in electric generators appear mainly due to large current requirements, which are manifested as large copper losses. The models described in Sections 4.2.1.1 and 4.2.1.2, for induction and permanent magnet machines, respectively, include the most important electric and mechanical dynamics and consider losses due to the Joule effect (i.e., copper losses in the stator and the rotor), core losses (i.e., stray losses) and mechanical losses (i.e., friction and windage losses). However, it

should be noted that iron losses are not included in the model, since they are considered negligible [313].

Figure 4.18 illustrates the losses in the different parts of an electric generator, from the rotor to the stator. Mechanical losses due to friction and windage ($P_{mech_{loss}}$) can be described as follows,

$$P_{mech_{loss}} = B_{wind}\omega_r^2, \tag{4.38}$$

while copper losses in the rotor (P^r_{copp}) and the stator (P^s_{copp}) are given as,

$$P^r_{copp} = R_r(i^2_{rd} + i^2_{rq}), \tag{4.39}$$

$$P^s_{copp} = R_s(i^2_{sd} + i^2_{sq}). \tag{4.40}$$

Stray-load losses (P_{stray}), which become important when operating at rated power, can be expressed [264] as:

$$P_{stray} = 0.005\frac{P_s^2}{P_N^2}, \tag{4.41}$$

where P_N is the nominal power of the electric generator.

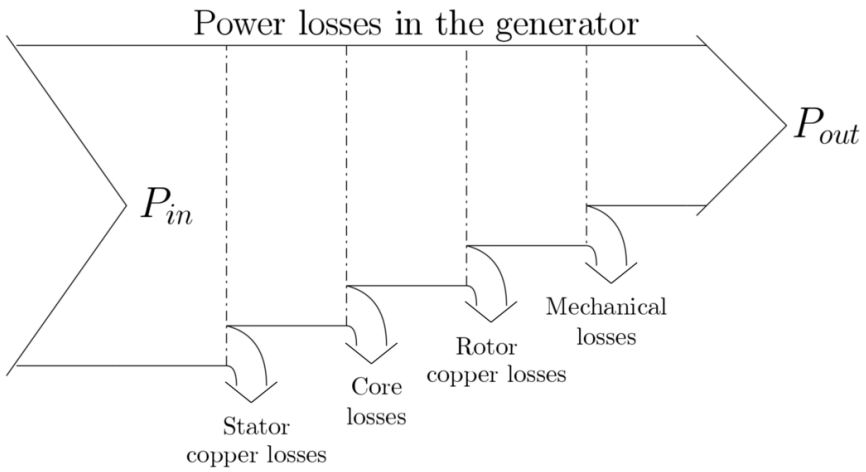

Figure 4.18: Specific power losses in electric generators.

4.2.3.2 Power converters

Power converter units comprise a number of power switches interconnected in a way that allows for the generation of AC signals from DC signals, and vice versa, by switching on and off these power switches at appropriate times.

Energy losses in converters arise from the non-ideal switching and conduction phases, illustrated in Figure 4.19, since power switches cannot switch on and off instantaneously. As a consequence, there exits a finite time window, referred to as ΔT_{on} or ΔT_{off} for switching on or off, respectively, where the non-zero overlap of collector-emitter voltage (V_{ce}) and current (i_{ce}) happens in the power switch. Figure 4.19 illustrates this non-zero overlap between V_{ce} and i_{ce}, and the power losses associated with switching operations in such a time window.

Switching losses, regardless of switching on or off, are commonly expressed as,

$$P_{switch} = f_{sw}\int_0^{\Delta T} i_{ce}(t)V_{ce}(t)dt, \tag{4.42}$$

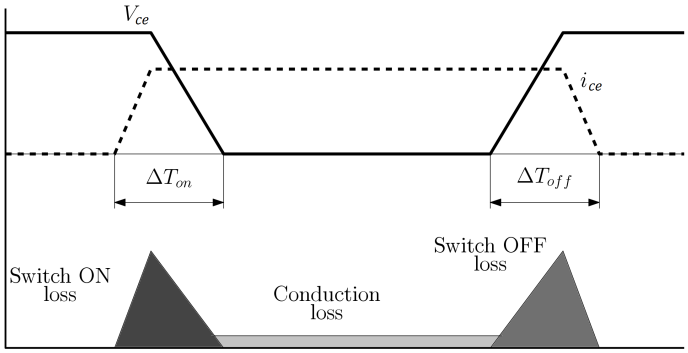

Figure 4.19: Diagram of a typical switching operation of a power switch that illustrates the (non-ideal) switching and conduction phases, and the power losses related to each phase.

where f_{sw} is the switching frequency, and ΔT is ΔT_{on} when switching on and ΔT_{off} when switching off. On the other hand, conduction losses can be calculated as follows,

$$P_{cond} = R_{ds} i_{ce}^2, \tag{4.43}$$

where R_{ds} is the resistance of the selected power switch. These conduction losses are constant for the whole period the power switch is conducting, as illustrated in Figure 4.19. However, if switching operations in the inverter are not included in the model, as described in Section 4.2.2, power losses cannot be calculated using Equations (4.42) and (4.43). Therefore, another alternative to evaluate power losses in the inverters, via experimental data, is suggested in Chapter 5.

4.3 Summary

This chapter presents the mathematical models for the hydraulic transmission system, including the constant- and variable-pressure HyPTO configurations, and the electrical system, with three different electric generators and power converters.

Section 4.1 focuses on the hydraulic transmission system, where the different configurations are described and the mathematical model for each component used in hydraulic transmission systems is provided. These mathematical models include the most relevant dynamics and losses of each component, and analyse different modelling possibilities. For example, the compressibility effect is evaluated via different mathematical models and different opening functions are suggested for valves. In the case of the hydraulic cylinder and motor, losses are incorporated into the mathematical model using manufacturers' data. Since the hydraulic motor used in the different hydraulic transmission system configurations is usually different, manufacturers' data for two hydraulic motors is presented, identifying loss model parameters for each case. Although manufacturers' data is provided for a limited range of operating conditions, model parameters are extrapolated so that the whole range of operating conditions is covered. In addition, the mathematical model for the hydraulic motor is scalable, meaning that the same model can be used for a variety of different motor sizes.

Section 4.2 describes the electrical system of the HyPTO system, divided into three main parts: the electric generator (Section 4.2.1), the B2B power converter (Section 4.2.2) and power losses in electrical systems (Section 4.2.3). Electric generators are three-phase electrical machines, but are typically represented via the two-phase dq reference frame. Thus, this dq reference frame is first introduced, explaining the transformation from a three-phase stationary to a two-phase rotational reference frame, and vice versa. Then, mathematical models for electric generators, including induction and permanent magnet rotational electric generators, are defined via the dq reference frame. The mathematical model of B2B power converters involves very high-frequency switching operations that reproduce the pulses generated in the PWM, but make the mathematical model computationally prohibitive. Therefore, PWM blocks are represented as unitary gains,

neglecting switching operations. Finally, the main power losses are studied in electric generators, including mechanical, stray-load and copper losses. Losses in power converters cannot be analysed if switching operations are neglected in the mathematical models and, thus, an alternative approach is required, which is described in Chapter 5.

Chapter 5

Validation of the *cHyW2W* model

The *cHyW2W* model presented in this thesis includes the most important dynamics, losses and constraints of each subsystem, as shown in Chapters 3 and 4. Nevertheless, in order to gain confidence in the *cHyW2W* model, it is crucial to validate the results against experimental data, ideally, or, in the absence of experimental results, against well-established high-fidelity software.

However, the large number of components included in the HyW2W models makes its validation, as a whole, quite challenging, mainly due to the complexity and cost of building a physical model where all the components are integrated. An alternative to validating the *cHyW2W* model as a whole, is to attempt to accomplish the validation by separately validating each subsystem or conversion stage of the model. The latter strategy is consistent with the way the *cHyW2W* model is implemented, since it is designed as a combination of inter-connected subsystems, as illustrated in Figure 2.22 and described later in Chapter 6.

Hence, this chapter presents the validation of the mathematical models described in Chapters 3 and 4. First, the different WSHI approaches, presented in Chapter 3, are compared against CNWT results in Section 5.1. Validation of WSHI models is often carried out in the literature by analysing absorber's motion under either uncontrolled or docile control conditions, meaning that the impact of nonlinear effects on the behaviour of the absorber is negligible. However, as demonstrated in Chapter 3, energy maximising control strategies can significantly enhance the impact of nonlinear effects. Therefore, a comparison of the different WSHI models is carried out under an aggressive control strategy, latching control. The comparison presented in Section 5.1.2 is a preliminary comparison, which only covers a single wave frequency/amplitude, and, thus, cannot be considered as a comprehensive validation. However, this preliminary comparison shows that the fidelity of mathematical models can be improved significantly by considering the most relevant nonlinear effects.

On the other hand, Section 5.2 shows the validation of the mathematical models for the hydraulic transmission system, including the constant- and variable-pressure configurations described in Section 4.1. Hence, two experimental test-rigs, one for each hydraulic transmission system configuration, are used. The details of the two experimental test-rigs are provided in Section 5.2.1, and results from the test-rigs are used to validate the mathematical models for the hydraulic cylinder, including the effect of the check valves, and the LP and HP accumulators. In the case of the hydraulic motor, due to the lack of experimental data, the well-known established simulation software *AMESim* [317] is used for the validation of the mathematical models presented in Section 4.1.2.4.

Finally, mathematical models for the electrical system are validated in Section 5.3, using experimental data generated in three different test-rigs, one for each electric generator topology described in Section 4.2.1. Mathematical models for these three electrical machines are validated across a broad range of operating conditions, using several different input signals, including part- and full-load conditions. To generate such input signals, the electric generator must be controlled via the power converters, which allows for the validation of the simplified mathematical model

suggested for power converters in Section 4.2.2.

5.1 Wave-structure hydrodynamic interactions

The validation of WSHI approaches is ideally carried out comparing the simulated behaviour of the absorber against results obtained from wave tank or open-sea experiments. However, results from such experiments are not always available, especially due to the high cost of the experiments, and, thus, alternative sources of data must be found for the validation. The mathematical approach, that provides results closest to real wave tank or open-sea experiments, is the fully-nonlinear CFD approach, as shown in Figure 2.23.

Therefore, in the present case, CNWT is implemented using the open-source software, OpenFOAM [318]. The main reason to select the OpenFOAM software, instead of other commercial software, is the open-source availability and the flexibility this provides. The source code can be accessed and manipulated as desired, which gives the user the total control over the software and allows for modification/augmentation, such as the coupling of the CNWT and the *cHyPTO* model, presented in Chapter 7. As for any CFD software, the OpenFOAM based CNWT captures all relevant hydrodynamic non-linearities when simulating WECs, by numerically solving the incompressible RANS equations shown in Equations (2.2) and (2.3).

Apart from the mathematical approach, simulation conditions are essential for a comprehensive validation, meaning that the complete operational space of the absorber must be covered, including a wide range of incoming waves and control conditions. In fact, when the absorber behaves as a wave follower, under docile control, mathematical models based on LPF theory show good agreement with wave tank experiments [179, 185, 319]. In contrast, when the motion of the absorber is enhanced via a control strategy, results from wave tank experiments or CNWTs, and from the LPF model diverge significantly [57, 188]. Therefore, when more aggressive control strategies are implemented, enhancing absorber's motion, mathematical models based on LPF theory become unreliable, overestimating motion and power absorption, as demonstrated in Section 3.2.4.

5.1.1 Case study

The BEM-based WSHI models suggested in Chapter 3 are evaluated for the spherical HPA, described in Section 3.1.3, using CNWT results as a benchmark. In this comparison, the B^{1}_{PTO} parameter is utilised, since it is the case that exaggerates the differences between the linear and nonlinear WSHI approaches, to the greatest extent. However, due to the prohibitive computational cost of CNWT simulations, only one case is selected to perform the comparison among all the monochromatic waves analysed in Section 3.2.4: $H_w = 1m$ and $T_w = 6s$. This specific case allows for the comparison of the different numerical approaches while the absorber never gets fully submerged or clear the water.

The setup of the CNWT is divided into three main parts: the tank, the boundary and the background mesh. The overall geometry of the tank is first defined using rectangular blocks. This overall geometry is defined based on the specific characteristics of the experiment to be analysed. More specifically, the water depth and the wavelength are the most important aspects. Finally, a symmetry plane is implemented in the $X0Z$ plane, which is defined as a boundary. *Wall* boundary is implemented in OpenFOAM for the seabed, while the *patch* boundary is implemented for the four walls of the tank and the top face.

Once the tank geometry and the boundaries are determined, the background mesh can be defined. This background mesh is one of the most important aspects of the CNWT. In fact, due to the exaggeration of the body motion under aggressive control conditions, a poor mesh can result in failure due to over-deformation of the cells. In addition, the accuracy of the generated waves also depends on the adequacy of the mesh. The mesh contains a central part where the density of cells, uniform cubic cells, is highest and stretches horizontally and vertically away from this

central block. Horizontally, the mesh stretches towards the back and front walls, reducing the overall number of cells. Vertically, the mesh is divided into three regions: air, interface and water. The interface region spans the area where the free-surface appears and is implemented with high mesh density. The water region has a moderate mesh density and stretches gradually from the interface region down to the tank floor. Finally, the air region has a rather low mesh density and the mesh stretches from the interface region up to the top of the tank.

There exist numerous methods to create and absorb waves in OpenFOAM. The case study analysed in this section uses the relaxation zone method implemented in the *waves2Foam* toolbox. The user selects a target solution for input waves and the relaxation zone method blends this solution smoothly, generating the desired input wave in the *wave creation zone* and absorbing the wave field in the *absorption zones* to avoid reflected waves from the tank walls. The recommended lengths for the *wave creation* and *absorption* zones are 1.5 and 3 times the wavelength, respectively [320], which result in a *wave creation zone* of 170m and an *absorption zone* of 335m.

With respect to the control conditions, absorber motion is enhanced in the present case via latching control, as described in Section 3.2.4.1, to enhance energy absorption from ocean waves. The latching control strategy, implemented in a CNWT, is presented in [321] for the first time and the same implementation is followed here. The algorithm to implement latching control in OpenFOAM uses the built-in function *sixDoFRigidBodyMotion*. This function was originally created to calculate the motion of the body under analysis, by integrating the forces applied on the absorber and solving Newton's second law. However, in order to highlight the relevance of control for validation purposes, all the different numerical approaches are compared under docile and aggressive control.

5.1.2 Preliminary comparison

Hence, results for the selected incoming wave under docile and aggressive control are calculated for six different approaches: *LFK*, *NLrest*, *NLFK*, *NLFKa*, *NLFKa* with externally added viscous effects following Equation (3.37) (*viscNLFKa*), and CNWT. In this comparison, results from the fully-nonlinear CNWT are taken as a fidelity benchmark, evaluating the results from the rest of the approaches against CNWT results. Displacement comparisons are used for evaluating the fidelity of the different approaches, and the deviation between these different approaches and the CNWT is calculated by means of the normalised root mean square deviation (NRMSD) as follows,

$$NRMSD = \frac{\sqrt{\frac{\sum_{k=1}^{n_t}(y(k)-\hat{y}(k))^2}{n_t}}}{\bar{y}}, \tag{5.1}$$

where $\hat{y}$ and y represent any variable (displacement in this specific case) obtained from the WSHI approach being evaluated and CNWT, respectively, n_t is the number of samples, and $\bar{y}$ represents the mean of the variable y. Thus, the NRMSD is bounded between 0 and 1, and the fidelity of the evaluated approaches expressed in percentage can be given as follows,

$$Fidelity = (1 - NRMSD) \times 100 \qquad [\%]. \tag{5.2}$$

However, another important characteristic of numerical models is the computational time, which also needs to be considered in this comparison. Figure 5.1 illustrates the fidelity of the different approaches versus their computational time requirements, under docile and aggressive control. Due to the high computational cost of the CNWT, compared to the rest of the approaches (up to 4 orders of magnitude higher), the computational cost of the different approaches are compared using the logarithmic scale and normalised against the computational time required by the *LFK* model (t_{CPU}^{norm}).

For the docile control case, all the approaches provide high fidelity results, always over 97% as shown in Figure 5.1 and Table 5.1. Thus, if the comparison is performed under docile control

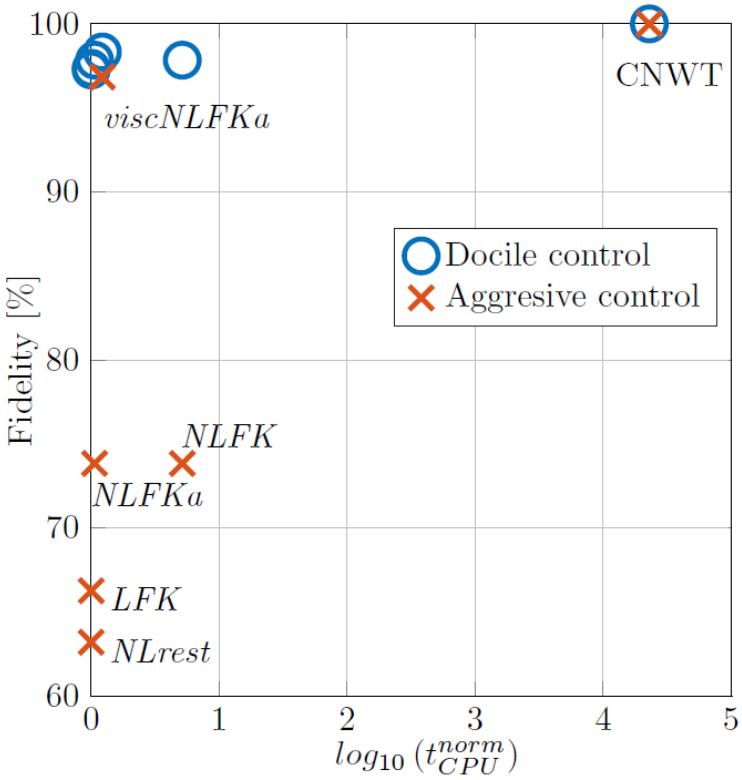

Figure 5.1: Fidelity of the different approaches versus their computational requirements, under docile and aggressive control for a monochromatic wave of 1m H_w and 6s T_p.

conditions, one could argue for the suitability of all the different mathematical models, including the *LFK* model. In fact, the comparison would conclude that the *LFK* model is the most adequate one, since it is computationally more appealing than the rest of the approaches. However, when a more aggressive control strategy, that maximises energy absorption, comes into play, results from different approaches diverge significantly, as shown in Figure 5.1.

Table 5.1: Fidelity [%] and normalised computational time under docile and aggressive control, using a regular wave of period T_w 6 s and H_w 1 m.

	LFK	*NLrest*	*NLFK*	*NLFKa*	*viscNLFKa*	CNWT
$\text{Fidelity}_{\text{Docile}}$ [%]	97.35	97.25	97.84	97.84	98.32	100
$\text{Fidelity}_{\text{Aggressive}}$ [%]	66.26	63.19	73.84	73.84	96.83	100
t^{norm}_{CPU}	1	1.09	5.15	1.26	1.35	23000

For the aggressive control case, the inaccuracy of the *LFK* and *NLrest* approaches is confirmed, as expected from the results presented in Chapter 3. In addition, one can notice that the *NLFK* and *NLFKa* approaches are equivalent in terms of accuracy, while differing significantly in computational time requirements, where the *NLFKa* approach reduces the computational time by a factor of 5. However, the implementation of the nonlinear FK forces is demonstrated to be insufficient to accurately represent the behaviour of the spherical HPA. Therefore, viscous effects have been added externally in the *viscNLFKa* approach, using $C_{drag} = 1$ as suggested in Section 3.2.3. The incorporation of viscous effects in the mathematical model provides reasonably high-fidelity results for a fraction of the computational time required for the CNWT approach, as illustrated in Figure 5.1 and Table 5.1.

In addition to the comparison in the fidelity/computational time plane presented in Figure 5.1 and Table 5.1, results of the comparison in time-domain are illustrated in Figure 5.2, in order to

show the impact of fidelity percentages on device motion.

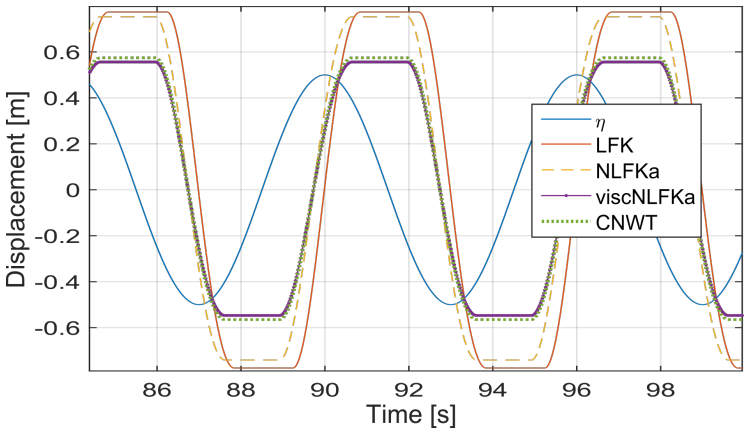

Figure 5.2: Displacement of the spheric HPA under latching control for the *LFK*, *NLFKa*, *viscNLFKa* and CNWT approaches for a monochromatic wave of 1m H_w and 6s T_p.

Since the complete operational space of the absorber should be covered in a comprehensive validation, the preliminary comparison presented in this section cannot be considered as a thorough validation study. However, this comparison is extended in [56] to include a wider range of incoming waves, where the conclusion is identical, highlighting the high fidelity of the *viscNLFKa* approach and, as a consequence, the need for nonlinear FK forces and viscous effects.

5.2 Hydraulic transmission system

The validation of hydraulic transmission system models includes two significantly different mathematical models, which require separate validation. Therefore, experimental data, generated by using two different test-rigs, are used in the validation. The performance of the hydraulic cylinder for both hydraulic system configurations is validated against experimental results, while the well-known simulation software *AMESim* [317] is used to validate the performance of the hydraulic motor, due to the lack of experimental results for the hydraulic motor.

5.2.1 Experimental setup

The particularities of each test-rig used in the validation of the mathematical models for the constant- and variable-pressure hydraulic transmission system configurations presented in Section 4.1 are discussed in the following subsections, but a number of commonalities should be reported before describing each test-rig.

Both test rigs were set-up on the same bed plate at the University of Bath's Centre for Power Transmission and Motion Control (CPTMC). Both rigs were driven by a double ended high precision linear actuator with 250 mm of stroke and piston area of 25 cm^2. This actuator was operated in position control and was powered by a power pack capable of delivering 52 L/min at pressures up to 195 bar. A Simulink Real-Time system was used for data logging and control purposes in both test rigs, using a National Instruments PCI6221 data acquisition (DAQ) board sampling at 1 kHz and a National Instruments PCI6229 DAQ board sampling at 100 Hz, on the constant- and variable-pressure rigs, respectively.

Both test rigs were also constructed from discrete components and, as a result, losses within the circuits are higher than would be expected within custom manufactured units of similar design. Maximising efficiency was not the intent of these test rigs, and so these losses were not of concern, as long as they could be quantified for the purpose of model validation.

It should be noted that the test-rigs and experiments presented in this section, which are used for the validation of the mathematical models presented in Section 4.1, were designed and carried out in previous projects, and so cannot be considered as a contribution of this thesis. However, it is important to describe the test-rigs and the experiments to better understand the validation described in Section 5.2.3.

5.2.1.1 Constant-pressure configuration

For the validation of the constant-pressure hydraulic transmission system configuration, a test-rig similar to the schematic illustrated in Figure 4.1 is necessary. However, the experimental test-rig implemented in the University of Bath's CPTMC slightly varies from that shown in Figure 4.1. The main difference is the use of an asymmetric cylinder, with an area ratio of approximately 2:1, as illustrated in Figure 5.3. Hence, to reproduce the behaviour of a test-rig with a symmetric cylinder and maintain similar flow rates in extension and retraction, further changes are necessary in the test-rig. Figure 5.3 shows the modified test-rig and Table 5.2 provides the details of the individual components. This test-rig was originally constructed by Chris Cargo for his PhD thesis in the University of Bath [322], where further information about the test-rig can be found.

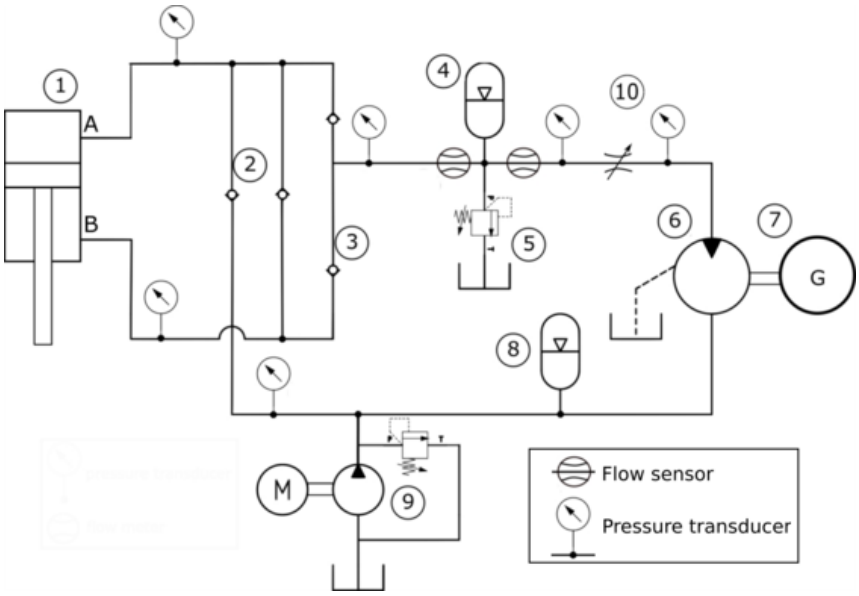

Figure 5.3: Experimental constant-pressure circuit.

Table 5.2: Constant pressure test rig components.

No.	Description	Details
1	Hydraulic cylinder	40 mm bore, 28 mm rod, 300 mm stroke
2	Regenerative check valves	0.35 bar preload
3	Rectification check valves	0.35 bar preload
4	HP accumulator	3.8 L, 10 bar precharge
5	Relief valve	100 bar cracking pressure
6	Gear motor	4.0 cc/rev
7	DC Generator	90 W at 3000 rpm
8	LP accumulator	1 L, 2 bar precharge
9	Boost pump	4 cc/rev, 7 bar relief pressure
10	Throttle valve	3/8" needle valve

Hence, when the hydraulic cylinder (1) is retracting, part of the fluid exiting the piston chamber (chamber A in Figure 5.3) is transferred, via the regenerative check valve (2), to the annulus chamber (chamber B in Figure 5.3). As a consequence, the rectified flow that goes through the rectification bridge (3) to the HP accumulator (4) and, eventually, to the hydraulic motor (6), is equal to the annular area multiplied by the piston velocity (or half the piston area multiplied by piston velocity, due to the 2:1 area ratio). In contrast, when the hydraulic cylinder is extending, the annulus flow is rectified to feed the motor, and the LP accumulator (8) and boost pump (9) provide make-up flow to the piston chamber A. A fixed-displacement motor is used in the test-rig along with a DC generator (7), and a throttle valve (10) is included in the circuit to mimic variations of the hydraulic motor displacement. Also, a relief valve (5) is implemented to avoid overpressure in the hydraulic circuit.

In Figure 5.3, the location of the six pressure sensors and two flow sensors used in the experimental test-rig can be identified. The pressure sensors themselves are all *Transinstrument 2000 series* rated to 250 bar and individually calibrated before installation. The flow meters are *Hydac EVS3100 series* capable of measuring flows between 6 L/min and 60 L/min, and are delivered pre-calibrated and with signal conditioning. The physical location of the different components included in the test-rig is shown in Figure 5.4.

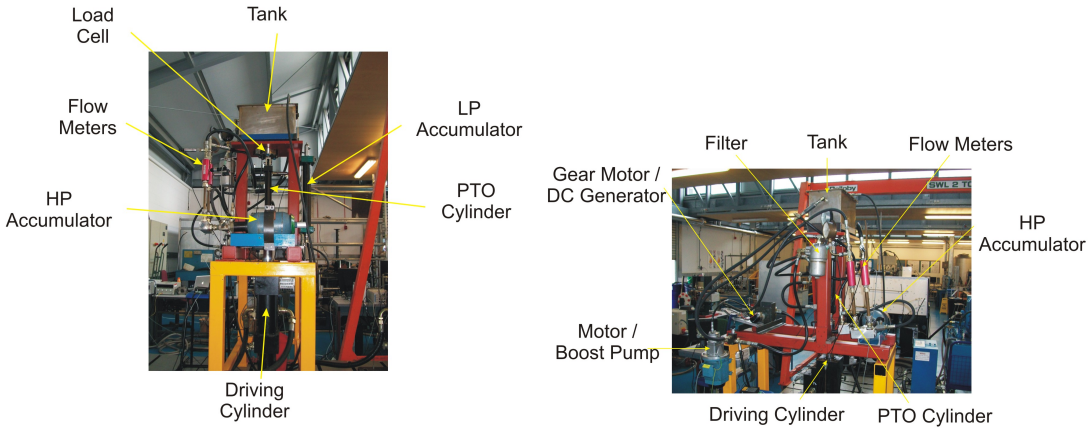

Figure 5.4: Front (a) and side view (b) of the constant-pressure configuration test-rig.

5.2.1.2 Variable-pressure configuration

The hydraulic circuit employed for the validation of the variable-pressure hydraulic transmission configuration is shown in Figure 5.5 and also includes a fixed displacement hydraulic motor (3), instead of the variable displacement motor shown in Figure 4.2. The leakage from the motor is directly returned to the circuit via a LP accumulator (5) and a pair of check valves (4), obviating the need for a boost pump. Pressure signals are measured by means of pressure sensors from the *Parker ASIC series* rated to 250 bar, which are calibrated at manufacture. Relief valves (2) to avoid overpressure in the circuit are also incorporated in this test-rig. Table 5.3 shows the details of each component for the variable-pressure test-rig.

Figure 5.6 illustrates the variable-pressure test-rig, where one can notice that there are two different hydraulic motors, since different sized motors were tested in the previous projects for which the test-rig was designed. However, all results discussed in this chapter are measured with the 7.8 cc/rev motor installed.

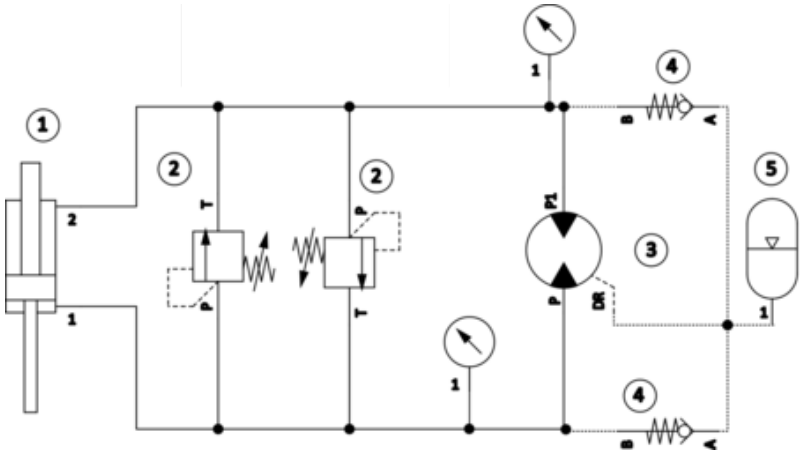

Figure 5.5: Experimental circuit of the variable-pressure.

Table 5.3: Variable pressure test rig components.

No.	Description	Details
1	Hydraulic cylinder	30 mm bore, 25 mm rod and 500 mm stroke
2	Relief valves	200 bar cracking pressure
3	Gear motor	7.8 cc/rev displacement
4	Leakage check	0.35 bar cracking pressure
5	LP accumulator	5 L, 1 bar precharge

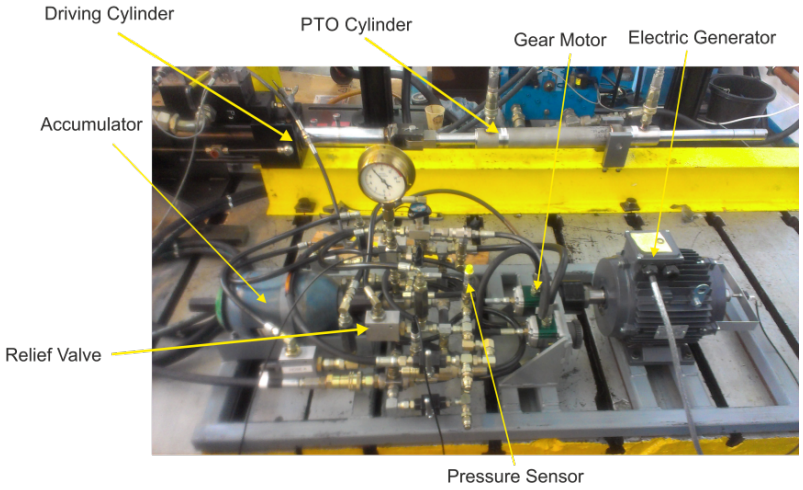

Figure 5.6: The physical variable-pressure test-rig.

5.2.2 Hydraulic motor model in *AMESim*

In the test-rigs presented in Sections 5.2.1.1 and 5.2.1.2, the results corresponding to the hydraulic motors are not available. Therefore, resort to a high-fidelity simulation platform was made to validate the mathematical model of the hydraulic motor presented in Section 4.1.2.4. Hence, a comparison between the model presented in Section 4.1.2.4, referred to as the Schlösser model in the following, and two different models created with the high-fidelity *AMESim* software, defined as the idealised and the detailed models, is presented. *AMESim* is a physical modelling and simulation package for mechatronic systems based on bond graph methods. It is used widely within the fluid power industry and there are numerous publications validating its results against empirical

data, including [323–326].

The idealised and detailed models created in *AMESim* reproduce the behaviour of a gear motor and use the pressure at the HP and LP accumulators, and the hydraulic motor's velocity from the numerical models, as inputs. The comparison between the Schlösser model, and the idealised and detailed *AMESim* models is carried out using the output torque at the motor shaft and flow at the outlet of the hydraulic motor.

5.2.2.1 Idealised model

The idealised model assumes a perfect motor with no losses and continuous flow. Therefore, motor flow in the idealised model is a linear function of the shaft velocity used as input. It is further assumed that there are no losses between the pressure sensors and the motor. This is the simplest model of a hydraulic motor and is created as a baseline for future models.

5.2.2.2 Detailed model

A second model is also created, which models the individual teeth of the gear motor, in addition to other effects. Thus, the displacement varies with the absolute rotational position of the motor. The pumping gears have a total of 12 driving and 12 driven teeth with a module of 2.65mm and width of 7mm each. This detailed hydraulic motor model is also coupled to a Wilson loss model, which uses the same efficiency map as shown in Figure 4.10, originally used to fit the hydraulic motor model developed in Section 4.1.2.4. The output torque measured in *AMESim* ignores the effect of inertia within the motor or generator, and so is more variable than the actual torque measured at the motor shaft.

5.2.3 Validation results

The two experimental set-ups described in Section 5.2.1 allow for complete validation of the mathematical models presented in Section 4.1, analysing the performance of the different components implemented in the constant- and variable-pressure hydraulic transmission systems, under different operating conditions.

The inputs to the mathematical models are, for both hydraulic transmission system configurations, piston position and velocity, and rotational speed of the electrical generator, as illustrated in Figure 2.22. Those inputs are taken directly from the experimental data and the outputs from the mathematical models are compared to the test-rig measurements and results from the high-fidelity software *AMESim*. Figures 5.7 (a) and (b) show the displacement and velocity of the piston, and the rotational speed, respectively, for one of the test cases simulated in the constant-pressure experimental set-up.

In the test-rig with the constant-pressure configuration, the hydraulic cylinder is coupled to a hydrodynamic model that reproduces the behaviour of a WEC by means of a hardware-in-the-loop (HIL) system. Further details about the WEC and the HIL system are given in [322]. However, these details are irrelevant for the validation presented in this section, since the hydrodynamic model computes the position and velocity of the WEC (and, thus, position and velocity of the piston in the hydraulic cylinder), which are used as the inputs to the experimental test-rigs.

Three test cases, based on regular waves, are studied in the constant-pressure test rig, which need to be scaled down (using a scaling factor of 10) to be implemented in the experimental test-rig:

- 10s (3.2s) wave period and 1.5m (15cm) amplitude,
- 10s (3.2s) wave period and 1m (10cm) amplitude, and
- 12s (3.8s) wave period and 1.25m (12.5cm) amplitude.

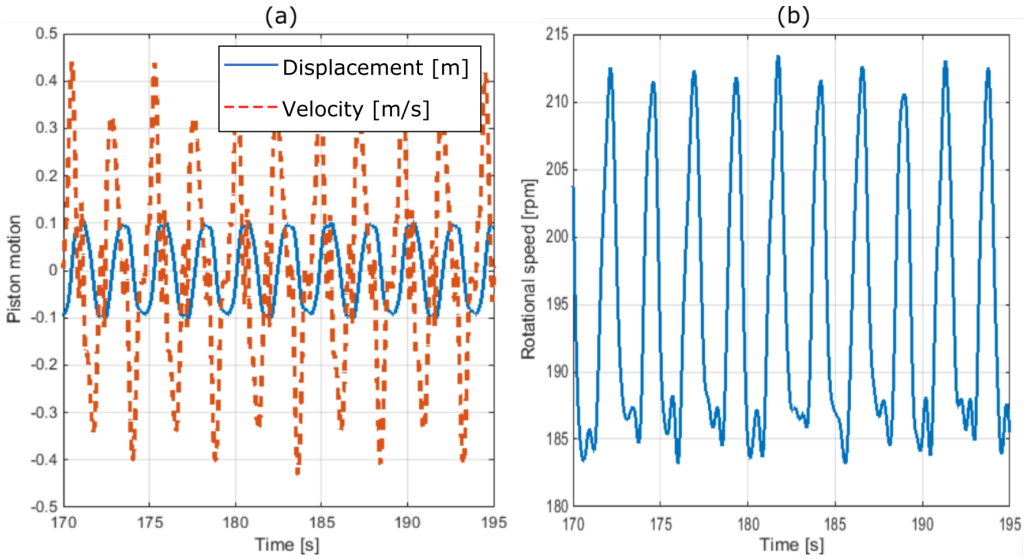

Figure 5.7: Inputs for the mathematical model: (a) position and velocity of the piston; and (b) rotational speed of the electric generator.

In the case of the variable-pressure configuration, no HIL system is implemented, and piston position and velocity from the experiments are directly used as inputs. A total of 20 test cases are analysed, combining four different sinusoidal input signals and five damping coefficients for the force control.

Hydraulic cylinders and motors are the most important components in hydraulic systems, because the performance of the whole system essentially depends on the performance of these two components. The major challenge when modelling hydraulic cylinders is to accurately reproduce losses and dynamics due to friction. In the case of the hydraulic motor, friction and leakage losses are the main challenge. Therefore, the validation of the mathematical models focuses on these two main components, carefully examining friction effects in hydraulic cylinders and losses in hydraulic motors.

5.2.3.1 Hydraulic cylinder

The performance of the hydraulic cylinder depends on the configuration of the hydraulic transmission system. In the case of constant-pressure configurations, the pressure in the cylinder chambers and, as a consequence, the force applied on the WEC, is practically constant, as illustrated in Figures 5.8 and 5.9, respectively. In contrast, the pressure in the cylinder chambers and the force of the hydraulic cylinder in the variable-pressure configuration follow the profile of the velocity, as shown in Figures 5.10 and 5.11, respectively.

5.2.3.1.1 Constant-pressure configuration

Pressure in the hydraulic cylinder is driven by the pressure in the hydraulic accumulators, which, in turn, depends on the pre-charge pressure and the oil volume, as shown in Equation (4.11). The pressure of the oil in the accumulator sets the threshold for the check valves, so that check valves open only when the pressure in the cylinder chamber is higher than in the HP accumulator.

As one can note from Figure 5.8, the hydraulic cylinder in the constant-pressure configuration repeats the same cycle during the simulation. When the piston reaches its final position (1 in Figure 5.8), the pressure in the high-pressure chamber starts to decrease, falling below the HP accumulator pressure level. At that point, check valves close and the piston starts to oscillate for a short period of time, which produces pressure fluctuations in both chambers (2 in Figure

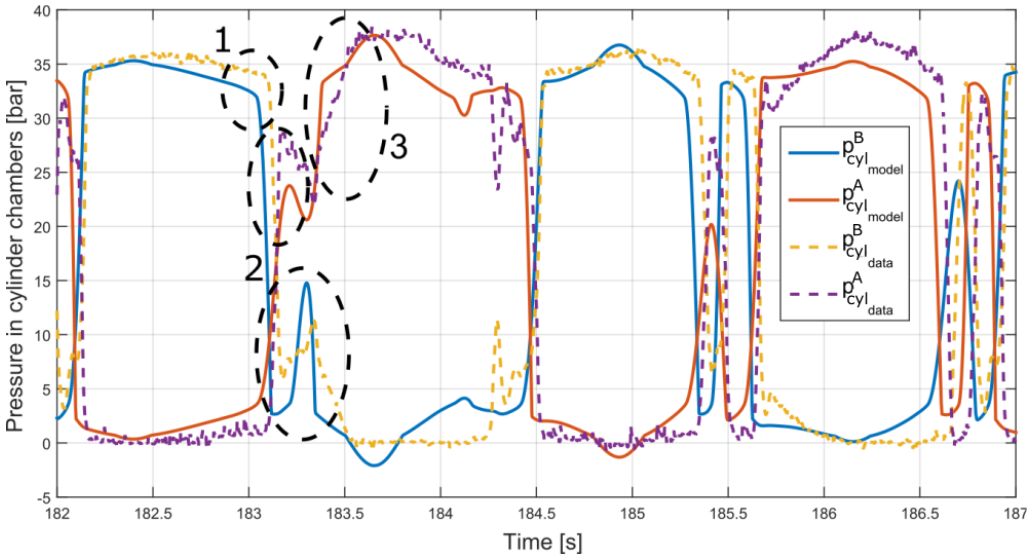

Figure 5.8: Pressure in the chambers A and B of the hydraulic cylinder from the experiments and the mathematical model for the constant-pressure configuration.

5.8). As soon as the pressure in any of the chambers increases again over the pressure in the HP accumulator, check valves open again, and the piston starts to move 'freely', pushing the oil in the chamber, and, consequently, increasing the pressure in the chamber (3 in Figure 5.8). When the piston again reaches its end point, the whole process repeats in the other chamber.

The behaviour of the hydraulic cylinder in the constant-pressure configuration is similar for all the test cases analysed in the validation, where the profile of the pressure signals is practically identical and only the magnitude of the signals changes from one test case to another. Figure 5.8 illustrates the pressure in the chambers of the hydraulic cylinder for the 12s period and 1.25m amplitude test case, showing good agreement between the experimental results and the results from the mathematical model, in the sense that the profile and magnitude of the pressure signals are similar. However, pressure signals in the experimental test-rigs appear to be slightly flatter at low pressure levels, while one can notice a negative overshoot in the results obtained from the mathematical model. This negative overshoot should not happen in the numerical model, since it would represent a negative volume in the LP accumulator. Therefore, the model of the LP accumulator should include a constraint to avoid these situations. In addition, a phase lag exists between the experimental measurement and the numerical simulation, as a result of the different pressure transitions. It should be noted that the opening of the check valves in the mathematical model follows the step function described in Figure 4.7, in order to reproduce the same valve opening profile as in the original study where the experimental data is taken from [322]. This step function results in an instantaneous pressure transition in the numerical simulations.

Similar agreement can be observed in Figure 5.9 for the piston force, where friction or inertia forces are also considered. The phase lag between the mathematical model and the experiments observed in the pressure signals remains, as expected, in the force signals. However, it should be noted that the effect of friction is rather low in these test cases, about 1% of power loss due to friction, based on the mathematical model.

5.2.3.1.2 Variable-pressure configuration

In the case of the variable-pressure configuration, agreement between the experiments and the numerical simulations is also good for the different test cases, as illustrated in Figure 5.10, where the pressure signal is clearly asymmetric. This asymmetry appears due to a non-symmetrical

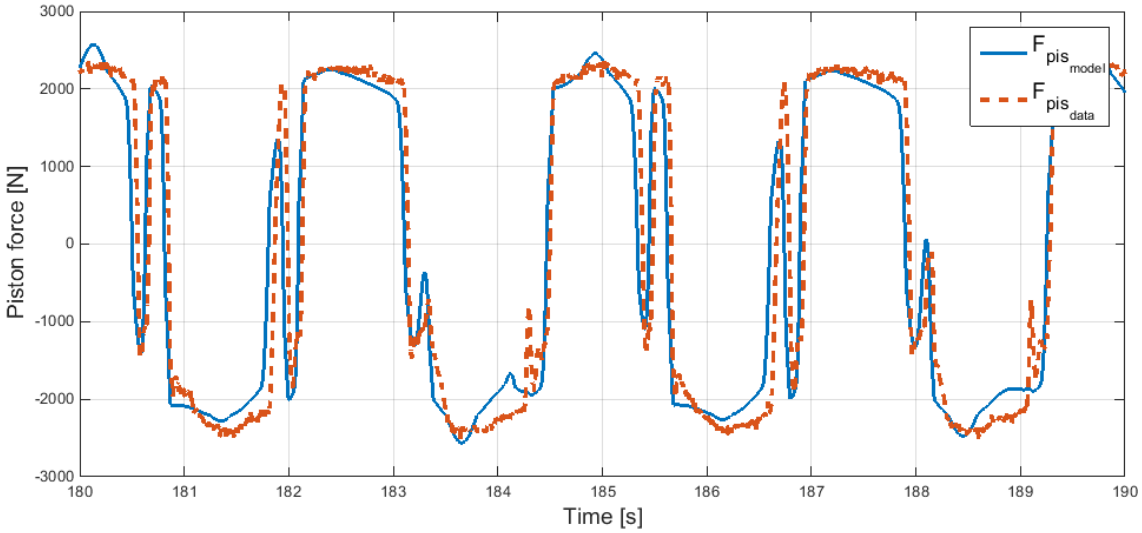

Figure 5.9: Pressure in the chambers A and B of the hydraulic cylinder from the experiments and the mathematical model for the constant-pressure configuration.

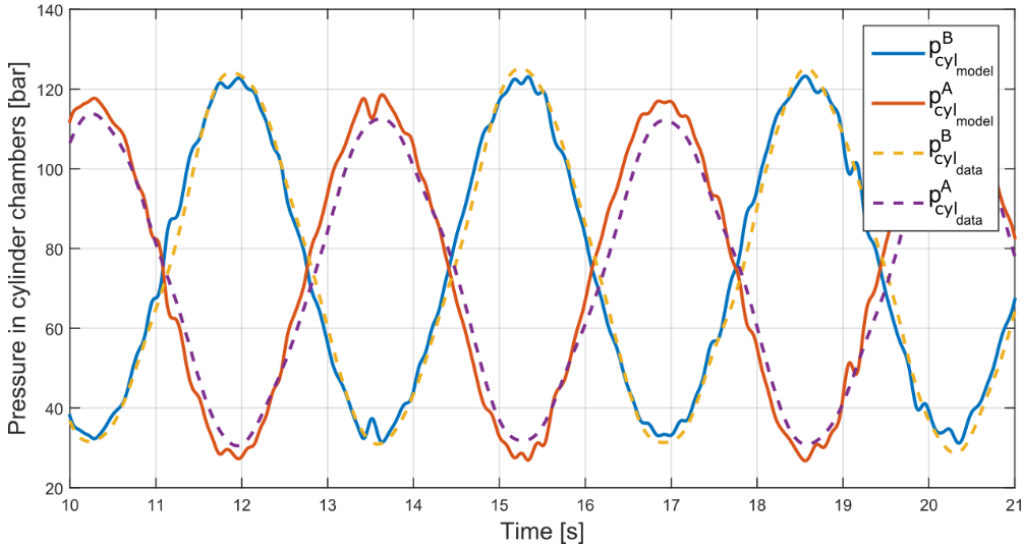

Figure 5.10: Piston force from the experiments and the mathematical model for the constant-pressure configuration.

control force signal, with a different damping coefficient for each direction of motion.

As for the constant-pressure configuration, the measured and simulated force signals match well, as illustrated in Figure 5.11. Apart from the total force signal, Figure 5.11 also shows the contribution of the different factors, such as pressure difference, friction and piston mass. Hence, one can observe that, for the pressure force, referred to as the force considering only the contribution of the pressure difference in the cylinder ($F_{\Delta P_{model}}$), the amplitude is lower than the experimental piston force ($F_{pis_{data}}$). In addition, the pressure force is, as expected, asymmetric, while the experimental piston force appears to be completely symmetric. However, when friction force and gravity force due to the piston mass are added to the pressure force, the total piston force obtained from the mathematical model ($F_{pis_{model}}$) accurately matches the experimental piston force.

Finally, the friction force signal shows the relevance of the Coulomb and static friction over the viscous friction and, as a consequence, the impact of the friction force is especially recognisable at low velocity. When the friction force suddenly changes from positive to negative, or vice versa, the force signal also shows an abrupt change, which can only be reproduced by accurately modelling

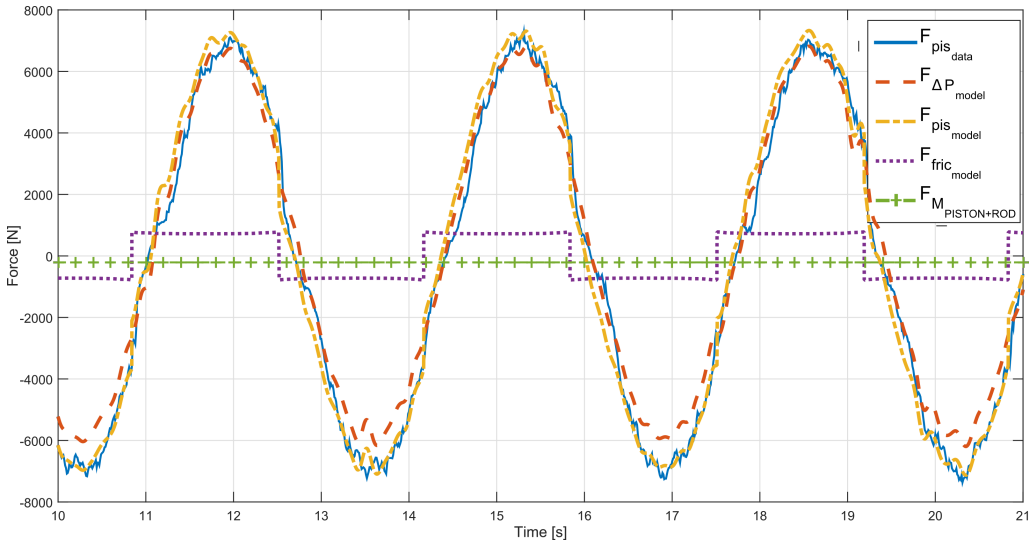

Figure 5.11: Contribution of the different forces in the hydraulic cylinder compared to the piston force measured in the test-rig with the variable-pressure configuration.

the effect of friction in the cylinder. Figure 5.12 illustrates the impact of the friction force at low velocity, where the force signal, considering the pressure difference alone, simply follows the velocity profile, while the signal that includes friction clearly shows an abrupt drop, similar to the measured force signal.

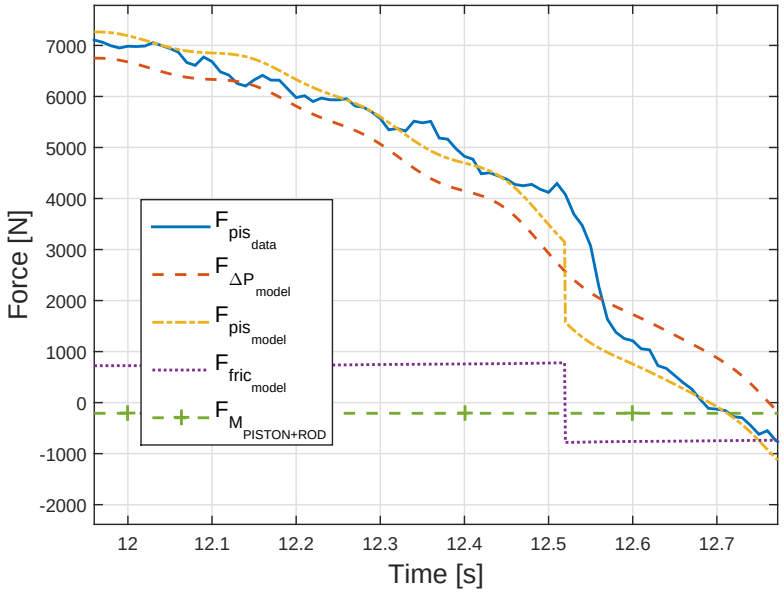

Figure 5.12: The effect of friction force at low velocity, comparing measured piston force and the contribution of the different effects obtained from the numerical model for the variable-pressure configuration.

5.2.3.2 Hydraulic motor

Losses in the hydraulic motor also depend on the operational characteristics, especially pressure difference and rotational speed, as described in the Schlösser model defined in Equations (4.14) and (4.15). Using the well-known simulation software *AMESim*, flow and torque outputs in the hydraulic motor are analysed, as illustrated in Figure 5.13, where results obtained from AMESim

are compared to the results from the Schlösser model.

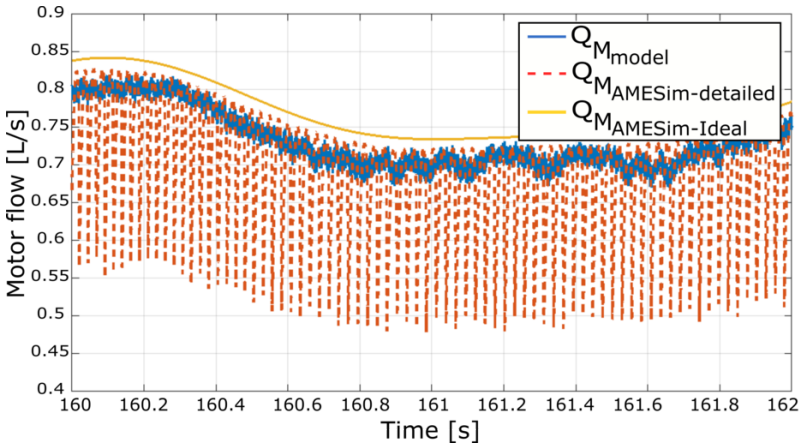

(a)

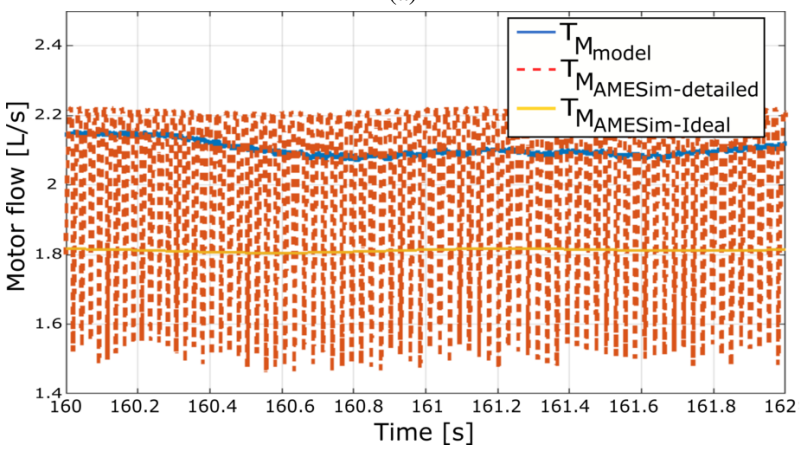

(b)

Figure 5.13: Flow (a) and torque (b) outputs of the hydraulic motor for the Schlösser model, presented in Section 4.1.2.4.1, and the detailed and ideal models implemented in *AMESim*.

Figures 5.13 (a) and (b) illustrate the motor flow and torque, respectively, where the flow of the Schlösser model stays always below the ideal flow, due to the losses neglected in the ideal *AMESim* model, and the torque stays always above the ideal *AMESim* model, to overcome the friction losses and supply the required torque. Compared to the detailed *AMESim* model, the flow and torque of the Schlösser model follow the upper envelope of the flow and torque outputs obtained from the detailed *AMESim* model, which suggests that the efficiency is similar for the detailed *AMESim* and Schlösser models. However, significantly more oscillation can be observed in the outputs of the detailed *AMESim* model, due to modelling of the movement of the individual pumping elements, which cannot be captured unless a detailed model is used.

5.3 Electrical system

The validation of the electrical system includes three different electric generators (SCIG, DFIG and PMSG), which need to be validated independently. Therefore, three independent test-rigs, one for each electric generator topology, are used to validate the mathematical models. In addition, the B2B power converter unit, including the GenSC and GridSC, as illustrated in Figure 4.17, is also part of the electrical system, which can be validated when coupled to any electric generator. In this case, all the test-rigs include the GenSC, but only the DFIG is connected to the grid in a B2B

configuration. Thus, the model for the B2B power converter is validated using the test-rig with the DFIG.

5.3.1 Experimental setup

The three electrical machines used for the validation of the mathematical models, presented in Sections 4.2.1.1 and 4.2.1.2, are installed in the University of the Basque Country in Eibar. The electrical machine is driven, in all cases, by a permanent magnet synchronous motor (PMSM), coupled to the rotor of the different generators. Among these different generators, only the DFIG is grid connected using a B2B configuration, while the SCIG and the PMSG are connected to a capacitor bank, where energy is stored. That capacitor bank is used as the energy source for the PMSM and as a sink for the energy generated in the SCIG and PMSG, forming a closed loop and avoiding the need to dissipate the generated energy.

To generate input signals for validation, a control platform is required in the experimental setting. The control platform is identical for the SCIG and PMSG and varies slightly in the case of the DFIG, since it is grid connected. Figure 5.14 illustrates the diagram of the experimental platform for the DFIG, including the B2B power converter and the control platform, where u is the voltage, i_g the grid current and subscripts a, b and c represent the three phases of the three-phase reference frame described in Figure 4.14. In the case of the SCIG and the PMSG, the second converter of the B2B power converter, illustrated inside the red dash-dotted rectangle in Figure 5.14, does not exist, and the first inverter of the B2B power converter is connected to the stator, instead of the rotor. An image of the experimental platform is shown in Figure 5.15, where all the components of the diagram illustrated in Figure 5.14 are shown: the PMSM, the DFIG, the control PC with the DS1103 controller board, and the GridSC and GridSC, referred to as RSC and GSC, respectively, in Figure 5.15.

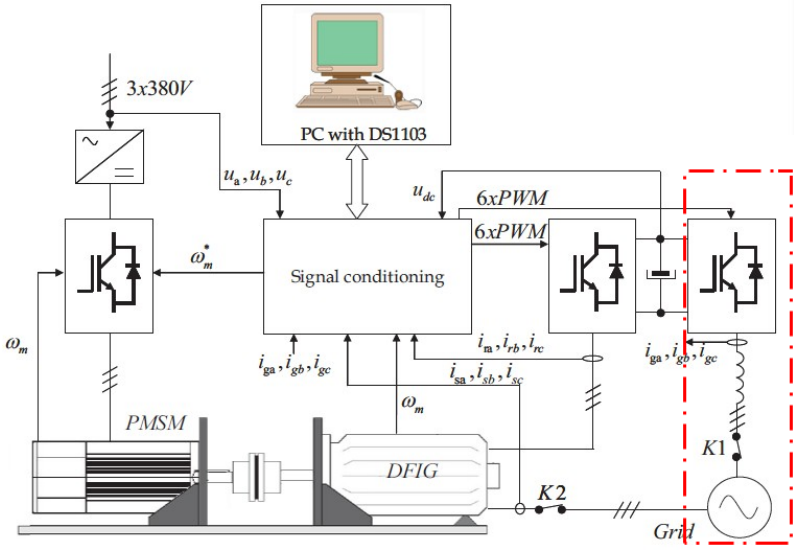

Figure 5.14: Diagram of the experimental platform for the DFIG [327].

The control platform shown in Figure 5.14, which has been employed to test several control strategies in the context of wind energy [327, 328], includes a PC with MATLAB/Simulink R2007a and dsControl 3.2.1 software, as well as the DS1103 Controller Board real-time interface using a dSpace system. The DS1103 Controller Board controls the GridSC and GridSC, generating the space vector PWM pulses with a maximum frequency of 7 kHz (143 μs).

The starting sequence of the machines varies for each generator. In the DFIG, the capacitor in the DC-link needs to be charged first. Once the DC-link is charged, the GridSC is connected to the grid by means of the connector *K1*, allowing for DC-link voltage regulation. Voltage in the

DC-link must be greater than the peak value of the grid voltage, which is about 540V for a grid RMS voltage of 380V. Therefore, the DC-link voltage is set to 570V in the experiments. After connecting the GridSC to the grid, the stator voltage is synchronised with the grid voltage. This voltage synchronisation is carried out by means of a phase locked loop (PLL), using measurements of the grid side voltage. Finally, the stator is connected to the grid by switching the connector *K2*.

In the SCIG and the PMSG, the capacitor in the DC-link must also be charged first, but the rest of the starting sequence is significantly different. In fact, the capacitor in the DC-link is a capacitor bank of 3300 μF and 1500 μF in the SCIG and PMSG, respectively, which is used as the voltage source for the GridSC. In the case of the SCIG, once the DC-link is charged, the rated flux is imposed in the generator via the control platform, so that the rotational speed regulation can only start after the rated flux is established in the generator. The PMSG, on the other hand, requires the determination of the initial position of the rotor before starting. To that end, a brief impulse is introduced to the generator, so that the encoder offset, with respect to the position of the rotor, can be determined. Hence, the rotational speed of the generator can be regulated using an adequate angle compensation.

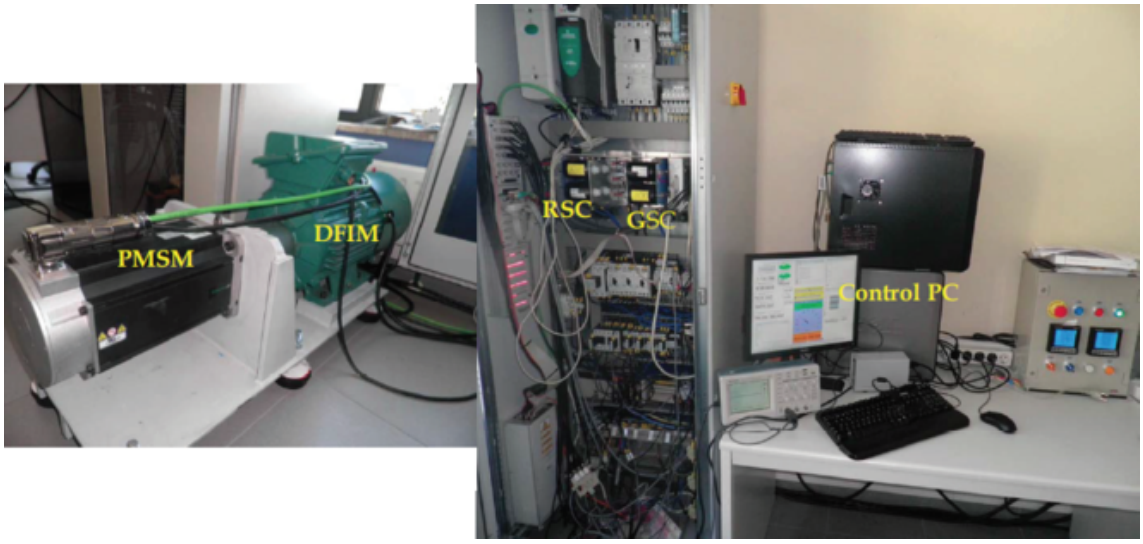

Figure 5.15: Picture of the experimental platform [327].

Sensors are essential in the experimental platform, for the measurement of currents, voltages and rotational speed in the generator. All the sensors are adapted and connected to the *DS1103 Controller Board*. Finally, it is important for the machines to be protected against overloading, and, thus, rotor and stator currents are limited to the nominal values of the machines. In addition, the operating conditions of the electric generators used in the validation are limited to sub-synchronous speeds, due to limitations of the experimental platform, as described further in Section 5.3.2.

All of the ratings and parameters for the SCIG, PMSG, DFIG and power converters included in the experimental test-rigs used in this section are provided in Table 5.4.

As for the hydraulic transmission system experimental setups described in Section 5.2.1, the test-rigs presented in this section, and used for the validation of the mathematical models presented in Section 4.2, were designed in previous projects, and so cannot be considered as a contribution of this thesis. Nevertheless, unlike in the case of the hydraulic transmission system, the experiments carried out to validate the electrical system are designed within the framework of this thesis and, as a consequence, can be considered as a contribution of this thesis.

Table 5.4: Ratings and parameters of the different electric generators and power converters.

Nominal power	7500 W
Stator voltage	380 V
Rated stator current	21 A
Rated speed	1450 rpm @50 Hz
Rated torque	50 Nm
Stator resistance	0.729 Ω
Rotor resistance	0.40 Ω
Magnetizing inductance	0.111 H
Stator leakage inductance	0.1152 H
Rotor leakage inductance	0.1138 H
Inertia moment	0.045 kg·m^2
Friction/windage damping	0.015 N·m·s

(a) Ratings and parameters of the SCIG.

Nominal power	3830 W
Stator voltage	380 V
Rated stator current	15 A
Rated speed	3000 rpm @50 Hz
Rated torque	12.2 Nm
Stator resistance	0.49 Ω
Stator (*d-axis*) leakage inductance	0.0069 H
Stator (*q-axis*) leakage inductance	0.039 H
Rotor permanent magnet flux	0.2484 Wb
Inertia moment	0.006 kg·m^2
Friction/windage damping	0.008 N·m·s

(b) Rating and parameters of the PMSG.

Nominal power	7500 W
Stator voltage	380 V
Rated stator current	18 A
Rated rotor current	24 A
Rated speed	1447 rpm @50 Hz
Rated torque	50 Nm
Stator resistance	0.42 Ω
Rotor resistance	0.70 Ω
Magnetizing inductance	0.055 H
Stator leakage inductance	0.06 H
Rotor leakage inductance	0.06 H
Inertia moment	0.04 kg·m^2
Friction/windage damping	0.001 N·m·s

(c) Ratings and parameters of the DFIG.

Nominal power	35 kW
Switching frequency	7 kHz
Inverter gain	310
Dead-time	1.4 µs

(d) Rating of the power converter units.

5.3.2 Experiment design

Having full access to the test-rigs with the electric generators allows experimental design freedom to adequately validate the mathematical models over the complete operational space of the system. The design of the experiments to validate mathematical models is not a trivial process. In particular, the input signals used in the experiments should excite the system over its complete range of operation, so that the experiments cover:

- the response to all the important frequencies and
- the full input/output signal ranges.

In addition, the experiments should cover the complete operational space in an efficient way, making a good use of the testing time. This is a common issue in system identification [191], where the information of the system's behaviour for the complete range of possible conditions is essential to accurately identify the parameters of the model. Multi-sinusoids, which contain a set of frequencies, or pseudo-random binary signals, which have a flat frequency spectrum, are typically used for the identification of linear systems [329]. However, nonlinear systems require a full operational range of both frequency and amplitude, for which pseudo-random signals with randomly varying amplitudes, also known as random-amplitude random-phase (RARP) sequences, are a good candidate [190].

Inputs for the electric generator system, which includes the generator, the GenSC and the controller, are T_M from the hydraulic motor and the reference rotational speed ω_r^*, as illustrated in Figure 5.16. Hence, ω_r^* in Figure 5.16 is the control-input to the electric generator validation system, which corresponds to the C_3 control-input illustrated in Figure 2.22. The same electric generator can be used for different hydraulic transmission system configurations, so the same inputs, T_M and ω_r^*, can be used for the validation of the three generators. However, the pattern of the T_M signal depends on the configuration of the hydraulic transmission system, where the T_M for a constant-pressure hydraulic transmission system varies slowly and is practically constant, while the T_M for a variable-pressure configuration is highly variable. Therefore, realistic operational conditions can be categorised into two groups: constant input torque and variable input torque. In addition, in the variable-pressure configuration, the efficiency of the HyPTO system can be improved by varying ω_r in the electrical generator [64], which significantly modifies the behaviour of the electric generator.

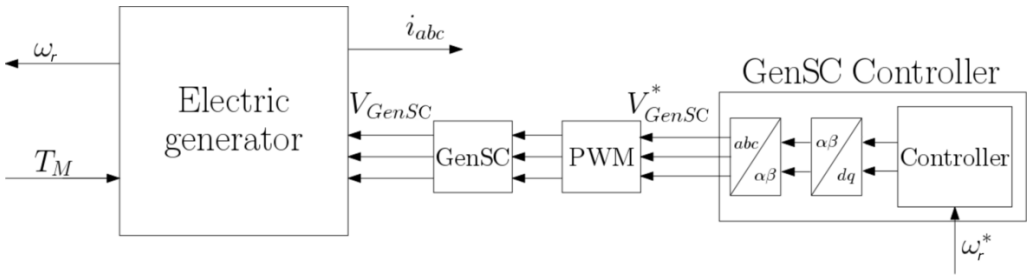

Figure 5.16: Diagram of the electric generator system, including the GenSC and the controller, where the inputs and outputs of the system are illustrated.

Consequently, the experiments utilised for the validation of electric generators should include, at least, three different test cases: constant input torque combined with constant rotational speed, variable input torque with constant rotational speed and variable torque with variable rotational speed. However, the amplitude and period of the input signals, for any of the three test cases, may vary considerably depending on the amplitude and period of the input waves. As a consequence, several different experiments should be considered for each test case, potentially resulting in an excessive number of experiments.

However, the full range of different amplitudes and periods can be efficiently covered by using RARP input signals. Therefore, the combination of RARP signals and realistic HyPTO signals can comprehensively cover the operational space of any electric generator coupled to a hydraulic transmission system, with a minimum number of experiments. Hence, six sets of combined T_M and ω_r^* are specified in total for the validation of each machine, three sets based on RARP sequences and three further sets based on realistic HyPTO signals. In the latter, input T_M signals are generated by implementing, in Simulink, the mathematical models for WSHIs and hydraulic transmission systems, described in Sections 3.3 and 4.1, respectively, and using the platform described in Section 5.3.1.

Although the experiments are specifically designed to validate the mathematical models of electric generators coupled to hydraulic transmission systems, this validation could equally serve for any other transmission system coupled to a rotary electric generator, since the input signals designed for the realistic HyPTO tests, described in Section 5.3.2.2, also correspond to typical inputs for other types of transmission systems. For example, the case that includes constant input torque combined with constant rotational speed, which represents a constant-pressure hydraulic transmission system, can also represent an overtopping device [268]. Similarly, the case that uses a variable input torque with a constant or variable rotational speed can represent the inputs from air turbines in OWC devices [330], or mechanical transmission systems [222, 272].

5.3.2.1 Random input signals

The three sets of RARP signals considered consist of two sets, where only one of the inputs varies randomly, while the other remains constant, and a third set, where both inputs vary randomly:

- Test 1a: Zero T_M and varying ω_r^*.
- Test 1b: Varying T_M and constant (rated) ω_r^*.
- Test 1c: Varying T_M and ω_r^*, as shown in Figure 5.17 (a).

The first 50s of Test 1c are shown in Figure 5.17 (a), for which the frequency content and the normalised amplitude distribution are shown in Figures 5.17 (b) and (c), respectively. The test duration is chosen to be 200s, which permits good coverage of the required amplitude and frequency ranges. In general, increasing the length of the signals results in a more even coverage of the amplitude range. However, increasing the signal duration beyond 200s, returns no substantial improvement in the coverage of frequency and amplitude. In contrast, the distribution of the frequency content is heavily influenced by the maximum allowable switching period of the signal, which is selected to be 1.4s [0.7072Hz], to enable a good coverage of the frequency range, as shown in Figure 5.17 (b).

All initially-generated RARP signals are normalised in amplitude, so that the same inputs can be implemented in different machines by multiplying the normalised signals with the rated torque and speed of the generator under analysis, given in Tables 5.4.

5.3.2.2 Realistic HyPTO input signals

Realistic HyPTO input signals are generated using the mathematical models described in Sections 3.3 and 4.1, producing input signals that an electric generator would experience when coupled to a realistic hydraulic transmission system, which, in turn, is connected to an absorber. The incoming waves, generated with the mathematical model implemented in Simulink, are polychromatic waves generated using a JONSWAP spectrum [75], and the spherical HPA described in Chapter 3 is used as the absorber. The JONSWAP spectrum is generated for a T_p of 10s, a H_s of 1.5m and a peak-enhancement factor $\gamma_J = 3.3$, which are typical values of the Atlantic ocean, and the polychromatic η_w is generated following Equation (3.19). Figure 5.18 illustrates the JONSWAP spectrum and the

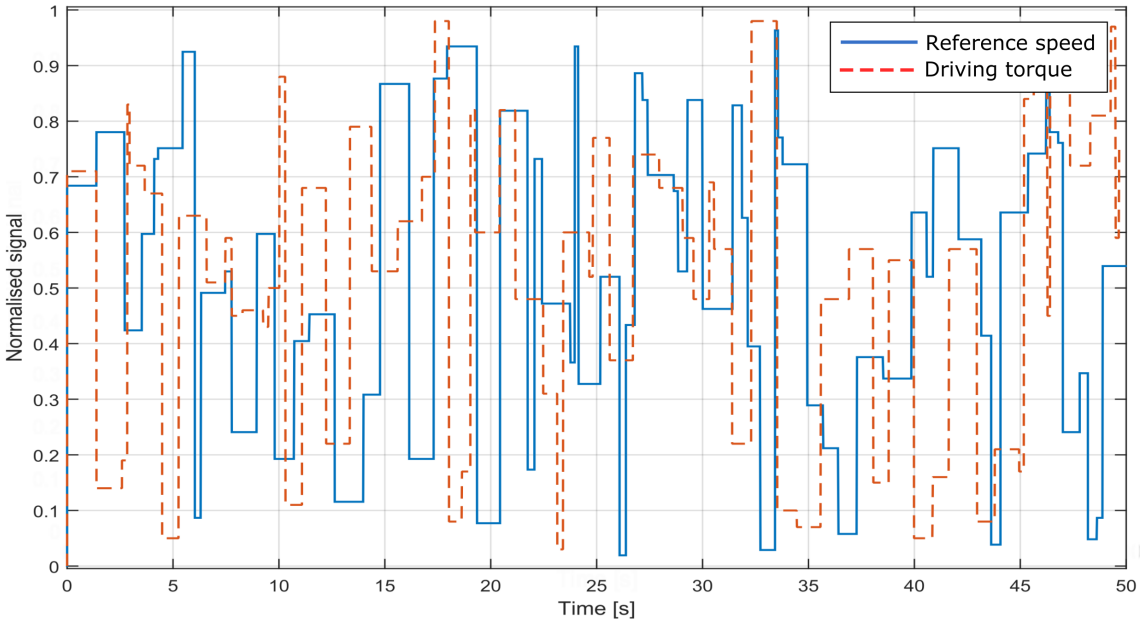

(a) RARP signal.

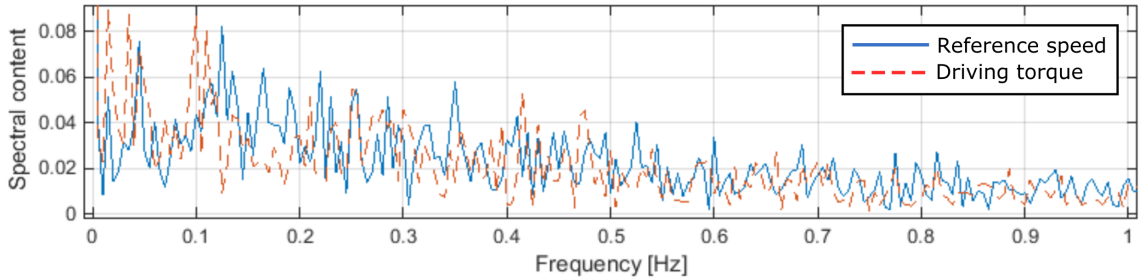

(b) RARP frequency spectrum.

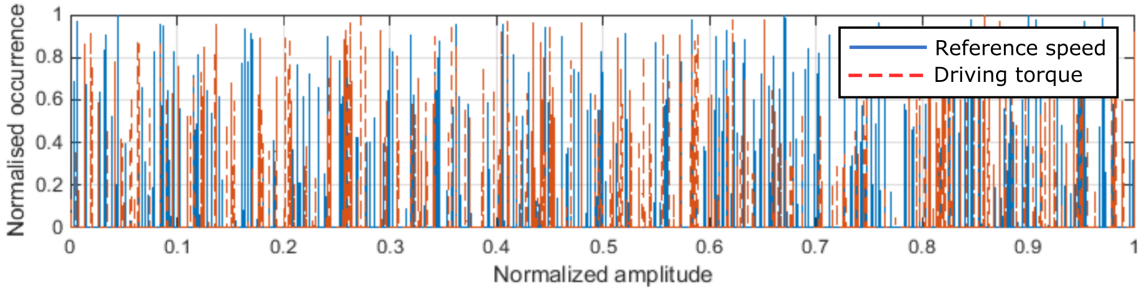

(c) RARP amplitude distribution.

Figure 5.17: RARP signals for the Test 1c test case, with the reference rotational speed and torque (a), and their spectral (b) and amplitude (c) properties.

free-surface elevation corresponding to the polychromatic wave analysed in the realistic HyPTO test cases.

Hence, following the constant- and variable-pressure hydraulic transmission system configurations described in Section 4.1, three sets of realistic HyPTO inputs are suggested:

- Test 2a: Practically constant T_M and constant (rated) ω_r^*, illustrated in Figure 5.19 (a).
- Test 2b: Varying T_M and constant (rated) ω_r^*, illustrated in Figure 5.19 (b).
- Test 2c: Varying T_M and varying ω_r^*, illustrated in Figure 5.19 (c).

In Test 2c, rotational speed follows the profile of the driving torque, but is constrained to the

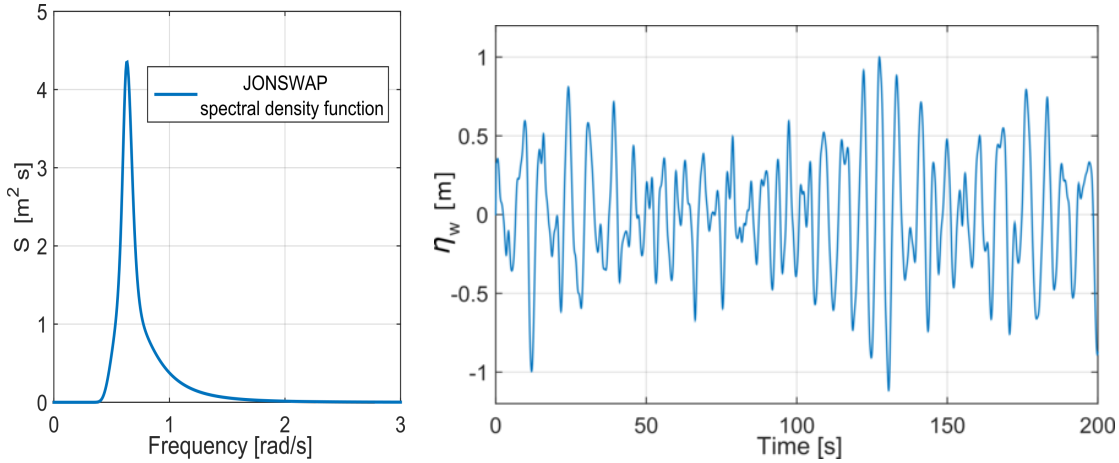

(a) (b)

Figure 5.18: Incoming waves included in the mathematical model to generate realistic HyPTO input signals, with the JONSWAP spectrum (a) and the free-surface elevation (b).

rated rotational speed of the generator, as shown in Figure 5.19c. Similarly to the RARP signals, realistic HyPTO signals are also initially normalised, so that they can be used for the validation of the three electric generators.

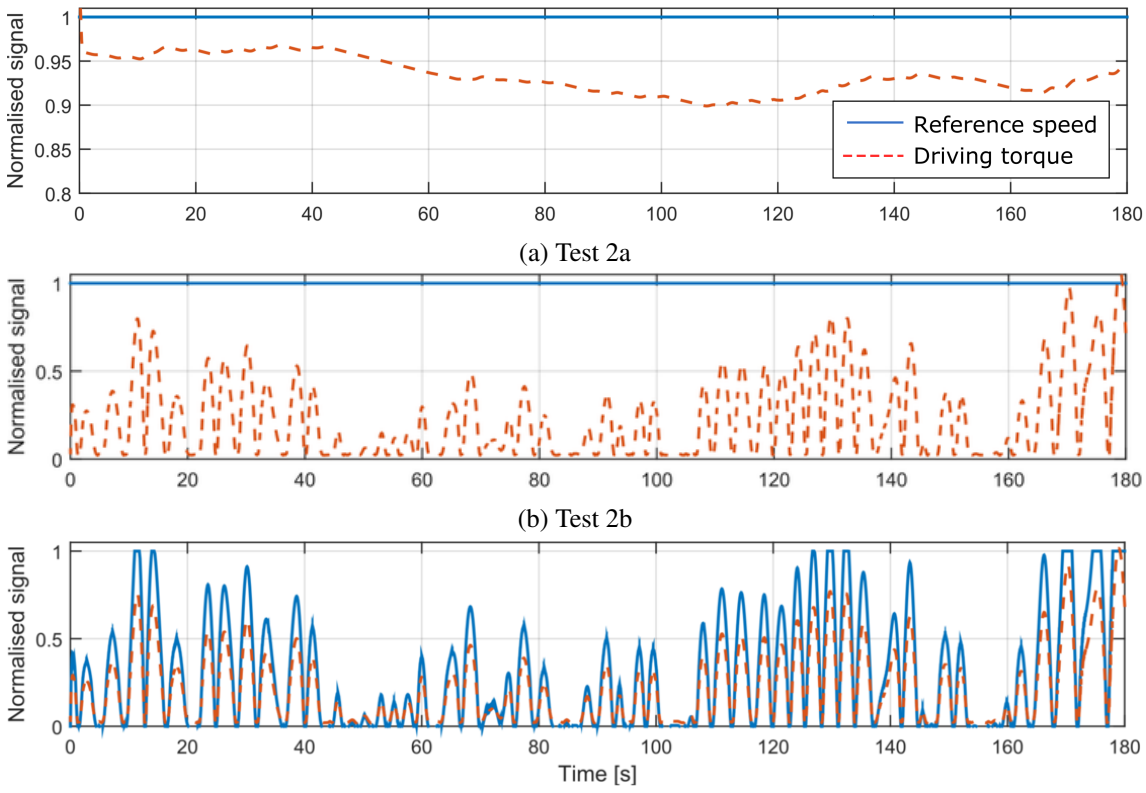

(a) Test 2a

(b) Test 2b

(c) Test 2c

Figure 5.19: The three signals based on realistic HyPTO systems: constant torque and rotational speed (a), variable torque and constant rotational speed (b) and variable torque and rotational speed (c).

5.3.3 Validation results

Electrical and mechanical dynamics of the generators are validated by comparing measurements from real machines to the corresponding output signals from the mathematical models. The output signals from the test-rigs are the rotational speed ω_r and three-phase stator current vector i_{abc}, as illustrated in Figure 5.16. However, the electromagnetic torque T_e, generated power (real power P_e and reactive power Q_e) and total power losses in the generators (P_{loss}) are also compared, to evaluate the fidelity of the mathematical models.

In the validation of electrical systems, a variety of variables from diverse test cases and different electric generators are studied. Hence, for the different error measures to be comparable, an error measure that is suitable for all variables is preferred. Normalised measures facilitate the comparison of diverse datasets with different scales, which is necessary in this case. Unfortunately, the popular mean average percentage error (MAPE) metric cannot be employed, since there are values in the datasets that are zero, or close to zero, which would potentially involve a division by zero. The NRMSE defined in Equation (5.1) is a suitable candidate.

However, when a single average values is used for normalisation, over the complete simulation, the NRMSE is susceptible to rapid shocks or variations, which are common in RARP signals, as illustrated in Figure 5.17 (a). Therefore, the validation is evaluated by means of a more robust measure, the moving average (also known as rolling average) normalised root mean square error (MANRMSE), presented in Equation (5.3). Hence, signals are divided into N_p parts, using a different average value in each part j to normalise the error. The bias of the error measure decreases as N_p increases, since the average value corresponding to each j part is more representative of the signal values in that j part. However, there is a value of N_p, beyond which further increases in N_p do not affect the error measure. In this study, the error measure was observed to be constant when the signals were divided into more than 40 parts, so $N = 40$ was chosen to obtain the fidelity measures.

$$MANRMSE = \frac{\sum_{j=1}^{N_p} \sqrt{\frac{\sum_{i=1}^{n_{t,j}} |y_j(k_i) - \hat{y}_j(k_i)|^2}{n_{t,j}}}}{\bar{y}_j} \Big/ N_p \tag{5.3}$$

where y_j and $\hat{y}_j$ are any variable measured in the test-rig and given by the mathematical models, respectively, at each part j, $\bar{y}_j$ the time-average of the measured variable, and $n_{t,j}$ the number of samples in each part j. Once the MANRMSE is calculated, the fidelity of the variables from the mathematical model in percentage terms can be obtained as follows,

$$Fidelity = (1 - MANRMSE) \times 100 \qquad [\%] \tag{5.4}$$

5.3.3.1 Electric generators

5.3.3.1.1 SCIG

Fidelity values shown in Table 5.5 for the SCIG show a good overall agreement between the machine and the mathematical model, where fidelity values above 90% are shown for most of the test cases and variables. Results from the mathematical models, considering all of the variables and test cases, show the ability to reproduce the behaviour of the real machine, as illustrated in Figure 5.20 for ω_r, T_e, P_e and Q_e.

The chaotic behaviour of the real power in Figure 5.20 (b) corresponds to abrupt variations of the input signal in the test case Test 1c, as shown in Figure 5.17 (a). Due to these abrupt variations, the generator rapidly varies from operating close to full-load conditions to part-load conditions, or vice versa. As a consequence, high power spikes appear, which can lead to negative power values when the generator need to draw energy from the grid to reach the new operation point. However, the measurements from the real machines show considerable high-frequency

Table 5.5: Fidelity measures [%] for the SCIG.

	Test 1a	***Test 1b***	***Test 1c***	***Test 2a***	***Test 2b***	***Test 2c***
ω_r	98.64	98.09	98.68	89.92	98.53	99.61
i_{abc}	93.33	97.72	94.26	86.47	97.05	94.03
T_e	96.43	95.22	95.33	82.15	95.57	94.42
P_e	97.25	93.78	96.13	81.03	92.70	93.80
Q_e	96.72	90.71	94.60	78.87	86.52	95.13
P_{loss}	97.01	96.25	91.87	79.98	85.74	92.49

fluctuations, as illustrated in Figure 5.20, which reduce the fidelity of the mathematical models. In fact, one can observe, from Figure 5.20, that such fluctuations are the main difference between the experimental and numerical results, in all the test cases.

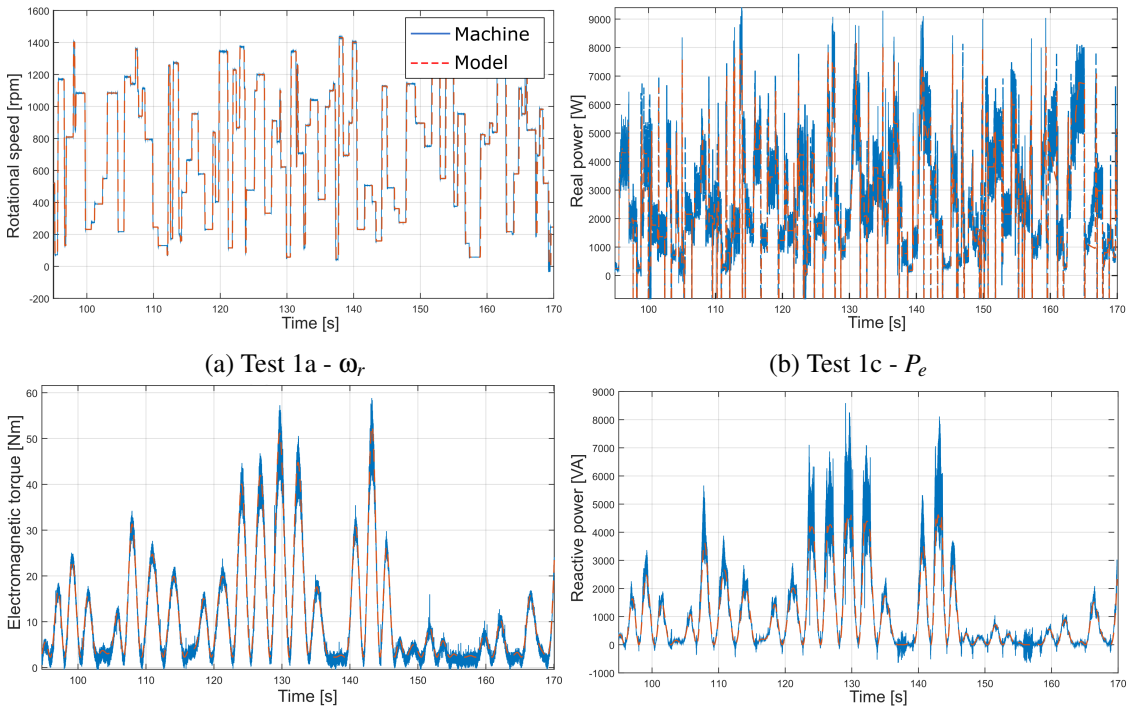

(a) Test 1a - ω_r

(b) Test 1c - P_e

(c) Test 2b - T_e

(d) Test 2c - Q_e

Figure 5.20: Comparative results from experiments and numerical models for the SCIG: rotational speed for Test1a (a), real power for Test1c (b), electromagnetic torque for Test2b (c) and reactive power for Test2c (d).

These high-frequency fluctuations appear in all of the test cases and variables, except for the rotational speed, as shown in Figure 5.20, because the inertia of the rotor shaft smooths out the rotational speed signal. However, the impact of these fluctuations in the measurements varies from one test case to another. In fact, the impact of these fluctuations is strongest for Test 2a, as illustrated in Figure 5.21 (a). It should be noted that fluctuations are similar for all the test cases and highest close to nominal values, as illustrated in Figure 5.21. Hence, since the variables remain almost constant close to nominal values through the whole simulation in Test 2a, the impact of these fluctuations is considerably higher in the fidelity results, as shown in Table 5.5.

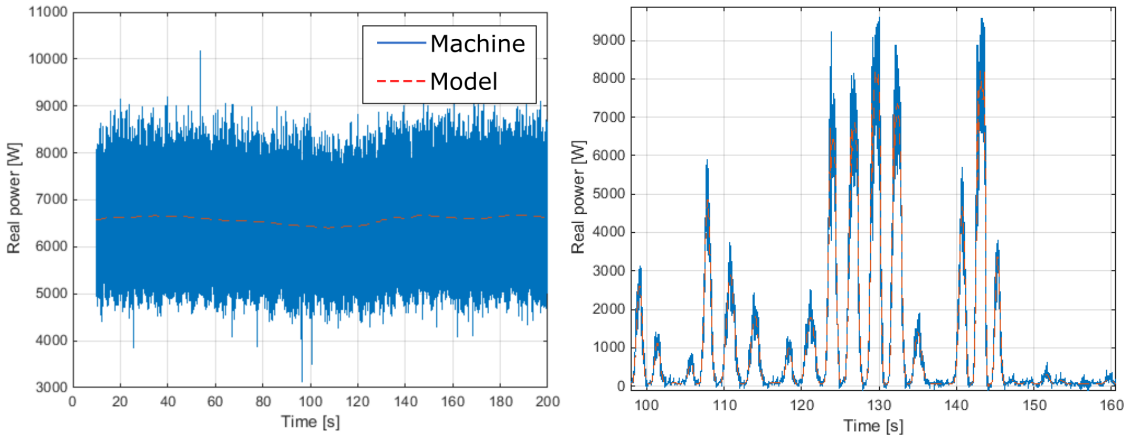

(a) Test 2b - P_e (b) Test 2a - P_e

Figure 5.21: Real power output for the test cases Test 2a (a) and Test 2c (b).

Two different sources are identified for these fluctuations: the harmonics generated by the power converters, and measurement noise. Harmonics inserted by power converters include fluctuations with a specific frequency, *i.e.* multiples of the fundamental frequency (f_0), while the noise added by virtue of the sensors, includes a (broadband) random error in the signal [331]. Figure 5.22 illustrates the frequency content of the stator voltage signal in Test2b, for which the fundamental frequency is 50 Hz for the complete simulation, because the rotational speed is constant (1500rpm). In addition to the fundamental frequency, one can clearly see the harmonics at two- and four-times the fundamental frequency, as well as the noise over the complete frequency range, in the case of the real machine. The mathematical models described in Section 4.2.2, however, do not incorporate the switching operations of the power converters and, as a consequence, results from mathematical models show no high-frequency fluctuations, as illustrated in Figure 5.20. The frequency content associated with the voltage signal of the mathematical model is, indeed, zero far from the fundamental frequency, as shown in Figure 5.22.

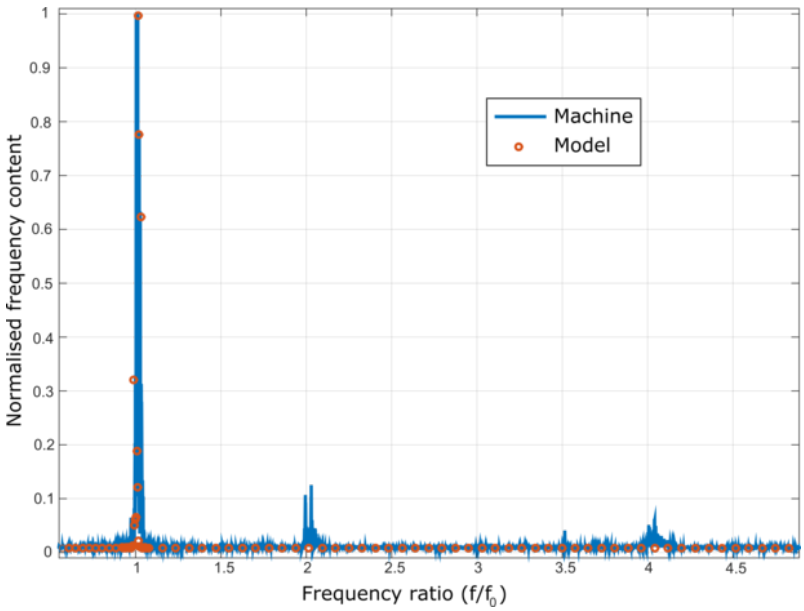

Figure 5.22: Frequency content of the stator voltage signals in Test2b, from machine measurements and model results.

5.3.3.1.2 PMSG

In the case of the PMSG, the fidelity values shown in Table 5.6 also show good agreement between the mathematical model and the real machine, with fidelity values over 90% for most of the test cases and variables. Similarly to the SCIG, test case Test 2a shows the results with the lowest fidelity values. However, fidelity values, in general, are lower in the PMSG than in the SCIG. These lower fidelity values are associated with stronger high-frequency fluctuations, as illustrated in Figure 5.23, where the level of high-frequency fluctuations is compared for the PMSG and the SCIG. Figure 5.23 (a) illustrates normalised real power values (normalised against rated power), and Figure 5.23 (b) shows the upper and lower envelopes of the normalized real power signals. The lower envelope for the SCIG and the PMSG in Figure 5.23 (b) is almost identical, while the upper envelope is considerably higher for the PMSG, which illustrates the greater level of high-frequency fluctuations in the PMSG.

Table 5.6: Fidelity measures [%] for the PMSG.

	Test 1a	***Test 1b***	***Test 1c***	***Test 2a***	***Test 2b***	***Test 2c***
ω_r	97.03	95.51	97.19	88.90	97.06	98.70
i_{abc}	94.55	94.69	94.59	81.84	90.29	93.98
T_e	93.58	93.13	94.31	72.72	92.20	92.14
P_e	94.66	91.34	95.02	77.45	87.28	94.95
Q_e	93.34	92.49	93.87	78.56	85.77	88.43
P_{loss}	92.59	91.00	94.50	75.35	84.39	87.85

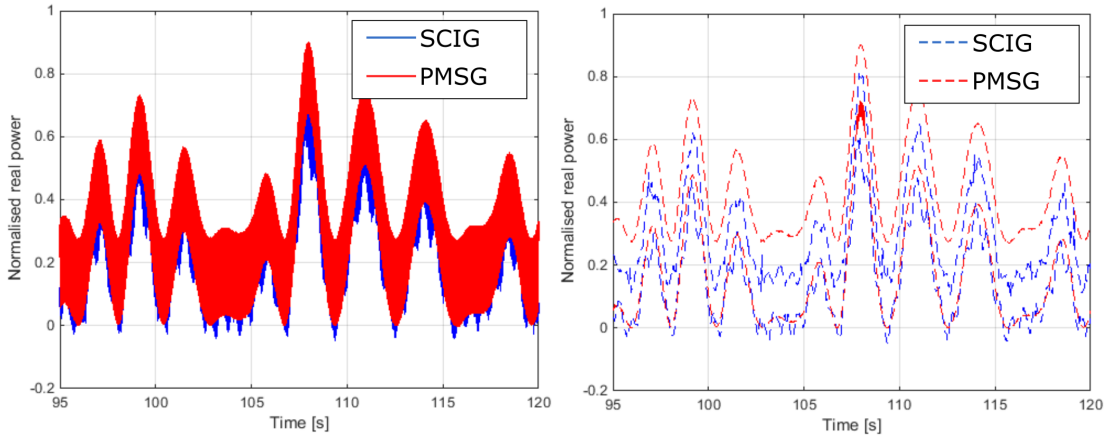

(a) (b)

Figure 5.23: Real power measurements in the SCIG and the PMSG for the Test 2c test case: power values (a) and normalised power showing the noise level (b).

Larger high-frequency fluctuations in the PMSG can arise due to the higher-rated rotational speed of the PMSG, which is twice as high as the rated rotational speed of the SCIG. The higher the rotational speed, the higher the frequency, which leads to faster pulses generated by the PWM voltage source converter and, as a consequence, to stronger fluctuations.

5.3.3.1.3 DFIG

Finally, fidelity figures for the DFIG, shown in Table 5.7, are similar to those obtained for the SCIG, which shows, once again, good agreement between the mathematical model and the real machine. Rated power and rotational speed are identical for the SCIG and the DFIG, which can explain why fidelity values for the SCIG and the DFIG are similar.

Table 5.7: Fidelity measures [%] for the DFIG.

	Test 1a	***Test 1b***	***Test 1c***	***Test 2a***	***Test 2b***	***Test 2c***
ω_r	99.08	98.49	99.05	91.46	97.86	98.06
i_{abc}	93.57	96.72	95.26	83.07	91.75	94.72
T_e	96.34	95.22	95.63	76.34	92.36	91.47
P_e	95.34	94.78	94.78	77.13	88.41	94.73
Q_e	93.72	91.26	94.21	79.91	86.97	89.66
P_{loss}	95.70	96.47	91.38	76.38	84.67	88.47

Apart from the dynamics of the machines, for which the effectiveness of the mathematical models has been demonstrated, accurately estimating the power losses associated with the generators is crucial. Therefore, efficiency values obtained from real machines and the corresponding mathematical models are compared for the three generators, using test case Test 1c. The reason why Test 1c is employed is because it is the test case that comprehensively covers the operational range of the generators, randomly varying ω_r^* and T_M, as shown in Figure 5.17. However, such random variations include abrupt spikes in the power and efficiency signals. In addition, because speed and torque input signals vary randomly, the electric generators operate at high rotational speed and low torque at some points during the simulation, which results in significant efficiency drops.

Therefore, Figures 5.24(a)-(c) illustrate the trend lines of the efficiency signals for the SCIG, PMSG and DFIG, respectively, as a function of the normalised rotational speed, providing satisfactory agreement between the trend lines from the real machines and the mathematical models. Rotational speed is normalised against the rated speed of each generator. The efficiency trend lines, shown in Figure 5.24, are fitted using a polynomial function, as follows,

$$y_{fit} = c_1 x_{\omega}^{c_2} + c_3 \tag{5.5}$$

where y_{fit} is the trend line, x_{ω} the variable on which the trend line is based (normalised rotational speed, in the case of the efficiencies), c_1 and c_3 are the coefficients and c_2 the exponent of the polynomial function that are identified to fit the data. The coefficients of the polynomial function for each generator, using results from the real machines and mathematical models, are given in Table 5.8, where subscripts $_{Ma}$ and $_{Mo}$ are used, respectively.

5.3.3.2 Power converters

The experiments carried out in the DFIG are also used to validate the B2B power converter implemented in the mathematical model, since the DFIG is grid connected in a B2B configuration. Hence, power losses in the GenSC and GridSC can be included in the simplified mathematical model, where the computationally prohibitive switching operations are neglected, modelling the PWM units as unit gain elements.

Table 5.8: Coefficients of the polynomial function used to fit the trend line of the real machines and model results.

	$\mathbf{SCIG_{Ma}}$	$\mathbf{SCIG_{Mo}}$	$\mathbf{PMSG_{Ma}}$	$\mathbf{PMSG_{Mo}}$	$\mathbf{DFIG_{Ma}}$	$\mathbf{DFIG_{Mo}}$
c_1	-264.1	-335.4	-164	-245.4	-20.88	-34.58
c_2	-0.2868	-0.3017	-0.1591	-0.2817	-0.3802	-0.3175
c_3	122.6	128.6	144	124.6	110.2	127.2

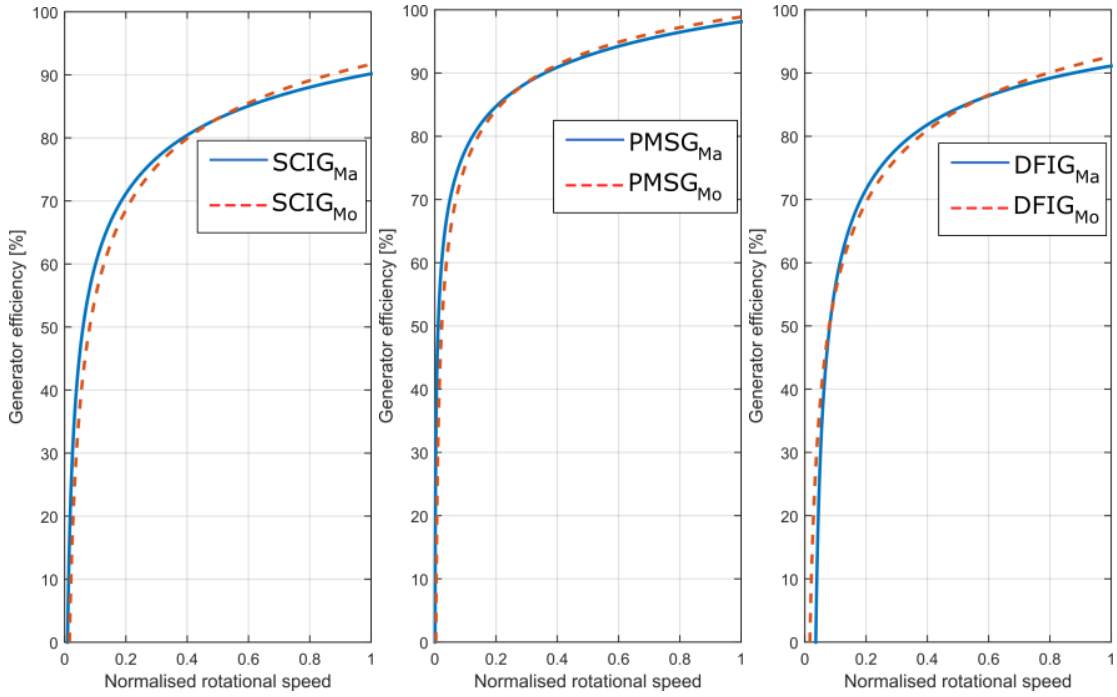

(a) (b) (c)

Figure 5.24: Efficiency of the SCIG (a); PMSG (b) and DFIG (c) for the Test 1c test case.

The main objective of the GenSC and GridSC, is the control of the electric generator and DC-link voltage, respectively. Therefore, apart from the power losses in the inverters, the capacity to reproduce the effects of the controllers are evaluated in this subsection. Figure 5.25 (a) illustrates the real power generation in the stator of the DFIG, comparing the power measured in the real machine and simulated in the simplified mathematical model, following test case Test 1c. Hence, it is demonstrated that the action of the controller in the GenSC can be accurately reproduced by only considering the fundamental harmonic. In addition, Figure 5.25 (b) compares the voltage in the DC-bus measured in the test-rig to that simulated in the mathematical model, illustrating the good agreement between the two signals and demonstrating the suitability of the simplified mathematical model of the GridSC to accurately control the voltage in the DC-bus.

As mentioned in Section 4.2.2, power losses in the B2B power converter can only be computed numerically if switching operations in the converters are considered, which is not the case in the mathematical model presented in this thesis. Therefore, power losses in the converters are considered in the simplified mathematical model using experimental analysis. To this end, active power is measured at the input and output of the B2B power converter, computing the losses between the input and the output, and calculating the efficiency of the B2B power converter for different operating conditions. In fact, the converter's efficiency varies as a function of load, with considerable efficiency drops at part-load and overload conditions [332]. However, measurements

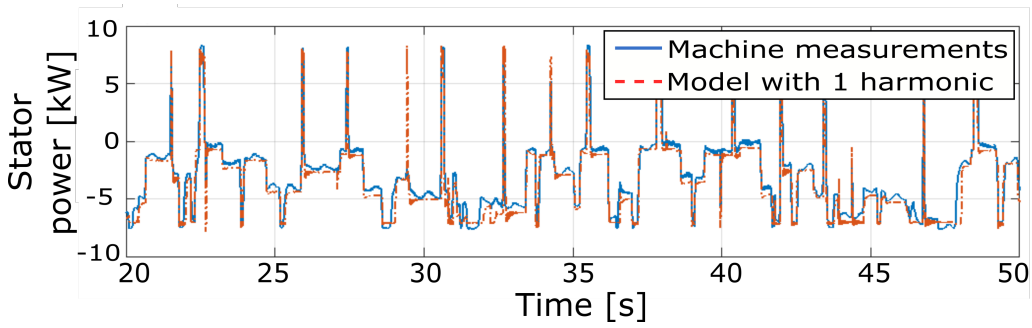

(a)

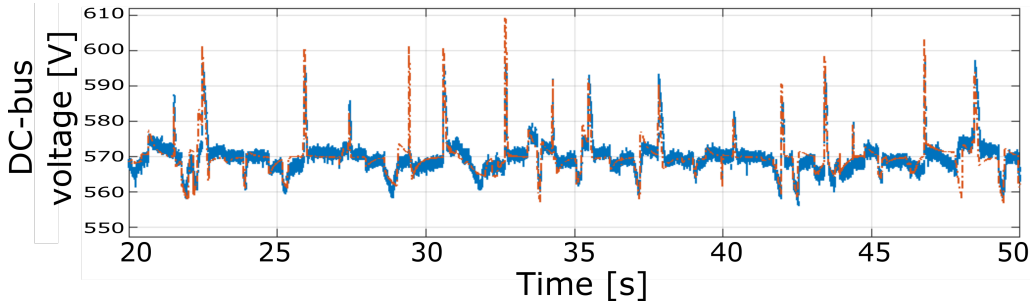

(b)

Figure 5.25: The efficacy of the control implemented in the GenSC and GridSC via the simplified mathematical model, compared to the measures of the real machine: power in the stator of the DFIG (a) and voltage at the DC-bus (b).

in the test-rigs only cover the part-load operation of the converters, since the rated power of the DFIG is significantly lower than the rated power of the converters used in the B2B converter.

Figure 5.26 (a) shows the efficiency of one converter in the B2B power converter as a function of normalised load, defined as the ratio between the input power to the B2B power converter and the rated power of the converters. The points from the experimental measurements clearly show the trend of the efficiency curve, at least for the part-load operating conditions. Thus, experimental data is used to fit a power trend-line, following Equation (5.5), as shown in Figure 5.26 (a). Using the fitted curve, power losses in the converters can be calculated without prohibitively increasing the computational requirements of the mathematical model. Hence, the power output of the B2B power converter is calculated using the power trend-line for all the different test cases, and is compared to the measures obtained from the test-rig with the DFIG. Figure 5.26 (b) illustrates this comparison for Test 1c.

Fidelity values, obtained by comparing the voltage in the DC-link and power losses in the B2B power converter from the experimental platform and the mathematical model, are presented in Table 5.9, showing very good agreement between the experimental and numerical results. In the case of power loss, the agreement is particularly good for Test 1c, since the power trend-line is fitted using the data from this test case.

Table 5.9: Fidelity measures for the B2B converter.

	Test 1a	***Test 1b***	***Test 1c***	***Test 2a***	***Test 2b***	***Test 2c***
V_{DC}	96.39	96.72	95.81	96.37	97.13	96.78
P_{loss}	94.61	95.27	98.47	87.43	95.71	94.86

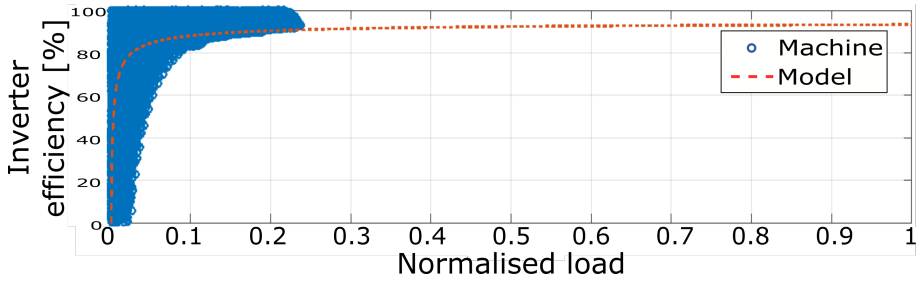

(a)

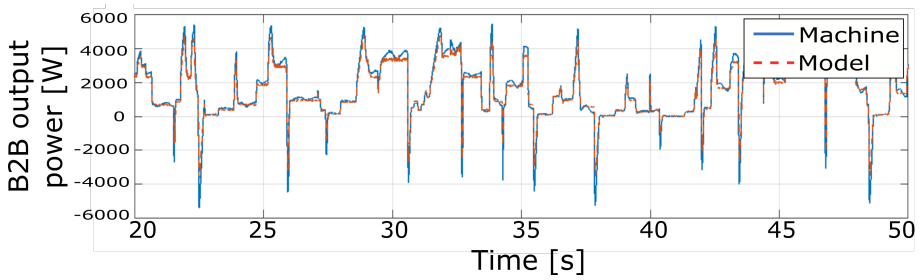

(b)

Figure 5.26: Efficiency of the converter, as a function of normalised load, including the fitted curve (a), and the power output of the B2B power converter for the test-rig and the model (b).

5.4 Summary

This chapter presents the validation of the different subsystems of the *cHyW2W* model. This validation has been divided into three main parts, based on the different conversion stages illustrated in Figure 2.22: *absorption* stage (Section 5.1), hydraulic *transmission* stage (Section 5.2), and *generation* and *conditioning* stages (Section 5.3). Hence, each of these parts has been validated independently using experimental data from different test-rigs or well-established high-fidelity software.

In the case of the *absorption* stage, several BEM-based mathematical models, which include different nonlinear effects, are compared against CFD. The comparison presented in Section 5.1 considers one regular wave condition and two control strategies, *i.e.* docile and aggressive control. All BEM-based mathematical models, including the *LFK* model, show high-fidelity levels under docile control. In contrast, only the *viscNLFKa* model shows high fidelity results when energy absorption is maximised by means of a more aggressive control strategy, providing results almost identical to CFD, but at a fraction of the computational cost, four orders of magnitude lower than CFD, due to the efficient algebraic solution presented in Section 3.3. However, a comprehensive coverage of the complete operational space of the WEC is necessary when validating numerical models. Accordingly, results for a single regular wave are insufficient to draw general conclusions. Thus, this comparison is extended in [56], including a wide range of incoming waves that adequately covers the operational space of the WEC, where the need for nonlinear FK forces and viscous effects is confirmed.

The mathematical model for the hydraulic transmission system is validated in Section 5.2, which includes two different hydraulic transmission system configurations commonly used in WECs: constant- and variable-pressure configurations. Experimental data for the validation of the hydraulic transmission system models is obtained from the CPTMC at University of Bath and covers different hydraulic transmission system configurations and operating conditions. Mathematical models show very good agreement, including the friction model in the hydraulic cylinder and the loss model in the hydraulic motor.

Finally, the electrical system, including the *generation* stage, with three different electric generators (*i.e.* a SCIG, DFIG and PMSG), and the *conditioning* stage, via a B2B power conversion

unit, is validated in Section 5.3. Experimental data is obtained using the facility of the University of the Basque Country in Eibar, where experiments, specifically designed to cover the complete operational space of an electrical system implemented in a WEC, are carried out. These experiments combine RARP and realistic HyPTO signals, described in Section 5.3.2, for which mathematical models provide excellent agreement, including losses in the different electric generators. In addition, an alternative method to include power losses of the B2B power conversion unit, avoiding the modelling of switching operations, is suggested in this chapter, where an efficiency curve based on a polynomial function is fitted to experimental data. Results using the fitted efficiency curve are compared to other experimental results, those that are not used in the identification of the polynomial parameters, showing good agreement and validating the use of the fitted efficiency curve.

Chapter 6

Efficient numerical implementation and simulation of the *cHyW2W* model

Mathematical models presented in Chapters 3 and 4, and validated in Chapter 5, need to be adequately combined to build the *cHyW2W* model. Due to the different components, which involve different dynamics, included in each subsystem described in Chapters 3 and 4, the *cHyW2W* model result in a complex multidisciplinary mathematical model. In addition, different absorbers and/or PTO systems may need to be implemented. Therefore, an adequate numerical implementation that allows for efficient simulation and facilitates the creation of different HyW2W models, is vital.

Hence, the numerical implementation presented in this chapter makes the *cHyW2W* model

- *generic*, in the sense they can, with appropriate modification, accommodate different
  - types of absorbers with one or multiple DoFs, single- or multi-body absorbers, or even an array of absorbers;
  - hydraulic PTO configurations, i.e. constant- or variable-pressure topologies;
  - rotational electric generators, fixed- or variable speed generators; and
  - grid connections, i.e. directly connected or through a B2B configuration.
- computationally *efficient*, mitigating their high computational requirements by utilising multi-rate (MR) time-integration schemes.
- *accurate*, with the subsystems of the HyW2W model validated against experimental data or well-established high-fidelity software.

The numerical implementation of the *cHyW2W* model is presented in the first part of this chapter (Section 6.1), describing the way in which the different mathematical models presented in Chapters 3 and 4 are combined. Section 6.1.1 analyses the selection of the optimum numerical method for each subsystem. In addition, the benefits of a MR time-integration scheme, compared to the traditional single-rate (SR) scheme, are illustrated.

Section 6.2 illustrates the results for two different variations of the *cHyW2W* model that include the same absorber, one coupled to a constant-pressure hydraulic transmission system topology and the second one to a variable-pressure topology. These two topologies are compared using different sea-states and control strategies. Finally, Section 6.2 shows the value of using the *cHyW2W* model when evaluating the impact of different HyPTO system configurations (Section 6.2.1) and control strategies (Section 6.2.2), and assessing the power production capabilities of a WEC (Section 6.2.3).

6.1 Model implementation

The *cHyW2W* model is designed as a combination of inter-connected sub-models that represent the different subsystems, as illustrated in Figure 2.22, which facilitates the interchange of any sub-model. The first subsystem, *Ocean waves*, generates the primary input η_w for the *cHyW2W* model following Equation (3.19), which is generated for the complete simulation time, prior to running the W2W simulation model.

The interconnection between ocean waves and the absorber is the only unidirectional interconnection, as illustrated in Figure 2.22. Therefore, any perturbation in any of the sub-models has an impact on the preceding and/or following sub-models due to the bi-directional interconnection. Hence, each sub-model in the *cHyW2W* model takes input variables from the preceding and/or following sub-models, independently solves the dynamical equations of the conversion stage it represents, and sends the output variables to the preceding and/or following sub-models, as appropriate. For example, the *Hydraulic transmission system* subsystem takes z_d and $\dot{z}$ from the preceding *Absorber* and ω_M from the following *Electric generator* subsystems, solves the equations associated with the different components of the hydraulic system, and sends F_{pis} and T_M to the preceding and following subsystems, respectively, as shown in Figure 2.4.

However, it should be noted that the coupling between the different sub-models is a *weak* coupling, since an offset exists in time-steps. That is, the variables calculated in one sub-model are only used at the same time-step in the down-wave sub-models, while in the up-wave sub-models, the variables are used in the next time-step. Following the same example used in the previous paragraph, the $T_M(t_i)$ calculated at time step t_i in the *Hydraulic transmission system* will be used in the *Electric generator* sub-model (down-wave) at the same time step t_i, while the $F_{pis}(t_i)$ will be used in the *Absorber* sub-model (up-wave) at time-step t_{i+1}. This weak coupling is computationally more efficient, since it does not require any intermediate iteration, but can be problematic in some cases, because the convergence is not guaranteed. Problems normally arise when the inertia effects in the different sub-models are equally important. However, in wave energy applications, inertia effects are significantly more important in the *Absorber* than in any other sub-model. Therefore, the *weak* coupling seems appropriate.

The *cHyW2W* model is coded in Matlab, with the aspiration of avoiding the use of proprietary Matlab functions or toolboxes where possible, so that it can be easily ported from Matlab to another coding language/environment if necessary. This transcription to another programming language may be needed, for instance, when implementing the *cHyW2W* model, either entirely or partly, in a HIL simulation or an energy maximising controller. The dynamical equations of the different subsystems are solved by means of a numerical method, which can be either fixed- or variable-step. Variable-step numerical methods have some important benefits, compared to fixed-step methods:

- Faster computation in systems with few disturbances,
- capability to adapt to the changing dynamics of the system, and
- numerical stability.

However, variable-step methods also include important disadvantages:

- The coding of the mathematical model becomes significantly more complex, since the appropriate step size must be identified at each step to achieve the accuracy requirement (or error tolerance), which needs to be specified beforehand.
- The processing time cannot be controlled and provides output vectors with values irregularly spaced, which may require interpolation. As a consequence, variable-step methods, either cannot be used or significantly complicate the implementation of the mathematical model for real-time applications.

- The implementation of parallel processing is also very complex.

In the specific case of the *cHyW2W* model, due to the different subsystems with very diverse dynamics implemented in the mathematical model, a SR time-integration scheme, *i.e.* an integration scheme that uses the same time-step for the whole model, requires that the whole model uses the time-step necessary in the subsystem with the fastest dynamics. Consequently, simulation time can increase substantially, since unnecessary computation is added in the components with slower dynamics. A solution to this issue, as presented later in Section 6.1.1.1, is a MR integration scheme, where each subsystem uses the time-step needed to accurately capture the specific dynamics of that subsystem. In this context, the lack of consistency of the processing time of variable-step numerical methods complicates the interconnection between the different subsystems in the *cHyW2W* model. Therefore, the *cHyW2W* model is implemented as a fixed-step simulation model in Matlab, using time-integration numerical methods coded by the author.

6.1.1 Time-integration schemes

Time-integration schemes or numerical methods are methods to find numerical approximations to the solution of differential equations. Different methods have been suggested in the literature to integrate a (system of) differential equation(s), which can be divided into two main categories [333]: one-step (Section B.1) and multi-step methods (Section B.2). Figure 6.1 classifies the different methods analysed in this chapter, where Euler's and Runge-Kutta (RK) methods are included in the one-step group [334], and Adams-Bashforth (AB) [335], Adams-Moulton (AM) [336] and backward differentiation function (BDF) [337] methods in the multi-step group.

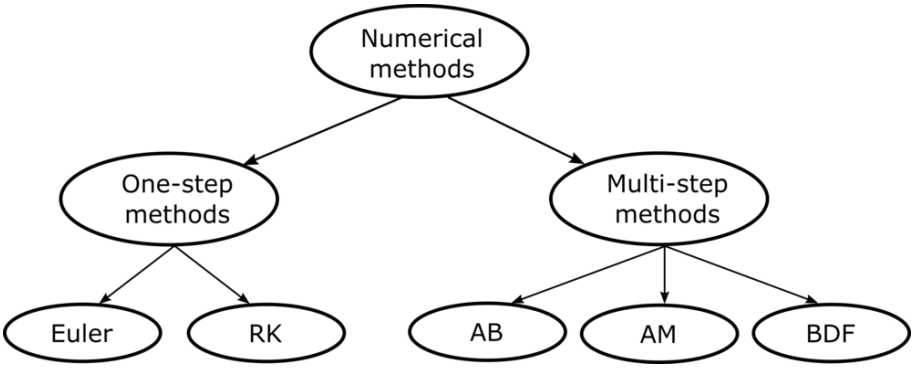

Figure 6.1: Classification of the different numerical methods.

One-step methods only use one previous step (y_i) and the derivative of that previous step (y'_i) to calculate the current step (y_{i+1}), while multi-step methods attempt to improve the efficiency of one-step numerical methods by utilising the information of several previous steps. More details about the different numerical methods illustrated in Figure 6.1 are provided in Appendix B, including the stability regions for each method.

6.1.1.1 Multi-rate scheme

Due to the different dynamics of the components included in the *cHyW2W* model, different sample periods are required to accurately reproduce the behaviour of the components described in each subsystem. For example, a sample period of 10ms ($\delta t_{HdM} = 10ms$) is suitable for wave-absorber interactions [338] (including linear and nonlinear hydrodynamics), while a period of 1ms ($\delta t_{Hyd} = 1ms$) is recommended for hydraulic transmission systems [233] and a period of 50μs ($\delta t_{ElecM} = 50\mu s$) for electric generators [339]. The suitability of these sample periods have been confirmed when validating each subsystem in Chapter 5, comparing the results from the mathematical models using different sample periods to the results from physical experiments or high-fidelity software.

Therefore, when a SR solver is implemented in the *cHyW2W* model, a sample period of 50μs is necessary to capture the dynamics of the fastest components. In contrast, the MR time-integration schemes permit the implementation of the required sampling period in each subsystem [340, 341]. Hence, the sub-models are connected by performing appropriate up-sampling and down-sampling on the output signals from each sub-model. Up- and down-sampling are performed by interpolating the signals (interpolation is required in down-sampling only when the time-steps of the interconnected sub-models are not integer multiples of each other), for which different interpolation methods, such as *linear*, *cubic* or *spline* interpolation, have been investigated. Identical results have been obtained for the different methods, which suggests that the *linear* interpolation is the most suitable, due to its appealing computational requirements.

The RK4 numerical method is initially employed to compare results from the model with the MR scheme against the results from the more conventional SR scheme, evaluating computational requirements and fidelity of the output variables in the three main sub-models: hydrodynamic sub-model (*HdM*), hydraulic transmission system sub-model (*HyM*) and electric sub-model (*ElecM*). The deviation between the results obtained with the SR and MR simulation models is calculated by means of the NRMSD presented in Equation (5.1), which is used to calculate the fidelity level of the different variables from the MR simulation model, following Equation (5.2).

The displacement and velocity of the absorber are evaluated in the *HdM* sub-model. Cylinder pressure difference and force, and motor flow and torque are studied in the *HyM* sub-model. Finally, current, voltage, active power and rotational speed are analysed in the *ElecM* sub-model. The overall fidelity of a sub-model is calculated as the straight average of the fidelities for all sub-model variables. Fidelity values, illustrated in Figure 6.2, exceed 99.5% for all the subsystems, with the deterioration attributed to the interpolation of the signals in up- and down-sampling. In order to illustrate the meaning of the fidelity values shown in Figure 6.2, time-domain results are illustrated in Figures 6.3 (a), (b) and (c) for hydrodynamic displacement, piston force applied from the HyPTO system to the spherical HPA, and the final electric power, respectively. As one can observe in Figure 6.3, differences between the SR and MR are almost imperceptible.

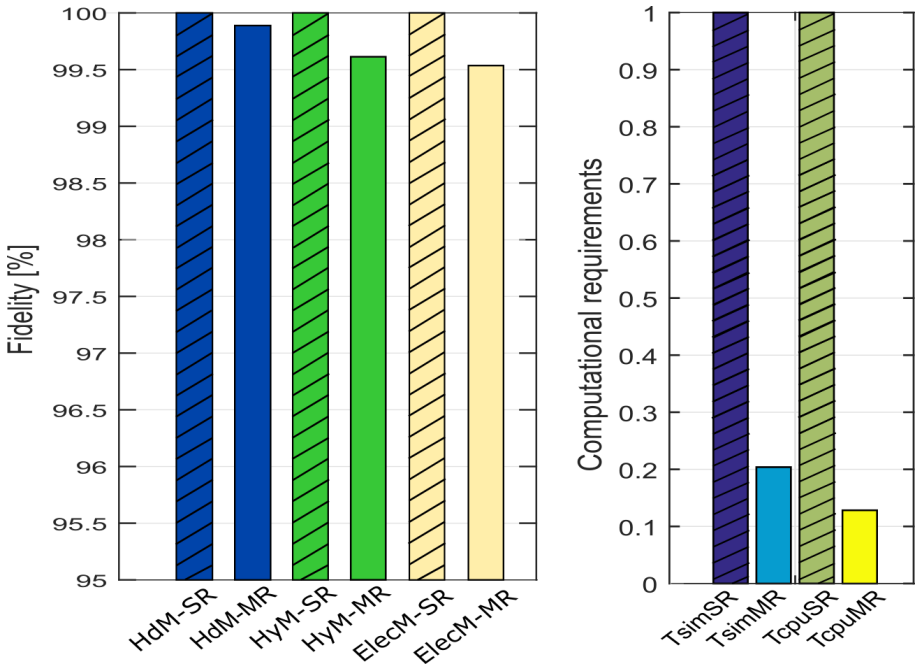

Figure 6.2: Fidelity and computational requirement characteristics of the SR and MR schemes using the RK4 method.

With respect to computational requirements, simulation time is reduced by a factor of 5 with the MR scheme, compared to the SR scheme, as shown in Figure 6.2, where all interpolation

calculations represent less than 0.05% of the total simulation time.

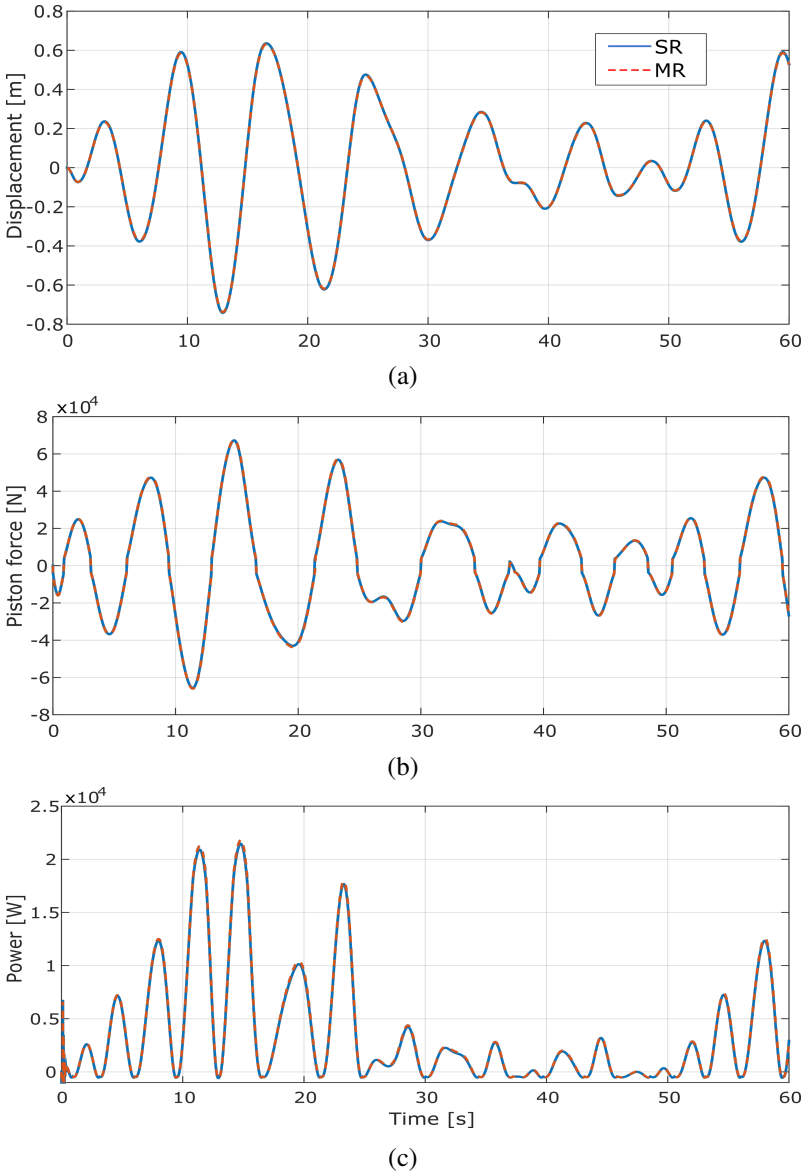

Figure 6.3: Comparison of the SR and MR time-integration schemes for body displacement (a), piston force (b) and generated power (c).

The RK4 integration method is, in the experience of the author, the most commonly implemented method in simulation models for wave energy applications, though little justification is offered. Therefore, a comparative study is carried out, in this section, to find the most efficient integration method, comparing different iterative and multi-step explicit and implicit methods presented in Sections B.1 and B.2: explicit RK (Section B.1.2), explicit AB (Section B.2.1), implicit AM (Section B.2.2) and implicit BDF (Section B.2.3) for orders between 2 and 4. Results from higher order methods, such as 5th order *Dormand-Prince*, are found to be identical to the results from RK4 for all the variables. Therefore, the SR model implementation with the numerical method RK4 (SR-RK4) is considered as the benchmark.

An extra complication may appear when modelling hydraulic transmission systems. Hydraulic systems are stiff systems due to the compressibility of the hydraulic fluid combined with the other relatively slow dynamics. Figures 6.4 (a) and (b) illustrate the motion of the device and the pressure in the hydraulic cylinder, respectively, using the second order RK solver for the first 30s and the second-order AB solver for the last 30s. Both solvers are numerically stable for the

hydrodynamic model, as shown in Figure 6.4 (a), while instability issues are evident in the last 30 seconds of the hydraulic transmission system simulation, as illustrated in Figure 6.4 (b), where numerical instabilities are highlighted in the zoomed dashed circle. Numerical instabilities, in this case, do not cause the solution to increase or decrease towards infinite values, but introduce rapid oscillations around the exact solution. Likewise, AM and BDF methods of order greater than two show stability problems when modelling the hydraulic transmission system, unless the sampling rate is significantly increased [336], since the absolute stability region reduces as the order increases, as shown in Figures B.3 and B.4. Consequently, AB methods of all orders and AM and BDF methods of order greater than two are directly discarded from the comparative study.

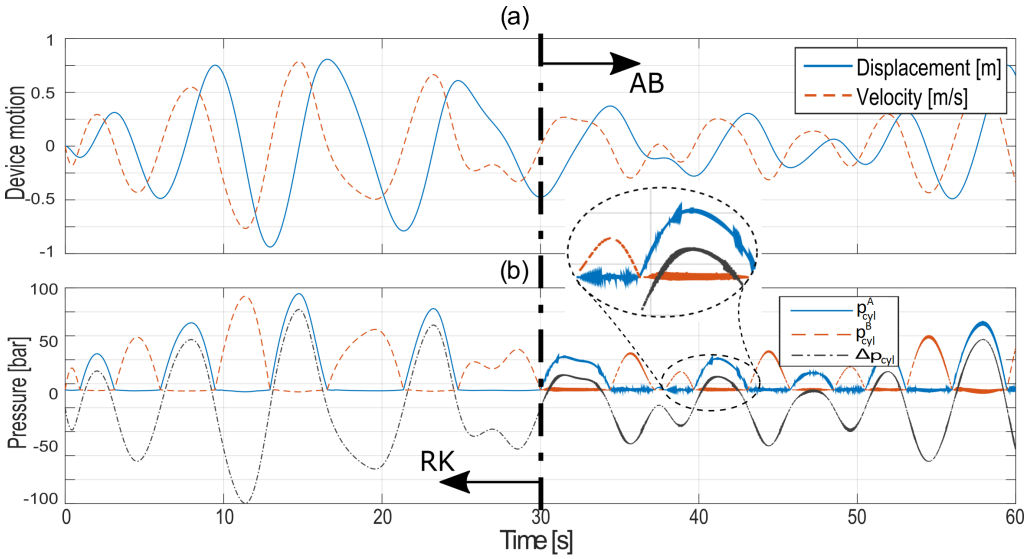

Figure 6.4: Hydrodynamic (a) and hydraulic subsystem (b) results for the RK and AB methods.

Hence, RK methods of order two, three and four, and AM and BDF methods of order two, are analysed in terms of accuracy and computational requirements, taking the SR-RK4 method as the benchmark. Figure 6.5 shows the fidelity values of each integration method for the different sub-models against the normalised computation time, where the colour code refers to the different sub-models again utilising the colour code used in Figure 6.2. As expected, second-order methods have the most appealing computational features, while higher-order RK methods are more accurate. However, RK2 exhibits both the appealing computational characteristics of the second-order methods and the accuracy of higher-order methods. Nevertheless, high-order RK methods could theoretically use larger time-steps than low-order RK methods, while providing similar fidelity levels. Therefore, to provide a fair comparison between high- and low order RK methods, a RK4 with a larger time-step (RK4a) is also included in the comparison. The time-steps for RK4a are defined so that computational requirements for RK2 and RK4a are similar: 20ms, 2ms and 75μs for the *HdM*, *HyM* and *ElecM*, respectively. Figure 6.5 shows that, compared to RK2, RK4a provides identical fidelity for *HdM*, but lower fidelity for *HyM* and, particularly, *ElecM*. In addition, stability issues appear in *HyM* when using RK4a, due to the larger time-steps.

As a consequence, MR-RK2 is demonstrated to be the most efficient method, providing almost indistinguishable results when compared to the results obtained using the SR-RK4 method, while requiring approximately a tenth of the time taken by SR-RK4.

However, in the event that the hydraulic transmission systems is modified so as to include more compression/expansion processes, a higher-order integration method, or a shorter time-step, may be necessary to accurately reproduce the more complex dynamics of such a hydraulic transmission system [233]. In such a case, the rest of the sub-models could still use the RK2 method, resulting in a MR multi-solver W2W model.

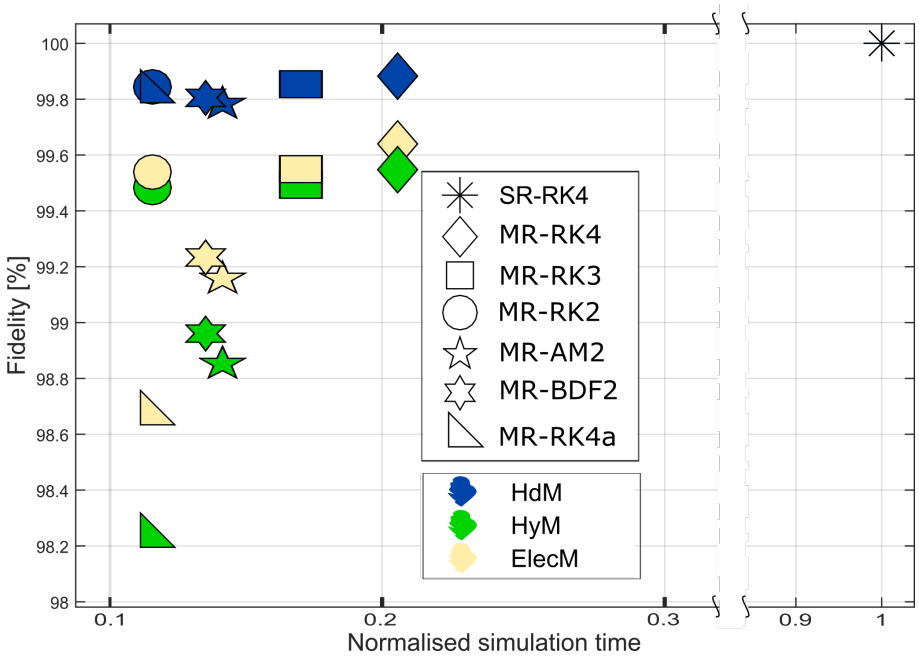

Figure 6.5: Fidelity versus normalised simulation time for each sub-model and integration method, when compared against the SR-RK4 method.

6.2 Application of the *cHyW2W* model

Using the *cHyW2W* model, implemented via the MR-RK2 integration scheme, the holistic performance of WECs can be evaluated accurately. Hence, a preliminary analysis is carried out to evaluate the holistic performance of the spherical HPA presented in Section 3.1.3, coupled to constant- and variable-pressure hydraulic transmission configurations described in Sections 4.1.1.1 and 4.1.1.2, respectively. It should be noted that the grid connection of the electric generator, in the constant- and variable-pressure hydraulic transmission system configurations, is different in this preliminary analysis. Constant-pressure configurations provide, in general, a smooth power output, which allows for a direct connection of the electric generator to the electricity grid, as shown in [238]. In contrast, the typical power output of variable-pressure hydraulic transmission system configurations is highly variable, which suggests that power converters are required for fulfilling the restrictions imposed by the electricity grid.

This preliminary analysis simulates the response of the spherical HPA for a polychromatic input wave based on a JONSWAP spectrum of 1.5m H_s and 9s T_p. In order to provide a fair comparison between the two HyPTO configurations, an identical hydraulic cylinder is used in both configurations, and the control forces used in both configurations are similar in magnitude. The reference PTO force (F^*_{PTO}) for the WEC is defined via Coulomb damping in the constant-pressure hydraulic transmission system configuration, while resistive control is used in the variable-pressure configuration. This F^*_{PTO} is used to determine the control input to the hydraulic motor (C_1 in Figure 2.22), which regulates α_M, controlling the fluid flow in the hydraulic motor and the pressure difference between the cylinder chambers. Hence, F^*_{PTO}, defined following Coulomb damping and resistive control, is given by:

$$F^*_{PTO} = C_{PTO}, \tag{6.1}$$

$$F^*_{PTO} = -B_{PTO}\dot{z}_d, \tag{6.2}$$

where C_{PTO} is the Coulomb damping term.

Results from the preliminary evaluation are summarised in Table 6.1, where the efficiencies of the different conversion stages, including the essential components of the hydraulic transmission

system and the electrical system, the efficiency of the HyPTO system as a whole (η_{PTO}), and the W2W efficiency (η_{W2W}) are presented. In addition, hydrodynamic power absorption efficiency (η_{Hyd}) is computed using the ratio of the absorbed power to the power available in the wave, as in [342].

Table 6.1: Efficiency of the different components included in the different variation of the *cHyW2W* model, with constant- and variable-pressure hydraulic transmission system configurations.

HyPTO configuration	η_{Hyd}	η_{Cyl}	η_{Mot}	η_{Hy}	η_{Gen}	η_{Inv}	η_{PTO}	η_{W2W}	P^{av}_{grid}	where
Constant-pressure	10.22	97.96	92.73	90.84	87.51	-	79.49	8.17	7.39 kW	$\eta = \frac{P_{out}}{P_{in}} \times 100\ [\%]$
Variable-pressure	16.15	95.27	72.92	71.91	76.63	92.47	51.67	8.34	7.54 kW	

In addition, Figures 6.6 (a) and (b) illustrate the velocity profile of the spherical HPA, and the PTO force applied by the hydraulic cylinder to the absorber, respectively, for the constant- and variable-pressure configurations. The velocity profile illustrated in Figure 6.6 (a) shows the different absorption modes for each HyPTO configuration, which shows higher peak values and less sharp edges in the variable-pressure case, compared to the constant-pressure case. Differences between constant- and variable-pressure configurations are more pronounced in Figure 6.6 (b), where the force profile in the constant-pressure case is, as expected, similar to a coulomb force, while the force profile in the variable-pressure case broadly follows the profile of absorber's velocity.

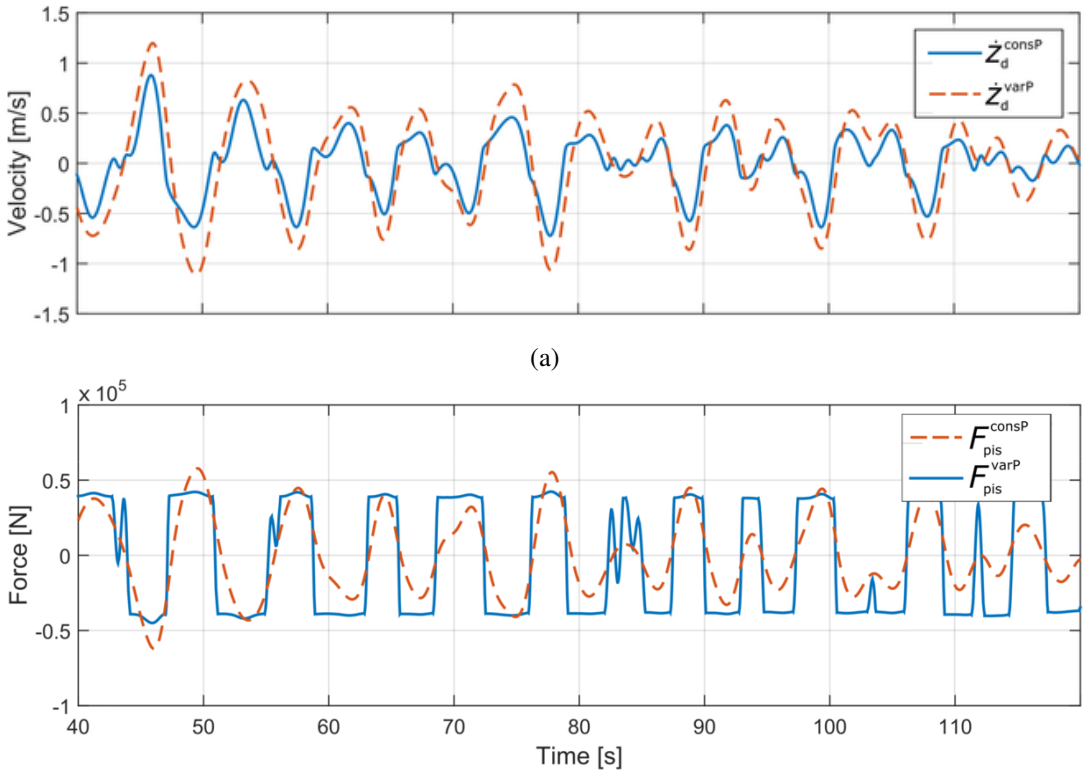

Figure 6.6: Absorption characteristics of the constant- and variable-pressure configurations: (a) absorber's velocity and (b) piston force. Superscripts consP and varP correspond to the constant- and variable-pressure hydraulic transmission system configurations, respectively.

Power outputs from the different conversion stages are shown in Figure 6.7, where the absor-

bed power signal is always positive for the variable-pressure HyPTO configuration, while negative values can be observed in the constant-pressure configuration. These negative values in the constant-pressure HyPTO configuration appear when the absorber reaches its final position and the check valves close, as explained in Section 5.2.3.1.1. At this point, the absorber starts moving in the opposite direction almost instantaneously, while the pressure in the cylinder chambers and, as a consequence, the force, needs more time to change. For a short period of time, the signs of the velocity and the force are the same, resulting in negative absorbed power results. Similar behaviour is observed in Section 5.2.3.1.1, when validating the mathematical model for the constant-pressure hydraulic transmission system configuration. Apart from the negative values, peaks in the absorbed power signal are twice as high in the case of the variable-pressure HyPTO configuration, compared to the constant-pressure case. As a result, absorption efficiency in Table 6.1 is almost 60% higher in the case of the variable-pressure HyPTO configuration. It should be noted that power absorption can be improved in both cases, by optimising control parameters C_{PTO} and B_{PTO} in Equations (6.1) and (6.2), respectively, or, in the case of the variable-pressure HyPTO configuration, by implementing real-time energy maximising control strategies, such as model-predictive [343], pseudo-spectral [344] or moment-domain control [345]. However, limitations of the constant-pressure HyPTO configuration, due to the HP accumulators installed between the hydraulic cylinder and motor, suggest that absorbed power will always be higher in the variable-pressure case.

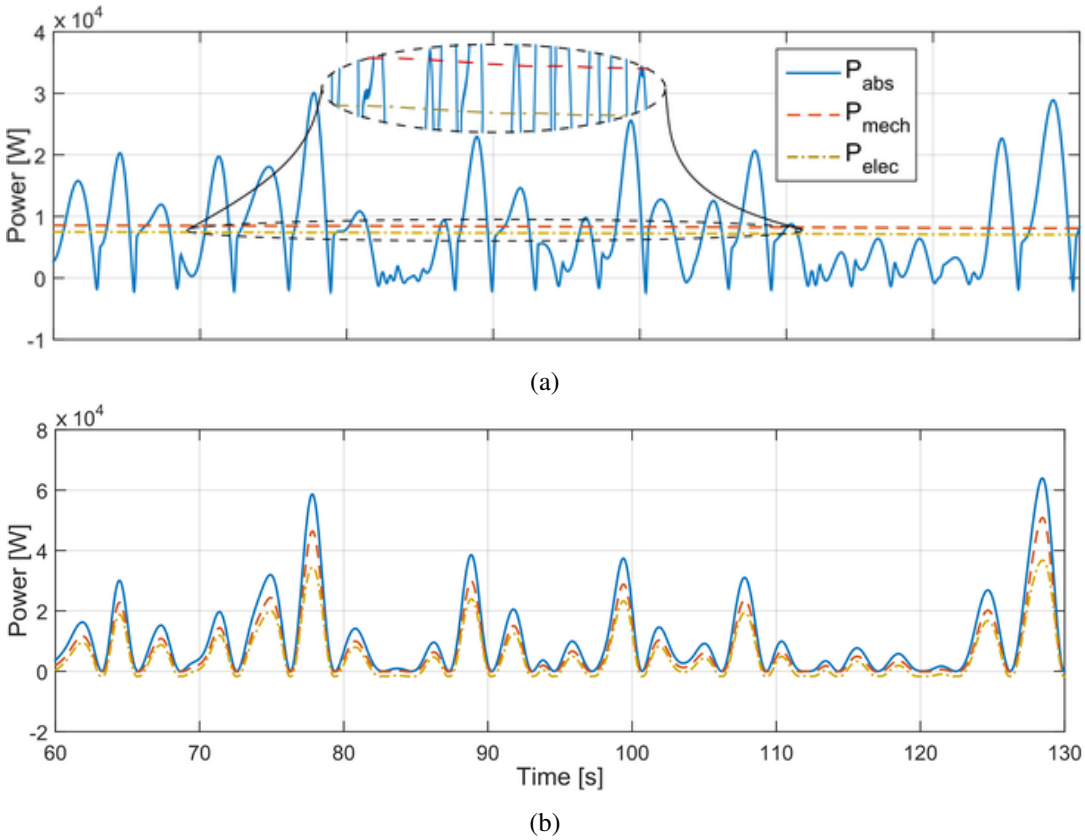

Figure 6.7: Absorbed, mechanical and electrical power for the constant- (a) and variable-pressure (b) configurations.

However, due to the HP accumulator in the constant-pressure HyPTO configuration, the output electrical power signal is smooth and practically constant, as illustrated in Figure 6.7 (a), which implies potentially higher hydraulic motor efficiency, as shown in Table 6.1. Mechanical and electrical power outputs (red dashed and yellow dash-dotted lines in Figure 6.7 (a), respectively), appear to be perfectly flat, since a very large accumulator is implemented (1000L). However, slow

power variation, due to the volume and pressure variation in the accumulator, can be observed in the zoomed dashed circle. In addition, since the generator operates at constant speed, the generator can be connected directly to the grid, avoiding power losses due to the inverters.

In contrast, the electrical power signal in the variable-pressure HyPTO configuration, as illustrated in Figure 6.7 (b), follows the profile of the absorbed power, which considerably reduces the HyPTO efficiency (approximately a 30% reduction compared to the constant-pressure HyPTO configuration), as shown in Table 6.1. Nevertheless, the W2W efficiency in the variable-pressure HyPTO configuration is higher than in the constant-pressure PTO configuration. Indeed, an improvement of the HyPTO efficiency in the variable-pressure HyPTO configuration is to be expected when the rotational speed of the electric generator and the hydraulic motor is actively controlled [64], since the rotational speed is held constant in the results shown in this chapter.

The results of the preliminary analysis shown in Table 6.1 demonstrate that a higher PTO efficiency does not necessarily imply a higher output power flow, which reinforces the idea that a holistic evaluation of a WEC is necessary to accurately assess the overall performance of a WEC. Therefore, a more comprehensive analysis is required to fully understand the relevance of the *cHyW2W* model. The impact of using the *cHyW2W* model is analysed for three specific applications presented in Chapter 2: selection of the HyPTO system configuration (Section 6.2.1), related to the *PTOopt* application; control strategy selection and optimisation (Section 6.2.2), related to the *MBC* application; and *PowAss* (Section 6.2.3).

6.2.1 HyPTO system configuration selection

Appropriate design of the PTO system is crucial for a WEC to efficiently convert absorbed wave energy into electricity. Different aspects must be considered when designing the PTO system of a WEC, such as the PTO mechanism to convert absorbed energy into electricity, the configuration and type of components included in that PTO system, and the sizing of these components. The comprehensive analysis evaluating constant- and variable-pressure HyPTO configurations is designed to cover the wide range of different possible sea conditions WECs can absorb energy from. Hence, three sea-states are defined in Table 6.2, *i.e.* low- (LE), medium- (ME) and high-energetic (HE) sea-states. Figure 6.8 presents the complete scatter diagram of the BIMEP test site in the bay of Biscay [346], showing the position of the three sea-states under analysis in the full scatter diagram.

Table 6.2: Sea-states analysed in the comparison of constant- and variable-pressure HyPTO configurations.

HyPTO	H_s [m]	T_p [s]
LE sea-state	1	6
ME sea-state	1.5	8
HE sea-state	3	11

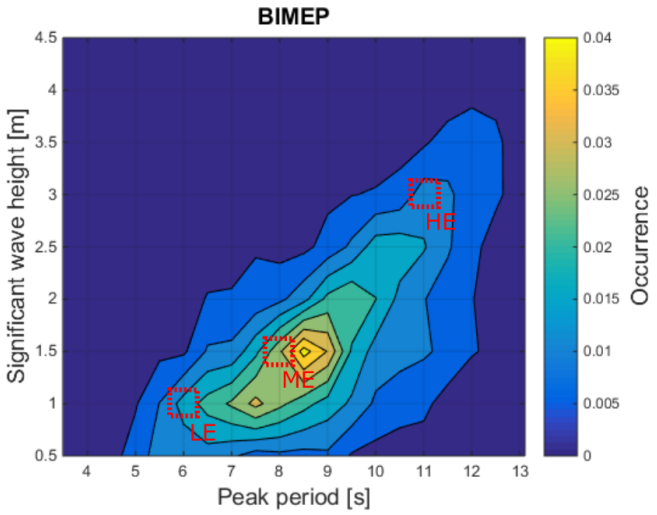

Figure 6.8: Scatter diagram of the BIEMP test site in the Bay of Biscay [346].

Similarly to the case in the preliminary analysis, the input η_w for each sea-state is generated by utilising the JONSWAP spectrum [75]. Figures 6.9 (a) and (b) illustrate the wave spectra and the η_w signals, respectively, for the three sea-states defined in Table 6.2.

The HyPTO systems used in this comparison have not been optimised, in the sense that the HyPTO components might be oversized, since the optimisation of the HyPTO systems is beyond the scope of this thesis. Thus, the components in the constant- and variable-pressure HyPTO system configurations used in this comparison, presented in Table 6.3, are designed so that they allow for satisfactory power absorption and generation all over the operational space presented in Figure 6.8.

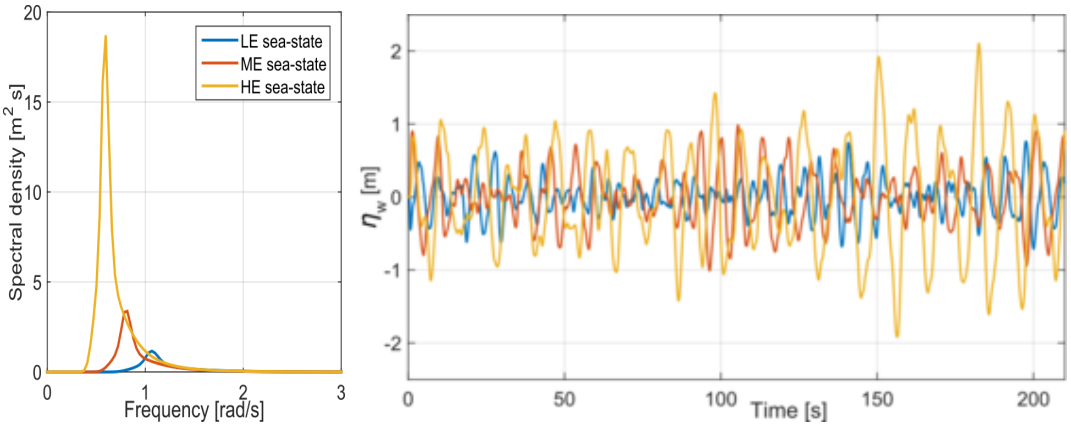

(a) (b)

Figure 6.9: Wave spectra (a) and η_w (b) for the three sea-states defined in Table 6.2.

In the case of the constant-pressure HyPTO configuration, the hydraulic cylinder is designed based on the maximum piston force and pressure allowed in the cylinder. Maximum pressure is usually set between 300-350 bar [64], while the maximum piston force is determined by optimising the power generation for the HE sea-state. The maximum piston force needed for optimal energy generation in the HE sea-state is about 100kN, so a maximum allowed piston force of 150kN is defined, which leaves a reasonable margin for (even) more-energetic sea-states. Dividing the maximum allowed piston force over the maximum allowed pressure (350 bar), gives the required A_p, which in this case is 70cm^2. Since the power output of the constant-pressure HyPTO system configuration is relatively flat, as shown in Figure 6.7 (a), the displacement of the hydraulic motor and the rated power of the electric generator can be selected based on the maximum expected average power. Thus, the hydraulic motor is designed so that it operates at 80% of its capacity at the HE sea-state, leaving a reasonable margin to absorb energy from (even) more-energetic sea-states, which results in a hydraulic motor of 60cc/rev. Finally, an electric generator of 36.6kW rated power is selected, which is the average power production expected in the most powerful sea-states within the power production region.

In contrast, the design of the variable-pressure HyPTO configuration needs to consider the high peak-to-average ratios (up to 17 and 58 for resistive and reactive control, respectively, [272]), which requires the analysis of the instantaneous generated power, in addition to the average power analysis. As a consequence of the high peak-to-average ratios, HyPTO components are significantly oversized, compared to the constant-pressure configuration, as one can notice in Table 6.3. The methodology to select A_p is the same as in the constant-pressure configuration, which results in $A_p = 140cm^2$ (assuming a maximum force of 420kN, based on [64]). The lack of hydraulic accumulators between the hydraulic cylinder and motor, results in the flow through the hydraulic motor being directly proportional to absorber's velocity. Therefore, the maximum displacement of the hydraulic motor is strongly related to the velocity constraint of the absorber. 2m/s is a common value for the velocity constraint in HPAs, which, assuming a maximum gene-

rator speed of 1500rpm, results in a hydraulic motor of 1120cc/rev capacity. Power fluctuations in variable-pressure configurations, illustrated in Figure 6.7 (b), complicate the selection of the electric generator. On the one hand, the electric generator should be large enough to deal with high power peaks. On the other hand, large electric generators involve frequent part-load operating conditions, significantly reducing the overall efficiency of the generator. Hence, the selection of the electric generator becomes a trade-off between the capacity to deal with power peaks and minimising losses due to frequent part-load operation. Although electric generators can operate in overload conditions for short periods of time, excessive overloading can cause serious damage [347]. However, to the best knowledge of the author, no study in the literature suggests a thorough analysis of the overloading operations in wave energy. Therefore, the power rating of the electric generator implemented in the variable-pressure configuration in this thesis, is determined as twice the average power generated in the HE sea-state: 74.5 kW.

Table 6.3: Main characteristics of the constant- and variable-pressure HyPTO system configurations.

	Constant-pressure HyPTO	Variable-pressure HyPTO
A_p	40cm^2	140cm^2
Cylinder length	2m	2m
V_{acc}	200L	-
D_ω	60cc/rev	1120cc/rev
P_e^{rated}	36.6kW	74.5kW
J_{shaft}	1.66kg·m^2	4.45kg·m^2

In this section, only resistive control is implemented in the variable-pressure HyPTO system configuration, following Equation (6.2). More aggressive control strategies, *e.g.* reactive control, are described and implemented later in Section 6.2.2, when analysing the effect of control strategies. Control parameters of the constant- and variable-pressure HyPTO system configurations are optimised for each sea-state. In the case of the constant-pressure configuration, the initial pressure in the accumulator, which determines the pressure difference between the hydraulic cylinder chambers and across the hydraulic motor, and the fractional-displacement α_M of the hydraulic motor, must be optimised. However, the optimisation needs to make sure that the hydraulic motor uses only the energy absorbed in the absorption stage and not the energy initially stored in the HP accumulator. Therefore, the optimisation is subject to a maximum of 5% difference between the energy entering and outgoing from the HP accumulator. Control parameter optimisation of the variable-pressure HyPTO configuration is simpler in that sense, where only the B_{PTO} coefficient needs to be optimised.

Power absorption and generation modes of the constant- and variable-pressure HyPTO system configurations are already described in Figures 6.7 (a) and (b), respectively. Therefore, power flows through the different conversion stages, and efficiencies of the different components in each conversion stage, are studied for the two HyPTO system configurations. Tables 6.4 and 6.5 show results for the constant- and variable-pressure HyPTO system configurations, respectively.

The extended comparison between constant- and variable-pressure HyPTO system configurations allows for a comprehensive discussion on the characteristics of the two HyPTO configurations. Absorption capabilities of the spherical HPA are significantly enhanced in the variable-pressure HyPTO configuration, particularly for medium- and high-energy sea-states, where the constant-pressure configuration absorbs up to 40% less energy from ocean waves. In fact, this difference can increase substantially when implementing a more aggressive control strategy in the variable-pressure configuration, as studied in Section 6.2.2.

However, absorbed energy needs to be converted into electricity to be delivered into the elec-

Table 6.4: Power flow through different conversion stages and efficiencies of different components for the constant-pressure HyPTO configuration.

SS	Ocean waves	Absorption		Hydraulic transmission				Electric generator		Power converter		W2W		
	P^{av}_{wave}	P^{av}_{abs}	η_{Abs}	η_{Cyl}	η_{Mot}	P^{av}_{Hy}	η_{Hy}	P^{av}_{Gen}	η_{Gen}	P^{av}_{Inv}	η_{Inv}	P^{av}_{grid}	η_{HyPTO}	η_{W2W}
LE	13.1	3.1	23.5	90.6	66.1	2.1	60.0	0.1	5.5	-	-	0.1	3.8	0.8
ME	39.1	7.4	18.9	92.0	82.7	5.8	76.1	3.7	64.3	-	-	3.7	50.4	9.5
HE	213.8	19.1	8.9	94.4	91.7	16.6	86.6	14.2	85.6	-	-	14.2	74.5	6.6

Table 6.5: Power flow through different conversion stages and efficiencies of different components for the variable-pressure HyPTO configuration under resistive control.

SS	Ocean waves	Absorption		Hydraulic transmission				Electric generator		Power converter		W2W		
	P^{av}_{wave}	P^{av}_{abs}	η_{Abs}	η_{Cyl}	η_{Mot}	P^{av}_{Hy}	η_{Hy}	P^{av}_{Gen}	η_{Gen}	P^{av}_{Inv}	η_{Inv}	P^{av}_{grid}	η_{HyPTO}	η_{W2W}
LE	13.1	3.4	25.7	93.2	14.3	0.4	13.3	-2.5	-	-3.2	-	-3.2	-	-
ME	39.1	9.8	25.1	96.5	57.8	5.5	55.8	3.8	69.8	1.9	50.5	1.9	20.1	4.9
HE	213.8	32.2	15.1	96.8	69.5	21.4	66.5	17.3	80.9	16.1	93.1	16.1	50.0	7.5

tricity grid, and this conversion is particularly inefficient for the variable-pressure configuration. In the LE sea-state, energy generation with the constant-pressure configuration is very low, with a HyPTO efficiency of just 4%. The efficiency of the HyPTO system increases to 50% in the ME sea-state and reaches a reasonably good 75% in the HE sea-state. Similar trends, with very low efficiency of the HyPTO system in LE sea-states, are presented in [276], where losses in the electric generator are neglected.

In the case of the variable-pressure HyPTO configuration, the average power generation is negative in the LE sea-state, meaning that the WEC needs to draw energy from the electricity grid to keep the electric generator rotating at synchronous speed. The variable-pressure HyPTO configuration includes oversized hydraulic and electric components to handle flow and power peaks at high-energy sea-states, which dramatically reduces conversion efficiencies at part-load operating conditions. In addition, based on the results shown in Table 6.5, the components of the variable-pressure HyPTO system designed in this chapter are clearly too large, which makes the variable-pressure HyPTO configuration even more inefficient.

These oversized components of the variable-pressure HyPTO configuration make electricity generation in LE and ME sea-states infeasible and very inefficient, respectively, as shown in Table 6.5. In fact, due to the highly variable hydraulic flow and power outputs, half of the energy absorbed from ocean waves is lost through the different HyPTO components, even in HE sea-states. Such low efficiencies of the HyPTO can be increased, without affecting the power absorption, by controlling the rotational speed of the hydraulic motor and electric generator via the B2B power converter, as shown in [64]. Another possibility to reduce losses at part-load operating conditions, is to use HyPTO components or configurations that allow for high-efficiency performance at part-load operating conditions, such as DDMs or DDCs coupled to accumulators with different pressure levels, as described in Section 2.3.4.

In any case, Tables 6.4 and 6.5 again show that lower efficiencies of the HyPTO system do not necessarily mean lower power production. Despite the excessively large HyPTO system components incorporated in the variable-pressure configuration, average power delivered into the electricity grid is higher in the variable-pressure (except for the LE sea-state), if the effect of the B2B power converter is neglected. The B2B power converter is included in the variable-pressure HyPTO configuration, which incurs significant losses at part-load operating conditions as illustrated in Table 6.5, but is not being used to control the rotational speed of the electric generator, since the electric generator rotates at constant synchronous speed, in all the analysed sea-states.

Differences between the constant- and variable-pressure HyPTO configurations, in terms of generated power, are relatively low. Thus, the smaller and, as a consequence, cheaper components, and the smoother power output of the constant-pressure configuration, as demonstrated in Figure

6.7, can tip the balance in favour of the constant-pressure configuration. However, the performance of the constant-pressure configuration is difficult to improve, apart from accurately optimising the size of the components, which would not excessively change the results shown in Table 6.4. In contrast, several alternatives to improve the performance of the variable-pressure configuration have been suggested: accurately optimising the size of the HyPTO components, including a DDM that reduces losses at part-load operating points, actively controlling the rotational speed of the generator and hydraulic motor and, most importantly, using an energy maximising control strategy to improve power absorption and generation of the WEC. The impact of a more aggressive control strategy, and the optimisation of control parameters using the *cHyW2W* model, is analysed in the following section.

6.2.2 Control strategy selection and optimisation

In order to evaluate more realistic capabilities of the variable-pressure HyPTO configuration, a more aggressive control strategy is implemented: reactive control. Reactive control is used to actively bring the absorber to resonance with the incident ocean waves, maximising energy absorption by harnessing reactive power flow through the HyPTO system. In essence, the absorber is actively forced, at specific instants throughout the simulation, using energy from the electricity grid, to enhance absorber's motion by putting it in phase with the excitation force and increase the average energy absorption from ocean waves. The PTO force under reactive control is given by

$$F^{*}_{PTO} = -B_{PTO}\dot{z}_d - K_{PTO}z_d, \tag{6.3}$$

where K_{PTO} is the PTO stiffness that brings the absorber to resonance.

The performance of the variable-pressure HyPTO configuration under reactive control, using control parameters (B_{PTO} and K_{PTO}), independently optimised for the LE, ME and HE sea-states, is illustrated in Table 6.6. These results can be compared to the results obtained from the same configuration under resistive control and the constant-pressure HyPTO configuration, presented in Tables 6.5 and 6.4, respectively.

Table 6.6: Power flow through different conversion stages and efficiencies of different components for the variable-pressure HyPTO configuration under reactive control.

SS	Ocean waves	Absorption		Hydraulic transmission				Electric generator		Power converter		W2W		
	P^{av}_{wave}	P^{av}_{abs}	η_{Abs}	η_{Cyl}	η_{Mot}	P^{av}_{Hy}	η_{Hy}	P^{av}_{Gen}	η_{Gen}	P^{av}_{Inv}	η_{Inv}	P^{av}_{grid}	η_{HyPTO}	η_{W2W}
LE	13.1	7.6	57.8	92.3	15.9	1.1	13.9	-2.1	-	-3.2	-	-3.2	-	-
ME	39.1	26.9	61.0	95.5	68.3	17.6	65.3	12.8	71.6	9.1	79.8	9.1	33.8	22.4
HE	213.8	70.1	32.8	97.7	79.0	50.5	72.1	39.1	77.4	34.5	88.2	34.5	49.3	16.1

The importance of actively controlling the WEC via aggressive control strategies is highlighted in Table 6.6, where average generated power values, compared to the variable-pressure configuration under resistive control, are shown to be significantly higher in ME and HE sea-states, about 350% and 115% higher, respectively. A large part of this improvement corresponds to the increase in absorbed power due to the more aggressive reactive control, which doubles the absorption efficiency in all the different sea-states presented in Table 6.2. However, the efficiency of the HyPTO system also increases in HE and, especially, in ME sea-states, which also contributes to the significant increase in generated power. The improvement in the absorption stage is a direct consequence of the more aggressive reactive control strategy and, thus, can be considered as a general rule, applicable to other type of absorbers and/or PTO mechanisms, as long as these aggressive control strategies can be implemented. In contrast, the improvement in HyPTO efficiency is rather circumstantial, and should not be considered as a general rule. In this specific case, due to the oversized HyPTO components, the more aggressive reactive control increases the pressure flow in the hydraulic circuit and the power peaks in the electric generator, which encourages the different components to operate closer to their ideal operating points.

The increase in average generated power under reactive control, shown in Table 6.6, also shows the superiority of the variable-pressure HyPTO configuration over the constant-pressure configuration. Hence, the capability to actively control the WEC, allowing generated energy to be maximised, is shown to be crucial in increasing the power delivered into the electricity grid. However, it should be noted, from Table 6.6, that the need for oversized HyPTO components, in the variable-pressure HyPTO configuration to deal with flow and power peaks, is a real problem in LE sea-states, illustrating the difficulty in designing a WEC that can efficiently generate energy from the wide range of conditions present in the ocean.

Equally important, as the implementation of a more aggressive control strategy to maximise energy generation from ocean waves, is accurately designing such controller, using a mathematical model that includes all the necessary information. Since the control strategies analysed in this section are resistive and reactive control, the accurate design of the controller is limited to accurately optimising the B_{PTO} and K_{PTO} control parameters. The impact of using the *cHyW2W* model for control parameter optimisation is analysed in this section, using the spherical HPA with a variable-pressure HyPTO configuration directly connected to the electricity grid, as illustrated in Figure 6.10.

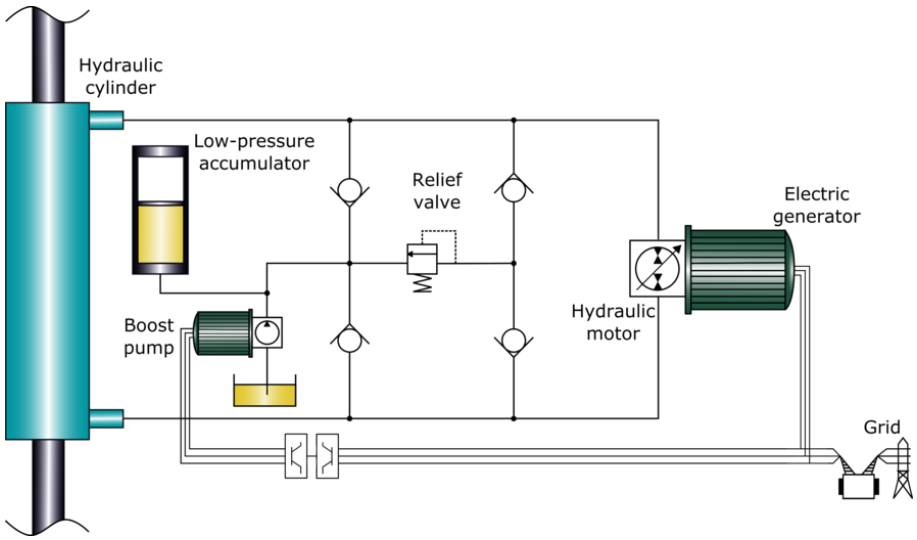

Figure 6.10: Diagram of the variable-pressure HyPTO system configuration.

These control parameters are usually optimised using mathematical models where the PTO mechanism is either neglected or excessively simplified. The only studies in the literature that use W2W models for control parameter optimisation are, to the best of author's knowledge, [64] and [271]. However, [64] optimises control parameters, considering losses in the PTO system by means of a constant efficiency parameter, while, in the W2W model suggested in [271], the electrical generator is added in the post-processing and is modelled using an efficiency coefficient that varies as a function of the rated power, neglecting the effects due to the inertia of the generator shaft.

Therefore, control parameters are optimised in this section using two significantly different mathematical models. On the one hand, the commonly used *viscLPF* method, based on Equation (3.28), coupled to an ideal HyPTO model, represented by Equation (6.3), is employed, henceforth referred to as *viscLPF+iPTO* model. The *viscLPF+iPTO* model includes three essential constraints of the HyPTO system: maximum absorber's displacement and velocity, and maximum PTO force. The maximum displacement constraint is implemented via the $F_{EndStop}$, which can be modelled as a spring and/or damping that is activated as soon as the motion amplitude reaches a threshold value close to the actual end-stop of the hydraulic cylinder. In this specific analysis, a linear damping ($B_{EndStop}$) is implemented. Note that, when an ideal HyPTO model is employed,

losses and dynamics of the HyPTO system are not included. Therefore, the hydrodynamic absorbed power and the generated electrical power are identical, and are given by:

$$P_{abs} = P_e = -\dot{z}_d F^*_{PTO}. \tag{6.4}$$

Results from the simplified *viscLPF+iPTO* model are compared to the *cHyW2W* model presented in this thesis, where all the essential dynamics, losses and constraints of the different components from ocean waves to the electricity grid are included. The latter is referred to as the $NLBEMW2W_{Cd=1}$ model in the following. The variable-pressure HyPTO system included in the $NLBEMW2W_{Cd=1}$ model is the same as that described in Table 6.3.

In order to comprehensively analyse the impact of the *cHyW2W* model on control parameter optimisation, the control parameters should be optimised over the complete operational space. Therefore, data from a real location is used to define that operational space. The selected location is Belmullet, off the west coast in Ireland, for which the Irish Marine Institute [348] provided the data. Belmullet has a high wave energy potential (one of the locations with the highest potential in Europe [346]). The scatter diagram for the location in Belmullet is shown in Figure 6.11 and the main characteristics of the location, such as the peak period and significant wave height with the highest frequency of occurrence (T'_p and H'_s, respectively), and the mean annual incoming wave energy per meter of wave front J, are presented in Table 6.7. Finally, it should be noted that the operational space of the WEC is limited to $H_s \leq 5m$, as illustrated by the red line in Figure 6.11, assuming that the WEC shifts to survival mode beyond that threshold value.

Table 6.7: Main characteristics of the Belmullet test site.

T'_p	11.3 s
H'_s	3.5 m
J	78kW/m

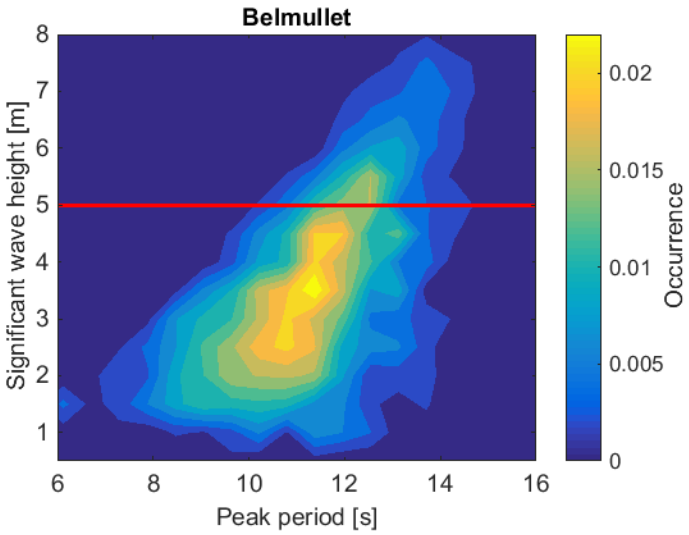

Figure 6.11: Scatter diagram of the Belmullet test site, where the red line shows the limit of the operational space.

Results from the *viscLPF+iPTO* and the $NLBEMW2W_{Cd=1}$ models are compared for both resistive and reactive control, where differences between the outputs from the *viscLPF+iPTO* and the $NLBEMW2W_{Cd=1}$ models are calculated, in percentage terms, as follows,

$$\Delta[\%] = \frac{y_{NLBEMW2W_{Cd=1}} - y_{viscLPF+iPTO}}{y_{NLBEMW2W_{Cd=1}}} \times 100, \tag{6.5}$$

where $y_{NLBEMW2W_{Cd=1}}$ and $y_{viscLPF+iPTO}$ are any output of the $NLBEMW2W_{Cd=1}$ and *viscLPF+iPTO* models, respectively. Note that Δ can take positive or negative values, negative values meaning that outputs from the *viscLPF+iPTO* model are overestimated, compared to the $NLBEMW2W_{Cd=1}$ model.

In the case of resistive control, differences between the control parameters (ΔB_{PTO}) optimised using the $NLBEMW2W_{Cd=1}$ and *viscLPF+iPTO* models are relatively important. Figure 6.12 il-

lustrates these differences over the complete operational space, where the *viscLPF+iPTO* model appears to overestimate control parameters for more energetic sea-states ($H_s \geq 3m$), while underestimation is evident for less energetic sea-states ($H_s \leq 3m$). One can observe, from Figure 6.12, that ΔB_{PTO} values are relatively low ($-10\% \leq \Delta \leq 10\%$) for medium sea-states ($1.5 \leq H_s \leq 3.5$), which suggests that the impact of inaccurate control parameters in that area may be lower.

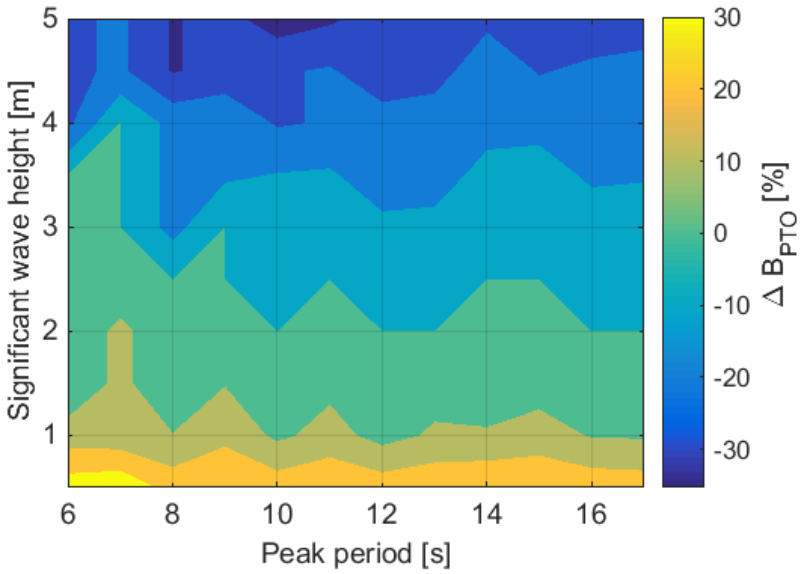

Figure 6.12: Resistive control parameter differences between the $NLBEMW2W_{Cd=1}$ and *viscLPF+iPTO* models over the complete operational space.

Table 6.8 presents the optimal control parameters and generated average power estimates ($P_e^{av,opt}$) for each model, and generated average power estimates from $NLBEMW2W_{Cd=1}$ using control parameters optimised with the *viscLPF+iPTO* model ($P_e^{av,viscLPF+iPTO}$), for resistive and reactive control at the sea-state with the highest occurrence in Belmullet ($T_p = 11.3s$ & $Hs = 3.5m$). For resistive control, the *viscLPF+iPTO* model is shown to overestimate the optimal control parameter by almost 9% and the generated power by over 30%.

Table 6.8: Optimal control parameters and corresponding generated power for the 11.3s peak period and 3.5m significant wave height sea-state, using resistive and reactive control.

		viscLPF+iPTO	$NLBEMW2W_{Cd=1}$	Δ [%]
Resistive control	B_{PTO} [kNs/m]	250	230	-8.7
	$P_e^{av,opt}$ [kW]	39.23	29.70	-32.1
	$P_e^{av,viscLPF+iPTO}$ [kW]	N/A[1]	29.24	-1.5
Reactive control	B_{PTO} [kNs/m]	90	130	30.8
	K_{PTO} [kN/m]	-175	-100	75
	$P_e^{av,opt}$ [kW]	123.7	53.6	-130.8
	$P_e^{av,viscLPF+iPTO}$ [kW]	N/A	*UnR*[2]	*UnR*

The abbreviation N/A is used for *not applicable*.
The abbreviation *UnR* is used for *unrealistic*.

However, if the B_{PTO} optimised with the *viscLPF+iPTO* model is used in the $NLBEMW2W_{Cd=1}$

model, generated power difference is low (about 1.5%). This means that the impact of the control parameter overestimation on the power estimation is low under resistive control. This difference is calculated by comparing $P_e^{av,viscLPF+iPTO}$ and $P_e^{av,opt}$ calculated with the $NLBEMW2W_{Cd=1}$ model, based on Equation (6.5), as follows,

$$\Delta[\%] = \frac{P_e^{av,opt} - P_e^{av,viscLPF+iPTO}}{P_e^{av,opt}} \times 100. \tag{6.6}$$

Conversely, differences are significantly larger under reactive control, as illustrated in Figure 6.13, where both control parameters and generated power, are significantly misestimated. Furthermore, the misestimation of control parameters has a dramatic impact on the performance of the WEC, since control parameters optimised with the *viscLPF+iPTO* model lead to unrealistic situations, as illustrated in Table 6.8 by the abbreviation *UnR*, where the WEC gets stuck at one of the cylinder end-stops for the whole simulation due to effect of the erroneously designed controller.

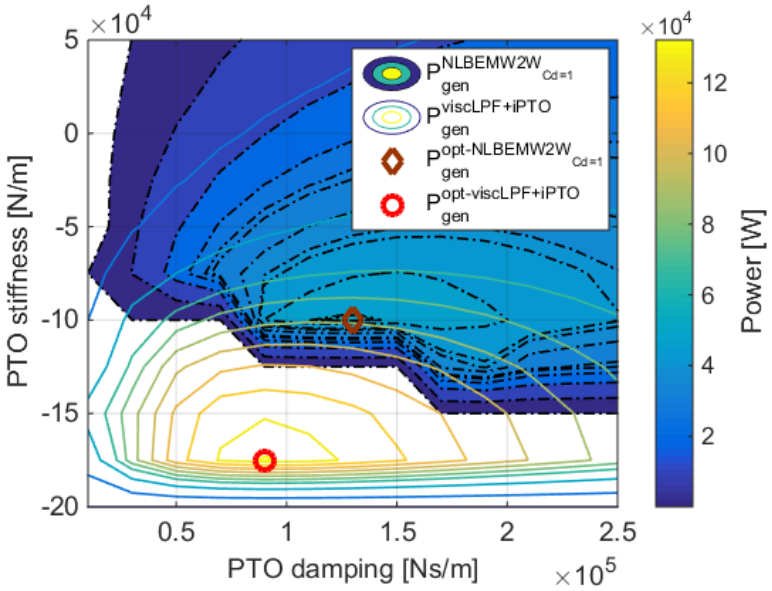

Figure 6.13: Reactive control parameter optimisation for the 11.3s T_p and 3.5m H_s, using $NLBEMW2W_{Cd=1}$ and *viscLPF+iPTO* models.

6.2.3 Power assessment

Accurate power production assessment is crucial for the development of WECs, since it allows the evaluation and comparison of different technologies in different geographic locations. Several studies in the literature analyse the power production assessment of different WECs, using either isolated devices [183, 271, 349–353] or arrays [346, 354] in the analysis. Power production assessment is also an essential tool to evaluate the economical viability of WECs or wave energy arrays, for which effects of the PTO systems should not be neglected. Finally, power production assessment is also used to evaluate the impact of wave resource variations on WECs [21, 22].

The predominant method for power production assessment consists of combining the wave scatter diagram of a specific location with the power output capabilities of a WEC for the different sea-states included in the scatter diagram, known as a power matrix. The wave scatter diagram is generated from the historical data collected over a reasonable time period (generally over a year), and the power matrix for the WEC is calculated using numerical models. Other methods for power production assessment, which avoid the use of power matrices, such as the full spectrum representation, are discussed in [353], where the potential inaccuracies of the power matrix approach are studied compared to the full spectrum representation.

The power matrix representation is used in this section, due to its simplicity and its appealing computational properties. In addition, the Belmullet location is particularly appropriate for this study, since the real spectra are similar to theoretical spectra, such as the JONSWAP spectrum, which reduces the inaccuracies due to the misrepresentation of the resource by the power matrix approach [353]. In any case, the objective of this section is to analyse the inaccuracies related to the WEC dynamical description, highlighting the impact of the *cHyW2W* model compared to the more common hydrodynamic models with an excessively simplified PTO system model. To that end, power production capabilities are assessed, under resistive and reactive control, using the *viscLPF+iPTO* and $NLBEMW2W_{Cd=1}$ models.

Figures 6.14 (a) and (b) illustrate the generated power matrices under reactive control for the *viscLPF+iPTO* and the $NLBEMW2W_{Cd=1}$ models, respectively. The pattern of the two power matrices in Figure 6.14 is very similar. Hence, the power absorption and generation modes of the WEC are not modified by the dynamics of the HyPTO system, suggesting that the HyPTO is able to adequately follow the reference force F^*_{PTO} created in the controller via Equations (6.2) and (6.3). Constraints and losses are probably one of the most influential aspects of the HyPTO system, but the fact that constraints are also included in the *viscLPF+iPTO* model makes the two power matrices very similar. The main difference between the two power matrices presented in Figure 6.14 is the magnitude of the generated power. Generated power estimates reach up to 200kW in the case of the *viscLPF+iPTO* model, while the maximum generated power estimate is about 80kW for the $NLBEMW2W_{Cd=1}$ model. This difference, a factor of 2.5, arises due to the losses of the different components in the HyPTO included in the $NLBEMW2W_{Cd=1}$ model, which are neglected in the *viscLPF+iPTO* model.

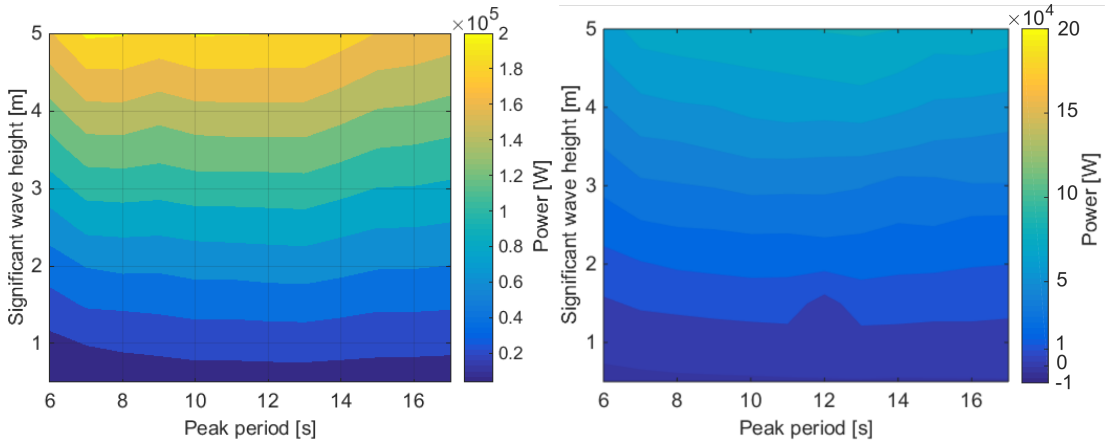

(a) *viscLPF+iPTO* model (b) $NLBEMW2W_{Cd=1}$ model

Figure 6.14: Generated power matrices obtained using (a) the *viscLPF+iPTO* and (b) the $NLBEMW2W_{Cd=1}$ models under reactive control.

In addition, one can observe, in Figure 6.14, that all generated power estimates over the complete operational space are positive in the case of the *viscLPF+iPTO* model, while negative values appear in the power matrix generated using the $NLBEMW2W_{Cd=1}$ model. These negative values appear at low-energy sea-states, as illustrated in Figure 6.14 (b), and arise due to the losses of the HyPTO system and the inertia effects in the electric generator. Negative generated power values appear both under resistive and reactive power, but always at less-energetic sea-states, since the power of ocean waves is too low to counteract the high inertia of the relatively large electric generator. However, such a large electric generator is necessary to deal with power peaks at more energetic sea-states. Similar trends are shown in Tables 6.5 and 6.6, where the energy delivered into the electricity grid at the LE sea-state is also negative. Although HyPTO system optimisation is beyond the scope of this thesis, it should be noted that an accurately optimised HyPTO system may improve the power generation of the WEC, allowing for power generation in all the sea-states,

including the less-energetic ones.

Differences between the two mathematical models are evaluated by means of the AMPP measure, and annual mean efficiencies of the HyPTO system (η_{HyPTO}^{AMPP}) and the whole WEC from ocean waves to the electricity grid (η_{W2W}^{AMPP}), calculated using AMPP values as follows,

$$\eta_{HyPTO}^{AMPP} = \frac{AMPP_{gen}}{AMPP_{abs}} \times 100, \tag{6.7}$$

$$\eta_{W2W}^{AMPP} = \frac{AMPP_{gen}}{P_{wave}^{av}} \times 100 = \frac{AMPP_{gen}}{J \times L_{charac}} \times 100, \tag{6.8}$$

where $AMPP_{abs}$ and $AMPP_{gen}$ are the absorbed and generated AMPP, respectively, and L_{charac} is the characteristic length of the absorber, its diameter in this case.

Generated AMPP and efficiency values are given in Table 6.9, where generated power overestimation of the *viscLPF+iPTO* model is shown again, as in Table 6.8: 40% under resistive control and 160% under reactive control. In addition, Table 6.9 demonstrates the importance of the holistic performance evaluation of the WEC by means of the η_{W2W}^{AMPP}, rather than η_{HyPTO}^{AMPP}.

Table 6.9: Power production assessment of the spherical HPA under resistive and reactive control, including optimal AMPP values, and HyPTO and W2W efficiencies obtained using the *viscLPF+iPTO* and $NLBEMW2W_{Cd=1}$ models; and AMPP values with misestimated control parameters ($AMPP_e^{av,viscLPF+iPTO}$).

		viscLPF+iPTO	$NLBEMW2W_{Cd=1}$	Δ [%]
Resistive control	$AMPP_e^{av,opt}$ [kW]	27.71	19.89	-39.32
	η_{HyPTO}^{AMPP} [%]	100	70.35	N/A
	η_{W2W}^{AMPP} [%]	7.11	5.26	N/A
	$AMPP_e^{av,viscLPF+iPTO}$ [kW]	N/A	19.62	-1.4
Reactive control	$AMPP_e^{av,opt}$ [kW]	94.23	36.17	-160.5
	η_{HyPTO}^{AMPP} [%]	100	59.07	N/A
	η_{W2W}^{AMPP} [%]	24.17	9.37	N/A
	$AMPP_e^{av,viscLPF+iPTO}$ [kW]	N/A	-17.34	-308.6

Most importantly, Table 6.9 shows the impact of the misestimation of the control parameters using the *viscLPF+iPTO* model. Under resistive control, since the area with low ΔB_{PTO} values in Figure 6.12 includes the sea-states with the highest frequency of occurrence (see Figure 6.11), the impact on $AMPP_{gen}$ is reasonably low (about 1.5% of difference, calculated following Equation (6.6)). In contrast, the impact of that misestimation is dramatic under reactive control.

Figure 6.15 illustrates the power matrix obtained using the $NLBEMW2W_{Cd=1}$ model with the control parameters optimised with the *viscLPF+iPTO* model. The blank spaces correspond to the unrealistic situations due to the erroneously designed controller, in which the WEC is considered to be non-operational. In addition, comparing Figure 6.15 with Figure 6.14 (b), one can note that positive values are significantly lower (up to a factor 3), while negative values are even more negative (up to a factor 2), which dramatically results in negative $AMPP_{gen}$, as shown in Table 6.9.

Despite the obvious benefits of the $NLBEMW2W_{Cd=1}$ model over the *viscLPF+iPTO* model, it should be noted that the computational requirements of the $NLBEMW2W_{Cd=1}$ model are prohibitive for any kind of optimisation and power production assessment purpose (over 100 times

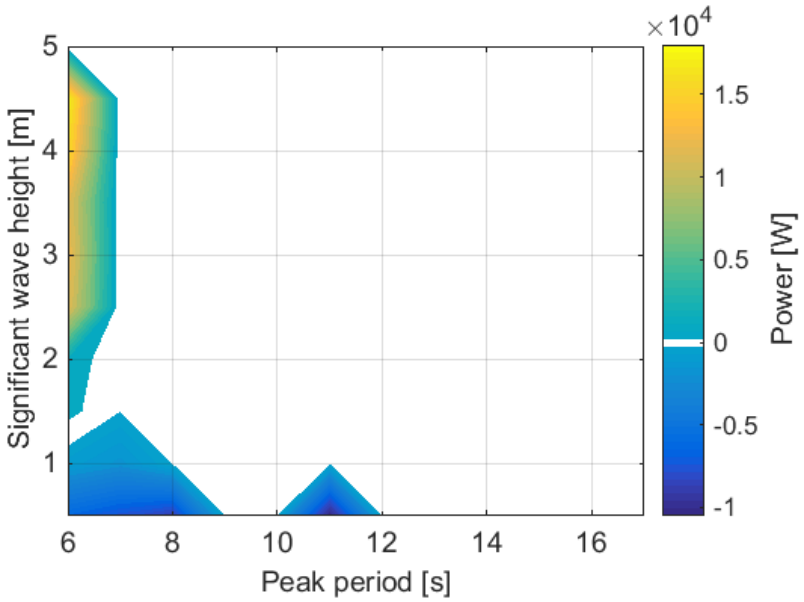

Figure 6.15: Power matrix obtained using the $NLBEMW2W_{Cd=1}$ model and misestimated control parameters optimised with the *viscLPF+iPTO* model, where blank spaces illustrate unrealistic situations due to erroneously designed controller.

slower than the *viscLPF+iPTO* model), mainly due to the extremely small time-steps required to capture the very fast electrical dynamics of the electric generator.

6.3 Summary

This chapter presents the numerical implementation and simulation of different variations of the *cHyW2W* model, and shows their relevance for different applications. Hence, the chapter is divided into two main parts. The first part of the chapter (Section 6.1) describes the numerical implementation of the *cHyW2W* model, comparing different time-integration schemes. The benefits of the MR time-integration scheme are highlighted over the SR scheme, which facilitates the use of a sampling period that is appropriate for each conversion-stage and avoids unnecessary computation in the components with slower dynamics. As a consequence, the computational requirements of the *cHyW2W* model are significantly reduced with a MR scheme, reducing the simulation time by a factor of 5. In addition to the integration schemes, different numerical integration methods, described in Appendix B, are analysed for each conversion stage. All the numerical methods analysed in this chapter provide accurate results for the *absorption*- and *generation*-stages, while the second-order RK method RK2 is shown to be the computationally most efficient method. In contrast, due to the fast dynamics included in the *transmission*-stage, mainly due to the compressibility effects of the hydraulic fluid, some numerical integration methods of order greater than two, such as the multi-step AB, AM or BDF, show stability issues, and, as a consequence, are directly discarded from the comparison. Thus, the RK2 numerical method with the MR integration scheme MR-RK2 is identified as the computationally most efficient numerical method, while providing almost indistinguishable results compared to the benchmark numerical implementation, which uses a SR integration scheme and the RK4 numerical method.

The second part of the chapter (Section 6.2) first presents a preliminary simulation of the *cHyW2W* model with the two different HyPTO system configurations described in Chapter 4: constant- and variable-pressure configurations. The absorption modes and generated power profiles for the spherical HPA with the two HyPTO configurations are compared, and the efficiency of each component included in the *cHyW2W* model is analysed. This preliminary simulation shows that a higher HyPTO efficiency does not necessarily imply higher power generation, highlighting

the importance of the absorption stage and the evaluation of the holistic performance of a WEC. In fact, the relevance of the *cHyW2W* model is studied in the same section via a more comprehensive analysis, which is divided into three subsections. Section 6.2.1 includes three sea-states that reasonably cover the wide operational space of the spherical HPA. In addition, the constant- and variable-pressure HyPTO configuration systems are designed, evaluating the performance of the spherical HPA using the constant-pressure configuration and the variable-pressure configuration under resistive control. The performance of the spherical HPA coupled to the variable-pressure HyPTO configuration and under a more aggressive control strategy, *i.e.* reactive control, is studied in Section 6.2.2. Hence, this extended evaluation again shows the need for evaluating the holistic behaviour of WECs, to accurately assess their power production capabilities, and particularly highlights the benefits of implementing more aggressive control strategies to maximise energy generation and using PTO systems that allow the implementation of these strategies. Hence, due to its higher flexibility in implementing energy maximising control strategies, the variable-pressure HyPTO configuration is selected to further evaluate the relevance of using the *cHyW2W* model. Finally, the impact of the *cHyW2W* model in control parameter optimisation, and assessment of power generation capabilities, is analysed in Sections 6.2.2 and 6.2.3, respectively. To that end, two significantly different mathematical models are compared: an excessively simplified mathematical model, *viscLPF+iPTO*, and the *cHyW2W* model, $NLBEMW2W_{Cd=1}$. Results show that, when optimising control parameters, the *viscLPF+iPTO* model misestimates the values of control parameters, where this misestimation is particularly important in the reactive control case. More importantly, it is demonstrated that using misestimated control parameters does not significantly affect power absorption in the resistive control case, but dramatically affects the performance of the WEC under reactive control. In fact, when using the misestimated control parameters in the real WEC, represented by the $NLBEMW2W_{Cd=1}$ model, the WEC may get permanently stuck at one of the end-stops, drawing energy from the electricity grid. With regard to power assessment, the *viscLPF+iPTO* model significantly overestimates power generation capabilities under resistive and, especially, reactive control. Finally the dramatic consequences of using misestimated control parameters in reactive control are shown, resulting in a negative AMPP value.

Chapter 7

HiFiWEC: coupled numerical wave tank and power take-off models

The commercial development of WECs is a slow, risky and expensive process, and the development trajectory towards the final commercial prototype involves several different stages. Figure 1.6 illustrates two different WEC development trajectories, where the ideal trajectory, suggested in [48], delays the expensive (large scale) prototype demonstration until a reasonably high level of confidence is gained in the concept. Hence, this ideal trajectory suggests first traversing the TPL scale at lower, less costly TRLs, as shown in Figure 1.6.

To gain confidence in the concept and traverse the TPL scale at lower TRLs, high-fidelity simulation models are vital. The need for the *cHyW2W* model for an accurate evaluation of the overall performance of WECs is demonstrated in Chapter 6, in particular for *PTOopt*, *MBC* and *PowAss* applications. However, the higher the TPL, the higher the level of accuracy needed to realistically assess the overall performance of the WEC. In contrast to the *PTOopt*, *MBC* and *PowAss* applications, the *VerVal* and *Ident* applications need W2W models of the highest possible fidelity, regardless of the computational cost required to provide such a high-fidelity level, as shown in Section 2.6.

This chapter describes a novel holistic high-fidelity W2W simulation platform, henceforth referred to as the *HiFiWEC*, which is the first attempt to couple a high-fidelity CNWT to a high-fidelity PTO model (the *cHyPTO* model presented in Chapter 4 and validated in Chapter 5). Hence, the *HiFiWEC* offers a high-fidelity simulation model for medium-high TPLs and low-medium TRLs, as shown in Figure 7.1.

The chapter is divided into four different parts, where the first part (Section 7.1) describes the *HiFiWEC*, including the CNWT and the inter-software coupling between the CNWT and the *cHyPTO* model. In addition, the area of application of the *HiFiWEC* is defined in Section 7.1, stating the particular applications for the *HiFiWEC*, and application areas for which the *HiFiWEC* is computationally prohibitive. Section 7.2 presents the case study utilised in this chapter, including the test cases, input waves, the CNWT setup and the HyPTO design. The inter-software coupling between the CNWT and the HyPTO model in the *HiFiWEC* is verified in Section 7.3, comparing the variables that are shared between the CNWT and the *cHyPTO* model, and the value of utilising the high-fidelity simulation platform offered by the *HiFiWEC* is highlighted in Section 7.4.

7.1 The *HiFiWEC*

The *HiFiWEC* is formed by coupling two high-fidelity mathematical models: a CNWT model that solves the fully nonlinear WSHI and the *cHyPTO* model that includes all the relevant dynamics, losses and constraints of hydraulic and electric PTO subsystems. Figure 7.2 illustrates the inter-

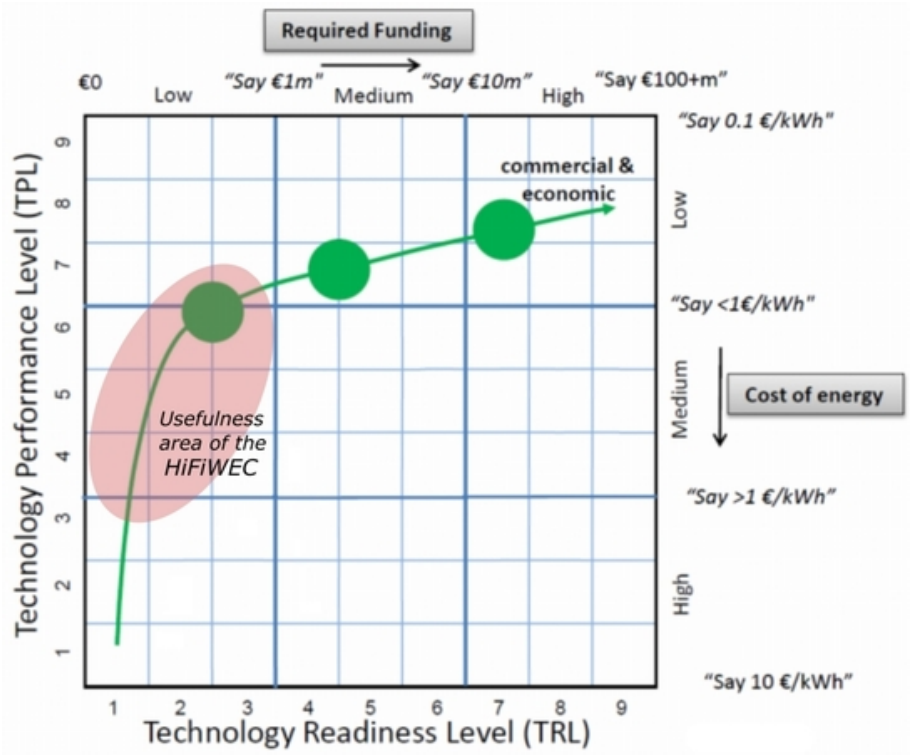

Figure 7.1: TRL and TPL matrix with the ideal development trajectory and the applicability area of the *HiFiWEC*, adapted from [48].

software coupling between the CNWT and *cHyPTO* models, where the simulation characteristics, such as the absorber and input waves η_w, are input to the CNWT, and the final output of the *HiFiWEC* is the generated electric power P_e. Since the CNWT and *cHyPTO* models are implemented in different software environments, and use different time-integration numerical methods, the platform requires a bespoke communication channel to couple the two models, which is described in more detail in Section 7.1.3.

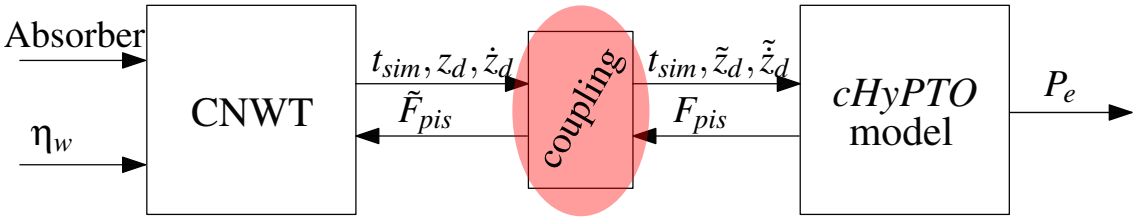

Figure 7.2: Scheme of the *HiFiWEC*, illustrating the inter-software coupling between the CNWT and the HyPTO model. Due to differences between the time-integration numerical methods, interpolation of variables is inevitable, which is illustrated with a tilde on the shared variables that are interpolated.

Likewise the coupling between the different sub-models in the *cHyW2W* model, the coupling between the CNWT and the *cHyPTO* model in the *HiFiWEC* is *weak*, in the sense that a time-step offset exists between the variable calculated in the *cHyPTO* model and the use of this variable back in the CNWT. This *weak* coupling may be problematic when the inertia effects in the different models that are coupled have a similar impact. However, in the wave energy case, as explained in Chapter 6, inertia effects of the absorber are always significantly higher than inertia effects in other sub-systems (*e.g.* the PTO system or the moorings). Therefore, the *weak* coupling, which is computationally more efficient due to the lack of any iterative process in the coupling, provides

accurate results in wave energy applications. In order to gain confidence in the coupling and demonstrate its suitability, the coupling implemented in the *HiFiWEC* is verified in this chapter.

The *HiFiWEC* is particularly useful (based on the seven applications defined in the introduction of Chapter 2):

a.i) as a benchmark to validate lower fidelity or computationally more efficient mathematical models (*ValVer* application),

a.ii) for system identification purposes, identifying the viscous drag coefficient or representative/parametric models under realistic operational conditions (*Ident* application), and

a.iii) to evaluate the efficacy of control strategies in realistic conditions (*ValVer* application).

While these applications would traditionally have required physical wave tank experiments, the *HiFiWEC* offers some advantages compared to its physical counterpart. The *HiFiWEC* can eliminate undesired influences of measurement equipment and the test environment, e.g. the unrepeatability of experiments [355], reflections from tank walls [356] and magnified friction effects from device restraints at small scale [185], but also has an ability to evaluate devices at full scale [357]. Also, the difficulty in evaluating the performance of full-scale PTO systems, and their impact on WSHIs, in wave tank experiments [358], is overcome in the *HiFiWEC*.

In contrast, it should also be noted that, due to the high computational cost, this high-fidelity platform is less useful for (based on the seven applications defined in the introduction of Chapter 2):

b.i) assessment of power production capabilities across a wide range of sea states (*PowAss* application),

b.ii) design of energy maximising control strategy (*MBC* application), or

b.iii) any kind of optimisation purpose (*MBC* or *PTOopt* applications).

Similarly to the *cHyW2W* model presented in Chapter 6, the validation of the *HiFiWEC* is accomplished by validating the CNWT and the *cHyPTO* model separately. The validation of the *cHyPTO* model is presented in Chapter 5, while the setup of the CNWT is first verified by comparing the performance of a WEC simulation in the CNWT against results of a BEM model [188, 359, 360], and then validated against physical experiments of a 1:10 scale WEC in [361, 362]. It should be noted that the implementation and the validation of the CNWT model are taken from previous publications and, as a consequence, are not an original contribution of this thesis. However, the setup of the CNWT is thoroughly described in Section 7.2.2, to demonstrate the high-fidelity level of the results obtained from the CNWT implemented in the *HiFiWEC*.

7.1.1 CFD-based numerical wave tank

The CNWT model in the *HiFiWEC* is based on the open-source CFD software, OpenFOAM [318]. The OpenFOAM based CNWT captures relevant hydrodynamic non-linearities when simulating WEC operation, by numerically solving the incompressible RANS equations using a cell-centred finite volume method. The RANS equations describe the conservation of mass and momentum, derived from Equations (2.2) and (2.3), respectively, given as:

$$\nabla v = 0, \tag{7.1}$$

$$\frac{\partial v}{\partial t} + (v\nabla)v = -\frac{1}{\rho_w}\nabla p_f + F + \frac{1}{\rho_w}\nabla T, \tag{7.2}$$

where T is the viscous stress tensor.

Turbulence is included in the CNWT using a *k-omegaSST* turbulence model, which is the most commonly employed turbulence model for WEC applications [139], and utilises the *kqR-WallFunction* for turbulence effects on the WEC boundary. The CNWT uses the *interDyMFOAM* solver to iteratively solve the RANS equations using the PIMPLE algorithm [363], and employs the VOF method to account for the two fluid phases in the CNWT (air and water) and capture the free surface interface.

The *interDyMFOAM* solver allows dynamic mesh deformation to accommodate the motion of the WEC within the numerical domain. The WEC motion, due to input waves and PTO forces, is calculated using the *sixDoFRigidBodyMotion* solver [364]. A range of numerical wave makers are available in OpenFOAM to generate and absorb waves [365]. For the present case study, the relaxation method is employed, via the *waves2Foam* toolbox [366], where target solutions for surface elevation and the velocity field are relaxed into the computational domain. Full details of the CNWT implementation can be found in [367].

7.1.2 Power take-off model

The variable-pressure *cHyPTO* model included in the *HiFiWEC*, and its implementation in Matlab, are thoroughly described in Chapters 4 and 6, respectively.

7.1.3 Platform coupling

The CNWT and the *cHyPTO* model are implemented on different software platforms, OpenFOAM and MATLAB®, respectively. Therefore, a communication channel, enabling the coupling between the CNWT and the *cHyPTO* model, is required. The coupling is achieved following similar procedures presented in [359, 368]. The method was first demonstrated in [368], where mooring forces on a floating WEC are calculated in MATLAB®, at each time-step of an OpenFOAM CNWT simulation. Similarly, OpenFOAM and MATLAB® are coupled in [359] for the evaluation of energy maximising control strategies, where an adaptive receding horizon pseudospectral control algorithm is implemented in MATLAB® to calculate the optimal PTO force applied to the absorber at each CNWT time-step.

The coupling is driven by the CNWT model, where, at each time-step, the CNWT simulation pauses, passes information to the *cHyPTO* model (t_{sim}, z_d and $\dot{z}_d$ at that time-step, as illustrated in Figure 7.2), and waits for the *cHyPTO* model to calculate and return F_{pis} at that time-step, before continuing. The CNWT adds $\tilde{F}_{pis}$, the interpolated F_{pis}, to the sum of fluid and gravity forces, and determines the total force acting on the absorber, from which the acceleration of the absorber and its resulting motion is calculated using the *sixDoFRigidBodyMotion* solver in OpenFOAM.

Due to the different time-integration solvers and time-steps implemented in the CNWT and the *cHyPTO* model, interpolation of the variables going through the communication channel is required. Similar interpolation procedures are also required in the *cHyPTO* model due to the MR scheme, as described in Section 6.1.1.1, where *linear* interpolation is demonstrated to be sufficiently accurate and computationally efficient. Therefore, *linear* interpolation is also used in the inter-software coupling between the CNWT and the *cHyPTO* model. A verification test is conducted in Section 7.2.1.1 to certify the satisfactory performance of the coupling.

7.2 Case study

The case study utilised to demonstrate the performance of the *HiFiWEC* considers the spherical HPA presented in Section 3.1.3, which is restricted to heave motion, similarly to the study presented in Section 6.2. The *HiFiWEC* is analysed for two different test cases, described in Section 7.2.1, where the same absorber connected to the same HyPTO system is used. The essential CNWT setup is also the same for both test cases, where only the size of the NWT and the mesh stretching ratio of the creation zone vary from one test case to the other (both are defined according

to the wavelength of the incoming wave, which is different in each test case). Therefore, in order to avoid repetition, the case study is described in this section for both test cases, including the CNWT setup and the design of the HyPTO system described in Sections 7.2.2 and 7.2.3, respectively.

7.2.1 Test cases

A verification test case is designed to ensure that the inter-software coupling between the CNWT and the *cHyPTO* model is implemented correctly and performing as expected. On the other hand, an evaluation test case is created to demonstrate the importance of utilising a high-fidelity simulation platform as the *HiFiWEC*.

7.2.1.1 Verification test case

The verification of the inter-software coupling is carried out by comparing results from the *HiFiWEC* to those obtained from a BEM-based HyW2W model with a linear WSHI model, referred to as the *LBEMW2W* model. The *LBEMW2W* model is similar to the $NLBEMW2W_{Cd=1}$ model presented in Section 6.2.2, except for the WSHI model, which is replaced with the linear model presented in Equation (3.28). Therefore, the viscous effects and nonlinear FK forces are neglected in the *LBEMW2W* model.

The *LBEMW2W* is implemented exclusively in MATLAB and, therefore, does not require any inter-software coupling as in the *HiFiWEC*. The mathematical model for the HyPTO system in the *LBEMW2W* model is the same as that in the *HiFiWEC*, so any variation in the results will arise due to differences in the hydrodynamic models or errors in the inter-software coupling of the *HiFiWEC*. Therefore, by choosing an input wave that ensures a linear hydrodynamic response of the absorber, any discrepancy between the *HiFiWEC* and the *LBEMW2W* models can be attributed to an erroneous inter-software coupling in the *HiFiWEC*.

To ensure linear hydrodynamic absorber behaviour, it is important to minimise variations in the wetted surface area, resulting in a perfect wave following absorber. This condition can be met with long waves of small amplitude, whose period is far from the absorber's natural period (3.17s in the case of the spherical HPA). However, the longer the wave, the higher the computational cost of the CNWT simulation, since a longer tank is required to ensure that waves are adequately generated and absorbed. Therefore, a monochromatic wave of 12s period and 0.5m height, illustrated in Figure 7.3 (a), is selected as a reasonable trade-off between wavelength and computation time, while ensuring linear absorber behaviour in the verification test.

Similarly, $\tilde{F}_{pis}$ applied to the absorber should not enhance the relative motion between the WEC and the water surface. However, a realistic $\tilde{F}_{pis}$, achievable by the HyPTO system utilised in the case study, needs to be applied in order to properly test the CNWT-*cHyPTO* coupling. A linear PTO damper, following Equation (6.2), with a $B_{PTO} = 100$kN is used, which is found to ensure proper operation of the HyPTO system and linear hydrodynamic behaviour of the absorber. Figures 7.3 (b) and (c) illustrate the excitation force and the displacement of the spherical HPA, respectively, using linear and partially nonlinear BEM-based WSHI models, the LPF and *viscNLFK* models presented in Chapter 3, respectively. Results for the linear and nonlinear WSHI models are shown to be identical, confirming the linear behaviour of the absorber for the input wave and the B_{PTO} coefficient value selected in the verification test case.

7.2.1.2 Evaluation test case

The evaluation test case considers a more realistic input wave signal, similar to the ME sea-state defined in Table 6.2 ($H_s = 1.5m$ & $T_p = 8s$), which corresponds to the sea-state with the highest occurrence in actual open-ocean sites, such as BIMEP in the Bay of Biscay, or Lisbon, in the Atlantic Ocean [183]. The ME polychromatic wave of $H_s = 1.5m$ and $T_p = 8s$, used in the evalua-

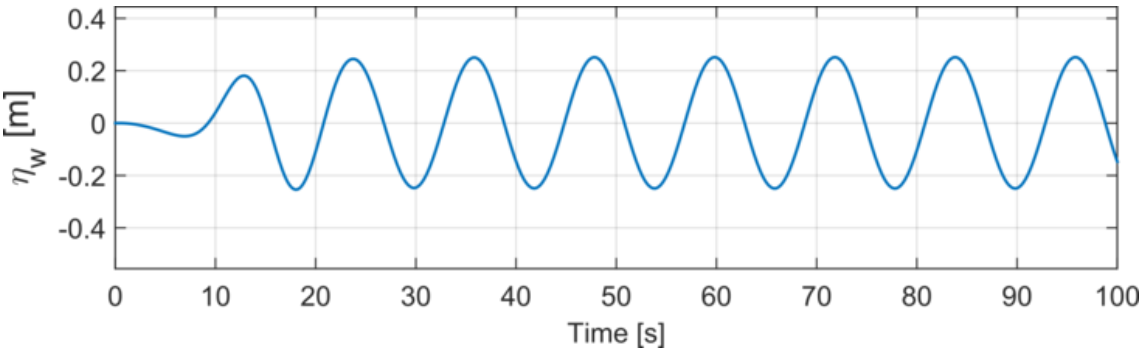

(a) Input waves.

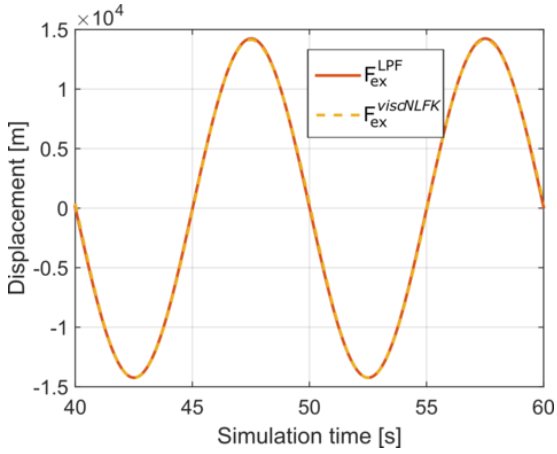

(b) Excitation force

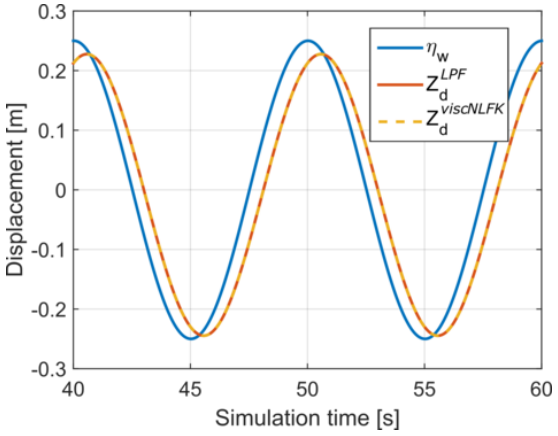

(c) Absorber displacement

Figure 7.3: The free-surface elevation signal for the verification test case (a), and the certification of the linear hydrodynamic behaviour of the absorber in the verification test case, comparing linear and nonlinear BEM-based WSHI models for excitation force (b) and displacement of the absorber (c).

tion test case, is generated using the idealised JONSWAP spectrum [75] with a peak-enhancement value $\gamma_J = 3.3$ and is illustrated in Figure 7.4.

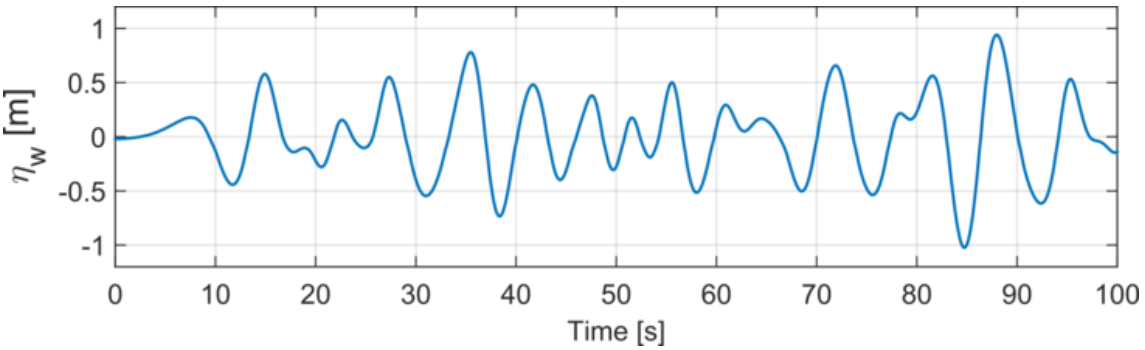

Figure 7.4: Input waves for the verification test case.

To evaluate the *HiFiWEC*, it is compared against four other HyW2W models, listed in Table 7.1, which combine different approaches to model the WSHI and the HyPTO system. In addition to the CNWT approach, the WSHI is modelled using both linear and nonlinear BEM-based models (described in Sections 3.1 and 3.2, respectively), where the latter includes nonlinear FK forces and a quadratic viscous damping term. The HyPTO system is modelled using, both the high-fidelity *cHyPTO* model, presented in Chapter 4, and an ideal HyPTO model, described in Section 6.2.2.

The coupling of the different HyW2W models which include the CNWT, is the same as that described in Section 7.1.3 for the HiFiWEC. However, the HyW2W models that represent the WSHI via BEM-based models, do not require any inter-software coupling, since all the different subsystems of the HyW2W model are implemented in the same environment, *i.e.* MATLAB.

Table 7.1: HyW2W models compared against the *HiFiWEC* in the evalutation test case.

Model name	Description
CNWT+iPTO	A CNWT coupled to an ideal HyPTO model
LPF+iPTO	Linear BEM-based hydrodynamic model coupled to an ideal HyPTO
$NLBEMW2W_{Cd=1}$	The *viscNLFK* BEM model, with $C_d = 1$ and the high-fidelity *cHyPTO*
$NLBEMW2W_{Cd=2}$	The *viscNLFK* BEM model, with $C_d = 2$ and the high-fidelity *cHyPTO*

Similarly to the analysis carried out in Section 6.2, the performance of the spherical HPA is assessed under resistive and reactive control in the evaluation test case, following Equations (6.2) and (6.3), respectively. The optimal B_{PTO} and K_{PTO} are taken from the analysis shown in Section 6.2.2, where control parameters are optimised for the same WEC as considered here, using the $NLBEMW2W_{Cd=1}$ model.

7.2.2 CNWT setup

Details of the CNWT, including wave generation, NWT geometry and mesh, and time-step of the solver, are presented in the following subsections for the two test cases.

7.2.2.1 Wave generation

The waves are first generated in the CNWT without the absorber in the tank, recording the free-surface elevation at the intended absorber position. The η_w signals are illustrated in Figures 7.3 (a) and 7.4. The recorded η_w is used as the input wave signal for the BEM-based models, and the CNWT simulations are run again, using exactly the same wave generation settings, with the absorber positioned in the tank. This ensures that results from CNWT- and BEM-based approaches are compared for identical input wave signals, removing the influence of any small errors in wave height or phase stemming from the numerical wave generation in a CNWT.

7.2.2.2 Tank geometry

For both test cases, the absorber is positioned at the centre of a simulation zone of 10 absorber radii (25m) length and 100m width. However, due to the different characteristic wavelengths considered, the water depth, and the creation and absorption zone lengths are different for each test case, as listed in Table 7.2.

Table 7.2: Numerical wave tank characteristics.

Test case	Wavelength	Creation zone	Absorption zone	Water zone
Verification	225m	337.5m	675m	160m
Evaluation	100m	150m	300m	70m

The length of the wave creation and absorption zones utilised in each test case are parametrised by the wavelength. This wavelength becomes the peak wavelength, the wavelength corresponding to the T_p of the sea-state, in the evaluation test case. Hence, the length of the wave creation zone is 1.5 times the wavelength and the absorption zone 3 times the wavelength. These values are selected based on the parameter study in [320], where the same sea-state used in the evaluation test case is analysed. In the case of the wave absorption zone, increasing the length decreases wave reflection. At a length of three times the peak wavelength the reflection coefficient drops below 1%.

For the wave creation zone, the parameter study in [320] considers a regular wave with the same period and wave height (8s & 1.5m, respectively), for which a wave creation zone of between 1 and 1.5 times the peak wavelength is found to provide the most accurate waves. Thus, the longer creation zone (1.5 time the peak wavelength) is chosen for the analysis, to allow for good absorption of radiated waves from the absorber travelling back towards the wave creation zone and to accurately generate waves in the polychromatic spectrum with wavelengths longer than the peak wavelength.

The wavelength of the verification and evaluation test cases, based on the wave period of the monochromatic wave and the T_p of the polychromatic wave, are 225m and 100m, respectively. The water depth of 70m, for the evaluation test, is chosen to be representative of the depth conditions at the BIMEP test site in the Bay of Biscay. However, in the verification test, for the 12s regular wave, the 70m water depth does not correspond to deep water and the resulting wave would not be completely monochromatic; therefore, the water depth is increased to approximately 70% of the wavelength to ensure deep water conditions.

The computational domain includes a 25m height above the equilibrium water level to the atmospheric boundary. To reduce the computational requirement, a symmetry plane is utilised through the centre of the tank, so that only half of the tank and WEC width is simulated. The influence of the symmetry plane on the body motion is investigated in [361] and found to be negligible.

7.2.2.3 NWT mesh

The mesh of the NWT, illustrated in Figure 7.5, consists of three main vertical regions: the air, the water and the interface region. The interface region is centred at the still water level and has a total height of 10m. The mesh of this interface region includes three different levels of discretisation, being the mesh finest close to the still water level. Hence, the whole interface region is first meshed vertically using uniform cells of height ΔC. These cells are then split in half at a distance of 2.5m above and 4.5m below the still water level, and split into half again 2m either side of the still water level, so that the cells in the region where the free surface will be generated have a height of $\Delta C/4$. Adjacent to the interface region, the mesh is stretched vertically towards the boundaries of the tank, using the grading ratio (GR), defined as the ratio between two subsequent cell sizes in the direction of stretching. In the water region, the mesh is stretched towards the tank floor with $GR = 1.075$. In the air region, the mesh is stretched to the atmosphere boundary with $GR = 1.2$.

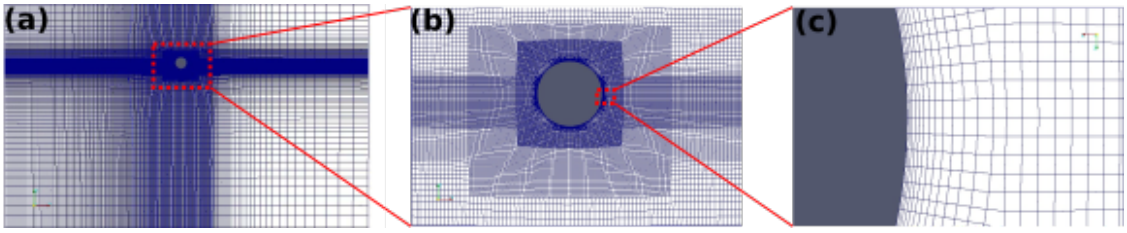

Figure 7.5: (a) The CNWT mesh (b) Zoom in of mesh around the absorber and (c) further zoom in of mesh refinement around absorber to ensure adequate y^+ values.

Horizontally, across the width of the tank, the mesh has a width of ΔC and then is stretched towards the side wall with $GR = 1.1$. Finally, along the length of the tank, the mesh is divided into three regions: creation, simulation and absorption zones. In the simulation zone, the mesh has a constant length of ΔC. In contrast, the meshes of the creation and absorption zones are stretched towards the up- and down-wave tank walls, respectively. The GR of the absorption zone is the same, $GR = 1.1$, for the verification and evaluation test cases, while the GR of the creation zone is larger, $GR = 1.075$, for the verification test case, compared to the evaluation test case, $GR = 1.01$. The reason why different *GR*s are utilised in the two cases is the fact that different wave regimes are used. It is important to have a specific number of cells per wave length, which can easily be determined for a regular wave. However, the wave spectrum utilised to generate the polychromatic wave for the evaluation test case contains a range of frequencies, meaning that the polychromatic η_w includes high-frequency waves with short wavelengths. Therefore, the cell length needs to be smaller for these shorter waves and, as a consequence, a smaller *GR* is used for the evaluation test case.

The *GR* values for the different regions are determined using two-dimensional (2D) trial runs, whereby the tank is only one cell wide, to reduce the overall cell count and allow many fast simulations. The *GR* was incremently increased until the solution began to diverge, identifying *GR* values that provide accurate solutions while ensuring the least amount of cells are used, which is vital for the subsequent three-dimensional simulations.

The mesh in the region around the absorber, illustrated in Figure 7.5 (b), needs to be refined too. Therefore, the cells are split in half in all directions within a box. This box extends a horizontal distance of three absorber radii from the centre of the absorber, and a vertical distance of three and two absorber radii downwards and upwards, respectively, from the centre of the absorber. A second refinement box, extending a distance of 1.5 absorber radii in all directions, is also included, where the cells are split into half again, so that the mesh within this second refinement box around the absorber has cells of length $\Delta C/4$. During this refinement procedure, the vertical cell lengths in the already refined interface regions remained unchanged, as illustrated in Figure 7.5 (b).

Once the structure of the mesh is defined, the value of ΔC needs to be determined. To that end, a mesh convergence study was undertaken, considering the wave generation and propagation for the polychromatic wave used in the evaluation test case (which is the most demanding test case). Three mesh resolutions were investigated, where ΔC was doubled between each mesh, resulting in a coarse ($\Delta C = 0.625m$), medium ($\Delta C = 0.3125m$) and fine ($\Delta C = 0.15625m$) mesh (these ΔC values were chosen as they are factors of 5m, allowing a clean division of the simulation and interface regions). The resulting η_w measured at the centre of the simulation zone, where the absorber is supposed to be placed, is plotted in Figure 7.6, with very little difference observed between the three meshes. However, as shown in the zoom box, results from the coarse mesh differ slightly, at some wave peaks and troughs, from the other two meshes which are shown to converge. Therefore, the medium mesh, with $\Delta C = 0.3125m$, is used for the case study. This relates to 19.2 cells per waveheight, which is consistent with predominant values reported in [139].

The final mesh parameter to be determined is the length of the first cell layer adjacent to the absorber, illustrated in Figure 7.5 (c), which can be adjusted using surface layers growing from the absorber to the background mesh. The length of the first cell layer, in conjunction with the fluid velocity in the cell, determines the non-dimensional wall distance y^+, which is important for the performance of the wall functions used within the turbulence model. The recommended y^+ values are $30 < y^+ < 500$ for fully developed turbulent flows in single phase fluids. However, a y^+ within this range is challenging to obtain in case studies with oscillating flows that include a free surface, as in the case of WECs. The pragmatic approach, generally taken when applying turbulence models to WECs [139], is to perform a sensitivity analysis of the results to these parameters.

Hence, the refinement around the absorber is implemented using an expansion ratio of 1.2 from the absorber to the background. Results for two different meshes, where *Mesh 1* uses 12 refinement layers, resulting in a first cell thickness of $0.010m$, and *Mesh 2* uses 9 refinement layers,

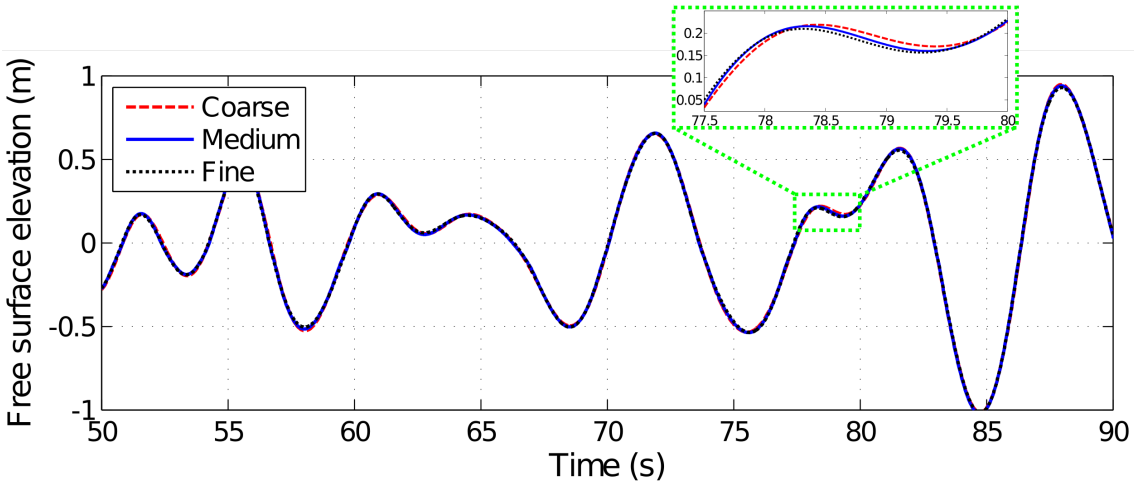

Figure 7.6: Free surface elevation for increasing mesh refinement.

resulting in a first cell thickness of $0.018m$, are shown in Figure 7.7. The y^+ values are calculated every $2s$ (since this requires cell values to be written to memory at each time step, increasing memory requirements and computation time), where the minimum and maximum values from all the cells surrounding the absorber are recorded. *Mesh 1* shows a y^+ range with minima of 16-64 and maxima of 211-478, while the y^+ range of *Mesh 2* includes minima of 44-114 and maxima of 410-835. Therefore, both meshes violate the ideal y^+ range ($30 < y^+ < 500$) in some instances. However, comparing the results depicted in Figure 7.7, one can observe that differences are insignificant, with differences in absorber motion of less than 0.2% at the peaks/troughs. Therefore, *Mesh 1* with a first cell thickness of 0.01m is used for the case study.

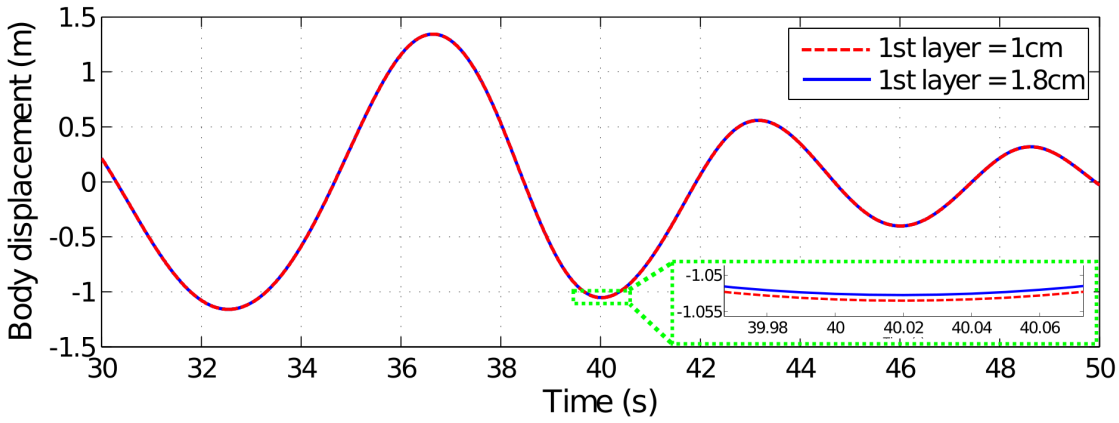

Figure 7.7: Absorber heave displacement for different mesh resolution around the body.

Overall, 1.3 and 1.7 million cells are used for the verification and evaluation test setups, respectively. Despite the large tank used for the verification test, the greater mesh stretching used in the creation zone gives an overall lower number of cells, compared to the evaluation test case.

7.2.2.4 Time-steps

The numerical integration method implemented in OpenFOAM offers the option of either variable- or fixed-step methods, where the variable-step method ensures adherence to a maximum specified Courant number. In this case, the fixed-step option is selected, due to the dependence on time-steps of the wave generation process using *waves2Foam*. Smaller mesh cells lead to smaller time-steps in the variable-step method, and, consequently, slightly different η_w signals are generated by

waves2Foam for cases with different meshes. Therefore, a mesh convergence study is impossible using a variable-step method with the *waves2Foam* toolbox. In addition, when introducing the absorber into the tank, the mesh of the NWT is modified, using smaller mesh cells to capture the boundary layer around the absorber. As a consequence, time-steps would be different for the waves-only and wave+absorber cases, meaning that the generated waves would be different too.

In order to select the optimum time-step, a convergence study is performed. A preliminary convergence study is presented in [320], where the static boundary method for wave generation is used with *waves2Foam*. Windt et al. [320] considers a regular wave with 8s period and 1.5m wave height, on a mesh with similar resolution as the mesh considered here (20 cells per waveheight), and finds a converged fixed time-step value of 0.02s.

For the present study, a further convergence study is required, where the absorber motion / fluid-structure interaction is included. However, if the absorber (the spherical HPA) is driven by waves generated via the wavemaker, the time-step dependence of the wavemaker may alter the convergence study. Therefore, in order to focus on the fluid-structure interaction, the convergence study opts to drive the absorber with the PTO force, as previously performed in [189]. To ensure representative dynamics, similar to the dynamics expected in the verification and evaluation test cases, the PTO force signal generated by the NLBEMW2W$_{Cd=1}$ model under reactive control, is used as the input to the absorber. Time step values of 0.04s, 0.02s, 0.01s and 0.005s are investigated in the convergence study. Results depicted in Figure 7.8 show that 0.01s and 0.005s time-steps provide identical results, which suggests 0.01s is the optimum time-step.

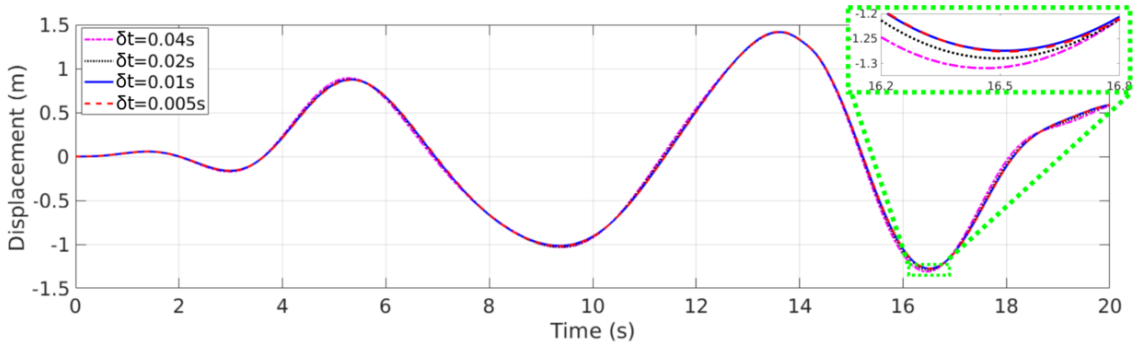

Figure 7.8: Absorber heave displacement for varying time step lengths.

7.2.3 PTO design

The specific design of the variable-pressure HyPTO system used in this case study is the same as that illustrated in Figure 6.10 and described in Table 6.3.

7.3 Verification of the platform coupling

Results from the *HiFiWEC* and the *LBEMW2W* model for the verification test case are compared in Figure 7.9, where the absorber heave displacement and the PTO force are plotted in Figures 7.9 (a) and (b), respectively, showing that the *HiFiWEC* and the *LBEMW2W* model agree extremely well for simulation times $t > 30s$.

The difference within the first 30s arises due to the way in which the BEM-based model interprets the input wave signal. The hydrodynamic coefficients for the BEM-based model are calculated using a frequency domain approach, where the excitation on a body for each frequency assumes interaction with a fully developed wave field of that single frequency. Therefore, the wave field exists both up-wave and down-wave from the body. However, for the CNWT, when the wave initially starts to interact with the body due to the up-wave pressure field, the fluid pressure on the

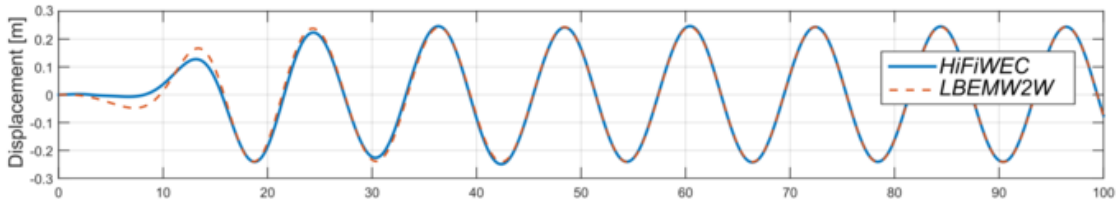

(a) Absorber displacement

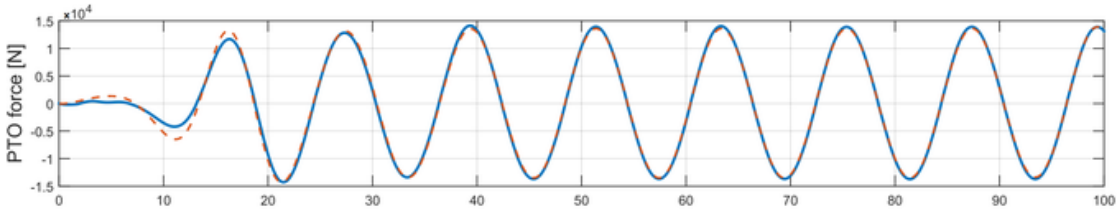

(b) PTO force

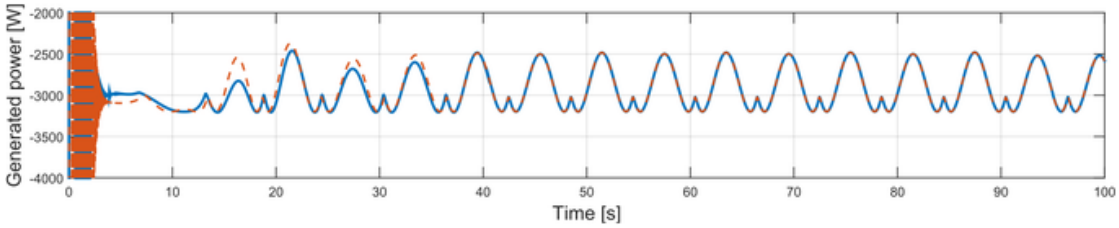

(c) Generated power

Figure 7.9: Verification test case results from the *HiFiWEC* and the *LBEMW2W* models for (a) displacement, (b) PTO force and (c) generated power.

down-wave side of the absorber is still at rest and, thus, the response of the absorber in the CNWT is inferior to that of the linear BEM model.

To complete the verification of the *HiFiWEC*, generated power signals obtained from the *HiFiWEC* and the *LBEMW2W* model are compared in Figure 7.9 (c). A notable characteristic of the generated power signal, for both models, is the high frequency oscillation during the first 5s. These oscillations correspond to the start-up of the induction generator, where the generator is accelerating until it reaches synchronous rotational speed. Once the generator is operating at synchronous speed, steady-state is reached at around 30s in the *LBEMW2W* model, while it takes about 10s longer in the *HiFiWEC*. Results again show a perfect match in steady-state. Thus, the correct performance of the coupling in the *HiFiWEC* is verified.

7.4 Evaluation of the *HiFiWEC* platform

For the evaluation test case, the WEC hydrodynamic behaviour and power generation, simulated by the *HiFiWEC*, is compared against the four other HyW2W models presented in Table 7.1. To remove any irrelevant initialisation effects, results are analysed for $t \geq 40s$, based on the observation from the verification test case.

The results from resistive control simulations are shown in Figure 7.10. The hydrodynamic behaviour of the WEC, illustrated by the body motion in Figure 7.10 (a), is similar for all five simulations. However, a small difference can be seen between the CNWT- and BEM-based approaches, highlighted in the zoomed snapshot in Figure 7.10 (a). With respect to the PTO force, Figure 7.10 (b) shows that, under resistive control, the force applied by the PTO system to the absorber is almost identical in all the HyW2W models. Small discrepancies can be observed between CNWT- and BEM-based approaches, likewise in Figure 7.10 (a), suggesting that discrepancies in the PTO force are mainly caused by differences in the hydrodynamic model.

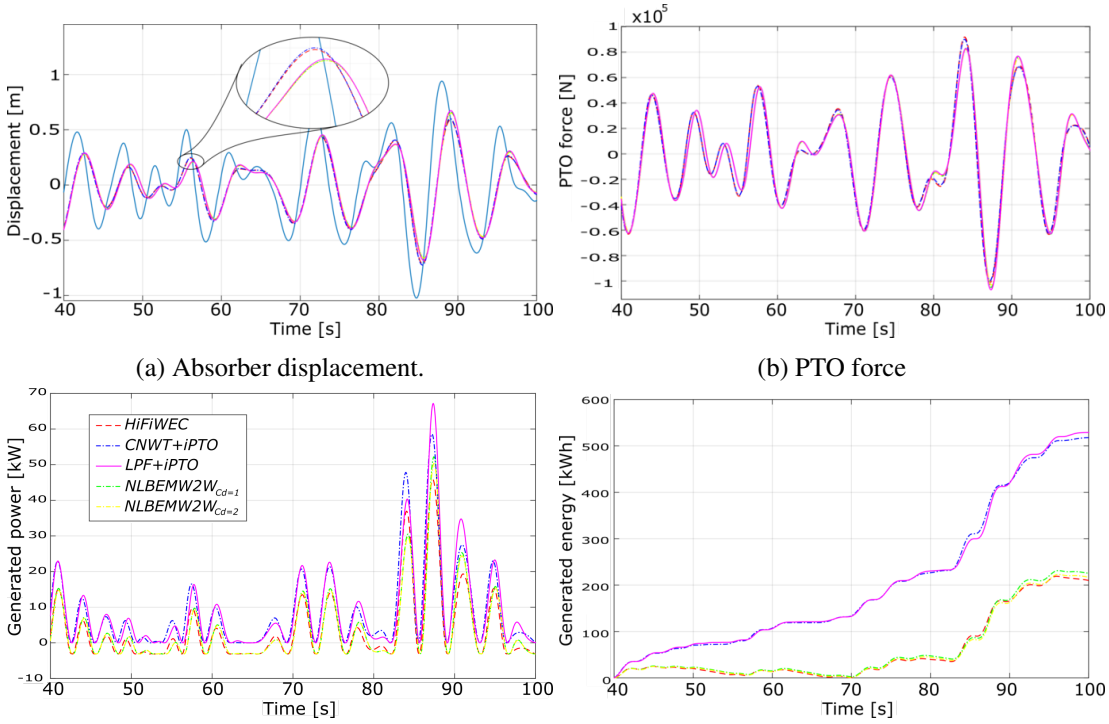

(a) Absorber displacement.

(b) PTO force

(c) Generated power.

(d) Generated energy.

Figure 7.10: Comparing results from the 5 different HyW2W models for (a) displacement, (b) PTO force, (c) generated power and (d) generated energy under resistive control.

However, although the impact of the high-fidelity *cHyPTO* model is negligible, with regard to PTO force, it significantly affects the generated power and energy estimates, as illustrated in Figures 7.10 (c) and (d). For example, generated power signals corresponding to the HyW2W models with the ideal PTO are always positive, while the power signals, corresponding to the HyW2W models with the high-fidelity HyPTO, reach negative values. Negative values in the simulation models with the high-fidelity HyPTO, also seen in Section 6.2.3, appear due to the need to draw energy from the electricity grid to keep the electric generator rotating at synchronous speed (1500rpm) when the mechanical energy is zero or close to zero. On the other hand, differences in the power peaks, between the HyW2W models with the ideal and the high-fidelity *cHyPTO* models, correspond to energy losses considered in the high-fidelity *cHyPTO* model, which result in significantly lower generated power peaks. The cumulative generated energy plotted in Figure 7.10 (d) illustrates that the HyW2W models with the ideal HyPTO model significantly overestimate power generation (by more than 100%), compared to the results from the HyW2W models with the high-fidelity *cHyPTO* model.

Table 7.3 compares the time-average absorbed and generated power values, P_{abs}^{av} and P_{e}^{av}, respectively, from the different HyW2W models against the values from the *HiFiWEC*, showing the deviation Δ between the different models and the *HiFiWEC*. As mentioned in Chapter 2, absorbed power refers to the mechanical power directly absorbed from ocean waves, which mainly depends on the hydrodynamic behaviour of the absorber, while generated power refers to the electric power output, where the components of the *transmission*- and *generation*-stages also play an important role. Deviation between the *HiFiWEC* and the other HyW2W models is calculated following Equation (6.5), with *HiFiWEC* as the benchmark. Table 7.3 shows low relative deviation values in absorbed power under resistive control, which is consistent with the results shown in Figure 7.10 (a). Regarding the generated power, the *NLBEMW2W* models, regardless of the C_{drag} value, provide results close to the *HiFiWEC*, with a relative deviation of -5.24% and -3.19% for $NLBEMW2W_{Cd=1}$ and $NLBEMW2W_{Cd=2}$, respectively. Interestingly, although $NLBEMW2W_{Cd=2}$ yields closer overall average *generated* power to the *HiFiWEC*, $NLBEMW2W_{Cd=1}$ yields closer

overall *absorbed* power, highlighting the importance of evaluating the overall performance of the WEC.

Table 7.3: Time-averaged absorbed and generated power values obtained from the *HiFiWEC* (in kW) and the deviation in percentage ($\Delta[\%]$) of the different HyW2W models.

HyW2W models	**Resistive control**		**Reactive control**	
	P_{abs}^{av}	P_{e}^{av}	P_{abs}^{av}	P_{e}^{av}
HiFiWEC [kW]	8.60	3.50	23.76	13.99
CNWT+iPTO Δ [%]	-0.32	-146.4	-3.03	-78.36
LPF+iPTO Δ [%]	-2.50	-151.8	-16.32	-97.52
$NLBEMW2W_{Cd=1}$ Δ [%]	-0.51	-5.24	7.60	2.87
$NLBEMW2W_{Cd=2}$ Δ [%]	1.81	-3.19	14.25	11.58

The results from reactive control simulations are shown in Figure 7.11. The hydrodynamic nonlinearities are seen to be enhanced under reactive control, where differences between the absorber motion simulated by the different HyW2W models, shown in Figure 7.11 (a), are more evident compared to the resistive control case. This is also evidenced in Table 7.3, where ΔP_{abs}^{av} increases by about an order of magnitude, compared to the resistive control case for all the different models. Consequently, differences between CNWT- and BEM-based approaches are also more evident in the PTO force profile, compared to the resistive control case, as illustrated in Figure 7.11 (b).

Overestimation of energy generation under reactive control, illustrated in Figure 7.11 (d), by HyW2W models with the ideal HyPTO model, compared to those with the high-fidelity *cHyPTO* model, is not as large as under resistive control. The efficiency of the HyPTO system is higher under reactive control for the input wave analysed in the evaluation test case, where the hydraulic system operates closer to its optimal operation point, due to increased fluid pressure in the hydraulic cylinder and motor. Similar findings are reported in Section 6.2, where η_{HyPTO} is higher under reactive control than under resistive control for similar wave conditions, as shown in Tables 6.6 and 6.5, respectively. As a consequence, the difference between the high-fidelity and ideal HyPTO models is smaller compared to the resistive control case. Similarly, generated power signals in Figure 7.11 (c) also illustrate smaller differences among the different HyW2W models.

An interesting finding is that, unlike under resistive control, ΔP_{e}^{av}, under reactive control, is lower for the $NLBEMW2W_{Cd=1}$ model than for the $NLBEMW2W_{Cd=2}$ model, which illustrates the inconsistency of the viscous model. In addition, ΔP_{abs}^{av}, under reactive control, is higher than ΔP_{e}^{av}, for both the $NLBEMW2W_{Cd=1}$ and $NLBEMW2W_{Cd=2}$ models, as opposed to the resistive control case, where the absolute ΔP_{e}^{av} is always higher. This again shows the inconsistency of the viscous model, which is shown to be particularly inconsistent when the motion of the device is exaggerated via reactive control.

Regarding computational requirements, the runtimes of the *HiFiWEC* are of the same order of magnitude as the *CNWT+iPTO*, because the CNWT is the computationally heaviest part in the *HiFiWEC*. Compared to the BEM-based approaches, both CNWT-based approaches are $O(1000)$ slower than any *NLBEMW2W* approach and $O(10000)$ slower than the *LPF+iPTO* model.

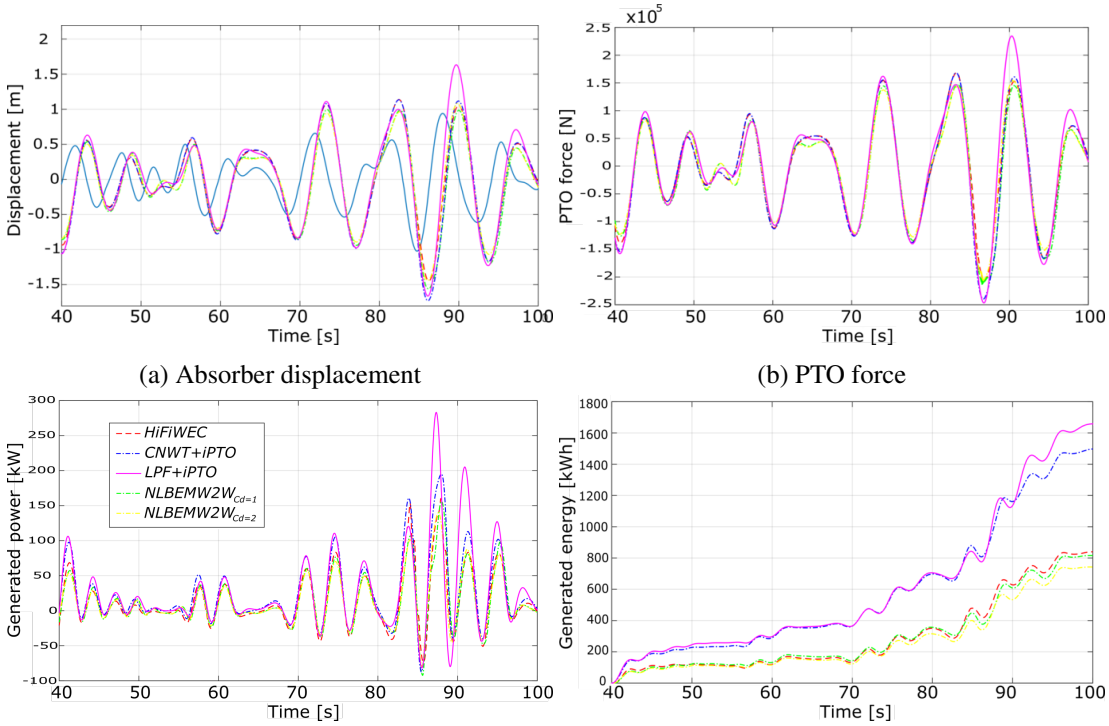

(a) Absorber displacement

(b) PTO force

(c) Generated power.

(d) Generated energy.

Figure 7.11: Comparing results from the 5 different HyW2W models for (a) displacement, (b) PTO force, (c) generated power and (d) generated energy under reactive control.

7.5 Summary and discussion

This chapter presents the high-fidelity HyW2W simulation platform *HiFiWEC*, coupling a CNWT to the high-fidelity *cHyPTO* model presented in Chapter 4, to accurately simulate the holistic performance of WECs. The *HiFiWEC* is first presented in Section 7.1, where potential applications of the platform are discussed. In addition, the different parts that comprise the *HiFiWEC* platform, *i.e.* the CNWT, the *cHyPTO* model and the inter-software coupling, are also described in Section 7.1.

The second part of the chapter (Section 7.2) presents the case study utilised to verify and evaluate the *HiFiWEC* platform, including the absorber, the different test cases and the details of the CNWT and the *cHyPTO* model. The verification of the simulation platform, verifying that the inter-software coupling between the CNWT and the *cHyPTO* model is implemented correctly and performing as expected, is shown in Section 7.3. For this verification, the variables that are shared between the CNWT and the *cHyPTO* model, and the final output of the *HiFiWEC*, are compared against a linear BEM-based mathematical model with the same high-fidelity *cHyPTO* model, under specific conditions. Finally, the *HiFiWEC* platform is evaluated in Section 7.4, comparing the *HiFiWEC* simulation platform to other HyW2W models.

Three potential applications (a.i-a.iii) for high-fidelity simulation platforms, such as the *HiFiWEC*, are mentioned in the introduction of this chapter. Regarding the use of the *HiFiWEC* as a benchmark to validate lower fidelity or computationally more efficient mathematical models (a.i), the results from the evaluation test case in Section 7.4 highlight the relative deficiencies of the different lower fidelity HyW2W modelling approaches, compared to the *HiFiWEC*. Similarly to the results shown in Chapter 6, the *LPF+iPTO* model, one of the most widely used approach in the literature for evaluating the power production of WECs, due to its simplicity and appealing computational requirements, is demonstrated to be highly inaccurate. Large relative deviation between the *LPF+iPTO* model and the *HiFiWEC* arise from excessive simplification of the WHSI and, especially, the HyPTO system.

Comparing the *CNWT+iPTO* model with the *HiFiWEC* isolates the importance of including a high-fidelity HyPTO model. The results show that neglecting the dynamics, constraints and losses of the HyPTO system, can lead to significant overestimation in the generated power output, up to 146% and 78% for the resistive and reactive control cases, respectively. Conversely, comparing the *NLBEMW2W* models to the *HiFiWEC*, isolates the importance of using the CFD approach to model the WSHI. The results show that using the BEM-based *viscNLFK* approach, which includes nonlinear FK forces and viscous effects, can reduce the deviation Δ in absorbed power to 7.6%, compared to the *HiFiWEC*. Therefore, for the particular absorber, HyPTO system and operating cases considered in this chapter, including the high-fidelity *cHyPTO* model, is seen to have a much larger influence on improving the accuracy of the simulated W2W system, compared to including the high-fidelity CFD model.

However, the *HiFiWEC* not only incorporates the individual benefits of high-fidelity WSHI and HyPTO models, but also offers the unique possibility of evaluating the holistic performance of a complete WEC system in high-fidelity. The significance of this is highlighted in Table 7.3, showing that the deviation in *NLBEMW2W* models alternates from absorbed to generated power, even though the HyPTO model is identical in the *HiFiWEC* and the *NLBEMW2W* models. This is relevant, since it implies that analysing the hydrodynamic WSHI and the HyPTO system independently, even with high-fidelity approaches, does not necessarily provide accurate results.

The price for such a high-fidelity platform is a high computational cost. Comparing the *HiFiWEC* to the *NLBEMW2W* models reveals a 1000-fold increase in run time. However, the results in the case study show a relative deviation in generated output power of 3-12%, which varies depending on the C_{drag} value and on the operating conditions (for example, the use of resistive or reactive control). A similar issue is also identified in [184], where the difficulty in consistently and accurately including viscous effects in BEM-based models is discussed. In this respect, the *HiFiWEC* is useful for the second application identified in the introduction of this chapter (a.ii): system identification purposes.

Despite the possibility of designing computationally more efficient mathematical models with reasonably low deviation, as shown in this chapter, some nonlinear effects can only be captured using fully-nonlinear approaches. Under certain circumstances, the performance of the best BEM-based approach, with the optimum C_{drag} value, may still provide inadequate results. Indeed, the spherical HPA analysed in this chapter is intentionally simple for demonstrative purposes whereas, in general, many WECs are significantly more complex, with several degrees of freedom and/or complicated geometries. In addition, the effect of mooring lines, which can influence the dynamical behaviour of the WEC, is often required (in which case the *HiFiWEC* must be extended to include coupling to high-fidelity mooring models [369]).

Finally, the suitability of the *HiFiWEC* to evaluate the efficacy of control strategies in realistic conditions (a.iii), is also demonstrated in this chapter. Apart from the differences among the different modelling approaches, the importance of actively controlling the WEC is clearly illustrated in Table 7.3, where the average generated power in the reactive control case is shown to be significantly higher (about 40% higher) than the average absorbed power in the resistive control case. This suggests that actively controlling the WEC will always result in a higher generated power, regardless of the efficiency of the HyPTO system. In addition, one can observe in Table 7.3, that the deviation for the absorption stage is very low for all the different mathematical models under resistive control, while increasing considerably under reactive control. Therefore, it can be concluded that an accurate representation of WSHIs, including all the nonlinear effects, is particularly important when the device is actively controlled to maximise the energy generation, as reported in Chapter 3.

Hence, the *HiFiWEC* is a vital numerical tool for the design of WECs with a high TPL in the early stage of (TRL) development, where open sea experimental tests are prohibitively expensive. As a complement to physical small-scale wave tank experiments, the *HiFiWEC* allows for a high-fidelity evaluation of the overall performance of full-scale WECs, including the dynamics, losses and constraints of the PTO system.

Chapter 8

Complexity reduction of wave-to-wire models

The high-fidelity HyW2W simulation platform *HiFiWEC*, presented in Chapter 7, provides a platform for accurately evaluating the holistic performance of a WEC, improving the results obtained from the *cHyW2W* model designed in Chapter 6, named as $NLBEMW2W_{Cd=1}$. Nevertheless, the price for such high-fidelity results obtained with the *HiFiWEC* is a significantly high computational cost, about three orders of magnitude higher than the $NLBEMW2W_{Cd=1}$ model, as shown in Chapter 7.

However, W2W models are required for several different applications, as described in the introduction to Chapter 2, which have potentially diverse requirements. Specific requirements of these potential applications are shown in Table 8.1, where the different requirements are organised into three main categories: accuracy and computational cost (Comp. cost in Table 8.1), specific dynamics and losses, and nonlinear effects, where nonlinear effects refers to the implications that nonlinear effects have in each application. For example, high-fidelity generated energy estimation (E_{gen}) is required for *ValVer* and *Ident*, including all the dynamics and losses from ocean waves to the electricity grid, and the computational cost of the mathematical model is largely irrelevant, since only few simulations are normally computed in these applications. Therefore, the *HiFiWEC* is the perfect simulation platform for *ValVer* and *Ident*, as stated in Chapter 7.

Table 8.1: Specific requirements of the potential applications that demand W2W models.

	Accuracy & Comp. cost		Specific dynamics & losses					
Potential applications	E_{gen} fidelity	Low comp. cost	WSHI	Hydraulic system dynamics	Hydraulic system losses	Electrical dynamics	Electric generator losses	Nonlinear effects
ValVer	+++	- - -	✓	✓	✓	✓	✓	✗
Ident	+++	- - -	✓	✓	✓	✓	✓	✓
SimWEC	++	-	✓	✓	✓	✓	✓	✗
PowSyst	++	-	✗	✗	✓	✓	✓	✗
MBC	++	+++	✗	✗	✓	✗	✓	✓
PowAss	++	++	✗	✗	✓	✗	✓	✗
PTOopt	++	++	✗	✓	✓	✗	✓	✗

However, the other applications presented in Table 8.1 require faster simulation models, as categorised in Section 2.6 for WSHI approaches. However, the need for low computational cost is less restrictive for some applications, such as *SimWEC* and *PowSyst*, compared to *MBC*, *PowAss* and *PTOopt*. In fact, modest computational cost is not the main requirement for *SimWEC* and *PowSyst*, but the inclusion of specific dynamics and losses. All dynamics and losses are important for *SimWEC*, while only losses in the HyPTO system and electrical dynamics of the electric

generator are necessary for *PowSyst*.

In contrast, reasonably fast mathematical models are essential for *PowAss*, *PTOopt* and, particularly, *MBC*, while relatively high-fidelity E_{gen} is required in all the three applications. In the case of *MBC* and *PowAss*, only the losses in the HyPTO system are necessary, while hydraulic system dynamics are also required for *PTOopt*, since evaluating the wear of the HyPTO components is crucial for the optimisation of PTO components. With respect to the impact of nonlinear effects, they are important only for *Ident* and *MBC*.

Unsurprisingly, Table 8.1 shows that reasonably high-fidelity results are required in all the applications, while low computational cost requirements are quite restrictive for some applications. However, combining high-fidelity and low computational cost in a mathematical model is a challenging task. Figure 8.1 illustrates the ideal fidelity/complexity characteristics of the application requirements and the modelling approaches commonly used for these applications, where the fidelity of the commonly used mathematical models is shown to decrease dramatically as complexity decreases. Thus, the discrepancy between the requirements and the usual models used for the applications is shown in Figure 8.1 to be significant, for certain applications.

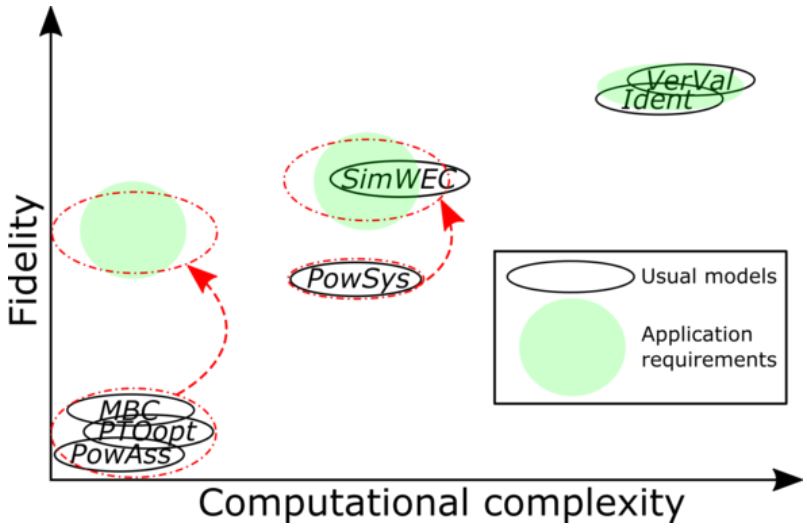

Figure 8.1: Fidelity/complexity trade-off of application requirements and the modelling approaches commonly used for these applications.

In order to fulfil all the requirements for each potential application, parsimonious HyW2W models specifically designed for each application are necessary. To that end, this chapter presents an application-sensitive *systematic* CR approach, using the *HiFiWEC* as the starting point for the *systematic* CR. Hence, the complexity level is systematically reduced to an acceptable level, while attempting to maximally retain those fidelity aspects of the model crucial to the application.

The complexity of a mathematical model ($\mathcal{C}$) depends on a number of aspects, such as the order of the dynamic system or the number of equations included in the model ($\mathcal{N}$), the nonlinearity degree of the system (χ), and the computational cost ($\mathcal{T}$).

$$\mathcal{C} = f(\mathcal{N}, \chi, \mathcal{T}), \tag{8.1}$$

where the determination of $\mathcal{N}$ and $\mathcal{T}$ is straightforward, and χ can be calculated via the nonlinearity measures described in Section 8.1. However, the relative weight of each component in $\mathcal{C}$ is very application-specific, meaning that a generic complexity measure is unattainable.

Complexity reduction techniques in the literature include model order reduction (MOR) approaches, linearisation techniques, and identification of compact parametric models utilising data from experiments or from well-established high-fidelity numerical models. Different MOR techniques can be classified into two main groups [370]. On the one hand, there exist singular-value-

decomposition-based methods, such as the balanced truncation [371], the Hankel-norm approximation [372], or the proper orthogonal decomposition (POD) [373]. An extension of the balanced truncation approach, the balanced POD, has also been recently suggested to deal with cases where a balanced truncation becomes complicated [374]. On the other hand, MOR techniques, based on approximation by moment matching, have been suggested [375], which are claimed to be numerically more efficient and reliable [376]. Specific to the wave energy field, research studies that apply these MOR techniques are scarce, to the best of the author's knowledge. One of the very few examples is [377], which applies the balanced POD technique to reduce a nonlinear WEC model implemented using a finite element method. The reduced-order model is then used to design an optimal controller for a WEC. Also with the aim of designing an optimal controller for a WEC, a moment matching approach is applied to a linear WEC model in [345].

Linearisation techniques are used in several different fields [378], providing a linear approximation of a nonlinear dynamical system around an operation point. These linearisation techniques are particularly appropriate for *MBC*, allowing for a control strategy based on linear control theory. However, due to the extreme variability of the wave resource, WECs do not have specific piecewise constant operating points, meaning that linearisation techniques are not as useful as in other fields. An extension to linearisation techniques in wave energy is the use of multi-linear or linear parameter-varying models, named as *mLPF* models in Section 2.2, defining multiple linear models for different operational points and switching between these linear models, depending on the operational space, as suggested in [160]. Finally, parametric models can be identified from input/output data generated from real processes or high-fidelity numerical platforms, as described in Section 2.2.3.3.

In this chapter, the measures for quantifying the nonlinearity degree of W2W models are presented in Section 8.1, using the *best linear approximation* identified through a minimisation problem. Two measures are suggested, *i.e.* the *original* and the *power* nonlinearity measures, where the *original* nonlinearity measure evaluates the nonlinear effects of the WSHIs and the *power* nonlinearity measure quantifies the nonlinear effects of the whole drivetrain with a power metric, including all the conversion stages from waves to the electricity grid.

The *systematic* CR approach is presented in Section 8.2, which is divided into two parts, where the *systematic* CR is applied to the WSHI and the HyPTO subsystems in Sections 8.2.1 and 8.2.2, respectively. Based on the reduced WSHI and HyPTO models, balanced reduced HyW2W models, that is, HyW2W models with a similar complexity/fidelity level for all the different subsystems of the drivetrain, are created in Section 8.2.3. Once different balanced reduced HyW2W models are created, the selection process, to allocate the optimum reduced model for each application, is presented in Section 8.2.4, which is divided into three steps: evaluation of computational cost and fidelity, examination of the specific dynamics required for each application, and quantification of the nonlinearity degree. Finally, the different balanced reduced HyW2W models are evaluated in Section 8.3, identifying the corresponding *Specific HyW2W* model to each application presented in Table 8.1.

8.1 Nonlinearity measures

The identification and quantification of nonlinear effects is crucial for *Ident* and *MBC*, since the inclusion of nonlinear effects may overcomplicate the structure of *ParaM*s or the identification process, and the control strategy, respectively. In the case of *Ident*, all the relevant nonlinear effects must be covered by the HyW2W model used for *Ident*, so that the identified model captures all the information, including nonlinear effects. In contrast, nonlinear effects should be linearised whenever possible for *MBC*, since including nonlinear effects in the controller significantly complicates the design of the controller. The first implication of including nonlinearities in the model used for *MBC* is the substantial increase in the numerical optimisation computation time [379],

which may challenge the real-time operation. In addition, regardless of the computation time, the optimisation problem may become non-convex when nonlinear effects are included [343].

8.1.1 A survey of nonlinearity measures

The degree of nonlinearity of a system can be analysed through nonlinearity tests, evaluating the degree of violation of a property that is specific to linear systems. In this area, [380] describes coherence analysis and [381] presents a variety of methods, such as a frequency method analysing the presence of sub-harmonics, and methods based on linear correlation and linear spectral density.

Alternatively, a nonlinearity measure can be employed, which, unlike a binary nonlinearity test, provides a means to quantify the nonlinearity degree of a nonlinear system. Several approaches to evaluate nonlinearity of dynamic systems have been suggested in the literature. A review of these different approaches is presented in [382], where different methods to evaluate nonlinearity are divided into two main groups: time-series-based and model-based methods.

Time-series-based approaches only use the output time-series of a process to evaluate nonlinearity. Indeed, one of the main benefits of time-series-based approaches is that no process model is required. Three main time-series-based methods have been suggested, based on bicoherence [383, 384], surrogate data [385], and harmonic analysis approaches [386]. Although time-series-based approaches only require the output data of the process to evaluate the nonlinearity of the system, this output data often needs to be adjusted (e.g. using correction factors that may include bias errors), or extended (e.g. generating synthetic or surrogate data).

Conversely, model-based approaches quantify the nonlinearity degree based on the input-output relationship of a nonlinear system. A *curvature measure* was first presented in [387] and extended in [388], where the nonlinearity of a process is quantified by measuring the first and second order sensitivities of the process model. This sensitivity is measured by analysing the contribution of the higher-order terms of the Taylor expansion of a nonlinear operator, relative to the contribution of the first-order terms. Thus, the *curvature measure* requires a Taylor expansion of the nonlinear system, which may be extremely complicated if the nonlinear system consists of different interconnected nonlinear subsystems, as is the case in the current application.

Other model-based approaches suggested in the literature measure the degree of nonlinearity by comparing the input-output behaviour of a nonlinear system to the *best linear approximation* of that nonlinear system. The first contribution to the identification of a *best linear approximation* is presented in [389], and several authors have used the same definition since then. The need for nonlinear models for modelling and control applications is studied in [390, 391], where variations of the *best linear approximation* are evaluated for different inputs. Similarly, the *best linear approximation* for the *worst input* case is defined in [392]. A generalisation of the approach suggested in [392] is presented in [393], which can be applied both to steady-state operation points and trajectory-dependent analyses.

8.1.2 Nonlinearity measures for wave energy

Among the different options presented in Section 8.1.1, nonlinearity tests appear to be a good option to identify whether the system is nonlinear or not, but do not provide a means to quantify the nonlinearity degree and, as a consequence, are not suitable for the present application. Time-series-based approaches only require output data, but often need to be somewhat subjectively adjusted, which can distort the results. Thus, time-series-based approaches are also discarded. In the category of model-based methods, the *curvature measure* requires the Taylor expansion of the nonlinear system, which is quite complicated in the present case. Therefore, the model-based comparative approach, based on the *best linear approximation*, suggested in [393], appears to be the sensible choice for the quantification of nonlinear effects in W2W models, especially if a W2W model is already available (the *cHyW2W* model).

8.1.2.1 *Original* nonlinearity measure

The definition of the nonlinearity measure presented in [393], which is a generic measure that can be used for any finite-dimensional multi-variable dynamic system, is summarised in this section. In this thesis, the nonlinearity measure suggested in [393] is referred to as the *original* nonlinearity measure, and is applied to WECs, which can be described by a set of nonlinear ordinary differential equations.

Hence, a nonlinear WEC model can be represented by a state-space description as follows,

$$\begin{aligned} \dot{\mathbf{x}}_N(t) &= \mathbf{f}(\mathbf{x}_N(t), \mathbf{u}_N(t)), \quad & \mathbf{x}_N(0) &= \mathbf{x}_{N,0}, \\ \mathbf{y}_N(t) &= \mathbf{h}(\mathbf{x}_N(t), \mathbf{u}_N(t)), \quad & 0 \leq t &\leq t_f, \end{aligned} \tag{8.2}$$

where $\mathbf{f}$ and $\mathbf{h}$ are vector mappings, and $\mathbf{u}_N$, $\mathbf{x}_N$, $\mathbf{x}_{N,0}$ and $\mathbf{y}_N$ the inputs, states, initial conditions and outputs of the nonlinear system, respectively. The system can be evaluated for a finite or infinite time interval ($t_f \leq \infty$). In this nonlinear system, $\mathbf{u}_N$ consists of elements of the space $\mathcal{U}_a$ of admissible inputs, $\mathbf{x}_N$ belongs to the space $\mathcal{X}$, $\mathbf{x}_{N,0}$ are elements of the space of admissible initial conditions $\mathcal{X}_{0,a}$, and $\mathbf{y}_N$ consists of elements of a normed space of outputs $\mathcal{Y}$.

The nonlinear system presented in Equation (8.2) can be defined using a nonlinear dynamic operator N that maps input signals $\mathbf{u}_N$, with $\mathbf{x}_{N,0}$ initial conditions, into output signals $\mathbf{y}_N$ as follows,

$$\mathbf{y}_N = N[\mathbf{u}_N, \mathbf{x}_{N,0}], \tag{8.3}$$

with $\mathbf{u}_N \in \mathcal{U}_a$, $\mathbf{x}_{N,0} \in \mathcal{X}_{0,a}$, and $\mathbf{y}_N \in \mathcal{Y}$.

To quantify the nonlinearity degree of the system defined with the operator N, the *best linear approximation* needs to be identified for the same input and output dimensions. As a consequence, a linear dynamic operator L can be defined, where L is an element of the time invariant linear space $\mathcal{L}$. Thus, any $L \in \mathcal{L}$ maps the input signals $\mathbf{u}_L$, with initial conditions $\mathbf{x}_{L,0}$, onto the output signals $\mathbf{y}_L$ as follows,

$$\mathbf{y}_L = L[\mathbf{u}_L, \mathbf{x}_{L,0}], \tag{8.4}$$

where $\mathbf{u}_L \in \mathcal{U}_L$, $\mathbf{x}_{L,0} \in \mathcal{X}_{0,L}$, $\mathbf{y}_L \in \mathcal{Y}_L$, $\mathcal{U}_L$ and $\mathcal{X}_{0,L}$ are the spaces of admissible inputs and initial conditions, respectively, and $\mathcal{Y}_L$ is the normed space of outputs.

In the present study, the author is only interested in measuring the nonlinearity of a WEC response at steady-state. Due to the slow variation of the conditions in the ocean, the transient-state can be neglected, as suggested in [345, 394] for energy maximisation control applications. Therefore, zero initial conditions can be assumed ($\mathbf{x}_{N,0} = \mathbf{x}_{L,0} = \mathbf{0}$).

Once the nonlinear and linear systems are defined, the *original* nonlinearity measure is represented as follows,

$$\phi_N^{\mathcal{S}} = \inf_{L \in \mathcal{L}} \sup_{(\mathbf{u},\mathbf{0}) \in \mathcal{S}} \frac{||L[\mathbf{u},\mathbf{0}] - N[\mathbf{u},\mathbf{0}]||}{||N[\mathbf{u},\mathbf{0}]||}, \tag{8.5}$$

with

$$\mathcal{S} = \{(\mathbf{u},\mathbf{0}) : \mathbf{u} \in \mathcal{U}_a, N[\mathbf{u},\mathbf{0}] \in \mathcal{Y}_a\}, \tag{8.6}$$

where $\mathbf{u}$ refers to the common input to the linear and the nonlinear systems, $\mathcal{Y}_a \subset \mathcal{Y}$ is the space of admissible outputs, and $||\cdot||$ is a suitable norm. The nonlinearity measure in Equation (8.5) assumes the existence of $\mathbf{y}$ and the boundedness of all norms for all $(\mathbf{u},\mathbf{0}) \in \mathcal{S}$.

The nonlinearity degree of a nonlinear system is given by the normalised largest difference between the nonlinear system and the *best linear approximation* for the *worst* input. This nonlinearity measure always provides a value between 0 and 1, where 0 means that N behaves as a linear system, and the closer to 1, the more nonlinear N is. A suitable norm applied in Equation (8.5) is the L_2-norm.

However, the computation of ϕ requires the solution of an infinite-dimensional nonlinear *min-max* problem, which is practically infeasible. Therefore, Equation (8.5) needs to be transformed into a finite-dimensional optimisation problem, replacing the *inf*-operator in Equation (8.5) with a *min*-operator.To that end, it is necessary to represent the *best linear approximation* L as a weighted sum of basis functions L_i as follows,

$$L[u_j, \mathbf{0}] = \sum_{i=1}^{m} d_{w,i} L_i[u_j, \mathbf{0}], \tag{8.7}$$

where $\mathbf{d_w} = [d_{w,1}, d_{w,2}, ..., d_{w,m}]$ is the vector of weights. The space spanned by the L_i basis functions should be dense in $\mathcal{L}$. As a consequence, the linear operator L is represented by linear transfer functions L_i, with corresponding time constants T_i,

$$L_i(s) = \frac{1}{1+T_i s}. \tag{8.8}$$

In addition, if an approximated space $\mathcal{S}_c \subset \mathcal{S}$ with a finite number of elements is defined, the *sup*-operator in Equation (8.5) can be replaced by a *max*-operator. Hence, the *inf-sup* problem becomes a *min-max* optimisation problem.

Finally, the *min-max* optimisation problem is transformed into a single convex minimization problem with constraints:

$$\begin{aligned} \theta_N^{\mathcal{S}_c} &= \min_{z \in \mathcal{R}, \mathbf{d} \in \mathcal{R}^m} z, \\ s.t. &\frac{L[u_j, \mathbf{0}] - N[u_j, \mathbf{0}]}{N[u_j, \mathbf{0}]} - z \leq 0, \\ &\forall (u_j, \mathbf{0}) \in \mathcal{S}_c. \end{aligned} \tag{8.9}$$

8.1.2.2 *Power* nonlinearity measure

In wave energy systems, F_{ex} is the typical input ($\mathbf{u}_N$ in Equation (8.3)) for WECs, while the output ($\mathbf{y}_N$ in Equation (8.3)) is typically z_d, $\dot{z}_d$ and/or P_e, as illustrated in Figure 8.2.

The *original* nonlinearity measure can quantify nonlinearities of the WEC system when using z_d or $\dot{z}_d$ as outputs. That way, θ can capture any nonlinearity of the WSHI. However, P_e, described in Equation (6.4) for the simplest representation of the WEC, is represented by a nonlinear combination of the outputs, $P_e = f(z_d, \dot{z}_d^2)$, assuming $F_{PTO} = f(z_d, \dot{z}_d)$ as shown in Equation (6.3). Consequently, using P_e as output results in a θ biased by the nonlinearities in the *measurement* Equation (6.4), rather than being focused on the nonlinearity degree of the WEC system. However, the nonlinearity degree of a WEC, including all the dynamics from waves to the electricity grid, can only be fully assessed using P_e as output. Therefore, for the nonlinearity measure to be appropriate for evaluating the nonlinearity degree of W2W models, θ must be adapted. The adaptation of θ is referred to as the *power* nonlinearity measure in the following. Figure 8.2 illustrates the application areas for the *original* and *power* nonlinearity measures.

Since P_e is obtained by multiplying $\dot{z}_d$ and F_{PTO}, the simplest way to measure the nonlinearity of a system, using P_e as output, is to include that multiplication between $\dot{z}_d$ and F_{PTO} in the nonlinearity measure itself. Thus, two linear operators L_1 and L_2, which represent $\dot{z}_d$ and F_{PTO}

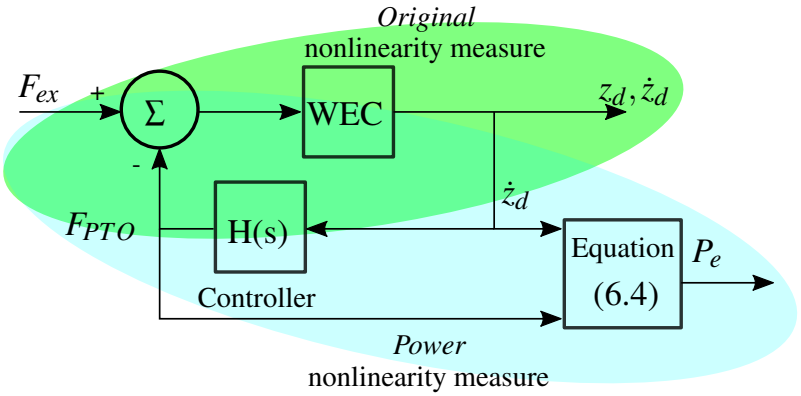

Figure 8.2: Diagram of a WEC, illustrating the applicability of the *original* and *power* nonlinearity measures.

individually, are defined so that the combination of any $L_1 \in \mathcal{L}$ and any $L_2 \in \mathcal{L}$ maps the input signals $\mathbf{u}_{L_{12}}$, with initial conditions $\mathbf{x}_{L_1,0}$ and $\mathbf{x}_{L_2,0}$ into the output signals $\mathbf{y}_{L_{12}}$ as follows,

$$\mathbf{y}_{L_{12}} = L_1[\mathbf{u}_{L_{12}}, \mathbf{x}_{L_1,0}] L_2[\mathbf{u}_{L_{12}}, \mathbf{x}_{L_2,0}], \tag{8.10}$$

with $\mathbf{u}_{L_{12}} \in \mathcal{U}_{L_{12}}$, $\mathbf{x}_{L_1,0}, \mathbf{x}_{L_2,0} \in \mathcal{X}_{0,L_{12}}$, and $\mathbf{y}_{L_{12}} \in \mathcal{Y}_{L_{12}}$.

The new *best* linear system is then formed by the combination of two linear operators L_1 and L_2 ($L_1[\mathbf{u},\mathbf{0}]L_2[\mathbf{u},\mathbf{0}]$), and the *power* nonlinearity measure can be defined as follows,

$$\psi_N^{\mathcal{S}_p} = \inf_{L_1,L_2 \in \mathcal{L}} \sup_{(\mathbf{u},\mathbf{0}) \in \mathcal{S}_p} \frac{||L_1[\mathbf{u},\mathbf{0}]L_2[\mathbf{u},\mathbf{0}] - N[\mathbf{u},\mathbf{0}]||}{||N[\mathbf{u},\mathbf{0}]||}, \tag{8.11}$$

with

$$\mathcal{S}_p = \{(\mathbf{u},\mathbf{0}) : \mathbf{u} \in \mathcal{U}_a, N[\mathbf{u},0] \in \mathcal{Y}_p\}, \tag{8.12}$$

where $L_1[\mathbf{u},\mathbf{0}] : \mathcal{U}_a \times \mathbf{0} \to \mathcal{Y}_a$ and $L_2[\mathbf{u},\mathbf{0}] : \mathcal{U}_a \times \mathbf{0} \to \mathcal{Y}_a$ are two linear dynamic operators belonging to the space of linear operators $\mathcal{L}$. Similarly to the measure presented in Equation (8.5), $\mathcal{U}_a$ and $\mathcal{Y}_a$ are the spaces of admissible inputs and outputs of the two linear operators, respectively. However, the combination of these two linear operators defines a new space of admissible outputs $\mathcal{Y}_p$. In addition, the nonlinearity measure in Equation (8.11) assumes the existence of $\mathbf{y}$ and the boundedness of all norms for all $(\mathbf{u},\mathbf{0}) \in \mathcal{S}$.

Similarly to the measure presented in Equation (8.5), the computation of the *power* nonlinearity measure needs an approximative computation scheme, transforming the practically infeasible infinite-dimensional problem into a finite-dimensional optimisation problem. For this purpose, an appropriate parametrization of the space of the linear operators L_1 and L_2 is chosen, using the weighted sum of basis functions L_i as in Equation (8.7),

$$\begin{aligned} L_1[u_j,\mathbf{0}] &= \sum_{i=1}^{m} d_{w1,i} L_i[uj,\mathbf{0}], \\ L_2[u_j,\mathbf{0}] &= \sum_{i=1}^{m} d_{w2,i} L_i[uj,\mathbf{0}], \end{aligned} \tag{8.13}$$

where $\mathbf{d_{w1}} = [d_{w1,1}, d_{w1,2}, ..., d_{w1,m}]$ and $\mathbf{d_{w2}} = [d_{w2,1}, d_{w2,2}, ..., d_{w2,m}]$ are the vectors of weights of L_1 and L_2, respectively. L_i functions are also represented by linear transfer functions, as shown in Equation (8.8), to ensure that the space spanned by the L_i functions is dense.

Similarly to the *original* nonlinearity measure, the *inf*- and *sup*-operators need to be replaced by *min*- and *max*-operators, respectively. Hence, ψ turns into a single constrained minimization problem,

$$\begin{aligned} \chi_N^{\mathcal{S}_{pc}} &= \min_{z\in\mathcal{R},\mathbf{d_1},\mathbf{d_2}\in\mathcal{R}^m} z, \\ s.t. &\frac{L_1[u_j,\mathbf{0}]L_2[u_j,\mathbf{0}]-N[u_j,\mathbf{0}]}{N[u_j,\mathbf{0}]} - z \leq 0, \\ &\forall (u_j,\mathbf{0}) \in \mathcal{S}_{pc}, \end{aligned} \tag{8.14}$$

where $S_{pc} \subset \mathcal{S}_p$ is the approximated space with a finite number of elements.

That way, the *best linear approximation* obtained from the *power* nonlinearity measure suggested in Equation (8.11) captures the quadratic response of the power signal, and is able to provide the nonlinearity measure expected for a linear model ($\chi = 0$). It is important to note that this coverage of the quadratic response does not distort the nonlinearity measure, since it only covers the quadratic response corresponding to power. Other nonlinearity sources are still captured by the *power* nonlinearity measure.

8.1.3 Verification of the nonlinearity measures

The performance of the *original* and *power* nonlinearity measures is verified by comparing the outputs from WEC models (y_N) and their *best linear approximation* (y_L), and evaluating the nonlinearity degree of WECs' response under different conditions. The first verification is shown in Figure 8.3, where the displacement of the spherical HPA, presented in Section 3.1.3, is analysed under different conditions. Figure 8.3 (a) compares the response of the spherical HPA for a monochromatic input wave of 2m wave height and 7s wave period under resistive control using the *LPF+iPTO* model, to its *best linear approximation*, where both are shown to be identical. Since the *LPF+iPTO* mathematical model is linear, the *best linear approximation* is able to perfectly replicate the displacement of the spherical HPA and, as a consequence, the nonlinearity measure $\theta = 0$.

In contrast, Figure 8.3 (b) illustrates the same WEC under the same conditions, but represented via the *viscNLFK+iPTO* model, where nonlinear FK forces and viscous effects are included in the WSHI. As a consequence, the response of the partially nonlinear model and its *best linear approximation* cannot be identical, although they are both reasonably close, resulting in a very low nonlinearity measure: $\theta = 0.04$. As shown in Sections 3.2.4 and 5.1, the spherical HPA under docile control, *i.e.* resistive control defined in Equation (6.2), shows linear behaviour, which is again confirmed in Figure 8.3 (b). However, if the spherical HPA is analysed under a more aggressive control strategy, allowing the WEC to resonate with the incident wave, nonlinear effects are enhanced, as shown in Sections 3.2.4 and 5.1. Therefore, Figure 8.3 (c) analyses the displacement of the spherical HPA for a monochromatic input wave of 2m wave height and 3s wave period, which is close to the natural period of the spherical HPA (see Table 3.2), and, thus, shows the spherical HPA at resonance. Consequently, differences between the displacement obtained from the *viscNLFK+iPTO* model and the *best linear approximation* are more significant and the nonlinearity measure is consequently higher: $\theta = 0.21$.

Another example is illustrated in Figure 8.4, where the *best linear approximation* and the *original* nonlinearity measure are evaluated for a heaving cone analysed in a fully-nonlinear CNWT. Results for this heaving cone are taken from [187], where the cone is excited with a monochromatic input force signal of 960N and 8s period. Figure 8.4 shows a reasonably nonlinear response, with a significant asymmetry with respect to the horizontal axis at the origin, and quite flat troughs. This nonlinear behaviour cannot be captured by the *best linear approximation* and, thus, results in a reasonably high nonlinearity measure of $\theta = 0.26$.

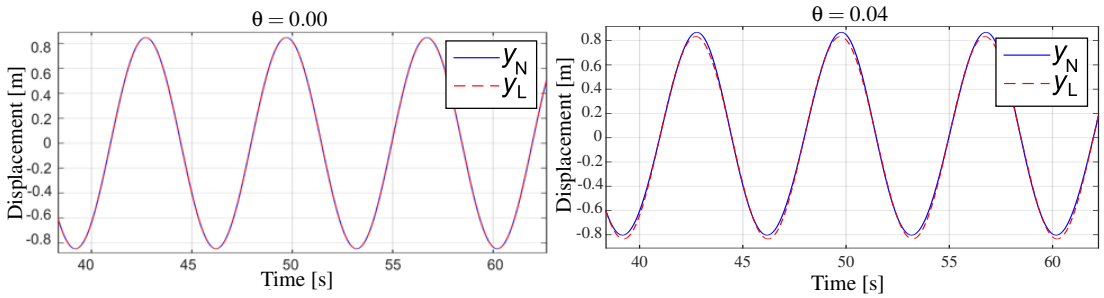

(a) *LPF+iPTO* model off-resonance $T_w = 7s$ & $H_w = 2m$.

(b) *viscNLFK+iPTO* model off-resonance $T_w = 7s$ & $H_w = 2m$.

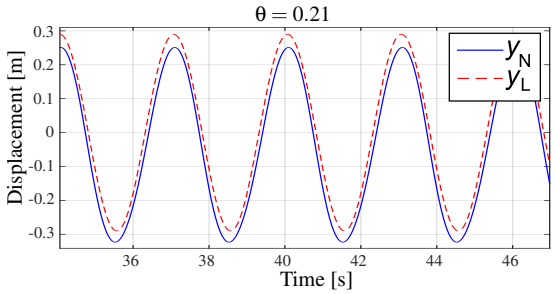

(c) *viscNLFK+iPTO* model at resonance $T_w = 3s$ & $H_w = 2m$.

Figure 8.3: The response of different WEC models for the spherical HPA under different conditions, their *best linear approximation*, and θ: (a) the *LPF+iPTO* mathematical model off-resonance, (b) the *viscNLFK+iPTO* model off-resonance, and (c) the *viscNLFK+iPTO* model at resonance.

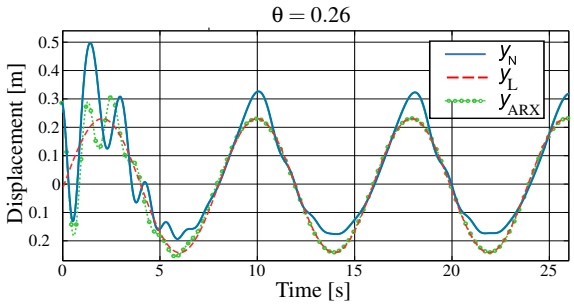

Figure 8.4: The response of the heaving cone analysed in a CNWT (y_N) and the approximation via ARX model (y_{ARX}) from [187], compared to the *best linear approximation* (y_L) using the *original* nonlinearity measure. Also, the nonlinearity degree θ of the cone's response.

Davidson et al. [187] attempts to replicate the response of the cone in the CNWT by utilising the linear ARX parametric model identified from the data generated in the CNWT. One can notice in Figure 8.4 that the output from the *best linear approximation* and the ARX model are identical once the response from the ARX has reached steady-state. After all, the ARX model and the *best linear approximation* calculated via Equation (8.9), if they are adequately identified, represent the best possible approximation to a nonlinear response using a linear model structure.

However, due to the quadratic response of the power signal, θ cannot capture the nonlinearity degree of a WEC model when using P_e as output. Figure 8.5 (a) illustrates the power output estimated with the *LPF+iPTO* model compared to its *best linear approximation* obtained using the *original* nonlinearity measure. The incapacity of the *original* nonlinearity measure to replicate the response of a linear model is clearly shown and, as a consequence, an unrealistically high nonlinearity measure, $\theta = 1$, is obtained. However, Figure 8.5 (b) shows the capability of the adapted *power* nonlinearity measure to capture the quadratic nonlinearity of the power signal and

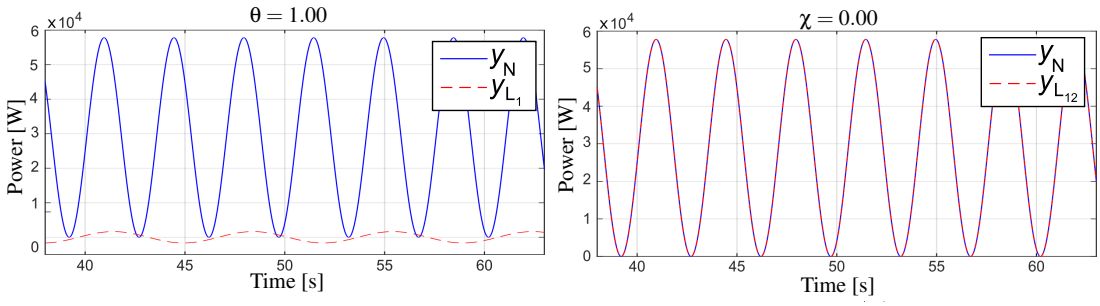

(a) *original* nonlinearity measure (b) *power* nonlinearity measure

Figure 8.5: P_e of the *LPF+iPTO* mathematical model and its *best linear approximation* for the *original* (a) and *power* nonlinearity measures (b).

provide the expected nonlinearity measure for a linear model: $\chi = 0$.

Despite the adequate performance of both nonlinearity measures, *i.e.* θ and χ, the nonlinearity degree of a WEC model, analysed under the very same conditions (identical input and control strategy), can vary significantly depending on the output signal selected for the evaluation of the nonlinearity degree. Figure 8.6 illustrates the *best linear approximation* and the nonlinearity degree of the $NLBEMW2W_{Cd=1}$ model, which includes a nonlinear description of the WSHI and all the dynamics of the HyPTO system, as described in Chapter 6. The nonlinearity degree is evaluated in Figures 8.6 (a), (b) and (c), under monochromatic wave excitation (3s period and 1m height, so close to resonance), using displacement (θ_{dis}), velocity (θ_{vel}) and power (χ), respectively, as output. The highest value of the nonlinearity measure is obtained with displacement as output ($\theta_{dis} = 0.56$), higher than with power ($\chi = 0.45$), which includes all the nonlinearities of the high-fidelity *cHyPTO* model described in Chapter 4. In addition, the nonlinearity degree is more than halved using θ_{vel}, compared to θ_{dis} ($\theta_{vel} = 0.21$).

This substantial difference between θ_{dis} and θ_{vel} appears due to the specific nature of the nonlinearity in this particular case. The main nonlinear phenomenon of the displacement signal is the asymmetry with respect to the horizontal axis at the origin, which can be represented by a constant offset in steady-state. However, because velocity is the derivative of the displacement, the offset of the displacement vanishes in the differentiation, dramatically reducing the indicated nonlinear behaviour.

The relevance of nonlinearities in different outputs depends on the required application of the nonlinear model. When nonlinearity is assessed for energy maximising control applications in wave energy, the implication of velocity nonlinearities may be significantly more influential than displacement nonlinearities, for two main reasons: On the one hand, velocity-dependent components are lossy, which strongly affects the final energy generation and, on the other hand, the control problem in wave energy is commonly tackled by optimising the velocity trajectory, as reviewed in [343]. In addition, Figure 8.6 (a) suggests that the displacement nonlinearity is affine, which can be relatively simple to tackle from a control perspective. Nonlinearities in the power signal are also important, since a precise description of the generated power is required to accurately maximise the generated energy of WECs.

Similarly to monochromatic waves, nonlinearity measures θ and χ can also be used with polychromatic waves. However, the parametrisation of the best linear approximation is different for monochromatic and polychromatic waves. In the case of monochromatic waves, only two basis functions are used, and the time constants must be selected in order to accurately characterise the steady-state response of the spherical HPA over the complete frequency range [395]: one time constant is placed close to the resonant frequency ($T_1 = 3s$) and the second time constant at a lower frequency ($T_2 = 0.3s$). For polychromatic waves, the *best linear approximation* is parametrized using 5 basis functions, with appropriately distributed time constants between 0.1s and 16s,

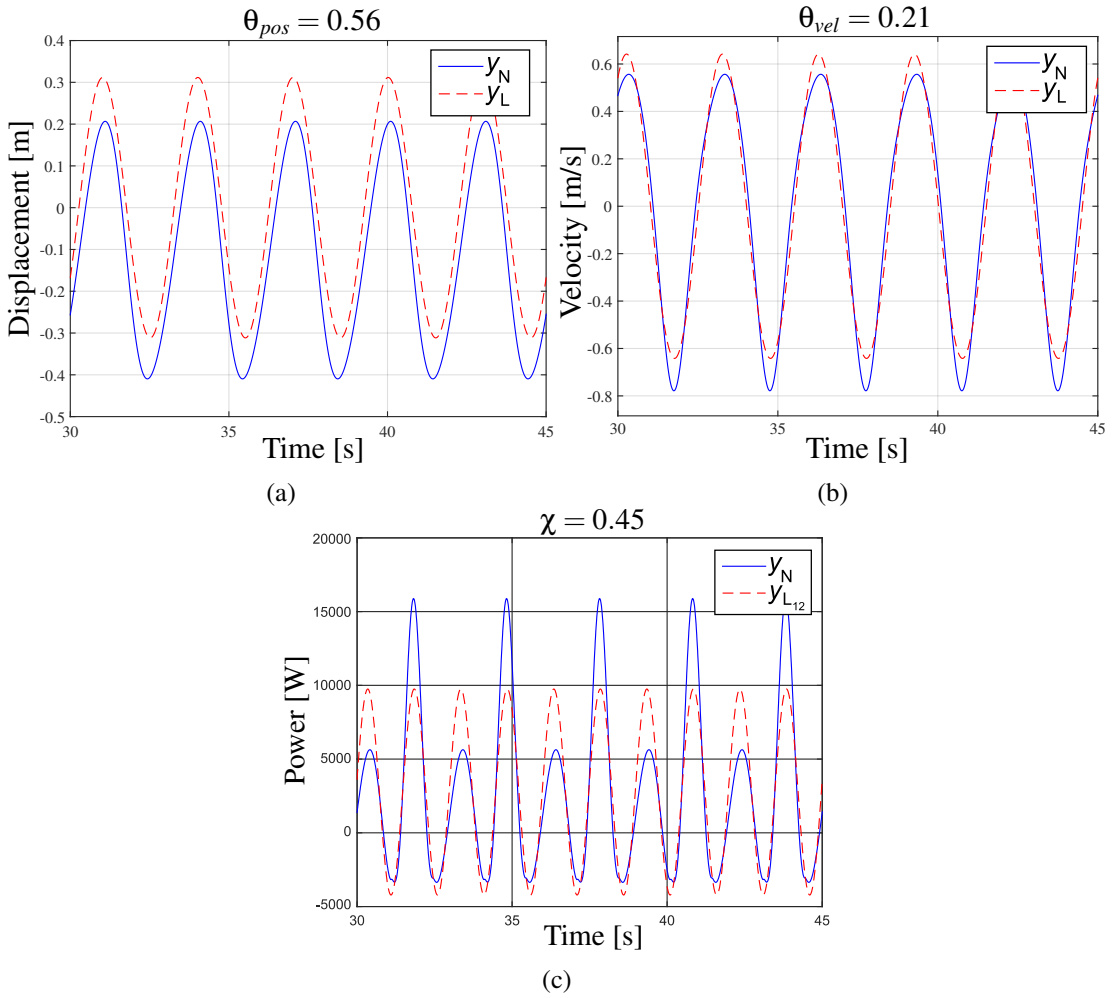

Figure 8.6: The *best linear approximation* and nonlinearity measures of the $NLBEMW2W_{Cd=1}$ model under monochromatic waves (3s wave period and 1m wave amplitude), when using (a) displacement, (b) velocity and (c) power as output.

which reasonably covers the range of possible wave periods. Figures 8.7 (a) and (b) illustrate the *best linear approximation* and θ_{vel} for the *LPF+iPTO* and *viscNLFK+iPTO* models, respectively, using a polychromatic input wave of 8s T_p and 2m H_s under resistive control, following Equation (6.2) using the control parameter optimised in Section 6.2.2.

8.1.4 Quantification of nonlinear effects

Using the different nonlinearity measures, the impact of the action of energy maximising control strategies on the nonlinear behaviour of WECs, suggested in Chapter 3, can be evaluated and quantified. Hence, the nonlinearity degree of the *viscNLFK+iPTO* model under docile and more aggressive control strategies, *i.e.* resistive and reactive control defined in Equations (6.2) and (6.3), respectively, is studied. Despite the lower nonlinearity measures obtained for velocity and power, as illustrated in Figure 8.6, special emphasis is given to velocity and power nonlinearities, due to their importance in the design of energy maximising control strategies for WECs. However, displacement nonlinearities are also quantified.

The nonlinearity degree of the *viscNLFK+iPTO* model is analysed over the complete operational space of a WEC defined by the scatter diagram of the BIMEP test site, depicted in Figure 6.8. Hence, Figures 8.8 (a) and (b) illustrate the nonlinearity measures of the *viscNLFK+iPTO* model, under resistive and reactive control, respectively, for each sea-state in the operational space. The

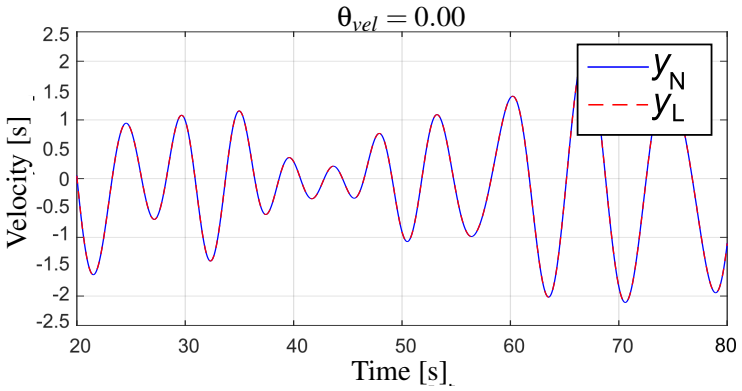

(a) *LPF+iPTO* model

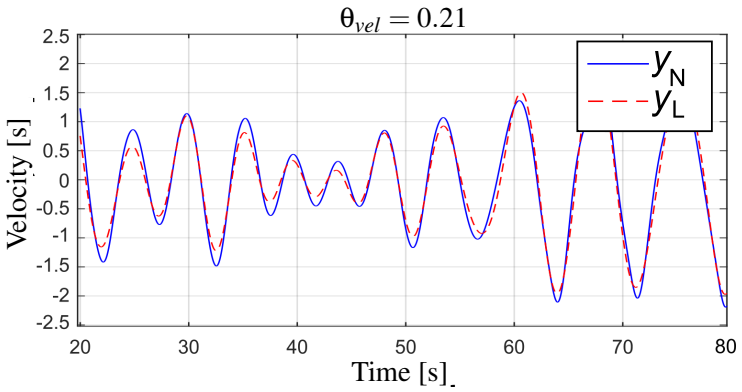

(b) *viscNLFK+iPTO* model

Figure 8.7: The *best linear approximation* and θ_{vel} for a polychromatic input wave (T_p =8s and H_s =2m) under reactive control, using (a) the *LPF+iPTO* and (b) *viscNLFK+iPTO* models.

maximum θ_{vel} is very similar in both cases ($\theta_{vel}^{max} \sim 0.33$) and is given for the same input wave (4s wave period and 4m wave height). In addition, θ_{vel} is highest with waves of 4s period for all wave heights, which suggests that the natural period of the device (3.17s using fully linear hydrodynamics) increases slightly due to the nonlinear effects in the WSHI, as previously reported in [321].

However, θ_{vel} decreases substantially when moving away from the resonant-period. For long period, small amplitude off-resonance waves, θ_{vel} vanishes under resistive control, as illustrated in Figure 8.8 (a), meaning that the WEC behaves linearly (as a wave follower) under these specific conditions. In contrast, θ_{vel} never vanishes in the case of reactive control, always staying above 0.1, as shown in Figure 8.8 (b). Differences between resistive and reactive control results are illustrated in Figure 8.8 (c), showing that θ_{vel} increases significantly far from the resonant-period due to reactive control. Similar trends can be observed using power as the output.

Table 8.2 presents the maximum nonlinearity measures for resistive and reactive control using monochromatic waves. However, maximum nonlinearity measures tend to describe the behaviour of the WEC close to resonance, while the main nonlinearity measure differences between the different controllers and models are observed far from the resonant-period, as shown in Figure 8.8. To capture an overall nonlinearity measure, mean values of the nonlinearity measures over the complete operational space are also considered in Table 8.2. Nonlinearity measures increase up to 25% from resistive to reactive control, which confirms the idea suggested throughout this thesis, that the action of energy maximising control strategies significantly affects the behaviour of WECs and enhances nonlinear effects of the WSHI.

Table 8.2 also shows the maximum and mean nonlinearity measures for the $NLBEMW2W_{Cd=1}$

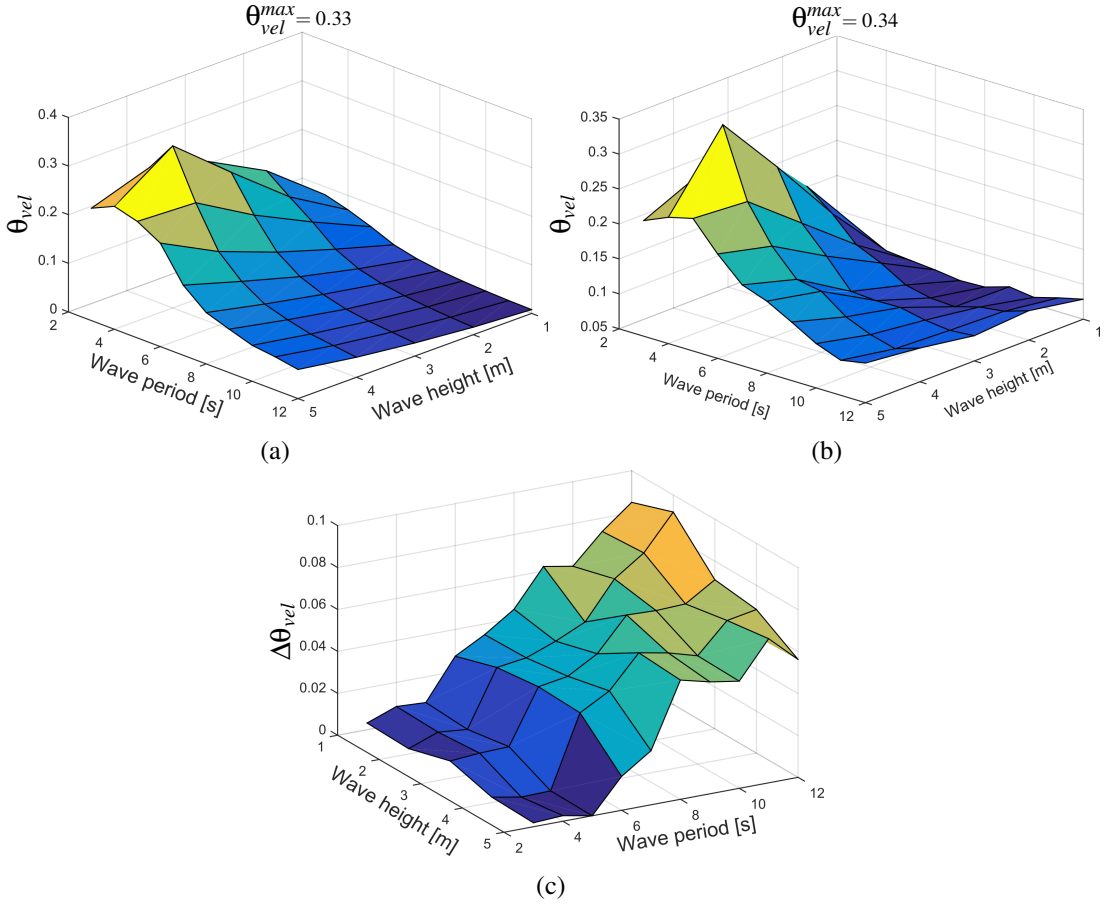

Figure 8.8: θ_{vel} over the complete operational space for the *viscNLFK+iPTO* model under (a) resistive and (b) reactive control, and (c) the difference between both.

Table 8.2: Maximum and mean nonlinearity measures for the *viscNLFK+iPTO* and *NLBEMW2W*$_{Cd=1}$ models when using different control strategies and outputs for monochromatic waves.

Monochromatic waves		*viscNLFK+iPTO*		*NLBEMW2W*$_{Cd=1}$	
		max	mean	max	mean
Resistive control	θ_{dis}	0.61	0.14	0.62	0.15
	θ_{vel}	0.33	0.10	0.36	0.10
	χ	0.46	0.15	0.51	0.17
Reactive control	θ_{dis}	0.66	0.16	0.69	0.20
	θ_{vel}	0.34	0.13	0.37	0.14
	χ	0.48	0.19	0.57	0.23

model, which allow the impact of the HyPTO system dynamics on WEC's nonlinear behaviour to be assessed. Under resistive control, maximum and mean nonlinearity measures are similar for the *viscNLFK+iPTO* and *NLBEMW2W*$_{Cd=1}$ models. Conversely, differences between the two mathematical models increase substantially under reactive control, where the highest maximum and mean nonlinearity measures are obtained for the *NLBEMW2W*$_{Cd=1}$ model, under reactive control ($\theta_{dis}^{max} = 0.69$ and $\chi^{mean} = 0.23$, respectively). However, it should be noted that nonlinearities in the case of the *NLBEMW2W*$_{Cd=1}$ model increase only by about 20%, compared to the *viscNLFK+iPTO* model with the ideal HyPTO model, meaning that the primary nonlinearity source in the *cHyW2W* model is the WSHI.

A similar analysis can be carried out for polychromatic waves. Figure 8.9 illustrates θ_{vel} for the *viscNLFK+iPTO* model under resistive control over the complete operational space, which, when compared to the same case with monochromatic waves illustrated in Figure 8.8 (a), three main differences can be observed: Firstly, θ_{vel}^{max} is substantially larger in polychromatic waves, approximately 40% higher; secondly, although θ_{vel} decreases when moving away from the resonant-period, the nonlinear behaviour of the WEC never vanishes completely as in the case with monochromatic input waves; and finally, θ_{vel} varies little with wave height.

Maximum and mean nonlinearity measures for all the different cases, using polychromatic waves, are presented in Table 8.3. Mean nonlinearity measures increase significantly (up to 30%) from monochromatic to polychromatic input waves, most likely due to the harmonics in the WEC response as a consequence of the frequency components added in the input polychromatic waves, meaning that nonlinear effects are more significant in polychromatic waves. Measures θ_{vel}^{max} and χ^{max} also increase significantly for all the cases, while θ_{dis}^{max} remains relatively unchanged.

The response of the WEC in polychromatic waves includes more harmonics, due to more frequency components included in the input wave, which incurs a more nonlinear behaviour of the WEC.

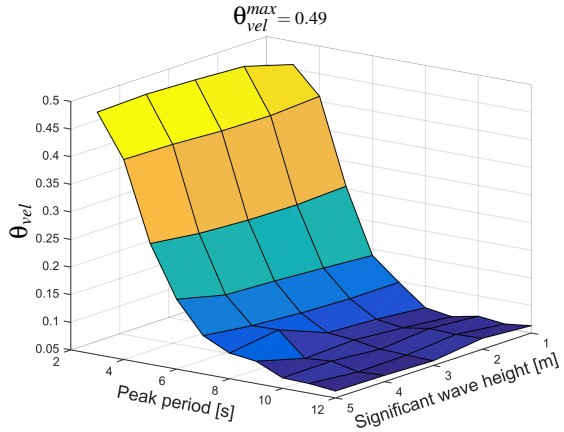

Figure 8.9: θ_{vel} over the complete operational space for the *viscNLFK+iPTO* model under resistive control and polychromatic waves.

Table 8.3: Maximum and mean nonlinearity measures for the *viscNLFK+iPTO* and *NLBEMW2W*$_{Cd=1}$ models when using different control strategies and outputs for polychromatic waves.

Polychromatic waves		*viscNLFK+iPTO*		*NLBEMW2W*$_{Cd=1}$	
		max	mean	max	mean
Resistive control	θ_{dis}	0.61	0.20	0.56	0.21
	θ_{vel}	0.49	0.18	0.59	0.22
	χ	0.45	0.17	0.49	0.26
Reactive control	θ_{dis}	0.63	0.21	0.62	0.21
	θ_{vel}	0.52	0.19	0.56	0.21
	χ	0.61	0.24	0.68	0.29

8.2 Systematic complexity reduction

Different reduced HyW2W (*rHyW2W*) models need to be designed for each application shown in Table 8.1, due to the specific requirements of each application. The ideal *rHyW2W* model for

each application, referred to as the *specific HyW2W* model, would be generated by means of an *algorithmic* CR approach that reduces the *HiFiWEC* considering the requirements of each application, as illustrated in Figure 8.10. However, such an *algorithmic* CR approach would be intractable, due to the complexity of the *HiFiWEC*, the difficulty in quantifying and, as a consequence, reducing the application-specific complexity, and the difficulty in articulating application requirements. Therefore, a *systematic* CR approach is suggested, progressively reducing the *HiFiWEC* model complexity.

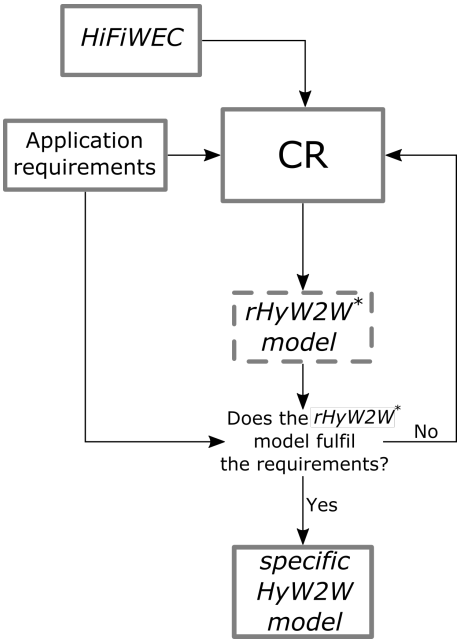

Figure 8.10: Algorithmic CR approach.

This *systematic* CR approach consists of removing or linearising different dynamics and loss models from the *HiFiWEC*. The reduced options for the WSHI and HyPTO models, referred to as the *rWSHI* and *rHyPTO* models, respectively, are analysed separately. Figures 8.11 (a) and (b) illustrate the model structure of the *HiFiWEC* and the different *rWSHI* and *rHyPTO* model possibilities, respectively, where red circles highlight the dynamics and/or loss models removed from the *cHyPTO* implemented in the *HiFiWEC*. Adequately combining the different *rWSHI* and *rHyPTO* models, a wide variety of *rHyW2W* models can be constructed.

The *HiFiWEC* could also be simplified in a single step via a *ParaM*, which would represent the whole drivetrain from ocean waves to the electricity grid, using η_w as input and P_e as output. Figure 8.11 (b) illustrates that option, where y_{ParaM} represents any output of the *ParaM*. Since the *HiFiWEC* includes the nonlinear effects due to the WSHI and HyPTO system, a nonlinear model structure, such as KGP [193] or ANN models [189, 194], must be chosen for the parametric model.

However, due to the complexity of the *HiFiWEC*, identifying the parameters of a nonlinear *ParaM* that accurately cover the complete operational space of a WEC without resulting in an overly complex model, may be extremely difficult. Therefore, *ParaMs* could be used to represent only one subsystem of the drivetrain, such as the WSHI, as shown in Section 2.2.3.3, the efficiency of the HyPTO system [278], or even a single effect within a subsystem, *e.g.* the fluid viscosity in the WSHI. The combination of multiple *ParaM*s, where each *ParaM* represents a single subsystem or effect, is also an alternative.

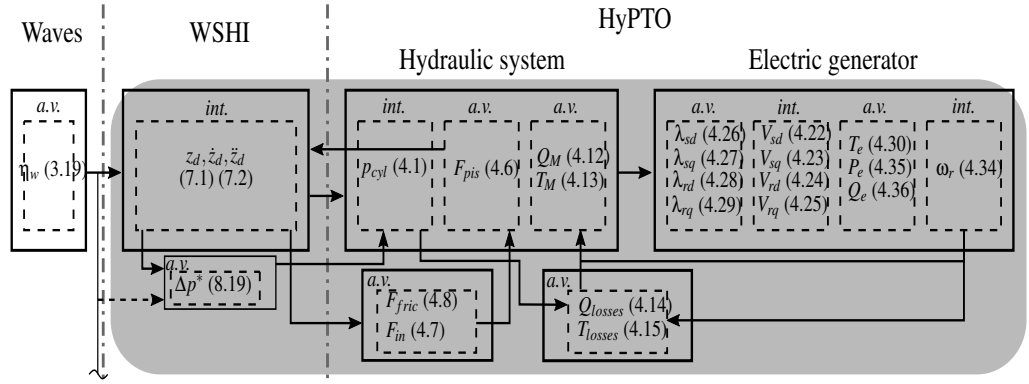

(a) The *HiFiWEC*.

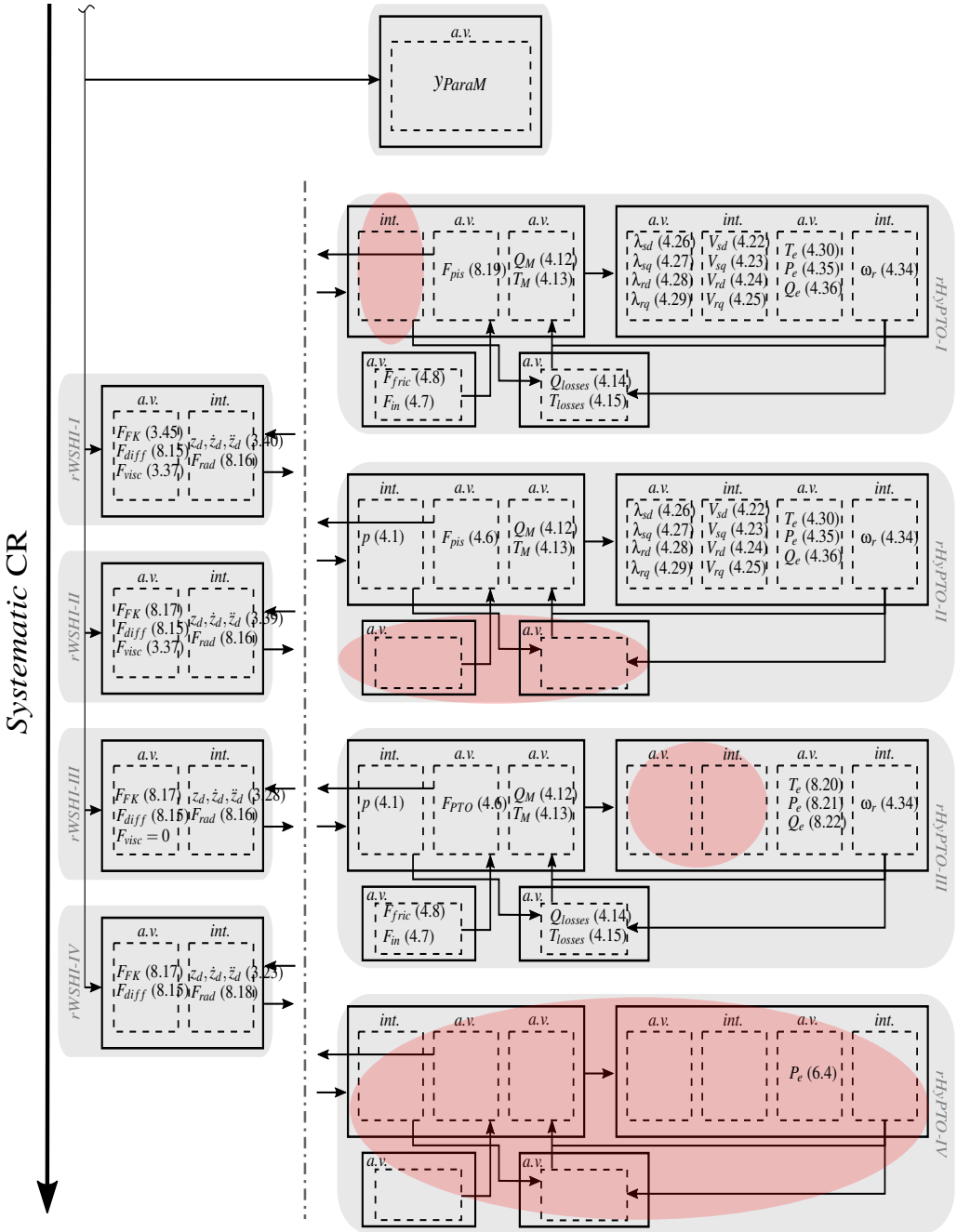

(b) Different *rWSHI* and *rHyPTO* models.

Figure 8.11: Schematic illustration of the *HiFiWEC* (a) and the different CR options (b) to design *rHyW2W* models. The abbreviations *a.v.* and *int.* mean algebraic variables and integration, respectively, red circles illustrate the part of the *cHyPTO* that has been removed, and the numbers in brackets after the variables represent the equations where the corresponding variables are defined.

8.2.1 WSHI reduction

Taking Equations (7.1) and (7.2) as the starting point, and excluding *ParaM*s, mathematical models based on potential flow are the next step in the progressive CR of the WSHI problem, as illustrated in Figure 2.23 (a). Therefore, all the *rWSHI* models assume the decomposition of the fluid force as in Equation (3.23). The different reductions suggested in this subsection result in WSHI models which have already been presented in Chapters 3 and 5.

8.2.1.1 *rWSHI-I*

The first reduced WSHI model, *i.e. rWSHI-I*, is based on Cummins' equation [86], and includes nonlinear FK forces, via Equation (3.45), and viscous effects added externally using a Morison-like equation [178], as in Equation (3.37). Diffraction and radiation forces remain linear, as in Equation (3.36), which can be represented as follows,

$$F_{diff} = \int_{-\infty}^{\infty} K_{diff}(t-\tau)\eta_w(\tau)d\tau, \tag{8.15}$$

$$F_{rad} = -\mu_{\infty}\ddot{z}_d(t) - \int_{-\infty}^{t} K_{rad}(t-\tau)\dot{z}_d(\tau)d\tau. \tag{8.16}$$

Hence, the *rWSHI-I* is the *viscNLFKa* model presented in Section 5.1.2.

8.2.1.2 *rWSHI-II*

The *rWSHI-II* model is also based on Cummins' equation, using the linearised version of the FK forces, as in Equation (3.28), represented as follows,

$$F_{FK} = \int_{-\infty}^{\infty} K_{FK}(t-\tau)\eta_w(\tau)d\tau. \tag{8.17}$$

In addition, viscous effects are included in the *rWSHI-II* model using the Morison-like equation, as in *rWSHI-I*. Hence, the *rWSHI-II* model is the same as the *viscLPF* model presented in Section 3.2.3.

8.2.1.3 *rWSHI-III*

Another step in the *systematic* CR is removing viscous effects, so that *rWSHI-III* model, also based on Cummins' equation, becomes the LPF model presented in Chapter 3.

8.2.1.4 *rWSHI-IV*

Finally, the radiation force can be replaced with a *M-D* system, neglecting the memory effects in the WSHI,

$$F_{rad} = B_{rad}\dot{z}_d + A_{rad}\ddot{z}_d. \tag{8.18}$$

8.2.2 HyPTO reduction

The *cHyPTO* model included in the *HiFiWEC*, presented in Chapter 4, can be simplified by neglecting or simplifying specific dynamics and losses of the hydraulic system and electric generator, as shown in Figure 8.11 (b). The *cHyPTO* includes a MR solver with different δt implemented in each subsystem of the drivetrain, as described in Chapter 6. However, the simplification or omission of certain (higher-frequency) dynamics allows the use of a larger δt, which can significantly reduce the computational cost of the *rHyW2W* model.

8.2.2.1 *rHyPTO-I*

In *rHyPTO-I*, fluid compressibility is neglected in the hydraulic system, meaning that Δp_{cyl} in Equation (4.6) is the same as Δp^*_{cyl}, as shown in Equation (8.19), where F^*_{PTO} is given by Equation (6.3). The omission of compressibility effects allows the use of a larger δt in the hydraulic system model: $\delta t_{HyM} = 10ms$.

$$\Delta p^*_{cyl} = F^*_{PTO}/A_p. \tag{8.19}$$

8.2.2.2 *rHyPTO-II*

Losses in the HyPTO system are neglected in *rHyPTO-II*. Hence, leakages and friction losses in the hydraulic cylinder ($F_{fric} = F_I = 0$) and motor ($Q_{losses} = T_{losses} = 0$) are neglected.

8.2.2.3 *rHyPTO-III*

The complexity of the electric generator is reduced in *rHyPTO-III*, where the electric dynamics are neglected. Hence, *rHyPTO-III* only includes the steady-state response of the electric generator, which permits the use of a larger time-step ($\delta t_{ElecM} = 10ms$), significantly reducing the computational cost.

Therefore, Equations (4.22)–(4.30), (4.35) and (4.36) are replaced with their steady-state representation [267] as follows,

$$T^{ss}_e = \frac{3\frac{Np}{2}R_r V_g^2}{s\omega_g[(R_s + R_r + \frac{1-s}{s}R_r)^2 + \omega_g(L_s + L_r)^2]}, \tag{8.20}$$

$$P^{ss}_e = 3V_g I^{ss}_e cos(\angle Z^{ss}), \tag{8.21}$$

$$Q^{ss}_e = 3V_g I^{ss}_e sin(\angle Z^{ss}), \tag{8.22}$$

where V_g is the grid voltage, s the generator slip and ω_g the frequency of the grid voltage. The current at the stator is given as,

$$I^{ss}_e = \frac{V_g}{Z^{ss}}, \tag{8.23}$$

with

$$Z^{ss} = \frac{Z_r Z_m}{Z_r + Z_m} + Z_s. \tag{8.24}$$

Z_r, Z_s and Z_m are the rotor, stator and magnetizing impedances, respectively.

8.2.2.4 *rHyPTO-IV*

rHyPTO-IV is the most simplistic case, where the HyPTO is completely idealised, meaning that generated power is the same as absorbed power, as shown in Equation (6.4).

8.2.3 Design of balanced reduced HyW2W

Reduced versions of the *HiFiWEC*, designed by combining the different options suggested in Sections 8.2.1 and 8.2.2, can lead to highly unbalanced (unbalanced complexity/fidelity levels for the WSHI and HyPTO models) and/or excessively simplified HyW2W models, *e.g.* the CNWT combined with *rHyPTO-IV* or *rWSHI-III* combined with *rHyPTO-IV* (the *CNWT+iPTO* model and the *LPF+iPTO* model presented in Table 7.1, respectively), which result in inaccurate HyW2W models as demonstrated in Section 7.2.1.2. In this section, a number of reasonably balanced *rHyW2W* models, presented in Table 8.4, are designed via the *systematic* CR approach. It should be noted that the *rHyW2W-I* model is the same as the $NLBEMW2W_{C_d=1}$ model presented in Sections 6.2 and 7.4.

Table 8.4: Configuration of the different balanced *rHyW2W* models.

Balanced **rHyW2W**	**WSHI**	**HyPTO**
rHyW2W-I	*rWSHI-I*	*cHyPTO*
rHyW2W-II	*rWSHI-III*	*cHyPTO*
rHyW2W-III	*rWSHI-I*	*rHyPTO-I*
rHyW2W-IV	*rWSHI-I*	*rHyPTO-II*
rHyW2W-V	*rWSHI-I*	*rHyPTO-III*
rHyW2W-VI	*rWSHI-I*	*rHyPTO-I & -III*

8.2.4 HyW2W model selection process

Among the initial set of *HyW2W* models, including the *HiFiWEC*, and the balanced *rHyW2W* models shown in Table 8.4, the *specific HyW2W* model must be selected for each application. Specific application requirements, presented in Table 8.1, are divided into three main groups: Accuracy and computational costs, specific dynamics and losses, and nonlinear effects. Hence, the selection process is also designed as an elimination process divided into three steps, following these three groups of specific requirements. Figure 8.12 illustrates the staggered selection process to select the *specific HyW2W* model.

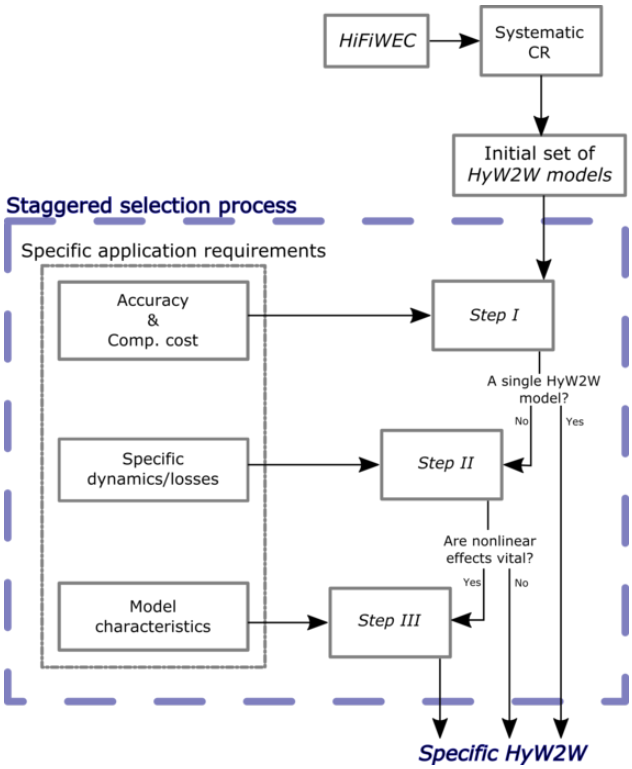

Figure 8.12: *Specific HyW2W* model selection process.

8.2.4.1 Selection *Step-I*

In *Step I* of the staggered selection process, the accuracy of E_{gen} estimation, and the computational cost of the different HyW2W models, are evaluated. Hence, the HyW2W models that cannot provide the required fidelity within the required computational cost are eliminated. If only one HyW2W model can meet the accuracy and/or computational cost requirements, then that HyW2W model will be the *specific HyW2W* model straightaway. Otherwise, the successful *HyW2W* models

are sorted from the computationally cheapest to the most expensive, before passing to *Step II*.

8.2.4.2 Selection *Step-II*

Among the *HyW2W* models that succeed to *Step II*, the inclusion of specific dynamics and losses is analysed. Hence, the *HyW2W* models that neglect the dynamics and/or losses, specifically required by the application, are eliminated in *Step II*. In a case where the inclusion of nonlinear effects is not a vital requirement of the application under analysis, the *HyW2W* model on the top of the list after *Step II*, that is, the computationally cheapest among the models that fulfil the requirements in *Steps I* and *II*, will be chosen as the *specific HyW2W* model.

8.2.4.3 Selection *Step-III*

Finally, the degree of nonlinearity of the HyW2W models that progress to *Step III* is evaluated. These successful HyW2W models are sorted from the most nonlinear to the least, according to the nonlinearity measure χ presented in Section 8.1.2.2. The implication of nonlinear effects is only relevant for *Ident* and *MBC*, as shown in Table 8.1, but with opposite requirements. In the case of *Ident*, retaining nonlinear effects is important, so the HyW2W model on top of the list, *i.e.* the most nonlinear model, is selected. Conversely, irrelevant nonlinear effects should be avoided when designing a model for *MBC*, so the HyW2W model on the bottom of the list, *i.e.* the least nonlinear, is chosen for *MBC*.

8.3 Evaluation of reduced models

For the evaluation of the different *rHyW2W* models suggested in Table 8.4, the spherical HPA presented in Section 3.1.3, coupled to the HyPTO system presented in Table 6.3, is used as the case study. In addition, all the *rHyW2W* models are analysed for the ME sea-state described in Table 6.2 ($T_p = 8s$, $H_s = 1.5m$, $\gamma_J = 3.3$) based on the JONSWAP spectrum [75], as described in Section 6.2.1. Due to the impact of control strategies on the behaviour of the spherical HPA, demonstrated in this thesis, resistive and reactive control are included in the analysis, for which the optimal B_{PTO} and K_{PTO} coefficients are obtained from Section 6.2.2.

Hence, for the initial step of the selection process, the fidelity of the E_{gen} estimates and the computational cost of the initial set of HyW2W models are studied, where the excessively simplified *LPF+iPTO* and the unbalanced *CNWT+iPTO* models are also included in the analysis, for the sake of completeness. The fidelity measure ($\mathcal{F}$) is given as a normalised value, following Equations (5.1) and (5.2), and using the *HiFiWEC* as benchmark, while the computational cost is given as the ratio between the simulation time and the real time required to run the simulation ($\mathcal{T}_{ratio} = {}^{t_{sim}}/_{t_{real}}$). Figure 8.13 illustrates the fidelity/computational cost compromise of the HyW2W models included in the initial set, under reactive control, where the extreme computational cost of the CNWT-based approaches, i.e. the *HiFiWEC* and the *CNWT-iPTO* model, is highlighted again. In addition, one can observe, in Figure 8.13, that, the high computational time and complexity of mathematical models, do not ensure high-fidelity results, especially if the HyPTO system is excessively simplified, as shown in the case of the *CNWT-iPTO* model.

The computational cost of the different HyW2W models is identical, regardless of the control implemented. In contrast, the fidelity of the HyW2W models may vary significantly, as seen in this thesis, under the action of docile and aggressive control strategies. Therefore, Figures 8.14 (a) and (b) illustrate the E_{gen} under resistive and reactive control, respectively, for the *HiFiWEC*, reduced models *rHyW2W-II*, *rHyW2W-IV* and *rHyW2W-VI*, and the *LPF+iPTO*. Figure 8.14 illustrates that the differences between a linear and a nonlinear model to solve WSHIs are particularly relevant under reactive control, while the simplification of the HyPTO model may lead to poor results under any type of control, as also highlighted in Chapter 7. The fidelity and computational cost

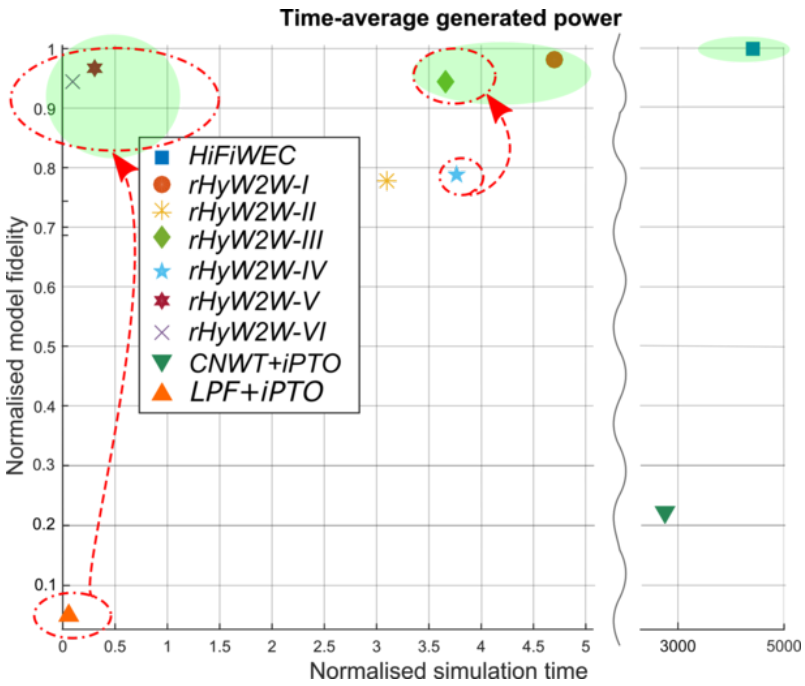

Figure 8.13: Fidelity/computational cost compromise of the different HyW2W models.

of all the *rHyW2W* models, under resistive and reactive control, are presented in Table 8.5, where *CNWT+iPTO* and *LPF+iPTO* models are excluded.

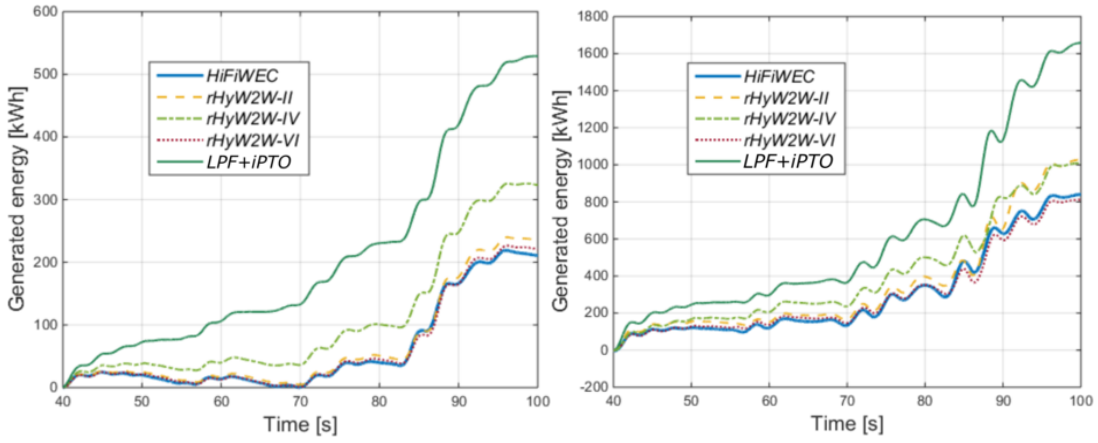

(a) (b)

Figure 8.14: Generated energy estimates of different HyW2W models under resistive (a) and reactive (b) control.

Although maximum fidelity can only be achieved with the *HiFiWEC*, Figure 8.13 and Table 8.5 show that reasonably high-fidelity results can also be obtained for a small fraction of the computational time required by the *HiFiWEC*. In fact, most of the *rHyW2W* models suggested in Table 8.4 provide fidelity values of over 90% under resistive and reactive control, with computational time reductions of, at least, three orders of magnitude, compared to the *HiFiWEC*. The only exceptions that return fidelity values below 90% are the reduced models *rHyW2W-II* and *rHyW2W-IV*, which neglect the nonlinear effects of the WSHI and the losses in the HyPTO system, respectively. However, it should be noted that the hydrodynamic models implemented in all the reduced HyW2W models, except for the *rHyW2W-II* model, use the C_d parameter, which must be identi-

Table 8.5: Fidelity, computational cost and nonlinearity characteristics of *rHyW2W* models.

HyW2W	$\mathcal{T}_{ratio}$	**Resistive control**		**Reactive control**	
		$\mathcal{F}$	χ	$\mathcal{F}$	χ
rHyW2W-I	4.7	0.95	0.23	0.97	0.12
rHyW2W-II	3.1	0.89	0.22	0.77	0.11
rHyW2W-III	3.7	0.94	0.15	0.94	0.09
rHyW2W-IV	3.8	0.51	0.21	0.79	0.11
rHyW2W-V	0.31	0.95	0.23	0.95	0.12
rHyW2W-VI	0.1	0.95	0.15	0.94	0.08

fied via a CNWT to ensure an acceptably accurate value. In addition, the inconsistency of C_d is demonstrated in Chapter 7 and [184], meaning that mathematical models which use a Morison-like equation, presented in Equation (3.37), to represent viscous losses of the WSHI, may lose fidelity, unless C_d is uniquely identified for each specific case.

Based on Table 8.5, the list of the HyW2W models that succeed in *Step I* of the selection process can now be defined for each application. In the case of *ValVer* and *Ident* applications, since the maximum fidelity is required, the *HiFiWEC* can be directly selected as the *specific HyW2W* model. In contrast, the list of HyW2W models that succeed in *Step I* for *SimWEC* and *PowSyst* applications includes four *rHyW2W* models, sorted from the computationally most efficient to the most demanding: *rHyW2W-VI*, *rHyW2W-V*, *rHyW2W-III* and *rHyW2W-I*. This list is reduced to just two candidates, i.e. *rHyW2W-VI* and *rHyW2W-V*, for the case of the *PTOopt*, *PowAss* and *MBC* applications, due to the excessive computational cost of the other models.

In *Step II* of the selection process, the *specific HyW2W* model is selected for all the applications except for *MBC*, for which the implication of the nonlinear effects is vital. For instance, the *SimWEC* application requires all the dynamics and losses to be included, which leaves the *rHyW2W-I* model, named as $NLBEMW2W_{Cd=1}$ in Chapters 6 and 7, as the only possible *specific HyW2W* model. On the other hand, the *PowSyst* application only requires electrical system dynamics and HyPTO losses, which are only included in models *rHyW2W-I* and *rHyW2W-III*, from which the computationally more efficient *rHyW2W-III* model is selected as the *specific HyW2W* model.

In the case of the *PTOopt* application, hydraulic system dynamics and HyPTO losses need to be considered, which are only covered by the *rHyW2W-V* model. Although the outputs from the *rHyW2W-V* and *rHyW2W-VI* models are almost identical at first glance, high-frequency dynamics, only covered by the *rHyW2W-V* model, as illustrated in Figure 8.15, have a significant impact on the wear of hydraulic components. Therefore, *rHyW2W-V* is the *specific HyW2W* model for the *PTOopt* application.

All the requirements for the *PowAss* application are included in the two candidates that progressed to *Step II*. Therefore, the *rHyW2W-VI* model is the *specific HyW2W* model for the *PowAss* application, due to its more appealing computational cost compared to the *rHyW2W-V* model. In fact, Table 8.5 shows that the *rHyW2W-VI* model can provide high fidelity results (always above 95% fidelity), but with a computational cost reduction of one order of magnitude, compared to *rHyW2W-I*.

Finally, the *specific HyW2W* model for the *MBC* application is selected in *Step III*, where the nonlinearity degree of the models is taken into consideration. Table 8.5 presents the χ measure for the different *rHyW2W* models, where all the χ measures are relatively low. In addition, the χ measure for the same model is different when the WEC operates under resistive and reactive control, as shown in Section 8.1.4. However, as opposed to the overall conclusion presented in Section 8.1.4, χ is higher under resistive control, compared to reactive control. This is linked to the power production profile of the spherical HPA under resistive and reactive control in this particular

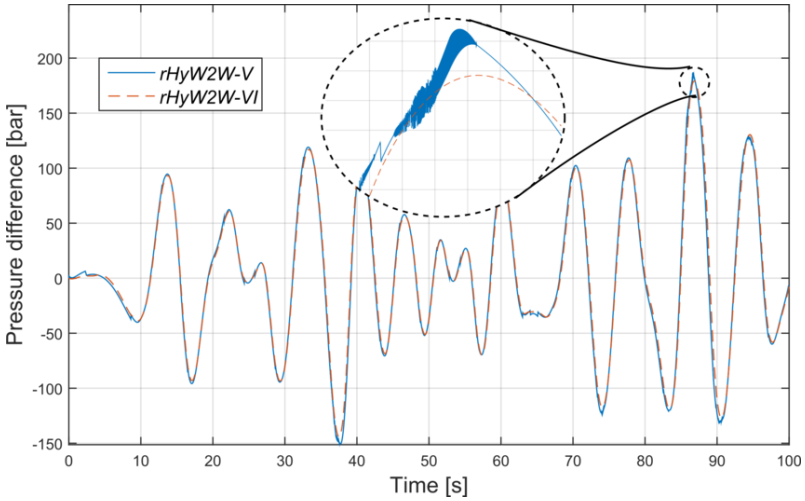

Figure 8.15: Pressure difference between the hydraulic cylinder chambers modelled with *rHyW2W-V* and *rHyW2W-VI*.

case, shown in Figure 8.16 for the *rHyW2W-I* model. The spherical HPA under resistive control, cannot produce enough energy to overcome the inertia of the electric generator at several stages of the simulation, as mentioned in Sections 6.2.3 and 7.4, which results in a generated power profile with rather flat troughs, as shown in Figure 8.16. This profile with flat troughs represents a more nonlinear behaviour of the spherical HPA than the profile shown under reactive control, which explains the higher χ values under resistive control, for this specific case.

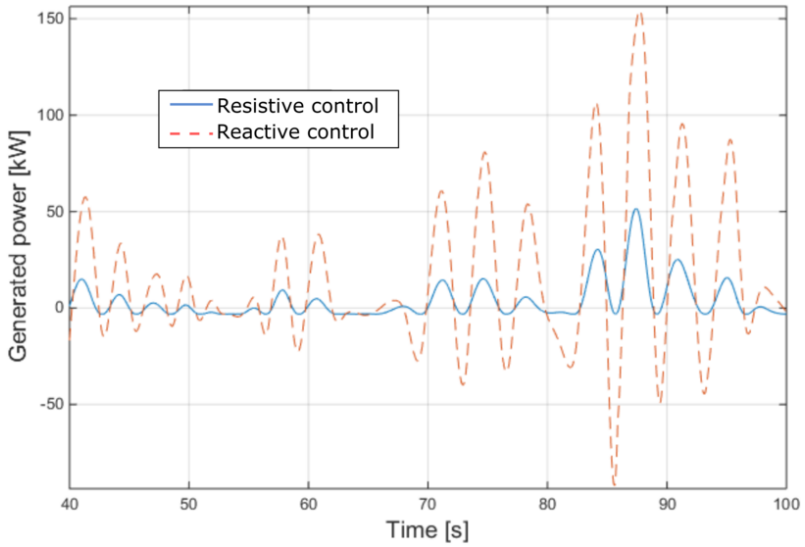

Figure 8.16: Generated power estimated with the *rHyW2W-I* model under resistive and reactive control.

The fidelity and computational cost characteristics of the *rHyW2W-V* and *rHyW2W-VI* models are very similar, but the *rHyW2W-V* model is more nonlinear, under both resistive and reactive control (up to 30% more). Therefore, the *rHyW2W-VI* model is considered as the *specific HyW2W* model for *MBC*.

8.3.1 *Specific HyW2W* models

Hence, the *specific HyW2W* model for each application is selected following the *systematic* CR approach, as shown in Table 8.6. The objective of this chapter, that is, reducing the complexity

of the *HiFiWEC* while retaining the specific fidelity required by each application, illustrated by the red arrows in Figure 8.1, is successfully accomplished, as illustrated by similar red arrows in Figure 8.13.

Table 8.6: The *specific HyW2W* model for each application.

	ValVer	*Ident*	*WECsim*	*PowSyst*	*PTOopt*	*PowAss*	*MBC*
Specific HyW2W model	*HiFiWEC*	*HiFiWEC*	*rHyW2W-I*	*rHyW2W-III*	*rHyW2W-V*	*rHyW2W-VI*	*rHyW2W-VI*

8.3.2 *rHyW2W* models for power assessment and controller design

Section 6.2 shows the incapacity of the *viscLPF+iPTO* model to accurately optimise control parameters and assess power production capabilities of the spherical HPA. In fact, Figure 6.15 illustrates the dramatic consequences of using an excessively simplified mathematical model for control parameter optimisation. Thus, a more accurate description of the WSHIs and the HyPTO system is required. However, the computational cost of the $NLBEMW2W_{Cd=1}$ model is shown to be prohibitive in Section 6.2, over 100 times slower than the commonly used *LPF+iPTO* or the *viscLPF+iPTO* models.

Using the *systematic* CR approach, the *rHyW2W-VI* model is selected as the optimum for *PowAss* and *MBC* applications, as shown in Table 8.6, for which the computational cost is comparable to the cost of the *LPF+iPTO* or the *viscLPF+iPTO* models. However, the fidelity of the *rHyW2W-VI* model is significantly higher, as illustrated in Figure 8.13. Therefore, the same analysis, carried out in Sections 6.2.2 and 6.2.3, using the *viscLPF+iPTO* and $NLBEMW2W_{Cd=1}$ models, is repeated in this section, using the *rHyW2W-VI* model. In this case, the suitability of the *rHyW2W-VI* model is analysed, and compared to the results shown in Sections 6.2.2 and 6.2.3. Following Equation (6.5), differences between the $NLBEMW2W_{Cd=1}$ and *rHyW2W-VI* models are analysed as follows,

$$\Delta[\%] = \frac{y_{NLBEMW2W_{Cd=1}} - y_{rHyW2W-VI}}{y_{NLBEMW2W_{Cd=1}}} \times 100, \tag{8.25}$$

where $y_{rHyW2W-VI}$ represents the outputs from the *rHyW2W-VI* model. Similarly to Equation (6.5), Δ can take positive or negative values, negative values meaning that outputs from the *rHyW2W-VI* model are overestimated, compared to the $NLBEMW2W_{Cd=1}$ model.

Table 8.7 presents control parameters optimised using the *rHyW2W-VI* and $NLBEMW2W_{Cd=1}$ models for the three sea-states described in Table 6.2. In addition, control parameters optimised with the *rHyW2W-VI* and $NLBEMW2W_{Cd=1}$ models are implemented in the $NLBEMW2W_{Cd=1}$ model to obtain power production estimates. The difference between the power estimates are given as ΔP_e^{av}. That way, the impact of using control parameters optimised with the *rHyW2W-VI* model is evaluated. Likewise in Section 6.2, control parameters are optimised under resistive and reactive control, as shown in Table 8.7.

In the case of resistive control, control parameters optimised utilising the *rHyW2W-VI* model are identical to those optimised with the $NLBEMW2W_{Cd=1}$ model, except for the LE sea-state, where B_{PTO} optimised with the *rHyW2W-VI* model is slightly overestimated. In the reactive control case, differences are slightly larger, especially for the K_{PTO} term, with overestimation of up to 15%. However, overestimation of control parameters has a very low impact on power production estimates. Differences between power production estimates are negligible under resistive control ($\Delta P_e^{av} < 0.03\%$) and remain reasonably low under reactive control ($\Delta P_e^{av} < 5.2\%$), where the highest differences are found for the LE sea-state. Note that all ΔP_e^{av} values in Table 8.7 are positive, meaning that control parameters optimised with the *rHyW2W-VI* model result in slightly underestimated power production estimates.

Table 8.7: Resistive and reactive control parameters optimised using the *rHyW2W-VI* and *NL-BEMW2W*$_{Cd=1}$ models, and the difference between power estimates obtained with the *NL-BEMW2W*$_{Cd=1}$ model using the different sets of control parameters. Units of B_{PTO} and K_{PTO} are $^{kNs}/_{m}$ and $^{kN}/_{m}$, respectively.

	rHyW2W-VI		*NLBEMW2W*$_{Cd=1}$		
Resistive control	B_{PTO}		B_{PTO}		ΔP_e^{av} [%]
LE	150		140		0.03
ME	210		210		0
HE	330		330		0
Reactive control	B_{PTO}	K_{PTO}	B_{PTO}	K_{PTO}	ΔP_e^{av} [%]
LE	70	-110	70	-120	5.2
ME	90	-160	90	-140	2.6
HE	150	-120	160	-140	3.2

Power production capabilities are evaluated over the complete operational space, illustrated in Figure 6.11, using the $AMPP_{gen}$ and η_{HyPTO}^{AMPP} measures, as in Table 6.9. In addition, the AMPP measure is calculated using the NLBEMW2W$_{Cd=1}$ model with control parameters optimised via the *rHyW2W-VI* model ($AMPP_{gen}^{rHyW2W-VI}$). Figures 8.17 (a) and (b) show the differences between the *rHyW2W-VI* and *NLBEMW2W*$_{Cd=1}$ models, when estimating power capabilities over the complete operational space under resistive and reactive control, respectively.

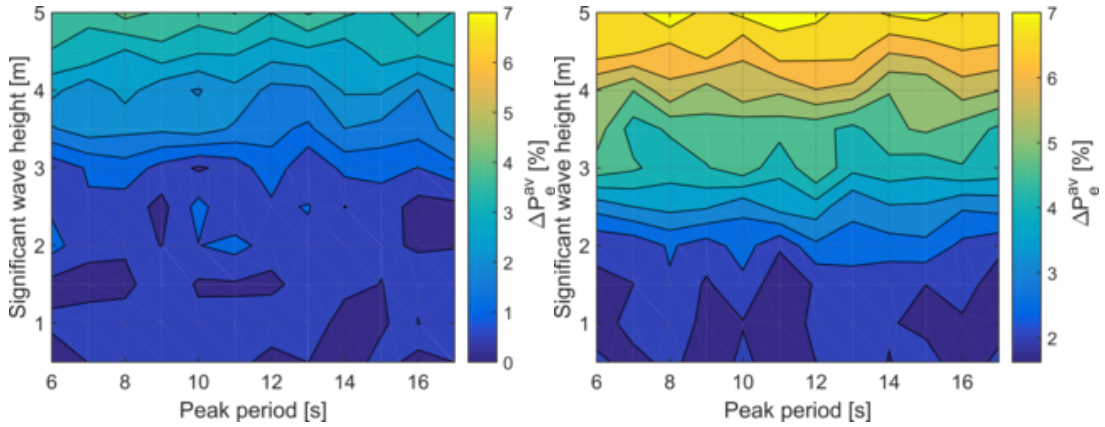

Figure 8.17: Differences between the power matrices obtained with the *NLBEMW2W*$_{Cd=1}$ and *rHyW2W-VI* models under (a) resistive and (b) reactive control.

Differences between the *rHyW2W-VI* and *NLBEMW2W*$_{Cd=1}$ models are relatively low across the complete operational space, for both control strategies. The *rHyW2W-VI* model always underestimates power production, this underestimation being highest at HE sea-states, up to 4% and 7% under resistive and reactive control, respectively. However, differences under resistive control remain remarkably low, below 1%, for LE and ME sea-states, and only increase for HE sea-states ($H_s \geq 3m$). Results for the ME sea-state are consistent with those presented in Table 8.5, where results from the *rHyW2W-VI* and the *NLBEMW2W*$_{Cd=1}$ models (*rHyW2W-I* in Table 8.5) are almost identical under resistive control and show a deviation of about 2% under reactive control.

Table 8.8 presents $AMPP_{gen}$, η_{HyPTO} and $AMPP_{gen}^{rHyW2W-VI}$ results, where differences between the *rHyW2W-VI* and *NLBEMW2W*$_{Cd=1}$ models are remarkably low. The *rHyW2W-VI* model is shown to underestimate the power production capabilities of the spherical HPA by 3.7% and 5.1% under resistive and reactive control, respectively. Due to the high occurrence of the HE sea-

states in Belmullet, differences between the two mathematical models are close to the differences at HE sea-states, shown in Figure 8.17. On the other hand, the impact of control parameters optimised using the *rHyW2W-VI* model on the estimation of power capabilities is demonstrated to be negligible under resistive control, a difference of 0.8%, and very low under reactive control, 2.6%.

Table 8.8: Power production assessment of the spherical HPA under resistive and reactive control, including $AMPP_{gen}$, η_{HyPTO}^{AMPP} and $AMPP_{gen}^{rHyW2W-VI}$. AMPP values are given in kW, while efficiencies are shown in percentage.

		rHyW2W-VI	$NLBEMW2W_{Cd=1}$	Δ [%]
Resistive control	$AMPP_{gen}$	19.16	19.89	3.7
	η_{HyPTO}^{AMPP}	67.8	70.3	N/A
	$AMPP_{gen}^{rHyW2W-VI}$	N/A	19.72	0.8
Reactive control	$AMPP_{gen}$	34.32	36.17	5.1
	η_{HyPTO}^{AMPP}	56.05	59.07	N/A
	$AMPP_{gen}^{rHyW2W-VI}$	N/A	35.48	2.6

The differences between the *rHyW2W-VI* and $NLBEMW2W_{Cd=1}$ models appear due to the slightly lower efficiency of the HyPTO system in the *rHyW2W-VI* model, as shown in Table 8.8. Figure 8.18 illustrates the power output of the *rHyW2W-VI* and $NLBEMW2W_{Cd=1}$ models for the ME sea-state under reactive control, where one can notice the underestimation of the *rHyW2W-VI* model at some power peaks, highlighted with transparent salmon circles.

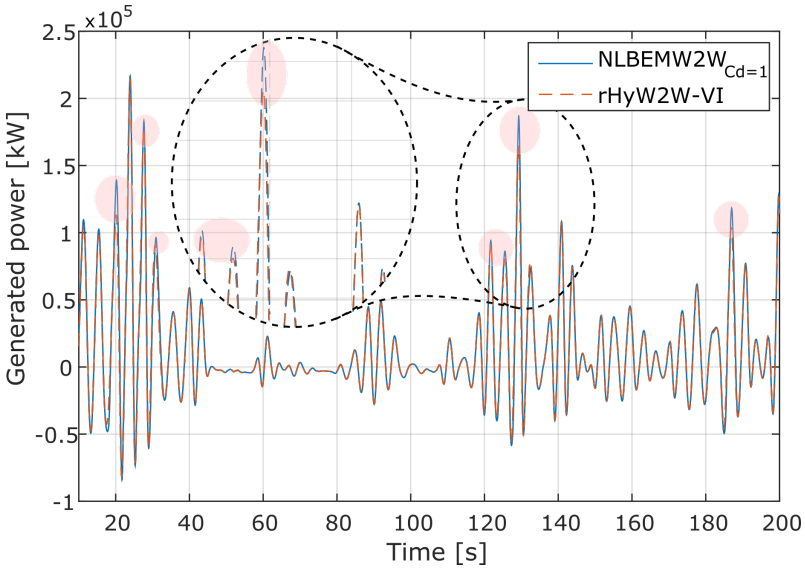

Figure 8.18: Generated power estimated with the *rHyW2W-VI* and $NLBEMW2W_Cd = 1$ models for the ME sea-state under reactive control.

In any case, differences between the *rHyW2W-VI* and the $NLBEMW2W_{Cd=1}$ models are relatively low, demonstrating that the *rHyW2W-VI* model provides sensible control parameters and reasonably high-fidelity power production estimates. In addition, the computational cost of the *rHyW2W-VI* model, reducing computational time in an order of magnitude, confirms that the *rHyW2W-VI* model is the most suitable candidate for controller design and power assessment purposes, as suggested in Table 8.6.

8.4 Summary

The present chapter presents a *systematic* CR approach to create application-sensitive HyW2W models, known as *specific HyW2W* models, for the different potential applications of W2W models, presented in Chapter 2. To that end, the specific requirements of each application are identified in the introduction of this chapter, which are divided into three main categories: accuracy and computational cost, specific dynamics and losses, and nonlinear effects. Based on these requirements, the fidelity/complexity trade-off of the different applications and the commonly used models for these applications are illustrated in Figure 8.1, where the gap between the required fidelity and the fidelity provided by the commonly used mathematical models is shown.

Due to the relevance of nonlinear effects for the complexity reduction of W2W mathematical models, two nonlinearity measures, the *original* and *power* nonlinearity measures, are presented in Sections 8.1.2.1 and 8.1.2.2, respectively. The two nonlinearity measures are based on the *best linear approximation* and are designed to identify and quantify nonlinearities in W2W mathematical models. The *original* nonlinearity measure θ quantifies the nonlinearity degree of the WSHI in W2W models, while the *power* nonlinearity measure χ is designed to quantify the nonlinearity degree of W2W models as a whole, including nonlinear effects from ocean waves to the electricity grid. Section 8.1.3 shows the potential of these two nonlinearity measures and Section 8.1.4 quantifies the nonlinearity degree of two different mathematical models that represent the spherical HPA: *viscNLFK+iPTO* and $NLBEMW2W_{Cd=1}$ models. For the quantification of the nonlinearity degree, the complete operational space of the spherical HPA is analysed, and the behaviour of the spherical HPA under resistive and reactive control strategies is evaluated. Hence, nonlinearities are shown to be significantly enhanced at resonance and the impact of a more aggressive control strategy on the enhancement of nonlinear effects, as discussed in Chapters 3, 5 and 7, is also demonstrated.

Section 8.2 presents the *systematic* CR approach, which uses the *HiFiWEC* simulation platform presented in Chapter 7 as the basis. The possible reductions, deletion or linearisation of different dynamics and/or loss models, in the WSHI and the HyPTO models are illustrated in Sections 8.2.1 and 8.2.2, respectively. Based on these reduced WSHI and HyPTO models, a set of balanced *rHyW2W* models, models where the complexity/fidelity level of the different subsystems is similar, is suggested in Section 8.2.3 and the process to select the *specific HyW2W* model is presented in Section 8.2.4. Finally, the *systematic* CR approach is evaluated for the spherical HPA case in Section 8.3, showing that significant reduction of the computational cost can be achieved while retaining the required fidelity level for each application. Hence, the *specific HyW2W* models for each application are presented in Section 8.3.1, and the *specific HyW2W* model for *PowAss* and *MBC* applications, the *rHyW2W-VI*, is tested in Section 8.3.2, providing very satisfactory results.

Chapter 9

Conclusions

Despite the significant development of different wave energy converter technologies during the recent decades, none of the technologies suggested so far has yet demonstrated economical viability. One of the difficulties for the development of wave energy converters is the prohibitive cost associated with the testing campaigns in wave tanks and, especially, in the open ocean, which are crucial to gain confidence on the prototype. The initial idea of the developers, as explained in Chapter 1, was that, once the technical viability and survivability of the prototype were demonstrated, the economical viability would arrive naturally. Therefore, developers focused on the technical viability, represented by the technology readiness level, trying to reach high technology readiness levels regardless of the cost, as shown by the traditional development methodology illustrated in Figure 1.6. However, the reality has demonstrated that the cost of the technology is crucial for the wave energy industry and that it has to be considered in the development of the prototypes from very early stages.

In this context, an improved development methodology, also illustrated in Figure 1.6, was suggested, where the expensive testing campaigns are delayed as much as possible, until confidence is gained in the prototype. To gain confidence on the prototype while avoiding or minimising the experimental campaigns, precise mathematical models are vital, which allow for the assessment of technical and economic performance of wave energy converters from the early development stages for a tiny fraction of the cost required in experimental campaigns. These mathematical models should include all the necessary dynamics (including nonlinear dynamics, if required), losses and constraints of the different conversion stages from ocean waves to the electricity grid, referred to as parsimonious wave-to-wire models. The literature review presented in Chapter 2 highlighted the need for different mathematical modelling approaches depending on the application of the model. Hence, all the different applications are divided into two main groups, based on two distinguishing dominant requirements: complexity vs. accuracy. This distinction is an important one when designing a mathematical model. Therefore, in this thesis, the author has attempted to create a procedure for designing specific wave-to-wire models for each application, starting from a comprehensive wave-to-wire model.

The starting point of the research study in this thesis is the design of the comprehensive wave-to-wire model, for which the different conversion stages are analysed separately. In the case of the wave-structure hydrodynamic interaction model, the appropriate mathematical approach depends both on the model application and the type of absorber, as shown in Tables 2.5 and 2.6. When creating a model that requires low computational costs, only the mathematical approaches based on potential flow are applicable, including the linear and the partially-nonlinear mathematical models, since the computational cost of other approaches, *i.e.* weakly- or fully-nonlinear potential flow models and numerical wave tanks based on computational fluid dynamics, becomes prohibitive. In addition, linear potential theory appears to be suitable only for oscillating wave surge converters, if viscous effects are included appropriately, while nonlinear Froude-Krylov forces included in the partially-nonlinear potential flow method are essential for floating oscillating water

column devices, heaving point absorbers and oscillating pitch converters.

The linear and the partially-nonlinear potential flow approaches require hydrodynamic coefficients, which are usually identified using a boundary element method solver, such as the commercial code WAMIT or the open-source code NEMOH. The capabilities of the open-source code NEMOH are evaluated in Appendix A, compared to results obtained from WAMIT. In the case of wave activated wave energy converters, such as point absorbers or oscillating wave surge converters, NEMOH provides excellent agreement with WAMIT. It is only when relatively thin elements, such as damping plates, are included in the device that NEMOH provides poor results, showing odd spikes in the radiation damping curve, as illustrated in Figure A.4 (b). One more issue NEMOH cannot yet solve is the presence of irregular spikes at relatively high frequencies, known as irregular frequencies, which can automatically be removed in WAMIT. However, these irregular frequencies can be removed manually, under post-processing, using interpolation methods to fill the gaps, as shown in Section 3.1.3. The modelling of oscillating water column devices is particularly challenging for NEMOH, since it fails to reproduce the hydrodynamic coefficients of the water column, when the water column is modelled as a thin disk. An alternative method is suggested in Section A.3.2, modelling the water column as a long cylinder, which provides reasonable results when only the heave motion is considered. However, the performance of this method should be analysed with more degrees of freedom before definitive conclusions can be drawn.

The case of a generic heaving point absorber, using a spherical heaving point absorber, is analysed in detail in Sections 3.2.4 and 5.1. The linear potential flow model is shown to be able to accurately estimate the behaviour of the spherical point absorber under docile control, when the relative motion of the device with respect to the free-surface elevation is not enhanced by the action of the controller. However, when more aggressive control strategies are implemented, latching or reactive control, for example, the impact of nonlinear effects on the behaviour of the absorber is significant. In order to quantify the impact of these nonlinear effects, two nonlinearity measures are presented in Section 8.1, which confirm that more aggressive control strategies enhance the nonlinear behaviour of wave energy converters, up to 25% more nonlinear under more aggressive control strategies, as shown in Section 8.1.4. These more relevant nonlinear effects, under more aggressive control strategies, lead to important displacement and power absorption overestimation of the linear model. Froude-Krylov forces, and, particularly, static Froude-Krylov forces, are demonstrated to be the most relevant nonlinear effect for heaving point absorbers. However, if only the static Froude-Krylov force is represented by a nonlinear approach, while using the linear representation for the dynamic part, the balance between the static and dynamic forces is broken, resulting in more significant motion and power overestimation, compared to the linear model.

The fact that the action of controller can significantly influence the suitability of a mathematical model suggests that any validation of mathematical models, either against high-fidelity well-established software or experimental results, should always consider the behaviour of the device under the action of an aggressive control strategy. Otherwise, when the validation is based on experimental results, where the device behaves as a wave follower, either because it is floating free on the free-surface or because it is tested under a docile control strategy, even mathematical models based on the linear potential flow method may provide excellent agreement with experimental results, as shown in Section 5.1.2. However, any further development based on these linear mathematical models, such as the design of the absorber geometry, the power take-off system or the energy maximising controller, may result in ineffective designs, leading to dramatic consequences, as shown in Section 3.2.4.

In addition to nonlinear Froude-Krylov and viscous effects, the impact of nonlinear waves is analysed in this thesis. Section 2.1 shows that waves in the power production region tend to be linear or low-order nonlinear, based on the data obtained from open ocean tests of three different devices. However, the implementation of nonlinear Froude-Krylov forces is theoretically more consistent when nonlinear waves are considered, since nonlinear boundary conditions are assumed at the free-surface. Results shown in Section 3.2.4.2 demonstrate that the linear representation of ocean waves is accurate enough when analysing a wave energy converter in the power production

region.

Therefore, including nonlinear Froude-Krylov forces, both static and dynamic, and viscous effects is vital to accurately design control strategies and evaluate the performance of heaving point absorbers. However, mathematical models with low computational cost are required for the design model-based control strategies and assessment of power production capabilities of wave energy converters. Therefore, the semi-analytical approach presented in Section 3.3 to implement nonlinear Froude-Krylov forces, which can also be extended to compute several degrees of freedom, is very convenient, providing identical results to other approaches that also include nonlinear Froude-Krylov forces, while reducing the computational cost by a factor of 5. With respect to the viscous effects, the most widely used Morison-like equation with a quadratic drag coefficient C_{drag} is found to be inconsistent, as shown in Section 7.4. In fact, the Morison-like viscous model is particularly inconsistent when the motion of the absorber is enhanced via an energy maximising control strategy. This highlights again the need for an accurate coverage of a wave energy converter's operational space, including large relative WEC/fluid motion amplitudes to emulate the action of an energy maximising control strategy, when carrying out experiments for the purpose of validation, or identification of mathematical models.

Including all the relevant components of the power take-off system, a hydraulic transmission system coupled to an electric generator in the case of the present thesis, is an essential part of comprehensive wave-to-wire modelling. However, these components are often neglected in the mathematical models presented in the literature, as illustrated in Section 2.6. Excessive simplification of the power take-off system can lead to generated power overestimation of up to 160%, as shown in Tables 6.9 and 7.3, which can vary depending on the control conditions.

With respect to hydraulic transmission systems, the main aspects to be considered are fluid compressibility, friction losses in the hydraulic cylinder and the losses in the hydraulic motor. Depending on the hydraulic system configuration, the effect of valves and hydraulic accumulators is also essential. Fluid compressibility is typically represented via the effective bulk modulus, which varies with the fluid pressure. However, Section 4.1.2.1.1 shows that the impact of these variations is negligible when estimating the pressure in the chambers of the hydraulic cylinder. Therefore, a constant value of the bulk modulus can be used to represent compressibility effects of the hydraulic oil. This constant value is usually calculated by reducing the air-free value provided by manufacturers by 40%. In order to include compressibility effects in the model of the hydraulic transmission system and capture the fast dynamics of the compressible fluid, the time-step of the mathematical model must be reduced to 1ms, which moderately increases the computational cost of the model.

Friction losses in the hydraulic cylinder and losses in the hydraulic motor are calculated using nonlinear loss models based on the Stribeck and the Schlösser models, respectively. The parameters of these models are identified using manufacturers' data. In the case of the hydraulic motor, since different hydraulic motor topologies can be used for different hydraulic system configurations, manufacturers' data for the required motor must be used. In addition, manufacturers often provide data for very specific operating points, *i.e.* one or two fractional displacement or rotational speed values. In that case, the parameters of the loss model identified using manufacturers' data must be interpolated to cover the whole operational space. However, this interpolation should be carried out carefully. If only data for two operating points is available, the linear interpolation is the only option, but if more operating points are available, that this linear interpolation can be inaccurate, as shown in Section 4.1.2.4.1. A second order interpolation function is shown to be accurate for all the different cases when more than two operational points are available. One of the advantages of the mathematical model suggested in this thesis for the hydraulic motor is the possibility of adapting the model, including the loss model, to hydraulic motors of different sizes by multiplying flow and torque equations by the ratio between the displacement of the baseline and the new motor. The models for the different hydraulic components are comprehensively validated over a wide range of operating conditions, demonstrating the suitability of the loss models identified using manufacturers' data.

Mathematical models for electric generators, are based on the conventional two-phase orthogonal rotating *dq* reference frame, which simplifies the analysis of three-phase machines. Therefore, iron losses in the generators are neglected, only considering copper, stray, and friction or windage losses. However, comparing the results from this conventional model against experimental results, excellent agreement is obtained, as illustrated in Section 5.3.3.1 for three different electric generator topologies, which suggests that iron losses can be neglected when modelling electric generators. However, the generators analysed for the validation in this thesis are small generators (around 10 kW). The relevance of iron losses in larger generators (around 1 MW) may be higher and, thus, a more detailed analysis is required before assuming iron losses are negligible, in general. In any case, if electrical dynamics are included in the mathematical model of the electric generator, the time-step must be reduced to 50μs, which significantly increases the computational cost of the mathematical model. The *dq* reference frame is also very convenient for control purposes. The control of electric generators is implemented via power converters and can be a highly valuable strategy, particularly rotational speed control, to improve the efficiency of the electric generator when generating power at part-load conditions.

The implementation of power converters in the mathematical model is more problematic than the implementation of electric generators. Power converters include extremely fast switching operations, reproducing the pulses generated in the pulse width modulator unit. However, these switching operations require very fine time-steps (about 1μs), which prohibitively increase the computational cost of the model. In fact, it is not only the computational time that increases prohibitively, but also memory requirements, rendering a simulation of more than a few seconds beyond the capability of most computing hardware. Therefore, the simplified alternative, suggested in this thesis, is to consider only the fundamental harmonic of the voltage signal and to model the pulse width modulator units as unit gain elements. The results from the simplified mathematical model show good agreement with experimental results, in terms of output power measurements and controller's efficacy, as presented in Section 5.3.3.2. However, power losses can only be considered if switching operations are included. Therefore, the efficiency of power converters in the mathematical model can be included by means of an efficiency curve measured from experimental tests. In fact, this strategy provides accurate results and significantly reduces the computational requirements, as shown in Section 5.3.3.2.

An essential aspect of comprehensive parsimonious wave-to-wire models is the efficient interconnection of the different mathematical models. However, the fact that each sub-model, which represents a conversion stage of the drivetrain, has different time-step requirements, and that the interconnections between the different sub-models are bidirectional, makes the combination of the different sub-models particularly complex. The use of a single-rate time-integration scheme simplifies the model implementation, which can be coded as a single large model. However, the use of a single-rate scheme involves that the time-step required to capture the fastest dynamics of the complete model, 50μs for the electrical dynamics in this specific case, to be used for all the different dynamics. This includes unnecessary computation for the slowest dynamics, which significantly increases the computational time and memory requirements of the mathematical model. The alternative multi-rate scheme divides the complete wave-to-wire model into different sub-models and uses the required time-step in each sub-model. That way, unnecessary computation can be avoided, reducing computational time and memory requirements by a factor of 5 and 8, respectively, as shown in Section 6.1.1.1. Due to the different time-steps used in the different sub-models, the variables shared between two consecutive sub-models need to be interpolated. The interpolation calculation can degrade results if a too simplistic interpolation technique is used, while complicated techniques can significantly increase the simulation time. Therefore, it is crucial to perform interpolation only when required (always in up-sampling, but only when the time-steps of the interconnected sub-models are not multiples of each other in down-sampling) and to use efficient interpolation techniques. In this specific case, as described in 6.1.1.1, linear interpolation is found to be accurate and to reduce computational costs, compared to other more complex techniques.

Apart from the time-integration scheme, diverse numerical methods to solve differential equations, one-step and multi-step methods, are compared for all the different sub-models. The use of the traditionally-used one-step fourth order Runge-Kutta method is found to be computationally inefficient for all the different sub-models. Lower order Runge-Kutta methods or multi-step predictor-corrector Adams-Moulton or backward differentiation functions can provide very similar fidelity levels for a fraction of the time required by the fourth order Runge-Kutta method, as depicted in Figure 6.5. However, when modelling stiff systems, such as hydraulic transmission systems, where compressibility effects are included, higher order Adams-Moulton or backward differentiation functions become unstable, unless the time-step is significantly reduced, as illustrated in Figure 6.4. Therefore, a second order Runge-Kutta method with the multi-rate integration scheme is found to be the most efficient numerical method, providing identical fidelity levels to the higher order Runge-Kutta method, while reducing computational requirements by a factor of 10, compared to the traditional single-rate fourth-order Runge-Kutta method.

High-fidelity comprehensive wave-to-wire models are essential to accurately evaluate the holistic performance of wave energy converters and design the different parts of the converters. For example, the power take-off technology or configuration can only be adequately specified if the overall performance of the wave energy converter is evaluated. If only the power take-off efficiency is evaluated, then the constant-pressure hydraulic transmission system appears to be the best candidate, with reasonably high efficiencies for all the components. However, the large accumulators included in the constant-pressure configuration remove the option to maximise energy absorption from ocean waves, as shown in Section 6.2.1. In contrast, if the overall performance of the wave energy converter is analysed, one can notice the potential of the variable-pressure hydraulic transmission system configuration to absorb and generate more energy (up to 260% and 140% more, respectively, as shown in Section 6.2), despite its lower power take-off efficiency. Similarly, the effect of the control strategy can only be accurately evaluated when the overall performance is analysed. A more aggressive control strategy, which maximises the energy absorption and generation by enhancing the motion of the absorber, is shown in Section 6.2.2 to significantly improve the performance of wave energy converters, increasing generated power by 350%, partly due to a significant increase in the power take-off efficiency. However, power generation can also be significantly increased by using a more aggressive control strategy (an increase of 115%) when the efficiency of the power take-off system is similar or lower, due to the substantial improvement in absorbed power (117% higher power absorption under more aggressive control strategies).

Similar conclusions can be drawn when using the HiFiWEC simulation platform, where a numerical wave tank, based on computational fluid dynamics, is coupled to the high-fidelity power take-off system model, providing the highest achievable fidelity level via numerical simulation. In fact, a heaving point absorber under a more aggressive control strategy is shown to generate 40% more electrical power than the mechanical power absorbed from ocean waves under a docile control strategy (see Table 7.3). This suggests that the use of an accurately designed aggressive control strategy would always improve the power production of a wave energy converter, regardless of the power take-off efficiency.

Parsimonious wave-to-wire models are also crucial for the design of control strategies and power assessment. Unless the essential dynamics, losses and constraints of the different conversion stages from ocean waves to the electricity grid are included in the mathematical model used for the design of the controller, energy generation cannot be adequately maximised and the performance of the wave energy converter is inefficient. More importantly, a poorly designed controller can lead to catastrophic consequences, as shown in Section 6.2.3, where the device is forced to follow an erroneous trajectory that can result in negative average generated power (consuming more energy from the electricity grid than the energy generated from ocean waves) or, more dramatically, stuck at one of the constraints of the power take-off, producing zero energy and potentially damaging the structure of the wave energy converter. Therefore, it is highly recommended to use high-fidelity simulation platforms, such as the HiFiWEC, to accurately evaluate the effectiveness of control strategies and evaluate the realistic performance of the wave energy converter.

Finally, wave-to-wire models specifically designed for each application can be created following a systematic complexity reduction approach, as shown in Section 8.2. That way, the relevance of the different dynamics in the drivetrain is analysed, keeping only the dynamics that are necessary for the purpose of each application. Electrical dynamics are necessary for electrical power systems modelling, electric generator fault analysis, power quality analysis or wave power integration into the electricity grid. However, modelling electrical dynamics requires short time-steps, which significantly increase the computational cost of the mathematical model. Therefore, if the computational cost requirement is very restrictive for an application, as in the case of an energy maximising controller's design or power production assessment of a wave energy converter, the electrical dynamics should be removed. Similarly, compressibility effects in the hydraulic transmission system are important when designing the servo controller (*e.g.* control of hydraulic valves) or even when designing and sizing the components of the hydraulic transmission system, since water hammer effects due to the compressibility of the fluid may influence the wear of the different components. However, for energy maximising controller design or power production assessment applications, these compressibility effects are negligible, and their omission can reduce computational costs significantly. In contrast, friction effects in the cylinder and losses in the hydraulic motor are important to accurately estimate the power generation capability of the wave energy converter, and add almost no extra computational cost, if they are efficiently implemented in the mathematical model.

Hence, reasonably high-fidelity results (about 95% fidelity) can be obtained by only including the essential dynamics, losses and constraints from ocean waves to the electricity grid, while reducing the computational cost of this comprehensive wave-to-wire model to similar values of the traditionally used excessively simplified mathematical models, as illustrated in Table 8.5.

9.1 Future work

The main contribution of this thesis is the construction of a unique comprehensive wave-to-wire model. However, for the sake of completeness, this wave-to-wire model still requires specific improvements:

- The wave-structure hydrodynamic interaction is so far defined for a single-degree-of-freedom point absorber, while real wave energy converters absorb energy from multiple degrees-of-freedom. Thus, in order to provide high-fidelity results of realistic wave energy converters, the inclusion of multiple degrees-of-freedom, including the necessary nonlinear effects in the different degrees of freedom, is vital. In addition, the improved version of the wave-structure hydrodynamic interaction model should allow for the implementation of absorbers with different geometric characteristics and working principles. In this sense, incorporating nonlinear effects may not be necessary in all the degrees-of-freedom, depending on the geometry and working principles of the absorber.

- The behaviour of a floating absorber moving in different degrees of freedom can be influenced by mooring lines, especially if the motion of the device is enhanced via an energy maximising control strategy. Therefore, including mooring lines is crucial in order to understand the complete dynamic behaviour of the device and to evaluate the holistic performance of realistic wave energy converters. Apart from the impact of mooring lines on the performance of the absorber, the mathematical model of mooring lines implemented in the comprehensive wave-to-wire model should also consider their internal dynamics, allowing for the evaluation of stresses and tensions in mooring lines, which is crucial for techno-economical analyses.

- Including different realistic wave energy converters involves the implementation of different power take-off systems, such as air-turbines, mechanical transmission systems and linear

generators. In the case of mechanical transmission systems, the implementation is straightforward, where only the mathematical model for the transmission stage needs to be replaced, keeping the remainder of the model as it is. The implementation of oscillating water column devices with air-turbines requires an additional subsystem with a thermodynamic model to consider compressibility effects of the air trapped in the chamber. In contrast, for the implementation of the linear generator, the transmission stage can be removed and the generation stage modified, replacing the rotational generator model with the linear generator model.

- Finally, the comprehensive wave-to-wire model should be extended to include arrays of several wave energy converters. Wave-to-wire models of arrays are essential for the analysis of wave power grid integration, the design of the electrical equipments, such as submarine cables to deliver electricity into the electricity grid, realistic power assessment of large wave energy converter farms, where interactions among the different absorbers are also considered, and the design of energy storage systems, if necessary. However, the implementation of arrays of comprehensive wave-to-wire models is likely to be challenging from a computational cost perspective. Due to the hydrodynamic interactions among the different absorbers implemented in the farm, the hydrodynamic model cannot be parallelised. However, power take-off systems are completely independent of each other, meaning that the parallelisation of the power take-off system models is possible, which can be computationally beneficial.

The impact of high-fidelity wave-to-wire models on the design of controllers has been widely demonstrated in this thesis. However, the control strategies employed in the thesis are rather simple control strategies. One of the interesting future research directions is the integration of the most relevant information of the comprehensive wave-to-wire model in more advanced control algorithms. These more advanced control strategies allow for generated energy maximisation (not only absorber energy) subject to certain constraints. These constraints can be used to minimise the wear of the different components, resulting in lower maintenance and operation costs and, as a consequence, lower the cost of wave energy. In addition, advanced control methods also include fault-tolerant control strategies, which can retain energy generation in the event of a fault in one or more components of the drivetrain. However, the integration of all the dynamics and losses, even when they are efficiently included in the optimisation problem, may be computationally prohibitive.

Last but not least, an important effort needs to be made in the wave energy community to include the appropriate economic metrics into the numerical models. The research study presented in this thesis only focuses on the technical aspects. However, in order to design wave energy converters that can achieve commercial viability, an accurate techno-economical analysis is necessary. Therefore, the author believes that high-fidelity mathematical models, such as the comprehensive wave-to-wire model presented in this thesis, are valuable tools, but need to be complemented with economic analysis in order to provide developers with the most accurate information. Only with the most accurate and complete information can developers make the correct decisions in the development of economically successful wave energy converters.

Appendix A

Verification of the NEMOH solver

The comparison between NEMOH and WAMIT is focused on the processing stage, that is, the stage where the BVP for the user-defined geometry is solved, providing the FD hydrodynamic coefficients. Other aspects, such as the pre-processing stage, where the files are prepared, and the post-processing stage, where the FD coefficients are converted into TD coefficients, are ignored in this section, but are considered in [396].

A.1 Geometry selection

The comparison between NEMOH and WAMIT is performed using the geometries of four different WECs for which real-life examples exist: a submerged axisymmetric point absorber (SAPA), a two-body point absorber (2BPA), an OWSC and a floating OWC. That way, most of the different types of WECs presented in Figure 1.4 are covered. In addition, two configurations of the 2BPA are analysed. The geometry of both 2BPAs is identical, except for the fact that one configuration includes a damping plate (Spar_{wdp}), while the second configuration does not ($\text{Spar}_{\text{nodp}}$). The main characteristics of the geometries used in the present comparison are given in Table A.1.

The mesh used in WAMIT and NEMOH simulations is identical for the SAPA, the 2BPA (in both configurations) and the OWSC, for which the mesh generated in NEMOH is converted into the WAMIT format (*.gdf*) to be used in WAMIT. Figure A.1 illustrates the meshes for these three geometries. The case of the OWC is slightly different, due to the different modelling options presented in the literature, and is treated separately in Section A.3.2.

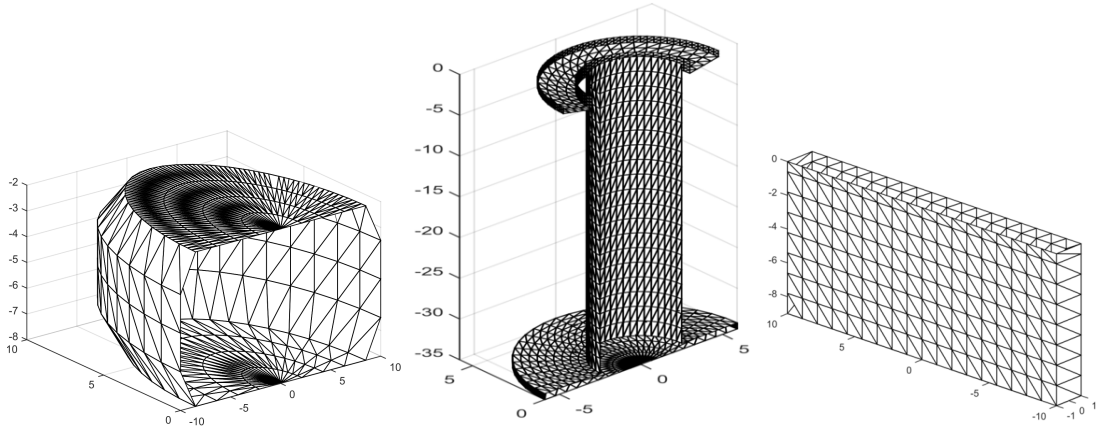

(a) SAPA (b) 2BPA (c) OWSC

Figure A.1: The low-order meshes for the SAPA, 2BPA and OWSC devices.

Table A.1: Main geometric characteristics* of the WECs used for the comparison.

Device type	Realistic WEC	DoFs	Principal dimensions	Water depth
SAPA	CETO [27]	surge (s_{11}) heave (h_{33}) pitch (p_{55})	$R^{geom} = 8.5$ $H^{geom} = 6$ $H_{FS}^{geom} = -2$	20
2BPA	OPT [29]	surge (s_{11}) heave (h_{33}) pitch (p_{55})	$R_{F_{out}}^{geom} = 4.75$ $R_{F_{in}}^{geom} = 3$ $T_F^{geom} = 2.25$ $R_S^{geom} = 2.5$ $R_{DP}^{geom} = 5.9$ $T_S^{geom} = 35$	∞
OWSC	Oyster [26]	pitch (p_{55})	$W^{geom} = 2$ $L^{geom} = 20$ $H^{geom} = 12$	13
OWC	Sparbuoy [34]	heave (h_{33})	$R_{out}^{geom} = 3$ $R_{in}^{geom} = 2$ $T^{geom} = 10$	∞

* In the *Principal dimensions* column, R^{geom} is the radius, H^{geom} the height, H_{FS}^{geom} the distance from the top of the device to the free-surface, T^{geom} the draft, W^{geom} the width and L^{geom} the length. In addition, subscripts $_{out}$ and $_{in}$ indicate the outside and inner radius, respectively, and $_F$, $_S$ and $_{DP}$ refer to the float, spar cylinder and the damping plate of the 2BPA, respectively. All the dimensions in the table are shown in metres.

A.2 Outcome selection

Only the processing capabilities are analysed in this section, by comparing the following FD hydrodynamic coefficients:

- F_{ex} [N/m],
- A_{rad} [Kg], and
- B_{rad} [Nm/s].

Due to the large number of cases to be compared (three devices with multiple DoFs, including cross coupling terms, and three different coefficients for each case, as illustrated in Table A.1), visual comparison of all the cases is impractical. Therefore, results need to be shown by means of similarity measures. However, discrepancies between NEMOH and WAMIT may arise due to diverse causes, but such discrepancies do not necessarily indicate a failure on the part of NEMOH. Thus, it is not possible to show the correspondence between the results obtained from the two solvers by using a single similarity measure. As a consequence, the comparison between NEMOH and WAMIT is shown by using three metrics based on two different measures, namely cross-correlation and the root mean square (RMS) ratio.

The cross-correlation measure compares two series as a function of the displacement of one relative to the other, and shows the similarity of the two signals for all the possible relative positions, as one signal progressively overlaps the second signal. For two series comprising n elements, the cross-correlation of the two signals results in a correlation vector with $2n$ values. Each value in the cross correlation vector lies between -1 and 1, where 1 means a perfect positive correlation, 0 indicates no correlation and -1 shows a perfect negative correlation between the two signals under analysis.

For the present study, where curves of hydrodynamic coefficients as function of frequency obtained from NEMOH and WAMIT are compared, two values from the correlation vector are considered. The first value of interest is the correlation when frequencies of the two curves align. This value is termed *XC*. The second value is the maximum correlation value, termed *maxXC*, which may not occur when the frequencies are aligned. Hence, *XC* shows the shape similarity of the curves from NEMOH and WAMIT when the frequencies are aligned, while *maxXC* highlights the best shape similarity of the curves, which corrects any potential frequency shift between NEMOH and WAMIT.

For example, these frequency shifts appear in geometries with a moonpool. Figure A.2 shows the B_{rad} coefficient for the pitch motion of the 2BPA float obtained from WAMIT and NEMOH, including the relative positions of the NEMOH curve corresponding to the *XC* and *maxXC* values, and the *XC* and *maxXC* values obtained from the cross-correlation analysis. When the frequencies of the WAMIT and NEMOH curves are aligned, the resonant frequency of the moonpool calculated with NEMOH and WAMIT is slightly different, showing strong spikes at different frequencies. As a consequence, the *XC* value is low. However, the agreement between the NEMOH and WAMIT curves, when frequencies of the curves are aligned, is relatively good, meaning that the *XC* value fails to provide a realistic similarity measure. Therefore, a second correlation value is necessary to realistically illustrate the agreement between the WAMIT and NEMOH curves. The *maxXC* value and the position of the NEMOH curve corresponding to the *maxXC* value shown in Figure A.2 demonstrate that the only discrepancy between NEMOH and WAMIT arises due to a small frequency shift. Hence, combining the *XC* and *maxXC* value, the shape agreement between WAMIT and NEMOH can be obtained. If there is no such frequency shift between the NEMOH and WAMIT curves, *XC* and *maxXC* values are identical.

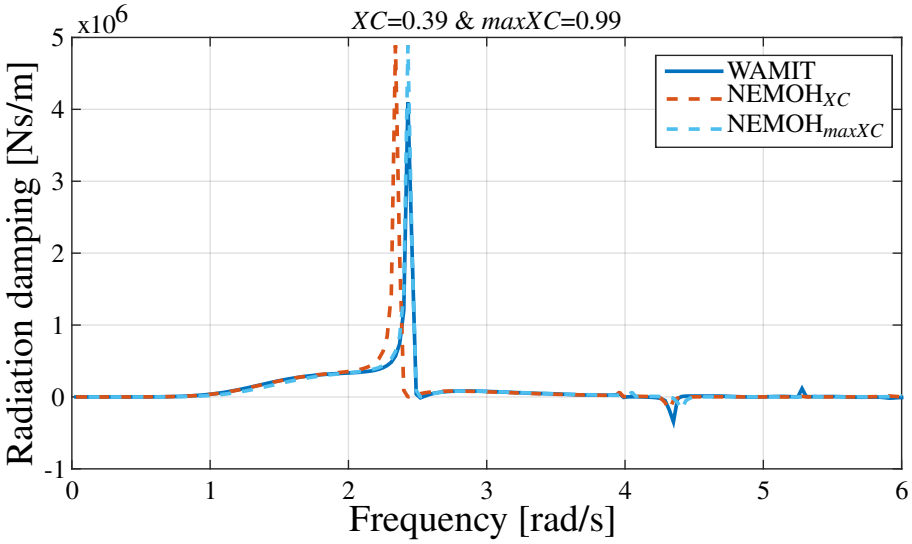

Figure A.2: Radiation damping for the pitch mode of the 2BPA float from WAMIT and NEMOH, illustrating the relative position of the curve obtained from NEMOH corresponding to the *XC* and *maxXC* measures.

A third metric is required, however, as the *XC* and *maxXC* values only show the similarity of the two curves in terms of their shape. These metrics give no indication as to the relative amplitudes of the two signals. Therefore, the RMS ratio (*RMSr*), defined in Equation (A.1), is used.

$$RMSr = \frac{RMS(C_{FD}^{WAMIT})}{RMS(C_{FD}^{NEMOH})}, \tag{A.1}$$

where C_{FD} represents the FD hydrodynamic coefficient under analysis.

A.3 BEM comparison

Results of the comparison between the hydrodynamic coefficients are shown in Table A.2, using the three measures described in Section A.2. In addition, a colour code with three colours (green, orange and red) indicates the level of agreement between NEMOH and WAMIT. Green colour indicates a cross-correlation or *RMSr* of between 0.9 and 1.1. Orange indicates a cross-correlation or *RMSr* between 0.8 and 0.9, and 1.1 and 1.2. Finally, red indicates any values outside these ranges.

Table A.2: Comparison of the hydrodynamic coefficients obtained with WAMIT and NEMOH for the four device types.

Devices		A_{rad}				B_{rad}				$\hat{F}_{ex}$			
		s_{11}	h_{33}	p_{55}	$s-p_{35}$	s_{11}	h_{33}	p_{55}	$s-p_{35}$	s_{11}	h_{33}	p_{55}	
SAPA		0.9998	0.9995	1.0000	0.9993	0.9993	0.9997	0.9998	0.9988	0.9998	0.9999	0.9996	*XC*
		0.9998	0.9995	1.0000	0.9993	0.9993	0.9997	0.9998	0.9988	0.9998	0.9999	0.9996	*maxXC*
		0.9358	0.9750	0.9568	0.9234	0.9233	0.9556	0.9626	0.8994	0.9821	0.9661	0.9654	*RMSr*
2BPA	Float	0.8996	0.9682	0.8655	0.7862	0.2657	0.7790	0.3949	0.2394	0.7348	0.9915	0.9105	
		0.8996	0.9682	0.9499	0.8539	0.9991	0.9879	0.9945	0.9994	0.9948	0.9915	0.9987	
		1.0210	0.9888	0.9197	0.9166	1.0681	0.9374	1.2165	1.1916	0.8524	0.9994	0.9582	
	$Spar_{nodp}$	0.9733	1.0000	0.8636	0.8561	0.2888	0.9995	0.2850	0.2870	0.8544	1.0000	0.7992	
		0.9733	1.0000	0.8819	0.8781	0.9985	0.9995	0.9986	0.9985	0.9963	1.0000	0.9963	
		0.9786	1.0348	0.8941	0.8881	1.1253	0.9760	1.1025	1.1107	0.9124	0.9996	0.8788	
	$Float\text{-}Spar_{nodp}$	0.8495	0.9990	0.7687	0.2754	0.2494	0.9900	0.3294	0.2492	N/A	N/A	N/A	
		0.8495	0.9990	0.8701	0.8518	0.9995	0.9900	0.9963	0.9995	N/A	N/A	N/A	
		0.9338	0.9898	0.7807	0.9269	1.0997	0.9827	1.1266	1.0855	N/A	N/A	N/A	
	$Spar_{wdp}$	0.8443	1.0000	0.3284	0.2270	0.1233	0.9242	0.1169	0.1198	0.8001	0.9995	0.6994	
		0.9803	1.0000	0.9904	0.9923	0.9907	0.9343	0.9902	0.9905	0.9942	0.9995	0.9948	
		0.9956	1.0404	1.0278	1.0241	1.2428	0.5858	1.2374	1.2345	0.9646	0.9954	0.9499	
	$Float\text{-}Spar_{wdp}$	0.0374	0.8127	0.1459	0.2216	0.0634	0.3933	0.1612	0.0645	N/A	N/A	N/A	
		0.9939	0.8127	0.9927	0.9943	0.9736	0.3933	0.9965	0.9735	N/A	N/A	N/A	
		1.1240	0.8255	0.9398	1.1177	1.2801	0.4474	1.1397	1.2705	N/A	N/A	N/A	
OSWC		N/A	N/A	0.9902	N/A	N/A	N/A	0.9779	N/A	N/A	N/A	0.9853	
		N/A	N/A	0.9902	N/A	N/A	N/A	0.9938	N/A	N/A	N/A	0.9927	
		N/A	N/A	1.0493	N/A	N/A	N/A	1.0753	N/A	N/A	N/A	1.0713	
OWC	Buoy	N/A	0.9996	N/A	N/A	N/A	0.9618	N/A	N/A	N/A	0.9978	N/A	
		N/A	0.9996	N/A	N/A	N/A	0.9618	N/A	N/A	N/A	0.9978	N/A	
		N/A	0.9395	N/A	N/A	N/A	0.8668	N/A	N/A	N/A	0.9860	N/A	
	Free-surface (thin disk)	N/A	0.4494	N/A	N/A	N/A	0.1698	N/A	N/A	N/A	0.5470	N/A	
		N/A	0.4494	N/A	N/A	N/A	0.3973	N/A	N/A	N/A	0.7167	N/A	
		N/A	0.8179	N/A	N/A	N/A	0.0011	N/A	N/A	N/A	0.4285	N/A	
	Free-surface (FC)	N/A	0.9998	N/A	N/A	N/A	0.8719	N/A	N/A	N/A	0.8990	N/A	
		N/A	0.9998	N/A	N/A	N/A	0.8837	N/A	N/A	N/A	0.8990	N/A	
		N/A	1.1823	N/A	N/A	N/A	1.2972	N/A	N/A	N/A	1.2324	N/A	

* Results for the added-mass column in the case of the OWC free-surface modelled via the FC technique are obtained using the total inertia term that includes the added-mass and the mass of the cylinder.
**N/A is used to show the corresponding measure is not applicable in that case.

Due to the difficulty to represent OWC devices with BEM solvers, the comparison between NEMOH and WAMIT is divided into two parts. Firstly, wave-activated bodies, that is, devices with moving elements that are directly activated by ocean waves, such the SAPA, 2BPA and OWSC devices, are analysed in Section A.3.1. Secondly, OWC devices are studied in Section A.3.2.

A.3.1 Wave-activated WECs

Overall, the performance of the NEMOH solver for the three wave-activated WECs (the SAPA, the 2BPA and the OWSC) is quite good. Similarity measures for the SAPA show a very good agreement between NEMOH and WAMIT for the three DoFs, including the cross coupling terms ($s - p_{35}$), as illustrated in Table A.2. In fact, the *XC* and *maxXC* measures are very close to 1, which would illustrate a perfect match, for all the DoFs and hydrodynamic coefficients. The main differences appear at curve peaks, where the curves from NEMOH reach slightly larger values, while results from NEMOH and WAMIT are almost identical for the rest of the curve, as illustrated in Figure A.3 (a).

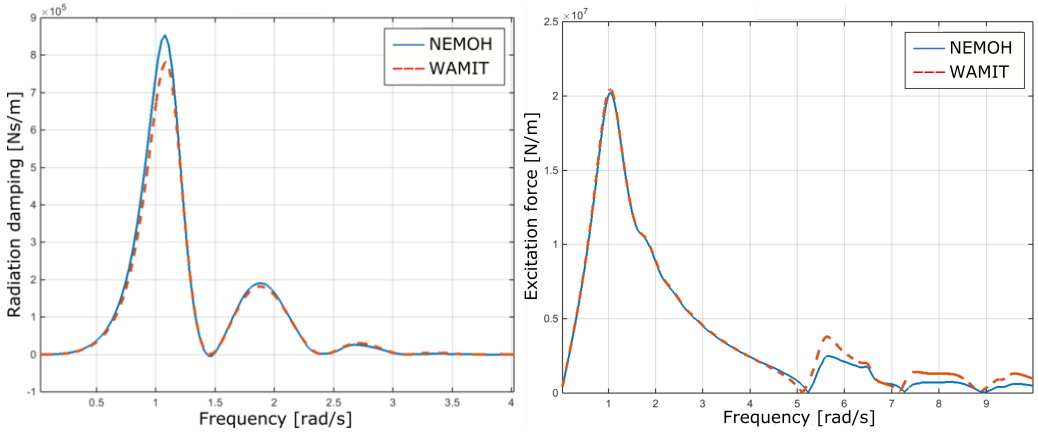

(a) SAPA - s_{11} (b) OWSC - p_{55}

Figure A.3: Radiation damping for surge mode of the SAPA device (a) and the excitation force for the pitch mode of the OWSC (b).

Similarly to the SAPA, the hydrodynamic coefficients from NEMOH and WAMIT for the OWSC are almost identical. The level of agreement between the two solvers is shown in Table A.2, where all the measures show that hydrodynamic coefficients match almost perfectly. The only difference between the coefficients obtained with NEMOH and WAMIT is the magnitude of the peak values, which in this case is always slightly lower in NEMOH, as illustrated in Figure A.3 (b).

The case of the 2BPA is slightly more complex, due to the damping plate of the central spar buoy, which may be an issue for NEMOH if represented by a thin element, and the presence of the moonpool between the float and the spar. Although it is well known that linear potential flow solvers cannot accurately represent such small moonpools, it is informative to compare the results between WAMIT and NEMOH when modelling this gap.

The similarity metrics given in Table A.2 for the two 2BPA configurations, with and without the damping plate, are divided into 5 different sections: the float, the $\text{Spar}_{\text{nodp}}$, interaction between the float and the $\text{Spar}_{\text{nodp}}$, the Spar_{wdp}, and interaction between the float and the Spar_{wdp}. Similarity measures show good agreement between NEMOH and WAMIT for the 2BPA without the damping plate (including the float and the spar cylinder). The mayor difference between NEMOH and WAMIT, for the 2BPA float, is the frequency shift, showing higher *maxXC* than *XC* for most of the coefficients. Figure, A.4 (a) illustrates, however, that results from NEMOH and WAMIT are almost identical for the 2BPA float, and, the fact that the moonpool frequency lies at a slightly higher frequency in NEMOH, should not be taken as an issue of the NEMOH solver. In addition, one can note irregular spikes at high frequencies (around 3.2, 4.3 and 4.8 rad/s, in this case) in the NEMOH curve, which are not present in the WAMIT curve. These spikes are known as irregular frequencies [177], which are frequencies for which the solution of the inner problem in the BEM solver is non-zero. These irregular frequencies appear only with free-surface piercing

bodies and generally at high frequencies, and arise due to a fundamental error in the formulation of the BEM solvers. Different methods have been suggested in the literature to solve the problem of irregular frequencies [397]. In fact, WAMIT results do not show such spikes, because WAMIT includes an option to remove irregular frequencies [398]. NEMOH also offers a preliminary option to remove them, but it is not fully implemented at this time, so it has not been included in this study [177].

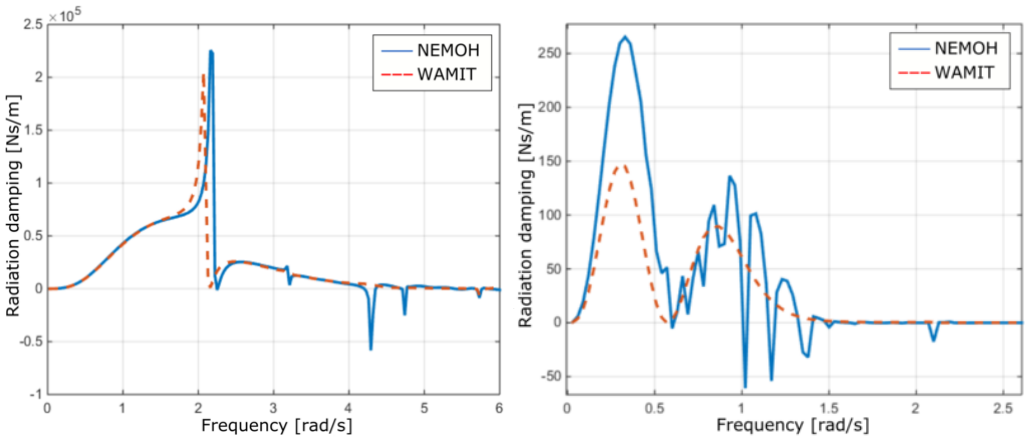

(a) 2BPA float - h_{33} (b) 2BPA spar - h_{33}

Figure A.4: Radiation damping for heave mode of the 2BPA float (a) and spar cylinder with damping plate (b).

However, the performance of the NEMOH solver decreases significantly when the damping plate is considered. Results are similar for A_{rad}, for which the frequency shift is the main source of discrepancy, while the calculation of B_{rad} for different DoFs appears to be problematic, as illustrated in FigureA.4 (b). The spar cylinder includes a relatively thin element at the bottom, which appears to be the source of odd spikes in the damping curve at relatively low frequencies.

A.3.2 Oscillating water column WECs

Modelling OWC devices using BEM codes, using either WAMIT or NEMOH, is especially challenging due to the very particular behaviour of the free-surface in the OWC chamber. The traditional method for modelling the free-surface inside the OWC chamber is to use an infinitely thin massless disk (lid) to represent the free-surface [399], referred to here as the thin disk method. However, WAMIT provides a number of methods to model OWC devices, including a generalised mode, which considers the free-surface at the moonpool as an extension of the body surface and assigns a new patch to represent the free-surface in the higher order method. Generalised modes are then applied to this patch, and the motion of the moonpool is modelled as the heave motion of this additional patch.

The only way the free-surface inside the chamber can be modelled in NEMOH is using the traditional method, *i.e* modelling a two-body system where the lid is modelled as a thin cylinder, as illustrated in Figure A.5 (a). An alternative method to model the free-surface is suggested in [400], where a cylinder of the same length as the water column is used. This method is referred to as the full cylinder (FC) method, and the mesh generated to apply the FC method is illustrated in Figure A.5 (b). Thus, in order to provide a fair comparison between the two solvers, while showing the full capabilities of both solvers, the two different two-body system models in NEMOH and WAMIT, plus a third case using the generalised modes in WAMIT, are compared.

Results shown in Table A.2 show good agreement between NEMOH and WAMIT for the OWC buoy, which is similar to the OPT float, and so good agreement was to be expected. However, when

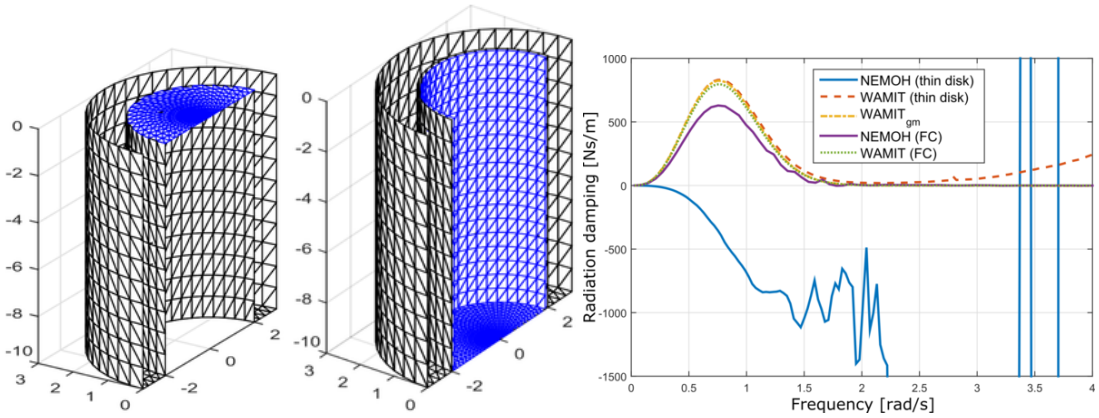

(a) OWC mesh - thin disk. (b) OWC mesh - FC. (c) OWC lid - h_{33}

Figure A.5: OWC meshes for the thin disk (a) and FC (b) modelling methods, and the B_{rad} for the moonpool free-surface modelled via the thin disk, FC and generalised modes methods (c).

modelling the free-surface of the moonpool using the thin disk method, NEMOH fails to produce hydrodynamic coefficients. While added-mass and excitation force coefficients in NEMOH are different from the WAMIT coefficients, these results appear to be reasonably realistic. In contrast, the radiation damping generated in NEMOH is clearly incorrect, showing negative values, as illustrated in Figure A.5 (c), which is unrealistic.

Results given by WAMIT, using the FC method, are identical to the results obtained using WAMIT with the thin disk method, except for the added-mass coefficient. However, when the total inertial term, which is the sum of the mass of the water in the water column and the added-mass of the cylinder, is considered, identical results are obtained in WAMIT for the two different two-body modelling techniques.

In addition, because no thin elements are used when modelling the OWC via the FC technique, NEMOH provides what appears to be realistic results for all the hydrodynamic coefficients, including radiation damping, as shown in Figure A.5 (c). Comparative metric values in Table A.2 for the FC modelling technique show that results from WAMIT and NEMOH are very similar, where an offset in amplitude between the WAMIT and NEMOH coefficients seems to be the only difference, as shown by the *RMSr* in Table A.2 and in Figure A.5 (c). It should be noted that the similarity values corresponding to the added-mass in the FC case are obtained by comparing the total inertia term.

Appendix B

Numerical methods

As described in Figure 6.1, the different numerical methods are divided into two main groups: one-step and multi-step numerical methods, defined in Sections B.1 and B.2, respectively. These methods can be explicit or implicit, where explicit methods calculate the response of a system at a later time-step only using the information of the system at the current and past time-steps, while implicit methods find a solution using the information at, both the current and later time-step. Obviously, implicit methods require an extra computation to obtain the information at the later time-step, but they can be useful for *stiff* problems. However, in this thesis, implicit methods are implemented using a predictor-corrector approach.

Stability is an important issue for numerical methods. A stable problem can be defined as a problem for which small changes in the initial conditions cause only small changes in the solution [334]. However, for some differential equations the application of standard explicit methods (*e.g.* Euler or higher-order RK methods) or even multi-step methods (*e.g.* the Adams-Bashforth method) exhibit numerical instabilities in the solution, unless the step size is significantly reduced. These problems are known as stiff problems. Instability exhibited by explicit methods in stiff problems does not necessarily mean that the solution quickly increases or decreases towards infinity, but can also involve oscillations about the expected solution [334].

Therefore, different numerical methods are described in this appendix, including the stability regions for different methods and method orders.

B.1 One-step numerical methods

All the one-step methods can be expressed [334] as follows,

$$y_{i+1} = y_i + \phi_s \delta t, \tag{B.1}$$

where ϕ_s is the slope or the increment function, and $\delta t = t_{i+1} - t_i$ the time-step. Hence, ϕ_s is used to estimate or extrapolate y_{i+1} from y_i over an interval δt. Depending on the one-step method employed, the slope ϕ_s is estimated following different approaches.

B.1.1 Euler' method

Euler's method is a first-order approach that estimates the slope ϕ_s using the first derivative of the function y' evaluated at instant i, as illustrated in Figure B.1 (a), for which Equation (B.1) can be replaced as,

$$y_{i+1} = y_i + y'_i \delta t. \tag{B.2}$$

The computational requirements of Euler's method are appealing, due to the few and simple calculation required to solve differential equations. As other first-order methods, Euler's method

uses straight lines to approximate the solution, which provides error-free predictions in the cases where the underlying function is a first-order polynomial function. In contrast, the accuracy of first-order methods, including Euler's method, decreases drastically for higher-order polynomial functions [334], unless the step-size is sufficiently small. However, decreasing the step-size considerably increases the computational time, cancelling the main advantage of Euler's method.

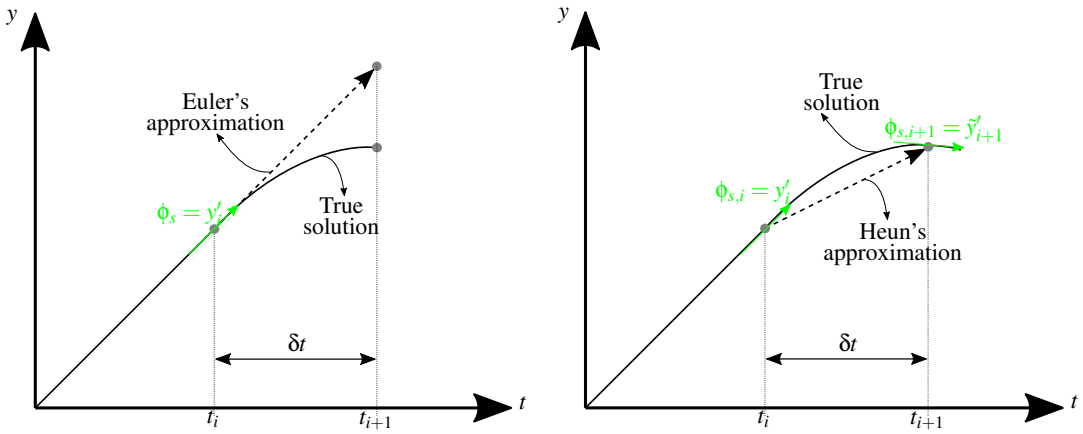

(a) Euler's method.

(b) Heun's method.

Figure B.1: Approximation with Euler's (a) and Heund's (b) methods, where the green arrows illustrate the slope ϕ_s estimated with the first derivative at different points of the interval δt.

B.1.2 Runge-Kutta

The inaccuracies of Euler's method arise, mainly, due to the assumption that, the derivative at the beginning of the interval can be applied across the whole interval δt. Thus, improving Euler's method involves the calculation of more derivatives at other points within δt. Different approaches have been suggested in the literature, but all these improved methods are considered as part of a larger group known as RK methods [334].

The simplest improvement of Euler's method is known as Heun's method, which calculates the derivative of the function at the beginning (t_i) and the end (t_{i+1}) of the interval, and uses the average of the two derivatives as the estimated slope in Equation (B.1), as illustrated in Figure B.1 (b). Hence, Equation (B.1) can be replaced [334] as follows,

$$y_{i+1} = y_i + \frac{y'_i + \tilde{y}'_{i+1}}{2}\delta t. \tag{B.3}$$

Heun's method is a *predictor-corrector* approach, where the initial prediction ($\tilde{y}_{i+1}$) using Euler's method is corrected by the average of the two derivatives calculated at t_i and t_{i+1}.

Another possible improvement of Euler's method is the *Midpoint* method [334], where Euler's method is used to predict the value of the function at the midpoint of the interval δt,

$$\tilde{y}_{\frac{i+1}{2}} = y_i + y'_i\frac{\delta t}{2}, \tag{B.4}$$

which is later used to calculate the slope at the midpoint ($\phi_{s,\frac{i+1}{2}} = \tilde{y}'_{\frac{i+1}{2}}$). This slope $\phi_{s,\frac{i+1}{2}}$ is assumed to be a valid average slope of the entire interval and is used to extrapolate the value y_{i+1}, following Equation (B.1):

$$y_{i+1} = y_i + \tilde{y}'_{\frac{i+1}{2}}\delta t. \tag{B.5}$$

The *Midpoint* method is superior to Euler's method, because it estimates the slope at the mid-point of the interval δt, instead of at the end of δt, which always provides a better approximation than the forward or backward finite-difference approximation [334].

Heun's method and the *Midpoint* method are only two variations of the second-order RK method (RK2), where the second derivative is calculated at t_{i+1} and $t_{\frac{i+1}{2}}$, respectively. Other variations consider this second derivative at other points within the interval δt, for example, at $t_{\frac{2(i+1)}{3}}$ in the case of Ralston's method [333]. However, the family of explicit RK methods also includes numerical methods of order higher than two. In fact, the most popular RK method is the fourth-order RK method (RK4), also known as the 'classical' RK method [333], which is a four-stage method, as illustrated in Figure B.2 (a).

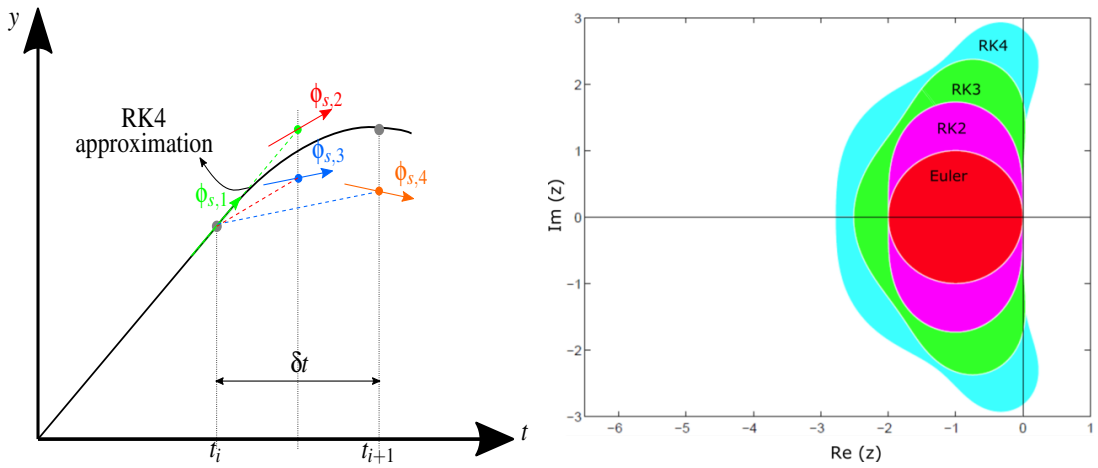

(a) RK4 method.

(b) RK stability regions.

Figure B.2: Approximation with the RK4 method (a), where the different colours of the arrows illustrate the slope ϕ_s at different stages, and the stability regions in the complex plane for different explicit RK method orders (b), adapted from [336].

The RK4 predicts the current value of the function y_{i+1} by estimating the slope at four different points of the interval δt, and calculating a weighted average of these slopes [333] as follows,

$$y_{i+1} = y_i + \left(\phi_{s,1} + 2\phi_{s,2} + 2\phi_{s,3} + \phi_{s,4}\right)\frac{\delta t}{6}. \tag{B.6}$$

The stability of numerical methods is an important aspect, specially when the numerical methods are used for solving stiff problems, *i.e.* problems with a combination of fast and slow dynamics. Stability regions for various explicit RK methods of different orders are illustrated in Figure B.2 (b), where it is shown that the stability region increases with the order.

Apart from the explicit RK methods, implicit RK methods also exist and have great stability characteristics. However, while the implementation of explicit RK methods is straightforward, implicit methods require solving a separate system of equations simultaneously, which are solved, in general, by means of an iterative process. In general, it is difficult to justify the use of implicit RK methods, due to the additional work and complexity involved in the implementation, and, thus, their use is restricted to very specific cases with critical stability issues [333].

B.2 Multi-step numerical methods

In contrast to one-step methods, multi-step methods use more information from several previous steps and, thus, compared to higher-order RK methods, multi-step methods require less function evaluations at each time-step. The most popular multi-step methods are the Adams family, with

AB and AM, and the BDF, as illustrated in Figure 6.1. These multi-step methods use linear combinations of function values at previous steps (y_i, y_{i-1}, ...), and slope predictions at previous ($\phi_{s,i}$, $\phi_{s,i-1}$, ...) and current steps $\phi_{s,i+1}$.

B.2.1 Adams-Bashforth

Adams-Bashforth methods are explicit methods, where the current step of the function y_{i+1} is predicted by combining only the function values and slopes of the previous steps [335]. Thus, the derivative of the function does not need to be estimated within the interval δt, as in RK methods. The predicted value of the function, using a second-order method, is obtained as follows,

$$y_{i+2} = y_{i+1} + \delta t\left(\frac{3}{2}\phi_{s,i+1} - \frac{1}{2}\phi_{s,i}\right), \tag{B.7}$$

where two previous steps are used. The corresponding coefficients for higher order methods can be found in [336].

Absolute stability regions for AB methods of different order are rather small and decrease when the order increases, as illustrated in Figure B.3 (a). These small absolute stability regions inspired an implicit version of the Adams method, namely the AM method.

B.2.2 Adams-Moulton

Implicit AM methods are similar to the explicit AB methods, where the main difference is the need to estimate the slope of the function at the end of the interval δt (t_{i+1}), as in Heun's method. Similarly to Heun's method, the value at t_{i+1} is used to correct the prediction, resulting in a predictor-corrector approach [336] as follows,

$$y_{i+1} = y_i + \frac{1}{2}\delta t\left(\phi_{s,i+1} + \phi_{s,i}\right), \tag{B.8}$$

which also shows the second-order method, even though only one previous step is used. The coefficients for higher order methods can also be found in [336].

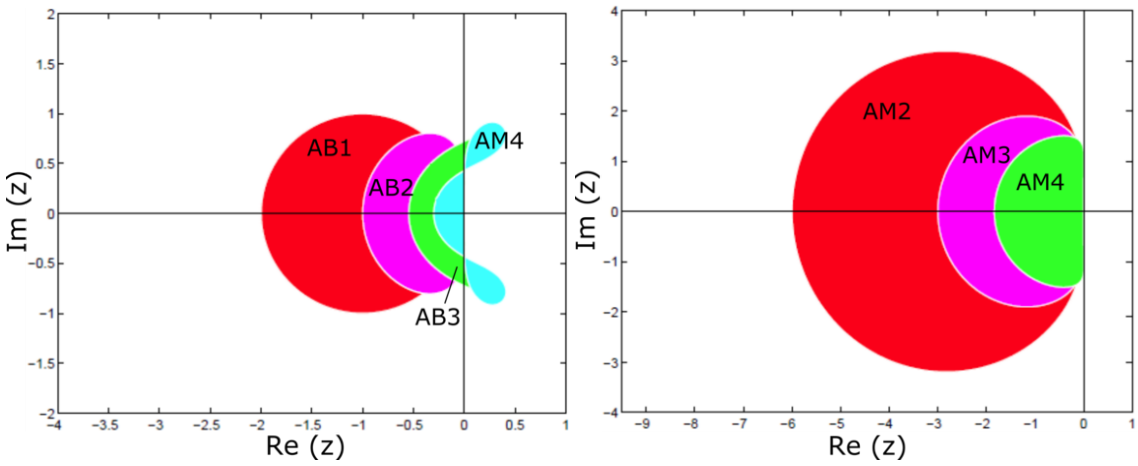

(a) AB. (b) AM.

Figure B.3: Absolute stability regions in the complex z-plane for different orders of AB (a) and AM methods (b), adapted from [336].

Adams-Moulton methods provide lower error values than the AB methods of the same order, and use one previous step less, for the same order, to predict y_{i+1}. In addition, the absolute stability regions of AM methods are significantly larger than those of AB methods, as shown in Figure B.3. However, AM methods are implicit methods and, thus, are often used together with AB methods,

yielding predictor-corrector pairs [336], where an AB method provides a preliminary prediction which is corrected by an AM method.

B.2.3 Backward differentiation function

The last multi-step method analysed in this thesis is the BDF. The BDF formulae are implicit methods and were created to solve stiff problems [337]. The current value of the function, using the second-order BDF method, can be predicted as,

$$y_{i+2} = \frac{4}{3}y_{i+1} - \frac{1}{3}y_i + \frac{2}{3}\delta t \phi_{s,i+2}, \tag{B.9}$$

where two previous steps are also used, as for the second-order AB method. Again, typical values of the coefficients in higher order methods can be found in [336].

The absolute stability regions for different orders of the BDF methods are illustrated in Figure B.4, where stability regions correspond to the space outside the shaded areas. Hence, stability regions for BDF methods are significantly larger than RK, AB and AM methods and, as in the case of AB and AM, the stability regions decrease in size as the order increases.

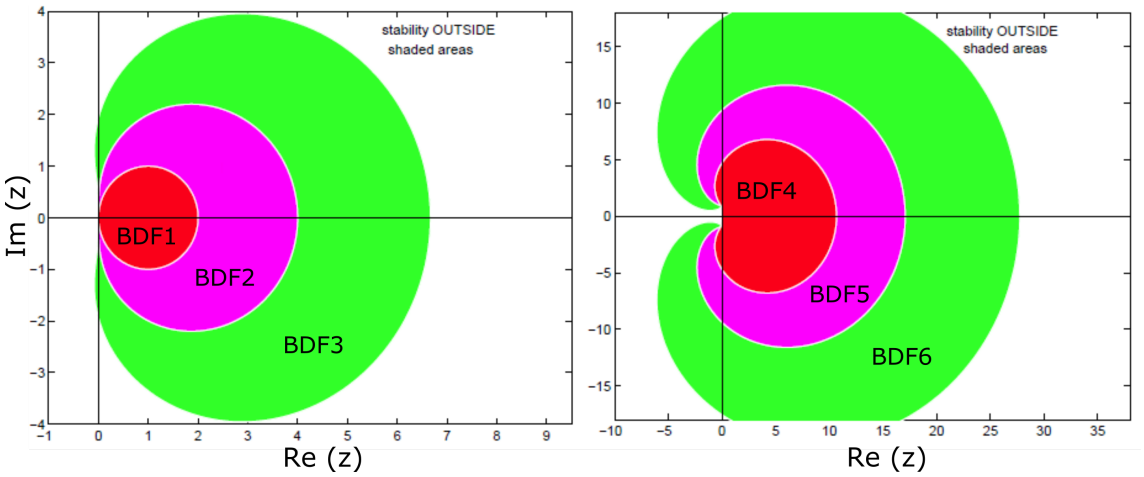

Figure B.4: Absolute stability regions in the complex z-plane for different orders of BDF methods, adapted from [336], where stability regions are outside the shaded areas.

Finally, since previous values of the function y are utilised in multi-step methods, initial values are required to start the process. For instance, for a N_{MS}-step method, N_{MS} initial values are needed. In addition, the accuracy of these initial values is important for accurate predictions of y_{i+1} from multi-step methods [336]. Therefore, these initial values are commonly obtained using an appropriate one-step method, since one-step methods do not require initial values.

Bibliography

[1] J. Schindler and W. Zittel, *Crude Oil - The Supply*. Energy Watch Group / Ludwig-Boelkow-Foundation, Ottobrunn, Germany, 2008. Available at https://www.aie.org.au/AIE/Documents/2008-02_EWG_Oil_Report_updated.pdf [Last accessed on 22 June 2018].

[2] K. Aleklett, M. Hök, K. Jakobsson, M. Lardelli, S. Snowden, and B. Söderbergh, "The peak of the oil age - analyzing the world oil production reference scenario in world energy outlook 2008," *Energy Policy*, vol. 38, no. 3, pp. 1398 – 1414, 2010.

[3] British Petroleum, "BP Statistical Review of World Energy 2017," 2017. Available at www.bp.com/content/dam/bp/en/corporate/pdf/energy-economics/statistical-review-2017/bp-statistical-review-of-world-energy-2017-full-report.pdf [Last accessed 22 June 2018].

[4] T. J. Crowley, "Causes of climate change over the past 1000 years," *Science*, vol. 289, no. 5477, pp. 270–277, 2000.

[5] NASA, "Long-term warming trend continued in 2017," January 2018. Available at https://climate.nasa.gov/news/2671/long-term-warming-trend-continued-in-2017-nasa-noaa/ [Last accessed on 22 June 2018].

[6] United Nations Department of Economic and Social Affairs, Population Division, "World Population Prospects: The 2017 Revision," 2017. Available at https://esa.un.org/unpd/wpp/Publications/Files/WPP2017_KeyFindings.pdf [Last accessed on 22 June 2018].

[7] N. Armaroli and V. Balzani, "The future of energy supply: Challenges and opportunities," *Angewandte Chemie International Edition*, vol. 46, no. 1-2, pp. 52–66, 2007.

[8] European Commision, "In-depth study of European Energy Security," 2017. Available at https://ec.europa.eu/energy/sites/ener/files/documents/20140528_energy_security_study.pdf [Last accessed 22 June 2018].

[9] M. Z. Jacobson, M. A. Delucchi, Z. A. Bauer, S. C. Goodman, W. E. Chapman, M. A. Cameron, C. Bozonnat, L. Chobadi, H. A. Clonts, P. Enevoldsen, J. R. Erwin, S. N. Fobi, O. K. Goldstrom, E. M. Hennessy, J. Liu, J. Lo, C. B. Meyer, S. B. Morris, K. R. Moy, P. L. O'Neill, I. Petkov, S. Redfern, R. Schucker, M. A. Sontag, J. Wang, E. Weiner, and A. S. Yachanin, "100% clean and renewable wind, water, and sunlight all-sector energy roadmaps for 139 countries of the world," *Joule*, vol. 1, no. 1, pp. 108 – 121, 2017.

[10] United Nations Framework Convention on Climate Change, "Adoption of the paris agreement," 2015. Available at https://unfccc.int/resource/docs/2015/cop21/eng/l09r01.pdf [Last accessed on 22 June 2018].

[11] REN 21, "Renewables 2017: Global status report," 2017. Available at http://www.ren21.net/gsr-2017/ [Last accessed on 22 June 2018].

[12] The European Wind Energy Association, "Pure power: Wind energy targets for 2020 and 2030," 2011. Available at http://www.ewea.org/fileadmin/files/library/publications/reports/Pure_Power_III.pdf [Last accessed on 22 June 2018].

[13] Ocean Energy Forum, "Ocean energy strategic roadmap 2016, building ocean energy for europe," 2016. Available at https://webgate.ec.europa.eu/maritimeforum/sites/maritimeforum/files/OceanEnergyForum_Roadmap_Online_Version_08Nov2016.pdf [Last accessed on 22 June 2018].

[14] G. Mork, S. Barstow, A. Kabuth, and M. T. Pontes, "Assessing the global wave energy potential," in *Proceedings of the ASME 29th International Conference on Ocean, Offshore and Arctic Engineering, Shanghai, China*, no. OMAE2010-20473, pp. 447–454, American Society of Mechanical Engineers, 2010.

[15] O. Edenhofer, R. Pichs-Madruga, Y. Sokona, K. Seyboth, P. Eickemeier, P. Matschoss, G. Hansen, S. Kadner, S. Schlömer, T. Zwickel, and C. V. Stechow, "IPCC Special Report on Renewable Energy Sources and Climate Change Mitigation," 2011. Available at http://srren.ipcc-wg3.de/report [Last accessed 22 June 2018].

[16] K. Gunn and C. Stock-Williams, "Quantifying the global wave power resource," *Renewable Energy*, vol. 44, pp. 296–304, 2012.

[17] International Energy Agency, "Key world energy statistics," 2017. Available at https://www.iea.org/publications/freepublications/publication/key-world-energy-statistics.html [Last accessed 22 June 2018].

[18] J. Cruz, *Ocean Wave Energy*. Springer, 2008.

[19] J. Portilla, J. Sosa, and L. Cavaleri, "Wave energy resources: Wave climate and exploitation," *Renewable Energy*, vol. 57, pp. 594–605, 2013.

[20] C. Maisondieu, "Wec survivability threshold and extractable wave power," in *Proceedings of the 11th European Wave and Tidal Energy Conference (EWTEC), Nantes, France*, no. 07D4-2, 2015.

[21] A. Ulazia, M. Penalba, G. Ibarra-Berastegui, J. Ringwood, and J. Saénz, "Wave energy trends over the Bay of Biscay and the consequences for wave energy converters," *Energy*, vol. 25, no. 2, pp. 44–45, 2018.

[22] M. Penalba, A. Ulazia, G. Ibarra-berastegui, J. Ringwood, and J. Sáenz, "Wave energy resource variation off the west coast of Ireland and its impact on realistic wave energy converters ' power absorption," *Applied Energy*, vol. 224, pp. 205–219, 2018.

[23] IPCC, *Mitigation of climate change: Contribution of working group III to the fourth assessment report of the Intergovernmental Panel on Climate Change*. Cambrige University Press, 2007. Available at https://www.ipcc.ch/pdf/assessment-report/ar4/wg3/ar4_wg3_full_report.pdf [Last accessed on 22 June 2018].

[24] International Renewable Energy Agency, "Wave Energy Technology Brief," 2014. Available at http://www.irena.org/documentdownloads/publications/wave-energy_v4_web.pdf [Last accessed 22 June 2018].

[25] Y. Torre-Enciso, I. Ortubia, L. López de Aguileta, and J. Marqués, "Mutriku wave power plant: from the thinking out to the reality," in *Proceedings of the 8th European Wave and Tidal Energy Conference*, pp. 319–329, 2009.

[26] T. Whittaker, D. Collier, M. Folley, M. Osterried, A. Henry, and M. Crowley, "The development of Oyster - a shallow water surging wave energy converter," in *Proceedings of the 7th European Wave and Tidal Energy Conference, Porto, Portugal*, 2007.

[27] J. Fiévez and T. Sawyer, "Lessons learned from building and operating a grid connected wave energy plant," in *Proceedings of the 11th European Wave and Tidal Energy Conference, Nantes*, no. 08D1-4, 2015.

[28] N. Meyer, M. M. Arnskov, L. Bennetzen, H. Burcharth, J. Bunger, V. Jacobsen, P. Maegaard, S. Vindelov, K. Nielsen, and J. Sørensen, "Bølgekraftprogram: Afsluttende rapport fra energistyrelsens rådgivende bølgekraftudvalg," 2002.

[29] K. Edwards and M. Mekhiche, "Ocean Power Technologies Powerbuoy®: System-Level Design, Development and Validation Methodology," in *Proceedings of the 2nd Marine Energy Technology Symposium (METS), Seattle, WA, USA*, no. 127, 2014.

[30] R. Henderson, "Design, simulation, and testing of a novel hydraulic power take-off system for the Pelamis wave energy converter," *Renewable energy*, vol. 31, no. 2, pp. 271–283, 2006.

[31] B. Drew, A. R. Plummer, and M. N. Sahinkaya, "A review of wave energy converter technology," *Proceedings of the Institution of Mechanical Engineers. Part A: Journal of Power and Energy*, vol. 223, 2009.

[32] A. d. O. Falcão, "Wave energy utilization: A review of the technologies," *Renewable and sustainable energy reviews*, vol. 14, no. 3, pp. 899–918, 2010.

[33] I. López, J. Andreu, S. Ceballos, I. M. de Alegría, and I. Kortabarria, "Review of wave energy technologies and the necessary power-equipment," *Renewable and Sustainable Energy Reviews*, vol. 27, pp. 413–434, 2013.

[34] A. F. Falcão, J. C. Henriques, and J. J. Candido, "Dynamics and optimization of the OWC Sparbuoy wave energy converter," *Renewable Energy*, vol. 48, pp. 369 – 381, 2012.

[35] A. Pecher, J. P. Kofoed, J. Espedal, and S. Hagberg, "Results of an experimental study of the Langlee wave energy converter," in *Proceedings of the Twentieth International Offshore and Polar Engineering Conference, Beijing, China*, no. ISOPE-I-10-048, 2010.

[36] E. Mehlum, "Tapchan," in *Proceedings of the International Symposium on the Hydrodynamics of Ocean Wave-Energy Utilization, Lisbon, Portugal* (D. Evans and A. Falcão, eds.), pp. 51–55, Springer, 1986.

[37] D. Ross, *Power from the Waves*. Oxford University Press, USA, 1995.

[38] G. Damy, "Production d'énergie à partie de la houle. bilan provisoire après 2 ans de déroulement du programme," Tech. Rep. TDI/CCTRME/82-31/GD-PV, IFREMER, 1982. Available at http://archimer.ifremer.fr/doc/00001/11265/ [Last accessed 22 June 2018].

[39] C. Miller, "Wave and tidal energy experiments in San Francisco and Santa Cruz," August 2004. Available at http://www.outsidelands.org/wave-tidal.php [Last accessed 22 June 2018].

[40] R. Dhaille, "Technique et rentabilité des dièdres à houle," in *Compte-rendu des 4èmes journées de l'hydraulique*, 1956.

[41] A. Babarit, *Ocean wave energy conversion: resource, technologies and performance*. London, UK: ISTE Press - Elsevier, 2016.

[42] S. H. Salter, "Wave power," *Nature*, vol. 249, no. 5459, pp. 720–724, 1974.

[43] D. Swift-Hook, B. Count, I. Glendenning, and S. Salter, "Characteristics of a rocking wave power device," *Nature*, vol. 254, no. 5500, p. 504, 1975.

[44] K. Budal and J. Falnes, "A resonant point absorber of ocean-wave power," *Nature*, vol. 256, no. 5517, p. 478, 1975.

[45] K. Budal and J. Falnes, *Power from sea waves*, ch. Interacting point absorbers with controlled motion, pp. 381–399. Academic Press, London, 1980.

[46] D. Evans, "A theory for wave-power absorption by oscillating bodies," *Journal of Fluid Mechanics*, vol. 77, no. 1, pp. 1–25, 1976.

[47] J. Falnes, "A review of wave-energy extraction," *Marine structures*, vol. 20, no. 4, pp. 185–201, 2007.

[48] J. Weber, "WEC technology readiness and performance matrix–finding the best research technology development trajectory," in *Proceedings of the 4th International Conference on Ocean Energy, Dublin, Ireland*, 2012.

[49] J. Weber, R. Costello, and J. Ringwood, "WEC technology performance levels (TPLs)-metric for successful development of economic WEC technology.," in *Proceedings of the 10th European Wave and Tidal Energy Conference, Aalborg, Denmark*, EWTEC, 2013.

[50] J. v. Hoff, "Real world challenges in designing a WEC PTO system," in *The 2nd NUIM Wave Energy Workshop, Maynooth, Ireland*, 2011.

[51] A. Henry, K. Doherty, L. Cameron, T. Whittaker, and R. Doherty, "Advances in the design of the Oyster wave energy converter," in *Proceedings of the Marine and Offshore Renewable Energy Conference, Royal Institution of Naval Architects, London, UK*, 2010.

[52] J.-C. Gilloteaux and J. V. Ringwood, "Control-informed geometric optimisation of wave energy converters," *IFAC Proceedings Volumes*, vol. 43, no. 20, pp. 366 – 371, 2010.

[53] P. B. Garcia-Rosa and J. V. Ringwood, "On the sensitivity of optimal wave energy device geometry to the energy maximizing control system," *IEEE Transactions on Sustainable Energy*, vol. 7, no. 1, pp. 419–426, 2016.

[54] M. Lawson, Y.-H. Yu, A. Nelessen, K. Ruehl, and C. Michelen, "Implementing nonlinear buoyancy and excitation forces in the WEC-Sim wave energy converter modeling tool," in *Proceedings of the ASME 33th International Conference on Ocean, Offshore and Arctic Engineering, San Francisco, Califormia, USA*, no. OMAE2014-24445, 2014.

[55] Y.-H. Yu and Y. Li, "Reynolds-Averaged Navier-Stokes simulation of the heave performance of a two-body floating-point absorber wave energy system," *Computers & Fluids*, vol. 73, pp. 104 – 114, 2013.

[56] G. Giorgi and J. V. Ringwood, "Nonlinear Froude-Krylov and viscous drag representations for wave energy converters in the computation/fidelity continuum," *Ocean Engineering*, vol. 141, pp. 164–175, 2017.

[57] A. Babarit, H. Mouslim, A. Clément, and P. Laporte-Weywada, "On the Numerical Modelling of the Non Linear Behaviour of a Wave Energy Converter," in *Proceedings of the ASME 28th International Conference on Ocean, Offshore and Arctic Engineering, Honolulu, Hawaii, USA*, no. OMAE2009-79909, pp. 1045–1053, 2009.

[58] M. Bhinder, A. Babarit, L. Gentaz, and P. Ferrant, "Effect of Viscous Forces on the Performanco of a Surging Wave Energy Converter," in *Proceedings of the Twenty-second International Offshore and Polar Engineering Conference, Rhodes, Greece*, no. ISOPE-I-12-194, 2012.

[59] H. Asmuth, P. Schmitt, A. Henry, and B. Elsaesser, "Determination of Non-linear Damping Coefficients of bottom-hinged Oscillating Wave Surge Converters Using Numerical Free Decay Tests ," in *Proceedings of the 1st International Conference on Renewable Energies Offshore, Lisbon, Portugal*, 2014.

[60] G. Giorgi and J. V. Ringwood, "Comparing nonlinear hydrodynamic forces in heaving point absorbers and oscillating wave surge converters," *Journal of Ocean Engineering and Marine Energy*, vol. 4, no. 1, pp. 25–35, 2017.

[61] G. Giorgi and J. V. Ringwood, "Importance of nonlinear wave representation for nonlinear Froude-Krylov force calculations for wave energy devices," in *Proceedings of the 12th European Wave and Tidal Energy Conference, Cork, Ireland*, no. 644, 2017.

[62] A. F. O. Falcão and J. C. C. Henriques, "Oscillating-water-column wave energy converters and air turbines: A review," *Renewable Energy*, vol. 85, pp. 1391–1424, 2016.

[63] A. C. O'Sullivan and G. Lightbody, "Co-design of a wave energy converter using constrained predictive control," *Renewable Energy*, vol. 102, Part A, pp. 142 – 156, 2017.

[64] R. H. Hansen, T. O. Andersen, and H. C. Pedersen, "Model based design of efficient power take-off systems for wave energy converters," *Proceedings of the 12th Scandinavian International Conference on Fluid Power*, 2011.

[65] L. O'Boyle, K. Doherty, v. J. Hoff, and J. Skelton, "The Value of Full Scale Prototype Data-Testing Oyster 800 at EMEC, Orkney," in *Proceedings of the 11th European Wave and Tidal Energy Conference, Nantes, France*, no. 08D1-1, 2015.

[66] D. Reeve, Y. Chen, S. Pan, V. Magar, D. Simmonds, and A. Zacharioudaki, "An investigation of the impacts of climate change on wave energy generation: The Wave Hub, Cornwall, UK ," *Renewable Energy*, vol. 36, no. 9, pp. 2404 – 2413, 2011.

[67] Sea Power, "Seapower platform power matrix," 2016. Available at http://www.seapower.ie/wp-content/uploads/Seapower-Powermatrix.png [Last accessed 22 June 2018].

[68] FLOW Science, "Waves," 2016. Available at https://www.flow3d.com/modeling-capabilities/waves/ [Last accessed 22 June 2018].

[69] G. Stokes, "On the theory of oscillatory waves," *Transactions of the Cambridge Philofophical Society*, vol. 8, pp. 441–455, 1847. Reprinted in: Stokes, G.G. (1880). Mathematical and Physical Papers, Volume I, Cambridge University Press. p.p. 197-229.

[70] J. Fenton, *The Sea: Ocean Engineering Science, Volume 9*, ch. Nonlinear Wave Theories, pp. 3–25. Harvard University Press, 1990.

[71] J. Fenton, "A high-order cnoidal wave theory," *Journal of Fluid Mechanics*, vol. 94, pp. 1329–161, 1979.

[72] M. Rienecker and J. Fenton, "A fourier approximation method for steady water waves," *Journal of Fluid Mechanics*, vol. 104, no. 1, pp. 119–137, 1981.

[73] J. D. Fenton, "Numerical methods for nonlinear waves," *Advances in coastal and ocean engineering*, vol. 5, pp. 241–324, 1999.

[74] W. Pierson and L. Moskowitz, "A proposed spectral form for fully developed wind seas based on the similarity theory of S.A. Kitaigorodskii," *Journal of Geophysical Research*, vol. 69, pp. 5181–5190, 1964.

[75] K. Hasselmann, T. Barnett, E. Bouws, H. Carlson, D. Cartwright, K. Enke, J. Ewing, H. Gienapp, D. Hasselmann, P. Kruseman, A. Meerburg, P. Muller, D. Olbers, K. Richter, W. Sell, and H. Walden, "Measurements of wind-wave growth and swell decay during the joint north sea wave project (JONSWAP)," Tech. Rep. A8 12, German Hydrographic Institute, Hamburg, 1973. Available at https://repository.tudelft.nl/islandora/object/uuid:f204e188-13b9-49d8-a6dc-4fb7c20562fc?collection=research [Last accessed 22 June 2018].

[76] C. Bretschneider, "Wave variability and wave spectra for wind-generated gravity waves," Tech. Rep. BEB-TM-118, Beach Erosion Board Engineer Research and Development Center, Washington DC, USA, 1959. Available at http://acwc.sdp.sirsi.net/client/en_US/search/asset/1008580;jsessionid=D9BE7CF3E6860183EE443CCBA96BA016.enterprise-15000 [Last accessed 22 June 2018].

[77] M. Ochi and E. Hubble, "Six-parameter wave spectra," *Coastal Engineering*, no. 15, pp. 301–328, 1976.

[78] A. Mérigaud and J. V. Ringwood, "Free-surface time-series generation for wave energy applications," *IEEE Journal of Oceanic Engineering*, vol. 43, no. 1, pp. 19–35, 2018.

[79] G. Giorgi and J. V. Ringwood, "Relevance of pressure field accuracy for nonlinear froude-krylov force calculations for wave energy devices," *Journal of Ocean Engineering and Marine Energy*, 2018.

[80] D. Dommermuth and D. Yue, "A high-order spectral method for the study of nonlinear gravity waves," *Fluid mechanics*, vol. 184, pp. 267–288, 1986.

[81] B. J. West, K. A. Brueckner, R. S. Janda, D. M. Milder, and R. L. Milton, "A new numerical method for surface hydrodynamics," *Journal of Geophysical Research: Oceans*, vol. 92, no. C11, pp. 11803–11824, 1987.

[82] F. Bonnefoy, G. Ducrozet, D. Le Touz'e, and P. Ferrant, *Advances in Numerical Simulation of Nonlinear Water Waves: Vol. 11*, ch. Time Domain Simulation of Nonlinear Water Waves Using Spectral Methods, pp. 129–164. World Scientific, 2009.

[83] G. Ducrozet, F. Bonnefoy, D. Le Touzé, and P. Ferrant, "3-D HOS simulations of extreme waves in open seas," *Natural Hazards and Earth System Science*, vol. 7, no. 1, pp. 109–122, 2007.

[84] G. Ducrozet, F. Bonnefoy, D. Le Touzé, and P. Ferrant, "Hos-ocean: Open-source solver for nonlinear waves in open ocean based on high-order spectral method," *Computer Physics Communications*, vol. 203, pp. 245–254, 2016.

[85] J. Falnes, *Ocean Waves and Oscillating Systems*. Cambridge University Press, 2002.

[86] W. Cummins, "The impulse response function and ship motion," *Schiffstechnik*, no. 9, pp. 101–109, 1962.

[87] J.-C. Gilloteaux, G. Bacelli, and J. Ringwood, "A nonlinear potential model to predict large-amplitude-motions: Application to a multy-body wave energy converter," in *Proceedings of the 10th World Renewable Energy Conference, Glasgow, UK*, pp. 934–939, 2008.

[88] A. Mérigaud, J. Gilloteaux, and J. Ringwood, "A nonlinear extension for linear boundary element method in wave energy device modelling," in *Proceedings of the ASME 31st International Conference on Ocean, Offshore and Arctic Engineering, Rio de Janeiro, Brazil*, no. OMAE2012-83581, pp. 615–621, 2012.

[89] O. Faltinsen, *Sea Loads on Ships and Offshore Structures*. Cambridge Ocean Technology Series, Cambridge University Press, 1993.

[90] G. H. Keulegan and L. H. Carpenter, "Forces on cylinders and plates in an oscillating fluid," *Journal of Research of the National Bureau of Standards*, vol. 2857, pp. 423–440, 1958.

[91] J. B. Rho, H. S. Choi, H. S. Shin, and I. K. Park, "A Study On Mathieu-type Instability of Conventional Spar Platform In Regular Waves ," *International Journal of Offshore and Polar Engineering*, vol. 15, no. 02, 2005.

[92] J. Paulling and R. Rosenberg, "On unstable ship motions resulting from nonlinear coupling," *Journal of Ship Research*, vol. 3, no. 1, pp. 36–46, 1959.

[93] N. N. Moiseyev and V. Rumyantsev, *Dynamic Stability of Bodies Containing Fluid*. Springer, Berlin, Heidelberg, 1968.

[94] Y. Zhang, Q.-P. Zou, and D. Greaves, "Airwater two-phase flow modelling of hydrodynamic performance of an oscillating water column device," *Renewable Energy*, vol. 41, pp. 159–170, 2012.

[95] D. Evans and R. Porter, "Wave energy extraction by coupled resonant absorbers," *Philosophical Transactions of the Royal Society A: Mathematical, Physical and Engineering Sciences*, vol. 370, no. 1959, pp. 315–344, 2012.

[96] S. Crowley, R. Porter, and D. Evans, "A submerged cylinder wave energy converter with internal sloshing power take off," *European Journal of Mechanics - B/Fluids*, vol. 47, pp. 108 – 123, 2014.

[97] A. Henry, P. Schmitt, T. Whittaker, A. Rafiee, and F. Dias, "The Characteristics of Wave Impacts on an Oscillating Wave Surge Converter ," in *Proceedings of the Twenty-third International Offshore and Polar Engineering Conference, Anchorage, Alaska*, no. ISOPE-I-13-182, 2013.

[98] L. Martinelli and P. Frigaard, "Example of overtopping time series. CRAFT program Low-Pressure Turbine and Control Equipment for Wave Energy Converters (Wave Dragon)," tech. rep., Hydraulics & Coastal Engineering Laboratory, Aalborg University, 1999.

[99] H. A. Wolgamot and C. J. Fitzgerald, "Nonlinear hydrodynamic and real fluid effects on wave energy converters," *Proceedings of the Institution of Mechanical Engineers, Part A: Journal of Power and Energy*, vol. 229, no. 7, pp. 772–794, 2015.

[100] M. WAMIT Inc., *WAMIT v7.0 manual*, 2013. Available at http://www.wamit.com/manualupdate/history/V70_manual_old.pdf [Last accessed 22 June 2018].

[101] A. W. ANSYS Inc., *AQWA manual Release 14.5*, 2012. Available at https://cyberships.files.wordpress.com/2014/01/wb_aqwa.pdf [Last accessed 22 June 2018].

[102] G. Delhommeau, "Seakeeping Codes AQUADYN and AQUAPLUS," in *Proceedings of the 19th WEGEMT School on Numerical Simulation of Hydrodynamics:Ships and Offshore Structures, Nantes, France*, 1993.

[103] M. T. Morris-Thomas, R. J. Irvin, and K. P. Thiagarajan, "An investigation into the hydrodynamic efficiency of an oscillating water column," *Journal of Offshore Mechanics and Arctic Engineering*, vol. 129, no. 4, pp. 273–278, 2007.

[104] R. Sykes, A. Lewis, and G. Thomas, "Predicting hydrodynamic pressure in fixed and floating OWC using a piston model," in *Proceedings of the 9th European Wave and Tidal Energy Conference, Southampton, UK*, 2011.

[105] D. Bull and P. Jacob, "Methodology for creating nonaxisymmetric WECs to screen mooring designs using a Morison Equation approach," in *Proceedings of the Oceans Conference, Hampton Roads, Virginia, USA*, 2012.

[106] R. Gomes, J. Henriques, L. Gato, and A. Falcão, "Testing of a small-scale floating owc model in a wave flume," in *Proceedings of the 4th International Conference on Ocean Energy, Dublin, Ireland*, pp. 1–7, 2012.

[107] G. Giorgi and J. V. Ringwood, "Analytical nonlinear model for parametric motion detection of an oscillating water column Sparbuoy," in *Proceedings of the 3rd International Conference on Renewable Energies Offshore, Lisbon, Portugal*, 2018.

[108] J. Armesto, R. Guanche, A. Iturrioz, C. Vidal, and I. Losada, "Identification of state-space coefficients for oscillating water columns using temporal series," *Ocean Engineering*, vol. 79, pp. 43–49, 2014.

[109] A. Iturrioz, R. Guanche, J. Armesto, M. Alves, C. Vidal, and I. Losada, "Time-domain modeling of a fixed detached oscillating water column towards a floating multi-chamber device," *Ocean Engineering*, vol. 76, pp. 65–74, 2014.

[110] J. Andersson and J. Pedersen, "Capturing Dynamic Effects in Ship Tanks - A coupling between HydroD and OpenFOAM," Master's thesis, Chalmers University of Technology, Gothenburg, Sweeden, 2011. Available at http://publications.lib.chalmers.se/records/fulltext/148448.pdf [Last accessed 22 June 2018].

[111] J. Kapell, "Analysis of the Inner Flow in the Wave Energy Converter WaveTube," Master's thesis, KTH School of Industrial Engineering and Management, Stockholm, Sweden, 2012. Available at http://www.diva-portal.org/smash/get/diva2:552195/FULLTEXT01 [Last accessed 22 June 2018].

[112] A. Zurkinden, F. Ferri, S. Beatty, J. Kofoed, and M. Kramer, "Nonlinear numerical modelling and experimental testing of a point-absorber wave energy converter," *Ocean Engineering*, vol. 78, pp. 11–21, 2014.

[113] M. Bhinder, A. Babarit, L. Gentaz, and P. Ferrant, "Assessment of Viscous Damping via 3D-CFD Modelling of a Floating Wave Energy Device," in *Proceedings of the 9th European Wave and Tidal Energy Conference, Southampton, UK*, 2011.

[114] G. Giorgi, M. Penalba, and J. V. Ringwood, "Nonlinear Hydrodynamic Force Relevance for Heaving Point Absorbers and Oscillating Surge Converters," in *Proceedings of the 3rd Asian Wave and Tidal Energy Conference, Singapore*, pp. 154–162, 2016.

[115] L. Tao and D. Dray, "Hydrodynamic performance of solid and porous heave plates," *Ocean Engineering*, vol. 35, no. 10, pp. 1006 – 1014, 2008.

[116] L. Tao and S. Cai, "Heave motion suppression of a spar with a heave plate," *Ocean Engineering*, vol. 31, no. 56, pp. 669 – 692, 2004.

[117] K. Tarrant and C. Meskell, "Investigation on parametrically excited motions of point absorbers in regular waves," *Ocean Engineering*, vol. 111, pp. 67–81, 2016.

[118] G. Giorgi and J. V. Ringwood, "Articulating parametric nonlinearities in computationally efficient hydrodynamic models," in *Proceedings of the 11th IFAC Conference on Control Applications in Marine Systems, Robotics, and Vehicles, Opatija, Croatia*, 2018.

[119] L. Letournel, C. Chauvigné, B. Gelly, A. Babarit, G. Ducrozet, and P. Ferrant, "Weakly nonlinear modeling of submerged wave energy converters," *Applied Ocean Research*, vol. 75, pp. 201–222, 2018.

[120] Y. Wei, T. Abadie, A. Henry, and F. Dias, "Wave interaction with an Oscillating Wave Surge Converter. Part II: Slamming," *Ocean Engineering*, vol. 113, pp. 319 – 334, 2016.

[121] A. Henry, O. Kimmoun, J. Nicholson, G. Dupont, Y. Wei, and F. Dias, "A Two Dimensional Experimental Investigation of Slamming of an Oscillating Wave Surge Converter," in *Proceedings of the Twenty-fourth International Ocean and Polar Engineering Conference, Busan, Korea*, no. ISOPE-I-14-448, 2014.

[122] A. Clément, A. Babarit, J.-C. Gilloteaux, C. Josset, and G. Duclos, "The SEAREV wave energy converter," in *Proceedings of the 6th European Wave and Tidal Energy Conference, Glasgow, UK*, 2005.

[123] T. Mäki, T. Mucha, and M. Vuorinen, "Waveroller one of the leading technologies for wave energy conversion," in *Proceedings of the 4th International Conference on Ocean Energy, Dublin, Ireland*, 2014.

[124] K. Tanizawa, "The state of the art on numerical wave tank," in *Proceeding of the 4th Osaka Colloquium on Seakeeping Performance of Ships*, 2000.

[125] J. Wackers, B. Koren, H. C. Raven, A. vander Ploeg, A. R. Starke, G. B. Deng, P. Queutey, M. Visonneau, T. Hino, and K. Ohashi, "Free-surface viscous flow solution methods for ship hydrodynamics," *Archives of Computational Methods in Engineering*, vol. 18, no. 1, pp. 1–41, 2011.

[126] P. Lin and P. Liu, "Free surface tracking methods and their applications to wave hydrodynamics," *Advances in Coastal and Ocean Engineering*, vol. 5, pp. 213–240, 1999.

[127] P. Queutey and M. Visonneau, "An interface capturing method for free-surface hydrodynamic flows," *Computers & Fluids*, vol. 36, no. 9, pp. 1481 – 1510, 2007.

[128] L. Gentaz, B. Alessandrini, and G. Delhommeau, "2D Nonlinear Diffraction Around Free Surface Piercing Body In a Viscous Numerical Wave Tank," in *Proceedings of the Twentieth International Offshore and Polar Engineering Conference*, no. ISOPE-I-99-287, 1999.

[129] C. Hirt and B. Nichols, "Volume of fluid (VOF) method for the dynamics of free boundaries," *Journal of Computational Physics*, vol. 39, no. 1, pp. 201–225, 1981.

[130] A. Iafrati, A. Di Mascio, and E. Campana, "A level set technique applied to unsteady free surface flows," *International Journal for Numerical Methods in Fluids*, vol. 35, no. 3, pp. 281–297, 2001.

[131] L. Larsson, F. Stern, and V. Bertram, "Benchmarking of Computational Fluid Dynamics for Ship Flows: The Gothenburg 2000 Workshop," *Journal of Ship Research*, vol. 47, no. 1, pp. 63–81, 2003.

[132] J. Ferziger and M. Peric, *Computational methods for fluid dynamics*. Springer, 2002.

[133] Y. Luo, Z. Wang, G. Peng, Y. Xiao, L. Zhai, X. Liu, and Q. Zhang, "Numerical simulation of a heave-only floating {OWC} (oscillating water column) device," *Energy*, vol. 76, pp. 799 – 806, 2014.

[134] Y. Wei, A. Rafiee, A. Henry, and F. Dias, "Wave interaction with an oscillating wave surge converter, Part I: Viscous effects," *Ocean Engineering*, vol. 104, pp. 185 – 203, 2015.

[135] P. Schmitt, S. Bourdier, T. Whittaker, D. Sarkar, E. Renzi, F. Dias, K. Doherty, and J. van't Hoff, "Hydrodynamic Loading On a Bottom Hinged Oscillating Wave Surge Converter ," in *Proceedings of the Twenty-second International Offshore and Polar Engineering Conference, Rhodes, Greece*, no. ISOPE-I-12-198, 2012.

[136] F. Menter, M. Kuntz, and R. Langtry, "Ten years of industrial experience with the SST turbulence model," *Turbulence, heat and mass transfer*, vol. 4, no. 1, pp. 625–632, 2003.

[137] S. M. El-Behery and M. H. Hamed, "A comparative study of turbulence models performance for separating flow in a planar asymmetric diffuser," *Computers & Fluids*, vol. 44, no. 1, pp. 248 – 257, 2011.

[138] P. Schmitt, T. Whittaker, D. Clabby, and K. Doherty, "The opportunities and limitations of using CFD in the development of wave energy converters," in *Proceedings of the Marine & Offshore Renewable Energy, London, UK*, pp. 89–97, 2012.

[139] C. Windt, J. Davidson, and J. Ringwood, "High-fidelity numerical modelling of ocean wave energy systems: a review of computational fluid dynamics-based numerical wave tanks," *Renewable and Sustainable Energy Reviews*, vol. 93, pp. 610–630, October 2018.

[140] J. Monaghan, *Theory and Applications of Smoothed Particle Hydrodynamics, in Frontiers in Numerical Analysis, pp. 143-193.* Springer, Heidelberg, Germany, 2005.

[141] R. Sampath, N. Montanari, N. Akinci, S. Prescott, and C. Smith, "Large-scale solitary wave simulation with implicit incompressible SPH," *Journal of Ocean Engineering and Marine Energy*, vol. 2, no. 3, pp. 313–329, 2016.

[142] J. Monaghan, "Smoothed particle hydrodynamics and its diverse applications," *Annual Review of Fluid Mechanics*, vol. 44, pp. 323–346, 2012.

[143] C. Ulrich, M. Leonardi, and T. Rung, "Multi-physics SPH simulation of complex marine-engineering hydrodynamic problems," *Ocean Engineering*, vol. 64, pp. 109 – 121, 2013.

[144] M. Müller, D. Charypar, and M. Gross, "Particle-based fluid simulation for interactive applications," in *Proceedings of the 2003 ACM SIGGRAPH/Eurographics symposium on Computer animation*, pp. 154–159, Eurographics Association, 2003.

[145] Q. Yang, V. Jones, and L. McCue, "Free-surface flow interactions with deformable structures using an SPH-FEM model," *Ocean Engineering*, vol. 55, pp. 136 – 147, 2012.

[146] A. Rafiee, B. Elsaesser, and F. Dias, "Numerical simulation of wave interaction with an oscillating wave surge converter," in *Proceedings of the ASME 32nd International Conference on Ocean, Offshore and Arctic Engineering, Nantes, France*, no. OMAE2013-10195, 2013.

[147] S. Yeylaghi, B. Buckham, B. Moa, P. Oshkai, S. Beatty, and C. Crawford, "Sph modeling of hydrodynamic loads on a point absorber wave energy converter hull," *Proceedings of the 11th European Wave and Tidal Energy Conference, Nantes, France*, no. 10A1-4, 2015.

[148] S. Yeylaghi, B. Moa, P. Oshkai, B. Buckham, and C. Crawford, "ISPH modelling of an oscillating wave surge converter using an OpenMP-based parallel approach," *Journal of Ocean Engineering and Marine Energy*, vol. 2, no. 3, pp. 301–312, 2016.

[149] A. Rafiee, *SPH Modeling of Multi-phase and Energetic Flows*. PhD thesis, University of Western Australia, Perth, Australia, 2012.

[150] A. Rafiee, S. Cummins, M. Rudman, and K. Thiagarajan, "Comparative study on the accuracy and stability of SPH schemes in simulating energetic free-surface flows," *European Journal of Mechanics - B/Fluids*, vol. 36, pp. 1 – 16, 2012.

[151] R. A. Gingold and J. J. Monaghan, "Smoothed particle hydrodynamics: theory and application to non-spherical stars," *Monthly notices of the royal astronomical society*, vol. 181, no. 3, pp. 375–389, 1977.

[152] P. W. Cleary, M. Prakash, J. Ha, and N. Stokes, "Smooth particle hydrodynamics: status and future potential," *Progress in Computational Fluid Dynamics: an International Journal*, vol. 7, no. 2, pp. 70–90, 2007.

[153] J. Monaghan, "Simulating Free Surface Flows with SPH," *Journal of Computational Physics*, vol. 110, no. 2, pp. 399 – 406, 1994.

[154] M. Gomez-Gesteira, B. D. Rogers, R. A. Dalrymple, and A. J. Crespo, "State-of-the-art of classical SPH for free-surface flows," *Journal of Hydraulic Research*, vol. 48, sup1, pp. 6–27, 2010.

[155] S. Koshizuka and Y. Oka, "Moving-particle semi-implicit method for fragmentation of incompressible fluid," *Nuclear science and engineering*, vol. 123, no. 3, pp. 421–434, 1996.

[156] C. Koh, M. Gao, and C. Luo, "A new particle method for simulation of incompressible free surface flow problems," *International Journal for Numerical Methods in Engineering*, vol. 89, no. 12, pp. 1582–1604, 2012.

[157] J. Westphalen, D. M. Greaves, A. Raby, Z. Z. Hu, D. M. Causon, C. G. Mingham, P. Omidvar, P. K. Stansby, and B. D. Rogers, "Investigation of Wave-Structure Interaction Using State of the Art CFD Techniques," *Open Journal of Fluid Dynamics*, vol. 4, no. 1, pp. 18–43, 2014.

[158] A. Crespo, J. Domínguez, C. Altomare, A. Barreiro, and M. Gómez-Gesteira, "Oscillating Water Column WEC modelling with a SPH model," in *2nd Second Iberian Workshop Advances on Smoothed Particle Hydrodynamics*, 2015.

[159] B. Edge, K. Gamiel, R. Dalrymple, A. Hérault, and G. Bilotta, "Application of GPUSPH to design of wave energy," in *Proceedings of the 9th International SPHERIC Workshop, Paris, France*, pp. 342–347, 2014.

[160] David Crooks, *Nonlinear Hydrodynamic Modelling of an Oscillating Wave Surge Converter*. PhD thesis, Queens University Belfast, Belfast, UK, 2016.

[161] J.-C. Gilloteaux, *Mouvements de grande amplitude d'un corps flottant en fluide parfait. Application à la récupération de l'énergie des vagues*. PhD thesis, Ecole Centrale de Nantes-ECN, Nantes, France, 2007. Available at https://tel.archives-ouvertes.fr/tel-00521689 [Last accessed 22 June 2018].

[162] G. Giorgi and J. V. Ringwood, "Computationally efficient nonlinear Froude–Krylov force calculations for heaving axisymmetric wave energy point absorbers," *Journal of Ocean Engineering and Marine Energy*, vol. 3, no. 1, pp. 21–33, 2017.

[163] J. H. S. Malenica, R. Eatock Taylor, "Second-order water wave diffraction by an array of vertical cylinders," *Journal of Fluid Mechanics*, vol. 390, pp. 349–373, 1999.

[164] J. Newman, "Second-order diffraction in short waves," *Journal of Ship Research*, vol. 49, no. 4, pp. 263–273, 2004.

[165] L. Letournel, P. Ferrant, A. Babarit, , and G. Ducrozet, "Développement dun outil de simulation numérique basé sur lapproche "weak-scatterer" pour létude des systèmes houlomoteurs en grands mouvements," in *Proceedings of the 13th Journées de lHydrodynamique, Chatou, France*, 2012.

[166] C. Chauvigné, L. Letournel, A. Babarit, G. Ducrozet, P. Bozonnet, J.-C. Gilloteaux, and P. Ferrant, "Progresses in the Development of a Weakly-Nonlinear Wave Body Interaction Model Based on the Weak-Scatterer Approximation," in *Proceedings of the ASME 34th International Conference on Ocean, Offshore and Arctic Engineering, St. John's, Newfoundland, Canada*, no. OMAE2015-41971, 2015.

[167] E. Guerber, M. Benoit, S. T. Grilli, and C. Buvat, "Numerical modeling of fully nonlinear interaction of ocean waves with a submerged moving body," *Proceedings of the 3rd International Conference on Ocean Energy, Bilbao, Spain*, 2010.

[168] E. Guerber, M. Benoit, S. T. Grilli, and C. Buvat, "A fully nonlinear implicit model for wave interactions with submerged structures in forced or free motion," *Engineering Analysis with Boundary Elements*, vol. 36, no. 7, pp. 1151–1163, 2012.

[169] S. T. Grilli, P. Guyenne, and F. Dias, "A fully non-linear model for three-dimensional overturning waves over an arbitrary bottom," *International Journal for Numerical Methods in Fluids*, vol. 35, no. 7, pp. 829–867, 2001.

[170] L. Letournel, P. Ferrant, A. Babarit, G. Ducrozet, J. C. Harris, M. Benoit, and E. Dombre, "Comparison of fully nonlinear and weakly nonlinear potential flow solvers for the study of wave energy converters undergoing large amplitude motions," in *Proceedings of the ASME 33th International Conference on Ocean, Offshore and Arctic Engineering, San Francisco, Califormia, USA*, no. OMAE2014-23912, 2014.

[171] P. Ferrant, L. Gentaz, C. Monroy, R. Luquet, G. Dupont, G. Ducrozet, B. Alessandrini, E. Jacquin, and A. Drouet, "Recent Advances Towards the Viscous Flow Simulation of Ships Manoeuvering in Waves," in *Proceedings of the 23rd International Workshop on Water Waves and Floating Bodies, Jeju, Korea*, 2008.

[172] C. Monroy, G. Ducrozet, F. Bonnefoy, A. Babarit, L. Gentaz, P. Ferrant, *et al.*, "RANS Simulations of a CALM Buoy in Regular and Irregular Seas using the SWENSE Method," in *Proceedings of the Twentieth International Offshore and Polar Engineering Conference, Beijing, China*, no. ISOPE-I-10-326, 2010.

[173] Z. Li, B. Bouscasse, G. Ducrozet, L. Gentaz, and P. Ferrant, "Challenges in developing a SWENSE two-phase CFD solver for complex wave conditions," in *Proceedings of the 33rd International Workshop on Water Waves and Floating Bodies,Brest, France*, 2018.

[174] L. G. G. D. Zhaobin Li, Benjamin Bouscasse and P. Ferrant, "Progress in Coupling Potential Wave Models and Two-Phase Solvers With the SWENSE Methodology," in *Proceedings of the ASME 37th International Conference on Ocean, Offshore and Arctic Engineering, Madrid, Spain*, no. OMAE2018-77466, 2018.

[175] B. T. Paulsen, H. Bredmose, and H. B. Bingham, "An efficient domain decomposition strategy for wave loads on surface piercing circular cylinders," *Coastal Engineering*, vol. 86, pp. 57 – 76, 2014.

[176] P. Schmitt, C. Windt, J. Nicholson, and B. Elsässer, "Development and validation of a procedure for numerical vibration analysis of an oscillating wave surge converter," *European Journal of Mechanics - B/Fluids*, vol. 58, pp. 9–19, 2015.

[177] A. Babarit and G. Delhommeau, "Theoretical and numerical aspects of the open source BEM solver NEMOH," in *Proceedings of the 11th European Wave and Tidal Energy Conference, Nantes, France*, no. 08C1, 2015.

[178] Morison, J.R., M., Johnson, J.W., Schaaf, and S.A., "The Force Exerted by Surface Waves on Piles," *Journal of Petroleum Technology*, vol. 2, no. 5, pp. 149–154, 1950.

[179] F. Ferri, M. M. Kramer, A. Pecher, *et al.*, "Validation of a wave-body interaction model by experimental tests," in *Proceedings of the Twenty-third International Offshore and Polar Engineering Conference, Anchorage, Alaska*, no. ISOPE-I-13-119, 2013.

[180] B. Molin, *Hydrodynamique des structures offshore*. Editions Technip, Paris, 2002.

[181] M. Folley, T. Whittaker, and A. Henry, "The performance of a wave energy converter in shallow water," in *Proceedings of the 6th European Wave and Tidal Energy Conference, Glasgow, Edinburgh*, 2005.

[182] K. Lok, T. Stallard, P. Stansby, and N. Jenkins, "Optimisation of a clutch-rectified power take off system for a heaving wave energy device in irregular waves with experimental comparison," *International Journal of Marine Energy*, vol. 8, pp. 1–16, 2014.

[183] A. Babarit, J. Hals, M. Muliawan, A. Kurniawan, T. Moan, and J. Krokstad, "Numerical benchmarking study of a selection of wave energy converters," *Renewable Energy*, vol. 41, pp. 44 – 63, 2012.

[184] G. Giorgi and J. V. Ringwood, "Consistency of viscous drag identification tests for wave energy applications," in *Proceedings of the 12th European Wave and Tidal Energy Conference, Cork, Ireland*, no. 643, 2017.

[185] S. Beatty, B. Buckham, and P. Wild, "Experimental comparison of self-reacting point absorber WEC designs," in *Proceedings of the 10th European Wave and Tidal Energy Conference, Aalborg, Denmark*, 2013.

[186] A. Iturrioz, R. Guanche, J. A. Armesto, C. Vidal, and Í. J. Losada, "Experimentally calibrated time-domain numerical model for a fixed owc device," in *Proceedings of ASME 32nd International Conference on Offshore Mechanics and Artic Engineering, Nantes, France*, no. OMAE2013-11177, 2013.

[187] J. Davidson, S. Giorgi, and J. Ringwood, "Numerical Wave Tank Identification of Nonlinear Discrete Time Hydrodynamic Models," in *Proceedings of the 1st International Conference on Renewable Energies Offshore, Lisbon, Portugal*, pp. 279–286, 2014.

[188] J. Davidson, S. Giorgi, and J. V. Ringwood, "Linear parametric hydrodynamic models for ocean wave energy converters identified from numerical wave tank experiments," *Ocean Engineering*, vol. 103, pp. 31–39, 2015.

[189] J. V. Ringwood, J. Davidson, and S. Giorgi, "Optimising numerical wave tank tests for the parametric identification of wave energy device models," in *Proceedings of the ASME 34th International Conference on Ocean, Offshore and Arctic Engineering, St. John's, Newfoundland, Canada*, no. OMAE2015-41529, 2015.

[190] J. Ringwood, J. Davidson, and S. Giorgi, *Numerical Modelling of Wave Energy Converters : State of the art techniques for single devices an arrays*, ch. 7: Identifying Models Using Recorded Data, pp. 123–147. Academic Press, Elsevier, 2016.

[191] L. Ljung, *System Identification: Theory for the User*. Pearson Education, 1998.

[192] O. Nelles, *Nonlinear System Identification: From classical approaches to Neural Networks and Fuzzy Models*. Springer-Verag, 2001.

[193] S. Giorgi, J. Davidson, and J. V. Ringwood, "Identification of wave energy device models from numerical wave tank data - Part 2: Data-based model determination," *IEEE Transactions on Sustainable Energy*, vol. 7, no. 3, pp. 1020–1027, 2016.

[194] E. Anderlini, D. Forehand, E. Bannon, and M. Abusara, "Reactive control of a wave energy converter using artificial neural networks," *International Journal of Marine Energy*, vol. 19, pp. 207–220, 2017.

[195] T. Heath, T. J. T. Whittaker, and C. B. Boake, "The Development and Installation of the Limpet Wave Energy Converter," in *Proceedings of the World Renewable Energy Congress VI, Brighton, UK*, pp. 1619–1622, 2000.

[196] J. Taylor and N. Caldwell, "Design and construction of the variable-pitch air turbine for the Azores wave energy plant," in *Proceedings of the 3rd European Wave and Tidel Energy Conference, Patras, Greece*, vol. 30, 1998.

[197] J. Rea, J. Kelly, R. Alcorn, and D. O'Sullivan, "Development and operation of a power take off rig for ocean energy research and testing," in *Proceedings of the 9th European Wave and Tidal Energy Conference, Southampton, UK*, 2011.

[198] R. Alcorn, A. Blavette, M. Healy, and A. Lewis, "FP7 EU funded CORES wave energy project: a coordinators' perspective on the Galway Bay sea trials," *Underwater Technology*, vol. 32, no. 1, pp. 51–59, 2014.

[199] Y. Washio, H. Osawa, Y. Nagata, F. Fujii, H. Furuyama, T. Fujita, *et al.*, "The offshore floating type wave power device "Mighty Whale": open sea tests," in *Proceedings of the Tenth International Offshore and Polar Engineering Conference, Seattle, Washington, USA*, no. ISOPE-I-00-054, 2000.

[200] A. J. N. A. Sarmento and A. F. O. Falcão, "Wave generation by an oscillating surface-pressure and its application in wave-energy extraction," *Journal of Fluid Mechanics*, vol. 150, pp. 467–485, 1985.

[201] R. Jefferys and T. Whittaker, "Latching control of an oscillating water column device with air compressibility," in *Hydrodynamics of Ocean Wave-Energy Utilization*, pp. 281–291, Springer, 1986.

[202] W. Sheng, R. Alcorn, and A. Lewis, "On thermodynamics in the primary power conversion of oscillating water column wave energy converters," *Journal of Renewable and Sustainable Energy*, vol. 5, no. 2, p. 023105, 2013.

[203] A. F. O. Falcão and P. A. P. Justino, "OWC wave energy devices with air flow control," *Ocean Engineering*, vol. 26, no. 12, pp. 1275 – 1295, 1999.

[204] J. C. C. Henriques, L. M. C. Gato, J. M. Lemos, R. P. F. Gomes, and A. F. O. Falcão, "Peak-power control of a grid-integrated oscillating water column wave energy converter," *Energy*, vol. 109, pp. 378 – 390, 2016.

[205] W. Sheng, R. Alcorn, and A. Lewis, "Assessment of primary energy conversions of oscillating water columns. II. Power take-off and validations," *Journal of Renewable and Sustainable Energy*, vol. 6, no. 5, p. 053114, 2014.

[206] A. F. O. Falcão and R. J. A. Rodrigues, "Stochastic modelling of OWC wave power plant performance," *Applied Ocean Research*, vol. 24, no. 2, pp. 59–71, 2002.

[207] A. Thakker, J. Jarvis, and A. Sahed, "Design charts for impulse turbine wave energy extraction using experimental data," *Renewable Energy*, vol. 34, no. 10, pp. 2264–2270, 2009.

[208] J. F. Kelly, W. M. D. Wright, W. Sheng, and K. O'Sullivan, "Implementation and Verification of a Wave-to-Wire Model of an Oscillating Water Column With Impulse Turbine," *IEEE Transactions on Sustainable Energy*, vol. 7, no. 2, pp. 546–553, 2016.

[209] S. L. Dixon and C. A. Hall, *Fluid mechanics and thermodynamics of turbomachinery*. Oxford, UK: Butterworth-Heinemann / Elsevier, seventh edition ed., 2014.

[210] A. F. O. Falcão and L. M. C. Gato, "Air turbines," in *Comprehensive Renewable Energy* (A. Sayigh, ed.), pp. 111 – 149, Oxford: Elsevier, 2012.

[211] A. A. Wells, "Fluid driven rotary transducer," September 1980. US Patent, US4221538A, Available at https://patents.google.com/patent/US4221538A/en [Last accessed 22 June 2018].

[212] T. Setoguchi, S. Santhakumar, H. Maeda, M. Takao, and K. Kaneko, "A review of impulse turbines for wave energy conversion," *Renewable Energy*, vol. 23, no. 2, pp. 261 – 292, 2001.

[213] R. Curran, T. Denniss, and C. B. Boake, "Multidisciplinary design for performance: ocean wave energy conversion," in *Proceedings of the Tenth International Offshore and Polar Engineering Conference, Seattle, Washington, USA*, no. ISOPE-I-00-063, 2000.

[214] T. Finnigan and D. Auld, "Model testing of a variable-pitch aerodynamic turbine," in *Proceedings of the Thirteenth International Offshore and Polar Engineering Conference, Honolulu, Hawaii, USA*, no. ISOPE-I-03-053, 2003.

[215] A. F. O. Falcão, L. M. C. Gato, and E. P. A. S. Nunes, "A novel radial self-rectifying air turbine for use in wave energy converters," *Renewable Energy*, vol. 50, pp. 289 – 298, 2013.

[216] S. Raghunathan, "The Wells air turbine for wave energy conversion," *Progress in Aerospace Sciences*, vol. 31, no. 4, pp. 335–386, 1995.

[217] G. Corey, "Rack and pinion wave motor power plant," August 1978. WO Patent, WO2009153329A3, Available at https://patents.google.com/patent/WO2009153329A3/en [Last accessed 22 June 2018].

[218] J. Eder and D. Stewart, "Wave energy converter and power take off system," July 2011. US Patent, US20110084488A1, Available at https://patents.google.com/patent/US20110084488A1/en?q=Wave&q=energy&q=converter&q=power [Last accessed 22 June 2018].

[219] J. Hals, S. G. Ásgeirsson, E. Hjálmarsson, J. Maillet, P. M oller, P. Pires, M. Guérinel, and M. Lopes, "Tank testing of an inherently phase controlled wave energy converter," in *Proceedings of the 11th European Wave and Tidal Energy Conference, Nantes, France*, no. 09B3-2, 2015.

[220] D. Albady and C. Öhman, "Characterization of a Cascade Gear Box for a Wave Energy Converter," Master's thesis, KTH Royal Institute of Technology, Stockholm, Sweden, 2013. Available at http://www.diva-portal.se/smash/get/diva2:684022/FULLTEXT01.pdf [Last accessed 22 June 2018].

[221] M. Metcalfe, "Gearing up for efficiency," *Gear Solutions*, vol. 10, no. 106, pp. 50–55, 2012.

[222] J. Sjolte, C. M. Sandvik, E. Tedeschi, and M. Molinas, "Exploring the potential for increased production from the wave energy converter Lifesaver by reactive control," *Energies*, vol. 6, no. 8, pp. 3706–3733, 2013.

[223] J. Sjolte, *Marine renewable energy conversion: Grid and off-grid modeling, design and operation*. PhD thesis, Norwegian University of Science and Technology, Trondheim, Norway, 2014. Available at https://brage.bibsys.no/xmlui/handle/11250/257868 [Last accessed 22 June 2018].

[224] A. Pecher, J. P. Kofoed, and T. Larsen, "Design specifications for the Hanstholm WEPTOS wave energy converter," *Energies*, vol. 5, no. 4, pp. 1001–1017, 2012.

[225] N. A. Hansen and K. K. Hansen, "Wave power machine," August 2005. US Patent, US6925800B2, Available at https://patents.google.com/patent/US6925800 [Last accessed 22 June 2018].

[226] K. Merk, "Device for generating energy using water waves," October 1999. WO Patent, WO2009153329A3, Available at https://patents.google.com/patent/WO2009153329A3/en [Last accessed 22 June 2018].

[227] Barness Industries Ltd, "Precision ball screws," 2016. Available at http://www.barnesballscrew.com/ball-screws [Last accessed 22 June 2018].

[228] SKF, "Roller screws. pub mt/p1 14489 en," 2014. Available at http://www.skf.com/binary/82-153959/14489-EN—Roller-screw-catalogue.pdf [Last accessed 22 June 2018].

[229] D. Stewart and J. Gerber, "Wave energy converter utilizing internal reaction mass and spring," February 2015. CA Patent, CA2632158C, Available at https://patents.google.com/patent/CA2632158C/en [Last accessed 22 June 2018].

[230] L. Ze, W. Yang, and C.-S. Wang, "Buoy and ball screw combined sea wave generator," May 2011. CN Patent, CN102042156A, Available at https://patents.google.com/patent/CN102042156A/en [Last accessed 22 June 2018].

[231] E. B. Agamloh, A. K. Wallace, and A. von Jouanne, "A novel direct-drive ocean wave energy extraction concept with contact-less force transmission system," *Renewable Energy*, vol. 33, no. 3, pp. 520 – 529, 2008.

[232] R. K. Holm, N. I. Berg, M. Walkusch, P. O. Rasmussen, and R. H. Hansen, "Design of a magnetic lead screw for wave energy conversion," *IEEE Transactions on Industry Applications*, vol. 49, no. 6, pp. 2699–2708, 2013.

[233] R. H. Hansen, *Design and Control of the PowerTake-Off System for a Wave Energy Converter with Multiple Absorbers*. PhD thesis, Aalborg University, Aalborg, Denmark, 2013. Available at http://vbn.aau.dk/en/publications/design-and-control-of-the-powertakeoff-system-for-a-wave-energy-converter-with-multiple-absorbers(f652ff2e-89d3-4560-b92b-eed3633fd16f).html [Last accessed 22 June 2018].

[234] C. Josset, A. Babarit, and A. H. Clément, "A wave-to-wire model of the SEAREV wave energy converter," *Proceedings of the Institution of Mechanical Engineers, Part M: Journal of Engineering for the Maritime Environment*, vol. 221, no. 2, pp. 81–93, 2007.

[235] P. Ricci, J. Lopez, M. Santos, P. Ruiz-Minguela, J. L. Villate, F. Salcedo, and A. F. O. Falcão, "Control strategies for a wave energy converter connected to a hydraulic power take-off," *IET renewable power generation*, vol. 5, no. 3, pp. 234–244, 2011.

[236] C. J. Cargo, A. R. Plummer, A. J. Hillis, and M. Schlotter, "Determination of optimal parameters for a hydraulic power take-off unit of a wave energy converter in regular waves," *Proceedings of the Institution of Mechanical Engineers, Part A: Journal of Power and Energy*, vol. 226, pp. 98–111, February 2012.

[237] C. J. Cargo, A. J. Hillis, and A. R. Plummer, "Optimisation and control of a hydraulic power take-off unit for a wave energy converter in irregular waves," *Proceedings of the Institution of Mechanical Engineers, Part A: Journal of Power and Energy*, vol. 228, pp. 462–479, June 2014.

[238] D. I. Forehand, A. E. Kiprakis, A. J. Nambiar, and A. R. Wallace, "A fully coupled wave-to-wire model of an array of wave energy converters," *IEEE Transactions on Sustainable Energy*, vol. 7, no. 1, pp. 118–128, 2015.

[239] Y. Kamizuru, *Development of hydrostatic drive trains for wave energy converters*. PhD thesis, RWTH Aachen University, Aachen, Germany, 2014.

[240] R. H. Hansen, M. M. Kramer, and E. Vidal, "Discrete displacement hydraulic power take-off system for the Wavestar wave energy converter," *Energies*, vol. 6, no. 8, pp. 4001–4044, 2013.

[241] A. Plummer and C. Cargo, "Power Transmissions for Wave Energy Converters: A Review," in *Proceedings of the 8th International Fluid Power Conference, Dresden, Germany*, 2012.

[242] M. Jelali and A. Kroll, *Hydraulic servo-systems: modelling, identification and control*. London, UK: Springer-Verlag, 2012.

[243] F. Yeaple, *Fluid power design handbook*. New York, NY, USA: CRC Press, 1995.

[244] V. Kalinin, "A wave energy conversion system," January 2011. WO Patent, WO2009153329A3, Available at https://patents.google.com/patent/WO2009153329A3/en [Last accessed 22 June 2018].

[245] D. Pizer, C. Retzler, and R. Yemm, "Floating apparatus and method for extracting power from sea waves," March 2000. WO Patent, WO2009153329A3, Available at https://patents.google.com/patent/WO2009153329A3/en [Last accessed 22 June 2018].

[246] R. H. Hansen, T. O. Andersen, H. C. Pedersen, and A. H. Hansen, "Control of a 420 kn discrete displacement cylinder drive for the wavestar wave energy converter," in *Proceedings of the ASME/BATH Symposium on Fluid Power and Motion Control, Bath, UK*, no. FPMC2014-7833, 2014.

[247] D. Helgerson, "Digital Displacement Pumps," 2018. Available at http://fluidpowerjournal.com/2018/03/digital-displacement-pumps/ [Last accessed 22 June 2018].

[248] R. Datta and V. T. Ranganathan, "Variable-speed wind power generation using doubly fed wound rotor induction machine - a comparison with alternative schemes," *IEEE Transactions on Energy Conversion*, vol. 17, no. 3, pp. 414–421, 2002.

[249] N. Mohan, *Advanced Electric Drives: Analysis, Control, and Modeling Using MATLAB/Simulink*. Hoboken, NJ, USA: John Wiley & Sons, 2014.

[250] T. Ahmed, K. Nishida, and M. Nakaoka, "Grid power integration technologies for offshore ocean wave energy," in *Proceedings of the IEEE Energy Conversion Congress and Exposition, Atlanta, GA, USA*, pp. 2378–2385, IEEE, 2010.

[251] K. Schlemmer, F. Fuchshumer, N. Böhmer, R. Costello, and C. Villegas, "Design and control of a hydraulic power take-off for an axi-symmetric heaving point absorber," in *Proceedings of the Ninth European Wave and Tidal Energy Conference, Southampton, UK*, 2011.

[252] M. Amundarain, M. Alberdi, A. J. Garrido, and I. Garrido, "Modeling and Simulation of Wave Energy Generation Plants: Output Power Control," *IEEE Transactions on Industrial Electronics*, vol. 58, no. 1, pp. 105–117, 2011.

[253] J. Sjolte, G. Tjensvoll, and M. Molinas, "Power collection from wave energy farms," *Applied Sciences*, vol. 3, no. 2, pp. 420–436, 2013.

[254] Z. Zhou, W. Knapp, J. MacEnri, H. C. Sorensen, E. F. Madsen, I. Masters, and P. Igic, "Permanent magnet generator control and electrical system configuration for Wave Dragon MW wave energy take-off system," in *Proceedings of the IEEE International Symposium on Industrial Electronics, Cambridge, UK*, pp. 1580–1585, 2008.

[255] N. J. Baker, *Linear generators for direct drive marine renewable energy converters*. PhD thesis, Durham University, Durham, UK, 2003. Available at http://etheses.dur.ac.uk/696/ [Last accessed 22 June 2018].

[256] O. Danielsson, *Wave energy conversion: linear synchronous permanent magnet generator*. PhD thesis, Uppsala University, Uppsala, Sweden, 2006. Available at http://www.diva-portal.org/smash/record.jsf?pid=diva2[Last accessed 22 June 2018].

[257] N. J. Baker, M. Mueller, and E. Spooner, "Permanent magnet air-cored tubular linear generator for marine energy converters," in *Proceedings of the Second International Conference on Power Electronics, Machines and Drives, Edinburgh, UK*, vol. 2, pp. 862–867, 2004.

[258] N. Hodgins, O. Keysan, A. S. McDonald, and M. A. Mueller, "Design and testing of a linear generator for wave-energy applications," *IEEE Transactions on Industrial Electronics*, vol. 59, no. 5, pp. 2094–2103, 2012.

[259] H. Polinder, M. E. C. Damen, and F. Gardner, "Linear PM Generator system for wave energy conversion in the AWS," *IEEE Transactions on Energy Conversion*, vol. 19, no. 3, pp. 583–589, 2004.

[260] F. Wu, X.-P. Zhang, P. Ju, and M. J. Sterling, "Modeling and control of AWS-based wave energy conversion system integrated into power grid," *IEEE Transactions on Power Systems*, vol. 23, no. 3, pp. 1196–1204, 2008.

[261] E. Spooner and C. J. Grimwade, "Snapper TM: an efficient and compact direct electric power take-off device for wave energy converters," in *Proceedings of the Second World Maritime Technology Conference, London*, pp. 6–10, 2006.

[262] P. O. Rasmussen, T. O. Andersen, F. T. Jorgensen, and O. Nielsen, "Development of a high-performance magnetic gear," *IEEE Transactions on Industry Applications*, vol. 41, no. 3, pp. 764–770, 2005.

[263] R. C. Crozier, H. Bailey, M. A. Mueller, E. Spooner, and P. McKeever, "Analysis, design and testing of a novel direct-drive wave energy converter system," *IET Renewable Power Generation*, vol. 7, no. 5, pp. 565–573, 2013.

[264] J. Tamura, "Calculation method of losses and efficiency of wind generators," in *Wind Energy Conversion Systems*, pp. 25–51, Springer, 2012.

[265] J. A. Baroudi, V. Dinavahi, and A. M. Knight, "A review of power converter topologies for wind generators," in *Proceedings of the IEEE International Conference on Electric Machines and Drives*, pp. 458–465, 2005.

[266] E. Dos Santos and E. R. da Silva, *Advanced Power Electronics Converters: PWM Converters Processing AC Voltages*, vol. 46. Hoboken, NJ, USA: John Wiley & Sons, 2014.

[267] A. Hughes and B. Drury, *Electric Motors and Drives: Fundamentals, Types and Applications*. Oxford, UK: Newnes - Elsevier, fourth ed., 2013.

[268] P. Igic, Z. Zhou, W. Knapp, J. MacEnri, H. C. Sorensen, and E. Friis-Madsen, "Multi-megawatt offshore wave energy converters - electrical system configuration and generator control strategy," *Renewable Power Generation, IET*, vol. 5, pp. 10–17, January 2011.

[269] A. J. Garrido, E. Otaola, I. Garrido, J. Lekube, F. J. Maseda, P. Liria, and J. Mader, "Mathematical modeling of oscillating water columns wave-structure interaction in ocean energy plants," *Mathematical Problems in Engineering*, vol. 2015, no. 727982, p. 11, 2015.

[270] J. C. C. Henriques, R. P. F. Gomes, L. M. C. Gato, A. F. O. Falcão, E. Robles, and S. Ceballos, "Testing and control of a power take-off system for an oscillating-water-column wave energy converter," *Renewable Energy*, vol. 85, pp. 714–724, 2016.

[271] H. Bailey, B. R. Robertson, and B. J. Buckham, "Wave-to-wire simulation of a floating oscillating water column wave energy converter," *Ocean Engineering*, vol. 125, pp. 248 – 260, 2016.

[272] E. Tedeschi, M. Carraro, M. Molinas, and P. Mattavelli, "Effect of Control Strategies and Power Take-Off Efficiency on the Power Capture From Sea Wave," *IEEE Transactions on Energy Conversion*, vol. 26, no. 4, pp. 1088–1098, 2011.

[273] G. Li and M. R. Belmont, "Model predictive control of sea wave energy converters–Part I: A convex approach for the case of a single device," *Renewable Energy*, vol. 69, pp. 453–463, 2014.

[274] T. K. A. Brekken, "On model predictive control for a point absorber wave energy converter," in *2011 IEEE Trondheim PowerTech*, 2011.

[275] Z. Yu and J. Falnes, "State-space modelling of a vertical cylinder in heave," *Applied Ocean Research*, vol. 17, no. 5, pp. 265–275, 1995.

[276] C. J. Cargo, A. J. Hillis, and A. R. Plummer, "Strategies for active tuning of Wave Energy Converter hydraulic power take-off mechanisms," *Renewable Energy*, vol. 94, pp. 32–47, 2016.

[277] H. Bailey, J. P. Ortiz, B. Robertson, B. J. Buckhamn, and R. S. Nicoll, "A Methodology for Wave-to-Wire WEC Simulations," *Proceedings of the 2nd Marine Energy Technology Symposium, Seattle, WA, USA*, 2014.

[278] J. F. Gaspar, M. Kamarlouei, A. Sinha, H. Xu, M. Calvário, F. X. Faÿ, E. Robles, and C. G. Soares, "Speed control of oil-hydraulic power take-off system for oscillating body type wave energy converters," *Renewable Energy*, vol. 97, pp. 769–783, 2016.

[279] P. B. Garcia-Rosa, J. P. Vilela Soares Cunha, F. Lizarralde, S. F. Estefen, I. R. Machado, and E. H. Watanabe, "Wave-to-Wire Model and Energy Storage Analysis of an Ocean Wave Energy Hyperbaric Converter," *IEEE Journal of Oceanic Engineering*, vol. 39, no. 2, pp. 386–397, 2014.

[280] G. Giorgi, M. Penalba, and J. V. Ringwood, "Nonlinear hydrodynamic models for heaving buoy wave energy converters," in *Proceedings of the 3rd Asian Wave and Tidal Energy Conference, Singapore*, pp. 144–153, 2016.

[281] S. J. Beatty, M. Hall, B. J. Buckham, P. Wild, and B. Bocking, "Experimental and numerical comparisons of self-reacting point absorber wave energy converters in regular waves," *Ocean Engineering*, vol. 104, pp. 370 – 386, 2015.

[282] M. Folley, T. Whittaker, and J. v. Hoff, "The Design of Small Seabed-Mounted Bottom-Hinged Wave Energy Converter," in *Proceedings of the 7th European Wave and Tidal Energy Conference, Porto, Portugal*, 2007.

[283] G. Knott and J. Flower, "Measurement of energy losses in oscillatory flow through a pipe exit," *Applied Ocean Research*, vol. 2, no. 4, pp. 155–164, 1980.

[284] Y. Luo, J.-R. Nader, P. Cooper, and S.-P. Zhu, "Nonlinear 2D analysis of the efficiency of fixed oscillating water column wave energy converters," *Renewable Energy*, vol. 64, pp. 255–265, 2014.

[285] A. Rafiee and J. Fiévez, "Numerical Prediction of Extreme Loads on the CETO Wave Energy Converter," in *Proceedings of the 11th European Wave and Tidal Energy Conference, Nantes, France*, no. 09A1-2, 2015.

[286] W. Wang, M. Wu, J. Palm, and C. Eskilsson, "Estimation of numerical uncertainty in computational fluid dynamics simulations of a passively controlled wave energy converter," *Proceedings of the Institution of Mechanical Engineers, Part M: Journal of Engineering for the Maritime Environment*, vol. 232, no. 1, pp. 71–84, 2018.

[287] M. Alves, *Numerical Modelling of Wave Energy Converters: State-of-the-Art Techniques for Single Devices and Arrays*, ch. 2: Frequency-Domain Models, pp. 11–30. London, UK: Elsevier Science & Technology Books, 2016.

[288] DNV-GL, "Frequency domain hydrodynamic analysis of stationary vessels - WADAM." Available at https://www.dnvgl.com/services/frequency-domain-hydrodynamic-analysis-of-stationary-vessels-wadam-2412 [Last accessed 22 June 2018].

[289] O. Masson, "Développements du programme achil3d," Tech. Rep. UMR6598, Laboratoire de Mécanique des Fluides CNRS, Ecole Central de Nantes, 1998.

[290] S. McKinley and M. Levine, "Cubic spline interpolation," 1998. Available at https://mse.redwoods.edu/darnold/math45/laproj/Fall98/SkyMeg/Proj.PDF [Last accessed 22 June 2018].

[291] T. Ogilvie, "Recent progress toward the understanding and prediction of ship motions," in *Proceedings of the 5th Symposium on Naval Hydrodynamics, Bergen, Norway*, pp. 3–128, 1964.

[292] P. Ricci, *Numerical Modelling of Wave Energy Converters: State-of-the-Art Techniques for Single Devices and Arrays*, ch. 3: Time-Domain Models, pp. 31–66. London, UK: Elsevier Science & Technology Books, 2016.

[293] J. Fenton, "Nonlinear wave theories," *the Sea*, vol. 9, no. 1, pp. 3–25, 1990.

[294] M. A. Bhinder, A. Babarit, L. Gentaz, and P. Ferrant, "Potential time domain model with viscous correction and CFD analysis of a generic surging floating wave energy converter," *International Journal of Marine Energy*, vol. 10, pp. 70 – 96, 2015.

[295] A. Babarit and A. Clément, "Optimal latching control of a wave energy device in regular and irregular waves," *Applied Ocean Research*, vol. 28, pp. 77–91, 2006.

[296] J. V. Ringwood and S. Butler, "Optimisation of a wave energy converter," *IFAC Proceedings Volume*, vol. 37, no. 10, pp. 155–160, 2004.

[297] J. Cordonnier, F. Gorintin, A. D. Cagny, A. Clément, and A. Babarit, "SEAREV: Case study of the development of a wave energy converter," *Renewable Energy*, vol. 80, pp. 40 – 52, 2015.

[298] A. F. O. Falcão, "Modelling and control of oscillating-body wave energy converters with hydraulic power take-off and gas accumulator," *Ocean engineering*, vol. 34, no. 14, pp. 2021–2032, 2007.

[299] D. R. Grandall, "The performance oand efficiency of hydraulic pumps and motors," Master's thesis, University of Minnesota, Minnesota, USA, 2010. Available at https://conservancy.umn.edu/bitstream/handle/11299/59818/1/Grandall_David_ January2010.pdf [Last accessed 22 June 2018].

[300] Y. Jinghong, C. Zhaoneng, and L. Yuanzhang, "The variation of oil effective bulk modulus with pressure in hydraulic systems," *Journal of dynamic systems, measurement, and control*, vol. 116, no. 1, pp. 146–150, 1994.

[301] H. E. Merritt, *Hydraulic control systems*. John Wiley & Sons, 1967.

[302] H. Olsson, K. J. Åström, C. C. De Wit, M. Gäfvert, and P. Lischinsky, "Friction models and friction compensation," *European journal of control*, vol. 4, no. 3, pp. 176–195, 1998.

[303] Fisher and Emerson Process Management, *Control Valve Handbook*. Fisher Controls International LLC, 2005.

[304] W. Wilson, "Rotary-pump theory," *Trans. ASME*, vol. 68, no. 4, pp. 371–384, 1946.

[305] D. McCandlish and R. Dorey, "The mathematical modeling of hydrostatic pumps and motors," *Proceedings of the Institution of Mechanical Engineers*, vol. 198B, no. 10, pp. 165–174, 1984.

[306] R. Dorey, "Modeling of losses in pumps and motors," in *Proceedings of the First Bath International Fluid Workshop, Bath, UK*, pp. 71–97, 1988.

[307] D. Mikeska, "A precise steady-state model of displacement machines for the application in virtual prototyping of power-split drives," in *Proceedings of the 2nd Fluid Power Net International Symposium, Modena, Italy*, pp. 3–6, 2002.

[308] W. Schlöesser, "Mathematical model for displacement pumps and motors," *Hydraulic power transmission*, pp. 252–257, 1961.

[309] W. Schlösser, "The overall efficiency of positive-displacement pumps," in *Proceedings of the 1st Fluid Power Symposium, Cranfield, UK*, no. 983, pp. 34–48, British Hydromechanics Research Association, 1968.

[310] Sauer-Danfoss, "Series 51 and 51-1 bent axis variable displacement motors technical information." Available at https://www.bibus.hu/fileadmin/editors/countries/bihun/product_data/sauer-danfoss/documents/sauerdanfoss_series_s51_motors_catalogue_en_520l0440.pdf [Last accessed 22 June 2018].

[311] Kawasaki, "Swash plate type axial piston pumps k3vl." Available at http://www.kpm-eu.com/files/Datasheets/P-200109-14-K3VL.aspx [Last accessed 22 June 2018].

[312] R. H. Park, "Two-reaction theory of synchronous machines generalized method of analysis-part I," *Transactions of the American Institute of Electrical Engineers*, vol. 48, no. 3, pp. 716–727, 1929.

[313] P. C. Krause, O. Wasynczuk, S. D. Sudhoff, and S. Pekarek, *Analysis of Electric Machinery and Drive Systems*. Hoboken, NJ, USA: Wiley-Blackwell, 3rd ed., 2013.

[314] M. Prasad, P. K. Gayen, and D. Chatterjee, "A harmonic elimination technique for voltage source inverter using embedded controller," in *Proceedings of the International Conference on Microelectronics, Computing and Communications, Durgapur, India*, 2016.

[315] R. Pena, J. Clare, and G. Asher, "Doubly fed induction generator using back-to-back PWM converters and its application to variable-speed wind-energy generation," *IEE Proceedings - IEE Electric Power Applications*, vol. 143, no. 3, pp. 231–241, 1996.

[316] H. Bai, F. Wang, and J. Xing, "Control strategy of combined PWM rectifier/inverter for a high speed generator power system," in *Proceedings of the 2nd IEEE Conference on Industrial Electronics and Applications, Harbin, China*, pp. 132–135, IEEE, 2007.

[317] Siemens PLM, "Simcenter Amesim." Available at https://www.plm.automation.siemens.com/global/en/products/simcenter/simcenter-amesim.html [Last accessed 22 June 2018].

[318] H. G. Weller, G. Tabor, H. Jasak, and C. Fureby, "A tensorial approach to computational continuum mechanics using object-oriented techniques," *Computers in physics*, vol. 12, no. 6, pp. 620 – 631, 1998.

[319] K. Ruehl, C. Michelen, S. Kanner, M. Lawson, and Y.-H. Yu, "Preliminary verification and validation of wec-sim, an open-source wave energy converter design tool," in *Proceedings of the ASME 33rd International Conference on Ocean, Offshore and Arctic Engineering, San Francisco, California, USA*, no. OMAE2014-24312, 2014.

[320] C. Windt, J. Davidson, P. Schmitt, and J. Ringwood, "A benchmark study for numerical wavemakers in CFD simulations," *submitted to Coastal Engineering*, 2018.

[321] G. Giorgi and J. V. Ringwood, "Implementation of latching control in a numerical wave tank with regular waves," *Journal of Ocean Engineering and Marine Energy*, vol. 2, no. 2, pp. 211–226, 2016.

[322] C. Cargo, *Design and Control of Hydraulic Power Take-Off for Wave Energy Converters*. PhD thesis, University of Bath, Bath, UK, 2012. Available at http://opus.bath.ac.uk/38460/ [Last accessed 22 June 2018].

[323] M. Borghi, M. Milani, M. Piraccini, and M. Flandoli, "Analysis of a F1 car hydraulic circuit dynamic behavior," in *Proceedings of the ransmission and Driveline Systems Symposium, Detroit, Michigan, USA*, pp. 225–230, SAE, 2001.

[324] S. Tikkanen, "Influence of line design on pump performance," in *Proccedings of the Bath Workshop on Power Transmission and Motion Control, Bath, UK*, pp. 33–46, John Wiley & Sons, 2001.

[325] S. Manco, N. Nervegna, and M. Rundo, "Effects of Timing and Odd/Even Number of Teeth on Noise Generation of Gerotor Lubricating Pumps for IC Engines," in *Proceedings of the International Off-Highway & Powerplant Congress, Milwaukee, Wisconsin, USA*, pp. 109–118, SAE, 2000.

[326] N. Nervegna, S. Manco, and M. Rundo, "Variable flow internal gear pump," in *Proceedings of the ASME International Mechanical Engineering Congress, New York, NY, USA*, vol. 8, pp. 81–92, 2001.

[327] O. Barambones, J. A. Cortajarena, P. Alkorta, and J. M. G. de Durana, "A real-time sliding mode control for a wind energy system based on a doubly fed induction generator," *Energies*, vol. 7, no. 10, pp. 6412–6433, 2014.

[328] J. A. Cortajarena and J. De Marcos, "Neural network model reference adaptive system speed estimation for sensorless control of a doubly fed induction generator," *Electric Power Components and Systems*, vol. 41, no. 12, pp. 1146–1158, 2013.

[329] R. Pintelon and J. Schoukens, *System identification: a frequency domain approach*. John Wiley & Sons, 2012.

[330] D. Ramirez, J. P. Bartolome, S. Martinez, L. C. Herrero, and M. Blanco, "Emulation of an OWC ocean energy plant with PMSG and irregular wave model," *IEEE Transactions on Sustainable Energy*, vol. 6, no. 4, pp. 1515–1523, 2015.

[331] S. G. Rabinovich, *Measurement errors and uncertainties: theory and practice*. Springer Science & Business Media, 2006.

[332] J. Mondol, "Sizing of grid-connected photovoltaic systems," 2007. Available at http://uir.ulster.ac.uk/2432/ [Last accessed 22 June 2018].

[333] W. C. Gear, *Numerical initial value problems in ordinary differential equations*. Englewood Cliffs, New Jersey, USA: Prentice-Hall, 1971.

[334] S. C. Chapra, *Applied Numerical Methods with MATLAB: for Engineers & Scientists*. New York, NY, USA: McGraw-Hill Higher Education, 3rd ed., 2011.

[335] E. Hairer, S. Nørsett, and G. Wanner, *Solving ordinary differential equations I: nonstiff problems*. New York, NY, USA: Springer-Verlag Berlin Heidelberg, 1993.

[336] U. M. Ascher and L. R. Petzold, *Computer methods for ordinary differential equations and differential-algebraic equations*, vol. 61. Siam, 1998.

[337] A. Iserles, *A first course in the numerical analysis of differential equations*. No. 44, Cambridge university press, 2009.

[338] A. Mérigaud and J. V. Ringwood, "A nonlinear frequency-domain approach for numerical simulation of wave energy converters," *IEEE Transactions on Sustainable Energy*, vol. 9, no. 1, pp. 86–94, 2018.

[339] B. Braconnier, "Dynamic phasor modeling of doubly-fed induction Machines including saturation effects of main flux linkage," Master's thesis, The University of British Columbia, Vancouver, Canada, 2009. Available at https://open.library.ubc.ca/media/download/pdf/24/1.0073304/1 [Last accessed on 22 June 2018].

[340] C. W. Gear and D. Wells, "Multirate linear multistep methods," *BIT Numerical Mathematics*, vol. 24, no. 4, pp. 484–502, 1984.

[341] C. Engstler and C. Lubich, "Multirate extrapolation methods for differential equations with different time scales," *Computing*, vol. 58, no. 2, pp. 173–185, 1997.

[342] R. Takaramoto, M. Kashiwagi, K. Sakai, *et al.*, "Wave energy absorption in irregular waves by a floating body equipped with interior rotating electric-power generator," in *Proceedings of the Twenty-fourth International Ocean and Polar Engineering Conference, Busan, Korea*, no. ISOPE-I-14-133, 2014.

[343] N. Faedo, S. Olaya, and J. V. Ringwood, "Optimal control, MPC and MPC-like algorithms for wave energy systems: An overview," *IFAC Journal of Systems and Control*, vol. 1, pp. 37–56, 2017.

[344] R. Genest and J. V. Ringwood, "Receding horizon pseudospectral control for energy maximization with application to wave energy devices," *IEEE Transactions on Control Systems Technology*, vol. 25, no. 1, pp. 29–38, 2017.

[345] N. Faedo, G. Scarciotti, A. Astolfi, and J. Ringwood, "Energy-maximising control of wave energy devices using a moment-domain representation," *Submitted to Control Engineering Practice*.

[346] M. Penalba, I. Touzón, J. Lopez-Mendia, and V. Nava, "A numerical study on the hydrodynamic impact of device slenderness and array size in wave energy farms in realistic wave climates," *Ocean Engineering*, vol. 142, pp. 224–232, July 2017.

[347] P. A. Lynn, *Electricity from wave and tide: an introduction to marine energy*. John Wiley & Sons, 2013.

[348] Irish Marine Institute. Available at http://www.marine.ie/Home/site-area/data-services/real-timeobservations/ wave-buoys [Last accessed 22 June 2018].

[349] R. Carballo and G. Iglesias, "A methodology to determine the power performance of wave energy converters at a particular coastal location," *Energy Conversion and Management*, vol. 61, pp. 8–18, 2012.

[350] A. D. de Andres, R. Guanche, J. Weber, and R. Costello, "Finding gaps on power production assessment on WECs: Wave definition analysis," *Renewable Energy*, vol. 83, pp. 171–187, 2015.

[351] E. Rusu and F. Onea, "Estimation of the wave energy conversion efficiency in the Atlantic Ocean close to the European islands," *Renewable Energy*, vol. 85, pp. 687–703, 2016.

[352] L. Rusu and F. Onea, "The performance of some state-of-the-art wave energy converters in locations with the worldwide highest wave power," *Renewable and Sustainable Energy Reviews*, vol. 75, no. November 2016, pp. 1348–1362, 2017.

[353] A. Mérigaud and J. V. Ringwood, "Power production assessment for wave energy converters: Overcoming the perils of the power matrix," *Proceedings of the Institution of Mechanical Engineers, Part M: Journal of Engineering for the Maritime Environment*, vol. 232, no. 1, pp. 50–70, 2018.

[354] B. Robertson, C. Hiles, E. Luczko, and B. Buckham, "Quantifying wave power and wave energy converter array production potential," *International Journal of Marine Energy*, vol. 14, pp. 143–160, 2016.

[355] P. Lamont-Kane, M. Folley, and T. Whittaker, "Investigating uncertainties in physical testing of wave energy converter arrays," in *Proceedings of the 10th European Wave and Tidal Energy Conference, Aalborg, Denmark*, 2013.

[356] S. Draycott, D. Noble, T. Davey, J. Steynor, and D. M. Ingram, "Application of Complex Wave and Current Conditions in a Laboratory Environment," in *Proceedings of the 12th European Wave and Tidal Energy Conference, Cork, Ireland*, no. 890, 2017.

[357] P. Schmitt and B. Elsässer, "The application of Froude scaling to model tests of Oscillating Wave Surge Converters," *Ocean Engineering*, vol. 141, pp. 108–115, 2017.

[358] S. Beatty, F. Ferri, B. Bocking, J. Kofoed, and B. Buckham, "Power Take-Off Simulation for Scale Model Testing of Wave Energy Converters," *Energies*, vol. 10, no. 7, p. 973, 2017.

[359] J. Davidson, R. Genest, and J. V. Ringwood, "Adaptive control of a wave energy converter simulated in a numerical wave tank," in *Proceedings of the 12th European Wave and Tidal Energy Conference, Cork, Ireland*, no. 747, 2017.

[360] R. Genest, J. Davidson, and J. V. Ringwood, "Adaptive control of a wave energy converter," *IEEE Transactions on Sustainable Energy*, vol. PP, no. 99, 2018.

[361] C. Windt, J. Davidson, A. Benazzou, and J. Ringwood, "Performance assessment of the overset grid method for numerical wave tank experiments in the openfoam environment," in *Proceedings of the ASME 37th International Conference on Ocean, Offshore and Arctic Engineering, Madrid, Spain*, no. OMAE2018-77564, 2018.

[362] B. Di Paolo, J. Lara, G. Barajas, A. Paci, and I. Losada, "Numerical analysis of wave and current interaction with moored floating bodies using overset method," in *Proceedings of the ASME 37th International Conference on Ocean, Offshore and Arctic Engineering, Madrid, Spain*, no. OMAE2018-77284, 2018.

[363] T. Holzmann, *Mathematics, numerics, derivations and OpenFOAM*, ch. 11: SIMPLE, PISO and PIMPLE algorithm, pp. 111 – 134. 4 ed., 2016.

[364] B. Devolder, P. Schmitt, O. Rauwoens, B. Elsaesser, and P. Troch, "A review of the implicit motion solver algorithm in OpenFOAM to simulate a heaving buoy," in *Proceedings of the 18th Numerical Towing Tank Symposium, Marstrand, Sweden*, 2015.

[365] C. Windt, J. Davidson, P. Schmitt, and J. V. Ringwood, "Assessment of numerical wave makers," in *Proceedings of the 12th European Wave and Tidal Energy Conference, Cork, Ireland*, no. 707, 2017.

[366] N. G. Jacobsen, D. R. Fuhrman, and J. Fredsoe, "A wave generation toolbox for the open-source cfd ligrary: OpenFOAM," *International Journal for Numerical Methods in Fluids*, vol. 70, pp. 1073–1088, 2012.

[367] J. Davidson, M. Cathelain, L. Guillemet, T. Le Huec, and J. Ringwood, "Implementation of an OpenFOAM Numerical Wave Tank for Wave Energy Expermethod," in *Proceedings of the 11th European Wave and Tidal Energy Conference, Nantes, France*, no. 09B1-1, 2015.

[368] J. Palm, C. Eskilsson, G. M. Paredes, and L. Bergdahl, "CFD simulation of a moored floating wave energy converter," in *Proceedings of the 10th European Wave and Tidal Energy Conference, Aalborg, Denmark*, 2013.

[369] J. Davidson and J. V. Ringwood, "Mathematical modelling of mooring systems for wave energy converters: A review," *Energies*, vol. 10, no. 5, p. 666, 2017.

[370] A. C. Antoulas, D. C. Sorensen, and S. Gugercin, "A survey of model reduction methods for large-scale systems," *Contemporary mathematics*, vol. 280, pp. 193–220, 2001.

[371] B. Moore, "Principal component analysis in linear systems: Controllability, observability, and model reduction," *IEEE Trasactions on Automatic Control*, vol. 26, pp. 17–32, February 1981.

[372] K. Glover, "All optimal hankel-norm approximations of linear multivariable systems and their L_∞ error bounds," *International Journal in Control*, vol. 39, no. 6, pp. 1115–1193, 1984.

[373] K. Willcox and J. Peraire, "Balanced model reduction via the proper orthogonal decomposition," *AIAA Journal*, vol. 40, no. 11, pp. 2323–2330, 2002.

[374] J. R. Singler and B. A. Batten, "A proper orthogonal decomposition approach to approximate balanced truncation of infinite dimensional linear systems," *International Journal of Computer Mathematics*, vol. 86, no. 2, pp. 355–371, 2009.

[375] A. Astolfi, "Model reduction by moment matching for linear and nonlinear systems," *IEEE Transactions on Automatic Control*, vol. 55, no. 10, pp. 2321–2336, 2010.

[376] A. C. Antoulas, *Approximation of Large-Scale Dynamical Systems*. Philadelphia, PA, USA: Society for Industrial and Applied Mathematics, 2005.

[377] E. S. J. Hesam, "An approach to reduce order modeling and feedback control for wave energy converters," Master's thesis, Oregon State University, Oregon, USA, 2014. Available at https://ir.library.oregonstate.edu/downloads/br86b600g [Last accessed 22 June 2018].

[378] D. Cheng, X. Hu, and T. Shen, "Linearization of nonlinear systems," in *Analysis and Design of Nonlinear Control Systems*, pp. 279–313, Springer, 2010.

[379] G. Bacelli, R. Genest, and J. V. Ringwood, "Nonlinear control of flap-type wave energy converter with a non-ideal power take-off system," *IFAC Annual Reviews in Control*, vol. 40, pp. 116–126, 2015.

[380] G. C. Carter, "Coherence and time delay estimation," *Proceedings of the IEEE*, vol. 75, no. 2, pp. 236–255, 1987.

[381] R. Haber, "Nonlinearity tests for dynamic processes," *IFAC Syposium on Identification and System Parameter Estimation*, vol. 18, no. 5, pp. 409–413, 1985.

[382] A. A. S. Choudhury, S. L. Shah, and N. F. Thornhill, *Diagnosis of process nonlinearities and valve stiction: data driven approaches*. Springer Science & Business Media, 2008.

[383] H. E. Emara-Shabaik, J. Bomberger, and D. E. Seborg, "Cumulant/bispectrum model structure identification applied to a pH neutralization process," in *Proceedings of the UKACC International Conference on Control, Exeter, UK*, pp. 1046–1051, IET, 1996.

[384] M. S. Choudhury, S. L. Shah, and N. F. Thornhill, "Diagnosis of poor control-loop performance using higher-order statistics," *Automatica*, vol. 40, no. 10, pp. 1719–1728, 2004.

[385] J. Theiler, S. Eubank, A. Longtin, B. Galdrikian, and J. D. Farmer, "Testing for nonlinearity in time series: the method of surrogate data," *Physica D: Nonlinear Phenomena*, vol. 58, no. 1-4, pp. 77–94, 1992.

[386] M. Ruel and J. Gerry, "Quebec quandary solved by Fourier transform," *Intech*, vol. 8, pp. 53–55, 1998.

[387] M. Guay, P. McLellan, and D. Bacon, "Measurement of nonlinearity in chemical process control systems: The steady state map," *The Canadian Journal of Chemical Engineering*, vol. 73, no. 6, pp. 868–882, 1995.

[388] M. Guay and P. McLellan, "Measurement of dynamic process nonlinearity," *IFAC Proceedings Volumes*, vol. 30, no. 9, pp. 589–594, 1997.

[389] C. Desoer and Y.-T. Wang, "Foundations of feedback theory for nonlinear dynamical systems," *IEEE Transactions on Circuits and Systems*, vol. 27, pp. 104–123, Feb 1980.

[390] M. Nikolaou, "When is nonlinear dynamic modeling necessary?," in *Proceedings of the American Control Conference, San Francisco, California, USA*, pp. 910–914, IEEE, 1993.

[391] M. Nikolaou and V. Hanagandi, "The 2-norm for nonlinear processes: application to modeling and control problems," *Proceedings of the 5th International Symposium on Process Systems Engineering, Kyongju, Korea*, pp. 971–976, 1994.

[392] F. Allgöwer, "Definition and computation of a nonlinearity measure," *IFAC Proceedings Volumes*, vol. 28, no. 14, pp. 257–262, 1995.

[393] A. Helbig, W. Marquardt, and F. Allgöwer, "Nonlinearity measures: definition, computation and applications," *Journal of Process Control*, vol. 10, no. 2, pp. 113–123, 2000.

[394] G. Bacelli and J. V. Ringwood, "Numerical optimal control of wave energy converters," *IEEE Transactions on Sustainable Energy*, vol. 6, no. 2, pp. 294–302, 2015.

[395] N. Faedo, Y. Pena-Sanchez, and J. Ringwood, "Finite-order hydrodynamic model determination for wave energy applications using moment-matching," *Submitted to Ocean Engineering*.

[396] M. Penalba, T. Kelly, and J. V. Ringwood, "Using NEMOH for modelling wave energy converters : A comparative study with WAMIT," in *Proceedings of the 12th European Wave and Tidal Energy Conference, Cork, Ireland*, no. 631, 2017.

[397] Y. Liu and J. M. Falzarano, "Irregular frequency removal methods: theory and applications in hydrodynamics," *Marine Systems & Ocean Technology*, vol. 12, no. 2, pp. 49–64, 2017.

[398] C.-H. Lee, J. Newman, and X. Zhu, "An extended boundary integral equation method for the removal of irregular frequency effects," *International Journal for Numerical Methods in Fluids*, vol. 23, no. 7, pp. 637–660, 1996.

[399] D. Evans, "The oscillating water column wave-energy device," *IMA Journal of Applied Mathematics*, vol. 22, no. 4, pp. 423–433, 1978.

[400] W. Sheng, R. Alcorn, and A. Lewis, "Hydrodynamics of oscillating water column wave energy converters," *Proceedings of the 1st International Conference on Renewable Energies Offshore, Lisbon, Portugal*, pp. 489–496, 2014.